JUNE 2009 VOLUME 11 NO.6
www.nature.com/naturecellbiology

nature cell biology

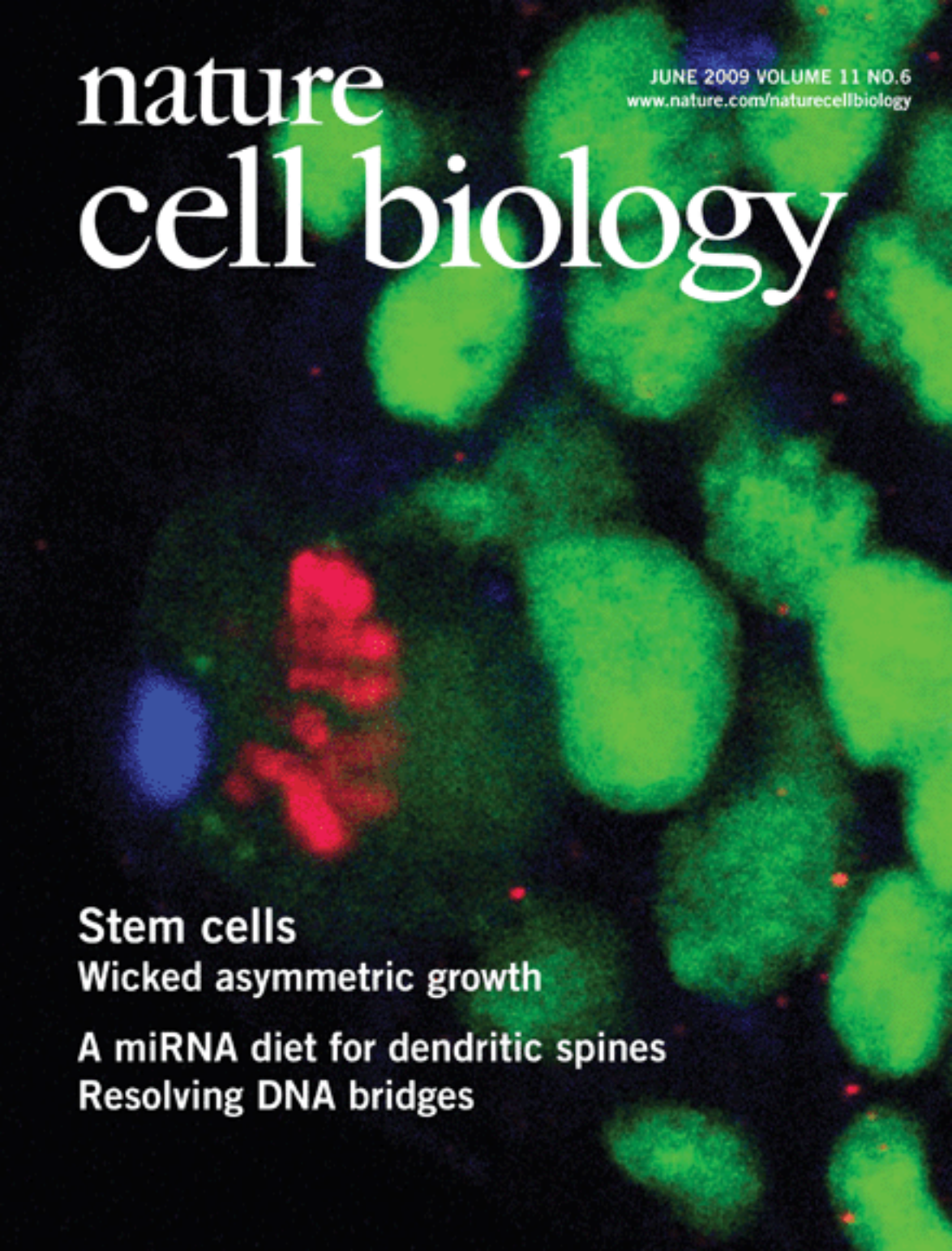

Stem cells
Wicked asymmetric growth

A miRNA diet for dendritic spines

Resolving DNA bridges

nature cell biology

EDITORIAL OFFICES

LONDON: cellbio@nature.com
The Macmillan Building, 4 Crinan Street, London N1 9XW
Telephone: +44 207 843 4924; Fax: +44 207 843 4794
EDITOR: Bernd Pulverer
SENIOR EDITORS: Alison Schuldt, Sowmya Swaminathan & Nathalie Le Bot
ASSOCIATE EDITORS: Silvia Grisendi & Christina Karlsson Rosenthal
PRODUCTION EDITOR: Karl Smart
ART EDITOR: Denis Mallet
COPY EDITOR: Tamra Poorun
EDITORIAL ASSISTANT: Alice Fuller

MANAGEMENT OFFICES

NPG LONDON: nature@nature.com
The Macmillan Building, 4 Crinan Street, London N1 9XW
Telephone: +44 207 833 4000; Fax: +44 207 843 4596/7
MANAGING DIRECTOR: Steven Inchcoombe, PUBLISHING DIRECTOR: Alison Mitchell
ASSOCIATE DIRECTORS: Jenny Henderson, Tony Rudland
EDITOR-IN-CHIEF, NATURE PUBLICATIONS: Philip Campbell
EDITORIAL PRODUCTION DIRECTOR: James McQuat
MANAGING PRODUCTION EDITOR: Donald McDonald
PRODUCTION DIRECTOR: Yvonne Strong
PRODUCTION CONTROLLER: Kelly Hopkins
SENIOR MARKETING MANAGER: Tim Redding

NPG NEW YORK: nature@natureny.com
75 Varick St F1 9, New York, NY 10013-1917
Telephone: +212 726 9200; Fax: +212 696 9006
EXECUTIVE EDITOR: Linda Miller
CHIEF TECHNOLOGY OFFICER: Howard Ratner

NPG TOKYO: nature@natureasia.com
Nature Japan K.K., Chiyoda Building 2–37 Ichigayatamachi, Shinjuku-Ku, Tokyo, 162-0843, Japan
Telephone: +81 3 3267 8751; Fax: +81 3 3267 8746
ASIA-PACIFIC PUBLISHER: Antoine E. Bocquet, MANAGER: Koichi Nakamura
ASIA-PACIFIC SALES DIRECTOR: Kate Yoneyama
ASIA-PACIFIC SALES: Ken Mikami
MARKETING/PRODUCTION MANAGER: Takeshi Murakami

DISPLAY ADVERTISING

display@natureny.com (US/Canada)
display@nature.com (Europe)
nature@natureasia.com (Asia)

GLOBAL HEAD OF DISPLAY ADVERTISING:
Andrew Douglas, Tel: 44 207 843 4960, Fax: 44 207 843 4996
ASIA-PACIFIC SALES MANAGER:
Ken Mikami, Tel: 81 3 3267 8765, Fax: 81 3 3267 8746

DISPLAY ACCOUNT MANAGERS:
WESTERN REGIONAL SALES MANAGER, WEST COAST SOUTH/WEST COAST CANADA:
George Lui, Tel: (415) 781 3804, Fax: (415) 781 3805
WEST COAST NORTH: Bruce Shaver, Tel: (415) 781 6422, Fax: (415) 781 3805
NEW ENGLAND/EAST COAST CANADA:
Sheila Reardon, Tel: (617) 399 4098, Fax: (617) 426 3717
NEW YORK, MID-ATLANTIC, SOUTHEAST:
Jim Breault, Tel: (212) 726 9334, Fax: (212) 696 9481
MIDWEST: Mike Rossi, Tel: (212) 726 9255, Fax: (212) 696 9481
GERMANY/SWITZERLAND/AUSTRIA:
Sabine Hugi-Fürst, Tel: 41 52761 3386, Fax: 41 52761 3419
UNITED KINGDOM/IRELAND/FRANCE/BELGIUM/EASTERN EUROPE:
Jeremy Betts, Tel: 44 207 843 4968, Fax: 44 207 843 4749
SCANDINAVIA/DENMARK/THE NETHERLANDS/ITALY/SPAIN/PORTUGAL/ISRAEL/ICELAND:
Graham Combe, Tel: 44 207 843 4914, Fax: 44 207 843 4749
GREATER CHINA/SINGAPORE: Gloria To, Tel: (852) 2811 7191, Fax: (852) 2811 0743

WORLD WIDE WEB

www.nature.com/naturecellbiology
WEB PRODUCTION MANAGER: Alex Thurrell
WEB PRODUCTION EDITOR: Deborah Anthony
WEB SERVICES: Anthony Barrera

NATUREJOBS

Please refer to panel at the start of the naturejobs section at the back of the issue.

VOLUME 11 NUMBER 6 JUNE 2009

nature cell biology

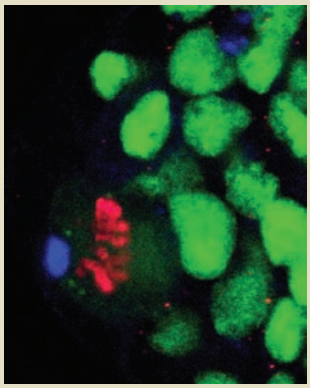

The U3 snoRNP component Wicked, which is required for pre-ribosomal RNA maturation (green), is localized asymmetrically in dividing *Drosophila* germline cells (DNA in red) and is critical for stem cell self-renewal.

[article p685]

EDITORIAL

BOOK REVIEW

REVIEWS

NEWS AND VIEWS

Nature Cell Biology® (ISSN 1465-7392) is published monthly by Nature Publishing Group (Porters South, 4 Crinan Street, London N1 9XW, UK). Editorial Office: Porters South, 4 Crinan Street, London N1 9XW, UK. Telephone: +44 (0)20 7843 4924. Fax: +44 (0)20 7843 4794. Email: cellbio@nature.com. North American Advertising: Nature Cell Biology, 75 Varick Street F19, New York NY 10013-1917, US. Telephone: +1(212) 726-9200. Fax: +1(212) 696-9006. European Advertising: Nature Cell Biology, Porters South, Crinan Street, London N1 9XW, UK. Telephone: +44 (0)20 7833 4000. Fax: +44 (0)20 7843 4596. New subscriptions/renewals/changes of address/back issues and all other customer service questions should be addressed to – North America: Nature Cell Biology, Subscription Dept, P.O. Box 5055, Brentwood, TN 37024-5055, USA. Outside North America: Subscriptions Department, Brunel Road, Basingstoke, Hants. RG21 6XS, UK. Annual subscription rates: Americas: US$225 (personal), US$3,060 (institutional); Europe: €287 (personal), €2,430 (institutional); UK: £185 (personal), £1,570 (institutional); Japan: ¥40,000 (personal), ¥345,000 (institutional). Back issues: US/Canada. $45 (Canada add 7% GST); Rest of World: surface US$43, air mail US$45. Application for periodical postage rate submitted and paid by New York, NY 10010 and additional mailing offices. Reprints: Nature Cell Biology Reprints Department, Porters South, Crinan Street, London N1 9XW, UK. Subscription information is available at the Nature Cell Biology homepage at http://www.nature.com/naturecellbiology POSTMASTER: Send address changes to Nature Cell Biology Subscriptions Department, Brunel Road, Basingstoke, Hants. RG21 6XS, UK or Nature Cell Biology Subscriptions Department PO Box 5054, Brentwood, TN 37024-5054, USA.

nature publishing group

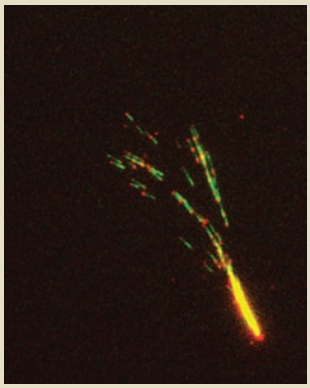

The fission yeast Kinesin-14 family member Klp2 mediates anti-parallel microtubule sliding and parallel microtubule cross-linking.

[letter p724]

ARTICLES

LETTERS

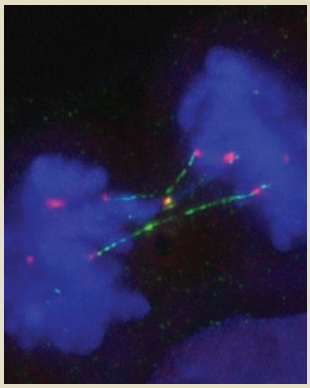

Replication perturbation induces formation of paired FANCD2 foci at sister genetic loci. Pairs of FANCD2 foci (red) are linked by a PICH-coated (green) ultra-fine DNA bridge in anaphase cells.

[letter p753]

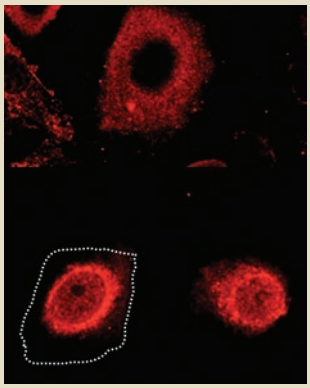

CLIC4 and Schnurri-2 enhance TGFβ signalling by protecting phospho-Smad2 and 3 from dephosphorylation.

[letter p777]

EDITORIAL

nature cell biology

How robust is your data?

New rules for the presentation of statistics.

Thanks to advanced imaging technologies and better integration with molecular and systems approaches, cell biology is undergoing something of a renaissance as a quantitative science. Robust conclusions from quantitative data require a measure of their variability. Cell biology experiments are often intricate and measure complex processes. Consequently the number of independent repeats of a measurement can be limited for practical reasons, yet the variability of the measurements can be rather high. Cell biologists have developed good intuition to guide their analysis of such constrained datasets. Biological complexity and the reliance on intuition can cause culture shock to physical scientists crossing over into cell biology (a kind of extension of the celebrated 'two cultures' concept of C. P. Snow).

With the arrival of quantitative information and '-omic' datasets, statistical analysis becomes a necessity to complement instinct. The problem is that statistical tools are built on basic assumptions such as the independence of replicate measurements and the normality of data distribution. Usually, sizeable datasets are prerequisite for statistical analysis. Alas, these can be as hard come by as a biostatistician (n is typically well below 5). The result is that all too often statistics (frequently undefined 'error bars') are applied to data where they are simply not warranted.

There are no easy solutions to rectify the prevalence of poor statistics in cell biology studies. However, an obvious recommendation is to consult a statistician when planning quantitative experiments. Consider whether n represents independent experiments (you may actually be publishing a measure of the quality of your pipette!) and whether it is large enough for the test applied. Avoid showing statistics when they are not justified; instead, show 'typical' data or, better still, all the measurements. Importantly, displaying unwarranted statistics attributes a misleading level of significance to the data. Always describe and justify any statistical analysis applied. We have updated our guidelines to reflect these recommendations (www.nature.com/ncb/pdf/gta.pdf). One key rule: if the number of independent repeats is less than the fingers of one hand, show the actual measurements rather than error bars. If you wish to present error bars, include the actual measurements alongside them.

Finally, please remember that you are interrogating a complex system — be careful not to discard 'outlier' data points on a whim, as they may well be as relevant as clustered measurements. One is naturally inclined to ignore data that does not match the hypothesis tested, but biology is rarely as black and white as we would like. Do not make 'hypothesis driven' research become 'hypothesis forced'!

Attribution and accountability

Author contribution statements are now mandatory and author responsibilities have been clarified.

Nature Cell Biology has encouraged author declarations for a decade and now almost 90% of papers carry them. The declaration is important as it adds transparency and accountability, as well as assigning credit. In an effort to standardize the information, we have now made it mandatory. While authors can structure them as they see fit, we require that every author is listed.

Although the corresponding author(s) of a paper is implicitly responsible for the accuracy and integrity of the data presented, we have refined our guidelines on author responsibility: in a collaboration, a senior researcher must take responsibility for the contribution of each group. This includes verifying that the data and conclusions accurately reflect the source data, that data analysis and image manipulations have been made in accordance with our guidelines (www.nature.com/ncb/authors/index.html), that the original data have been archived and that materials, data and algorithms have been deposited in the appropriate databases and will be distributed to interested parties. Corresponding authors are responsible for ensuring that all co-authors agree with the content and author list of a manuscript and for informing them of issues that arise before and after publication; they must certify that their manuscript fulfils the policies outlined at www.nature.com/authors/editorial_policies/authorship.html as part of the online submission process.

Reproducible methods

***Nature Cell Biology* will publish online methods in more detail.**

A central tenet of academic research is that the data are exposed to public scrutiny. Data that survive debate and experimental validation form the basis of new research, which nurtures the tree of knowledge (the shedding of the odd branch in a storm of controversy is a healthy part of the process). The dissemination of new research is commonly facilitated by publication in peer reviewed journals, ensuring that data pass a set of standards set by the research community and applied by referees and editors.

An essential part of the process is that scientific papers are sufficiently detailed to allow for assessment of the data and for independent reproduction of experiments (we have commented previously on the decline of reproduction of data; Editorial *Nature Cell Biol.* 8, 541; June 2006). In an effort to improve the information provided by the papers we publish, we have previously called for a ban on 'data not shown' (Editorial *Nature Cell Biol.* 8, 541; June 2006) and it is our policy to display uncropped data (Editorial *Nature Cell Biol.* 8, 203; March 2006), as well as the sequences of nucleotide probes and antigens (Editorial *Nature Cell Biol.* 9, 481; May 2007). We have also set clear policies for the sharing of research materials (Editorial *Nature Cell Biol.* 8, 425; May 2006).

However, a criticism rightly levied at journals with an intentionally terse format is that excessively tight word limits are not compatible with methods sufficiently detailed for reproducibility. Most read papers online, and this format allows for the cost-effective display of limitless information. As a result, we have joined the other *Nature* titles to present our 'Methods' sections online only. Although we have relaxed our format guidelines for this section, we suggest that methods are limited to around 1,600 words.

Notably, the 'Methods' section will remain integral to the main online paper and it will be copy edited. Although references in the 'Methods' will only be included in the online edition of the manuscript, they will be taken into account for impact factor calculations.

All the policies discussed above are listed in our online 'Guide to authors' (http://www.nature.com/ncb/authors/index.html)

New fashion models

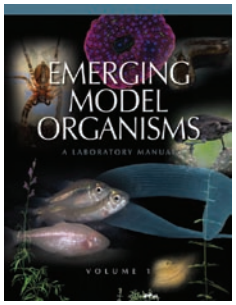

Emerging Model Organisms:
A Laboratory Manual, volume 1

Cold Spring Harbor Press 2009, 592pp
Price: $89/ £55
http://cshprotocols.cshlp.org/emo/

Reviewed by Christian Braendle and Marie-Anne Félix

Barnacles, pigeons and slave-making ants served as model organisms to shape the mind of the man who laid the foundations for modern evolutionary biology. Many other 19th century biologists were also highly promiscuous in their use of study organisms. The pioneering cellular studies of E. B. Wilson, for example, involved an impressive juggle between polychaete worms, amphioxus, grasshoppers, snails and sea urchins. However, during the last 100 years there has been a dramatic bottleneck, restricting much of laboratory research to a handful of model organisms that have come to dominate cellular, molecular and developmental biology. Whereas some serendipity accompanied the choice and success of these models, their numerous advantages are obvious: ease of culturing, feasible genetics, relatively short generation times and — after decades of intensive research efforts — extremely effective resources and techniques at hand.

Although nobody will dispute the power of such models, their study is insufficient to understand all of biology. First, organismal diversity itself cannot be captured by studying a minuscule fraction of it. Second, extrapolating biological information from one organism to another may simply be wrong. Luckily, yet driven solely by professional necessity, naturalists, taxonomists and ecologists have always been studying numerous non-model organisms. Now, many of their favourite organisms are finally ready to be dissected using molecular and genetic tools. The recent interest in establishing new laboratory organisms stems in part from the surge in studies on changes in organism development during evolution (evo-devo) as well as the availability of universally applicable techniques, such as DNA sequencing. Nevertheless, even with a whole genome sequence at hand, an organism of choice may be still very far from being a tractable model system.

The first volume of the laboratory manual *Emerging Model Organisms* symbolizes the ongoing rediscovery of many neglected study organisms. The book covers 23 eukaryotic organisms in various stages and forms of laboratory domestication, ranging from choanoflagellates and mosses to wandering spiders and fruit bats. Many of these species turn out to be re-invading laboratories rather than merely emerging for the first time. Chapters on each organism detail biological background information and established experimental protocols and are written by aficionados. Surprisingly, the book omits the presentation of the over-arching evolutionary context and relationships between organisms, ultimately reading like a collection of short stories, allowing us a glimpse at the wonders of an 18th century cabinet of curiosities. The presentation of organisms differs among chapters, with some being quite short on biological content or too technical on anatomy. Most chapters are, however, nicely balanced to educate and intrigue the curious neophyte, outlining singular properties and experimental advantages of the organism. Two sources of amazement spring from the book: how much of biological diversity we ignore and how many unique techniques were developed to allow the manipulation of an organism of choice.

Not parting with the tradition of practical laboratory manuals, the available experimental techniques and protocols are described in detail for each organism. We envy the laboratory that could fully exploit the protocols provided within this volume. Imagine starting your day with a snorkle to collect some fresh *Amphimedon* samples (sponge), following by beef liver paste preparation for your hungry planarians and rounding up the day by doing an *in situ* hybridization of your latest collection of *Monodelphis* embryos (opossum). In brief, the book represents the diversity of a Woods Hole Embryology Course brought to you in Cold Spring Harbor Laboratory manual style. Although fun to browse through, the protocol section of each chapter could have been exclusively presented in the accompanying website, www.cshprotocols.org/emo, to leave more space for biological background in the printed volume. Nevertheless, the protocols may provide a rich resource for biologists aiming to develop new techniques and, in any case, may be an inspirational source for embracing emerging model organisms.

Overall, the book is attractive to anyone interested in biological research, and in particular to those looking for a new muse or seeking to convert to a new organism. What is in this book for cell biologists? Certainly a important reminder that cells exist in many different shapes and forms, including some that evade the specific paradigm of idiosyncratic yeasts and a couple of fast-growing animals or plants. The emergence of new model organisms will thus create novel perspectives on key questions as well as open new avenues in addressing specific problems, such as the mechanisms and evolution of cell-type diversity. Importantly, addressing evolutionary problems in cell biology, as in developmental biology, will need to go beyond studying apparent conservation or differences among phylogenetically distant species, and rather needs to characterize intra-species variation and variation among closely related species. Studying this biological diversity is essential to understand how mechanisms function in different contexts and how the same mechanism can generate diversity.

The first volume of *Emergent Model Organisms* illustrates the bewildering variety of natural histories and rapidly advancing techniques that have been developed to work with a wide spectrum of organisms. If Darwin were around now, he would have been the first to happily make use of this manual — and would be impatiently awaiting the forthcoming tome, describing the emergence of honeybees, squids, ascidians, rabbits, ants… and many more.

Christian Braendle is at the Institute of Developmental Biology and Cancer, CNRS - Université de Nice Sophia Antipolis, Parc Valrose, 06108 Nice cedex 2, France. Marie-Anne Félix is at the Institut Jacques Monod, CNRS - Université de Paris 7, 15 rue Hélène Brion, 75205 Paris cedex 13, France.
e-mails: felix@ijm.jussieu.fr; braendle@unice.fr

STIMulating store-operated Ca^{2+} entry

Michael D. Cahalan

Calcium influx through plasma membrane store-operated Ca^{2+} (SOC) channels is triggered when the endoplasmic reticulum (ER) Ca^{2+} store is depleted — a homeostatic Ca^{2+} signalling mechanism that remained enigmatic for more than two decades. RNA-interference (RNAi) screening and molecular and cellular physiological analysis recently identified STIM1 as the mechanistic 'missing link' between the ER and the plasma membrane. STIM proteins sense the depletion of Ca^{2+} from the ER, oligomerize, translocate to junctions adjacent to the plasma membrane, organize Orai or TRPC (transient receptor potential cation) channels into clusters and open these channels to bring about SOC entry.

Cells are preoccupied by the control of cytosolic calcium concentration, and with good reason. Calcium ions shuttle into and out of the cytosol — transported across membranes by channels, exchangers and pumps that regulate flux across the ER, mitochondrial and plasma membranes. Calcium regulates both rapid events such as cytoskeleton remodelling or release of vesicle contents, and slower ones such as transcriptional changes. Moreover, sustained cytosolic calcium elevations can lead to unwanted cellular activation or apoptosis.

Among the long-standing mysteries in the Ca^{2+} signalling field is the nature of feedback mechanisms between the ER and the plasma membrane. Studies in the late 1980s and 1990s established that the depletion *per se* of ER Ca^{2+}, but not the resulting rise of cytosolic Ca^{2+}, is the initiating signal that, following $InsP_3$-induced release of ER Ca^{2+}, triggers SOC entry (SOCE) through Ca^{2+} channels in the plasma membrane[1]. The best-characterized SOC current was, and still is, the Ca^{2+} release-activated Ca^{2+} (CRAC) current in lymphocytes and mast cells[2–4]. However, the molecular mechanism remained undefined until recently. The key breakthroughs came from RNAi screening, which first identified STIM proteins as the molecular link from ER Ca^{2+} store depletion to SOCE and CRAC channel activation in the plasma membrane, and then identified Orai (CRACM) proteins that comprise the CRAC channel pore-forming subunit. STIM proteins will be referred to generically as STIM, the *Drosophila melanogaster* protein as Stim and the two mammalian homologues as STIM1 and STIM2.

Origins of STIM

STIM proteins first came to light outside the Ca^{2+} signalling field. STIM1 was originally identified in a library screen by its ability to confer binding of pre-B lymphocytes to stromal cells. Originally named SIM (stromal interacting molecule)[5], the name later morphed into STIM — fortuitously suggestive of its function in stimulating calcium influx across the plasma membrane. *Drosophila* and *Caenorhabditis elegans* have one STIM protein, but representative amphibians, birds and mammals have two STIM homologues (and teleost fish have four)[6,7], suggesting gene duplication at the invertebrate-vertebrate transition. In addition, STIM1 (formerly known as GOK)[8] was implicated in cell transformation and growth by its chromosomal localization (human 11p15.5) to a region associated with paediatric malignancies, and by its ability to induce cell death when transfected into rhabdomyosarcoma and rhabdoid tumour cells[9]. It was originally characterized biochemically as a glycosylated phosphoprotein with ~25% expression in the plasma membrane by surface biotinylation[6,10,11]. The human *STIM2* gene, sharing 61% sequence identity with *STIM1*, localizes in a region (4p15.1) implicated in squamous carcinoma and breast tumours[6]. The sole *Drosophila* homologue, Stim, has 31% identity and 60% sequence similarity to STIM1. STIM proteins from *Drosophila* and mammals are shown diagrammatically in Fig. 1.

Inspection of the primary polypeptide sequence of STIM proteins reveals a modular construction. Two protein–protein interaction domains are separated by a single membrane-spanning segment and, as a type I membrane protein, the amino terminus is predicted to reside either within the ER lumen or facing the extracellular space. Between the N-terminal signal peptide sequence and the sterile alpha motif (SAM) protein interaction domain, two adjacent regions containing negative charges, one typical of an EF-hand Ca^{2+}-binding domain, are found. At the other end, in the cytoplasm, a lengthy bipartite coiled-coil is predicted within a region containing an ezrin/radixin/moesin (ERM) domain leading to the C terminus. This end of the molecule diverges substantially, the *Drosophila* (and *C. elegans*) protein notably lacking a proline-rich region and a lysine-rich tail.

RNAi screens identify STIM and Orai

The key breakthroughs in identifying the molecular constituents of SOC signalling arose from RNAi screening. A critical role of STIM in SOCE was first revealed by two concurrent and independent candidate RNAi screens[12,13], using thapsigargin to deplete the ER Ca^{2+} store. Thapsigargin blocks the ER-resident SERCA (sarcoplasmic/endoplasmic reticulum calcium) pump, causing a decline in luminal Ca^{2+} store content as Ca^{2+}

Michael D. Cahalan is in the department of Physiology and Biophysics and Institute for Immunology, University of California, Irvine, CA 92697–4561, USA.
e-mail: mcahalan@uci.edu

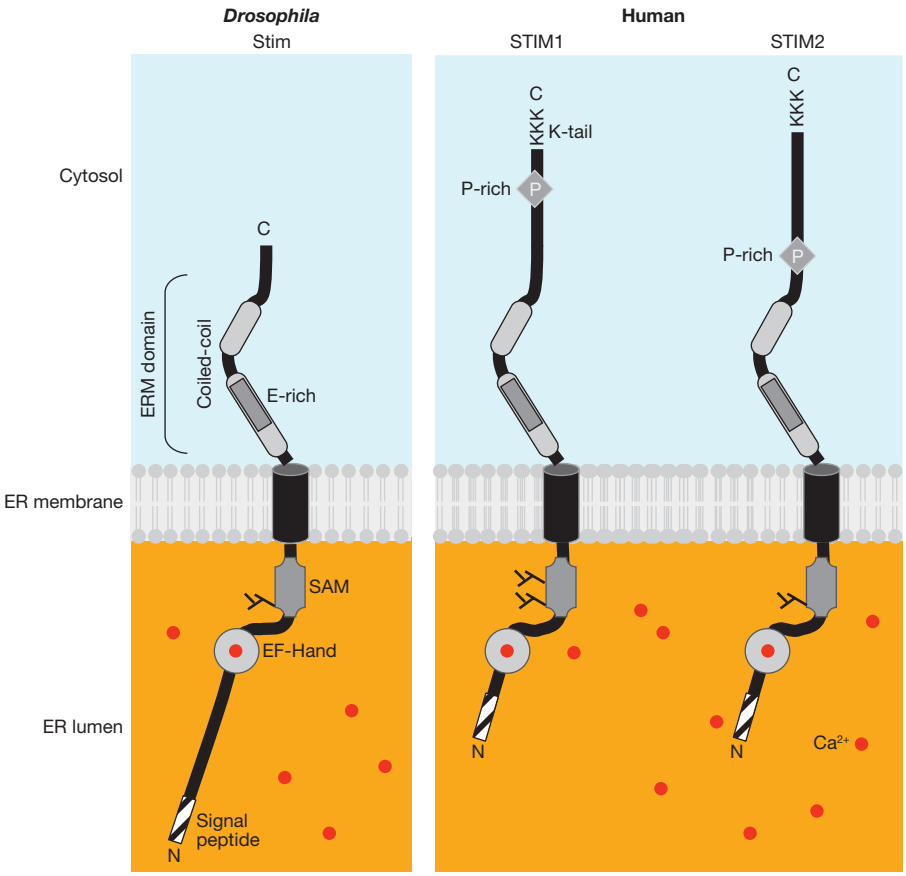

Figure 1 Domains of STIM proteins. *Drosophila* and human STIM proteins are situated in the ER membrane. Modules of STIM1, STIM2 and Stim include: the signal peptide, the predicted EF-hand and SAM domains, the transmembrane region and two regions predicted to form coiled-coil structures comprising the ERM domain. Proline-rich domains (P) and the lysine-rich C-terminal regions are unique to the mammalian STIM family members. *Drosophila* Stim contains an N-terminal sequence in the ER that is not present in either STIM1 or STIM2. The *N*-linked glycosylation sites at the SAM domain, experimentally verified for STIM1 (refs 11, 85), are also indicated. Background colours represent basal Ca^{2+} concentrations of ~50 nM in the cytosol and > 400 μM in the ER lumen. Ca^{2+} ions are shown as red dots, including Ca^{2+} bound to the EF-hand domain.

leaks out of the ER passively, unopposed by active re-uptake through the pump. *Drosophila* S2 cells used in one screen[13] have functional CRAC currents closely similar in activation requirements and biophysical characteristics to those in human T lymphocytes[14]. Hits were defined by decreased SOCE and confirmed in single cells by Ca^{2+} imaging and whole-cell recording. The S2 cell screen yielded one hit (Stim)[13], and the human HeLa cell screen identified both mammalian homologues, STIM1 and STIM2 (ref. 12). It soon became clear that several mammalian cell types rely primarily on STIM1 for SOCE and CRAC channel activation[12,13,15]; an additional screen showed that STIM2 functions in regulating basal Ca^{2+} levels[16].

STIM triggers SOCE but does not form the CRAC channel itself. Following the success of the candidate screening approach, the search for the CRAC channel continued as genome-wide RNAi screening in S2 cells was performed independently by three research groups[17–19]. This led to the identification of several additional genes required for Ca^{2+} signalling, including the previously unheralded *Orai* (also known as *CRACM,* formerly known as *olf186-F*), a *Drosophila* gene with three mammalian homologues. A parallel genetic screen by one of the three groups led to the remarkable discovery that a point mutation (corresponding to R91W) in human *Orai1* on chromosome 12 causes a rare but lethal disorder SCID (severe combined immunodeficiency disorder) — the first identified channelopathy of the immune system[17]. Orai proteins have four predicted transmembrane segments, but apart from being a multi-span transmembrane protein Orai has no other similarity to known ion channels. Evidence that Orai forms the CRAC channel itself came from two further discoveries. First, the unique biophysical fingerprint of the CRAC channel in patch clamp studies is duplicated, but with currents that are amplified 10 to 100-fold, when STIM and Orai are overexpressed together in heterologous cells[19–22]. Second, Orai and Orai1 were confirmed as CRAC channel pore-forming subunits by the marked alteration of ion selectivity that results from point mutation of a key glutamate residue in the loop between transmembrane segments 1 and 2 (refs 23–25).

Sensing luminal ER Ca^{2+}

The essential function of STIM as a non-channel intermediary of SOCE and CRAC channel activation has been explored by mutagenesis and subcellular localization. The presence of an EF-hand motif near the N terminus, localized in the ER lumen, suggested a role in sensing ER Ca^{2+}. It was soon discovered that expression of EF-hand mutants engineered to prevent Ca^{2+} binding resulted in constitutive Ca^{2+} influx and CRAC channel activation, but without depletion of the ER Ca^{2+} store[12,26]. This ability of the EF-hand mutants to bypass the

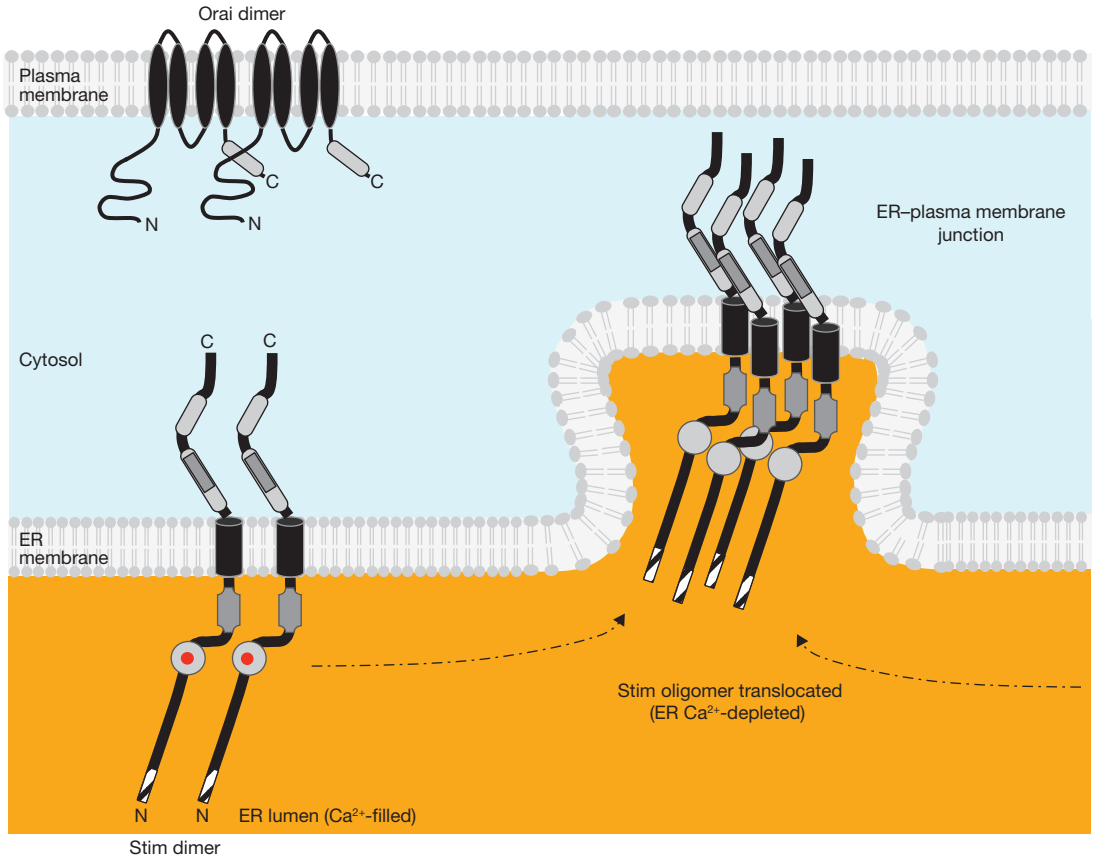

Figure 2 STIM Ca^{2+} sensor, signal initiation and messenger functions. STIM molecules are shown in the basal state as dimers (left); the Ca^{2+} sensor EF-hand domain has bound Ca^{2+} (red dots) when the ER Ca^{2+} store is filled. Background colours represent basal Ca^{2+} concentrations of ~50 nM in the cytosol and > 400 μM in the ER lumen. ER Ca^{2+} store depletion causes Ca^{2+} to unbind from the low affinity EF-hand of STIM; this is the molecular switch that leads to STIM oligomerization and translocation (dashed arrows) to ER–plasma membrane junctions. Non-conducting Orai channel subunits are shown as dimers.

requirement for Ca^{2+} store depletion convincingly demonstrated that the Ca^{2+}-unbound state of STIM leads to CRAC channel activation. The resting concentration of Ca^{2+} within the ER lumen is hundreds of micromolar — much higher than in the cytoplasm — and is maintained by ongoing activity of the SERCA pump. Ca^{2+} binding to the isolated EF-SAM portion of STIM1 was shown to have a dissociation constant in the range of hundreds of micromolar and a 1:1 binding stoichiometry[27]. Low-affinity binding of Ca^{2+} to the EF-hand domain is compatible with the proposal that Ca^{2+} is bound when the ER store is full and STIM releases Ca^{2+} when the ER is depleted, thus initiating a process that leads to CRAC channel activation.

Signal initiation by oligomerization

In the basal state when ER Ca^{2+} stores are filled, STIM is a dimer stabilized by C-terminal coiled-coil interactions, as shown by several lines of evidence. Intact STIM proteins heteromultimerize under basal conditions[6,28,29], and Stim forms dimers[30]. Moreover, the isolated C-terminal portion of STIM1 forms dimers[31], whereas the isolated N-terminal ER-SAM domain is monomeric at basal ER Ca^{2+} concentration. When the ER Ca^{2+} store is depleted, further STIM1 oligomerization occurs within seconds in intact cells[32,33], and this is mediated by the SAM domain adjacent to the EF-hand domain, as shown by the formation of multimers at reduced Ca^{2+} levels in biochemical and nuclear magnetic resonance structural studies of the isolated N-terminal portion of STIM1 (refs 34, 35). In intact cells, oligomerization precedes and triggers translocation of STIM to the plasma membrane and activation of CRAC channel activity[32,33,36].

Conveying the message to the plasma membrane

After Ca^{2+} store depletion, the EF-hand domain releases bound Ca^{2+} and oligomers of STIM physically translocate 'empty-handed', thereby conveying the message to the plasma membrane that the ER store has been depleted (Fig. 2). Native STIM1 and tagged constructs were first shown by light microscopy, and then by electron microscopy, to form clusters (also termed 'puncta' or 'hotspots', with surface areas in the order of 1–10 μm^2) immediately adjacent to the plasma membrane, following Ca^{2+} store depletion[12,20,26,28,37]. Whereas native untagged STIM1 colocalized with ER-resident proteins in the resting state when the Ca^{2+} store was filled, it was shown to translocate to the plasma membrane following store depletion[26]. Moreover, activating EF-hand mutant STIM1 proteins were localized predominantly at the plasma membrane even when the Ca^{2+} store remained full[12,26]. The marked redistribution of STIM1 after Ca^{2+} store depletion was not accompanied by any obvious changes in the bulk ER structure[12,26,37]. Instead, as seen from Förster resonance energy transfer (FRET) measurements, ER STIM1 oligomerizes and subsequently accumulates at specific predetermined foci in the peripheral ER[32,33,38,39], representing points of close ER–plasma membrane apposition[37]. Total internal reflectance fluorescence (TIRF) microscopy placed

Box 1 Surface expression, plasma membrane insertion and tags

Native STIM1 is localized primarily in the ER but is also detected by surface biotinylation, indicative of plasma membrane expression of a sizeable fraction (20–30%) of the total pool [10,26,82,83]. Moreover, it was reported to insert into the plasma membrane following store depletion by thapsigargin treatment[26,83]. Neither STIM2 nor EF-hand mutant STIM1 was detected under conditions that revealed plasma membrane expression through surface accessible biotinylated STIM1[15,82]. However, surface expression experiments using anti-tag antibodies, electron microscopy and the failure to observe acute quenching of pH-sensitive forms of GFP by acidic pH did not show covalently tagged STIM1 in the plasma membrane (when tagged with GFP, YFP, HRP or HA— haemagglutinin — at the N-terminus[12,20,32,37,50,84] or CFP — cyan fluorescent protein — at the C-terminus[84]). Thus, it appears that trafficking of STIM1 to the plasma membrane may be perturbed by protein tags. Consistently, a very small tag (hexahistidine) at the N terminus of STIM1 was shown to externalize following thapsigargin treatment, whereas co-expressed C-terminal CFP-tagged STIM1 remained within the ER[84]. Direct fusion events of STIM1-containing ER tubules to lipid raft domains of the plasma membrane have been reported using C-terminal-tagged YFP imaged by TIRF microscopy[45]. Membrane insertion will clearly need to be evaluated using other methods. Collectively, these results imply that STIM1 is in the plasma membrane and the ER, that tags (N-terminal YFP, GFP, HRP, HA and C-terminal CFP) can prevent surface localization and that the native protein may insert acutely following store depletion. It now seems clear that regardless of whether STIM1 is present in the plasma membrane or inserts acutely into it following store depletion, translocation to the plasma membrane without STIM1 insertion is sufficient to activate the CRAC channel, as STIM1 or Stim tagged with YFP or with other fluorescent proteins functions perfectly well in activating robust SOC influx and CRAC current[12,20,30,32,37,50]. Moreover, the presence of plasma membrane STIM1 is not required for ER-resident-tagged STIM1 to function in triggering SOCE[28]. Plasma membrane STIM1 may be involved with other functions such as cell adhesion, as originally suggested in the first report on 'SIM', where it was defined as a protein required for adhesion to stroma[5], and as suggested in very recent evidence favouring a role of plasma membrane STIM1 in SOC channel activation[82]. In addition, STIM1 in the plasma membrane may be essential for activation of arachidonate-regulated Ca^{2+} (ARC) channels[85] that include ORAI1 and ORAI3 as essential components[86].

yellow fluorescent protein (YFP)-tagged STIM1 clusters to within 100–200 nm of the cell surface[12,28,32,37] (Supplementary Information, Movie 1), and electron microscopy visualization of horseradish peroxidase (HRP)-tagged STIM1 demonstrated that it migrates to within 10–25 nm of the plasma membrane[37]. Tagging may prevent surface expression of STIM1 (Box 1), but tagged proteins are effective in evoking SOCE and CRAC currents indicating that acute insertion of STIM1 into the plasma membrane is not a required step. Clustering of STIM1 adjacent to the plasma membrane is rapid (occurring before CRAC channels open), spatially reproducible and rapidly reversible on signal termination and refilling of the ER Ca^{2+} store[32,38–40]. In addition to the refilling of the ER Ca^{2+} store, the disassembly of STIM1 clusters may also result from Ca^{2+} influx and the resulting rise in cytosolic Ca^{2+}, implying a local negative feedback mechanism that may contribute to CRAC channel inactivation[41].

Oligomerization of STIM is necessary and sufficient for its translocation to ER–plasma membrane junctions[36]. STIM1 clustering and translocation begins when ER luminal Ca^{2+} concentration falls below ~300 μM[16,36], consistent with low-affinity binding of Ca^{2+} to the EF-hand–SAM region of STIM1 (ref. 27). STIM1 clustering at the plasma membrane was found to be heavily dependent on ER Ca^{2+} concentration (a Hill coefficient of ~4, far steeper than the Ca^{2+} concentration dependence of binding to the EF-hand domain of STIM1), suggesting that STIM1 oligomers, but not monomers or dimers, accumulate near the plasma membrane. Moreover, CRAC channel activation closely matched the steep Ca^{2+} dependence of STIM1 aggregation and translocation to the peripheral ER, suggesting sequential processes triggered by aggregation[36]. Importantly, chemically induced oligomerization of STIM1 also resulted in translocation and activation of CRAC channels without ER Ca^{2+} store depletion[36]. These key experiments confirm that STIM oligomerization is sufficient to induce translocation to the plasma membrane and CRAC channel activation.

During even modest depletion of the ER Ca^{2+} store, STIM2 formed clusters at the plasma membrane, even as STIM1 remained localized in the bulk ER[16]. A distinct function of STIM2 in basal Ca^{2+} regulation, STIM2 having a lower 'effective affinity' for luminal ER Ca^{2+} than STIM1 (400 and 200 μM, respectively), is probably linked to differences in coupling between the EF-hand domain and the adjacent SAM domain[34].

So how does STIM migrate within the ER under basal conditions and then accumulate at the plasma membrane following store depletion? When the ER Ca^{2+} store is filled, STIM1 colocalizes with microtubules and appears to have a role in organizing and remodelling the ER, as the tubulovesicular distribution of STIM1 and the ER itself are disrupted when microtubules are depolymerized[28,42,43] and ER extension is stimulated by STIM1 overexpression[43]. STIM1 binds to the microtubule plus-end tracking protein EB1 (end binding protein 1) and associates with tubulin at the growing plus-end of microtubules[43]. TIRF microscopy imaging revealed rapid comet-like movement of ER STIM1 along fibrillar microtubule tracks near the cell surface[28,43–45] (Supplementary Information, Movie 1). As a plus-end microtubule-tracking protein, STIM1 can cover long distances within the cell. STIM1 proteins in tubular ER structures have been reported to associate with lipid raft regions of the plasma membrane, colocalizing with the ganglioside GM1 and caveolin[45,46]. A role for microtubules in SOCE and CRAC channel function remains controversial, some studies showing partial inhibition upon microtubule depolymerization[44,47] and others reporting no effect[28,48]. Microtubules interact with, and appear to guide, the intracellular trafficking of STIM1 as it migrates within the ER under basal conditions, but are neither required for cluster formation nor for functional activation of SOCE or CRAC channels when STIM1 is overexpressed[28,44].

Organizing the elementary unit of Ca^{2+} signalling

After ER Ca^{2+} store depletion, STIM clusters are found in the ER, close enough to the cell surface to allow for direct interaction with plasma membrane proteins. There are important precedents for ER–plasma membrane protein–protein signalling interactions, including excitation-contraction coupling in muscle. However, unlike STIM-mediated

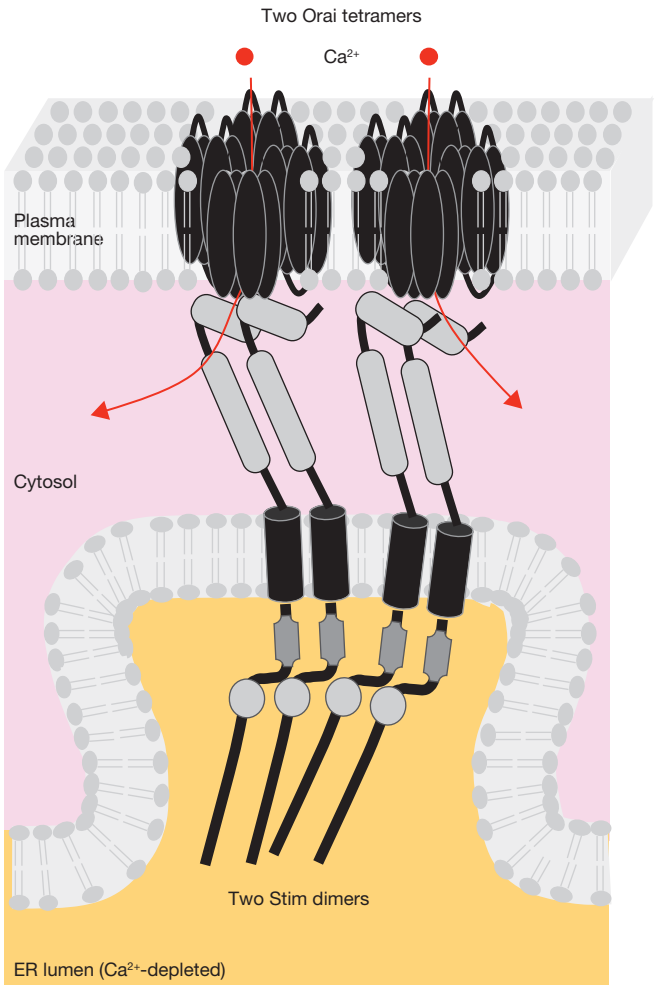

Figure 3 STIM-mediated organization of the elementary unit and activation of Orai channels. STIM accumulation induces Orai channels to cluster in the adjacent plasma membrane. The C-terminal effector domain of STIM induces Orai channels to open by direct binding of the distal coiled-coil domain, and Ca^{2+} enters the cell (red arrows). Two STIMs can activate a single CRAC channel consisting of an Orai tetramer; channel activation of Orai may involve a preliminary step of assembling Orai dimers into a functional tetramer. Background colours represent changes in cytosolic Ca^{2+} concentration (from that in the basal state as represented in Figs 2 and 3) to > 1 μM due to Ca^{2+} entry, and ER luminal Ca^{2+} to < 300 μM.

Ca^{2+} signalling, the primary signal in excitation-contraction coupling is from the plasma membrane to the sarcoplasmic reticulum, through a molecular coupling between plasmalemmal voltage-gated Ca^{2+} channels and ryanodine receptor Ca^{2+} release channels in the sarcoplasmic reticulum. In contrast, CRAC channel activation involves physical migration of ER-resident STIM to ER–plasma membrane junctions and subsequent aggregation of the Ca^{2+} influx channel. Not only does STIM serve as both Ca^{2+} sensor and messenger, it also organizes Orai subunits into adjacent plasma membrane clusters[30,49,50]. The clusters of messenger STIM and corresponding Orai channel proteins have been termed the 'elementary unit' of SOCE and CRAC channel activation, as Ca^{2+} influx through CRAC channels occurs precisely at STIM–Orai clusters[49]. Induced aggregation of Orai channels serves to concentrate local Ca^{2+} signalling at the particular regions of the cell where STIM and Orai cluster. Based on cluster size and number, estimates of the single-channel CRAC conductance, total number of channels per cell[19] and on direct fluorescence measurements[31], STIM and Orai clusters contain hundreds to thousands of molecules packed into a few square micrometres in the overexpression systems.

A particularly notable example of altered subcellular localization of STIM and Orai occurs at the region of contact — the 'immunological synapse' — between lymphocytes and antigen-presenting cells. When a T lymphocyte contacts an antigen-presenting cell, local signalling events lead rapidly to a cascade of tyrosine phosphorylation, $InsP_3$ generation and release of Ca^{2+} from the ER store. STIM1 and Orai1 colocalize to the immunological synapse, resulting in localized Ca^{2+} entry into the T cell region immediately next to the synapse[51]. STIM1–Orai1 clustering at the synapse was confirmed and also detected at the distal pole of the T cell in cap-like membrane aggregates[52]. Interestingly, following the initial phase of T cell activation, all three Orai isoforms and STIM1 are upregulated and Ca^{2+} signalling is enhanced, implying a positive feedback mechanism that sensitizes T cells to antigen during the first day of an immune response[51].

Orai channel activation by STIM

Stim activates Orai[19], and STIM1 couples functionally to all three Orai homologues in expression systems[20,53,54], forming very large CRAC-like currents with subtle differences in biophysical properties after store depletion. Evidence for a physical interaction between Stim and Orai was first obtained by co-immunoprecipitation studies demonstrating an increased interaction strength after Ca^{2+} store depletion[25]. A direct nanoscale molecular interaction was suggested by FRET measurements between donor and acceptor fluorescent protein tags at the C termini of STIM1 and Orai1 (refs 33, 42, 52, 55). Abundant evidence indicates that the cytosolic C terminus of STIM functions as the effector domain to open Orai and TRPC channels. Most importantly, the truncated C-terminal portion of either Stim or STIM1 ('C-STIM') is sufficient, when expressed as a cytosolic protein, to constitutively activate native CRAC current, as well as expressed Orai, Orai1 and TRPC1 channels[30,31,33,56–58], bypassing the requirement for Ca^{2+} store depletion. Cytosolic C-STIM was found by colocalization, co-immunoprecipitation and FRET analysis to interact with Orai independent of ER Ca^{2+} store depletion, but without forming clusters typical of full-length STIM after store depletion[30,31,33]. Together, these studies identify the C terminus as the effector of STIM and show that CRAC channel activation does not necessarily require cluster formation. Further deletion analysis and fragment-expression experiments have recently defined even smaller portions of STIM1 as the effector[59–61]. A minimal activating sequence of approximately 100 amino acids spanning the distal coiled-coil of STIM1 was shown to activate the Orai1 current[60,61] and to bind directly to purified Orai1 protein[60]. Interestingly, the Orai1 current induced by the minimal fragment of STIM1 reportedly lacks the normal CRAC channel property of rapid Ca^{2+}-dependent inactivation[60,62].

Stoichiometry: STIM in Orai channel subunit assembly

Many ion channels are stable tetramers that surround a conducting pore, but examples of trimers, pentamers and hexamers are also well known. STIM1 oligomerization is sufficient to cause its translocation adjacent to the plasma membrane where activation of Orai1 channels occurs[36] (Fig. 3). How many STIM and Orai molecules are required to activate the channel? To date, four studies have investigated the

Box 2 Knockouts, STIMopathies and knockdown

Corresponding to its widespread expression pattern and documented role in Ca^{2+} signalling, *Stim1* knockout has devastating effects *in vivo*. *Stim1*$^{-/-}$ mice generated in various ways perished *in utero* or soon after birth of respiratory failure, although early embryos appeared to develop normally[80,87–89]. STIM2-deficient animals were born, but died at 4–5 weeks[88]. A difference in STIM1 and STIM2 function has been confirmed *in vivo* in T cells from single- and double-knockout mice[88]. Consistent with RNAi studies on cells in culture[12,13], deletion of *Stim1* resulted in a more profound reduction of SOCE in primary T cells and embryonic fibroblasts than deletion of *Stim2* (ref. 88). CRAC currents were nearly abolished in T cells when *Stim1* was deleted but were scarcely reduced by *Stim2* knockout. Yet effects on cytokine production were profound in both *Stim1*- and *Stim2*-knockout T cells. One possible explanation is that STIM2 continues to provide sufficient Ca^{2+} influx to promote gene expression responses at late times when STIM1 has redistributed back to the bulk ER. CD4-CRE mice doubly deficient in both STIM1 and STIM2 developed a lymphoproliferative disorder due to impaired function of regulatory T cells[88]. *Stim1* knockout also profoundly reduced SOCE in fetal liver-derived mast cells and acute degranulation was nearly abolished[87]. Secretion of cytokines was strongly reduced, and in heterozygous *Stim1*$^{+/-}$ mice anaphylactic responses were mildly reduced. A gene-trap knockout to generate *Stim1*$^{-/-}$ mice resulted in neonatal lethality with growth retardation and a severe skeletal myopathy[89]. Functional analysis of myotubes from gene-trap-knockout *Stim1*$^{gt/gt}$ mice indicated reduced SOCE, attenuated CRAC-like current and increased fatiguability during repetitive action potentials. A role of STIM1 in platelets relating to cerebrovascular function was also inferred[80]. SOCE, agonist-dependent Ca^{2+} influx and platelet aggregation was reduced in platelets from STIM1-deficient mice, also generated by insertion of an intronic gene-trap cassette. Of potential clinical significance, bone-marrow chimaeric mice with STIM1 deficiency in haematopoietic cells, including platelets, had improved outcomes in a brain infarction model of stroke using transient occlusion of a cerebral artery to induce neuronal damage[80]. STIM1 also has a vital role in FCγ receptor-mediated functions in macrophages, including the secretion of inflammatory cytokines and phagocytosis[90]. In the same study, mice lacking STIM1 in haematopoietic cells were shown to be resistant in experimental models of thrombocytopenia and autoimmune hemolytic anaemia. Furthermore, transgenic mice expressing an EF-hand mutant STIM1 exhibited a bleeding disorder associated with elevated Ca^{2+} and reduced survival of platelets that led to reduced clotting in this induced 'STIMopathy' (ref. 91). Collectively, these studies show that Ca^{2+} signalling was dramatically reduced in T lymphocytes, fibroblasts, mast cells, skeletal muscle, platelets and macrophages from Stim1 knockouts.

Recently, an immune deficiency syndrome due to mutation of STIM1 was identified in a human family[92]. This first human STIMopathy arises from a truncation mutation in the SAM domain that introduces a premature STOP codon and results in undetectable levels of *Stim1* mRNA and protein expression. SOCE was absent in patient fibroblasts, and the patients exhibited a complex syndrome of combined immunodeficiency with infections and autoimmunity associated with hepatosplenomegaly, hemolytic anaemia, thrombocytopenia and reduced numbers of regulatory T cells. In addition, patients exhibited muscular hypotonia and an enamel dentition defect, similarly to patients with immunodeficiency due to mutations in Orai1.

STIM1 has also been implicated by RNAi knockdown of SOCE or CRAC channel function in a variety of primary cells and cell lines, including: Jurkat T[13], HEK293 (refs 13, 93), HeLa[12,94], PC12 (ref. 95), neuroblastoma/glioma[75] and breast cancer[96] cell lines; airway and vascular smooth muscle[75,97–101]; hepatocytes[102] and liver cell lines[103–105]; and salivary and mandibular gland cells[70]. In addition, parallels in STIM1 expression and SOCE function are reported in primary megakaryocytes and platelets[106], resting and activated human T cells[51] and vascular smooth muscle[107,108]; STIM1 translocation has been studied in a pancreatic cell line[40].

oligomerization status of Orai. In biochemical experiments (glycerol gradient centrifugation, native gel systems and cross-linking)[30,63], Orai appears predominantly as a stable dimer. Yet strong functional evidence favouring a tetramer also exists; tandem tetramers of Orai1 were resistant to dominant-negative suppression by a non-conducting Orai1 monomer[64]. Two recent studies took the different, single-molecule approach of counting the number of photobleaching steps to determine the number of GFP (green fluorescent protein)-tagged Orai subunits per channel[30,31]. Both studies showed that a tetramer predominates when the channel is activated. However, using biochemical analysis and single-molecule photobleaching, we found that when Orai was expressed alone (without Stim or activating C-Stim) it appeared as a stable dimer and no change in oligomerization status was seen in resting cells expressing Stim and Orai[30]. In contrast, another study found that STIM1 and Orai1 co-expression always resulted in tetrameric Orai1 in both closed and open states[31]. Further studies are needed to determine the kinetics and reversibility of the dimer-to-tetramer transition. A similar photobleaching approach applied to C-STIM1 suggests that two STIM1 molecules are required to activate the tetrameric Orai channel[31].

TRPC channel activation by STIM1

Are all SOC channels actually STIM-Operated Ca^{2+} channels with a variety of different pore-forming subunits? The coupling between STIM1 and Ca^{2+}-permeable channels appears to be promiscuous, a property that may potentially help to resolve an often tendentious discussion of what is, and what is not, a SOC channel. From a biophysical perspective, it has been puzzling to note the very different properties of ion selectivity and rectification of SOC channels in various cell types. CRAC channels in the immune system are very selective for Ca^{2+}, have an inwardly rectifying current-voltage relationship and an unusually low single-channel conductance in the femtosiemens range; in contrast,TRPC channels are less Ca^{2+}-selective and have more linear current-voltage relationships and higher single channel conductances in the picosiemens range. The promiscuity of STIM1 coupling potentially resolves this conundrum. 'Classic' CRAC current is identified as originating from Orai channels, whereas the less selective SOC influx may be due to TRPC family members. So far, STIM1 has been implicated in activating Ca^{2+}-permeable TRPC1, C2, C3, C4, C5 and C6 (but not TRPC7) channels[45,46,56,61,65–70]. As shown previously for native CRAC channels, the C terminus of STIM1

activates TRPC1 and TRPC3 channels and interacts with TRPC1, C2, C4 and C5 (as shown by co-immunoprecipitation)[56,57], leading to the conclusion that STIM1 heteromultimerizes TRPC channels and confers function as SOC channels[57]. For TRPC1, channel activation is mediated through a charge–charge interaction that requires the C-terminal lysine-rich domain of STIM1 (ref. 71). TRPC1 is reportedly recruited by STIM1 to lipid raft domains in the surface membrane, resulting in a store-dependent mode of TRPC1 channel activation[45,46]. A further level of complexity was suggested on the basis of RNAi suppression, dominant-negative suppression and biochemical pulldown experiments that point to interactions between TRPC and Orai channels[68,70,72,73]. However, the functional relationship between STIM, TRPC and Orai proteins will need further investigation to confirm the extent of inter-family heteromultimerization and to ensure that TRPC channels are activated directly by STIM1 following store depletion and not through an indirect route.

Conclusion and remaining questions

In this review, the modular organization and five distinct functions of STIM that link ER Ca^{2+} store depletion to the activation of SOC channels in the plasma membrane are highlighted: Ca^{2+} sensing, signal initiation by oligomerization, translocation to ER–plasma membrane junctions, inducing Orai subunits to cluster and activating Ca^{2+} influx. This entire intracellular spatiotemporal signalling sequence can occur within a minute in small cells. Molecular feedback mediated by STIM1 shuttling between the ER and the plasma membrane ensures that Ca^{2+} influx occurs locally across the plasma membrane, refilling the ER Ca^{2+} store near the site of signal initiation in large cells and producing sustained and global Ca^{2+} signalling in small cells. Local Ca^{2+} signalling is likely to have important consequences for amplifying the Ca^{2+} signal near lipid raft domains as, for example, in the region of the immunological synapse. Knockout and RNAi knockdown experiments suggest important functions and potential therapeutic targets that involve Ca^{2+} signalling and homeostasis during development and in several different organ systems and cell types (Box 2).

Despite rapid progress since the initial discovery of STIM's role in SOCE, we still do not understand several aspects of how STIM functions. We are uncertain how ER-resident STIM migrates rapidly along microtubules, how it accumulates at the plasma membrane following store depletion and how it is retrieved when the Ca^{2+} store is refilled. Many questions are posed. Are there additional scaffolding functions of STIM to anchor microtubules or to keep the ER intact? Is STIM translocation active or passive? What defines ER–plasma membrane junctions and how stable is the organization? When STIM arrives at the plasma membrane, does it induce Orai to accumulate using a diffusion trap? Or something else? Is the assembly of Orai dimers into a tetramer a dynamic and rapidly reversible process during channel gating? Finally, how exactly does STIM open the Ca^{2+} channel formed by Orai?

Other than STIM and Orai, there may be additional molecular components to the mechanism. After all, there were dozens of hits in genome-wide screens for SOCE function; to date, however, attention has been focused on STIM and Orai. Is there a 'CRAC-osome', and if so what is it? Suggestions that there are other components include size constraints involved in migration of Orai1 into clusters[39], evidence old and recent that a Ca^{2+} influx factor might be involved[74–76] and evidence that several proteins can be recruited to clusters[77]. On the other hand, overexpression of STIM and Orai alone, without a third protein, amplifies the number of functional CRAC channels to a remarkably high expression level (> 10^5 per cell) in many cell types, indicating that expression levels of other proteins are not limiting, at least up to very high channel densities. Furthermore, EF-hand mutant STIM1 and C-STIM N-terminal fragments bypass ER Ca^{2+} store depletion in activating robust CRAC current, arguing strongly against the hypothesis that a Ca^{2+} influx factor-like substance liberated by store depletion is required. How is it that STIM1 interacts with Orai1 and also with structurally unrelated TRPC channels? And concerning the function of STIM2, how is it that mammals have two STIMs, whereas flies function successfully with one? How does STIM1 (but not STIM2) insert into the plasma membrane? In addition to resolving mechanistic questions, future work may target STIM–channel interactions in the design of new immunosuppressant drugs[78,79] or to ameliorate cerebrovascular damage following stroke[80]. Finally, and again referring to early discoveries relating to its chromosomal localization[9,81], it will be of interest to learn if STIM has a role in tumorigenesis.

Note: Supplementary Information is available on the Nature Cell Biology website.

ACKNOWLEDGEMENTS

I thank members of the Cahalan and Parker laboratories at UCI who participated in a Stim/Orai Symposium (SOS), where discussions of the literature were extremely helpful; A. Penna and K. Németh-Cahalan for contributions to figures, and I. Parker, A. Demuro and A. Penna for providing the TIRF microscopy Supplementary Movie.

Published online at http://www.nature.com/naturecellbiology/
Reprints and permissions information is available online at http://npg.nature.com/reprintsandpermissions/

1. Parekh, A. B. & Putney, J. W. Jr Store-operated calcium channels. *Physiol. Rev.* **85,** 757–810 (2005).
2. Hoth, M. & Penner, R. Depletion of intracellular calcium stores activates a calcium current in mast cells. *Nature* **355,** 353–356 (1992).
3. Lewis, R. S. & Cahalan, M. D. Mitogen-induced oscillations of cytosolic Ca^{2+} and transmembrane Ca^{2+} current in human leukemic T cells. *Cell Regul.* **1,** 99–112 (1989).
4. Zweifach, A. & Lewis, R. S. Mitogen-regulated Ca^{2+} current of T lymphocytes is activated by depletion of intracellular Ca^{2+} stores. *Proc. Natl Acad. Sci. USA* **90,** 6295–6299 (1993).
5. Oritani, K. & Kincade, P. W. Identification of stromal cell products that interact with pre-B cells. *J. Cell Biol.* **134,** 771–782 (1996).
6. Williams, R. T. *et al.* Identification and characterization of the *STIM* (stromal interaction molecule) gene family: coding for a novel class of transmembrane proteins. *Biochem. J.* **357,** 673–685 (2001).
7. Cai, X. Molecular evolution and functional divergence of the Ca^{2+} sensor protein in store-operated Ca^{2+} entry: stromal interaction molecule. *PLoS ONE* **2,** e609 (2007).
8. Parker, N. J., Begley, C. G., Smith, P. J. & Fox, R. M. Molecular cloning of a novel human gene (D11S4896E) at chromosomal region 11p15.5. *Genomics* **37,** 253–256 (1996).
9. Sabbioni, S., Barbanti-Brodano, G., Croce, C. M. & Negrini, M. *GOK*: a gene at 11p15 involved in rhabdomyosarcoma and rhabdoid tumor development. *Cancer Res.* **57,** 4493–4497 (1997).
10. Manji, S. S. *et al.* STIM1: a novel phosphoprotein located at the cell surface. *Biochim. Biophys. Acta* **1481,** 147–155 (2000).
11. Williams, R. T. *et al.* Stromal interaction molecule 1 (STIM1), a transmembrane protein with growth suppressor activity, contains an extracellular SAM domain modified by Nlinked glycosylation. *Biochim. Biophys. Acta* **1596,** 131–137 (2002).
12. Liou, J. *et al.* STIM is a Ca^{2+} sensor essential for Ca^{2+}-store-depletion-triggered Ca^{2+} influx. *Curr. Biol.* **15,** 1235–1241 (2005).
13. Roos, J. *et al.* STIM1, an essential and conserved component of store-operated Ca^{2+} channel function. *J. Cell Biol.* **169,** 435–445 (2005).
14. Yeromin, A. V., Roos, J., Stauderman, K. A. & Cahalan, M. D. A store-operated calcium channel in *Drosophila* S2 cells. *J. Gen. Physiol.* **123,** 167–182 (2004).
15. Soboloff, J. *et al.* STIM2 is an inhibitor of STIM1-mediated store-operated Ca^{2+} Entry. *Curr. Biol.* **16,** 1465–1470 (2006).
16. Brandman, O., Liou, J., Park, W. S. & Meyer, T. STIM2 is a feedback regulator that stabilizes basal cytosolic and endoplasmic reticulum Ca^{2+} levels. *Cell* **131,** 1327–1339 (2007).
17. Feske, S. *et al.* A mutation in Orai1 causes immune deficiency by abrogating CRAC channel function. *Nature* **441,** 179–185 (2006).
18. Vig, M. *et al.* CRACM1 is a plasma membrane protein essential for store-operated Ca^{2+} entry. *Science* **312,** 1220–1223 (2006).
19. Zhang, S. L. *et al.* Genome-wide RNAi screen of Ca^{2+} influx identifies genes that regulate Ca^{2+} release-activated Ca^{2+} channel activity. *Proc. Natl Acad. Sci. USA* **103,** 9357–9362 (2006).

20. Mercer, J. C. *et al.* Large store-operated calcium selective currents due to co-expression of Orai1 or Orai2 with the intracellular calcium sensor, Stim1. *J. Biol. Chem.* **281,** 24979–24990 (2006).
21. Peinelt, C. *et al.* Amplification of CRAC current by STIM1 and CRACM1 (Orai1). *Nature Cell Biol.* **8,** 771–773 (2006).
22. Soboloff, J. *et al.* Orai1 and STIM reconstitute store-operated calcium channel function. *J. Biol. Chem.* **281,** 20661–20665 (2006).
23. Prakriya, M. *et al.* Orai1 is an essential pore subunit of the CRAC channel. *Nature* **443,** 230–233 (2006).
24. Vig, M. *et al.* CRACM1 multimers form the ion-selective pore of the CRAC channel. *Curr. Biol.* **16,** 2073–2079 (2006).
25. Yeromin, A. V. *et al.* Molecular identification of the CRAC channel by altered ion selectivity in a mutant of Orai. *Nature* **443,** 226–229 (2006).
26. Zhang, S. L. *et al.* STIM1 is a Ca^{2+} sensor that activates CRAC channels and migrates from the Ca^{2+} store to the plasma membrane. *Nature* **437,** 902–905 (2005).
27. Stathopulos, P. B., Li, G. Y., Plevin, M. J., Ames, J. B. & Ikura, M. Stored Ca^{2+} depletion-induced oligomerization of stromal interaction molecule 1 (STIM1) via the EF-SAM region: An initiation mechanism for capacitive Ca^{2+} entry. *J. Biol. Chem.* **281,** 35855–35862 (2006).
28. Baba, Y. *et al.* Coupling of STIM1 to store-operated Ca^{2+} entry through its constitutive and inducible movement in the endoplasmic reticulum. *Proc. Natl Acad. Sci. USA* **103,** 16704–16709 (2006).
29. Dziadek, M. A. & Johnstone, L. S. Biochemical properties and cellular localisation of STIM proteins. *Cell Calcium* **42,** 123–132 (2007).
30. Penna, A. *et al.* The CRAC channel consists of a tetramer formed by Stim-induced dimerization of Orai dimers. *Nature* **456,** 116–120 (2008).
31. Ji, W. *et al.* Functional stoichiometry of the unitary calcium-release-activated calcium channel. *Proc. Natl Acad. Sci. USA* **105,** 13668–13673 (2008).
32. Liou, J., Fivaz, M., Inoue, T. & Meyer, T. Live-cell imaging reveals sequential oligomerization and local plasma membrane targeting of stromal interaction molecule 1 after Ca^{2+} store depletion. *Proc. Natl Acad. Sci. USA* **104,** 9301–9306 (2007).
33. Muik, M. *et al.* Dynamic coupling of the putative coiled-coil domain of ORAI1 with STIM1 mediates ORAI1 channel activation. *J. Biol. Chem.* **283,** 8014–8022 (2008).
34. Stathopulos, P. B., Zheng, L. & Ikura, M. Stromal Interaction Molecule (STIM) 1 and STIM2 calcium sensing regions exhibit distinct unfolding and oligomerization kinetics. *J. Biol. Chem.* **284,** 728–732 (2009).
35. Stathopulos, P. B., Zheng, L., Li, G. Y., Plevin, M. J. & Ikura, M. Structural and mechanistic insights into STIM1-mediated initiation of store-operated calcium entry. *Cell* **135,** 110–122 (2008).
36. Luik, R. M., Wang, B., Prakriya, M., Wu, M. M. & Lewis, R. S. Oligomerization of STIM1 couples ER calcium depletion to CRAC channel activation. *Nature* **454,** 538–542 (2008).
37. Wu, M. M., Buchanan, J., Luik, R. M. & Lewis, R. S. Ca^{2+} store depletion causes STIM1 to accumulate in ER regions closely associated with the plasma membrane. *J. Cell Biol.* **174,** 803–813 (2006).
38. Smyth, J. T., Dehaven, W. I., Bird, G. S. & Putney, J. W. Jr Ca^{2+}-store-dependent and -independent reversal of Stim1 localization and function. *J. Cell Sci.* **121,** 762–772 (2008).
39. Varnai, P., Toth, B., Toth, D. J., Hunyady, L. & Balla, T. Visualization and manipulation of plasma membrane-endoplasmic reticulum contact sites indicates the presence of additional molecular components within the STIM1-Orai1 Complex. *J. Biol. Chem.* **282,** 29678–29690 (2007).
40. Tamarina, N. A., Kuznetsov, A. & Philipson, L. H. Reversible translocation of EYFP-tagged STIM1 is coupled to calcium influx in insulin secreting β-cells. *Cell Calcium* **44,** 533–544 (2008).
41. Malli, R., Naghdi, S., Romanin, C. & Graier, W. F. Cytosolic Ca^{2+} prevents the subplasmalemmal clustering of STIM1: an intrinsic mechanism to avoid Ca^{2+} overload. *J. Cell Sci.* **121,** 3133–3139 (2008).
42. Calloway, N., Vig, M., Kinet, J. P., Holowka, D. & Baird, B. Molecular clustering of STIM1 with Orai1/CRACM1 at the plasma membrane depends dynamically on depletion of Ca^{2+} stores and on electrostatic interactions. *Mol. Biol. Cell* **20,** 389–399 (2009).
43. Grigoriev, I. *et al.* STIM1 is a MT-plus-end-tracking protein involved in remodeling of the ER. *Curr. Biol.* **18,** 177–182 (2008).
44. Smyth, J. T., DeHaven, W. I., Bird, G. S. & Putney, J. W. Jr Role of the microtubule cytoskeleton in the function of the store-operated Ca^{2+} channel activator STIM1. *J. Cell Sci.* **120,** 3762–3771 (2007).
45. Alicia, S., Angelica, Z., Carlos, S., Alfonso, S. & Vaca, L. STIM1 converts TRPC1 from a receptor-operated to a store-operated channel: Moving TRPC1 in and out of lipid rafts. *Cell Calcium* **44,** 479–491 (2008).
46. Pani, B. *et al.* Lipid rafts determine clustering of STIM1 in endoplasmic reticulum-plasma membrane junctions and regulation of store-operated Ca^{2+} entry (SOCE). *J. Biol. Chem.* **283,** 17333–17340 (2008).
47. Oka, T., Hori, M. & Ozaki, H. Microtubule disruption suppresses allergic response through the inhibition of calcium influx in the mast cell degranulation pathway. *J. Immunol.* **174,** 4584–4589 (2005).
48. Bakowski, D., Glitsch, M. D. & Parekh, A. B. An examination of the secretion-like coupling model for the activation of the Ca^{2+} release-activated Ca^{2+} current I(CRAC) in RBL-1 cells. *J. Physiol.* **532,** 55–71 (2001).
49. Luik, R. M., Wu, M. M., Buchanan, J. & Lewis, R. S. The elementary unit of store-operated Ca^{2+} entry: local activation of CRAC channels by STIM1 at ER-plasma membrane junctions. *J. Cell Biol.* **174,** 815–825 (2006).
50. Xu, P. *et al.* Aggregation of STIM1 underneath the plasma membrane induces clustering of Orai1. Biochem. Biophys. Res. Commun. **350,** 969–976 (2006).
51. Lioudyno, M. I. *et al.* Orai1 and STIM1 move to the immunological synapse and are up-regulated during T cell activation. *Proc. Natl Acad. Sci. USA* **105,** 2011–2016 (2008).
52. Barr, V. A. *et al.* Dynamic movement of the calcium sensor STIM1 and the calcium channel Orai1 in activated T-cells: puncta and distal caps. *Mol. Biol. Cell* **19,** 2802–2817 (2008).
53. Lis, A. *et al.* CRACM1, CRACM2, and CRACM3 are store-operated Ca^{2+} channels with distinct functional properties. *Curr. Biol.* **17,** 794–800 (2007).
54. DeHaven, W. I., Smyth, J. T., Boyles, R. R. & Putney, J. W. Jr Calcium inhibition and calcium potentiation of Orai1, Orai2, and Orai3 calcium release-activated calcium channels. *J. Biol. Chem.* **282,** 17548–17556 (2007).
55. Navarro-Borelly, L. *et al.* STIM1-Orai1 interactions and Orai1 conformational changes revealed by live-cell FRET microscopy. *J. Physiol.* **586,** 5383–5401 (2008).
56. Huang, G. N. *et al.* STIM1 carboxyl-terminus activates native SOC, I(crac) and TRPC1 channels. *Nature Cell Biol.* **8,** 1003–1010 (2006).
57. Yuan, J. P., Zeng, W., Huang, G. N., Worley, P. F. & Muallem, S. STIM1 heteromultimerizes TRPC channels to determine their function as store-operated channels. *Nature Cell Biol.* **9,** 636–645 (2007).
58. Zhang, S. L. *et al.* Store-dependent and -independent modes regulating Ca^{2+} release-activated Ca^{2+} channel activity of human Orai1 and Orai3. *J. Biol. Chem.* **283,** 17662–17671 (2008).
59. Muik, M. *et al.* A cytosolic homomerization and a modulatory domain within STIM1 C-terminus determine coupling to ORAI1 channels. *J. Biol. Chem.* **284,** 8421–8426 (2009).
60. Park, C. Y. *et al.* STIM1 clusters and activates CRAC channels via direct binding of a cytosolic domain to Orai1. *Cell* **136,** 876–890 (2009).
61. Yuan, J. P. *et al.* SOAR and the polybasic STIM1 domains gate and regulate Orai channels. *Nature Cell Biol.* **11,** 337–343 (2009).
62. Zweifach, A. & Lewis, R. S. Rapid inactivation of depletion-activated calcium current (ICRAC) due to local calcium feedback. *J. Gen. Physiol.* **105,** 209–226 (1995).
63. Gwack, Y. *et al.* Biochemical and functional characterization of Orai proteins. *J. Biol. Chem.* **282,** 16232–16243 (2007).
64. Mignen, O., Thompson, J. L. & Shuttleworth, T. J. Orai1 subunit stoichiometry of the mammalian CRAC channel pore. *J. Physiol.* **586,** 419–425 (2008).
65. Cheng, K. T., Liu, X., Ong, H. L. & Ambudkar, I. S. Functional requirement for Orai1 in store-operated TRPC1-STIM1 channels. *J. Biol. Chem.* **283,** 12935–12940 (2008).
66. Jardin, I., Lopez, J. J., Salido, G. M. & Rosado, J. A. Orai1 mediates the interaction between STIM1 and hTRPC1 and regulates the mode of activation of hTRPC1-forming Ca^{2+} channels. *J. Biol. Chem.* **283,** 25296–25304 (2008).
67. Kim, M. S. *et al.* Native store-operated Ca^{2+} influx requires the channel function of Orai1 and TRPC1. *J. Biol. Chem.* **284,** 9733–9741 (2009).
68. Liao, Y. *et al.* Functional interactions among Orai1, TRPCs, and STIM1 suggest a STIM-regulated heteromeric Orai/TRPC model for SOCE/Icrac channels. *Proc. Natl Acad. Sci. USA* **105,** 2895–2900 (2008).
69. Ma, H. T. *et al.* Canonical transient receptor potential 5 channel in conjunction with Orai1 and STIM1 allows Sr^{2+} entry, optimal influx of Ca^{2+}, and degranulation in a rat mast cell line. *J. Immunol.* **180,** 2233–2239 (2008).
70. Ong, H. L. *et al.* Dynamic assembly of TRPC1-STIM1-Orai1 ternary complex is involved in store-operated calcium influx. Evidence for similarities in store-operated and calcium release-activated calcium channel components. *J. Biol. Chem.* **282,** 9105–9116 (2007).
71. Zeng, W. *et al.* STIM1 gates TRPC channels, but not Orai1, by electrostatic interaction. *Mol. Cell* **32,** 439–448 (2008).
72. Liao, Y. *et al.* Orai proteins interact with TRPC channels and confer responsiveness to store depletion. *Proc. Natl Acad. Sci. USA* **104,** 4682–4687 (2007).
73. Liao, Y. *et al.* A role for Orai in TRPC-mediated Ca^{2+} entry suggests that a TRPC:Orai complex may mediate store and receptor operated Ca^{2+} entry. *Proc. Natl Acad. Sci. USA* **106,** 3202–3206 (2009).
74. Bolotina, V. M. Orai, STIM1 and iPLA2β: a view from a different perspective. *J. Physiol.* **586,** 3035–3042 (2008).
75. Csutora, P. *et al.* Novel Role for STIM1 as a Trigger for Calcium Influx Factor Production. *J. Biol. Chem.* **283,** 14524–14531 (2008).
76. Randriamampita, C. & Tsien, R. Y. Emptying of intracellular Ca^{2+} stores releases a novel small messenger that stimulates Ca^{2+} influx. *Nature* **364,** 809–814 (1993).
77. Redondo, P. C., Jardin, I., Lopez, J. J., Salido, G. M. & Rosado, J. A. Intracellular Ca^{2+} store depletion induces the formation of macromolecular complexes involving hTRPC1, hTRPC6, the type II IP(3) receptor and SERCA3 in human platelets. *Biochim. Biophys. Acta* **1783,** 1163–1176 (2008).
78. Cahalan, M. D. *et al.* Molecular basis of the CRAC channel. *Cell Calcium* **42,** 133–144 (2007).
79. Oh-hora, M. & Rao, A. Calcium signaling in lymphocytes. *Curr. Opin. Immunol.* **20,** 250–258 (2008).
80. Varga-Szabo, D. *et al.* The calcium sensor STIM1 is an essential mediator of arterial thrombosis and ischemic brain infarction. *J. Exp. Med.* **205,** 1583–1591 (2008).
81. Sabbioni, S. *et al.* Exon structure and promoter identification of *STIM1* (alias *GOK*), a human gene causing growth arrest of the human tumor cell lines G401 and RD. *Cytogenet. Cell Genet.* **86,** 214–218 (1999).
82. Hewavitharana, T. *et al.* Location and function of STIM1 in the activation of Ca^{2+} entry signals. *J. Biol. Chem.* **283,** 26252–26262 (2008).

83. Lopez, J. J., Salido, G. M., Pariente, J. A. & Rosado, J. A. Interaction of STIM1 with endogenously expressed human canonical TRP1 upon depletion of intracellular Ca^{2+} stores. *J. Biol. Chem.* **281,** 28254–28264 (2006).
84. Hauser, C. T. & Tsien, R. Y. A hexahistidine-Zn^{2+}-dye label reveals STIM1 surface exposure. *Proc. Natl Acad. Sci. USA* **104,** 3693–3697 (2007).
85. Mignen, O., Thompson, J. L. & Shuttleworth, T. J. STIM1 regulates Ca^{2+} entry via arachidonate-regulated Ca^{2+}-selective (ARC) channels without store depletion or translocation to the plasma membrane. *J. Physiol.* **579,** 703–715 (2007).
86. Mignen, O., Thompson, J. L. & Shuttleworth, T. J. Both Orai1 and Orai3 are essential components of the arachidonate-regulated Ca^{2+}-selective (ARC) channels. *J. Physiol.* **586,** 185–195 (2008).
87. Baba, Y. *et al.* Essential function for the calcium sensor STIM1 in mast cell activation and anaphylactic responses. *Nature Immunol.* **9,** 81–88 (2008).
88. Oh-Hora, M. *et al.* Dual functions for the endoplasmic reticulum calcium sensors STIM1 and STIM2 in T cell activation and tolerance. *Nature Immunol.* **9,** 432–443 (2008).
89. Stiber, J. *et al.* STIM1 signalling controls store-operated calcium entry required for development and contractile function in skeletal muscle. *Nature Cell Biol.* **10,** 688–697 (2008).
90. Braun, A. *et al.* STIM1 is essential for Fcγ receptor activation and autoimmune inflammation. *Blood* **113,** 1097–1104 (2009).
91. Grosse, J. *et al.* An EF hand mutation in Stim1 causes premature platelet activation and bleeding in mice. *J. Clin. Invest.* **117,** 3540–3550 (2007).
92. Picard, C. *et al.* STIM1 mutation associated with a syndrome of immunodeficiency and autoimmunity. *N. Engl. J. Med.* **360,** 1971–1980 (2009).
93. Wedel, B., Boyles, R. R., Putney, J. W. Jr & Bird, G. S. Role of the store-operated calcium entry proteins Stim1 and Orai1 in muscarinic cholinergic receptor-stimulated calcium oscillations in human embryonic kidney cells. *J. Physiol.* **579,** 679–689 (2007).
94. Jousset, H., Frieden, M. & Demaurex, N. STIM1 knockdown reveals that store-operated Ca^{2+} channels located close to sarco/endoplasmic Ca^{2+} ATPases (SERCA) pumps silently refill the endoplasmic reticulum. *J. Biol. Chem.* **282,** 11456–11464 (2007).
95. Thompson, M. A., Pabelick, C. M. & Prakash, Y. S. Role of STIM1 in regulation of store-operated Ca^{2+} influx in pheochromocytoma cells. *Cell. Mol. Neurobiol.* **29,** 193–202 (2009).
96. Yang, S., Zhang, J. J. & Huang, X. Y. Orai1 and STIM1 are critical for breast tumor cell migration and metastasis. *Cancer Cell* **15,** 124–134 (2009).
97. Aubart, F. C. *et al.* RNA interference targeting STIM1 suppresses vascular smooth muscle cell proliferation and neointima formation in the rat. *Mol. Ther.* **17,** 455–462 (2009).
98. Dietrich, A. *et al.* Pressure-induced and store-operated cation influx in vascular smooth muscle cells is independent of TRPC1. *Pflugers Arch.* **455,** 465–477 (2007).
99. Guo, R. W. *et al.* An essential role for stromal interaction molecule 1 in neointima formation following arterial injury. *Cardiovasc. Res.* **81,** 660–668 (2009).
100. Peel, S. E., Liu, B. & Hall, I. P. A key role for STIM1 in store operated calcium channel activation in airway smooth muscle. *Respir. Res.* **7,** 119 (2006).
101. Takahashi, Y. *et al.* Functional role of stromal interaction molecule 1 (STIM1) in vascular smooth muscle cells. *Biochem. Biophys. Res. Commun.* **361,** 934–940 (2007).
102. Jones, B. F., Boyles, R. R., Hwang, S. Y., Bird, G. S. & Putney, J. W. Calcium influx mechanisms underlying calcium oscillations in rat hepatocytes. *Hepatology* **48,** 1273–1281 (2008).
103. El Boustany, C. *et al.* Capacitative calcium entry and transient receptor potential canonical 6 expression control human hepatoma cell proliferation. *Hepatology* **47,** 2068–2077 (2008).
104. Aromataris, E. C., Castro, J., Rychkov, G. Y. & Barritt, G. J. Store-operated Ca^{2+} channels and Stromal Interaction Molecule 1 (STIM1) are targets for the actions of bile acids on liver cells. *Biochim. Biophys. Acta* **1783,** 874–885 (2008).
105. Litjens, T. *et al.* Phospholipase C-γ1 is required for the activation of store-operated Ca^{2+} channels in liver cells. *Biochem. J.* **405,** 269–276 (2007).
106. Tolhurst, G. *et al.* Expression profiling and electrophysiological studies suggest a major role for Orai1 in the store-operated Ca^{2+} influx pathway of platelets and megakaryocytes. *Platelets* **19,** 308–313 (2008).
107. Berra-Romani, R., Mazzocco-Spezzia, A., Pulina, M. V. & Golovina, V. A. Ca^{2+} handling is altered when arterial myocytes progress from a contractile to a proliferative phenotype in culture. *Am. J. Physiol. Cell. Physiol.* **295,** C779–790 (2008).
108. Lu, W., Wang, J., Shimoda, L. A. & Sylvester, J. T. Differences in STIM1 and TRPC expression in proximal and distal pulmonary arterial smooth muscle are associated with differences in Ca^{2+} responses to hypoxia. *Am. J. Physiol. Lung Cell. Mol. Physiol.* **295,** L104–113 (2008).

Wicked views on stem cell news

Ralph A. Neumüller and Juergen A. Knoblich

Stem cells achieve the remarkable task of generating both identical copies of themselves and lineage-restricted daughter cells that ultimately undergo terminal differentiation. The differential regulation of ribosomal protein biosynthesis helps to generate these two outcomes in *Drosophila melanogaster*.

In stem cell lineages, some cells retain the potential to self-renew, whereas others eventually differentiate to replace cells in the target tissue. How this is achieved in mammals is largely unclear, but work done mainly in invertebrate model organisms has identified two distinct mechanisms. In one case, the tissue architecture of the stem cell niche allows only some daughter cells to receive growth factor signals essential for stem cell fate[1–3]. Alternatively, the stem cell undergoes an intrinsically asymmetric division in which differentiation factors are inherited by only one of the two daughter cells[4,5]. On page 685 of this issue, Fichelson and colleagues challenge this distinction between the two mechanisms, and demonstrate that asymmetric segregation of critical stem cell regulators occurs even in *Drosophila* ovarian stem cells that were previously thought to be a model for purely extrinsic cell fate diversification[6].

The fruit fly *Drosophila* has emerged as one of the best understood model systems for stem cell biology. *Drosophila* ovaries consist of 14–16 germaria that each contain 2–3 stem cells. Ovarian germline stem cells are in close contact with cap cells from which they receive a signal mediated by the TGF-like growth factor Dpp (Decapentaplegic)[1,2]. In the stem cell, Dpp is essential for self-renewal. When the stem cell divides, the mitotic spindle is oriented perpendicularly to the surface of the stem cell niche through E-cadherin-dependent anchoring to the cap cells. Therefore, one of the two daughter cells (called the cystoblast) is always placed away from the niche, no longer receives Dpp and upregulates the differentiation factor Bam (Bag of marbles). As a consequence, this cell undergoes four rounds of incomplete mitotic division to generate a cyst of 16 interconnected cystocytes (Fig. 1a, left). Ultimately, one of these cells forms the oocyte, whereas the others undergo several rounds of endoreplication to form the nurse cells. Although it is known that a cytoplasmic structure called the spectrosome is preferentially segregated into the stem cell, it is generally assumed that extrinsic signals provided by the stem cell niche are primarily responsible for controlling self renewal in the ovarian germline stem cell lineage[1,2].

In a genetic screen for mutants that affect ovarian stem cell maintenance, Fichelson and colleagues identified a gene they call *wicked*. When *wicked* was inactivated, mutant germline stem cells were lost from the stem cell niche (Fig.1a, right). This is not because they underwent apoptosis, but because they differentiated prematurely. *Wicked* encodes for a nucleolar protein that is essential for correct processing of ribosomal RNA (rRNA). In the absence of Wicked, immature rRNA intermediates accumulate at the expense of the final product due to defects in the early maturation steps. This might lead to defects in ribosome assembly and a decrease in overall protein biosynthesis rates that could be responsible for stem cell loss.

Quite unexpectedly, Wicked does not seem to be controlled by extracellular Dpp signalling, but instead is asymmetrically distributed between the two daughter cells. In the study, the authors developed a live imaging procedure for Wicked::GFP in dividing ovarian stem cells to demonstrate that the protein accumulates in cytoplasmic dots during mitosis. In metaphase, these dots accumulate on the side of the cell facing the cap cells. In anaphase and telophase, they segregate into the daughter cell that will remain a stem cell, whereas the other daughter cell inherits around seven times fewer particles. Thus, Wicked is the first protein that is both asymmetrically distributed and required for stem cell maintenance in the *Drosophila* ovary.

The asymmetry of Wicked is not restricted to ovarian stem cells. A similar asymmetric segregation is seen in *Drosophila* neuroblasts, a cell type whose asymmetric division is thought to rely on intrinsic mechanisms[4,5]. Neuroblasts are stem cell-like progenitors in the *Drosophila* central nervous system. They typically divide into one cell that remains a neuroblast and continues to proliferate and one ganglion mother cell (GMC) that undergoes just one more division to generate two terminally differentiating neurons (Fig. 1b, left). During each neuroblast division, the proteins Numb, Prospero and Brat segregate into the GMC where they are thought to inhibit self-renewal and induce terminal differentiation. As in germline stem cells, Wicked accumulates in cytoplasmic dots during neuroblast division, and those dots are preferentially inherited by the daughter cell that maintains stem cell identity. W*icked* mutant neuroblasts are only half the size of normal neuroblasts and generate half the number of GMCs, indicating that the Wicked protein is required for cell growth and proliferation in neuroblasts (Fig. 1b, right).

In both neuroblasts and ovarian germline stem cells, Wicked-positive granules are inherited by the daughter cell that retains stem cell potential. This is interesting because several previous observations suggest that this daughter cell has a higher growth rate after mitosis[7,8].

Ralph A. Neumüller and Juergen A. Knoblich are at the Institute of Molecular Biotechnology of the Austrian Academy of Sciences (IMBA), Dr. Bohr Gasse 3, 1030 Vienna, Austria.
e-mail: Juergen.Knoblich@imba.oeaw.ac.at

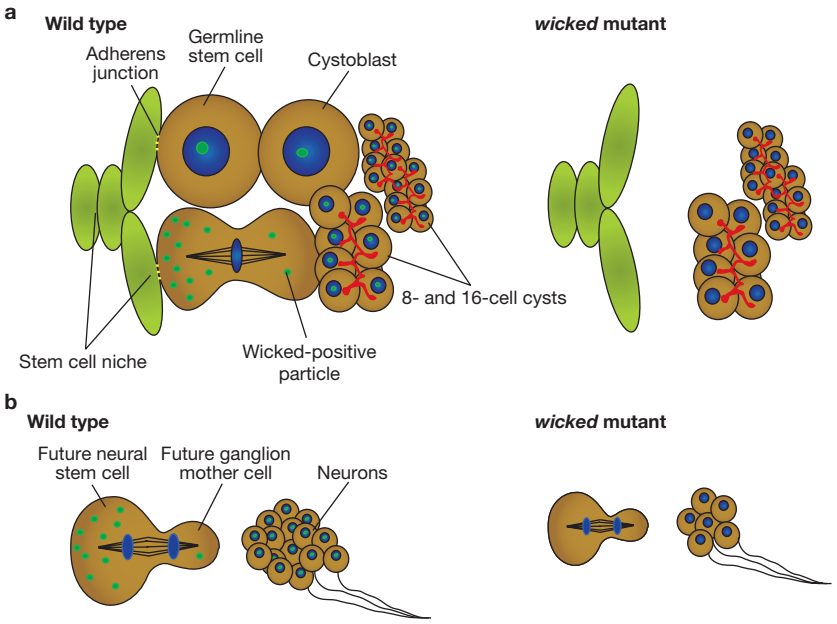

Figure 1 Wicked segregates into stem cells and is required for proliferation and growth. (**a**) Germline stem cells (brown) are in direct contact with the stem cell niche (green). After mitosis, one of the two daughter cells is no longer in contact with the niche and becomes the cystoblast, which divides four times to form a 16-cell cyst. Wicked-positive particles (green) are preferentially segregated into the future stem cell (left). *wicked* mutant germline stem cells differentiate prematurely, presumably due to a growth defect (right). Red indicates thefusome, a membranous organelle that connects all the cells of one cyst. (**b**) Neuroblasts divide into another neuroblast and a ganglion mother cell that terminally divides to produce two neurons. On division Wicked-positive particles are segregated into the future neuroblast. *wicked* mutant neuroblasts are smaller than their wild-type counterparts and produce fewer neurons.

In the neuroblast lineage, cell size is more or less constant; this means that loss of cytoplasm during mitosis is compensated by constant growth. For the quiescent neuron, on the other hand, it means that growth is insignificant before axonogenesis. In the ovarian stem cell lineage, the stem cell grows back to its original size between each division, whereas the cystoblast and cyst cells slow down cell growth so that cystocytes become smaller with each division. Thus, both in ovaries and in the nervous system it seems that the stem cells that inherit the Wicked protein grow at a faster rate.

Could Wicked be responsible for these differences in growth rate? Wicked resides in the nucleolus, the major site of ribosomal RNA synthesis. As ribosome biogenesis and overall protein biosynthesis rates are correlated with cell growth, this localization is consistent with a rate limiting function in growth control. In *wicked* mutant neuroblasts, both cell size and division rates are reduced, indicating that cell growth is significantly slowed down. As neurons and GMCs do not show a similar reduction in size, Wicked is at least partially responsible for generating the growth difference between neuroblasts and neurons. In ovaries, quantification of *wicked* mutant stem cell size is difficult because mutant germline stem cells are lost from the niche and undergo premature differentiation. Loss of germline stem cells has also been described in other situations where cell growth is compromised. Germline stem cells that, for example, lack the transcription factor *dMyc* are preferentially lost from the niche, whereas *dMyc* overexpression outcompetes other stem cells that express normal levels of the protein[9]. Similarly, overexpression of the growth inhibitor Mei-P26 results in premature differentiation[8]. Thus, Wicked is probably a rate-limiting factor for cell growth in stem cell lineages.

From this, we can conceive a simple model where the preferential segregation of Wicked granules into the stem cell increases the rate of cell growth. Indeed, both in neuroblast and ovarian germline stem cell lineages, the nucleolus is larger in the stem cell and this correlates with a higher requirement for Wicked in this cell[7,8]. However, the fraction of Wicked protein contained in the granules is minimal, and so their asymmetric inheritance only marginally increases Wicked levels in one of the two daughter cells. In addition, the overexpression of Wicked does not cause any strong phenotypes, indicating that other factors exist that limit cell growth in differentiating daughter cells. It is therefore more likely that Wicked is a permissive, rather than a regulatory, factor of protein biosynthesis and cellular growth, and its asymmetric inheritance simply reflects (rather than causes) the differential requirements for ribosome biogenesis in the two daughter cells.

Wicked seems to be part of a protein network that restricts cell growth in stem cell lineages. Other components of this network are dMyc and its regulators Brat and Mei-P26 (refs 7–9). In ovaries, *dMyc* is highly expressed in the stem cell but its expression is downregulated as cysts go through their transit-amplifying divisions[8]. In *mei-P26* mutants, this downregulation does not occur leading to the formation of an ovarian tumour[8]. In neuroblasts, the Mei-P26 related protein Brat restricts growth and proliferation and thereby prevents the formation of a neuroblast-derived brain tumour[7,10,11]. Either directly or indirectly, Brat also inhibits dMyc, suggesting a common mechanism for controlling stem cell growth[7]. Identifying how Wicked fits into this mechanism will be an important task for the future. One of the main effects of dMyc is to stimulate rRNA biosynthesis and increase the size of the nucleolus[12–14], the site where Wicked functions. It is conceivable that regulation of nucleolar size through dMyc and regulation of the activity of Wicked through asymmetric segregation feed into the same pathway that controls protein biosynthesis rates and therefore cellular growth. As both Brat and Mei-P26 prevent stem cells from becoming tumorigenic, characterization of this pathway and its regulation will have important implications for research in tumorigenesis.

1. Wong, M. D., Jin, Z. & Xie, T. *Annu. Rev. Genet.* **39,** 173–195 (2005).
2. Fuller, M. T. & Spradling, A. C. *Science* **316,** 402–404 (2007).
3. Morrison, S. J. & Spradling, A. C. *Cell* **132,** 598–611 (2008).
4. Knoblich, J. A. *Cell* **132,** 583–597 (2008).
5. Doe, C. Q. *Development* **135,** 1575–1587 (2008).
6. Fichelson, P. *et al. Nature Cell Biol.* **11,** 685–693 (2009).
7. Betschinger, J., Mechtler, K. & Knoblich, J. A. *Cell* **124,** 1241–1253 (2006).
8. Neumuller, R. A. *et al. Nature* **454,** 241–245 (2008).
9. Rhiner, C. *et al. Development* **136,** 995–1006 (2009).
10. Lee, C. Y., Wilkinson, B. D., Siegrist, S. E., Wharton, R. P. & Doe, C. Q. *Dev. Cell* **10,** 441–449 (2006).
11. Bello, B., Reichert, H. & Hirth, F. *Development* **133,** 2639–2648 (2006).
12. Grewal, S. S., Li, L., Orian, A., Eisenman, R. N. & Edgar, B. A. *Nature Cell Biol.* **7,** 295–302 (2005).
13. Arabi, A. *et al. Nature Cell Biol.* **7,** 303–310 (2005).
14. Grandori, C. *et al. Nature Cell Biol.* **7,** 311–318 (2005).

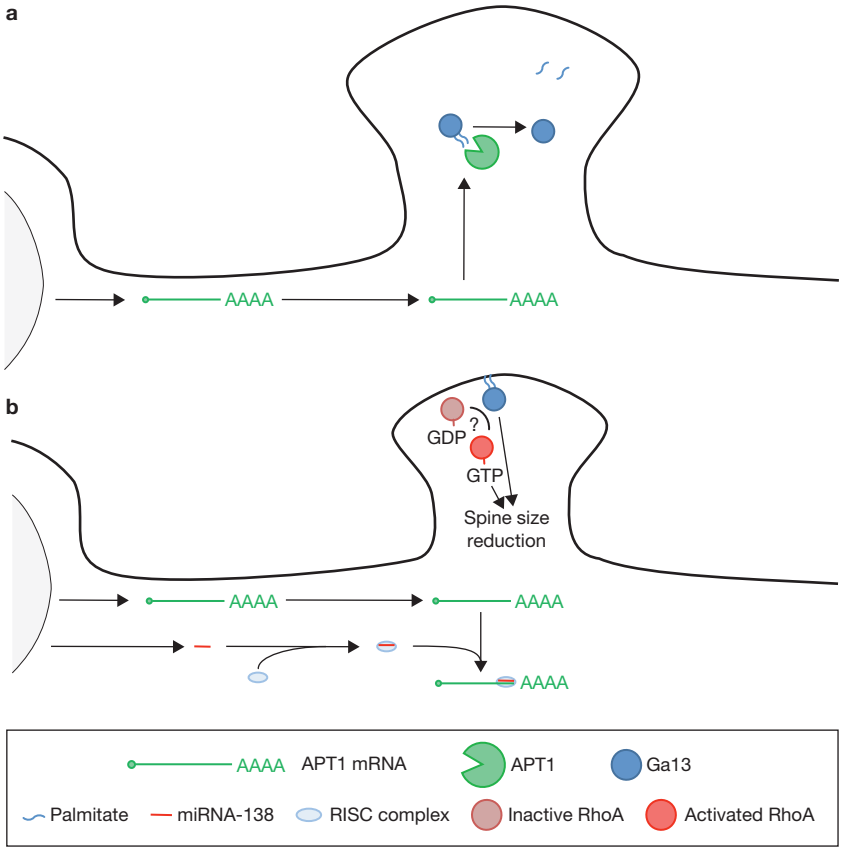

Figure 1 RNA-138 may control spine size in response to synaptic activity by regulating APT1-mediated palmitoylation of Gα13. (**a**) In the absence of miRNA-138, APT1 is expressed in dendritic spines and depalmitoylates synaptic proteins such as Gα13, preventing its membrane localization. (**b**) APT1 mRNA is located in dendrites; when present, miRNA-138 (recruited by the RNA-induced silencing complex, RISC) binds APT1 mRNA and inhibits APT1 synthesis, which in turn increases the palmitoylation state of the APT1 target Gα13 and its membrane localization. The result is shrinkage of the spine, possibly through a pathway involving RhoA (Ras homologue gene family, member A) activation.

It has also been suggested that some miRNAs affect synaptic plasticity in the adult brain. For example, miRNA-134 inhibits the expression of LIM-kinase 1, regulating the size of dendritic spines[8]. However, the mechanisms underlying miRNA action are still not well understood.

Siegel and colleagues used microarrays to identify miRNAs that are enriched in the immediate proximity of synapses and thus might regulate synaptic plasticity. They used RNA from synaptosomes as a source of synaptic miRNA and compared miRNA levels in this fraction with those in total brain extracts. Using this technique, they identified several miRNAs consistently enriched in the synaptic compartment. After confirming the neuronal expression and dendritic localization of candidate miRNAs using northern blotting and *in situ* hybridization, the authors set out to investigate the role of these miRNAs in regulating dendritic spine morphology, an indicator of synaptic plasticity. For this, the authors used 2'-O'methyl modified antisense oligoribonucleotides that inhibit the action of target miRNAs[9]. Expression of antisense oligoribonucleotides against two candidates resulted in an increase in dendritic spine volume. The authors then decided to focus their study on one of the two candidates, miRNA-138, the physiological function of which is unknown in the nervous system.

Using duplex RNA, the authors found that overexpression of miRNA-138 decreased spine volume. Furthermore, this effect was not the result of a more global change in dendrite morphology as modification of miRNA-138 expression did not have any effect on other dendrite characteristics, such as spine density and dendrite branching. As expected when spine size is decreased, the authors were able to correlate the overexpression of miRNA-138 with a decrease in AMPA (α-amino-3-hydroxy-5-methyl-4-isoxazolepropionic acid) receptor cluster size and the miniature excitatory postsynaptic currents (mEPSCs) mediated by these receptors. The specific effect of miRNA-138 on dendritic spine size suggests a potential role in regulating synaptic plasticity rather than in regulating other characteristics of neuronal function.

A key feature of this work was to identify relevant target(s) for miRNA-138. Siegel and colleagues first used a computational approach to find potential targets and then selected those exhibiting a biochemical activity that could be linked to synaptic function. The effect of miRNA-138 overexpression on these candidates was subsequently assessed using reporter constructs containing their 3′untranslated region (3′UTR) after the luciferase coding region. The most striking effect was observed with the 3′UTR of the enzyme APT1. Interestingly, APT1 catalyses the depalmitoylation of target proteins but its function in neurons is unknown. Palmitoylation has recently been implicated in the regulation of synaptic plasticity[10,11], and changes in spine structure have been linked to a dynamic balance between the addition of palmitate to, and removal from, synaptic proteins[11]. Therefore, the authors hypothesized that APT1 may regulate spine morphology in response to neuronal activity.

Other findings confirmed APT1 as a target of miRNA-138. In particular, the authors found that inhibition of endogenous miRNA-138 increased synthesis of APT1, and they identified a unique binding site for miRNA-138 in the 3′UTR region of *APT1*. This region is necessary for the regulation of the synthesis of APT1 protein. In addition, the presence of *APT1* mRNA in dendrites further points to local control of APT1 synthesis near the synapse. With this evidence in hand, the authors then determined whether miRNA-138-mediated regulation of dendritic spine morphology directly involves the downregulation of APT1 protein. The authors used siRNA against *APT1* to inhibit its synthesis or pharmacological agents to inhibit the enzymatic activity of APT1. In both cases, the increase in spine volume associated with miRNA-138 inhibition was significantly reduced, demonstrating that APT1 is an important mediator of miRNA-138 action in dendritic spines and that the mode of action of APT1 is to depalmitoylate target proteins. Siegel and colleagues then extended their experiments further and determined the target of APT1.

They chose to focus on the G protein subunit Gα13, a previously identified substrate of APT1 (ref. 12), which must be palmitoylated for it

to localize to the membrane and to function in Rho-dependent signalling[13]. The authors showed that APT1 negatively regulates the membrane localization of Gα13, suggesting that APT1 effectively depalmitoylates Gα13. In addition, overexpression of miRNA-138, which downregulates APT1, increased the membrane localization of Gα13, indicating that the three molecules belong to a common pathway (Fig. 1). The authors established a new link between Gα13 and the regulation of spine size, as overexpression of Gα13 counteracted the spine growth observed after inhibition of miRNA-138. Although the authors could not directly implicate the palmitoylation of Gα13 by APT1 in the regulation of spine size, they provided evidence that the association of Gα13 with the membrane is necessary to rescue the effect of miRNA-138 inhibition.

This study by Siegel and colleagues is the first to show a direct link between miRNA and the dynamic regulation of post-translational modification of synaptic proteins leading to changes in spine morphology. Thus, these findings open up a new direction for the study of synaptic plasticity by focusing on local events that occur in the dendrite and are regulated through miRNA activity.

1. Hering, H. & Sheng, M. *Nature Rev. Neurosci.* **2,** 880–888 (2001).
2. Bramham, C. R. & Wells, D. G. *Nature Rev. Neurosci.* **8,** 776–789 (2007).
3. Siegel, G. *et al. Nature Cell Biol.* **11,** 705–716 (2009).
4. Bartel, D. P. *Cell* **116,** 281–297 (2004).
5. Lee, R. C. *et al. Cell* **75,** 843–854 (1993).
6. Ambros, V. *Nature* **431,** 350–355 (2004).
7. Kosik, K. S. *Nature Rev. Neurosci.* **7,** 911–920 (2006).
8. Schratt, G. M. *et al. Nature* **439,** 283–289 (2006).
9. Meister, G. *et al. RNA* **10,** 544–550 (2004).
10. El-Husseini Ael, D. *et al. Cell* **108,** 849–863 (2002).
11. Kang, R. *et al. Nature* **456,** 904–909 (2008).
12. Yeh, D. C. *et al. J. Biol. Chem.* **274,** 33148–33154 (1999).
13. Bhattacharyya, R. & Wedegaertner, P. B. *J. Biol. Chem.* **275,** 14992–14999 (2000).

RESEARCH HIGHLIGHTS

Ribosome clearance: ubiquitin steps in

Four ribosomal RNAs (rRNAs) and about 80 proteins constitute the small (40S) and large (60S) subunits that form a functional (80S) ribosome. rRNAs are prone to synthesis errors and genotoxic stress, and defective ones are eliminated through non-functional rRNA decay (NRD). Although the molecular mechanism of NRD remains ill-understood, elimination through increased susceptibility to nucleases has been suggested. Ohno and colleagues (*Genes Dev*. **23,** 963–974; 2009) have uncovered a more specific mechanism: Rtt101p and Mms1p, two non-ribosomal components of an E3 ubiquitin ligase previously known for its role in DNA repair, mediate the ubiquitin-dependent degradation of non-functional copies of the 60S component 25S rRNA.

Loss of Mms1p and Rtt101p, identified through a yeast genetic screen for elevated levels of specific mutant rRNAs, resulted in reduced cell growth rates and accumulation of catalytically inactive 60S and 80S subunits containing mutant 25S rRNAs. Ribosomes purified from cells expressing mutant 25S rRNAs were enriched in ubiquitylated proteins, which were not detected in *mms1p*- and *rtt101p*-deficient cells, and inhibition of ubiquitylation stabilized the defective 25S rRNAs. although the ubiquitylation targets remain to be identified, these findings reveal a potential cellular strategy for the coordinated control of DNA and RNA damage. SG

Kinetochore mono-orientation

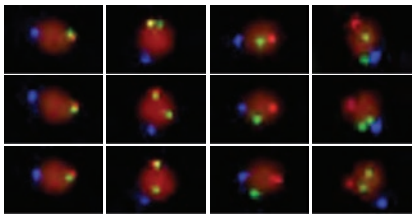

During the reductional division in meiosis I, homologous chromosomes recombine and then segregate to opposite spindle poles, while sister chromatids move to the same pole. The co-orientation of sister chromatids requires alignment of their kinetochores but it is unclear how this is achieved. Watanabe and colleagues (*Nature* **458,** 852–858; 2009) now elegantly show that differences in where cohesion is established determines kinetochore geometry. From monitoring GFP-labelled core centromeres in fission yeast, the authors conclude that cohesion occurs during meiosis I. In mitosis, however, core centromeres separate before anaphase. Since the ectopic expression of cohesin cannot reverse separation in mitosis, core centromere cohesion appears to be actively prevented. In meiosis I, an artificial tether of centromere cores restores kinetochore mono-orientation in mutants with deficient core cohesion. Interestingly, the artificial core centromere tether also results in increased monopolar attachment in mitotic divisions. In mutants lacking cohesion along the entire chromosome arms, artificial tethers of pericentromeric regions cause more bi-orientation, whereas the core centromeric tether favours more mono-orientation. Thus, cohesion in the core and pericentromeric regions seems to induce side-by-side and back-to-back orientation of kinetochores, respectively. Further work is needed to elucidate in more detail how kinetochore geometry is achieved and whether the model applies to other organisms. CK

Smurfs shaping asymmetry

The proteins that control planar cell polarity (PCP) are distributed asymmetrically within the cell. A report by Wrana and colleagues (*Cell* **137,** 295–307; 2009) finds that asymmetric localization of the PCP protein Prickled1 (Pk1) is achieved by Smurf-mediated degradation functioning downstream of non-canonical Wnt signalling.

Smurfs are E3 ubiquitin ligases that act as effectors of the polarity protein Par6. Wrana and colleagues show that mice deleted for both Smurf1 and Smurf2 have defective convergent extension and neural tube closure — two phenotypes seen in PCP mutants. A PCP phenotype was also seen in sensory cells of the inner ear.

Smurf1/2 interacts with the PCP protein Dishevelled2 (Dvl2). This association depends on constitutive binding of Dvl2 and Par6, and Dvl2 phosphorylation in response to non-canonical Wnt signalling. This trimeric complex then triggers Pk1 ubiquitylation and degradation. In the absence of Smurf, Pk1 levels are increased and asymmetric Pk1 localization is lost in the neuroepithelium and the inner ear.

This study thus provides a basis for the previously observed antagonistic relationship between Dvl and Pk, and reveals how non-canonical Wnt signalling can drive the asymmetric degradation of a key PCP protein to regulate the generation of polarity. AS

Decoding Alzheimer's: γ-secretase targets EphA4

Takai and colleagues report that the ephrin receptor EphA4 is processed by γ-secretase, a protease whose aberrant activity is associated with Alzheimer's disease (*J. Cell Biol.* doi: 10.1083/jcb.200809151; 2009). They found that presenilin1 (PS1), the catalytic subunit of γ-secretase, localises to synapses, and that inactivating γ-secretase results in altered dendritic spine morphology. EphA4 was identified as a new synaptic target for γ-secretase *in vitro* and *in vivo*. Moreover, increasing synaptic activity led to enhanced EphA4 processing.

Intramembrane processing of substrates, such as the amyloid precursor protein, by γ-secretase releases their intracellular domains. Indeed, overexpression of the intracellular domain of EphA4 suppresses the effects of γ-secretase inhibition on dendritic spine morphology and loss of EphA4 abolishes the effects of γ-secretase inhibition. Thus, EphA4 appears to be a key γ-secretase target in dendritic spine morphogenesis. The EphA4 intracellular domain activates Rac signalling, which regulates dendritic spine morphology through Rac1. Interestingly, EphA4 processing is reduced in cells expressing the PS1 mutation associated with familial Alzheimer's disease. Whether EphA4 processing is also impaired in patients and mouse models remains to be addressed.

Previous work has noted a loss of synaptic function in Alzheimer's disease. Identifying EphA4 as a γ-secretase target provides important inroads into understanding the pathology of Alzheimer's. SS

By Silvia Grisendi, Christina Karlsson Rosenthal, Alison Schuldt and Sowmya Swaminathan

nature cell biology

Live-imaging of single stem cells within their niche reveals that a U3snoRNP component segregates asymmetrically and is required for self-renewal in *Drosophila*

Pierre Fichelson[1,4,6], Clara Moch[1,3,6], Kenzo Ivanovitch[1,4], Charlotte Martin[2,3], Clara M Sidor[1,5], Jean-Antoine Lepesant[1], Yohanns Bellaiche[2,3] and Jean-René Huynh[1,3,7]

Stem cells generate self-renewing and differentiating progeny over many rounds of asymmetric divisions. How stem cell growth rate and size are maintained over time remains unknown. We isolated mutations in a *Drosophila melanogaster* gene, *wicked* (*wcd*), which induce premature differentiation of germline stem cells (GSCs). Wcd is a member of the U3 snoRNP complex required for pre-ribosomal RNA maturation. This general function of Wcd contrasts with its specific requirement for GSC self-renewal. However, live imaging of GSCs within their niche revealed a pool of Wcd-forming particles that segregate asymmetrically into the GSCs on mitosis, independently of the Dpp signal sent by the niche. A fraction of Wcd also segregated asymmetrically in dividing larval neural stem cells (NSCs). In the absence of Wcd, NSCs became smaller and produced fewer neurons. Our results show that regulation of ribosome synthesis is a crucial parameter for stem cell maintenance and function.

During development or after injury, stem cells face the dual task of generating tissue and maintaining their own cell population with identical properties for tissue homeostasis[1]. One of these properties is stem cell size, which is restored rapidly after division. How stem cell growth is regulated and whether this regulation is required for their function is poorly characterized.

Drosophila GSCs are a good model to study actively proliferating stem cells, as they produce gametes throughout adult life[2]. In females, GSCs are located at the apex of a structure called the germarium[3,4] (Fig. 1a). Two to three GSCs adhere to a niche of somatic cells, providing signals that prevent GSC differentiation, such as Decapentaplegic (Dpp, a bone morphogenetic protein)[5,6]. GSCs divide asymmetrically, generating daughter cells with distinct fates[7]. Upon division, the orientation of the mitotic spindle allows at least one daughter to remain within the niche and adopt the GSC fate, while its sibling positioned outside the niche differentiates into a cystoblast[8,9]. The cytoblast undergoes four rounds of asymmetric divisions with incomplete cytokinesis, producing a cyst of 16 cells (cystocytes) interconnected by cytoplasmic bridges called ring canals[10,11]. The asymmetry of the GSC division relies mainly on extrinsic mechanisms[3,4]. The only known intrinsic asymmetry of female GSC division is the differential segregation of the spectrosome, a cytoplasmic structure made of vesicles kept together by components of the submembraneous cytoskeleton[8,12]. During the four cyst divisions, a spectrosome-like structure, the fusome, anchors one pole of each spindle and ensures that an invariant pattern of divisions is followed[13]. This pattern is important as the oocyte differentiates from one of the two cells with four ring canals, which are called pro-oocytes. Cystocyte size decreases after each division, whereas GSC size is maintained over time and many divisions[14]. How GSC growth is regulated remains unknown.

Cell growth depends primarily on ribosome biogenesis, as the amount of ribosomes in a cell determines the quantity of proteins that can be synthesised[15–17]. Ribosome biogenesis begins with transcription of the ribosomal genes, and maturation of the 47S pre-ribosomal RNA (pre-rRNA) in the nucleolus[18]. The pre-rRNA matures through methylations and pseudouridylations together with endonucleolytic and exonucleolytic cleavages of external and internal transcribed spacers (ETS and ITS). These maturation steps are carried out by complexes containing small nucleolar RNAs (snoRNAs) together with associated proteins called small nucleolar ribonucleoproteins (snoRNPs)[19]. The release of 18S rRNA from the pre-rRNA requires U3 snoRNA, which is associated with pre-rRNA processing components such as Fibrillarin (Fib). Once cleaved, the matured rRNAs assemble with ribosomal proteins and form the 60S and 40S ribosome subunits. Although ribosome biogenesis has been well

[1]Institut Jacques Monod, CNRS, Universités Paris 6 et 7, 2, place Jussieu, F-75251 Paris, Cedex 05, France. [2]Institut Curie, UMR 144, 26 rue d'Ulm, 75248 Paris, Cedex 05, France. Current addresses: [3]Institute Curie, Department of Genetics and Developmental Biology (U934/UMR3215), 26 rue d'Ulm, 75248 Paris, Cedex 05, France; [4]Medical Research Council, Laboratory for Molecular Cell Biology and Cell Biology Unit, Department of Anatomy and Developmental Biology, University College London, Gower Street, London, WC1E 6BT, United Kingdom; [5]Cancer Research UK, London Research Institute, 44 Lincoln's Inn Field, London, WC2A 3PX, United Kingdom.
[6]These authors contributed equally to this work.
[7]Correspondence should be addressed to J.-R.H. (e-mail: jean-rene.huynh@curie.fr)

Received 14 November 2008; accepted 10 February 2009; published online 10 May 2009; DOI: 10.1038/ncb1874

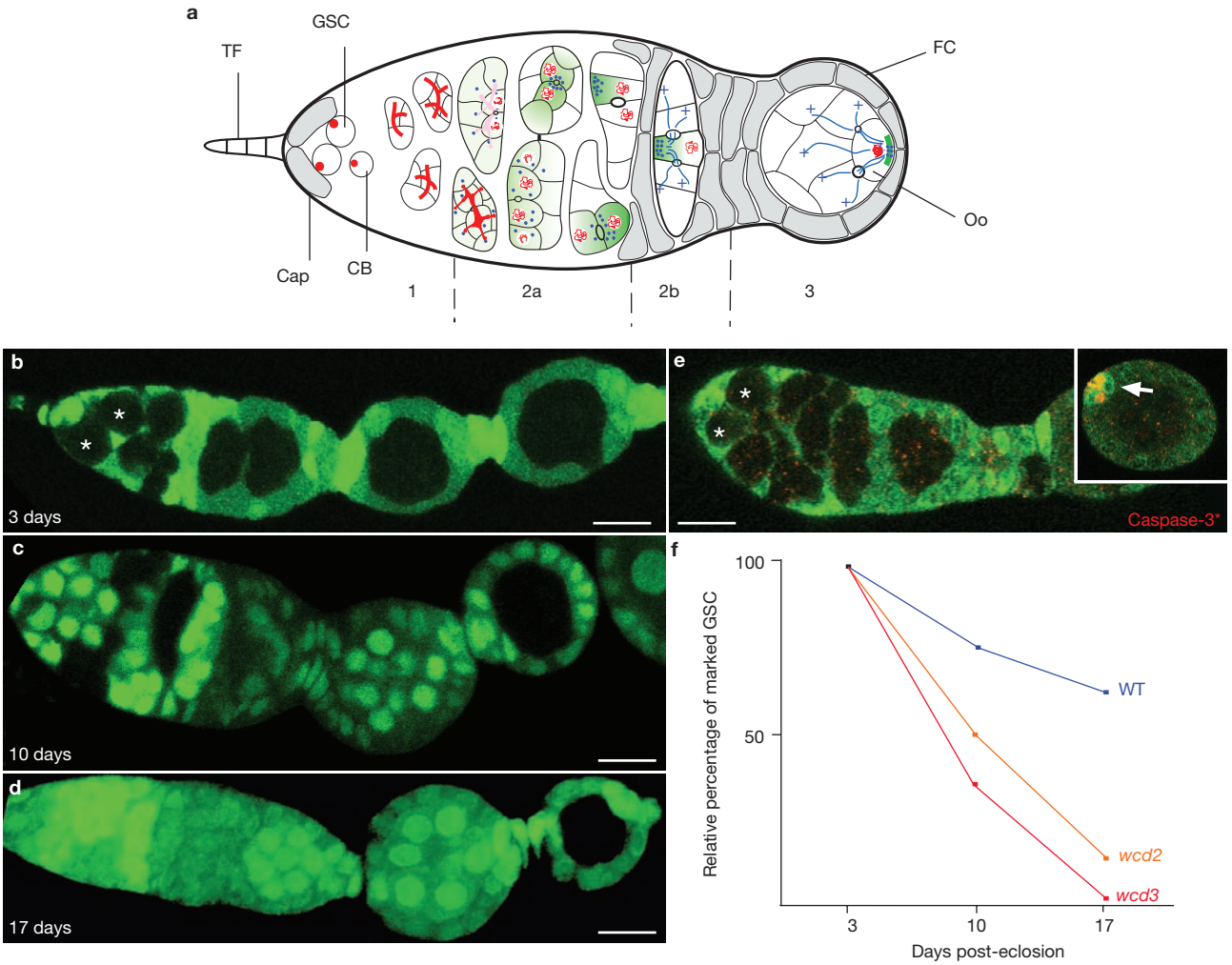

Figure 1 *Wcd* is required for GSC self-renewal. (**a**) *Drosophila* early oogenesis. An egg chamber comprises 16 germline cells surrounded by follicle cells (FC). The germarium is divided into 4 regions along the anterior–posterior axis (1, 2a, 2b, 3). GSCs reside at the tip of the germarium (left) in a microenvironment created by cap cells (Cap) and terminal filament cells (TF). GSCs produce cytoblasts, which divide four times and generate germline cysts of 16 cells connected by ring canals. The GSCs and cystoblasts contain a spectrosome (red circles), which develops into a branched fusome orienting cystoblast divisions. In region 2a, the synaptonemal complex (SyC, red lines) forms in the 2 cells with 4 ring canals (the pro-oocytes) as they enter meiosis. The SyC then appears transiently in the 2 cells with 3 ring canals, before becoming restricted to the pro-oocytes. By region 2b, the oocyte (Oo) is selected, and is the only cell to remain in meiosis. In region 2a, cytoplasmic proteins, mRNAs, mitochondria (green) and centrosomes (blue circles) accumulate progressively at the anterior of the oocyte. In region 2b, the minus ends of the microtubules are focused in the oocyte, and the plus ends extend through the ring canals into the nurse cells. The follicle cells (grey) start to migrate and surround the germline cells. As the cyst moves to region 3, the oocyte adheres to the posterior follicle cells and repolarizes along its anterior–posterior axis, with the microtubules (MT) minus ends and specific cytoplasmic components now localized at the posterior cortex. (**b**–**e**) *wcd* cells are labelled by the lack of GFP, in green. *wcd* GSCs (asterisks) can frequently be observed 3 days after hatching (**b**) but become rarer and rarer at 10 (**c**) and 17 (**d**) days after hatching. No activated caspase-3 (in red) is observed in *wcd* GSCs (**e**, asterisks). Endogenous apoptosis in polar cells serves as a positive control (arrow). (**f**) Relative percentage of negatively marked GSCs observed at 3, 10 and 17 days after hatching. The loss rate of wcd^2 and wcd^3 GSCs is more pronounced than that of wild-type (WT) GSCs. Scale bars, 10 μm.

described in yeast, its regulation in specific cell types and its involvement in cell differentiation remain unclear in multicellular organisms.

RESULTS

Wcd is essential for GSC maintenance

Screening for mutations affecting early oogenesis with the FLP/FRT system[20], we found one line that showed a marked decrease in the production of mutant clones in aged flies. We named this mutant *wicked*^{1} (wcd^1) because of the severity of the phenotype. We identified and generated two additional alleles (see Methods), wcd^2 and wcd^3, and observed the same phenotype with all three mutations. To test the involvement of *wcd* in GSC self-renewal, we generated negatively labelled wild-type or *wcd* GSCs and compared their rates of loss (Fig. 1b). We observed a gradual decrease of negatively labelled WT GSCs, reflecting their described half-life (Fig. 1f, Table 1). In contrast, the rate of loss of *wcd* GSCs was much more pronounced: after seventeen days, *wcd* GSCs were recovered in 2.8% of wcd^2 ($n = 355$) and in 0.4% of wcd^3 mosaic germaria ($n = 233$) (Fig. 1b–d, f). This loss of mutant GSCs could have been caused by increased cell death or premature differentiation. To distinguish between these possibilities, we used markers of apoptosis in *wcd* GSCs and did not detect DNA fragmentation or activation of caspase-3 ($n = 58$; Fig. 1e), indicating that GSC loss was not the result of apoptosis. Instead, our data

Table 1 Marked GSC clones

Genotypes	3 days	10 days	17days
Wild type *(FRTG13)*	21.5%/100% (265)	16.1%/75% (380)	12.2%/58% (287)
wcd^{2}	17.8%/100% (157)	9.1%/51% (395)	2.8%/16% (355)
wcd^{3}	17.4%/100% (149)	6.1%/35% (396)	0.4%/2% (233)

Data are expressed as the percentage of germaria with at least one GFP-negative stem cell over the percentage of germaria normalized at the first time-point. The numbers in parentheses are the total numbers of germaria scored for each time-point.

indicate that *wcd* GSCs differentiated prematurely. *Wcd* thus seems to be essential in the balance between GSC self-renewal and differentiation.

Wcd encodes the *Drosophila* homologue of UTP18, a conserved nucleolar protein

We mapped the *wcd*^{1} mutation to a substitution from Asp to Val in position 277 of the *l(2)k07824* gene, herein named *wicked* (Fig. 2a). *Wcd* is a 1.5 kb gene with no intron, encoding an evolutionarily conserved protein consisting of 506 amino acids that is predicted to contain four WD40 repeats (Supplementary Information, Fig. S1a). Its human homologue WDR50 was identified in a proteomics study of nucleoli[21]. The yeast homologue, U3 snoRNA-associated protein18 (UTP18), is part of a large ribonucleoprotein complex required for 18S rRNA biogenesis[22]. We identified and generated two null alleles, *wcd*^{2} and *wcd*^{3} (Fig. 2a; Supplementary Information, Fig. S1c–e). Transgenic lines expressing an RFP::Wcd fusion protein in *wcd*^{2} clones completely rescued GSC self-renewal and germline cyst development (Fig. 2b), confirming the involvement of *wcd* at these steps and showing the functionality of RFP::Wcd. The localization of Wcd was determined using an antibody directed against the amino-terminal half of the protein (Supplementary Information, Fig. S1a–b). Both endogenous Wcd and its GFP/RFP-tagged versions were distributed within the nucleus, although not evenly (Supplementary Information, Fig. S2 shows a comparison of the distributions of endogenous Wcd and GFP/RFP::Wcd expressed in the presence or absence of endogenous protein). Wcd was localized in two nuclear sub-regions where DNA staining was weak or absent, both in germ and follicle cells (Supplementary Information, Fig. S2c–e and data not shown). In the oocyte, Wcd was present throughout the germinal vesicle (Supplementary Information, Fig. S2a2). Double-labelling with the nucleolar marker Fib showed perfect colocalization with the main pool of Wcd (Fig. 2d, d′′; Supplementary Information, Fig. S3g1–3), demonstrating that Wcd is nucleolar. However, we found that Wcd did not colocalize with Fib in the Cajal body (Supplementary Information, Fig. S3g1–3). The second and smaller pool of Wcd colocalized with LSM11 (Fig. 2e, e′′) indicating that it is part of the histone locus body, which contains the U7 small nuclear RNP (snRNP) and the stem-loop binding protein (Slbp), which are both required for the 3′-end cleavage of histone pre-mRNA[23–25]. However, in contrast to *wcd* mutations, complete deletions of the U7 snRNA and null mutations in *Slbp* affect only late stages of oogenesis[23,24]. We thus focused on the function of nucleolar Wcd.

Wcd is a functional component of the *Drosophila* U3 sno-RNP required for pre-rRNA maturation.

To test whether Wcd could be part of the U3 snoRNP, we performed immunoprecipitation experiments on ovarian extracts using the Fib antibody. Western blot analysis after immunoprecipitation showed that Wcd is present in a complex with Fib (Fig. 3a). This was confirmed using an anti-Wcd antibody for immunoprecipitation and revealing the presence of Fib within the Wcd-containing complex (Fig. 3b). By contrast, no Fib was detected when immunoprecipitation was carried out using the Wcd pre-immune serum. Wcd and Fib are thus part of a nucleolar complex *in vivo*. To analyse whether the Wcd-containing complex is associated with the U3 snoRNA, we performed similar immunoprecipitation experiments followed by northern blotting using a probe directed against the U3 snoRNA. A specific band the size of U3 was observed after immunoprecipitation with the anti-Wcd antibody, indicating that Wcd is part of the U3 snoRNP (Fig. 3c). Following the same approach using a probe directed against the first ITS of the pre-rRNA, we observed that the pre-rRNA can also be found in a complex with Wcd, consistent with a role in its maturation (Fig. 3c). To test this, we treated S2 cells with dsRNA directed against the first half of the *wcd* mRNA, which resulted in efficient knockdown (Fig. 3e). We then performed northern blot analysis using probes directed against regions within the ETS, ITS1, ITS2, 18S and 28S sequences of the pre-rRNA (Fig. 3f and data not shown). The sequential cleavages of the pre-rRNA led to a series of intermediates, designated a–e (Fig. 3d); two alternative processing pathways, A and B, have been described previously[26]. We observed an accumulation of the long form of the pre-rRNA in *wcd* RNAi treated cells compared with the control (Fig. 3f), indicating defects in the early maturation steps. We also noticed a decrease in the amounts of intermediate b and an accumulation of intermediate d (Fig. 3f). These results strongly suggest that Wcd is required for cleavage 2 and/or 3 of processing pathway A. They also support the hypothesis that, when pathway A is compromised, maturation occurs through pathway B[27]. Together these experiments show that Wcd is a functional component of the U3 snoRNP required for pre-rRNA maturation.

A fraction of Wcd forms particles segregating asymmetrically into the GSCs and pro-oocytes

This general function of Wcd contrasts with its specific requirement for GSC self-renewal. To investigate this paradox, we studied the localization of Wcd during divisions of GSCs and germline cysts. Surprisingly, in metaphase Wcd concentrated as one or more bright cytoplasmic dots that segregated into the future stem cell during anaphase (Fig. 4a–d). We observed the same behaviour on fixed samples expressing Wcd::GFP (Fig. 4a, a′) or the endogenous Wcd (n = 20, Fig. 4b; Supplementary Information, Fig. S3b–f). To further analyse the distribution of Wcd during mitosis, we devised an experimental set-up to image dividing GSCs within their niche *ex vivo* (see Methods). Upon nuclear envelope breakdown, bright dots of Wcd formed and moved to the metaphase plate on the side of the future GSC and then preferentially segregated into the GSC (n = 6, Fig. 4c1–3, d1–3; Supplementary Information, Movies 1, 2). Smaller dots localizing in the cytoblast were also visible. Fluorescence of Wcd::GFP in particles in the GSC and in the cytoblast was measured and the ratio of these quantities calculated: 7 (6.9 ± 2.5) times more particles segregated into the GSC than into the cytoblast (Supplementary Information, Fig. S4a). However, these particles represent only a fraction

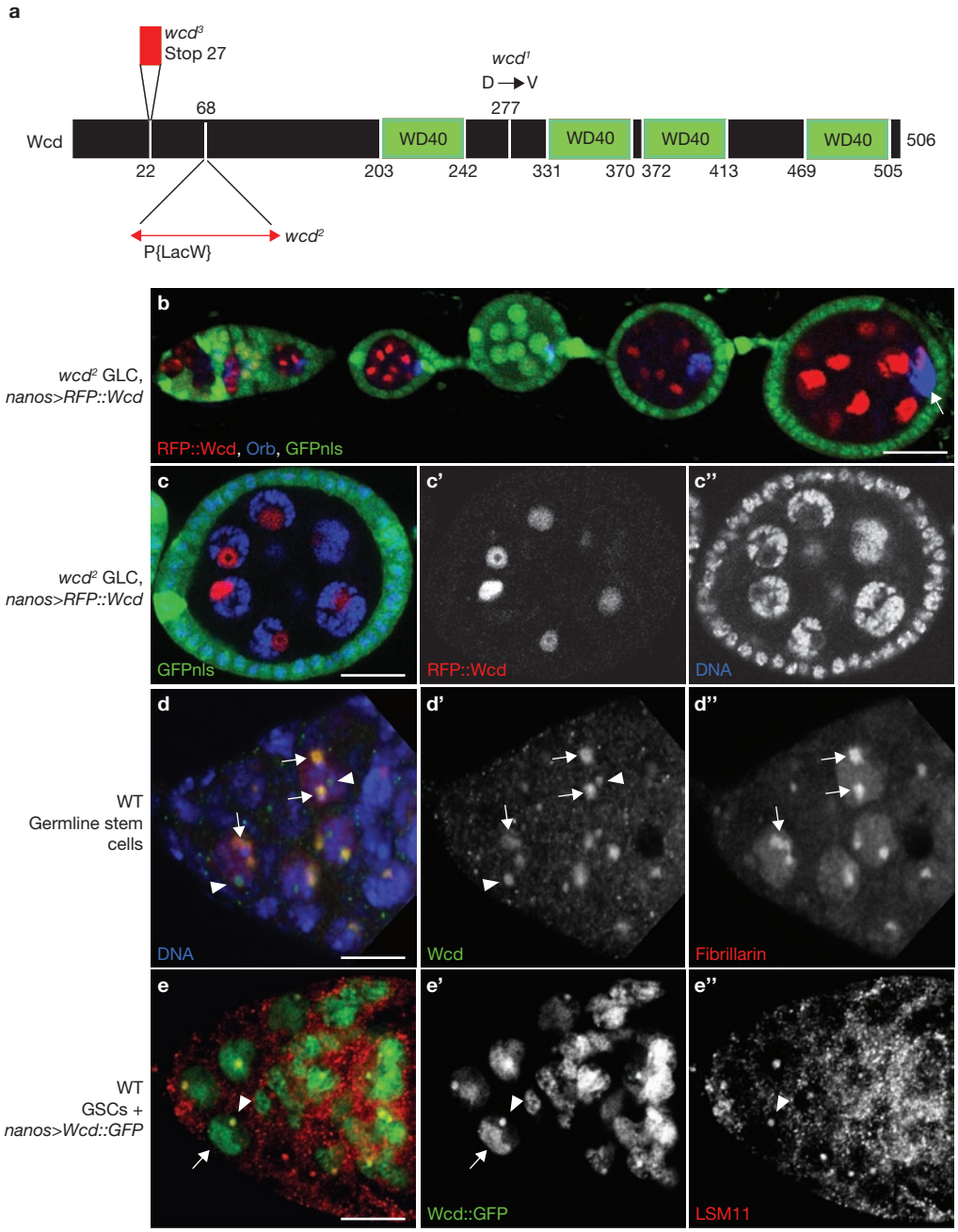

Figure 2 *Wcd* encodes a nucleolar protein containing four WD40 motifs. (**a**) Schematic representation of the Wcd protein (black bar). The *wcd*^{1} mutation leads to an amino acid substitution (Asp to Val) in position 277. The *wcd*^{2} mutation corresponds to a lethal transposable element insertion 68 base pairs downstream of the start site. The *wcd*^{3} mutation results from the imprecise excision of this transposable element, which leads to the presence of a stop codon at position 27. (**b**, **c**) *wcd*^{2} mutant cells are labelled by the lack of GFP, in green. The expression of RFP::Wcd, in red, was driven within *wcd*^{2} germline clones (GLC) using *nanos*–GAL4. (**b**) Expression of RFP::Wcd leads to a complete rescue of the growth phenotype. In addition, Orb, in blue, is correctly relocalized to the posterior of the oocyte (arrow). (**c**, **c**′′) RFP::Wcd (red in **c** and white in **c**′) accumulates in nuclear regions where the DNA staining (blue in **c** and white in **c**′′) is weak or absent. (**d**–**d**′′) The endogenous Wcd protein is green in **d** and white in **d**′. The nucleolar marker Fib is red in **d** and white in **d**′′. Fib overlaps perfectly with the main pool of Wcd (arrows) but a small fraction of Wcd resides in another nuclear sub-compartment (arrowheads). (**e**–**e**′′) Wcd–GFP is green in **e** and white in **e**′. The HLB marker LSM11 is red in **e** and white in **e**′′. The main pool on Wcd::GFP is nucleolar (arrow), whereas the small pool of Wcd::GFP colocalizes with LSM11 (arrowhead). Scale bars, 20 μm (**b**, **c**) and 4 μm (**d**, **e**)

of the total amounts of Wcd::GFP (Supplementary Information, Fig. S5b). As GSCs and cytoblasts have similar sizes immediately after mitosis[14], the ratio of the total amounts of Wcd::GFP in the GSC and cytoblast is marginally above 1 (Supplementary Information, Fig. S4c), although the localization of Wcd::GFP is clearly asymmetric.

We further found that Wcd forms particles segregating preferentially into the two pro-oocytes during germline cyst divisions (Wcd::GFP in Fig. 4e1–4, f1–3; Supplementary Information, Movies 3, 4; endogenous Wcd in Supplementary Information, Fig. S3b1, 2). Our live-imaging analysis demonstrates that a pool

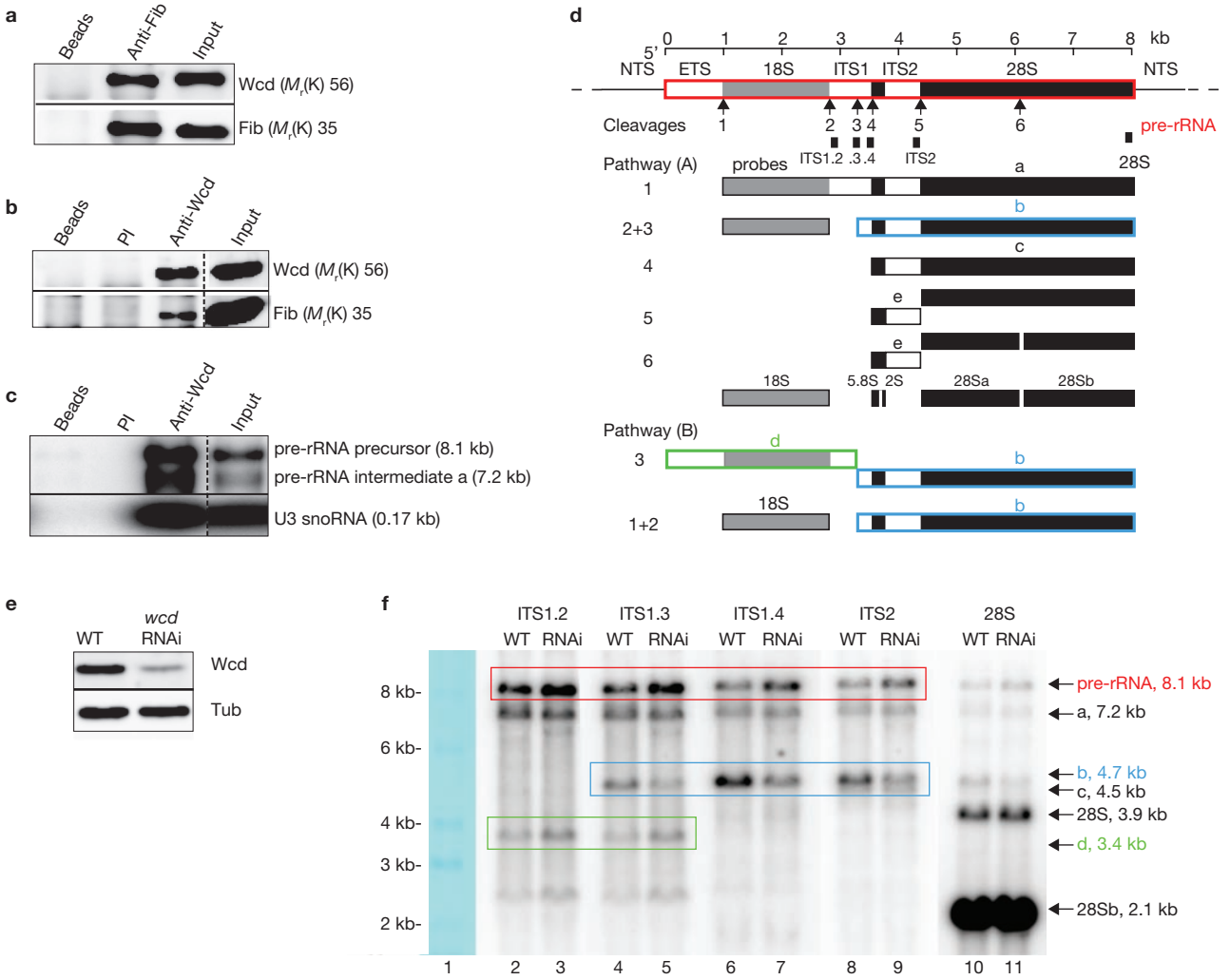

Figure 3 Wcd is a functional component of the U3 snoRNP required for pre-rRNA maturation. (**a**–**c**) Immunoprecipitation performed on ovarian extracts using anti-Fib (**a**) or anti-Wcd antibodies (**b**, **c**). PI, pre-immune serum. Wcd and Fib can be specifically co-immunoprecipitated (**a**, **b**). Western-blot analysis of the immunoprecipitate using anti-Wcd (upper panel) or anti-Fib (lower panel) antibodies. Northern-blot analysis of the immunoprecipitate using a radiolabelled probe directed against the pre-rRNA (**c**, top panel) or against the U3 snoRNA (**c**, bottom lane). A complex containing Wcd, the pre-rRNA and the U3 snoRNA can be specifically co-immunoprecipitated using anti-Wcd antibody (bottom lane). Data in the upper and lower gels (**a**, **b**) and top and middle panels (**c**) are from two different gels. Dashed lines in **b** and **c** indicate that lanes from the same gel have been juxtaposed. (**d**) Schematic representation of the pre-rRNA processing pathways A and B (adapted from Long and Dawid[26]). The top line shows the structure of the pre-rRNA; the ETS and ITS are shown in white, the 18S subunit in grey and the 5.8S, 2S and 28S subunits in black. The cleavage sites are numbered from 1 to 6. The different maturation intermediates indicated by the letters a–e. The probes used for northern blot analysis are represented as black boxes. (**e**) Western blot analysis of *wcd* RNAi-treated S2 cells, using anti-Wcd antibody (upper panel) or anti-tubulin (Tub) antibody (lower panel). *wcd* RNAi treatment resulted in an efficient and specific knockdown of Wcd (compare wild-type (WT) cells, left lane, with RNAi treated cells in the right lane. (**f**) Northern blot analysis of *wcd* RNAi-treated S2 cells using the probes described in **d**. Arrows on the right highlight the pre-rRNA and the different maturation intermediates. Knockdown of Wcd leads to an increase in the amount of pre-rRNA (compare lanes 3, 5, 7, 9 with lanes 2, 4, 6, 10), an increase in the amount of the intermediate d (compare lanes 3 and 5 with lanes 2 and 4) and a decrease in the amount of intermediate b (compare lanes lanes 5, 7, 9 with lanes 4, 6, 8). The 28S probe served as an internal loading control. Full gel scans for **a**–**c**, **e** and **f** can be seen in Supplementary Information, S7.

of Wcd forms asymmetrically segregating particles during the GSC and germline cyst mitosis and reveals an intrinsic asymmetry of the GSC division.

Wcd asymmetric localization is independent of the Dpp signal

The asymmetric outcome of the GSC division is controlled mainly by Dpp, which is secreted by the niche and promotes GSC fate[28–30]. Accordingly, overactivation of the Dpp pathway induces an overproliferation of GSCs or GSC-like cells in 'stem cell tumours' filling up the germarium. To test whether the asymmetric distribution of Wcd depends on the Dpp pathway, we expressed an activated form of the Dpp receptor Thickveins (Tkv) in the GSCs[29,31]. Germaria were filled with single cells dividing away from the niche with random orientations (Fig. 5a). Our movies showed that Wcd::GFP was still segregating into only one of the two daughter cells ($n = 8$, Fig. 5d1–3; Supplementary Information, Movies 5, 6). This asymmetry was not undirected as Wcd::GFP always localized into the cell retaining the original spectrosome: 10.5 ± 5.5 times more Wcd::GFP segregated into that cell ($n = 22$, Fig. 5b, c; Supplementary Information, Fig. S4a), representing

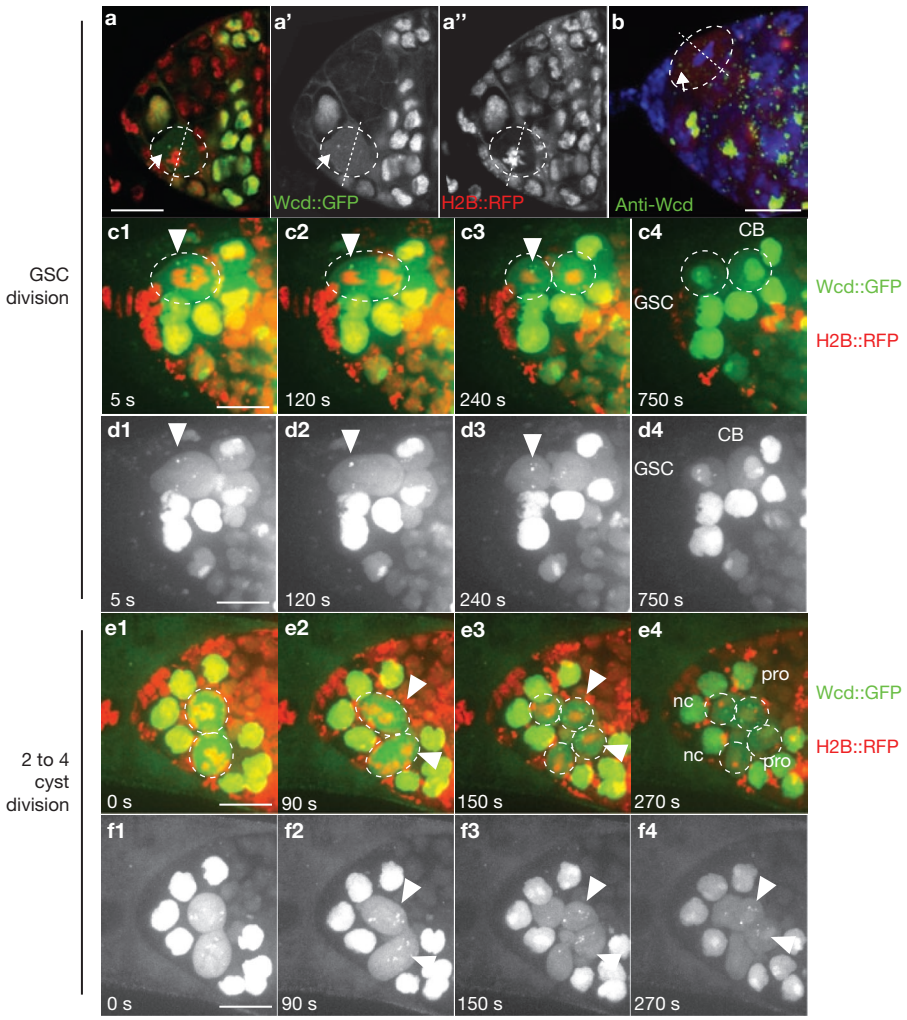

Figure 4 Wcd is asymmetrically segregated upon GSC mitosis. (**a**, **c**, **e**) Wcd::GFP is in green. The DNA marker histoneH2B::RFP (H2B::RFP) is in red. The dividing GSC is highlighted by a white dashed circle (**a**–**c**) and the orientation of the metaphase plate is indicated by a white straight dashed line (**a**, **b**). Wcd::GFP forms a dot upon GSC division (arrow), which is located on the side of the future GSC (**a**). Single channels are shown for Wcd::GFP (**a**′) and H2B::RFP (**a**′′). (**b**) Wcd is in green and DAPI staining is in blue. The endogenous Wcd protein also segregates asymmetrically as a dot upon GSC division (arrow), which is located on the side of the future GSC. (**c**, **d**) *Ex-vivo* imaging of GSC division. Time (s) is indicated at the bottom left of each panel. The Wcd::GFP channel is shown on its own in **d**. Soon after nuclear envelope breakdown, Wcd::GFP forms a bright dot (arrowhead) that segregates into the new GSC. Once the two daughter cells have re-formed, the dot relocalizes to the nucleus of the GSC and cytoblast. (**e**, **f**) *Ex-vivo* imaging of germline cyst division, which leads to the formation of a four-cell cyst. The dividing cyst is highlighted by a white dashed line (**e**). The Wcd::GFP channel is shown on its own in **f**. Soon after nuclear envelope breakdown, Wcd::GFP forms several bright dots that are preferentially segregated into two of the four daughter cells (arrowheads), which we identify as the two pro-oocytes (pro) based on their positions. nc: nurse cells. Scale bars, 4 μm.

3 ± 1.6% of the total amounts of Wcd::GFP. Therefore, although the outcome of division is symmetric in terms of fate, the mitosis itself is asymmetric regarding the spectrosome and the distribution of Wcd::GFP[32].

Wcd particles segregate asymmetrically into neural stem cells and are required for stem cell growth

Overall, Wcd distribution is similar to the partially (as opposed to all or nothing) asymmetric behaviour of the fusome during GSC and cyst divisions in wild-type and mutant conditions. To test whether the asymmetric segregation of Wcd is germline-specific or whether it occurs in other cell types, we analysed Wcd dynamics during neural stem cell (NSC) divisions, which are well-characterized asymmetric divisions with no fusome[33]. Larval neuroblasts are NSCs generating dozens of neurons in the fly central nervous system after repeated rounds of self-renewing asymmetric divisions during which a new neuroblast and a smaller ganglion mother cell (GMC) are generated. The GMC divides once more to produce two ganglion cells. *Ex-vivo* imaging of neuroblast division revealed dots of Wcd::GFP reproducibly segregating into the neuroblast (13/16, Fig. 6a1–3; Supplementary Information, Movies 7, 8). The dots formed during early anaphase, later than in the GSCs, and had segregated into neuroblasts by telophase. Five (5.38 ± 3.3) times more particles of Wcd::GFP segregated into neuroblasts than into GMCs (Supplementary Information, Fig. S4a), representing 1.4 ± 1% of the total amount of Wcd::GFP (Supplementary Information, Fig. S4b). Similar temporal and spatial behaviour was found for the endogenous protein (Supplementary Information, Fig. S3d1, 2). Wcd also segregated asymmetrically during mitosis of the precursor cell of the bristle lineage (pI cell), albeit infrequently (2/19, Supplementary Information, Fig. S5, Movie 9). These results show that Wcd can localize

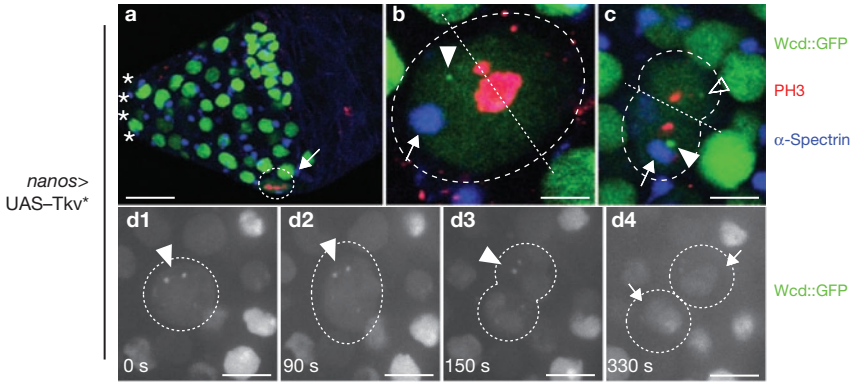

Figure 5 Asymmetric segregation of Wcd is independent of the Dpp signal. (**a**–**d**) Overexpression of activated Tkv under the control of the *nanos*–GAL4 driver. The mitotic marker phospho-histoneH3 (PH3) is in red and the spectrosome marker α-Spectrin is in blue (**a**–**c**). The orientation of the metaphase plate is indicated by a white straight dashed line (**b**, **c**). A GSC-like cell (highlighted by a white dashed circle) dividing at a distance from the niche (**a** arrow). Asterisks highlight the niche cells. Metaphase (**b**): Wcd::GFP segregates asymmetrically upon GSC-like cell division (arrowhead), together with the spectrosome (arrow). Anaphase (**c**): asymmetric segregation of Wcd::GFP as a dot (arrowhead) together with the spectrosome (arrow). A smaller dot of Wcd::GFP also segregates into the other daughter cell (empty arrowhead). *Ex-vivo* imaging of GSC-like division (**d**). Dots of Wcd::GFP form soon after entry into mitosis (arrowheads) and disappear in late telophase when the nuclei of the daughter cells re-form (arrows). Scale bars, 5 μm (**a**), 0.5 μm (**b**) and 0.7 μm (**c**, **d**)

asymmetrically in the absence of a fusome. More importantly, the unequal segregation of a U3snoRNP component is a conserved feature in germ and neural cells. Furthermore, Wcd segregates into the larger and/or self-renewing cell in all cases.

We analysed the requirement of *wcd* in ventral nerve cord neuroblasts using the MARCM system[34] (Fig. 6b, c). We found that *wcd* neuroblasts sequentially produced early-born Chinmo$^+$ ganglion cells and late-born Br-C$^+$ ganglion cells[35] (Supplementary Information, Fig. S6). However, *wcd* neuroblasts generated only half the number of ganglion cells produced by wild-type NSCs ($n = 20$; Fig. 6d). To test whether this reduction reflected an increase in cell death, we performed activated caspase-3 stainings and found no difference between *wcd* and wild-type clones (data not shown). We also expressed the inhibitor of apoptosis p35 (ref. 36) in wild-type and mutant MARCM clones and found that *wcd* neuroblasts still generated about half the number of ganglion cells produced by wild-type neuroblasts ($n = 22$; Fig. 6d). We then investigated whether this phenotype was associated with changes in neuroblast size by measuring the volume of wild-type and mutant neuroblasts. On average, *wcd* neuroblasts were half the size of wild-type neuroblasts ($n = 20$, Fig. 6e). Wcd is thus required for NSC proliferation and growth.

DISCUSSION

We identified *wcd* as a *Drosophila* gene required for stem cell self-renewal. We characterized its molecular function and validated our results *in vivo* in a multicellular organism. Live-imaging of single stem cells and analysis of fixed samples revealed asymmetric segregation of Wcd particles upon mitosis both in GSCs and NSCs. Overall, our results show that the regulation of cell size by ribosome synthesis is an important parameter for stem cell maintenance and function.

Large and/or rapidly dividing stem cells face the challenge of sustaining a high growth rate to maintain their size and function over long periods of time. They must, therefore, be particularly sensitive to mutations that decrease ribosome production, such as *wcd*. Their growth must also be tightly regulated, as mutations that increase ribosome biogenesis can cause stem cells to overproliferate and form tumours[37]. For example, mutations in the *brat* gene induce overproliferation of certain NSCs and the formation of tumours in *Drosophila* brain[38–41]. Brat was shown to repress growth by acting in part through the repression of ribosome biogenesis[40,42]. Interestingly, Brat segregates asymmetrically into pIIb cells and GMCs during divisions of pI cells and NSCs, respectively, which is opposite to Wcd in both cases. Similarly, mutations in the *brat* homologue *mei-P26* generate tumours specifically in the germarium[43]. Mei-P26 expression is low in GSCs and high in differentiating germline cysts, where it restricts growth[14]. In the absence of *Mei-P26*, cystocytes grow abnormally and fail to differentiate. The current model is that *brat* and *mei-P26* regulate cell and nucleolus size in stem cell lineages by inhibiting ribosome biogenesis in the differentiating daughter cells[14]. Our results suggest a twofold process in which ribosome formation is decreased in the smaller differentiating cell and increased in the larger and/or self-renewing cell.

An alternative possibility is that Brat, Mei-P26 or Wcd may associate with cell-type-specific ribosomal proteins or ribosome biogenesis pathways performing specialized functions, as shown in yeast[44]. Support for this hypothesis comes from microarray analysis of female GSCs in *Drosophila*, which showed enrichment in specific isoforms of ribosomal proteins and regulators of ribosome biogenesis[32]. Neither alternative, based respectively on quantitative or qualitative differences in the ribosome biogenesis pathway, is exclusive.

Is the asymmetric segregation of Wcd responsible for differential growth? To address this question, we overexpressed Wcd in the germline and nervous system, but did not observe any phenotype, suggesting that overexpression of Wcd is insufficient to induce overgrowth (data not shown). However, there are several explanations for this result, limiting the interpretation of this kind of experiment. First, although Wcd is required for growth, it is probably not an essential limiting factor as mutant GSCs and NSCs were observed several days after the loss of *wcd*. Second, the localization of Wcd is not an all-or-nothing asymmetry as is the segregation of Numb in the nervous system[45]. Wcd is expressed in every cell and only a small fraction of Wcd segregates preferentially into the stem cell during mitosis (Supplementary Information, Fig. S4b). Third, even if Wcd levels were increased in the cystoblast/GMC, endogenous Mei-P26

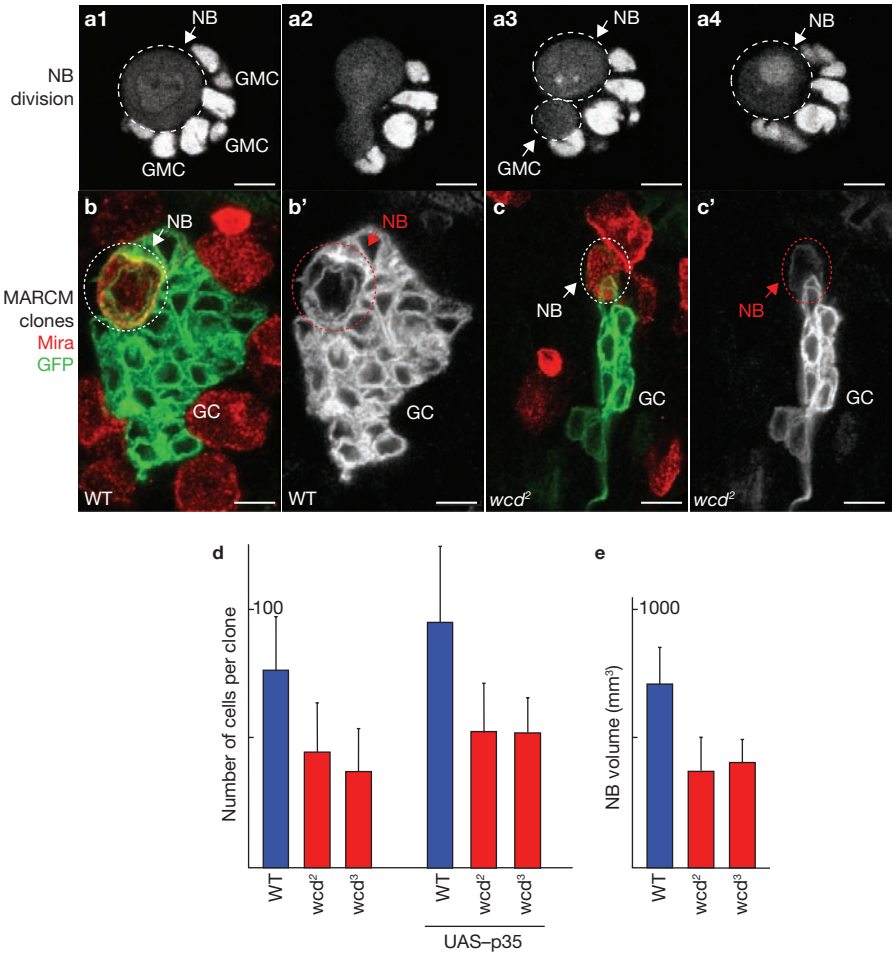

Figure 6 Wcd is asymmetrically segregated upon neuroblast division in the larval central nervous system and is required for neural stem cell proliferation and growth. (**a**) Wcd::GFP is in white. (**b**, **c**) Membrane-associated GFP positively labels the clones in green. The neuroblast (NB) marker Miranda (Mira) is shown in red. (**a**) An *ex-vivo* NB (indicated by an arrow) with several of its daughter ganglion mother cells (GMCs). Wcd::GFP forms two large dots (**a3**, arrowhead), which are inherited asymmetrically by the NB (white circle). The nucleolus then re-forms at telophase (**a4**). (**b**) A GFP-labelled wild-type (WT) NB, (white circle) and part of its progeny (GC). (**b**′) GFP channel. (**c**) A GFP-labelled *wcd*^{2} NB and part of its progeny (GC). (**c**′) GFP channel. (**d**, **e**) *wcd* mutant NBs produce fewer GCs (**d**) and are smaller (**e**) than WT NBs. (**d**) Average number of GCs observed in WT (blue bar) and *wcd* mutant clones (red bars) when apoptosis can occur (**d**, left panel, $n = 20$) or when apoptosis is inhibited by overexpression of the caspase inhibitor p35 (UAS–p35, **d**, right panel, $n = 22$). (**e**) Measurement of the volume of WT (blue bar) and *wcd* mutant (red bars) NBs ($n = 20$). Data are mean ± s.d.; scale bars, 10 μm.

and Brat would still be present and repress ribosome synthesis[14,40]. Overall, we have shown that Wcd is required for stem cell maintenance; however, whether its asymmetric localization has an instructive role is unclear and difficult to test experimentally. Nevertheless, our work and other studies published recently[14,40] support the idea that differential ribosome biogenesis *per se* regulates asymmetric growth and self-renewal in stem cell lineages. There is a clear correlation between Wcd, Brat and Mei-P26 distribution and cell size. Wcd segregates into the larger GSC, NSC and pIIa cell. In contrast, Brat localizes into the smaller GMC and pIIb cell[38–41]. Similarly, Mei-P26 is highly expressed in the small cystocytes and at low levels in the larger GSCs[14]. Finally, Wcd does not form particles and is partitioned equally in symmetrically dividing follicle cells (Supplementary Information, Fig. S3h1–3, Movie 10). Increasing ribosome biogenesis is sufficient to induce differentiating cells to form tumours. In *brat* and *mei-P26* mutants, the nucleolus enlarges, suggesting an increase in ribosome formation[40]. Consequently cells overgrow and fail to exit the cell cycle and to differentiate, leading to the formation of tumours. Decreasing ribosome biogenesis triggers premature stem cell differentiation: the absence of Wcd induces severe rRNA maturation defects and leads to the differentiation of GSCs. Similarly, overexpression of Mei-P26 reduces nucleolus size and triggers stem cell loss[14,40].

Another question arising from our work is whether the differential segregation of Wcd is a cause or a consequence of the asymmetry of stem cell division. In the germline, the main source of asymmetry is the Dpp signal sent by the niche, and expression of activated Tkv is sufficient to transform the asymmetric GSC division into one producing two identical GSCs or GSC-like cells[29,31]. Under these conditions, Wcd and the spectrosome co-segregated preferentially into one cell, demonstrating that their asymmetric distribution is independent of Dpp signalling. This reveals an intrinsic asymmetry of GSC or GSC-like divisions independent of the niche's signals and adhesion. It also shows that artificially activating the Dpp pathway is sufficient to induce both daughter cells to become GSCs, regardless of the spectrosome and Wcd asymmetry. This suggests that the extrinsic signals from the niche have a primary influence over intrinsic factors on cell fate in the ovary. This

conclusion may also hold true under specific wild-type conditions, as the fusome is still unequally partitioned when a GSC divides perpendicular to the anterior-posterior axis so that both daughter cells remain in the niche and become stem cells[9].

Better understanding of stem-cell-driven regeneration is likely to arise from live-imaging of single stem cells within their microenvironment over long periods of time, with a good spatial and temporal resolution[46]. We show the possibility of maintaining and imaging *ex vivo* the entire ovarian niche for several hours. This has allowed us to uncover a transient asymmetry in the segregation of Wcd, which would have been difficult to detect in fixed tissues. We believe that this technique will allow new questions to be addressed and, together with a combination of genetic and biochemical approaches, will help uncover essential processes underlying the extraordinary properties of stem cells.

METHODS

Methods and any associated references are available in the online version of the paper at http://www.nature.com/naturecellbiology/

Note: Supplementary Information is available on the Nature Cell Biology website.

ACKNOWLEDGMENTS

We are especially grateful to Danièle Hernandez-Verdun, Bruno Bello, Frank Hirth, Andrew Vaughan and the Imaging facilities at IJM for experimental advice; to Danièle Hernandez-Verdun, Acaimo Gonzalez-Reyes, Antoine Guichet, Juliette Mathieu, Emily Richardson and Ralph Neumuller for critical reading. We are also grateful for reagents provided by Danièle Hernandez-Verdun, Joe Gall, Acaimo Gonzalez-Reyes, Fumio Matsuzaki, Christophe Antoniewski, Antoine Guichet, Christian Lehner, Alex Gould, Tzumin Lee, Barry Thompson, DHSB (Iowa University) and Bloomington *Drosophila* Stock center. We wish to thank Franck Pichaud (MRC-LMCB, UCL) in whose lab part of this work was performed. This work was funded by grants to J.R.H. (CNRS, ARC # 3802, and ANR # 06-JCJC-0092-01), P.F. (ARC post-doctoral fellowhip and EMBO long term fellowship), CM (CNRS), J.A.L. (CNRS, ARC# 3802) Ch.M. and Y.B. (CNRS, Curie).

COMPETING FINANCIAL INTERESTS

The authors declare no competing financial interests.

Published online at http://www.nature.com/naturecellbiology/
Reprints and permissions information is available online at http://npg.nature.com/reprintsandpermissions/

1. Birnbaum, K. D. & Sanchez Alvarado, A. Slicing across kingdoms: regeneration in plants and animals. *Cell* **132,** 697–710 (2008).
2. Morrison, S. J. & Spradling, A. C. Stem cells and niches: mechanisms that promote stem cell maintenance throughout life. *Cell* **132,** 598–611 (2008).
3. Gilboa, L. & Lehmann, R. How different is Venus from Mars? The genetics of germ-line stem cells in *Drosophila* females and males. *Development* **131,** 4895–4905 (2004).
4. Wong, M. D., Jin, Z. & Xie, T. Molecular mechanisms of germline stem cell regulation. *Annu. Rev. Genet.* **39,** 173–195 (2005).
5. Song, X. & Xie, T. DE-cadherin-mediated cell adhesion is essential for maintaining somatic stem cells in the *Drosophila* ovary. *Proc. Natl Acad. Sci. USA* **99,** 14813–14818 (2002).
6. Xie, T. & Spradling, A. C. Decapentaplegic is essential for the maintenance and division of germline stem cells in the *Drosophila* ovary. *Cell* 94**,** 251–260 (1998).
7. Fichelson, P. & Huynh, J. R. Asymmetric divisions of germline cells. *Prog. Mol. Subcell. Biol.* **45,** 97–120 (2007).
8. Deng, W. & Lin, H. Spectrosomes and fusomes anchor mitotic spindles during asymmetric germ cell divisions and facilitate the formation of a polarized microtubule array for oocyte specification in *Drosophila*. *Dev. Biol.* **189,** 79–94 (1997).
9. Xie, T. & A, S. A niche maintaining germline stem cells in the *Drosophila* ovary. *Science* **290,** 328–330 (2000).
10. de Cuevas, M., Lilly, M. A. & Spradling, A. C. Germline cyst formation in *Drosophila*. *Annu. Rev. Genet.* **31,** 405–428 (1997).
11. Huynh, J. R. & St Johnston, D. The origin of asymmetry: early polarisation of the *Drosophila* germline cyst and oocyte. *Curr. Biol.* **14,** R438–449 (2004).
12. de Cuevas, M. & Spradling, A. C. Morphogenesis of the *Drosophila* fusome and its implications for oocyte specification. *Development* **125,** 2781–2789 (1998).
13. Huynh, J. R. Fusome as a cell–cell communication channel of *Drosophila* ovarian cyst (Landes Biosciences, 2006).
14. Neumuller, R. A. *et al.* Mei-P26 regulates microRNAs and cell growth in the *Drosophila* ovarian stem cell lineage. *Nature* (2008).
15. Rudra, D. & Warner, J. R. What better measure than ribosome synthesis? *Genes Dev.* **18,** 2431–2436 (2004).
16. Frescas, D., Guardavaccaro, D., Bassermann, F., Koyama-Nasu, R. & Pagano, M. JHDM1B/FBXL10 is a nucleolar protein that represses transcription of ribosomal RNA genes. *Nature* **450,** 309–313 (2007).
17. Maaloe, O. & Kjedgaard, N. *Control of macromolecular synthesis*, (W. A. Benjamin, New York, 1966).
18. Boisvert, F. M., van Koningsbruggen, S., Navascues, J. & Lamond, A. I. The multifunctional nucleolus. *Nature Rev. Mol. Cell Biol.* **8,** 574–585 (2007).
19. Matera, A. G., Terns, R. M. & Terns, M. P. Non-coding RNAs: lessons from the small nuclear and small nucleolar RNAs. *Nature Rev. Mol. Cell Biol.* **8,** 209–220 (2007).
20. Xu, T. & Rubin, G. Analysis of genetic mosaics in developing an adult *Drosphila* tissues. *Development* **117,** 1223–1237 (1993).
21. Scherl, A. *et al.* Functional proteomic analysis of human nucleolus. *Mol. Biol. Cell* **13,** 4100–4109 (2002).
22. Dragon, F. *et al.* A large nucleolar U3 ribonucleoprotein required for 18S ribosomal RNA biogenesis. *Nature* **417,** 967–970 (2002).
23. Godfrey, A. C. *et al.* U7 snRNA mutations in *Drosophila* block histone pre-mRNA processing and disrupt oogenesis. *RNA* **12,** 396–409 (2006).
24. Lanzotti, D. J. *et al. Drosophila* stem-loop binding protein intracellular localization is mediated by phosphorylation and is required for cell cycle-regulated histone mRNA expression. *Mol. Biol. Cell* **15,** 1112–1123 (2004).
25. Liu, J. L. *et al.* The *Drosophila melanogaster* Cajal body. *J. Cell Biol.* **172,** 875–884 (2006).
26. Long, E. O. & Dawid, I. B. Alternative pathways in the processing of ribosomal RNA precursor in *Drosophila melanogaster*. *J. Mol. Biol.* **138,** 873–878 (1980).
27. Giordano, E., Peluso, I., Senger, S. & Furia, M. *minifly*, a *Drosophila* gene required for ribosome biogenesis. *J. Cell Biol.***144,** 1123–1133 (1999).
28. Chen, D. & McKearin, D. Dpp signaling silences bam transcription directly to establish asymmetric divisions of germline stem cells. *Curr. Biol.* **13,** 1786–1791 (2003).
29. Casanueva, M. O. & Ferguson, E. L. Germline stem cell number in the *Drosophila* ovary is regulated by redundant mechanisms that control Dpp signaling. *Development* **131,** 1881–1890 (2004).
30. Song, X. *et al.* Bmp signals from niche cells directly repress transcription of a differentiation-promoting gene, bag of marbles, in germline stem cells in the *Drosophila* ovary. *Development* **131,** 1353–1364 (2004).
31. Bolivar, J., Pearson, J., Lopez-Onieva, L. & Gonzalez-Reyes, A. Genetic dissection of a stem cell niche: the case of the *Drosophila* ovary. *Dev. Dyn.* **235,** 2969–2979 (2006).
32. Kai, T., Williams, D. & Spradling, A. C. The expression profile of purified *Drosophila* germline stem cells. *Dev. Biol.* (2005).
33. Betschinger, J. & Knoblich, J. A. Dare to be different: asymmetric cell division in *Drosophila, C. elegans* and vertebrates. *Curr. Biol.* **14,** R674–685 (2004).
34. Lee, T. & Luo, L. Mosaic analysis with a repressible cell marker for studies of gene function in neuronal morphogenesis. *Neuron* **22,** 451–461 (1999).
35. Maurange, C., Cheng, L. & Gould, A. P. Temporal transcription factors and their targets schedule the end of neural proliferation in *Drosophila*. *Cell* **133,** 891–902 (2008).
36. Clem, R. J., Fechheimer, M. & Miller, L. K. Prevention of apoptosis by a baculovirus gene during infection of insect cells. *Science* **254,** 1388–1390 (1991).
37. Al-Hajj, M. & Clarke, M. F. Self-renewal and solid tumor stem cells. *Oncogene* **23,** 7274–7282 (2004).
38. Bowman, S. K. *et al.* The tumor suppressors Brat and Numb regulate transit-amplifying neuroblast lineages in *Drosophila*. *Dev. Cell* **14,** 535–546 (2008).
39. Bello, B., Reichert, H. & Hirth, F. The brain tumor gene negatively regulates neural progenitor cell proliferation in the larval central brain of *Drosophila*. *Development* **133,** 2639–2648 (2006).
40. Betschinger, J., Mechtler, K. & Knoblich, J. A. Asymmetric segregation of the tumor suppressor brat regulates self-renewal in *Drosophila* neural stem cells. *Cell* **124,** 1241–1253 (2006).
41. Lee, C. Y., Wilkinson, B. D., Siegrist, S. E., Wharton, R. P. & Doe, C. Q. Brat is a Miranda cargo protein that promotes neuronal differentiation and inhibits neuroblast self-renewal. *Dev. Cell* **10,** 441–449 (2006).
42. Frank, D. J., Edgar, B. A. & Roth, M. B. The *Drosophila melanogaster* gene brain tumor negatively regulates cell growth and ribosomal RNA synthesis. *Development* **129,** 399–407 (2002).
43. Page, S. L., McKim, K. S., Deneen, B., Van Hook, T. L. & Hawley, R. S. Genetic studies of mei-P26 reveal a link between the processes that control germ cell proliferation in both sexes and those that control meiotic exchange in *Drosophila*. *Genetics* **155,** 1757–1772 (2000).
44. Komili, S., Farny, N. G., Roth, F. P. & Silver, P. A. Functional specificity among ribosomal proteins regulates gene expression. *Cell* **131,** 557–571 (2007).
45. Knoblich, J., Jan, L. & Jan, Y. Asymmetric segregation of Numb and Prospero during cell division. *Nature* **377,** 624–627 (1995).
46. Schroeder, T. Imaging stem-cell-driven regeneration in mammals. *Nature* **453,** 345–351 (2008).

METHODS

Fly strains and genetics. *wcd*^{1} was identified as a second site mutation on a chromosome also mutant for *shotgun*$^{P34-1}$ (DE-cadherin) during a pilot screen for mutations affecting the early steps of oogenesis (M. Jagut, L. Mihaila-Bodart, M. F. Alin, J. A. Lepesant and J. R. Huynh, in preparation). The two mutations were separated by outcrossing with w^{1118}, FRTG13 flies. *wcd*^{1} failed to complement *Df(2R)Exel6063* (Bloomington-7545) and *Df(2R)Exel7142* (Bloomington-7886). P-element insertions in the overlapping region were tested for complementation and the insertion *l(2)k07824* [*wcd*^{2}] inserted in the *CG7989* failed to complement *wcd*^{1}. *wcd*^{2} is a lethal P- element insertion 68 base pairs downstream of the start site (*l(2)k07824*$^{[k07824]}$, Fig. 2a). Given the insertion site, *wcd*^{2} was likely to be a null allele. This was confirmed by *in situ* hybridization and antibody staining in *wcd*^{2} mutant clones (Supplementary Information, Fig. S1c and data not shown). Precise excisions of *l(2)k07824* restored viability. Lethal $w^{-/-}$ excisions were screened by PCR for the presence of a fragment smaller than the wild-type *CG7989* locus. *wcd*^{3} is an imprecise excision of this P-element, resulting in the presence of a stop codon after amino acid 26 and a deletion of the downstream part of the gene (Fig. 2a). *wcd*^{3} is therefore very likely to be another null mutation (Supplementary Information, Fig. S1d, e1–4). The FLP/FRT system was used in combination of GFP for homozygous mutant clones selection. Germline clones were induced by heat-shock for 2 h at 37 °C for 2–3 consecutive days on third instar larvae. The following stocks were used: *y*, *w*, hsFLP12; FRT[G13]-ubiGFPnls; *nanos*–Gal4; H2B::RFP (gift from C. Lehner, University of Zurich, Switzerland); UASp–*tkv** (gift from A. Gonzalez-Reyes, CSIS-Universidad Pablo doe Olavide, Spain); w; *insc*-Gal4/+; *neuralized*^{P72}–Gal4 (ref. 47). To produce wild-type, *wcd*^{2} and *wcd*^{3} MARCM clones, the same number of *y w* hsFLP; FRTG13, *tubP*–GAL80/(CyO,*Act*GFPJMR1); *tubP*–GAL4, UAS–mCD8::GFP/TM6,*Tb,Hu* (gift from B.Bello, BioZentrum, Switzerland) virgins were crossed with the same number of FRTG13, FRTG13-*wcd*^{2} and FRTG13-*wcd*^{3} males respectively. To prevent apoptosis, the same experiments were carried using the following stocks: FRTG13; UAS-p35, FRTG13-*wcd*^{2};UAS–p35, and FRTG13-*wcd*^{3}; UAS–p35. Flies were left laying for 6 h at 25 °C and the egg collection was then kept for 22 h at 25 °C, followed by heatshock for 1 h at 37 °C. The heatshocked population of first instar larvae (aged between 0 and 6 h after hatching) was kept for four days at 25 °C. Wandering third instar larvae were then dissected and antibody staining performed. Quantifications of Wcd::GFP amounts were made using the ImageJ software. Cells were outlined manually and particles were defined as pixels above a threshold of fluorescence intensity. The amount of Wcd::GFP in particles is the sum of all pixel intensities above this threshold in each cell.

The volume of ventral nerve cord neuroblasts was measured using Miranda staining. Three-dimensional reconstructions and measurements were performed using Volocity software. Neuroblasts were first manually outlined at the level of their largest diameter and reconstructed in 3D. Only objects above a background threshold were analysed by the software. A noise-removing filter was applied and only objects bigger than 50 μm^3 were considered. Holes within such objects were filled and the total volume of pixel contained within these objects was measured, reflecting neuroblast size.

Rescue construct and fluorescently tagged proteins. A PCR fragment corresponding to the whole *wcd* cDNA sequence was amplified from the DGRC cDNA clone no. LD16320 using primers 5′-CACCATGAGTTCAGACGAGTCCAG-3′ and 5′-ATAACCCTTGAAGTACTTAAGCCTAAAG-3′ and cloned into the pENTR/D-TOPO Gateway entry vector using the pENTR directional TOPO cloning kit (Invitrogen). The *wcd* cDNA was then transferred to *Drosophila* transgenic expression vectors by LR recombination using the Gateway LR clonase II enzyme mix (Invitrogen). Destination vectors pPRW and pPWG were obtained from Terence Murphy's laboratory *Drosophila* Gateway Vector Collection at Carnegie Institution (http://www.ciwemb.edu/labs/murphy/Gateway%20vectors.html). The two resulting transgenic constructs consist of either mRFP N-terminal tagged (RFP::Wcd) or eGFP C-terminal tagged (Wcd::GFP) Wcd fusion proteins, both under the control of the UASp promoter, allowing GAL4-driven somatic and female germline expression. Transgenic lines were generated by standard methods.

Generation of anti-Wcd antisera. A PCR fragment was amplified from w^{1118} genomic DNA using primers 5′-AGCATGctcgagATGAGTTCAGACGAGTCC-3′ and 5′-cgtgacCTCGAGttaATATGTGGCCCTGTTCAG-3′, which corresponds to the 203 first N-terminal amino acids of Wcd (shown in Supplementary Information, Fig. S1a), thus excluding the WD40 motifs, with *Xho*I sites at both ends and a downstream stop codon. This PCR fragment was inserted at *Xho*I site in-frame into an N-terminal His-tag expression vector pET-16b (Novagen) and the DNA sequence was verified. Recombinant fusion protein expression was induced by IPTG in *Escherichia coli* strain BL21(DE3)pLysS (Invitrogen). The His–Wcd fusion protein was purified under native conditions using nickel-chelate-nitrilotriacetic acid (Ni-NTA) Superflow columns according to the supplier's instructions (Qiagen), followed by dialysis on Centricon YM-10 concentrators (Millipore). The final concentration of recombinant protein was achieved by SDS–PAGE on 12% gels and His–Wcd-containing polyacrylamide gel fragments were cut and used directly for immunization. A standard 3-month immunization protocol was performed by Eurogentec using two rabbits numbered 6011 and 6012. No further purification of the crude polyclonal antisera was needed, as both gave very little cross-immunoreactivity with other *Drosophila* epitopes. Both anti-Wcd antisera were used at a dilution of 1/5,000 for western blots and 1/500 for immunohistochemistry.

Live imaging. Ovaries were dissected in oil (10S, Halocarbon, Sigma). The muscular sheath around each ovariole was removed and germarium were made to stick to coverslips in oil. Germaria were imaged for 30–40 min with an Ultraview spinning disk (CSU10) operated by Metamorph on an inverted Leica DM IRBE microscope.

Larval NSCs. Third-stage larvae brains were obtained from larvae of the following genotype: w; *insc*-Gal4/+; UAS-*wcd*::GFP/+. Larval brains were dissected in dissection buffer (NaCl 136 mM, KCl 2.6 mM, NaH2PO4 0.36 mM, NaHCO3 12mM, glucose 5 mM in 100 ml water). The brains were dissociated in 0.2 mg ml^{-1} collagenase and washed in M3 medium. The neuroblasts were transfered to a chamber containing feeding buffer (Schneider's medium, 10% FCS, 5% fly extract, 1% penicillin/streptomycin, 1 mg ml^{-1} glucose, 5 $\mu g\ ml^{-1}$ insulin) and imaged. Images were acquired on an inversed LSM510 Zeiss confocal at 22 °C. SOP (pI cell) were imaged as described previously[48].

Co-immunoprecipitation. These experiments were performed with 50 µl of nProtein A Sepharose 4 Fast Flow (GE Healthcare) per experimental condition. Beads were first equilibrated by three 15-min washes in RIPA buffer (50 mM Tris-HCl pH 7.4, 2 mM EDTA, 100 mM NaCl, 0.5% IGEPAL CA-630 (Sigma), 10% glycerol, Complete EDTA-free protease inhibitor cocktail (Roche), phosphatase inhibitor cocktail set II (Calbiochem) and 200 units ml^{-1} RNasin RNase inhibitor (Promega)), and then incubated for 1 h at 4 °C in blocking buffer (RIPA buffer supplemented with 10% bovine serum albumin), followed by three more washes in RIPA buffer. Ovaries from 50 adult w^{1118} females per experimental condition were homogenized on ice and lysed for 30 min at 4°C in 300 µl of RIPA buffer. Homogenate was clarified by microfuge centrifugation for 15 min at 4 °C. The lysate was then cleared for 1 h at 4 °C with 50 µl of treated beads to eliminate non-specific direct interactions, and after centrifugation the supernatant was used as input for immunoprecipitation experiments. For Fib immunoprecipitation experiments, the ovarian extract was first incubated with 12 µl of anti-Fib antibody (ab5821, Abcam) overnight at 4 °C on a shaking table, before adding beads for another 4-h incubation. For Wcd immunoprecipitation experiments, beads were first incubated for 4 h at 4 °C on a shaking table with 20 µl of anti-Wcd antibody (or 20 µl of the corresponding pre-immune serum as a control), and then briefly washed once in RIPA buffer before adding the ovarian extract for an overnight incubation. In both Fib and Wcd immunoprecipitation experiments, a control with only beads and the ovarian extract (without any antibody) was included. Finally, beads were washed six times with 1 ml of RIPA buffer and then homogenized either in 50 µl of Laemmli buffer for protein extraction or in 1 ml of TRIzol reagent (Invitrogen) for RNA extraction. Each resulting protein or RNA extract was divided into two halves for loading on two gels of western or northern blot respectively.

Western blots. Denatured proteins were fractionated by SDS–PAGE using 10–12% gels and electroransferred to Protran nitrocellulose membranes (Schleicher & Schuell). The membranes were blocked overnight at 4 °C in blocking buffer (PBS buffer supplemented with 0.1% Tween 20 and 5% milk) and then incubated for 2 h in the same buffer containing primary antibodies at the following dilutions: anti-Wcd at 1/5,000 and anti-Fib (Abcam) at 1/500. After three washes in PBS-T

DOI: 10.1038/ncb1874

(PBS buffer supplemented with 0.1% Tween 20), membranes where incubated for 1 h with the secondary antibody in blocking buffer containing a peroxydase-conjugated light-chain-specific anti-rabbit IgG (Jackson Immunoresearch) diluted at 1/10,000. After three washes in PBS-T, bands were detected with the SuperSignal West Pico Chemiluminescent Substrate (Pierce) and visualized using a LAS-3000 Imaging System (Fujifilm).

Northern blots. Total RNAs from wild-type or RNAi-treated S2 cells, co-immunoprecipitation samples or polysome gradient fractions were prepared with TRIzol reagent following the supplier's instructions (Invitrogen). Glycogen (35 µg; MP Biomedicals) was added as a carrier for RNA precipitation of all co-immunoprecipitation samples and polysome gradient fractions. Denatured RNA samples were run overnight on either 1% (in the case of high molecular weight pre-rRNAs) or 2% (in the case of the U3 snoRNA) agarose formadehyde gels in sodium phosphate buffer and were then transferred in 20 × SSC to Hybond N^+ membranes (GE Healthcare). After methylene blue staining, membranes were pre-hybridized for 4 h in 3 × SSC, 0.2% (w/vol) polyvinylpyrrolidone 40, 0.2% (w/vol) Ficoll 400, 1% (w/vol) glycine, 5% (w/vol) polyethylene glycol 6000, 1% (w/vol) SDS and 100 µg $ml^{-1}$of denatured DNA from salmon sperm, before an overnight hybridization under the same conditions. Oligonucleotide probes were labelled at their 5′ ends with g-^{32}P-ATP (GE Healthcare) using T4 polynucleotide kinase (New England Biolabs). DNA fragments used as probes were labelled by random priming with a-^{32}P-dCTP (GE Healthcare) using the Megaprime DNA labelling system (GE Healthcare). All probes were purified on Probe Quant G50 micro-columns (GE Healthcare). Pre-hybridization, hybridization and washing steps were carried out at 42 °C for oligonucleotide probes and at 65 °C for DNA fragment probes. Membranes were subjected to phosphoimager analysis using a Typhoon Trio Imaging System (GE Healthcare). Oligonucleotide probes, corresponding to different regions of the pre-rRNA precursor, are shown in Fig. 3d and have the following sequences: ITS1.2 is 5′-GATTTTAACTTTTGATTCCATGGAATC-3′, ITS1.3 is 5′-GAAATTAAAAATACACCATTTTACTGGC-3′, ITS1.4 is 5′-GTCAATTATGTTTTTATTGAAAGAAATTAAAAATAC-3′, ITS2 is 5′-GAATCATTAATAAGAGACAATTCTAGATG-3′ and 28S is 5′-GTTACAAAAGTCGTTTACAATTGATTC-3′. The pre-rRNA precursor was also detected with a DNA probe corresponding to the ITS1 region, obtained by PCR amplification from w^{1118} genomic DNA using primers 5′-GTATGTTGTGCGTATTTGTG-3′ and 5′-TAATCTGGTTGGTTATGGGG-3′. Detection of the U3 snoRNA was performed using as probe a PCR fragment amplified from w^{1118} genomic DNA using primers 5′-CTTTCACACTAGCTGAAAGCCAAGT-3′ and 5′-ACCACTCAGAATTCGCTCTATCCG-3′.

Cell culture and RNA interference. *Drosophila* S2 cells were grown in Schneider's *Drosophila* medium (Invitrogen) supplemented with 10% heat-inactivated fetal bovine serum (Biowest), 100 units ml^{-1} penicillin and 100 µg ml^{-1} streptomycin (Sigma) at 25 °C. RNA interference was performed as described previously[49] with little modification. A PCR fragment containing 5′ T7 RNA polymerase-binding sites and corresponding to *wcd* 465 first nucleotides was amplified from plasmid DNA (DGRC cDNA clone no. LD16320), using primers 5′-gaattgtaatacgactcactatagggATGAGTTCAGACGAGTCCA-3′ and 5′-gaattgtaatacgactcactatagggGACCTTCTTTTCCGCCCACT-3′. This DNA template was transcribed using the Megascript RNAi kit following the supplier's instructions (Ambion). S2 cells were seeded in 25- or 75-cm^2 flasks at a density of 10^6 cells ml^{-1} and 10^5 cells/cm^2, and treated with *wcd* RNAi (25 µg per 10^6 cells) for 1 h in 1 ml of serum-free Schneider's medium per 10^6 cells, followed by 4 days in a total of 3 ml of complete Schneider's medium per 10^6 cells. The efficiency of *wcd* RNAi-mediated depletion was assessed by western blot.

Immunostaining and *in situ* hybridization. For immunostaining, ovaries were dissected in PBS, fixed in 4%PFA-PEPS, permeabilized in PBT (0,2%Triton) for 30 min, washed 2 h in PBS, left overnight with primary antibodies in PBS at room temperature, washed 2 h in PBS, left with secondary antibody for 2hr at room temperature, washed 1 h in PBS and mounted in Cityfluor. We used the following primary antibodies: rabbit anti-Wcd at 1/500; mouse anti-Orb (orb4H8 and orb6H4 DHSB) 1/250; rabbit anti-C(3)G at 1/1,000 (ref. 50); anti-H3K27me3; anti-H3K9me2; anti-activated caspase3 (AbCam); human anti-Fib at 1/500 (gift from D. Hernandez-Verdun, Institut Jacques Monod, France); rabbit anti-Fib at 1/500 (AbCam); rabbit anti-LSM11 at 1/1000 (ref. 25); rabbit anti-phosphoHistoneH3 (Upstate) 1/1,000; mouse anti-α-Spectrin (3A9, DHSB), rabbit anti-Chinmo 1/1,000 (ref. 51), rabbit anti-Br-C 1/500, and rabbit anti-Miranda[52]. Secondary antibodies conjugated with Cy3, Cy5 and TRITC (Jackson laboratories) were used at 1/200. Samples were examined either with a Leica DMR microscope or by confocal microscopy using a Leica SP5 AOBS microscope. *In-situ* hybridizations were performed as published previously[53]

47. Bellaiche, Y., Gho, M., Kaltschmidt, J. A., Brand, A. H. & Schweisguth, F. Frizzled regulates localization of cell-fate determinants and mitotic spindle rotation during asymmetric cell division. *Nature Cell Biol.* **3,** 50–57 (2001).
48. Gho, M., Bellaiche, Y. & Schweisguth, F. Revisiting the Drosophila microchaete lineage: a novel intrinsically asymmetric cell division generates a glial cell. *Development* **126,** 3573–3584 (1999).
49. Worby, C. A., Simonson-Leff, N. & Dixon, J. E. RNA interference of gene expression (RNAi) in cultured *Drosophila* cells. *Sci. STKE* 2001, PL1 (2001).
50. Hong, A., Lee-Kong, S., Iida, T., Sugimura, I. & Lilly, M. A. The p27cip/kip ortholog dacapo maintains the *Drosophila* oocyte in prophase of meiosis I. *Development* **130,** 1235–1242 (2003).
51. Zhu, S. *et al.* Gradients of the *Drosophila* Chinmo BTB-zinc finger protein govern neuronal temporal identity. *Cell* **127,** 409–422 (2006).
52. Ikeshima-Kataoka, H., Skeath, J. B., Nabeshima, Y.-i., Doe, C. Q. & Matsuzaki, F. Miranda directs Prospero to a daughter cell during *Drosophila* asymmetric divisions. *Nature* **390,** 625–629 (1998).
53. González-Reyes, A., Elliott, H. & St Johnston, D. Polarization of both major body axes in *Drosophila* by *gurken-torpedo* signalling. *Nature* **375**, 654–658 (1995).

nature cell biology

DOI: 10.1038/ncb1874

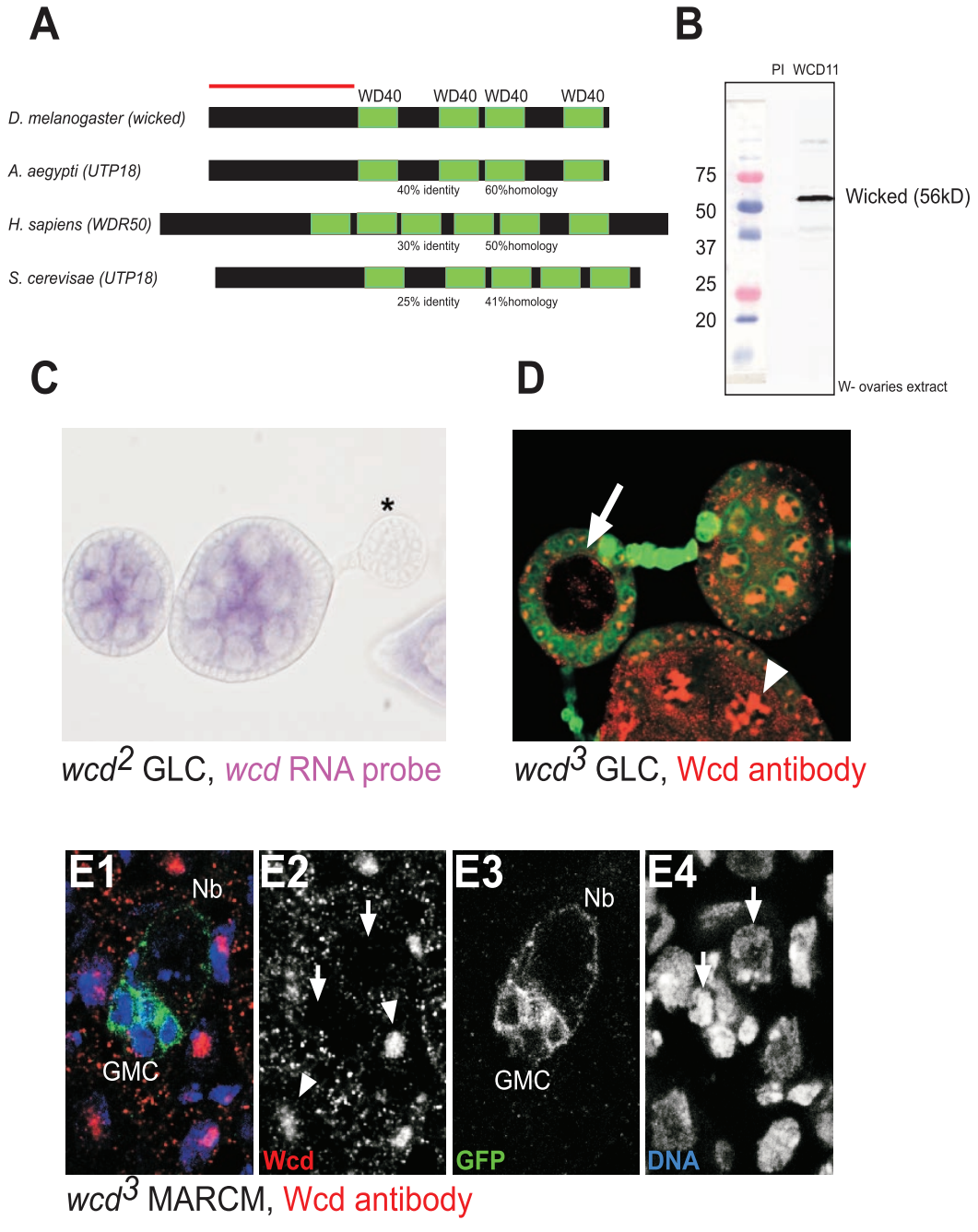

Figure S1 Wcd homologues and specificity of the antibody. **(A)** Wcd homologues. The WD40 domains are in green. In red the region used to make the antibody. **(B)** Western blot using the Wcd antibody on ovarian extracts. One major band at the expected size is detected. **(C)** *In situ* hybridization with a *wcd* RNA probe on *wcd* mutant germline clone. No signal is detected in the homozygous mutant egg chamber (asterisk). **(D)** Immunostaining using the Wcd antibody on a wcd^3 mutant germline clone. Wcd is in red and the clone is labelled by the lack of nuclear GFP (in green). No signal is detected in the homozygous mutant egg chamber (arrow) and Wcd is nucleolar in WT cells (arrowhead pointing at a WT nurse cell nucleus). **(E)** wcd^3 MARCM clone in the larval ventral nerve cord. **(E1)** The endogenous Wcd protein is in red, the DAPI staining in blue labels DNA and mutant cells are labelled by the presence of membrane associated GFP. Single channels are shown in **(E2-E4)**. No Wcd protein is detected in wcd^3 mutant NBs or GCs (arrows). WT NBs show strong nucleolar Wcd staining (arrowheads in **E2**).

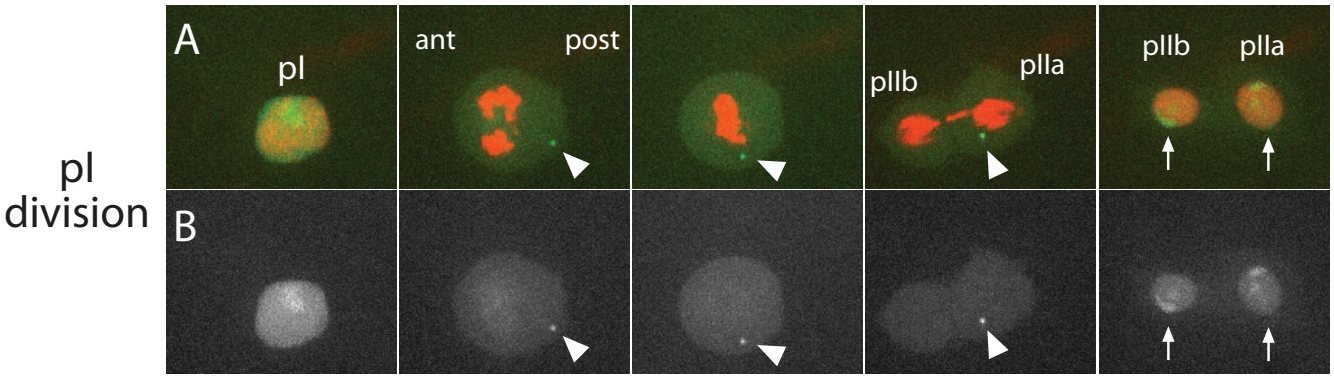

Figure S2 Asymmetric segregation of Wcd during pI division in the peripheral nervous system. Wcd::GFP is in green. H2B::RFP is in red. **(A)** Wcd::GFP forms a dot when the nuclear envelop breaks down (arrowhead) upon pI division. The dot is located on the side of the future pIIa cell. At the end of telophase, both nucleoli reform (arrow). Single channel is shown in **(B)** Wcd::GFP.

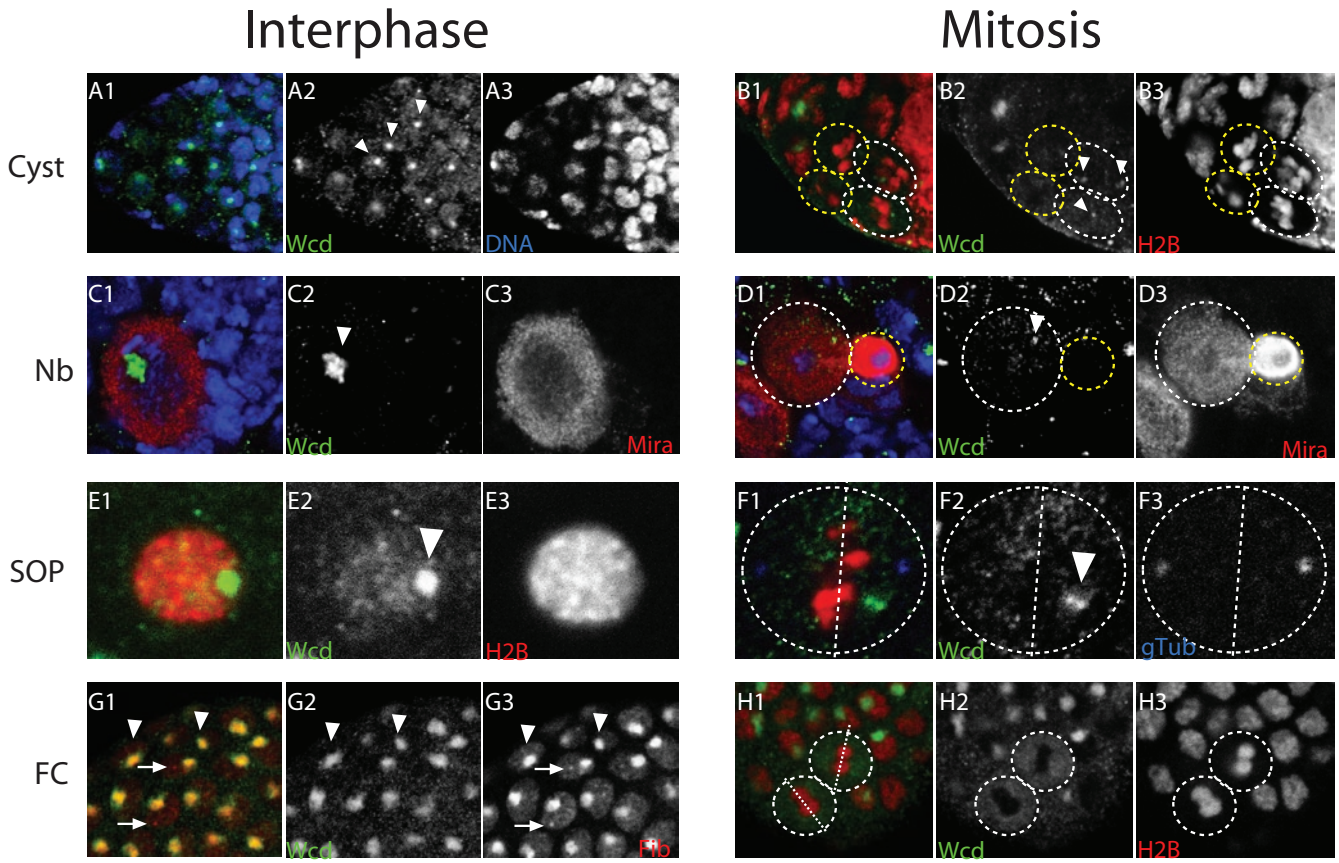

Figure S3 Localisation of the endogenous Wcd protein in cyst cells, neuroblasts, sensory organ precursors and follicle cells during interphase and mitosis. **(A1, B1, C1, D1, E1, F1, G1, H1)** The endogenous Wcd protein is in green. **(A, C, E, G)** Cells in interphase. **(B, D, F, H)** Mitotic cells. **(A,B)** Cyst cells. **(C, D)** NBs. **(E,F)** Sensory organ precursor cells (SOPs). **(G,H)** Follicle cells (FC). **(A)** Wcd is nucleolar in cyst cells during interphase (arrowheads in **A2**). The DAPI staining is in blue in **(A1)**. Single channels are shown in **(A2, A3)**. **(B)** Particles of Wcd are asymmetrically segregated upon cyst cell division (arrowheads in **B2**) into the two pro-oocytes (highlighted by white dashed circles). The yellow dashed circles highlights the two nurse cells. The H2B::RFP fusion protein is shown in red in **(B1)**. Single channels are shown in **(B2, B3)**. **(C)** Wcd is nucleolar in NBs during interphase (arrowhead in **C2**). **(C1)** Mira is in red and the DAPI staining is in blue. Single channels are shown in **(C2, C3)**. **(D)** Particules of Wcd are asymmetrically segregated upon NB division (arrowhead in **D2**) into the NB (highlighted by a white dashed circle). The yellow dashed circle highlights the future ganglion mother cell. **(D1)** Mira is in red and the DAPI staining is in blue. Single channel are shown in **(D2, D3)**. **(E)** Wcd is nucleolar in SOPs during interphase (arrowhead in **E2**). **(E1)** H2B::RFP is in red. Single channels are shown in **(E2, E3)**. **(F)** Particles of Wcd that do not co-localise with centrosomes are asymmetrically segregated upon SOP division (arrowhead in **F2**). The white dashed circle highlights the dividing SOP and the orientation of the metaphase plate is indicated by a white straight dashed line. **(F1)** H2B::RFP is in red and the centrosome marker γ-tubulin is in blue. Single channel are shown in **(F2, F3)**. **(G)** Wcd co-localises with Fibrillarin in the nucleolus of the follicle cells (arrowheads) but only Fibrillarin is detected in the Cajal Body (arrows). **(G1)** Fibrillarin is in red. Single channels are shown in **(G2, G3)**. **(H)** Wcd is symmetrically distributed upon follicle cell division. The white dashed circles highlight dividing follicle cells and the orientation of the metaphase plate is indicated by a white straight dashed line. H2B::RFP is in red in **(H1)** and single channels are shown in **(H2, H3)**.

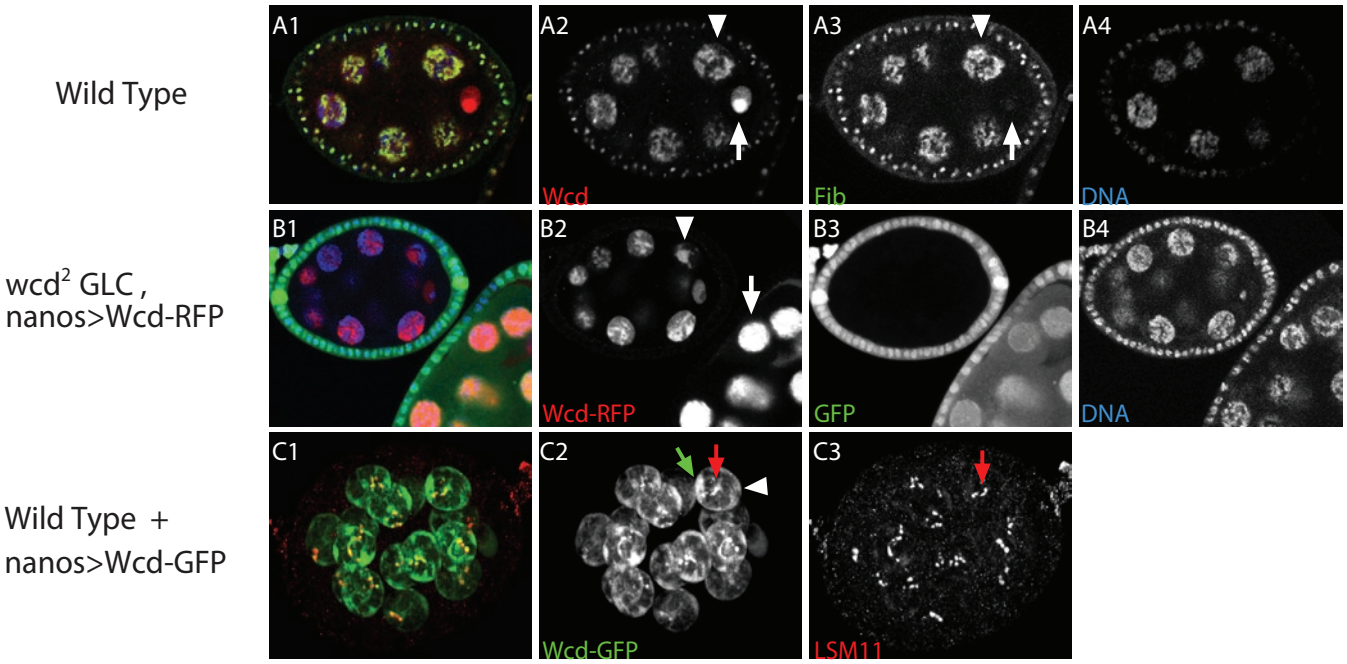

Figure S4 (Fichelson et al.)

Figure S4 Comparison of the localisation of the endogenous Wicked protein with RFP- or GFP-tagged Wicked in stage 5 egg chambers. **(A)** The endogenous Wcd protein perfectly colocalises with Fibrillarin in the nucleolus of the nurse cells (arrowhead) but is present without Fibrillarin in the gernminal vesicle (arrow). **(A1)** Wcd is in red, Fibrillarin in green and the DAPI staining is in blue. Single channels are shown in **(A2-A4)**. **(B)** RFP::Wcd localisation in the absence of the endogenous Wcd protein (rescue experiment). Cells lacking endogenous Wcd are labelled by the lack of nuclear GFP. **(B1)** RFP::Wcd is in red, GFP is in green and the DAPI staining is in blue. Single channels are shown in **(B2-B4)**. In the context of a rescue, RFP::Wcd is nucleolar, similarly to the endogenous Wcd (arrowhead in **B2**). When RFP::Wcd is expressed in the presence of the endogenous Wcd protein, the fusion protein fills most of the nucleus (arrow in **B2**). **(C)** Mild over-expression of Wcd::GFP in the presence of the endogenous Wcd protein. **(C1)** Wcd::GFP is in green and the histone locus body marker LSM11 is in red. Single channels are shown in **(C2, C3)**. Although the endogenous protein is present, Wcd::GFP accumulates in descrete regions of the nucleus: in the nucleolus (green arrow in **C2**) and in the histone locus body (red arrow in **C2, C3**). The rest of the nucleoplasm shows only low levels of Wcd::GFP (white arrowhead in **C2**).

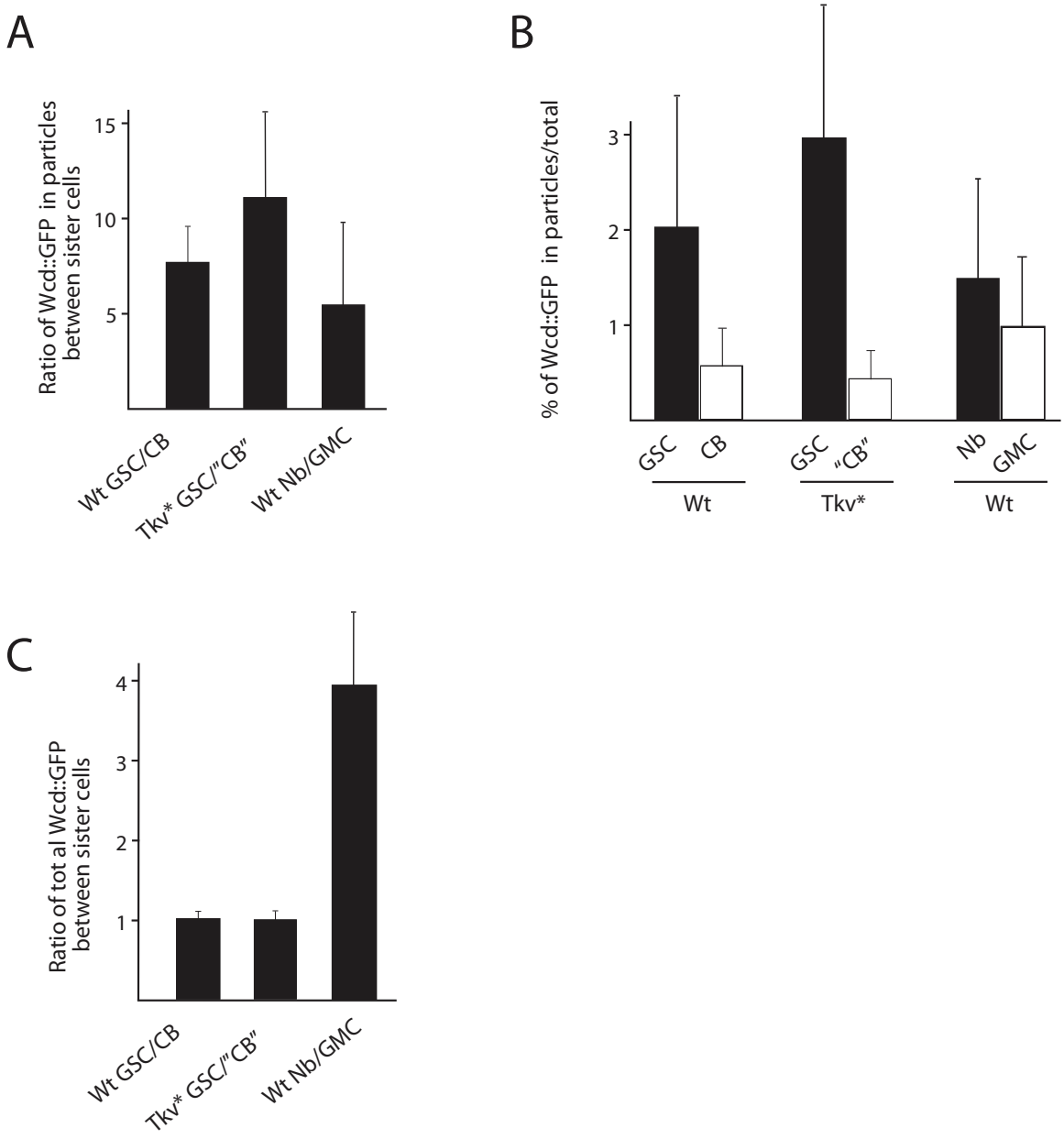

Figure S5 Quantification of the asymmetric distribution of the Wcd particles in different cell types upon mitosis. **(A)** Ratio of Wcd::GFP in particles between sister cells during the division of WT GSCs, GSCs expressing the activated form of thick veins (tkv*-GSC) and WT NBs. CB: cystoblast. GMC: ganglion mother cell. **(B)** Percentage of Wcd::GFP present in particles in WT GSCs and WT CBs; tkv*-GSC and "CB"; NBs and GMCs. **(C)** Ratio of total Wcd::GFP between sister cells upon WT GSCs division, tkv*-GSC division and NB division.

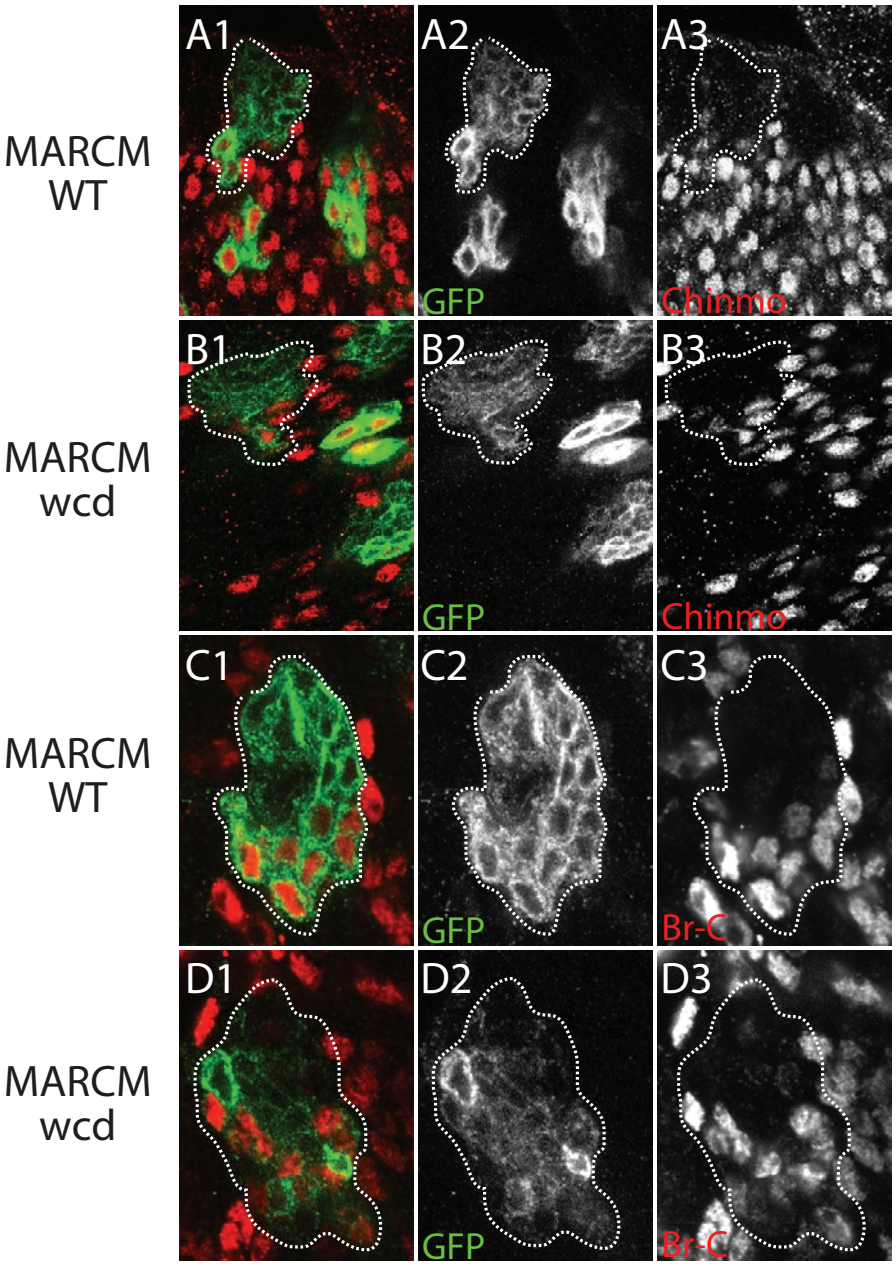

Figure S6 *wcd* mutant neuroblasts produce cells expressing the correct postmitotic transcription factors. **(A, C)** WT MARCM clone. **(B, D)** *wcd*^{3} MARCM clone. **(A-D)** The clone is labelled by the presence of a membrane associated GFP and highlighted by a white dashed line. **(A1, B1, C1, D1)** GFP is in green. **(A,B)** A subset of the clone expresses Chinmo (in red in A1 and B1), whether in the presence **(A)** or in the absence of Wcd **(B)**. Single channels are shown in **(A2, A3, B2, B3)**. **(C-D)** A subset of the clone expresses Broad-Complex (Br-C, in red in **C1** and **D1**), whether in the presence **(C)** or in the absence of Wcd **(D)**. Single channels are shown in **(C2, C3, D2, D3)**.

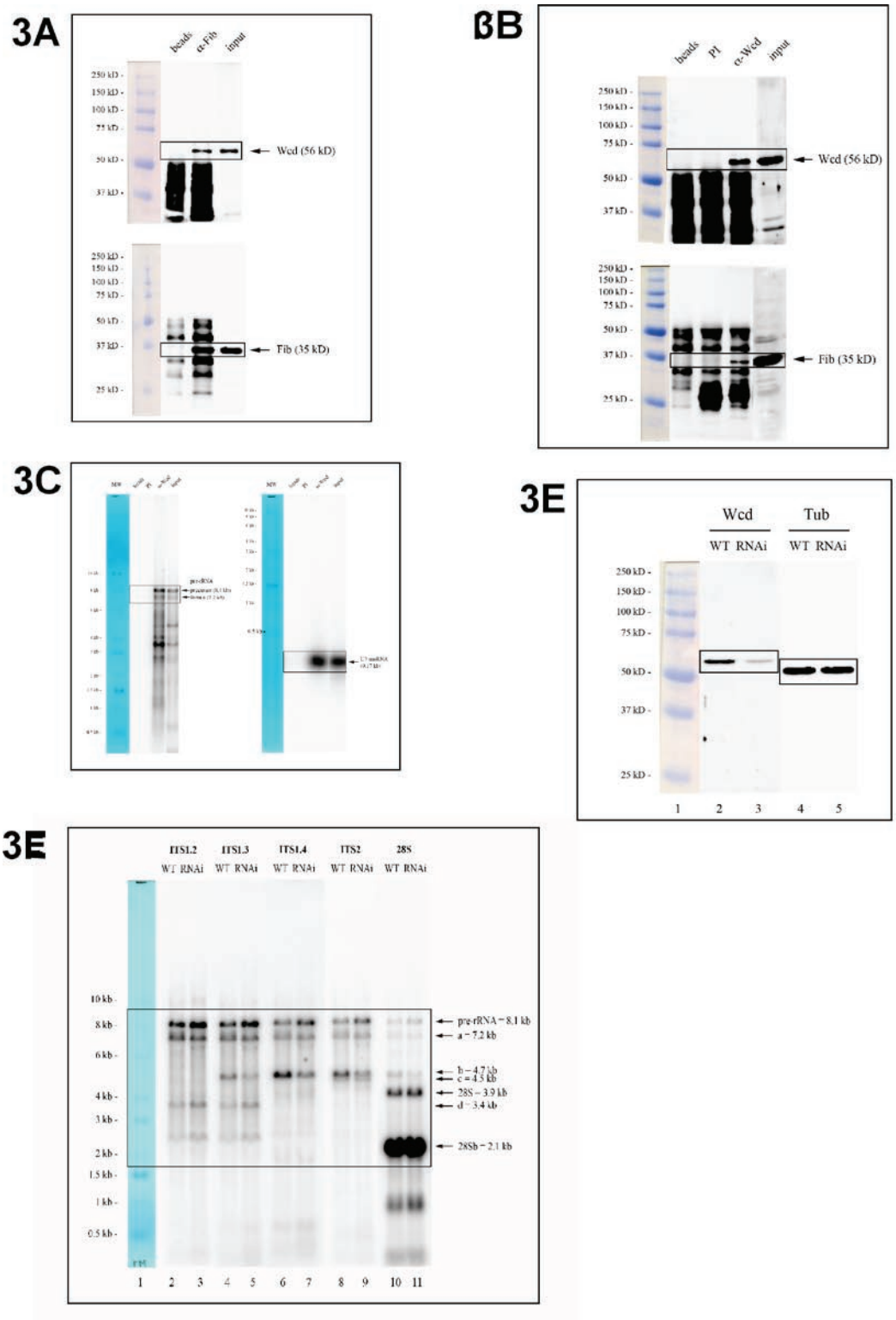

Figure S7 Full gel scans

Supplementary Movie Legends

Movie 1 Wcd segregates asymmetrically into the germline stem cell (anaphase). Wcd::GFP is in green and HistoneH2B::RFP (H2B::RFP) is in red. Arrowhead: large dot of Wcd::GFP segregating into the germline stem cell (GSC). Note that some Wcd::GFP also segregates into the cystoblast (CB).

Movie 2 Wcd segregates asymmetrically into the germline stem cell (metaphase). Wcd::GFP is in green and H2B::RFP is in red. One dot of Wcd::GFP (arrowhead) forms at nuclear envelop break down (NEB) and localizes at the anterior side of the metaphase plate toward the GSC.

Movie 3 Wcd segregates asymmetrically into the pro-oocytes. Wcd::GFP is in green and H2B::RFP is in red. Synchronous division of a 2-cell cyst to form a 4-cell cyst. Large aggregates of Wcd::GFP localize into the two pro-oocytes (arrowheads). Note that the two future nurse cells also inherit some Wcd::GFP (arrows).

Movie 4 Wcd segregates asymmetrically into the pro-oocytes. Wcd::GFP is in green and H2B::RFP is in red. Synchronous division of a 2-cell cyst to form a 4-cell cyst. One dot of Wcd::GFP forms after NEB in each cell (only one is first shown then both with an arrowhead) and segregate into the two inner cells (white circles, pro-oocytes). Yellow circles: pro-nurse cells.

Movie 5 Wcd segregates asymmetrically in germline cells expressing an activated form of thickvein. Wcd::GFP is in white. Overexpression of Tkv under the control of the *nanos*-GAL4 driver. Two dots of Wcd::GFP (arrowheads) segregate into only one cell.

Movie 6 Wcd segregates asymmetrically in germline cells expressing an activated form of thickvein. Wcd::GFP is in white. Overexpression of Tkv under the control of the *nanos*-GAL4 driver. Two independent GSC-like cells dividing away from the niche. Wcd::GFP forms aggregates (arrowhead) at nuclear envelop break down (NEB). Wcd::GFP (arrowheads) segregates into only one cell in both cases.

Movie 7 Wcd segregates asymmetrically during larval neuroblast division. Wcd::GFP is in white. One neuroblast (NB) is shown with part of its progeny (GMC). Two dots of Wcd::GFP (arrowheads) segregate into the neuroblast (white circle) at anaphase and fuse with the nucleolus at interphase.

Movie 8 Wcd segregates asymmetrically during larval neuroblast division. Wcd::GFP is in white. One neuroblast (NB) is shown with part of its progeny (GMC). Two dots of Wcd::GFP (arrowheads) segregate into the neuroblast (white circle) at anaphase and fuse with the nucleolus at interphase.

Movie 9 Wcd segregates asymmetrically into the pIIa cell during Sensory Organ Precursor division (SOP). Wcd::GFP is in green and H2B::RFP is in red. Two SOP divisions are shown. One dot of Wcd::GFP (arrowhead) forms at nuclear envelop breakdown (NEB) and segregates into the posterior pIIa cell in both cases.

Movie 10 Wcd segregates symmetrically during follicle cell divisions. Wcd::GFP is in white. Armadillo::GFP is also in white and labels the adherens junctions at the cortex of follicle cells (only a few junctions are visible in this movie). 3 follicle cells divisions are shown. No particle form after nuclear envelop breakdown (NEB) and cytoplasmic Wcd::GFP is partitioned equally between sister cells.

nature cell biology

p53 controls cancer cell invasion by inducing the MDM2-mediated degradation of Slug

Shu-Ping Wang[1], Wen-Lung Wang[1], Yih-Leong Chang[2], Chen-Tu Wu[2], Yu-Chih Chao[1], Shih-Han Kao[3], Ang Yuan[4], Chung-Wu Lin[5], Shuenn-Chen Yang[6], Wing-Kai Chan[7], Ker-Chau Li[8], Tse-Ming Hong[9,11] and Pan-Chyr Yang[4,6,10,11,12]

The tumour suppressor p53 is known to prevent cancer progression by inhibiting proliferation and inducing apoptosis of tumour cells. Slug, an invasion promoter, exerts its effects by repressing E-cadherin transcription. Here we show that wild-type p53 (wtp53) suppresses cancer invasion by inducing Slug degradation, whereas mutant p53 may stabilize Slug protein. In non-small-cell lung cancer (NSCLC), mutation of *p53* correlates with low MDM2, high Slug and low E-cadherin expression. This expression profile is associated with poor overall survival and short metastasis-free survival in patients with NSCLC. wtp53 upregulates MDM2 and forms a wtp53–MDM2–Slug complex that facilitates MDM2-mediated Slug degradation. Downregulation of Slug by wtp53 or MDM2 enhances E-cadherin expression and represses cancer cell invasiveness. In contrast, mutant p53 inactivates Slug degradation and leads to Slug accumulation and increased cancer cell invasiveness. Our findings indicate that wtp53 and p53 mutants may differentially control cancer invasion and metastasis through the p53–MDM2–Slug pathway.

Cancer metastasis is the most common cause of treatment failure and death in cancer patients[1]. Although metastasis is a complicated process involving multiple factors and genetic events, increased migratory and invasive capabilities are critical to the initiation of the metastatic process[1]. Tumorigenesis and metastasis are two distinct aspects of cancer progression; the clinical significance of tumour suppressor activity is enhanced if both cancer invasion and metastasis are inhibited.

The well-characterized tumour suppressor p53 is normally maintained at low levels by MDM2, which mediates the ubiquitylation and proteasomal degradation of p53 (ref. 2). Oncogene activation or genotoxic stress can activate p53, resulting in cell cycle arrest, apoptosis, DNA repair and cell differentiation[3,4]. Mutations in *p53* occur frequently in cancers and are present in about 50% of non-small-cell lung cancers (NSCLCs)[4–6]. *p53* mutations in NSCLC are associated with increased neoangiogenesis, higher proliferative index and decreased overall survival[6]. In addition, *p53* mutations are associated with decreased E-cadherin expression[7] and increased cancer invasiveness[8]. Recently, two groups have generated p53-mutant mouse models and found that the tumours developing in these mice metastasize[9,10], indicating that mutant p53 may mediate a gain-of-function metastatic phenotype. Moreover, several reports have indicated that p53 is involved in cancer progression by specifically regulating cancer invasion[11–13].

Downregulation of E-cadherin is a hallmark of epithelial–mesenchymal transition (EMT), a process that allows epithelial cells to separate from their neighbours and migrate to distant regions during development or metastasis[14]. E-cadherin is a suppressor of invasion and metastasis. Its downregulation is associated with the development of malignant epithelial cancers[15–17]. Forced expression of E-cadherin suppresses cancer metastasis, whereas functional knockout of E-cadherin confers a metastatic phenotype on benign tumour cells[18,19].

The predominant mechanism responsible for E-cadherin silencing in most carcinomas is transcriptional repression[20,21]. Slug (also known as SNAI2), a member of the Snail family of transcriptional repressors, is capable of repressing E-cadherin expression and triggering EMT[22–24], suggesting that it may act as an invasion promoter. Recently, we have found that Slug promotes NSCLC cell invasion by downregulating E-cadherin and upregulating matrix metalloproteinase-2 (ref. 25). Consistent with the view that Slug can promote invasion, aberrant upregulation of Slug is correlated with reduced E-cadherin expression and is associated with malignant transformation and metastatic progression in numerous cancers[25–30].

Here we report an additional mechanism by which p53 regulates cancer invasion. We show that wild-type p53 is able to suppress cancer cell invasion by inducing MDM2-mediated Slug degradation. Furthermore, we

[1]Graduate Institute of Life Sciences, National Defense Medical Center, Taipei 11490, Taiwan. [2]Department of Pathology and Graduate Institute of Pathology, National Taiwan University, Taipei 10043, Taiwan. [3]Graduate Institute of Molecular Biology, College of Medicine, National Taiwan University, Taipei 10043, Taiwan. [4]Department of Internal Medicine, National Taiwan University Hospital, Taipei 10043, Taiwan. [5]Department of Pathology, National Taiwan University Hospital, Taipei 10043, Taiwan. [6]Institute of Biomedical Sciences, Academia Sinica, Taipei 11529, Taiwan. [7]Department of Medical Research, National Taiwan University Hospital, Taipei 10043, Taiwan. [8]Institute of Statistical Science, Academia Sinica, Taipei, 11529, Taiwan. [9]Institute of Clinical Medicine, National Cheng Kung University, Tainan 70101, Taiwan. [10]NTU Center for Genomic Medicine, College of Medicine, National Taiwan University, Taipei 10043, Taiwan.
[11]These authors contributed equally to this work.
[12]Correspondence should be addressed to P.-C Y. (e-mail: pcyang@ntu.edu.tw)

Received 29 October 2008; accepted 19 February 2009; published online 17 May 2009; corrected online 19 May 2009; DOI:10.1038/ncb1875

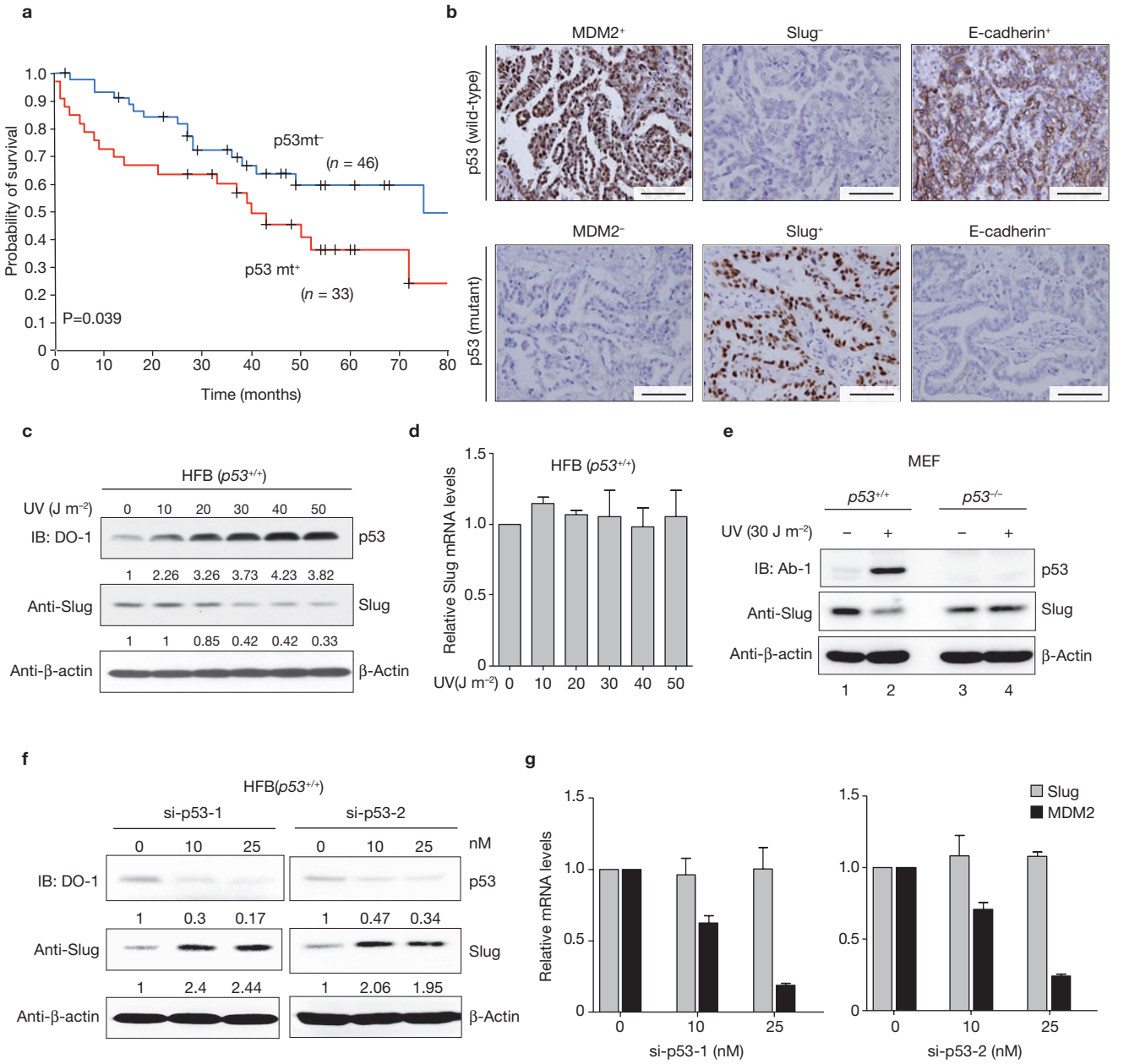

Figure 1 *p53* mutation is associated with poor clinical outcome in patients with NSCLC, and p53 can regulate Slug protein expression. (**a**) Kaplan–Meier plots of overall survival for patients with NSCLC with (p53mt⁺) or without (p53mt⁻) *p53* mutation. (**b**) Immunohistochemistry of MDM2, Slug and E-cadherin in serial sections of NSCLC tumour specimens with wild-type or mutant p53. Scale bars represent 100 μm. (**c**–**e**) UV-induced p53 activation decreases the level of Slug protein but not that of *Slug* mRNA. Cell lysates were analysed by immunoblotting (IB) (**c**) or real-time PCR analysis (**d**) 12 h after different doses of UV radiation. β-Actin protein served as a control for equal loading. Data are shown as means and s.e.m. for three independent experiments ($n = 3$). (**e**) $p53^{+/+}$ and $p53^{-/-}$ MEFs were exposed to UV (30 J m^{-2}) radiation or left untreated. Cell lysates were analysed by immunoblotting 12 h after UV irradiation. (**f**, **g**) HFBs transfected with different concentrations of *p53*-siRNA oligonucleotides (si-p53-1 or si-p53-2) were lysed and analysed by immunoblotting (**f**) or real-time PCR analysis (**g**) 72 h after transfection. Data are shown as means and s.e.m. for three independent experiments ($n = 3$). Numbers below the panels of the immunoblots indicate the densitometric values normalized to the respective β-actin value. Uncropped images of the scans in **c**, **e** and **f** are shown in Supplementary Information, Fig. S4.

demonstrate that mutant p53 represses MDM2 expression, thereby stabilizing Slug protein in cancer cells and promoting cancer cell invasiveness.

RESULTS

Mutation of *p53* correlates with outcomes of patients with NSCLC

Mutations of *p53* occur frequently in lung cancer[5,6]. Mutant p53 has recently been shown to regulate breast and oesophageal cancer progression by specifically promoting cancer cell invasion[11,13]. To assess the role of mutant p53 in lung cancer progression, we collected a cohort of 79 patients with NSCLC and determined the *p53* mutation status in lung tumour specimens by direct DNA sequencing, as well as p53 protein expression with immunohistochemistry (Table 1; Supplementary Information, Fig. S1a). The clinical characteristics of the patients with NSCLC are shown in Supplementary Information, Table S1. Among the 79 patients with NSCLC, 33 samples

Table 1 Relationship between p53 mutation status and the protein expression of p53, MDM2, Slug, and E-cadherin in tumour specimens from 79 NSCLC patients

		p53 mutation		
	Protein expression*	Positive (n = 33)	Negative (n = 46)	P †
p53	High	18 (54.5%)	13 (28.3%)	
	Low	15 (45.5%)	33 (71.7%)	0.018
MDM2	High	11 (33.3%)	36 (78.3%)	
	Low	22 (66.7%)	10 (21.7%)	<0.001
Slug	High	25 (75.8%)	13 (28.3%)	
	Low	8 (24.2%)	33 (71.7%)	<0.001
E-cadherin	High	5 (15.2%)	39 (84.8%)	
	Low	28 (84.8%)	7 (15.2%)	<0.001

* High expression, more than 50%; low expression, 50% or less.
† Pearson Chi-Square test.

(41.8%) harboured mutant *p53*, which correlated with high p53 protein expression ($P = 0.018$; Table 1) and poor overall survival of patients with NSCLC ($P = 0.039$; Fig. 1a).

Mutation of *p53* is associated with high expression of Slug and low expression of E-cadherin in NSCLC tumour specimens

To determine whether *p53* mutation can influence the expression of cancer-invasion-related genes, we investigated the immunohistochemistry of Slug and E-cadherin in serial sections of NSCLC tumour specimens (Fig. 1b). Most tumours with mutant *p53* were associated with high expression of Slug and low expression of E-cadherin. In contrast, tumours with wild-type *p53* were associated with low expression of Slug and high expression of E-cadherin ($P < 0.001$ and $P < 0.001$, respectively; Table 1).

Wild-type p53 inhibits Slug protein expression

We then investigated the mechanisms by which p53 regulates Slug expression and modulates cancer cell invasion. In p53-deficient H1299 cells, overexpression of wtp53 induced a substantial and dose-dependent decrease in Slug protein levels without a change in *Slug* messenger RNA levels (Supplementary Information, Fig. S1b, c). There was no obvious apoptosis in the transfected cells, suggesting that the effect of wtp53 overexpression on Slug was not due to p53-induced cytotoxicity. To determine whether endogenous Slug is downregulated by p53 in response to stress, we subjected human fibroblasts (HFBs) endogenously expressing wtp53 to treatment with ultraviolet (UV) radiation. At 12 h after UV irradiation, Slug protein levels were significantly decreased in parallel with increased wtp53 accumulation (Fig. 1c) but *Slug* mRNA levels did not change (Fig. 1d), indicating that Slug is not transcriptionally regulated by wtp53. Conversely, the effects of UV irradiation on Slug levels were abolished in $p53^{-/-}$ mouse embryo fibroblasts (MEFs), confirming that Slug downregulation is through p53 (Fig. 1e). In further confirmation of the negative regulation of Slug by wtp53, we knocked down ectopically expressed wtp53 in H1299 cells as well as endogenous wtp53 in HFBs by two independent *p53* RNA-mediated interference (RNAi) species. We found that Slug protein expression gradually increased (Fig. 1f; Supplementary Information, Fig. S1d), whereas the *Slug* mRNA levels did not change (Fig. 1g). These results suggest that an intrinsic function of wtp53 may limit the intracellular concentration of Slug protein.

Wild-type p53 is required for Slug protein degradation

To determine whether the p53-mediated downregulation of Slug reflects altered Slug protein stability, we measured the half-life of Slug in HFBs. In wtp53-containing cells, Slug protein had a shorter half-life of about 40 min, but this increased markedly in the presence of the proteasome inhibitor MG132 (Fig. 2a, b). Conversely, Slug protein was highly stable in p53-deficient H1299 cells (Fig. 2c, d), as demonstrated by the unchanged haemagglutinin (HA)-tagged Slug concentration after a [^{35}S]methionine pulse chase (Fig. 2c, upper panel). The introduction of wtp53 into H1299 cells stimulated Slug protein turnover (Fig. 2c, lower panel), indicating that wtp53 promotes Slug protein degradation.

Wild-type p53 induces MDM2-mediated ubiquitylation and degradation of Slug

p53 modulates cellular responses by inducing gene transcription or by direct protein–protein interactions[31,32]. To determine whether p53 triggers Slug degradation through a transcription-dependent mechanism or a transcription-independent one, we transfected $p53^{-/-}$ H1299 cells with either wild-type or mutant p53. We found that degradation of Slug was efficiently induced by wtp53 but not by p53 mutants deficient in DNA binding, namely V173L, N247I, R248W and R273H (Fig. 3a). Moreover, a transactivation-deficient p53 double mutant (L22Q/W23S) capable of binding DNA failed to trigger Slug degradation (Fig. 3a), suggesting that the transcriptional activity of p53 is required for Slug degradation.

p53 is both a transcriptional inducer of the ubiquitin ligase MDM2 (ref. 2) and its target. Functional knockdown of p53 decreased MDM2 expression levels and stabilized Slug protein (Figs 1f, g and 3a), indicating that MDM2 might also function as a p53-dependent ubiquitin ligase for Slug. This supposition is supported by the observation that Slug interacts with MDM2 *in vivo* (Fig. 3b). To determine whether MDM2 promotes Slug ubiquitylation, we examined ubiquitylated Slug species in H1299 cells expressing HA–Slug with or without Myc-tagged ubiquitin (Myc–Ub) and/or MDM2 (Fig. 3c). Ubiquitylated HA–Slug was detected in cells co-expressing Myc–Ub, and the ubiquitylation extent was increased in the presence of MG132 (Fig. 3c, lane 5). Coexpression of MDM2 further increased ubiquitylated Slug (Fig. 3c) and decreased the corresponding unconjugated HA–Slug levels (Fig. 3d, left panel). MDM2-dependent Slug ubiquitylation was further enhanced by treatment with MG132 (Fig. 3c), which also partly rescued the decreased HA–Slug levels (Fig. 3d, right panel). The findings suggest that MDM2 facilitates the ubiquitylation and subsequent degradation of Slug. Moreover, the exogenous expression of MDM2 in $p53^{-/-}Mdm2^{-/-}$ MEFs significantly enhanced Slug ubiquitylation (Supplementary Information, Fig. S1e). The result confirmed that MDM2 modulates Slug ubiquitylation *in vivo*. Conversely, knocking down MDM2 increased endogenous Slug levels in HFBs (Supplementary

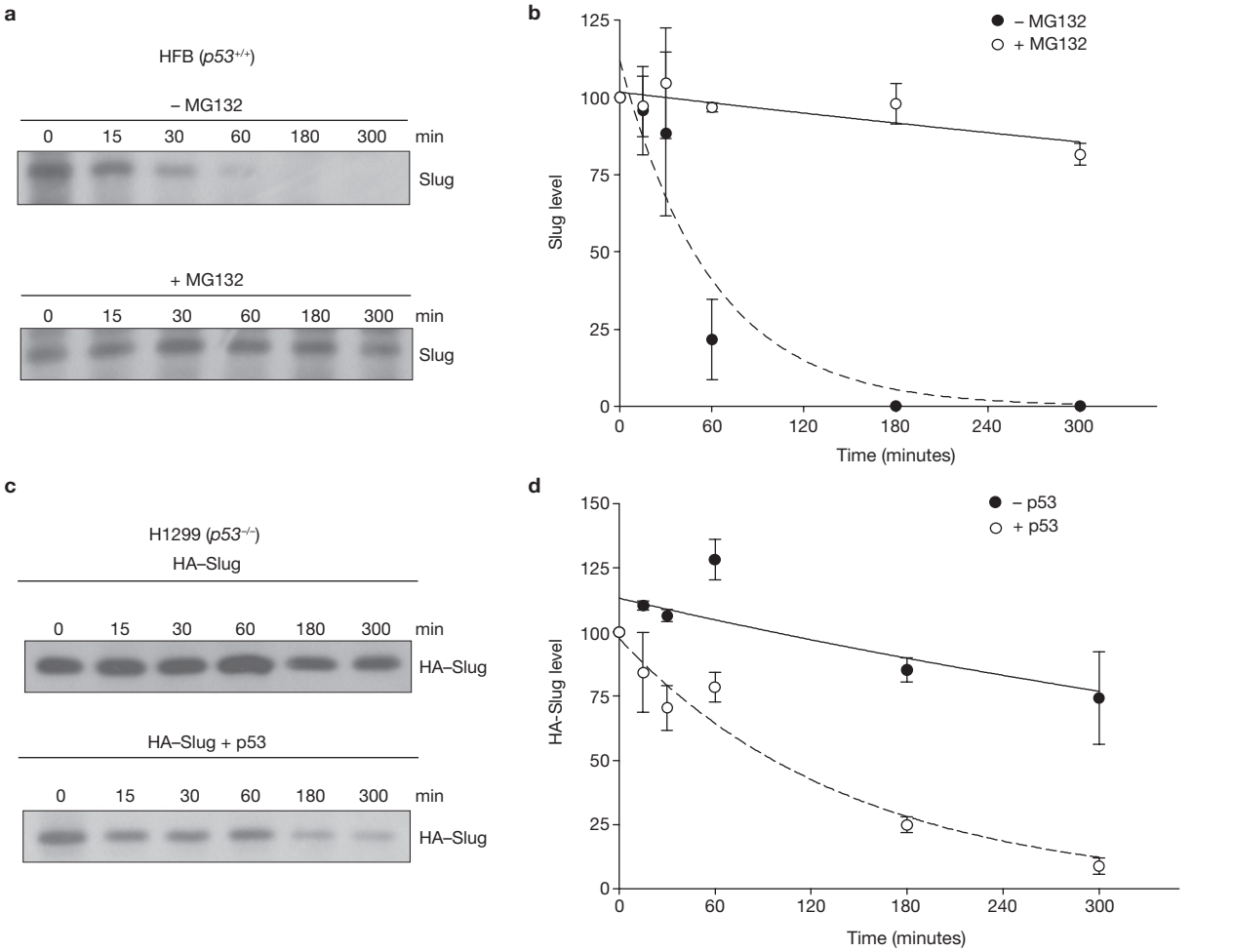

Figure 2 Slug is unstable in $p53^{+/+}$ cells and is regulated by the 26S proteasome. (**a**, **b**) The stability (half-life) of endogenous Slug from HFBs ($p53^{+/+}$) was determined by [^{35}S]methionine pulse–chase assays. HFBs were pretreated with 10 μM MG132 or left untreated, followed by analysis with [^{35}S]methionine pulse–chase assays as described in Methods. Data were quantified. (**c**, **d**) Slug protein turnover is dependent on p53. HA–Slug from H1299 ($p53^{-/-}$) cells co-transfected with an empty vector or p53 was analysed by [^{35}S]methionine pulse–chase assays. Signals in **a** and **c** were quantified by densitometry with ImageQuant software (Molecular Dynamics). Relative densitometry results of Slug are plotted in **b** and **d**. Data are shown as means ± s.e.m. for three independent experiments ($n = 3$).

Information, Fig. S1f). These data indicate that Slug degradation depends on the MDM2 ubiquitin ligase–proteasome pathway.

To show that Slug expression is regulated by p53 and MDM2, we compared the levels of Slug proteins in $p53^{+/+}$, $p53^{-/-}$ and $p53^{-/-}Mdm2^{-/-}$ MEFs. As expected, the level of Slug protein was increased in $p53^{-/-}$ and $p53^{-/-}Mdm2^{-/-}$ MEFs compared with that in $p53^{+/+}$ MEFs (Fig. 3e). Exogenous expression of wtp53 decreased Slug levels in $p53^{-/-}$ MEFs but not in $p53^{-/-}Mdm2^{-/-}$ MEFs, confirming that p53 acts through MDM2 to promote Slug degradation (Fig. 3f). Moreover, we measured the Slug levels in UV-irradiated HFBs expressing a lentivirus-based *Mdm2* short hairpin RNA (shRNA) (Fig. 3g). UV-induced wtp53 accumulation was associated with an increase in MDM2 expression and a concurrent decrease in Slug expression (Fig. 3g, lane 2). Conversely, MDM2 knockdown increased endogenous Slug levels and decreased p53-induced Slug degradation (Fig. 3g). Although MDM2 could not be completely abolished because of p53 activation under UV treatment, the decrease in MDM2 expression was sufficient to cause the accumulation of Slug. Taken together, our findings demonstrate that MDM2 functions as a ubiquitin ligase for Slug that acts downstream of p53 to mediate Slug degradation.

Wild-type p53 forms a complex with Slug and MDM2

The ability of p53 to interact with Slug *in vivo* (Fig. 4a) suggests that p53 may bind directly to the Slug–MDM2 complex. We therefore examined the interactions between endogenous wtp53, MDM2 and Slug in cells. The reciprocal protein complexes involving wtp53, MDM2 and Slug could be detected in both epithelial (SK-MEL-5 or HEK293) cells and HFBs (Fig. 4b; Supplementary Information, Fig. S2a, b). A two-step co-immunoprecipitation assay with H1299 cells co-expressing Flag–Slug, wtp53 and MDM2 showed that Slug can bind wtp53 and MDM2 simultaneously (Fig. 4c), confirming the existence of the wtp53–MDM2–Slug complex in both fibroblastic and epithelial cells.

The wtp53–MDM2–Slug complex facilitates Slug degradation

The fact that wtp53, MDM2 and Slug form a complex raises the possibility that this interaction may facilitate the MDM2-mediated ubiquitylation and degradation of Slug. To test this hypothesis, we knocked down wtp53 and/or MDM2 in HFBs. Knockdown of wtp53 or MDM2 increased Slug levels in HFBs only partly; however, simultaneous knockdown of wtp53 and MDM2 greatly enhanced Slug levels (Fig. 4d). Furthermore,

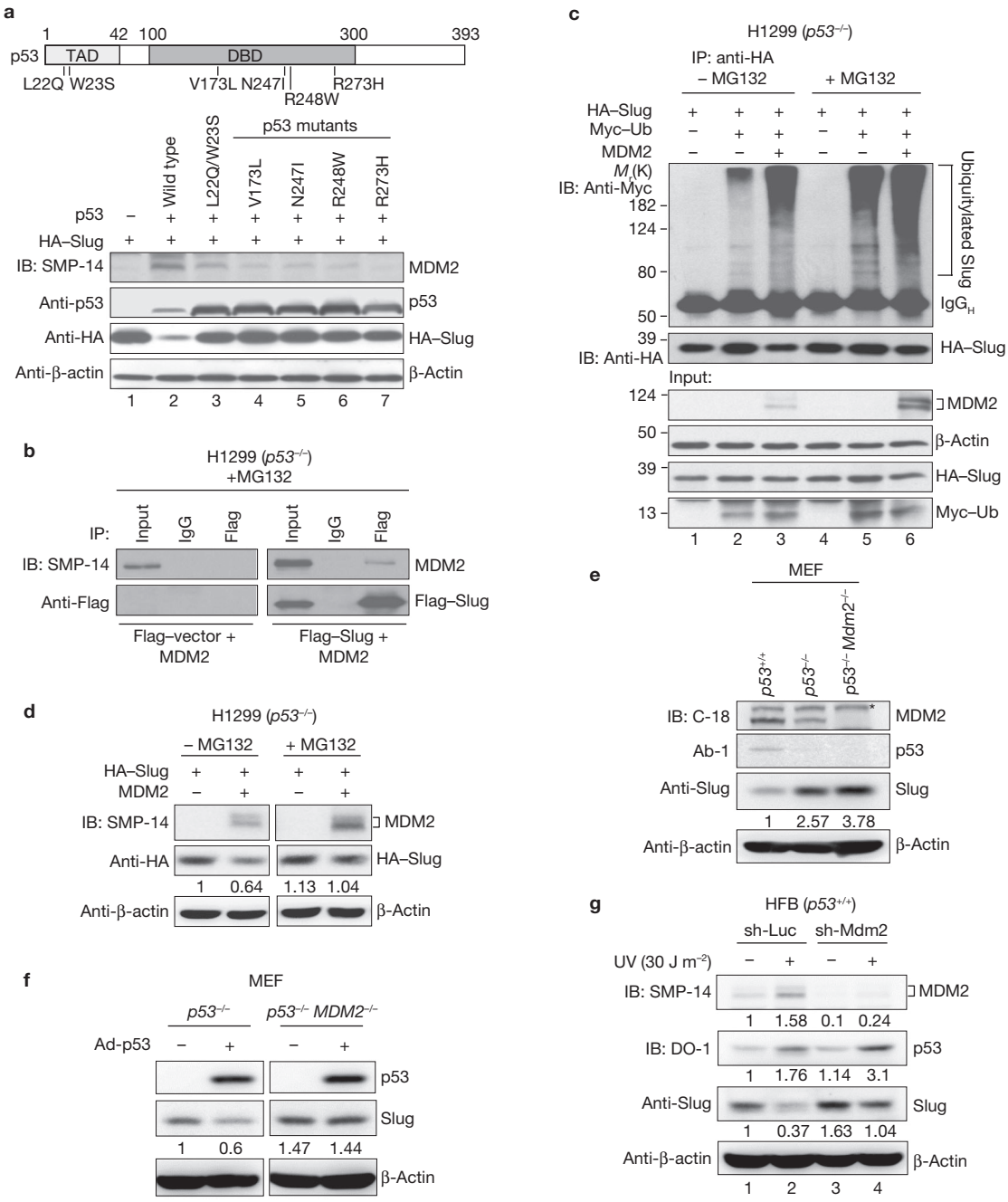

Figure 3 MDM2 ubiquitin E3-ligase is involved in p53-induced Slug degradation. (**a**) The transactivating function of p53 is important for Slug degradation. The schematic diagram (top) depicts the p53 domain structure and the location of mutation sites. TAD, transactivation domain; DBD, DNA-binding domain. Bottom: H1299 cells were transfected with HA–Slug together with wild-type or mutant forms of p53 (or an empty vector). After 36 h, expression of the indicated proteins was evaluated by immunoblotting. (**b**) MDM2 interacts with Slug *in vivo*. H1299 cells were co-transfected with MDM2 and Flag–Slug (or an empty vector) and treated with MG132 for 5 h. At 36 h after transfection, cell lysates were immunoprecipitated (IP) with anti-Flag or mouse IgG and analysed by immunoblotting. (**c**) MDM2 promotes poly-ubiquitylation of Slug. H1299 cells were co-transfected with the indicated combinations of HA–Slug, MDM2 and Myc–Ub expression plasmids for 36 h, and then treated (or not) with MG132. Top: after immunoprecipitation of Slug with anti-HA, the ubiquitylated Slug complexes were detected by immunoblotting with an anti-Myc antibody. Bottom: 50 μg of whole cell lysates immunoblotted with the indicated antibodies. (**d**) MDM2 promotes proteasomal degradation of Slug. H1299 cells were co-transfected with HA–Slug and MDM2 (or an empty vector) under the same conditions as in **c**. Cell lysates were analysed by immunoblotting with the indicated antibodies. (**e**) Lysates from $p53^{+/+}$, $p53^{-/-}$ and $p53^{-/-}Mdm2^{-/-}$ MEFs were analysed by immunoblotting with the indicated antibodies. The asterisk indicates a non-specific band. (**f**) p53-induced Slug degradation is MDM2-dependent. $p53^{-/-}$ and $p53^{-/-}Mdm2^{-/-}$ MEFs were infected with a p53 adenovirus for 48 h, and cell lysates were analysed by immunoblotting with the indicated antibodies. (**g**) MDM2 knockdown attenuates p53-induced Slug degradation. HFBs were infected with lentivirus containing sh-Luc or sh-Mdm2, and stable transductants were selected with 0.75 μg of puromycin. Cells were exposed to UV (30 J m^{-2}) or left untreated, and cell lysates were analysed by immunoblotting 12 h after UV irradiation. Numbers below the panels of the immunoblots indicate the densitometric values normalized to the respective β-actin value. Uncropped images of the scans in **e**, **f** and **g** are shown in Supplementary Information, Fig. S4.

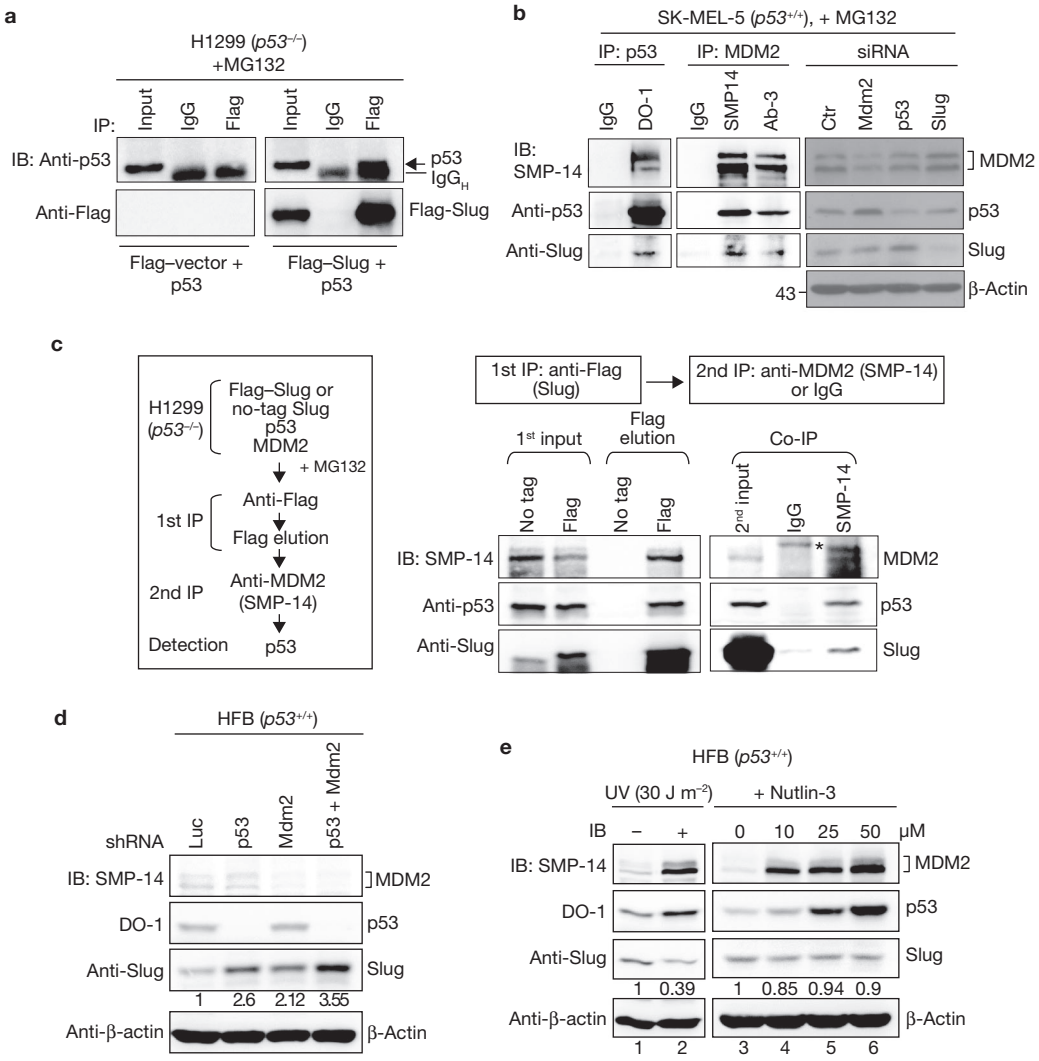

Figure 4 The p53–MDM2–Slug complex facilitates Slug degradation. (**a**) p53 interacts with Slug *in vivo*. H1299 cells were co-transfected with p53 and Flag–Slug (or an empty vector) and treated with MG132 for 5 h. At 36 h after transfection, cell lysates were immunoprecipitated (IP) with anti-Flag or mouse IgG and analysed by immunoblotting. (**b**) Interactions of endogenous p53, MDM2 and Slug. Left: SK-MEL-5 cells were treated with 10 μM MG132. After 6 h, cell lysates were immunoprecipitated with anti-p53 (DO-1), two independent anti-MDM2 antibodies (SMP-14 and Ab-3), or mouse IgG before being immunoblotted with the indicated antibodies. Right: the protein bands detected in co-immunoprecipitation assays were characterized by specific siRNAs. (**c**) Two-step co-immunoprecipitation identifies a p53–MDM2–Slug complex. The procedure from ref. 42 is outlined in the box at the left. H1299 cells were co-transfected with p53, MDM2 and Flag–Slug (or untagged Slug as control) and treated with MG132. Cell lysates were first precipitated with anti-Flag M2 agarose and eluted with a 3 × Flag peptide. Eluates were then immunoprecipitated with anti-MDM2 (SMP-14) or mouse IgG. Protein samples from each step were analysed by immunoblotting with the indicated antibodies. The asterisk indicates a non-specific band. (**d**) p53 and MDM2 are both required for Slug degradation. Cell lysates from HFBs, stably transduced with a lentiviral vector containing sh-Luc, sh-p53, sh-Mdm2 or sh-p53 plus sh-Mdm2, were analysed by immunoblotting with the indicated antibodies. (**e**) Blocking p53–MDM2 binding eliminates Slug degradation. UV-treated (30 J m^{-2}) or untreated HFB cells, and HFB cells treated with a range of Nutlin-3 concentrations, were lysed after 12 h and immunoblotted with the indicated antibodies. Numbers below the panels of the immunoblots indicate the densitometric values normalized to the respective β-actin value. Uncropped images of the scans in **b**, **c** and **e** are shown in Supplementary Information, Fig. S4.

Slug was heavily ubiquitylated in $p53^{+/+}$ MEFs but the ubiquitylated Slug level in $p53^{-/-}$ MEFs was markedly decreased (Supplementary Information, Fig. S2c). When graded p53 was co-expressed with MDM2 in $p53^{-/-}Mdm2^{-/-}$ MEFs, the endogenous Slug levels were decreased in a dose-dependent manner (Supplementary Information, Fig. S2d). These results support the idea that the formation of a complex containing MDM2 and wtp53 may be a prerequisite for Slug degradation. However, the transcriptional activity of wtp53 is required for MDM2-mediated Slug degradation (Fig. 3a). To test whether this dual requirement for wtp53 and MDM2 is independent of p53–MDM2 interaction, we treated HFBs with Nutlin-3, which inhibits the interaction (Fig. 4e). In contrast to cells not treated with Nutlin-3, in which UV-induced p53 and MDM2 led to Slug degradation (Fig. 4e, lanes 1 and 2), in Nutlin-3-treated cells p53 and MDM2 were upregulated without degradation of Slug (Fig. 4e, lanes 3–6).

Next we generated a series of deletion mutants to determine the reciprocal interacting domains of Slug, wtp53 and MDM2 (Fig. 5). A minimal domain around residues 21–29 of Slug was required for p53 interaction, and residues 27–66 were required for MDM2 binding (Fig. 5a–c). Thus, p53 and MDM2 seem to interact with Slug by means of nearly overlapping, adjacent regions. Our results further show that the Slug-binding

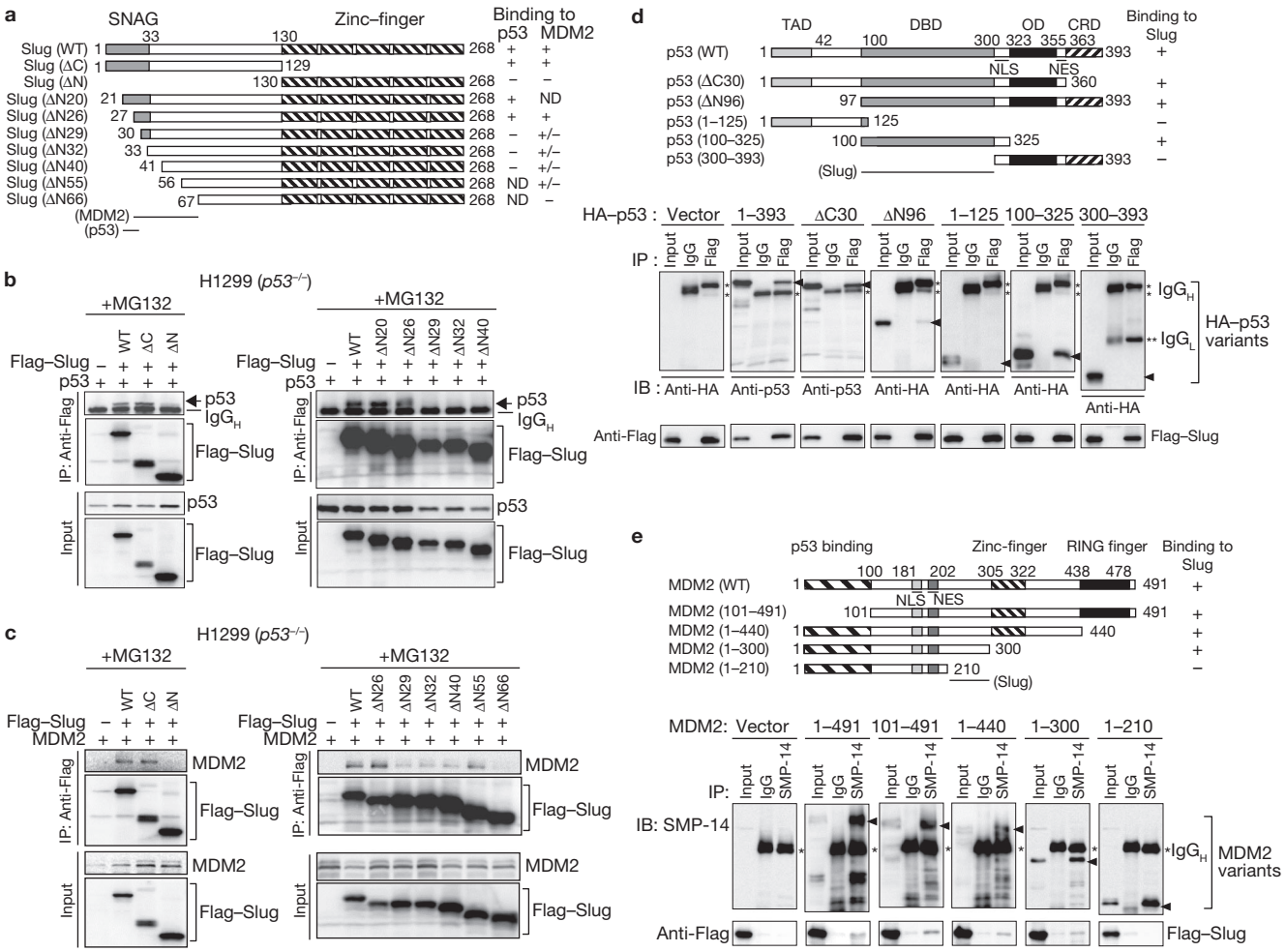

Figure 5 Domain mapping of the p53–MDM2–Slug complex. (**a**) Schematic diagram of Slug and Slug deletion mutants. The interaction of each fragment with p53 and MDM2 is shown at right; regions that interact with p53 and with MDM2 are indicated at the bottom. ND, not determined. SNAG, Snail/GFI-1 repression domain. (**b**, **c**) H1299 cells transfected with p53 (**b**) or MDM2 (**c**) were co-transfected with different Flag–Slug deletion mutants (or an empty vector) and treated with MG132 for 5 h. At 36 h after transfection, cell lysates were immunoprecipitated (IP) with anti-Flag and anti-mouse IgG antibodies, respectively, and analysed by immunoblotting (IB). (**d**) Top: schematic diagram of p53 and p53 deletion mutants. TAD, transactivation domain; DBD, DNA-binding domain; OD, oligomerization domain; CRD, C-terminal regulatory domain. The interaction of each fragment with Slug is shown at the right; the Slug-interacting region is indicated below. Bottom: H1299 cells were co-transfected with Flag–Slug and different HA–p53 deletion mutants (or an empty vector), then treated with MG132 for 5 h. At 36 h after transfection, cell lysates were immunoprecipitated with anti-Flag and anti-mouse IgG antibodies, respectively, and analysed by immunoblotting. (**e**) Top: schematic diagram of MDM2 and MDM2 deletion mutants. The interaction of each fragment with Slug is shown at the right; the Slug-interacting region is indicated below. Bottom: H1299 cells were co-transfected with Flag–Slug and different MDM2 deletion mutants (or an empty vector), then treated with MG132 for 5 h. At 36 h after transfection, cell lysates were immunoprecipitated with anti-MDM2 (SMP-14) and anti-mouse IgG antibodies, respectively, and analysed by immunoblotting.

domain of p53 is located within its DNA-binding domain (residues 100–300), and the Slug-binding domain of MDM2 lies between residues 211–300 (Fig. 5d, e).

wtp53-mediated Slug degradation represses Slug-mediated cancer cell invasion

To determine whether p53-mediated Slug degradation contributes to the suppression of cancer cell invasion, we examined the effects of *p53* silencing in the low-invasiveness cancer line MCF7, which expresses wtp53 and low Slug levels. As shown in Fig. 6a, p53 knockdown increased Slug levels and decreased E-cadherin expression in MCF7 cells, suggesting that endogenous wtp53 might normally keep Slug at low levels and limit cell invasiveness. Indeed, overexpression of Slug in MCF7 cells with Lenti-Slug significantly decreased E-cadherin levels and increased cell invasiveness accompanied by a modest downregulation of steady-state p53 levels (Fig. 6b, lanes 1 and 2). It is consistent with previous findings[33] that forced expression of Slug can overcome p53-mediated Slug downregulation and enhance cell invasiveness. Overexpression of wtp53 or MDM2 in Lenti-Slug-MCF7 cells significantly decreased Slug protein levels and concomitantly upregulated E-cadherin expression and suppressed cell invasiveness (Fig. 6b, lanes 3 and 4). These data indicate that wtp53 and MDM2 can repress the aberrantly expressed Slug in cancer cells, thereby inhibiting Slug-induced cancer cell invasiveness.

Mutant p53 upregulates Slug and enhances cancer cell invasion

As shown in Table 1, *p53* mutation was correlated with high Slug and low E-cadherin expression in NSCLCs. We speculated that mutant p53 might contribute to Slug upregulation. We chose a highly invasive NSCLC line,

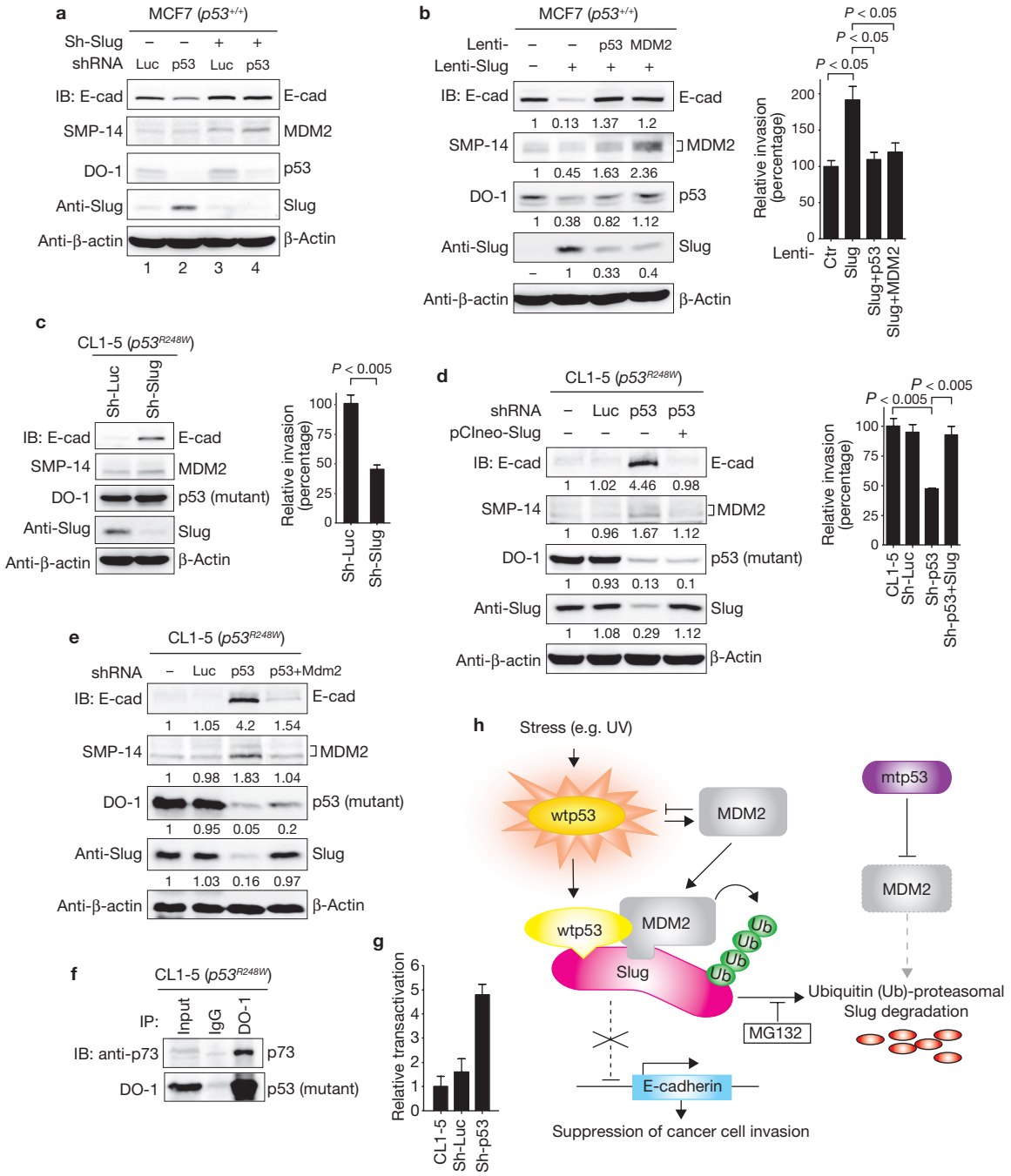

Figure 6 The effects of wtp53 and mutant p53 on Slug-mediated cancer cell invasion. (**a**) wtp53 represses Slug protein expression in MCF7 cells of low invasiveness. Expression of the indicated proteins in MCF7 cells, stably transduced with sh-Luc or sh-p53 alone or in combination with sh-Slug, was assessed by immunoblotting. E-cad, E-cadherin. (**b**) Overexpression of wtp53 or MDM2 represses Slug-induced cancer cell invasion. Expression of the indicated proteins in MCF7 cells, stably transduced with control lentivirus or Lenti-Slug alone or in combination with Lenti-p53 or Lenti-MDM2, was assessed by immunoblotting (left panel). Invasive ability was determined with the Matrigel invasion assay (right panel; see Methods). (**c**) The effects of *Slug* silencing in CL1-5 cells were assessed by immunoblotting and the Matrigel invasion assay, respectively. (**d**) The effects of mutant *p53* silencing on MDM2, Slug and E-cadherin expression and cancer cell invasiveness. Expression of the indicated proteins and invasiveness were determined by immunoblotting and the Matrigel invasion assay, respectively, in CL1-5 parental cells and in cells stably transduced with sh-Luc, sh-p53, or sh-p53 in combination with stable Slug expression (pCIneo-Slug). All of the invasion data are shown as means and s.e.m. for three independent experiments ($n = 3$). (**e**) Knockdown of MDM2 reverses the effects of mutant *p53* silencing on the expression of Slug and E-cadherin. Numbers below the panels of the immunoblots indicate the densitometric values normalized to the respective β-actin value. (**f**) p73 interacts with p53R248W in CL1-5 cells. Cell lysates were immunoprecipitated with anti-p53 (DO-1) or mouse IgG and then immunoblotted with the indicated antibodies. (**g**) Transcriptional activation of a *p53* reporter gene in mutant *p53*-silenced CL1-5 cells. p53–Luc, a p53 responsive promoter–reporter construct, was transfected into each CL1-5 cell clone as indicated. The luminescence signal from the p53–Luc reporter (firefly luciferase) was normalized to that of co-transfected pRL-SV40 vector (*Renilla* luciferase) to control for transfection efficiency. Data are shown as means and s.e.m. for three independent experiments ($n = 3$). (**h**) Proposed model illustrating opposing regulatory influences of wild-type and mutant p53 on Slug degradation and cancer cell invasion. Uncropped images of the scans in **a**, **b**, **d** and **e** are shown in Supplementary Information, Fig. S4.

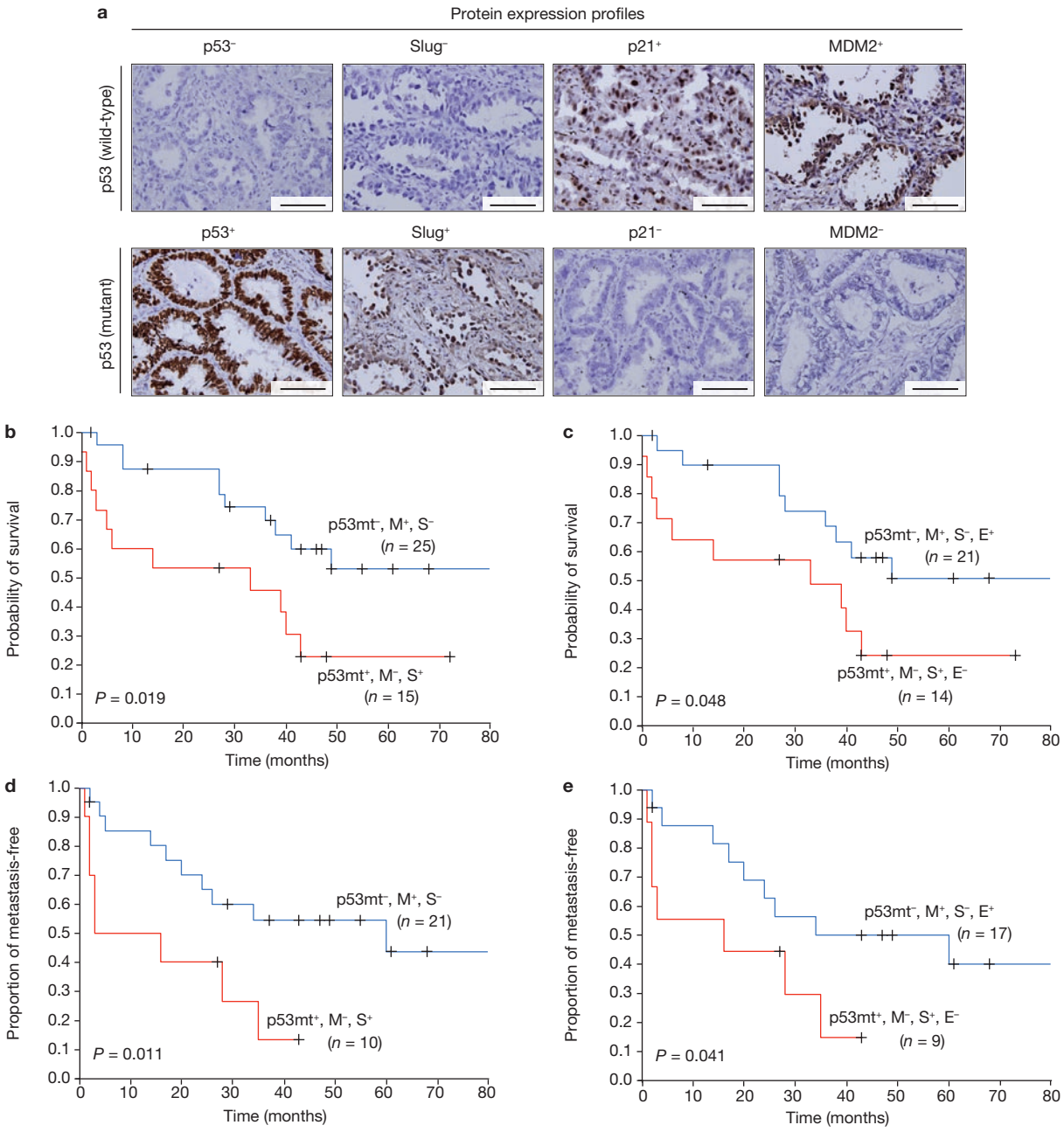

Figure 7 The signature of *p53* mutation (p53mt), low MDM2 (M), high Slug (S) and low E-cadherin (E) expression is correlated with poor overall survival and early metastasis in patients with NSCLC. (**a**) Immunohistochemistry of p53, Slug, p21 and MDM2 in serial sections of NSCLC tumour specimens with wild-type or mutant p53. Superscript + or – means tumours with or without overexpression of the indicated protein. Scale bars, 100 μm. (**b**) Kaplan–Meier analysis of overall survival for patients with NSCLC with p53mt⁻, MDM2⁺, Slug⁻ versus p53mt⁺, MDM2⁻, Slug⁺. (**c**) Kaplan–Meier analysis of overall survival for patients with NSCLC with p53mt⁻, MDM2⁺, Slug⁻, E-cadherin⁺ versus p53mt⁺, MDM2⁻, Slug⁺, E-cadherin⁻. (**d**) Kaplan–Meier analysis of metastasis-free survival for patients with NSCLC with p53mt⁻, MDM2⁺, Slug⁻ versus p53mt⁺, MDM2⁻, Slug⁺. The metastasis information of nine patients was not available. (**e**) Kaplan–Meier analysis of metastasis-free survival for patients with NSCLC with p53mt⁻, MDM2⁺, Slug⁻, E-cadherin⁺ versus p53mt⁺, MDM2⁻, Slug⁺, E-cadherin⁻. The metastasis information of nine patients was not available.

CL1-5^{p53R248W}, as our model. We first confirmed that Slug confers high invasiveness on CL1-5 cells through its suppression of E-cadherin (Fig. 6c; Supplementary Information, Fig. S3a). We further silenced the mutant *p53* gene in CL1-5 cells by using two independent *p53*-shRNAs to test whether *p53* mutation affects Slug levels and causes the high invasiveness of CL1-5 cells. We observed a significantly decreased Slug level accompanied by increased E-cadherin expression and decreased cancer cell invasiveness in *p53*-knockdown CL1-5 cells, and this effect was reversed by reconstituting Slug (Fig. 6d; Supplementary Information, Fig. S3b). These results indicate that mutant p53 upregulates Slug and enhances cancer cell invasiveness. The same results were also observed in two other mutant p53-expressing cancer lines, MDA-MB-231^{p53R280H} and SW620^{p53R273H} (Supplementary Information, Fig. S3c, d), supporting a general function of mutant p53 on Slug upregulation and cancer cell invasion. Moreover, our results showed

that MDM2 levels were markedly elevated in p53 shRNA-transduced cells (Fig. 6d; Supplementary Information, Fig. S3c, d). This suggests that mutant p53 may repress MDM2 expression, thereby stabilizing Slug protein. Indeed, knocking down MDM2 in *p53*-shRNA-expressing CL1-5 cells largely restored Slug and E-cadherin repression (Fig. 6e), confirming that the decrease in Slug levels could result from MDM2 upregulation.

p53 mutants have been proposed to interact with p63 and p73 and eliminate their transactivation of *Mdm2* (refs 34, 35). Consistent with this mechanism, p73 could be co-immunoprecipitated with p53 mutants in CL1-5, MDA-MB-231 and SW620 cells (Fig. 6f; Supplementary Information, Fig. S3e, f). Furthermore, luciferase reporter experiments in CL1-5 cells demonstrated that p53 reporter activity was increased after knockdown of p53R248W (Fig. 6g), indicating that p53R248W binding interferes functionally with the transcriptional activity of p73. Thus, our findings suggest that mutant p53 protein may repress MDM2 expression by inhibiting p73 function, thereby stabilizing Slug protein in cancer cells and promoting cancer cell invasion.

The signature of *p53* mutation, low MDM2, high Slug and low E-cadherin expression correlates with poor overall survival and early metastasis in patients with NSCLC

Wild-type p53 and its mutants may differentially modulate MDM2 levels and hence control the expression of Slug and E-cadherin in cell models. To examine whether the p53–MDM2–Slug–E-cadherin pathway exists in human lung cancers, we checked the relationship between the *p53* mutation (mt) status and the expression profiles of MDM2, Slug and E-cadherin in 79 patients with NSCLC. The tumours with mutant p53 were correlated with low MDM2, high Slug and low E-cadherin expression, whereas wild-type p53 was correlated with high MDM2, low Slug and high E-cadherin expression ($P < 0.001$, $P < 0.001$ and $P < 0.001$, respectively; Fig. 1b and Table 1). We found that more than half of the patients with NSCLC showed the profile of p53mt$^-$-MDM2$^+$-Slug$^-$ or p53mt$^+$-MDM2$^-$-Slug$^+$ (see Supplementary Information, Table S2). A tree diagram for the preferential profiles and the conditional probabilities of *p53* mutation, MDM2, Slug and E-cadherin expression is also shown in Table S2. These data suggest that the p53–MDM2–Slug–E-cadherin pathway may exist in patients with NSCLC. To confirm that mutant p53 upregulates Slug through inhibiting p73 function in patients with NSCLC, we investigated the expression of the p73 targets p21 and MDM2 in tumour specimens. Indeed, p21 and MDM2 expression was significantly downregulated in the NSCLC tumours expressing Slug and mutant p53 ($P = 0.001$ and $P = 0.010$, respectively; Fig. 7a; Supplementary Information, Table S3a).

We then investigated the prognostic significances of *p53* mutation and MDM2, Slug and E-cadherin expression status in NSCLCs by Kaplan–Meier analysis and log-rank test. The patients with a p53mt$^+$-MDM2$^-$-Slug$^+$ expression profile had a significantly poorer overall survival than the p53mt$^-$-MDM2$^+$-Slug$^-$ group ($P = 0.019$; Fig. 7b). Similarly, patients with a p53mt$^+$-MDM2$^-$-Slug$^+$-Ecad$^-$ expression profile had a poorer overall survival than the p53mt$^-$-MDM2$^+$-Slug$^-$-Ecad$^+$ group ($P = 0.048$; Fig. 7c). These poor-survival signatures also indicated early metastasis in patients with NSCLC. As shown in Fig. 7d, e, our data show that the patients with these poor-survival signatures had a higher proportion of metastasis ($P = 0.011$ and $P = 0.041$, respectively). Thus, these results support the contention that Slug accumulation by mutant p53 promotes metastasis in NSCLC and results in a poor prognosis.

DISCUSSION

Emerging evidence has suggested that p53 can specifically regulate cancer invasion[11–13] and can extend its role beyond apoptosis and cell cycle arrest[3,31]. Here we show an additional mechanism by which p53 suppresses cancer cell invasion through negative regulation of Slug, an invasion-promoting factor (Fig. 6h). We find that p53 induces MDM2-mediated Slug degradation and the concomitant E-cadherin upregulation. Formation of the p53–MDM2–Slug complex is important for Slug degradation. Moreover, *p53* mutation is associated with low MDM2, high Slug and low E-cadherin expression in cancer cells, as well as with poor overall survival and short metastasis-free survival in patients with NSCLC. Thus, the role of p53 as a tumour suppressor[4–6,36] may need to be reinterpreted in the light of the fact that p53 also suppresses cancer invasion and metastasis.

In addition, we showed that *p53* dysfunction (either loss or mutation) disrupts the Slug degradation pathway, which may result in the abnormal Slug accumulation observed in some tumour types[28–30]. Our findings provide a mechanistic basis for recent reports about *p53* dysfunction and its roles in decreased E-cadherin expression[7,37], increased metastatic abilities in cancer cells[8,38,39] and poor prognosis in various cancers[5,6,36]. On the basis of our findings, we speculate that in p53-dysregulated tumours, upregulation of Slug and the subsequent loss of E-cadherin contribute to the clinically observed cancer progression and metastasis.

We found that p73 transactivation on *Mdm2* is inhibited by its association with p53 mutants (p53R248W, R280K or R273H) in several cancer lines. p73 inhibition by mutant p53 was closely correlated with MDM2 downregulation and Slug upregulation in cancer cell lines and NSCLC tumours. These results may provide a molecular framework for explaining the origin of metastatic phenotypes in mice with *p53* mutations[9,10].

Although many patients with NSCLC showed the expression profile of p53mt$^-$-MDM2$^+$-Slug$^-$ or p53mt$^+$-MDM2$^-$-Slug$^+$ (Supplementary Information, Table S2), there was no significant correlation between MDM2 and Slug expression (Supplementary Information, Table S3b). A possible explanation might be attributed to the complex regulation between MDM2 and Slug, because a recent report has indicated that Slug can repress *Mdm2* transcription[40]. Further investigations are therefore needed to unravel the Slug–MDM2 regulatory pathway and to explain our observations in clinical tumour specimens.

p53 acts as a DNA damage sensor, responding to the severity of the damage by selectively inducing cell-cycle arrest or apoptosis-related genes[31]. It has recently been reported[41] that a lethal dose of γ-irradiation induces a p53-dependent transactivation of Slug that protects hematopoietic progenitor cells from apoptosis. Conversely, our data show that p53 induces Slug degradation in response to a sublethal dose of UV damage but has no effect on *Slug* gene expression. Intriguingly, although p53 activation by a UV stimulus downregulated Slug in association with the induction of the pro-arrest genes *p21* and *Mdm2*, we found that pro-apoptotic modification of p53 (phospho-Ser 46) led to the mild induction of the *Slug* gene and to cell death (Supplementary Information, Fig. S3g, h). We speculate that the affinity of p53 for different promoters (that is, those for *Mdm2* and *Slug*) might be selectively influenced by the nature and extent of the damage stimulus[31]. These potentially divergent regulatory roles of Slug warrant further investigation.

Our findings provide new insights into the molecular mechanism by which wild-type and mutant forms of p53 exert opposite effects on an invasion-promoting factor, Slug, thus regulating cancer invasion and

metastasis. The finding that p53 forms a complex with MDM2 and Slug to mediate Slug degradation and interrupt cancer cell invasion may offer new targets for treatments to prevent cancer metastasis. □

METHODS

Methods and any associated references are available in the online version of the paper at http://www.nature.com/naturecellbiology/

Note: Supplementary Information is available on the Nature Cell Biology website.

ACKNOWLEDGEMENTS

We thank H. K. Sytwu (Graduate Institute of Medical Sciences, National Defense Medical Center, Taipei, Taiwan) for providing the plasmids for the lentivirus infection system, Pei-Fang Hung and Lu-Kai Wang for technical assistance, and Pei-Ying Lin for English language editing. This work was supported by the National Science Council and Department of Health, Executive Yuan of the Republic of China, through the National Research Program for Genomic Medicine Grants (DOH94-TD-G-111-020, DOH95-TD-G-111-010, DOH96-TD-G-111-009, DOH97-TD-G-111-018, DOH98-TD-G-111-007, NSC97-3112-B-002-033 and NSC97-2314-B-002-146-MY3). shRNA constructs were obtained from the National RNAi Core Facility at the Institute of Molecular Biology/Genomic Research Center, Academia Sinica, Taipei, Taiwan.

AUTHOR CONTRIBUTIONS

T.-M.H. and P.-C.Y. directed the project and contributed equally to this work. S.-P.W. performed and analysed most of the experiments. W.-L.W., Y.-C.C., S.-H.K., S.-C.Y. and W.-K.C. provided reagents and materials, and performed data analysis. Y.-L.C., C.-T.W., A.Y., C.-W.L and K.-C.L. collected and analysed samples from lung cancer patients.

Published online at http://www.nature.com/naturecellbiology
Reprints and permissions information is available online at http://npg.nature.com/reprintsandpermissions/

1. Steeg, P. S. Tumor metastasis: mechanistic insights and clinical challenges. *Nature Med.* **12,** 895–904 (2006).
2. Michael, D. & Oren, M. The p53–Mdm2 module and the ubiquitin system. *Semin. Cancer Biol.* **13,** 49–58 (2003).
3. Vousden, K. H. & Lane, D. P. p53 in health and disease. *Nature Rev. Mol. Cell Biol.* **8,** 275–283 (2007).
4. Vogelstein, B., Lane, D. & Levine, A. J. Surfing the p53 network. *Nature* **408,** 307–310 (2000).
5. Soussi, T. & Beroud, C. Assessing TP53 status in human tumours to evaluate clinical outcome. *Nature Rev. Cancer* **1,** 233–240 (2001).
6. Yuan, A. *et al.* Aberrant p53 expression correlates with expression of vascular endothelial growth factor mRNA and interleukin-8 mRNA and neoangiogenesis in non-small-cell lung cancer. *J. Clin. Oncol.* **20,** 900–910 (2002).
7. Bukholm, I. K., Nesland, J. M., Karesen, R., Jacobsen, U. & Borresen-Dale, A. L. Expression of E-cadherin and its relation to the p53 protein status in human breast carcinomas. *Virchows Arch.* **431,** 317–321 (1997).
8. Hsiao, M. *et al.* Gain-of-function mutations of the p53 gene induce lymphohematopoietic metastatic potential and tissue invasiveness. *Am. J. Pathol.* **145,** 702–714 (1994).
9. Lang, G. A. *et al.* Gain of function of a p53 hot spot mutation in a mouse model of Li–Fraumeni syndrome. *Cell* **119,** 861–872 (2004).
10. Olive, K. P. *et al.* Mutant p53 gain of function in two mouse models of Li–Fraumeni syndrome. *Cell* **119,** 847–860 (2004).
11. Mehta, S. A. *et al.* Negative regulation of chemokine receptor CXCR4 by tumor suppressor p53 in breast cancer cells: implications of p53 mutation or isoform expression on breast cancer cell invasion. *Oncogene* **26,** 3329–3337 (2007).
12. Chen, Y. W. *et al.* Loss of p53 and Ink4a/Arf cooperate in a cell autonomous fashion to induce metastasis of hepatocellular carcinoma cells. *Cancer Res.* **67,** 7589–7596 (2007).
13. Okawa, T. *et al.* The functional interplay between EGFR overexpression, hTERT activation, and p53 mutation in esophageal epithelial cells with activation of stromal fibroblasts induces tumor development, invasion, and differentiation. *Genes Dev.* **21,** 2788–2803 (2007).
14. Thiery, J. P. & Sleeman, J. P. Complex networks orchestrate epithelial-mesenchymal transitions. *Nature Rev. Mol. Cell Biol.* **7,** 131–142 (2006).
15. Mareel, M. & Leroy, A. Clinical, cellular, and molecular aspects of cancer invasion. *Physiol Rev.* **83,** 337–376 (2003).
16. Bremnes, R. M. *et al.* High-throughput tissue microarray analysis used to evaluate biology and prognostic significance of the E-cadherin pathway in non-small-cell lung cancer. *J. Clin. Oncol.* **20,** 2417–2428 (2002).
17. Frixen, U. H. *et al.* E-cadherin-mediated cell–cell adhesion prevents invasiveness of human carcinoma cells. *J. Cell Biol.* **113,** 173–185 (1991).
18. Handschuh, G. *et al.* Tumour-associated E-cadherin mutations alter cellular morphology, decrease cellular adhesion and increase cellular motility. *Oncogene* **18,** 4301–4312 (1999).
19. Perl, A. K., Wilgenbus, P., Dahl, U., Semb, H. & Christofori, G. A causal role for E-cadherin in the transition from adenoma to carcinoma. *Nature* **392,** 190–193 (1998).
20. Hajra, K. M., Ji, X. & Fearon, E. R. Extinction of E-cadherin expression in breast cancer via a dominant repression pathway acting on proximal promoter elements. *Oncogene* **18,** 7274–7279 (1999).
21. Hennig, G. *et al.* Progression of carcinoma cells is associated with alterations in chromatin structure and factor binding at the E-cadherin promoter *in vivo*. *Oncogene* **11,** 475–484 (1995).
22. Nieto, M. A. The snail superfamily of zinc-finger transcription factors. *Nature Rev. Mol. Cell Biol.* **3,** 155–166 (2002).
23. Bolos, V. *et al.* The transcription factor Slug represses E-cadherin expression and induces epithelial to mesenchymal transitions: a comparison with Snail and E47 repressors. *J. Cell Sci.* **116,** 499–511 (2003).
24. Hajra, K. M., Chen, D. Y. & Fearon, E. R. The SLUG zinc-finger protein represses E-cadherin in breast cancer. *Cancer Res.* **62,** 1613–1618 (2002).
25. Shih, J. Y. *et al.* Transcription repressor slug promotes carcinoma invasion and predicts outcome of patients with lung adenocarcinoma. *Clin. Cancer Res.* **11,** 8070–8078 (2005).
26. Castro, A. C. *et al.* Slug is overexpressed in gastric carcinomas and may act synergistically with SIP1 and Snail in the down-regulation of E-cadherin. *J. Pathol.* **211,** 507–515 (2007).
27. Shioiri, M. *et al.* Slug expression is an independent prognostic parameter for poor survival in colorectal carcinoma patients. *Br. J. Cancer* **94,** 1816–1822 (2006).
28. Martin, T. A., Goyal, A., Watkins, G. & Jiang, W. G. Expression of the transcription factors snail, slug, and twist and their clinical significance in human breast cancer. *Ann. Surg. Oncol.* **12,** 488–496 (2005).
29. Uchikado, Y. *et al.* Slug expression in the E-cadherin preserved tumors is related to prognosis in patients with esophageal squamous cell carcinoma. *Clin. Cancer Res.* **11,** 1174–1180 (2005).
30. Gupta, P. B. *et al.* The melanocyte differentiation program predisposes to metastasis after neoplastic transformation. *Nature Genet.* **37,** 1047–1054 (2005).
31. Aylon, Y. & Oren, M. Living with p53, dying of p53. *Cell* **130,** 597–600 (2007).
32. Manfredi, J. J. p53 and apoptosis: it's not just in the nucleus anymore. *Mol. Cell* **11,** 552–554 (2003).
33. Kajita, M., McClinic, K. N. & Wade, P. A. Aberrant expression of the transcription factors snail and slug alters the response to genotoxic stress. *Mol. Cell Biol.* **24,** 7559–7566 (2004).
34. Lozano, G. The oncogenic roles of p53 mutants in mouse models. *Curr. Opin. Genet. Dev.* **17,** 66–70 (2007).
35. Levrero, M. *et al.* The p53/p63/p73 family of transcription factors: overlapping and distinct functions. *J. Cell Sci.* **113,** 1661–1670 (2000).
36. Havrilesky, L. *et al.* Prognostic significance of p53 mutation and p53 overexpression in advanced epithelial ovarian cancer: a Gynecologic Oncology Group study. *J. Clin. Oncol.* **21,** 3814–3825 (2003).
37. Cano, A. *et al.* Expression pattern of the cell adhesion molecules. E-cadherin, P-cadherin and $\alpha 6\,\beta 4$ integrin is altered in pre-malignant skin tumors of p53-deficient mice. *Int. J. Cancer* **65,** 254–262 (1996).
38. Lewis, B. C. *et al.* The absence of p53 promotes metastasis in a novel somatic mouse model for hepatocellular carcinoma. *Mol. Cell Biol.* **25,** 1228–1237 (2005).
39. Derksen, P. W. *et al.* Somatic inactivation of E-cadherin and p53 in mice leads to metastatic lobular mammary carcinoma through induction of anoikis resistance and angiogenesis. *Cancer Cell* **10,** 437–449 (2006).
40. Bermejo-Rodriguez, C. *et al.* Mouse cDNA microarray analysis uncovers Slug targets in mouse embryonic fibroblasts. *Genomics* **87,** 113–118 (2006).
41. Wu, W. S. *et al.* Slug antagonizes p53-mediated apoptosis of hematopoietic progenitors by repressing puma. *Cell* **123,** 641–653 (2005).
42. Harada, J. *et al.* Requirement of the co-repressor homeodomain-interacting protein kinase 2 for ski-mediated inhibition of bone morphogenetic protein-induced transcriptional activation. *J. Biol. Chem.* **278,** 38998–39005 (2003).

METHODS

Sample collection, *p53* mutation analysis and immunohistochemistry. Seventy-nine patients who underwent surgical resection for NSCLC at the National Taiwan University Hospital between January 1996 and December 2005 were studied. NSCLC tumours were staged in accordance with the American Joint Committee on Cancer Staging (AJCC)[43]; histology was performed with World Health Organization standards[44]. The *p53* mutation analysis was performed as described previously[45]. In brief, genomic DNA was extracted from microdissected cells in paraffin-embedded tissues and used for each PCR reaction. Exons 5–8 of p53 with short flanking intronic sequences were amplified by nested PCR with specific primers and subjected to sequencing analysis. Multiple sequence alignments of exon sequences were conducted with Sequencer 4.14 (Gene Codes) for mutation identification. Immunohistochemistry of paraffin-embedded, formalin-fixed surgical specimens was performed with specific antibodies against p53 (1:500 dilution; Oncogene), MDM2 (1:150; Santa Cruz), Slug (1:75; ABGENT), E-cadherin (1:400; TaKaRa Bio Inc) and p21 (1:50; Thermo Fisher Scientific). For negative controls, PBS instead of primary antibody was applied in immunohistochemistry. The immunohistochemistry results were reviewed and scored independently by two pathologists. This study was approved by the Institutional Review Board and was conducted with the informed written consent of all patients.

Plasmids and transfection. The Slug expression plasmid pSG5-HA–Slug was constructed by cloning the full-length human *Slug* cDNA containing an N-terminal HA tag into the pSG5 vector (Stratagene). The expression vector for human MDM2 was a gift from S.-Y. Shieh; Y.-S. Lin provided the human wtp53 expression vector, pCEP4-p53. The deletion constructs of p53 and MDM2 were generated by PCR-subcloning relevant cDNA into pcDNA3.0-HA (a gift from C.-Y. Huang) or pcDNA3 vector (Invitrogen), respectively. p53 mutants were generated by site-directed mutagenesis with a QuikChange kit (Stratagene) and verified by DNA sequencing. All transfection experiments were performed with Lipofectamine 2000 reagents (Invitrogen) in accordance with the manufacturer's protocols.

Viruses and transduction. Luciferase, p53, Slug and Mdm2-shRNA-containing lentiviral vectors were obtained from the National RNAi Core Facility (Academia Sinica, Taiwan) and prepared in accordance with standard protocols. Cells were infected with lentivirus (multiplicity of infection 5 or 10) in medium containing polybrene (8 μg ml^{-1}). At 24 h after infection, cells were treated with 0.75 μg ml^{-1} puromycin to select for a pool of puromycin-resistant clones.

Cell culture. The H1299, MCF7 and human fibroblast (HFB) cells were cultured in DMEM containing 10% FBS. The CL1-5 cell is a highly invasive subline selected by a Transwell invasion assay from parental CL1-0 cells[46]. CL1-5, MDA-MB-231 and SW620 cells were cultured in RPMI medium containing 10% FBS and L-glutamine. *p53*$^{-/-}$ and *p53*$^{-/-}$*Mdm2*$^{-/-}$ MEFs were obtained from G. Lozano (M. D. Anderson Cancer Center). Stably transduced, pooled clones (sh-Luc, sh-p53, sh-Slug, sh-Mdm2 and sh-p53-pCIneo-Slug) were selected and maintained in the above-described medium supplemented with 0.75 μg ml^{-1} puromycin or puromycin plus 400 μg ml^{-1} G418, as appropriate for the corresponding selection markers.

Quantitative real-time PCR. Total RNA was prepared with RNA-Bee RNA isolation solvent (Tel-test). Of total RNA (1 μg) was used in cDNA synthesis with random hexamer primers using Superscript III reverse transcriptase (Invitrogen). The resulting cDNA (1:10 dilution) was used to detect the expression of endogenous *Slug* and *Mdm2* mRNA by quantitative Taqman real-time PCR. The primer sets for Slug (Hs00161904_m1) and Mdm2 (Hs01066930_m1) were purchased from Applied Biosystems. No-reverse-transcription (no-RT) controls were performed with 100 ng of total RNA from each individual sample as template to ensure that amplification was not due to contamination with DNA. No signal could be detected in the no-RT control. Relative mRNA expression was calculated with the comparative C_t method ($\Delta\Delta C_t$). GAPDH was used for normalization.

Cell lysate preparation, immunoprecipitation and immunoblotting. All experiments were performed in accordance with standard protocols. In brief, cell lysates for immunoblotting were prepared in RIPA buffer (1% Nonidet P40, 0.5% sodium deoxycholate, 0.1% SDS) containing 1 × complete protease inhibitor cocktail (Roche). For co-immunoprecipitation, cell lysates were prepared with IP lysis buffer (20 mM Tris pH 7.5, 100 mM NaCl, 1% Nonidet P40, 100 μM Na_3VO_4, 50 mM NaF, 30 mM sodium pyrophosphate) containing 1 × complete protease inhibitor cocktail (EDTA-free) (Roche). Two-step co-immunoprecipitations were performed essentially as described previously[42]. In brief, six 60-mm dishes of H1299 cells were transfected with plasmids expressing p53, MDM2 and Flag–Slug for 31 h, and then treated with MG132 (10 μM) for 5 h. Cells were then lysed with IP lysis buffer, passed several times through a 21-gauge needle, and centrifuged. The supernatant was incubated with anti-Flag M2-agarose (100 μl) for 2 h at 4 °C. After centrifugation, the beads were washed three times with IP lysis buffer containing 150 mM NaCl, and the Flag–Slug protein complex was eluted with 300 μl of IP lysis buffer containing 250 mM NaCl and 3 × Flag peptide (300 μg ml^{-1}) for 2 h at 4 °C. An untagged Slug expression plasmid (pCIneo-Slug) was used as a control in the first immunoprecipitation. For the second immunoprecipitation, anti-MDM2 (SMP-14) or control mouse IgG was added to eluates from the first immunoprecipitation, followed by the addition of Protein G-Sepharose. Protein samples were separated by SDS–PAGE, transferred to a poly(vinylidene difluoride) membrane and probed with the indicated antibodies. Proteins were detected by chemiluminescence.

Antibodies. Primary antibodies used for immunoblotting were as follows: monoclonal anti-HA (HA11; Covance), anti-p53 (DO-1; Santa Cruz; or Ab-1; Oncogene), anti-MDM2 (SMP-14; Santa Cruz; or Ab-3; Calbiochem), anti-E-cadherin (BD Biosciences), anti-Myc (9E11; Covance), anti-p73 (ER-15; Calbiochem), and anti-p21 (Santa Cruz); polyclonal anti-Slug (Santa Cruz), anti-p53 (NB200-171; Novus), anti-MDM2 (C-18; Santa Cruz), and anti-phospho-p53 (Ser 46) (Cell Signaling).

Pulse–chase analysis. Cells were incubated in methionine/cysteine-free DMEM supplemented with glutamine and 5% dialysed FBS (all from Invitrogen), pulse-labelled with 250 μCi ml^{-1} [^{35}S]methionine/cysteine mix (Perkin-Elmer) for 90 min, and chased with DMEM supplemented with 10% FBS and 2 mM unlabelled methionine and cysteine for the indicated durations. Cells were harvested for immunoprecipitation with anti-HA or anti-Slug antibody, respectively, and analysed by SDS–PAGE and fluorography.

RNA interference. Cells were transfected with specific siRNA oligonucleotides for *p53* (si-p53-1 and si-p53-2), *Slug* (si-Slug) or *Mdm2* (si-Mdm2) (all from Invitrogen) by using RNAiFect Transfection Reagent (Qiagen). Efficacy of gene silencing was analysed 72 h after transfection. Lentivirus-based shRNAs were used to create stable Slug, p53 and/or Mdm2 knockdown clones.

Matrigel invasion assay. Transwell chambers (8 μm or 3 μm (for SW620) pore size; Falcon) were coated with Matrigel (Becton Dickinson Labware), seeded with 10^5 cells per well and incubated for 24 h. Cells that invaded the Matrigel were fixed in methanol and stained with propidium iodide, photographed under a fluorescence microscope and counted with AIS software (Imaging Research). Each condition was assayed in triplicate.

Statistical analysis. Data are presented as mean ± s.e.m.The differences between two groups were analysed with Student's *t*-test for continuous variables or Pearson's χ^2 test for categorical variables. The overall survivals for patient groups with different expression signatures were estimated with the Kaplan–Meier method, and two-sided log-rank tests were applied to compare the differences. For correlating the poorer prognostic signatures detected in overall survival analysis (p53mt$^+$, M$^-$, S$^+$, or p53mt$^+$, M$^-$, S$^+$, E$^-$) with the earlier metastasis, we applied one-sided log-rank tests to the metastasis-free survival times. Statistical analyses were performed with SPSS for Windows (version 10.0; SPSS, Inc.). $P < 0.05$ was considered statistically significant.

43. Mountain, C. F. Revisions in the international system for staging lung cancer. *Chest* **111,** 1710–1717 (1997).
44. Travis, W., Brambilla, E., Müller-Hermelink, H. K. & Harris, C. C. *Pathology and Genetics of Tumors of the Lung, Pleura, Thymus and Heart* (IARC Press, 2004).
45. Chang, Y. L. *et al.* Clonality and prognostic implications of p53 and epidermal growth factor receptor somatic aberrations in multiple primary lung cancers. *Clin. Cancer Res.* **13,** 52–58 (2007).
46. Chu, Y. W. *et al.* Selection of invasive and metastatic subpopulations from a human lung adenocarcinoma cell line. *Am. J. Respir. Cell Mol. Biol.* **17,** 353–360 (1997).

nature cell biology

DOI: 10.1038/ncb1875

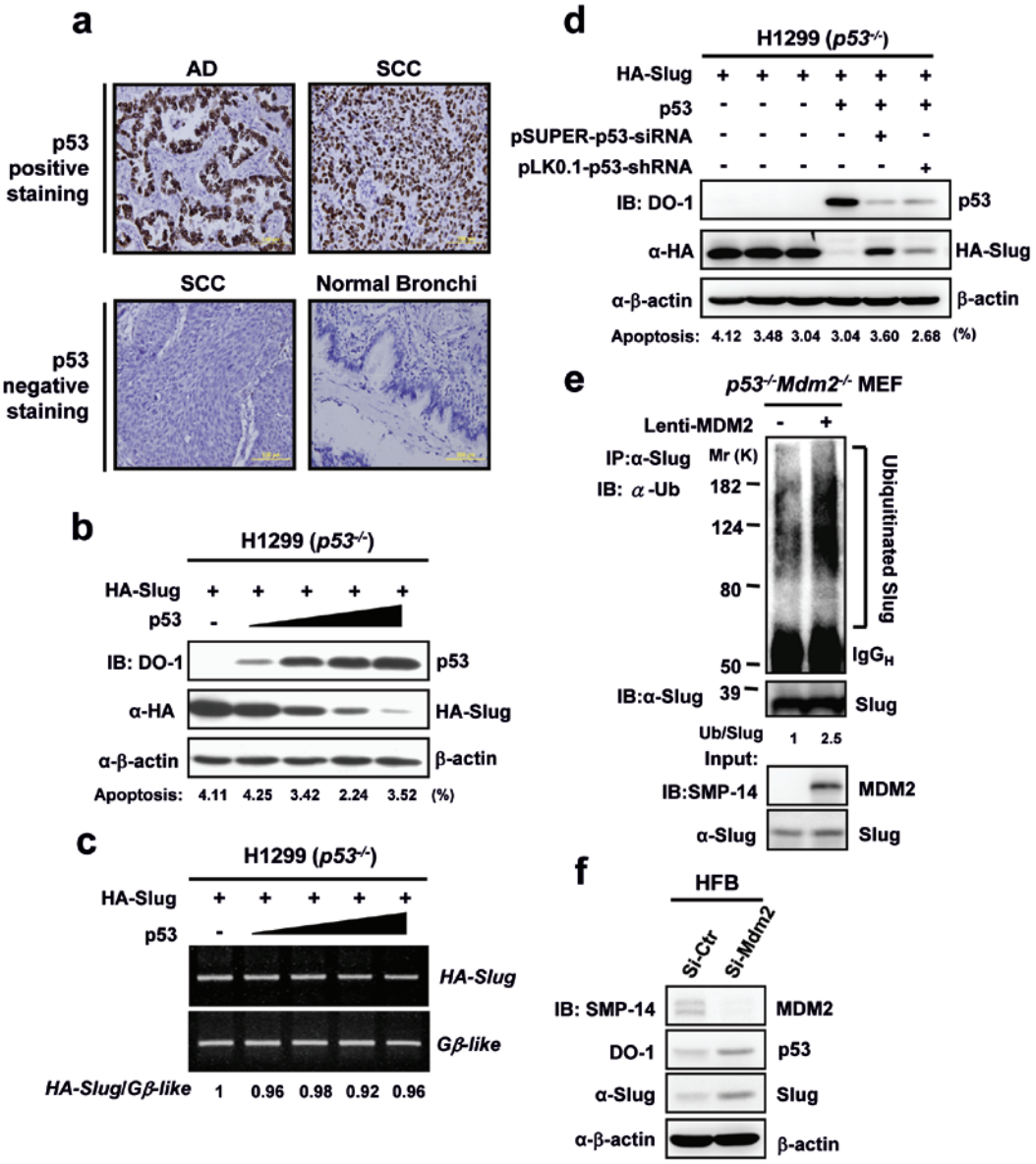

Figure S1 (**a**) The 79 surgical specimens from NSCLC patients were analysed by immunohistochemistry with an anti-p53 antibody and control serum (data not shown). The normal bronchi served as the negative control. Scale bars represent 100 μm. AD, adenocarcinoma; SCC, squamous cell carcinoma. (**b, c**) p53 overexpression decreases the level of Slug protein but not mRNA. H1299 cells were transfected with increasing concentrations of p53 and a constant amount of HA-Slug. At 36 h post-transfection, cell lysates were analysed by immunoblotting (IB) (**b**) or RT-PCR analysis (**c**). β-actin protein and *Gβ-like* mRNA, respectively, served as controls for equal loading. Numbers below the row of the RT-PCR indicate the densitometric values normalised with the relative *Gβ-like* value. (**d**) RNAi knockdown of *p53* reverses p53-mediated Slug downregulation. H1299 cells were co-transfected with HA-Slug, p53 and pSUPER-p53-siRNA or pLK0.1-p53-shRNA in different combinations and protein expression was evaluated by immunoblotting 36 h post-transfection. Apoptosis was quantified by FACS analysis and the percentage of sub-G1 cells is shown. (**e**) MDM2 promotes Slug ubiquitination *in vivo*. *p53*$^{-/-}$*Mdm2*$^{-/-}$ MEFs were infected with Lenti-MDM2 for 48 h, and then treated with MG132. After immunoprecipitation of Slug with α-Slug, the ubiquitinated-Slug complexes were detected by immunoblotting using an α-Ub antibody. (**f**) Knockdown of MDM2 stabilises Slug protein. HFBs transfected with control or *Mdm2*-siRNA oligonucleotides were lysed and analysed by immunoblotting 72 h after transfecting.

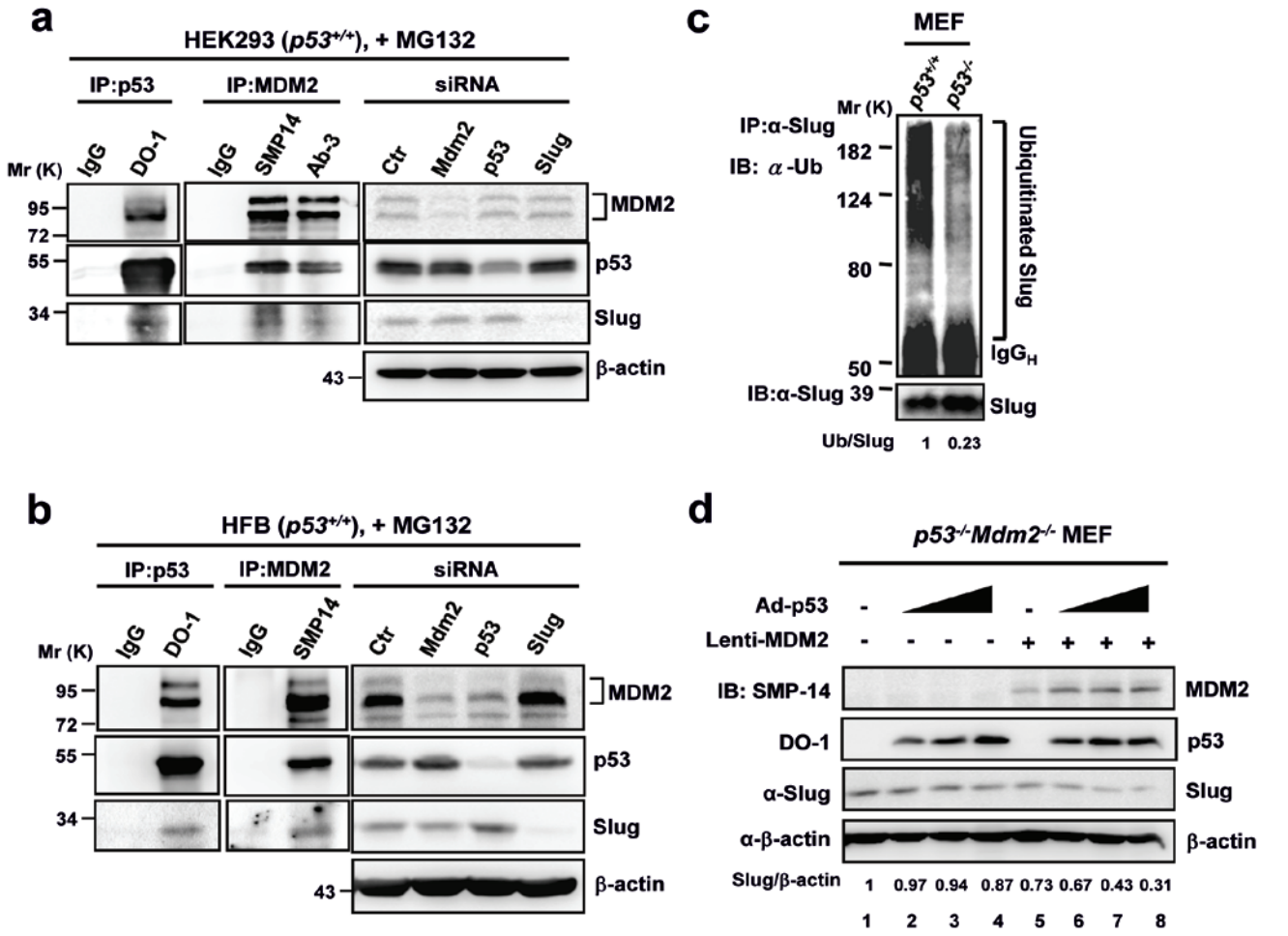

Figure S2 (**a, b**) Interactions of endogenous p53, MDM2, and Slug in HEK293 and HFB cells. Cells were treated with 10 μM MG132. After 6 h, cell lysates were immunoprecipitated with α-p53 (DO-1), two independent α-MDM2 (SMP-14 and/or Ab-3), or mouse IgG before immunoblotted with specific antibodies (SMP-14, α-p53 or α-Slug). Right panel: the protein bands detected in co-IP assays were characterised by specific siRNAs. (**c**) Loss of p53 expression reduces the levels of Slug ubiquitination. *p53*$^{+/+}$ or *p53*$^{-/-}$ MEFs were treated with 10 μM MG132 for 6 h. After immunoprecipitation of Slug with α-Slug, the ubiquitinated-Slug complexes were detected by immunoblotting using an α-Ub antibody (Pierce). (**f**) p53 enhances the MDM2-mediated degradation of Slug. *p53*$^{-/-}$*Mdm2*$^{-/-}$ MEFs stably transduced with Lenti-MDM2 or control Lenti-eGFP were infected with differential doses of Ad-p53. After 48 h, cells were lysed and analysed by immunoblotting with indicated antibodies. Numbers below the respective panels of the immunoblots indicate the densitometric values normalised with the relative control (as indicated) value.

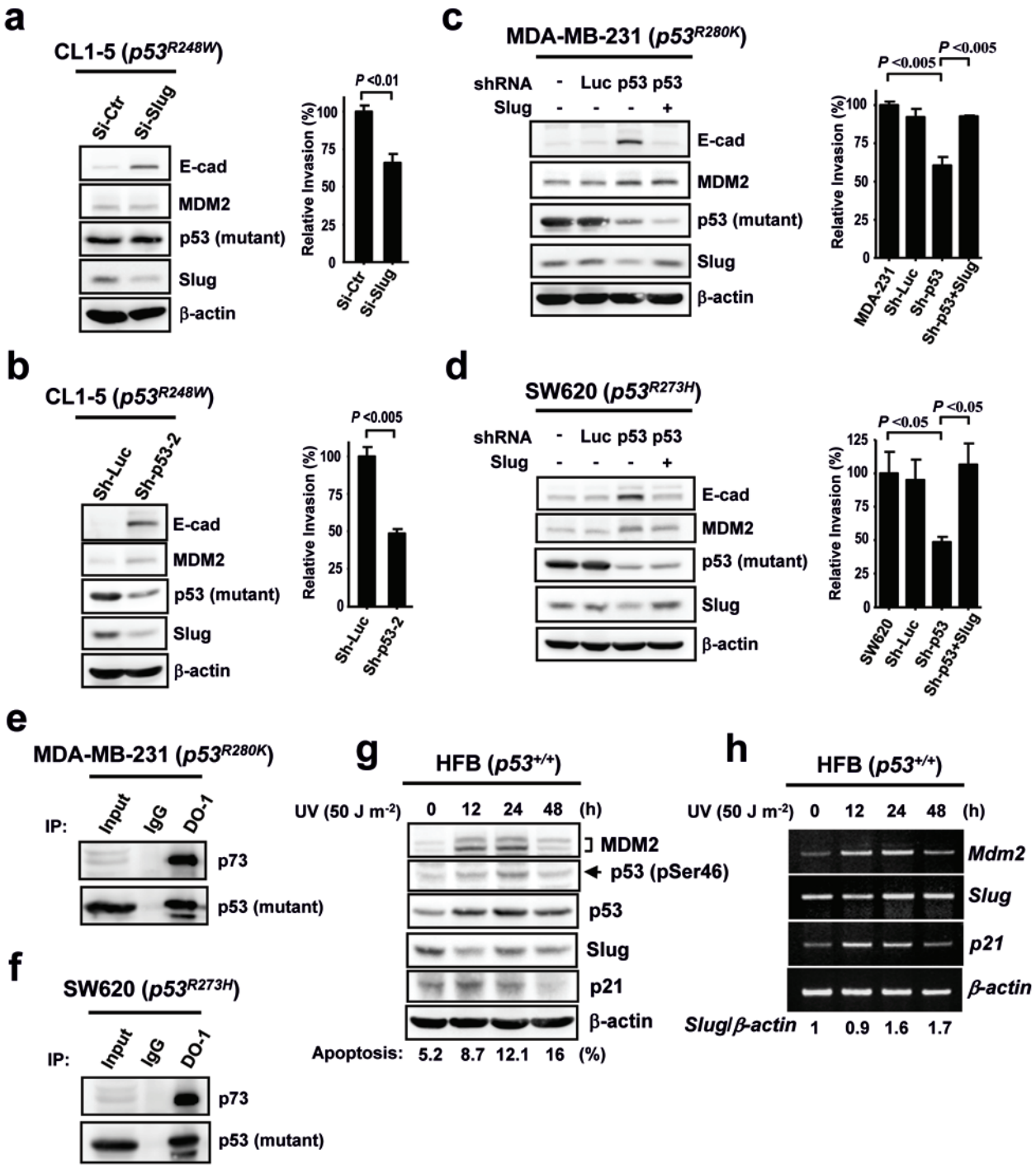

Figure S3 (**a**) Knockdown of Slug in CL1-5 cells by *Slug*-siRNA oligonucleotides increases E-cadherin expression and decreases cell invasiveness. (**b**) The effects of mutant *p53* silencing on MDM2, Slug, E-cadherin, and cancer cell invasiveness can be observed by an independent p53-shRNA (sh-p53-2). (**c, d**) The effects of mutant *p53* silencing on MDM2, Slug, E-cadherin, and cancer cell invasiveness can be observed in other mutant p53-expressing cancer cell lines, MDA-MB-231 (**c**) and SW620 (**d**). Data are shown as mean ± SEM from three independent experiments (n=3). (**e, f**) p73 interacts with p53R280K in MDA-MB-231 cells (**e**) or with p53R273H in SW620 cells (**f**). (**g, h**) Correlation of p53 activation, Slug expression, and p21 and Mdm2 induction with apoptosis in UV-irradiated HFB (*p53*$^{+/+}$) cells. HFB cells were exposed to 50 J m^{-2} of UV radiation. At different time points after UV radiation, cells were lysed and analysed for expression of p53, MDM2, p21 and Slug by immunoblotting (**g**) and RT-PCR analysis (**h**). Phosphorylation of p53 at Ser46 was also evaluated by immunoblotting. β-actin served as an internal control for both immunoblotting and PCR analyses. Numbers below the RT-PCR indicate the densitometric values normalised with the relative β-*actin* value. Apoptotic cells were detected using an Annexin V-PI FACS-based assay. The percentage of PI-negative, annexin V-positive cells at different time points after UV radiation is indicated.

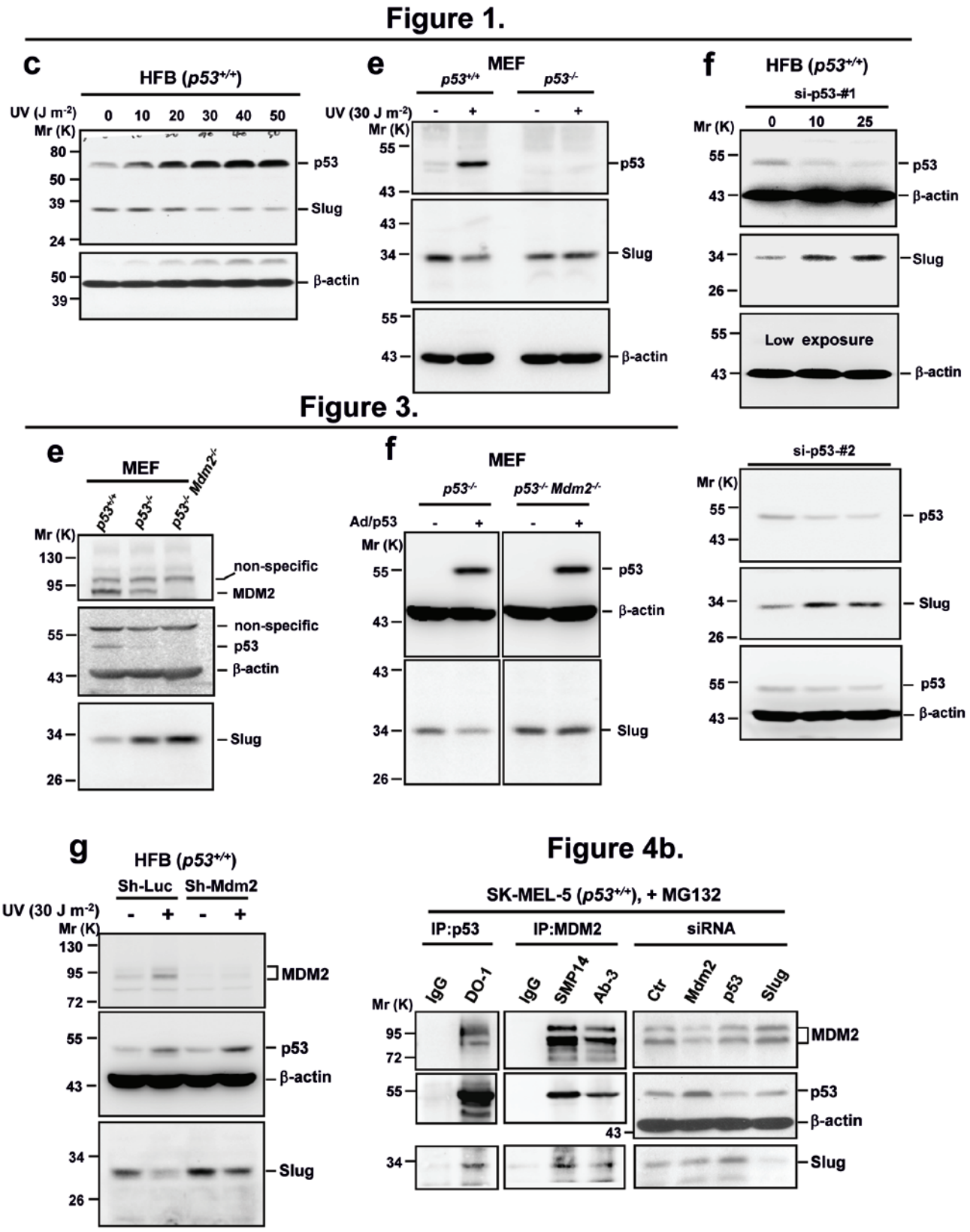

Figure S4 Full scans of key Western data shown in the regular Figures 1c, 1e, 1f, 3e, 3f, 3g, 4b, 4c, 4e, 6a, 6b, 6d, 6e, and Supplementary Information, Figure S2d.

Figure 4.

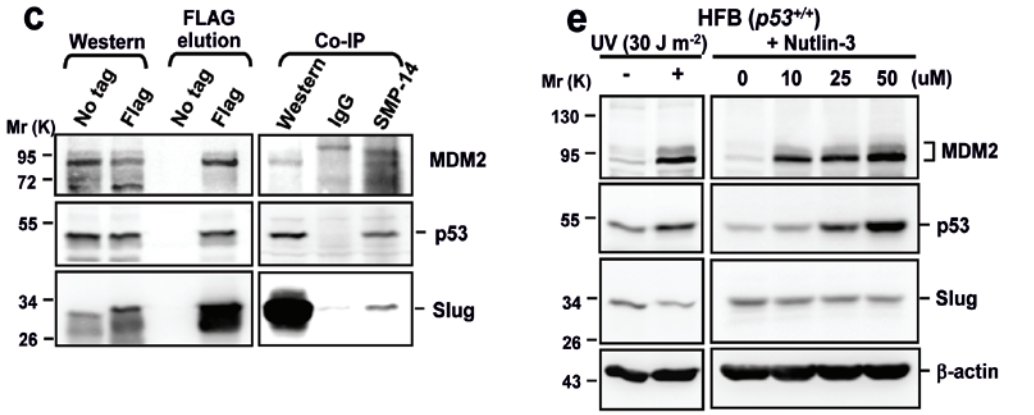

Figure 6.

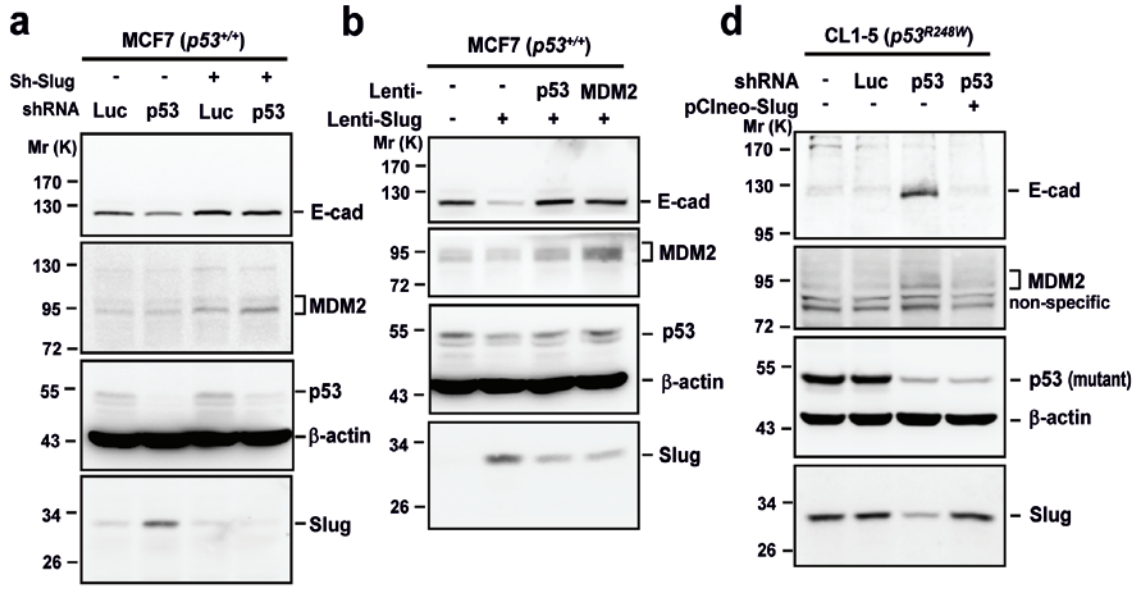

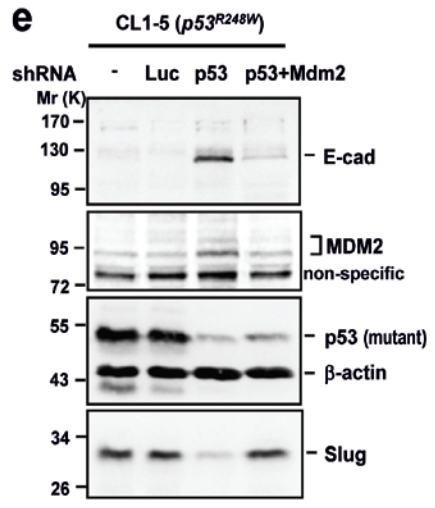

Figure S2d

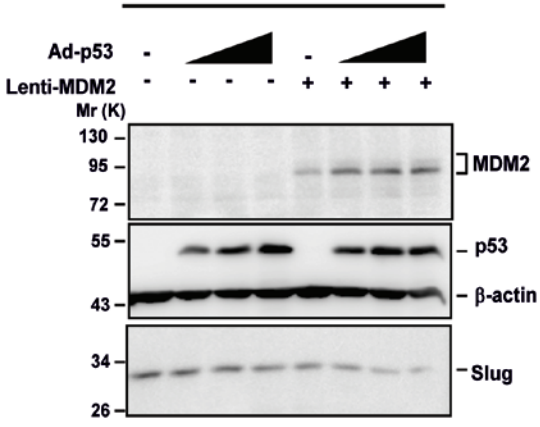

Figure S4 continued

Figure S4 continued

Table S1. The p53 mutation status as well as the MDM2, Slug, and E-cadherin expression profiles with relation to clinical and pathologic characteristics

	Patient	p53 mutation			MDM2 expression			Slug expression			E-cadherin expression		
Characteristics	no.	Negative	Positive	*P*-value*	Low	High	*P*-value*	Low	High	*P*-value*	Low	High	*P*-value*
Patient number	79	46 (58.2%)	33 (41.8%)		32 (40.5%)	47 (59.5%)		41 (51.9%)	38 (48.1%)		35 (44.3%)	44 (55.7%)	
Sex													
Male	49	24 (49.0%)	25 (51.0%)		26 (53.1%)	23 (46.9%)		24 (49.0%)	25 (51.0%)		25 (51.0%)	24 (49.0%)	
Female	30	22 (73.3%)	8 (26.7%)	0.033	6 (20.0%)	24 (80.0%)	0.004	17 (56.7%)	13 (43.3%)	0.507	10 (33.3%)	20 (66.7%)	0.125
Histological type†													
Squamous cell carcinoma	12	6 (50.0%)	6 (50.0%)		10 (83.3%)	2 (16.7%)		5 (41.7%)	7 (58.3%)		8 (66.7%)	4 (33.3%)	
Adenocarcinoma	63	38 (60.3%)	25 (39.7%)	0.506	21 (33.3%)	42 (66.7%)	0.001	33 (52.4%)	30 (47.6%)	0.496	24 (38.1%)	39 (61.9%)	0.067
Tumor stage													
Stage II	20	13 (65.0%)	7 (35.0%)		10 (50.0%)	10 (50.0%)		12 (60.0%)	8 (40.0%)		10 (50.0%)	10 (50.0%)	
Stage III	38	22 (57.9%)	16 (42.1%)		14 (36.8%)	24 (63.2%)		19 (50.0%)	19 (50.0%)		18 (47.4%)	20 (52.6%)	
Stage IV	21	11 (52.4%)	10 (47.6%)	0.714	8 (38.1%)	13 (61.9%)	0.603	10 (47.6%)	11 (52.4%)	0.693	7 (33.3%)	14 (66.7%)	0.489

*Pearson Chi-Square test.

†Adenosquamous carcinomas are not included

Table S2. The p53 mutation status and protein expression pattern of MDM2 and Slug in 79 NSCLC patients.

Expression pattern	p53 mutation	MDM2 overexpression	Slug overexpression	Total (%)
1	+	+	+	10 (12.7)
2	+	+	–	1 (1.3)
3	+	–	+	15 (19.0)
4	+	–	–	7 (8.9)
5	–	+	+	11 (13.8)
6	–	+	–	25 (31.7)
7	–	–	+	2 (2.5)
8	–	–	–	8 (10.1)
Total				79 (100)

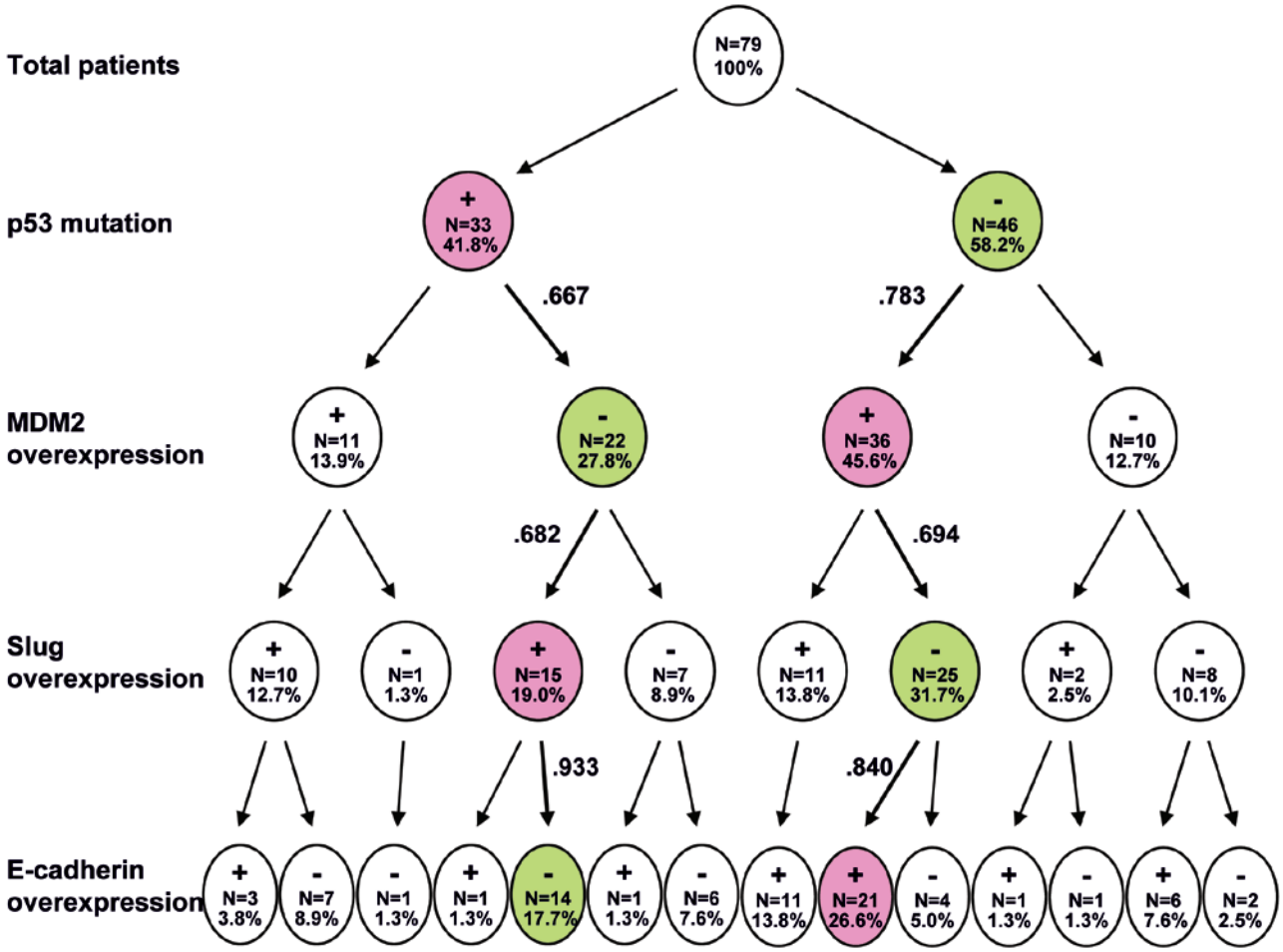

A tree diagram for the preferential expression patterns of p53, MDM2, Slug, and E-cadherin. Numbers along edges indicate the conditional probabilities of choosing nodes in a path. Pink codes + and green codes - .

Table S3a. The p73 targets, p21 and MDM2, were significantly downregulated in mutant p53- and Slug-expressing NSCLC tumours.

	p21 expression			MDM2 expression			
Expression pattern	**Low**	**High**	***P-value****	**Low**	**High**	***P-value****	**Total**
p53 mutation+ p53+ Slug+	11 (78.6%)	3 (21.4%)		9 (64.3%)	5 (35.7%)		14
p53 mutation - p53 - Slug -	5 (21.7%)	18 (78.3%)	0.001	5 (21.7%)	18 (78.3%)	0.010	23

*Pearson Chi-Square test.

Table S3b. The relationship between MDM2 and Slug expression in tumour specimens from 79 NSCLC patients

		MDM2		
Protein expression		**High (>50%, n=47)**	**Low (≤50%, n=32)**	***P-value****
Slug	**High (>50%)**	21 (44.7 %)	17 (53.1 %)	
	Low (≤50%)	26 (55.3 %)	15 (46.9 %)	0.461

*Pearson Chi-Square test.

Supplementary discussion

The phosphorylation and ubiquitin-mediated proteasomal degradation of Snail (SNAI1) has recently been described[1]. Unlike SNAI1, little is known about the post-translational regulation of Slug. Vernon et al. have shown that, in *Xenopus*, the partner of paired (Ppa) protein, the F-box component of a modular E3 ligase, regulates the degradation of Slug in neural crest cells[2]. Here we found that human Slug is a labile protein whose degradation is mediated by p53 and MDM2 in normal cells and cancer cells. Because the Slug protein plays essential functions in embryonic development and cancer progression, multiple sophisticated mechanisms are likely involved in controlling its activity. Our findings imply that the stability of Slug is normally under fine control, and dysregulation of Slug catabolism may invigorate tumour malignancy[3].

It has been shown that p53, through its p53 DNA-binding domain, interacts directly with bcl-xL and bcl-2 to mediate apoptosis (ref. 32 in main text), indicating that this domain possesses functions apart from transcriptional regulation. In our study, we showed that p53 can bind to Slug via its DNA-binding domain, forming a complex with Slug and MDM2 that facilitates Slug degradation. These results corroborate a previous report that p53 guides the recognition and recruitment of HIF-1α to MDM2-ubiquitin ligase, facilitating ubiquitin-dependent degradation by the proteasome[4]. In addition, we showed that an N-terminal region (amino acids 21-66) of Slug is responsible for binding p53 and MDM2 and is likely critical for Slug degradation. A more refined characterization of the interacting domains within the p53-MDM2-Slug complex and a functional analysis of their contributions to Slug degradation may assist in the rational design of new cancer therapies.

Supplementary references

1. Peinado, H., Olmeda, D., & Cano, A. Snail, Zeb and bHLH factors in tumour progression: an alliance against the epithelial phenotype? *Nat. Rev. Cancer* **7,** 415-428 (2007).

2. Vernon, A. E. & LaBonne, C. Slug stability is dynamically regulated during neural crest development by the F-box protein Ppa. *Development* **133,** 3359-3370 (2006).

3. Perez-Mancera, P. A. *et al.* SLUG in cancer development. *Oncogene* **24,** 3073-3082 (2005).

4. Ravi, R. *et al.* Regulation of tumor angiogenesis by p53-induced degradation of hypoxia-inducible factor 1alpha. *Genes Dev.* **14,** 34-44 (2000).

nature cell biology

A functional screen implicates microRNA-138-dependent regulation of the depalmitoylation enzyme APT1 in dendritic spine morphogenesis

Gabriele Siegel[1,11], Gregor Obernosterer[1,11], Roberto Fiore[1], Martin Oehmen[3], Silvia Bicker[1], Mette Christensen[1,4], Sharof Khudayberdiev[1], Philipp F. Leuschner[2], Clara J. L. Busch[2], Christina Kane[5], Katja Hübel[6], Frank Dekker[6], Christian Hedberg[9], Balamurugan Rengarajan[6], Carsten Drepper[7,10], Herbert Waldmann[6], Sakari Kauppinen[4,8], Michael E. Greenberg[5], Andreas Draguhn[3], Marc Rehmsmeier[7,10], Javier Martinez[2,12] and Gerhard M. Schratt[1,12]

The microRNA pathway has been implicated in the regulation of synaptic protein synthesis and ultimately in dendritic spine morphogenesis, a phenomenon associated with long-lasting forms of memory. However, the particular microRNAs (miRNAs) involved are largely unknown. Here we identify specific miRNAs that function at synapses to control dendritic spine structure by performing a functional screen. One of the identified miRNAs, miR-138, is highly enriched in the brain, localized within dendrites and negatively regulates the size of dendritic spines in rat hippocampal neurons. miR-138 controls the expression of acyl protein thioesterase 1 (APT1), an enzyme regulating the palmitoylation status of proteins that are known to function at the synapse, including the α_{13} subunits of G proteins ($G\alpha_{13}$). RNA-interference-mediated knockdown of APT1 and the expression of membrane-localized $G\alpha_{13}$ both suppress spine enlargement caused by inhibition of miR-138, suggesting that APT1-regulated depalmitoylation of $G\alpha_{13}$ might be an important downstream event of miR-138 function. Our results uncover a previously unknown miRNA-dependent mechanism in neurons and demonstrate a previously unrecognized complexity of miRNA-dependent control of dendritic spine morphogenesis.

The functioning of the mammalian brain relies on the proper formation of intricate neuronal circuits. Neurons within these circuits are synaptically connected, and most excitatory synaptic connections between neurons form on dendritic spines, specialized protrusions emanating from the dendritic shaft[1,2]. The structural and functional plasticity of dendritic spines correlates with long-lasting changes in synaptic transmission that underlie higher cognitive functions[3,4]. Dendritic spine abnormalities are a hallmark of a variety of neurological diseases, including several forms of learning disability[5]. A plethora of molecular mechanisms involved in dendritic spine plasticity have been elucidated during the last decade, including actin cytoskeletal dynamics, post-translational protein modifications, protein trafficking, gene transcription and protein turnover[6–10]. The synthesis of proteins *de novo* is of particular importance for creating enduring changes in synaptic transmission that are associated with long-term memory[11,12]. Proteins can be either synthesized in the soma and transported to dendritic spines, or synthesized locally from a pool of dendritic messenger RNAs within or next to spines[13–15].

The local translation of dendritic mRNAs is regulated tightly by RNA-binding proteins and non-coding RNAs that bind preferentially to the 3′ untranslated region (UTR) of the mRNAs[16,17]. miRNAs, a diverse class of 20–24-nucleotide non-coding RNAs, regulate local mRNA translation in dendrites, thereby affecting the morphology of dendritic spines in rat hippocampal neurons[18,19].

miRNAs are expressed in essentially all cell types and regulate important biological processes, including differentiation, apoptosis and cellular transformation[20,21]. miRNAs inhibit mRNA translation by binding

[1]Interdisziplinäres Zentrum für Neurowissenschaften, SFB488 Junior Group, Universität Heidelberg, and Institut für Neuroanatomie, Universitätsklinikum Heidelberg, Im Neuenheimer Feld 345, 69120 Heidelberg, Germany. [2]Institute of Molecular Biotechnology, IMBA, Austrian Academy of Sciences, Dr. Bohr Gasse 3, 1030 Vienna, Austria. [3]Institut für Physiologie und Pathophysiologie, Universität Heidelberg, Im Neuenheimer Feld 326, 69120 Heidelberg, Germany. [4]Wilhelm Johannsen Center for Functional Genome Research, Department of Cellular and Molecular Medicine, University of Copenhagen, Blegdamsvej 3, DK-2200 Cph N, Denmark. [5]Department of Neurobiology, Harvard Medical School, 220 Longwood Avenue, Boston, Massachusetts 02115, USA. [6]Max-Planck-Institut für molekulare Physiologie, Abteilung Chemische Biologie, and Technische Universität Dortmund, Fakultät Chemie, Chemische Biologie, Otto-Hahn-Strasse 11, 44227 Dortmund, Germany. [7]Center for Biotechnology (CeBiTec), Universität Bielefeld, 33594 Bielefeld, Germany. [8]Santaris Pharma, Boege Alle 3, DK-2970 Hoersholm, Denmark. [9]Max Planck Institute of Molecular Physiology, Chemical Biology, Otto-Hahn-Strasse 11, 44227 Dortmund, Germany.
[10]Present addresses: Institute for Clinical Neurobiology, ZEMM, Zinklesweg 10, Würzburg University, 97078 Würzburg, Germany (C.D.); Gregor Mendel Institute of Molecular Plant Biology, Dr. Bohr-Gasse 3, 1030 Vienna, Austria (M.R.).
[11]These authors contributed equally to this work.
[12]Correspondence should be addressed to J.M. (e-mail: javier.martinez@imba.oeaw.ac.at) or G.M.S. (e-mail: schratt@ana.uni-heidelberg.de)

Received 18 December 2008; accepted 10 February 2009; published online 24 May 2009; DOI:10.1038/ncb1876

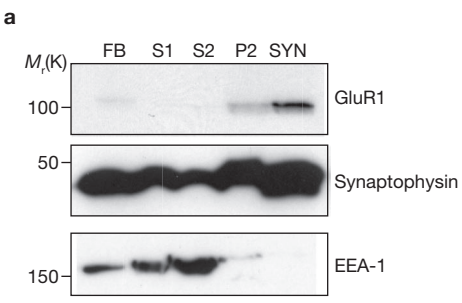

b

miRNA	Fold enrichment	STDV
miR-29a	4.60	2.45
miR-7	3.71	1.65
miR-341	3.41	1.09
miR-218	3.39	1.17
miR-137	3.27	0.61
miR-9	2.66	1.39
miR-335	2.25	0.45
miR-376b	2.20	0.44
miR-98	2.19	0.51
miR-138	2.16	0.51
miR-143	0.36	0.07
miR-150	0.25	0.10
miR-145	0.20	0.06
miR-126	0.05	0.01

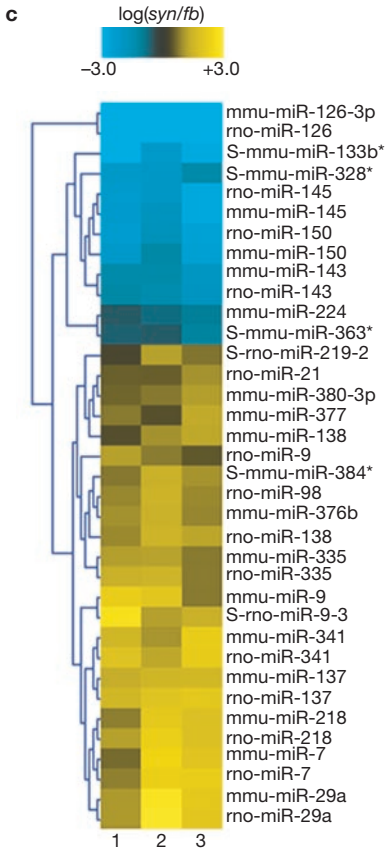

Figure 1 Expression profiling of miRNAs in synaptososomes. (**a**) Western blot analysis of protein extracts derived from P15 rat forebrain (FB), low-speed centrifugation supernatant (S1), high-speed centrifugation supernatant (S2), high-speed centrifugation pellet (P2) or synaptosomes (SYN). Whereas synaptosomes are enriched in presynaptic (synaptophysin) and postsynaptic (GluR1) proteins, cytoplasmic EEA-1 is depleted from P2 and synaptosomes. (**b**) miRNAs that displayed an at least twofold change in expression between synaptosomes and forebrain in three different experiments, s.d. (**c**) Hierarchical clustering of miRNAs displaying significantly different expression between whole forebrain and synaptosomes in three different experiments. Colour coding: enrichment in synaptosomes versus whole forebrain on a logarithmic scale; yellow, higher level in synaptosomes; blue, lower level in synaptosomes.

to cognate sites in the 3′ UTR of target mRNAs[22]. In the mammalian nervous system, miRNAs function during cell specification (miR-124a and miR-9), neurite outgrowth (miR-132) and spine development (miR-134)[23]. Microarray and cloning experiments have shown that a large number of miRNAs are expressed in the postnatal mammalian brain at times of synapse development, but their role in synapse formation and plasticity is largely unknown[24–26]. Here we present a functional screen that led to the identification of miRNAs that are involved in dendritic spine morphogenesis. Among these miRNAs, miR-138 was found to robustly inhibit the growth of dendritic spines, an effect that was mediated by downregulation of APT1, an enzyme catalysing the depalmitoylation of several signalling proteins[27]. Our findings define a previously unknown mechanism by which miRNAs control dendritic spine morphogenesis and indicate a hitherto unrecognized complexity of miRNA function in the regulation of synaptic plasticity in mammalian neurons.

RESULTS

Large-scale identification of synaptically enriched miRNAs

To identify miRNAs that function during synaptic development, we undertook a combination of expression profiling of miRNAs in the synaptodendritic compartment and subsequent functional inhibitory screening in primary hippocampal neurons.

We reasoned that miRNAs that are important for synapse function might reside primarily near the synapse, where they could locally regulate the translation of critical target mRNAs. Synaptosomes, a biochemical fraction highly enriched for synaptic membranes, preserve components of local protein synthesis, including polyribosomes, mRNAs and regulatory RNAs (ref. 28, Fig. 1a, and data not shown). We therefore conclude that synaptosomes are a suitable source for synaptic miRNAs. Total RNA was extracted from postnatal day 15 (P15) rat forebrains and synaptosomes and simultaneously hybridized to microarrays that contained probes for all mouse and rat mature miRNAs listed in the Sanger database (miRBase, version 7.1; http://www.sanger.ac.uk/Software/Rfam/mirna/). In this manner we identified ten mature miRNAs that displayed an at least twofold enrichment in synaptosomes compared with whole forebrain in three biological replicates. Conversely, four mature miRNAs were strongly depleted from synaptosomes (Fig. 1b, c; Supplementary Information, Table S1).

The observed enrichment of several miRNAs in RNA preparations from synaptosomes was validated for selected candidates by northern blot analysis (Fig. 2a). In accordance with the microarray data, we found higher levels of miR-218 (3.02-fold) and miR-138 (1.67-fold) in total RNA prepared from synaptosomes than in whole forebrain. In contrast, mature miR-124 was not enriched (0.96-fold) and pre-miR-124 was undetectable in synaptosomes, confirming that only specific miRNAs are enriched at the synapse.

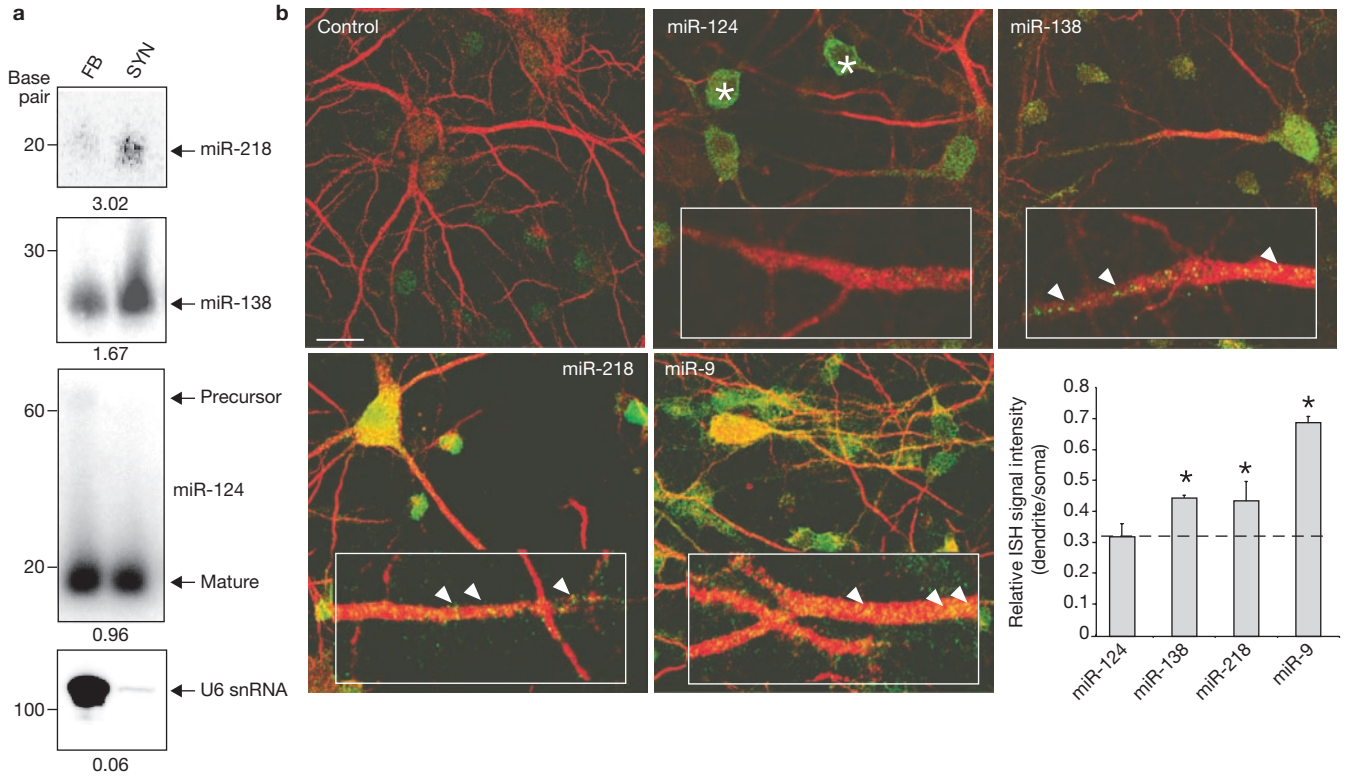

Figure 2 A subset of neuronal miRNAs is localized in the synaptodendritic compartment. (**a**) Validation of microarray results by northern blotting. RNA was extracted from P15 rat forebrain (FB) or P15 rat synaptosomes (SYN), separated by 15% PAGE and probed for the presence of miR-218, miR-138, miR-124 or U6 snRNA. Numbers represent fold enrichment in synaptosomes. Note the absence of pre-miR-124 from synaptosomes. (**b**) Subcellular localization of synaptically enriched miRNAs in hippocampal neurons. *In situ* hybridization was performed on hippocampal neurons at 18 DIV with fluorescein isothiocyanate-coupled LNA probes directed against miR-9, miR-218 and miR-124, a digoxigenin-coupled LNA probe directed against miR-138 or a digoxigenin-coupled control LNA probe. Asterisks indicate prominent staining of miR-124 in neuronal cell bodies; arrowheads indicate dendritic staining of miR-9, miR-218 and miR-138. Scale bar, 20 μm. Bottom right: quantification of ISH signal. Values are expressed as the ratio between dendritic and somatic signal intensities. Dendrite/soma ratios of miR-138, miR-218 and miR-9 are significantly higher than that of the somatic miR-124. Asterisk, $P < 0.05$ (*t*-test, $n = 3$).

To monitor the subcellular localization of miRNAs identified in our screen, we performed *in situ* hybridization (ISH) in rat hippocampal neurons at 18 days *in vitro* (DIV), using probes for miR-9, miR-218, miR-138 and miR-124 as a control (Fig. 2b). All candidate miRNAs were readily detected in cultured hippocampal neurons by using locked nucleic acid (LNA) oligonucleotides as detection probes. We confirmed the specificity of our ISH protocol by using a scrambled LNA control oligonucleotide (Fig. 2b, upper left panel). Neuronal expression of miR-138 was further confirmed by ISH in brain slices (Supplementary Information, Fig. 1a, b), quantitative RT–PCR and northern blotting with RNA from dissociated primary neurons (Supplementary Information, Fig. 1c, d). Whereas miR-124 was localized mainly within the cell body (Fig. 2b, asterisks), the signals for miR-138, miR-218 and miR-9 extended well into neuronal processes that were identified as dendrites by co-staining for the dendritic marker protein MAP2 (Fig. 2b, arrowheads). Quantification of the ISH signals (Fig. 2b, lower right panel) confirmed the enrichment of miR-138, miR-218 and miR-9 in dendrites relative to the cell-body-restricted miR-124. Taken together, our microarray, northern blot and ISH data show that a specific subset of miRNAs is enriched in the synaptodendritic compartment of rat neurons. These findings suggest the existence of a dendritic miRNA regulatory network.

Functional screening identifies miR-138 as a negative regulator of dendritic spine size

To study the functional relevance of the miRNA regulatory network in dendrites, we interfered with the function of candidate miRNAs identified in the microarray analysis by transfecting cells with miRNA antagonists (2′-*O*-methyl (2′*O*-Me) modified antisense (AS) oligoribonucleotides)[29]. We speculated that some of the miRNAs identified in the screen might affect dendritic spine morphology, a correlate of the maturity and strength of excitatory synapses[3,4,30] (Fig. 3a).

Using a single cell fluorescent sensor assay[31], we found that transfection of 2′*O*-Me AS oligonucleotides significantly decreased miRNA-mediated sensor cleavage for three selected miRNAs (miR-138, miR-132 and miR-218) that are endogenously expressed in hippocampal neurons (10–18 DIV; Supplementary Information, Fig. 1e). Therefore, 2′*O*-Me AS oligonucleotides are suitable for achieving specific inhibition of individual miRNAs. We analysed candidate miRNAs that showed an at least twofold enrichment in synaptosomes compared with whole brain. In addition, miR-132 was included because it regulates dendritic outgrowth[32]. Inhibition of miRNA function by 2′*O*-Me AS oligonucleotides resulted in a significant change in dendritic spine volume for two of the miRNAs tested (miR-138 and miR-132) in comparison with control transfected neurons (Fig. 3b). Inhibition of miR-138 function resulted in a robust and significant increase in spine volume (Fig. 3b, c) without altering the total number of synaptic puncta

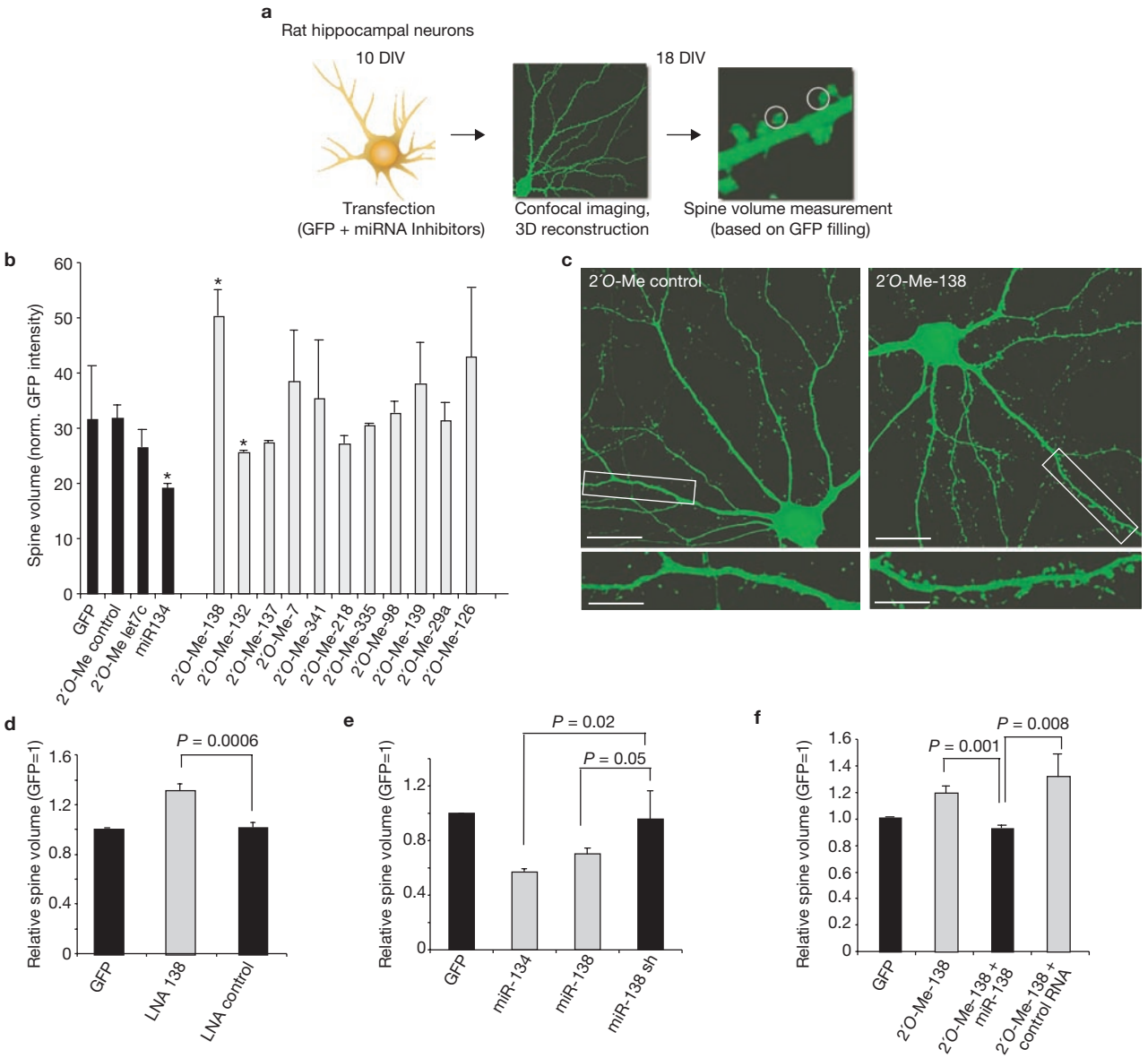

Figure 3 Synaptically enriched miR-138 regulates dendritic spine size. (**a**) Flowchart of the functional screen for the identification of miRNAs controlling dendritic spine size. Rat hippocampal neurons (10 DIV) were transfected with GFP together with miRNA inhibitors (40 nM) or 134 duplex RNA (20 nM), and processed at 18 DIV for confocal microscopy. The fluorescence intensity of the freely diffusible GFP within three-dimensional projections was used to calculate the relative spine volume. (**b**) Quantitative analysis of relative spine volume of hippocampal neurons transfected with the indicated double-stranded RNA (20 nM) or antisense 2′-*O*-methyl (2′*O*-Me) oligonucleotides (40 nM). Values are shown as mean ± s.d. ($n = 3$; at least 750 spines from 15 neurons). Asterisk, $P < 0.05$ (compared with 2′*O*-Me control conditions). (**c**) Representative hippocampal neurons (18 DIV) transfected with GFP together with either 2′*O*-Me control (left) or 2′*O*-Me-138 (40 nM). Boxed insets show spines at higher magnification. Scale bars, 20 μm (main panels); 8 μm (insets). (**d**) LNA-mediated inhibition of miR-138 increases spine volume. Average spine volume of neurons treated with the indicated LNA antisense oligonucleotides (100 nM). Values were normalized to the GFP-only condition and are shown as mean ± s.d. ($n = 3$; at least 1,200 spines from 15 neurons). $P = 0.001$ (ANOVA). The P value of a pairwise Student's t-test is indicated. (**e**) Overexpression of miR-138 in hippocampal neurons decreases spine volume. Duplex RNAs representing the full-length version of miR-138, a 3′ truncated miR-138 (miR-138 sh) or miR-134 were transfected as in **b** and the relative spine volume was determined. Values were normalized to the GFP-only condition and are shown as mean ± s.d. ($n = 3$; at least 1,200 spines from 15 neurons). $P = 0.029$ (ANOVA). P values of pairwise Student's t-tests are indicated. (**f**) Restoring miR-138 function rescues increased spine size caused by miR-138 inhibition. Average spine volume was determined from neurons transfected with 2′*O*-Me-138 (40 nM) together with synthetic miR-138 duplex RNA (20 nM) or control duplex RNA (20 nM, let-7c). Values were normalized to the GFP-only condition and are shown as mean ± s.d. ($n = 3$; at least 1,200 spines from 15 neurons). $P = 0.0067$ (ANOVA). P values of pairwise Student's t-tests are indicated.

(Supplementary Information, Fig. 2a). Introducing 2′*O*-Me AS oligonucleotides directed against the other nine candidate miRNAs or three control sequences (2′*O*-Me control, 2′*O*-Me let7c and 2′*O*-Me-126) did not significantly affect spine volume (Fig. 3b), demonstrating that we can specifically interfere with dendritic spine morphogenesis.

Because inhibition of miR-138 changed dendritic spine size very robustly, and the role of miR-138 in the nervous system and synaptic development was completely unknown, we decided to focus on miR-138. To corroborate our findings, we employed another AS oligonucleotide inhibitor of different chemistry (LNA). Similarly to 2′*O*-Me-138,

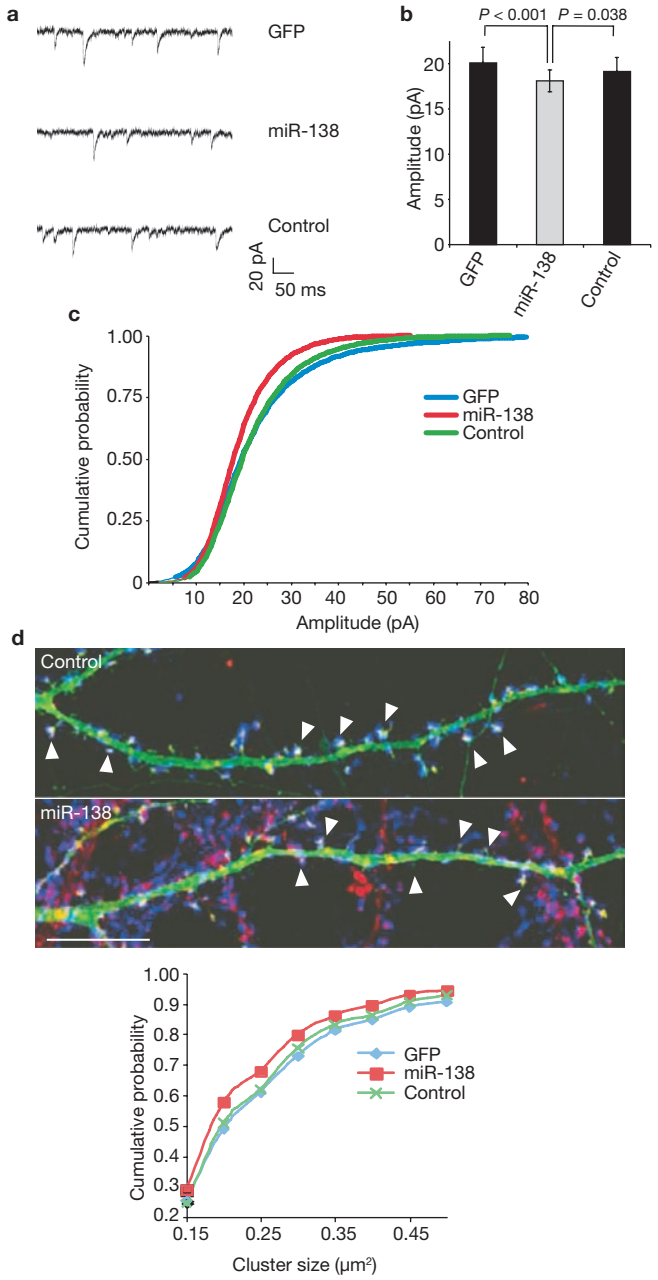

Figure 4 miR-138 negatively regulates miniature synaptic transmission at excitatory synapses. (**a**) Original recordings of mEPSCs in cultured hippocampal neurons in the presence of tetrodotoxin and gabazine. Cells were voltage clamped at −70 mV. Traces show representative data from cells expressing GFP only, GFP + miR-138 duplex RNA, and GFP + control duplex RNA. (**b**) Decrease in median mEPSC amplitudes in miR-138-expressing neurons. Results are shown as medians and s.d. for each group (GFP, $n = 14$; miR-138 $n = 16$; control duplex RNA $n = 12$). P values (pairwise Student's t-test) are indicated above the bar graph. (**c**) Cumulative amplitude distributions of mEPSCs recorded from neurons transfected as in **a**. Data were pooled from 14 cells (GFP), 16 cells (mir-138) and 12 cells (control duplex RNA). Note the leftward shift of the cumulative curve for miR-138 ($P < 0.001$, Kolmogorov–Smirnov test). (**d**) GluR2 surface staining of cells transfected as in **a**. Top panels: representative dendrites of neurons transfected with either miR-138 or control duplex RNA and stained for GluR2 (red) and synapsin (blue). Arrowheads depict large GluR2 clusters in spine heads of control neurons and small or absent GluR2 clusters in protrusions of miR-138-expressing neurons. Scale bar, 10 μm. Bottom panel: cumulative distribution of GluR2 surface cluster sizes plotted for the indicated conditions. Kolmogorov–Smirnov test: $P = 0.001$; $D = 0.0927$ (miR-138 versus control transfected cells).

transfection of LNA-138 specifically increased the average spine volume of hippocampal neurons (Fig. 3d). Conversely, transfection of miR-138 duplex RNA significantly decreased average spine volume, supporting an inhibitory role for miR-138 in spine growth (Fig. 3e). miR-138 duplex RNA, but not a control RNA (let-7c), was able to completely revert the spine-growth-promoting effect observed on inhibition of miR-138, demonstrating the specificity of the effect on spine size (Fig. 3f). Overexpression of either duplex RNA had no significant effect on dendritic spine density or the dendritic branching index (Supplementary Information, Fig. 2b, c), indicating that overall dendritic morphology was not compromised by the introduction of synthetic small RNAs.

We therefore identified miR-138 as a critical component of a regulatory pathway that orchestrates dendritic spine growth. Calcium influx into cortical neurons as induced by membrane depolarization led to a rapid and progressive decline of pre-miR-138 expression (Supplementary Information, Fig. 2d) and miR-138 cleavage activity (Supplementary Information, Fig. 2e), indicating that miR-138 could be regulated during activity-dependent spine development.

miR-138 regulates synaptic transmission and α-amino-3-hydroxy-5-methyl-4-isoxazole propionic acid receptor (AMPAR) surface staining

We next examined whether the observed changes in spine morphology on perturbation of miR-138 are associated with corresponding alterations in excitatory synaptic function. We recorded miniature excitatory postsynaptic currents (mEPSCs; Fig. 4a) from cultured hippocampal neurons that had been transfected with miR-138, with control duplex RNA or with a vector expressing green fluorescent protein (GFP) only. In miR-138-expressing neurons, the median amplitude of mEPSCs was significantly decreased in comparison with both control transfections (Fig. 4b, c). The frequency of events was not different between all three types of cell. This result is consistent with our previous observations that miR-138 expression leads to a 25% decrease in spine volume (Fig. 3d) but has no effect on spine density (Supplementary Information, Fig. 2b). mEPSCs were sensitive to 6-cyano-7-nitroquinoxaline (CNQX) and were therefore largely mediated by AMPARs (data not shown). Accordingly, we found a decrease in the median size, but not in the density, of GluR2-containing AMPAR clusters in dendrites of miR-138-expressing neurons (Fig. 4d and data not shown; $P < 0.001$ (Kolmogorov–Smirnov test). Thus, miR-138-mediated spine shrinkage correlates with a decrease in the amplitude of postsynaptic currents and AMPAR cluster size.

mRNA encoding acyl-protein thioesterase 1 (APT1) is a miR-138 target in neurons

Using the RNAhybrid program we predicted miR-138 target mRNAs that might mediate the miR-138 effect on spine morphogenesis[33,34]. We selected four putative miR-138 target mRNAs that seemed to be particularly interesting in terms of synaptic function: EphrinB3 (ref. 35), PLEKHB1 (ref. 36), RIMS2 (ref. 37) and APT1 (ref. 38).

To validate the functionality of the identified binding sites within these mRNAs, full-length 3′ UTRs of the candidate miR-138 targets were cloned downstream of the luciferase coding region and these constructs were transfected into cortical neurons along with miR-138 duplex RNA. The *APT1* 3′ UTR conferred the most robust decrease in luciferase activity upon miR-138 co-transfection in both HeLa

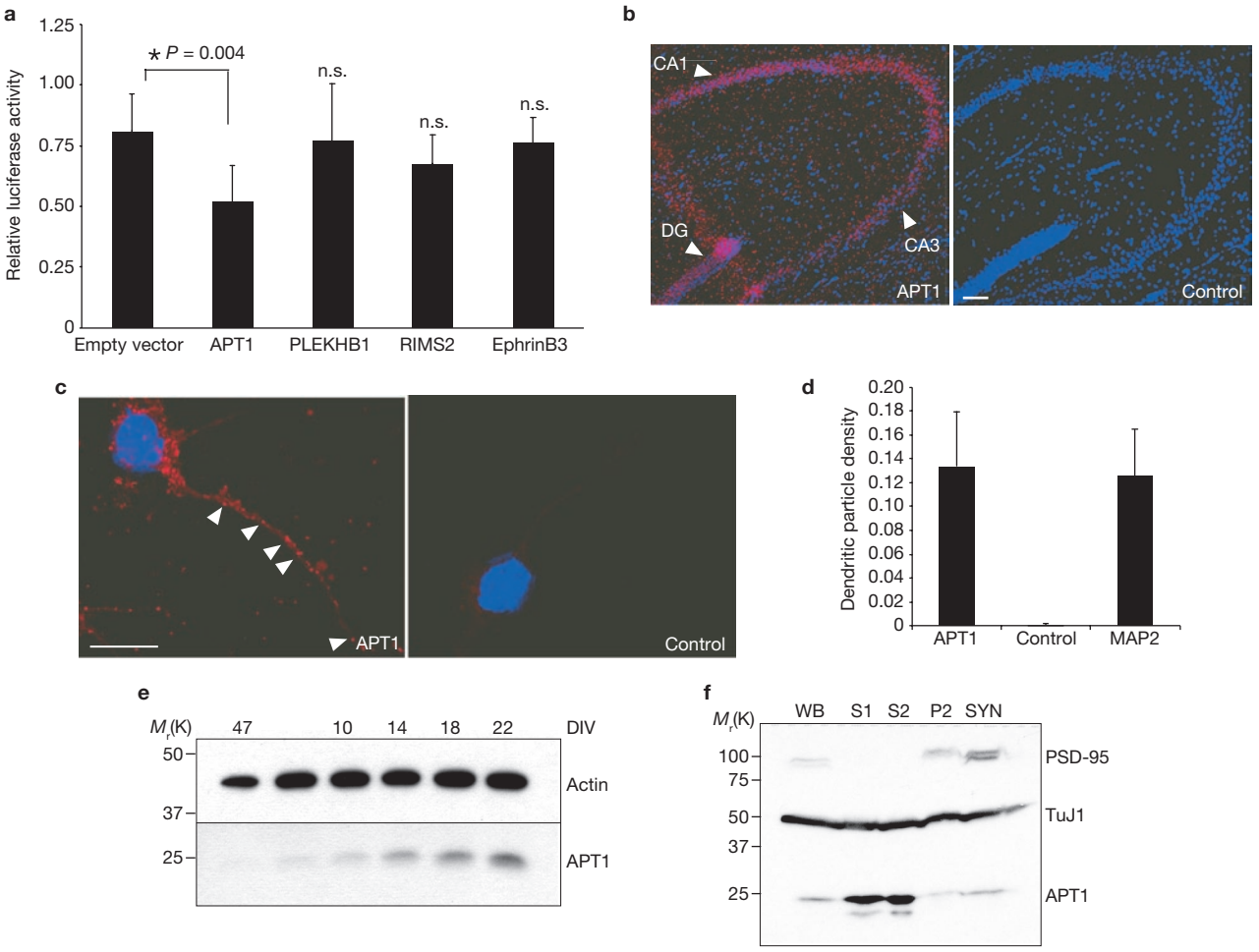

Figure 5 APT1 is expressed in neuronal dendrites during synapse development. (**a**) Validation of predicted miR-138 target mRNAs by dual-luciferase reporter assay in cortical neurons (5 DIV). 3′ UTR regions of the indicated genes were cloned downstream of the firefly-luciferase-coding region within pGL3, and the resulting vectors were transfected into neurons together with miR-138 duplex RNA (20 nM). The percentage firefly luciferase activity, normalized to the internal *Renilla* luciferase control, of miR-138-expressing cells compared with control-transfected cells is plotted for each individual reporter construct. Results are shown as means ± s.d. (empty vector, $n = 5$; APT1, $n = 6$), each performed in duplicate. Asterisk, $P < 0.05$ (pairwise Student's *t*-test; individual *P* values are indicated above each bar). n.s., not significant. (**b**) *APT1* mRNA is expressed in mouse hippocampus. ISH was performed in adult mouse hippocampal slices with the use of a probe perfectly complementary to mouse *APT1* mRNA (red signal in left panel) or a mismatch control probe (right panel). Cell nuclei were revealed with Hoechst counterstain (blue signal). DG, dentate gyrus. Scale bar, 0.1 μm. (**c**) *APT1* mRNA localizes to dendrites of primary hippocampal neurons. ISH was performed in 9–10 DIV primary dissociated hippocampal neurons as described for **b**. Note the presence of multiple dendritic *APT1* mRNA-containing granules along the entire length of dendrites (arrowheads). Scale bar, 20 μm. (**d**) Quantification of ISH signals obtained in **c**. Data are shown as means and s.d. for each of the indicated ISH probes (APT1 and control, $n = 6$; MAP2, $n = 8$). (**e**) APT1 protein expression is upregulated during the development of primary cortical neurons in culture. Whole cell extracts were prepared from the indicated stages of cortical neuron development and simultaneously probed with a rabbit antiserum against APT1 (lower band) and a mouse monoclonal anti-β-actin antibody as a loading control (upper band). (**f**) APT1 protein is present at low levels in synaptosomal extracts. P15 rat brains were fractionated into cytosolic fractions (S1 and S2), membrane fraction (P2) and synaptosomes (SYN), and fractions were probed for the presence of PSD-95, APT1 and TuJ1 as a loading control. Protein levels in whole forebrain before fractionation (WB) are shown for comparison.

cells lacking endogenous miR-138 and primary neurons (Fig. 5a; Supplementary Information, Fig. 3a). We therefore decided to focus on APT1 and study its regulation by miR-138 in more detail. Introduction of miR-138 into cortical neurons did not significantly alter steady-state APT1–luciferase mRNA levels (Supplementary Information, Fig. 3b), suggesting that the inhibitory effect of miR-138 on APT1 expression is due mainly to impaired translation of *APT1* mRNA. APT1 catalyses the removal of palmitate, a lipid modification with important roles in the localization and function of proteins[39]. The expression and function of APT1 in the nervous system were completely unknown, but the fact that dynamic palmitoylation of synaptic proteins has been implicated in the regulation of synaptic efficacy[40] made APT1 an interesting candidate in the context of dendritic spine morphology. To test for the physiological significance of the interaction of miR-138 with the APT1 3′ UTR we explored the expression of *APT1* mRNA and protein with the use of brain slices and isolated primary neurons. By ISH, mouse *APT1* mRNA was detected in multiple brain regions, including the principal layers of the hippocampus (Fig. 5b, data not shown). In hippocampal neurons, *APT1* mRNA localized to the somatic and dendritic compartment (Fig. 5c). In a similar manner to the known dendritic mRNA encoding MAP2, *APT1* mRNA was concentrated in granule-like structures along the length of dendrites (Fig. 5d). APT1 protein

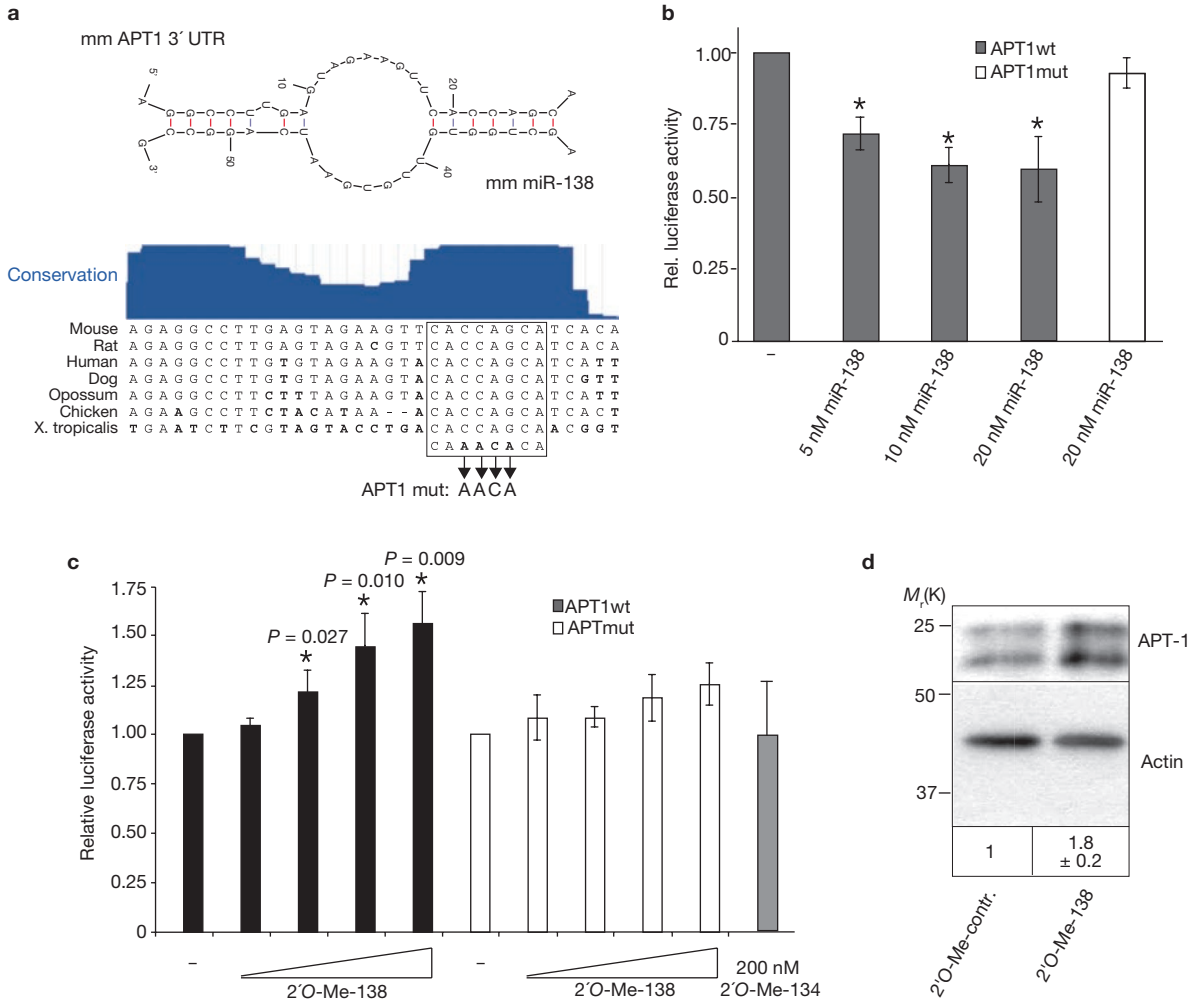

Figure 6 *APT1* mRNA is a miR-138 target in neurons. (**a**) Top: schematic representation of the mouse miR-138–*APT1* 3′ UTR duplex as determined by RNAfold algorithm (rna@tbi.univie.ac.at). G•C base pairs are indicated by red dots, and A•U and G•U base pairs by blue dots. Bottom: sequence conservation of the miR-138 target site within the *APT1* 3′ UTR across the indicated vertebrate species. Note the extensive conservation of nucleotides at both ends of the duplex that are engaged in base-pairing, and the less extensive conservation in the internal bulge structure (adopted from the University of California Santa Cruz genome browser at http://genome.ucsc.edu/). Nucleotide substitutions in the APT1 mut construct are indicated. *X. tropicalis*, *Xenopus tropicalis*. (**b**) Importance of the 'seed' region within the *APT1* 3′ UTR for miR-138-mediated downregulation in primary rat cortical neurons (5 DIV). Luciferase assay was performed with wild-type APT1 (APT1wt) and mutated 3′ UTR constructs (APT1mut) in the presence of the indicated concentrations of miR-138 duplex RNA. Values are expressed relative to the internal *Renilla* luciferase activity and normalized to the activity of the wild-type APT1 reporter under basal conditions. Results are shown as means ± s.d. (10 nM, $n = 6$; 20 nM, $n = 18$, APT1mut, $n = 8$). Asterisk, $P < 0.00001$ (pairwise Student's *t*-test between corresponding values of wild-type and mutated reporter). (**c**) Endogenous miR-138 inhibits APT1 luciferase reporter gene expression. Wild-type or mutated APT1 luciferase reporter genes were co-transfected together with increasing amounts of 2′*O*-Me-138 AS oligonucleotide (50–200 nM) into hippocampal neurons (16 DIV) and luciferase activity was measured two days later. Results are shown as mean ± s.d. ($n = 5$). Activity of the wild-type APT1 and mutated reporters under basal conditions was arbitrarily set to 1. Asterisk, $P < 0.01$ (pairwise Student's *t*-test between corresponding values of wild-type and mutated reporter; *P* values are shown above bar graphs). (**d**) Endogenous miR-138 inhibits the accumulation of APT1 protein. Cholesterol-modified 2′*O*-Me antisense oligonucleotides directed against miR-138 or an unrelated sequence were introduced into hippocampal neurons at 13 DIV at a concentration of 1 μM, and protein extracts were prepared for western blotting at 18 DIV. The average fold increase in the APT1 signal is indicated ($n = 3$; 2′*O*-Me control set to 1).

gradually increased over three weeks of cortical neuron development *in vitro* (Fig. 5e). At the subcellular level, APT1 protein was present in both the cytosolic fractions (low-speed and high-speed centrifugation supernatants) and membrane fractions (high-speed centrifugation pellet and synaptosomes) of P15 rat brain (Fig. 5f). However, in contrast with PSD-95, most of the APT1 protein accumulated in the soluble cytosolic fractions. These results are consistent with the idea that at least part of the negative regulatory interaction between miR-138 and *APT1* mRNA occurs locally in the synaptodendritic compartment.

We next tested whether the predicted miR-138-binding site within the *APT1* 3′ UTR is sufficient for miR-138-mediated translational inhibition. The duplex between the target site of the *APT1* 3′ UTR and miR-138 features extensive complementarity, especially within a highly conserved region at the 5′ end of the miRNA known as the 'seed' region (Fig. 6a). Accordingly, point mutations within this seed region (APT1 mutant) rendered the APT1–luciferase construct insensitive to miR-138-mediated inhibition (Fig. 6b). Therefore, inhibition of APT1 expression by miR-138 is mediated through a single conserved miR-138-binding site within the *APT1* 3′ UTR.

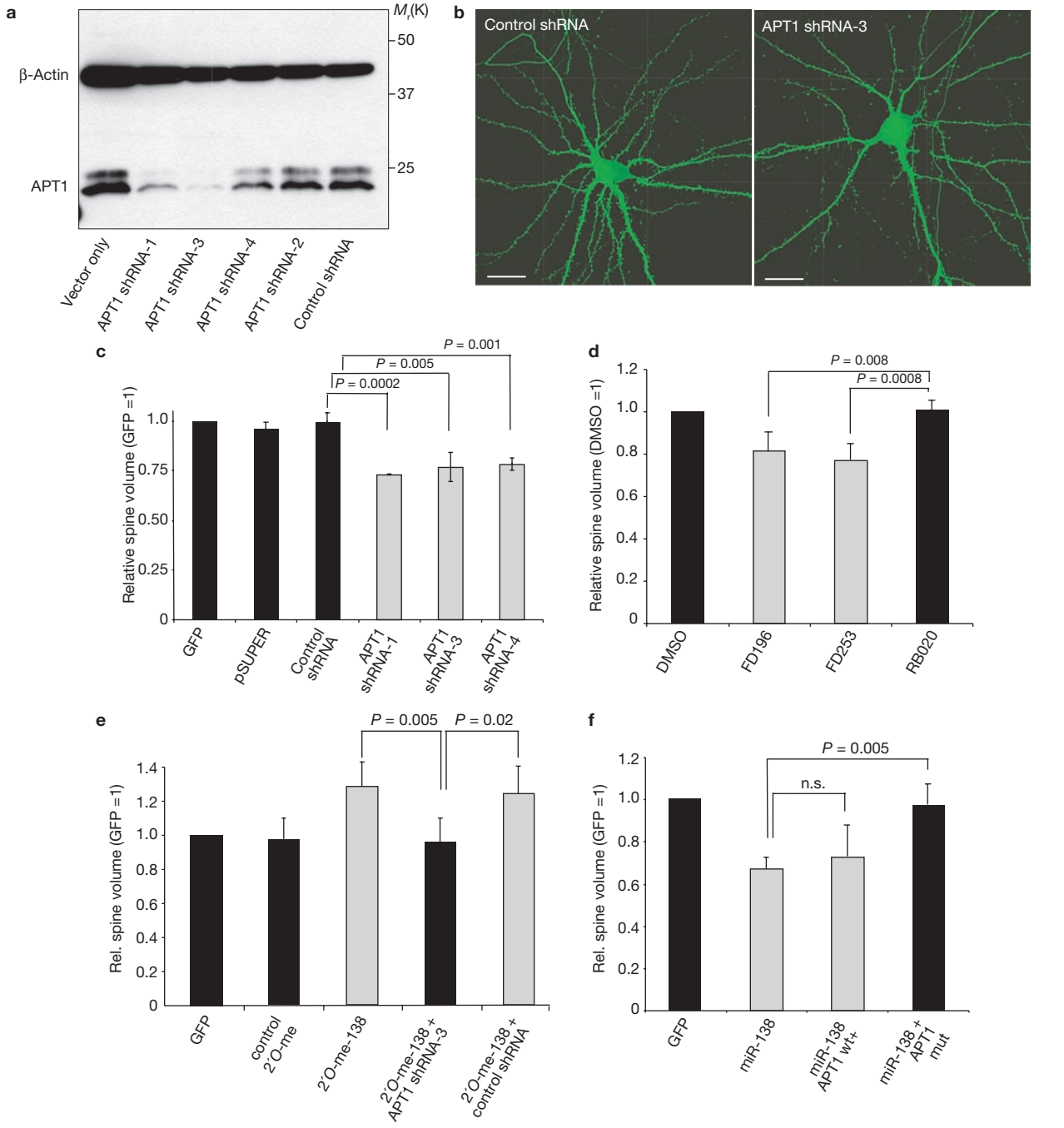

Figure 7 APT1 activity is required for the control of dendritic spine size. (**a**) shRNA-mediated knockdown of endogenous APT1 in primary neurons. pSUPER shRNA vectors (2 μg) were electroporated into cortical neurons, and the expression of endogenous APT1 and β-actin was determined by western blotting (7 DIV). (**b**) Interfering with APT1 expression in neurons decreases dendritic spine volume. Representative hippocampal neurons at 18 DIV transfected with enhanced GFP and either control shRNA (left panel) or pSUPER-APT1-shRNA-3 are shown. Scale bar, 20 μm. (**c**) shRNA-mediated knockdown of endogenous APT1 in neurons decreases dendritic spine volume. Rat hippocampal neurons (14 DIV) were transfected with GFP alone or together with pSUPER-expressing shRNAs directed against *APT1* mRNA (*APT1* shRNA-1, shRNA-3 and shRNA-4) or an unrelated sequence (control shRNA; 5 ng each). Values were normalized to the GFP-only condition and are shown as means and s.d. ($n = 3$; at least 1,800 spines from 18 neurons). $P < 0.0001$ (ANOVA). *P* values of pairwise Student's *t*-tests are indicated. (**d**) Pharmacological inhibition of APT1 in neurons decreases dendritic spine volume. Hippocampal neurons (18 DIV) were treated for 6 h with either inactive control compound (RB020) or specific APT1 inhibitors (FD196, FD253, 10 μM each) before analysis of spine volume. Values were normalized to the dimethylsulphoxide (DMSO)-only condition and are shown as means and s.d. ($n = 3$; 1,800 spines from 18 neurons). $P = 0.044$ (ANOVA). *P* values of pairwise Student's *t*-tests are indicated. (**e**) shRNA-mediated knockdown of APT1 suppresses the increase in spine volume caused by miR-138 inhibition. Rat hippocampal neurons (14 DIV) were transfected with the indicated 2′*O*-Me antisense oligonucleotides (40 nM) together with *APT1* shRNA-3 or control shRNA (5 ng of each). Values are shown as means and s.d. ($n = 4$; at least 2,400 spines from 24 neurons). $P = 0.0075$ (ANOVA). *P* values of pairwise Student's *t*-tests are indicated. (**f**) APT1 expression rescues miR-138-mediated spine shrinkage. Rat hippocampal neurons (10 DIV) were transfected with miR-138 duplex RNA (20 nM) in combination with wild-type APT1 or APT1 mut expression constructs (250 ng each). Values were normalized to the GFP-only condition and are shown as means and s.d. ($n = 3$; at least 1,800 spines from 18 neurons). $P = 0.029$ (ANOVA). *P* values of pairwise Student's *t*-tests are indicated.

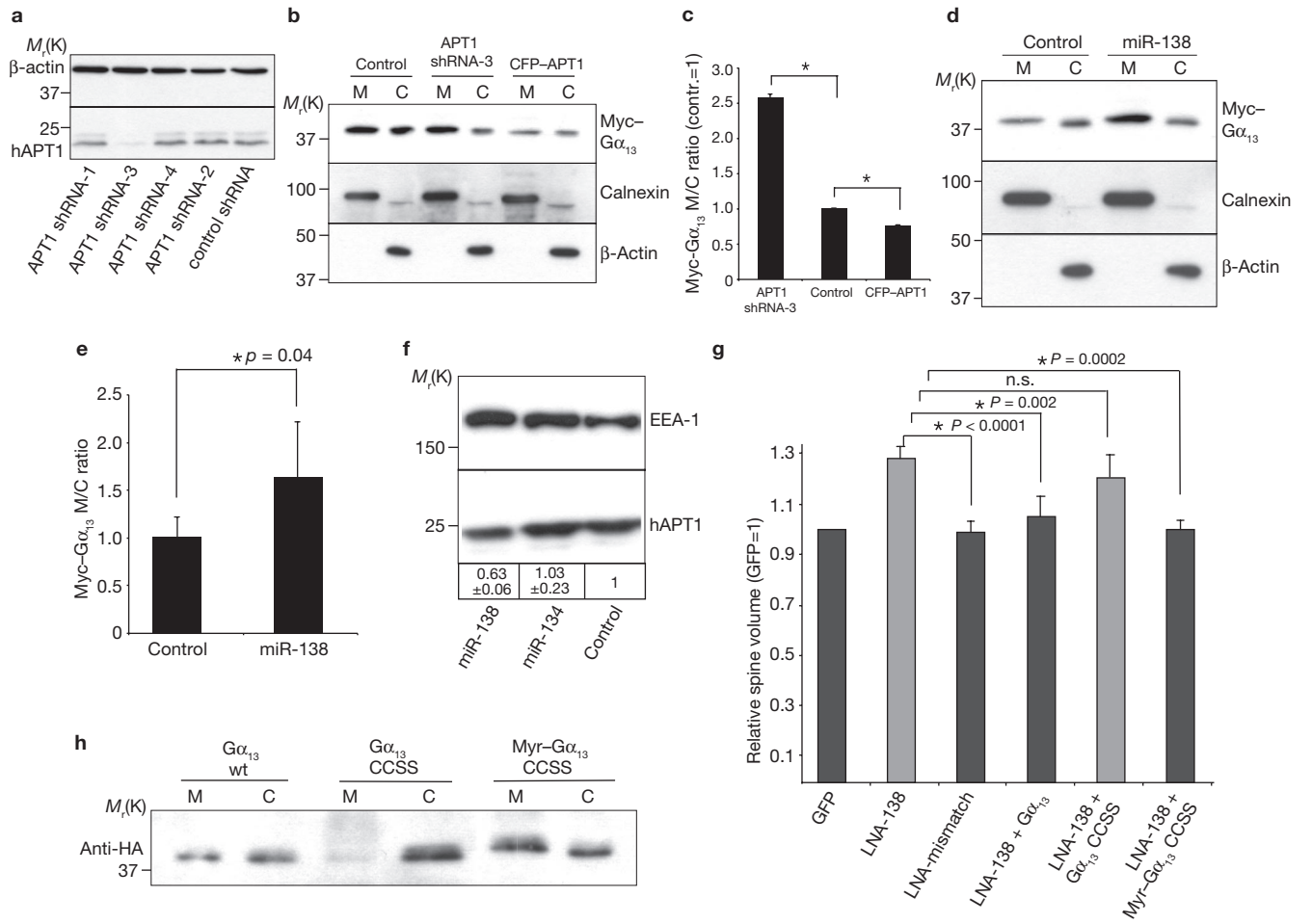

Figure 8 miR-138 regulated membrane-association of $G\alpha_{13}$ is required for the control of dendritic spine size. (**a**) Western blot of total lysates from HEK293 cells transfected with control shRNA or *APT1* shRNA-1–4 using anti-β-actin (top) or anti-APT1 (bottom) antibodies. A representative blot is shown ($n = 3$). Note that only the *APT1* shRNA-3 target site is conserved in human and rat. (**b**) shRNA-mediated knockdown of endogenous APT1 increases the fraction of membrane-bound Myc–$G\alpha_{13}$ in HEK293 cells. Western blot of membrane (M) or cytosolic (C) lysates expressing Myc–$G\alpha_{13}$ together with *APT1* shRNA-3 or a control shRNA, using anti-Myc (top), anti-calnexin (middle) or anti-β-actin (bottom) antibodies. (**c**) Quantification of signals obtained by western blotting in **b**. $*P < 0.05$ ($n = 3$; pairwise Student's *t*-test). (**d**) Expression of miR-138 increases the fraction of membrane-bound Myc–$G\alpha_{13}$ in HEK293 cells. Western blot of membrane (M) or cytosolic (C) lysates expressing Myc–$G\alpha_{13}$ with or without synthetic miR-138 duplex (40 nM), using anti-Myc (top) anti-calnexin (middle) or anti-β-actin (bottom) antibodies. (**e**) Quantification of signals obtained by western blotting in **d**. $*P < 0.05$ ($n = 4$; pairwise Student's *t*-test). (**f**) Expression of miR-138 decreases endogenous APT-1 protein levels in HEK293 cells. Western blot of whole cell lysates transfected with miR-134, miR-138 or control duplex RNA (10 nM), using anti-APT-1 (bottom) or anti-EEA-1 (top) antibodies. Quantification of independent blots is shown at the bottom ($n = 3$; control duplex RNA = 1). Note the modest decrease in endogenous hAPT1 protein levels as a result of low co-transfection efficiency of miR-138 duplex RNA (about 50–60%). (**g**) Expression of membrane-targeted $G\alpha_{13}$ rescues spine enlargement caused by miR-138 inhibition. Rat hippocampal neurons (10 DIV) were transfected with the indicated LNA oligonucleotides (100 nM) together with $G\alpha_{13}$ expression constructs (250 ng each). Values were normalized to the GFP-only condition and are shown as means and s.d. ($n = 3$; at least 1,800 spines from 18 neurons). $P = 0.019$ (ANOVA). *P* values of pairwise Student's *t*-tests are indicated. (**h**) Expression levels and subcellular distribution of $G\alpha_{13}$ variants. Western blot of membrane (M) or cytosolic (C) lysates from HEK293 cells expressing the indicated $G\alpha_{13}$ mutants.

To test whether endogenous miR-138 regulates the translation of *APT1* mRNA in neurons, we transfected the APT1–luciferase reporter into mature, miR-138-expressing neurons (14–16 DIV; Fig. 6c). Inhibition of endogenous miR-138 by 2′*O*-Me-138 specifically upregulated APT1–luciferase expression in a dose-dependent manner. This inhibitory function of endogenous miR-138 on the APT1 reporter construct was dependent on a functional miR-138-binding site (Fig. 6c; Supplementary Information, Fig. 3c). The effect of 2′*O*-Me-138 on APT1 expression was specific, because it was effectively competed for by the transfection of miR-138 duplex RNA (Supplementary Information, Fig. 3d). Quantitative transduction of primary neurons by bath application of cholesterol-modified 2′*O*-Me-138 led to a reproducible and specific upregulation of APT1 protein as assessed by semi-quantitative western blotting (Fig. 6d). In summary, our results establish *APT1* mRNA as a genuine miR-138 target, thereby implicating miR-138 in the regulation of palmitoylation in neurons.

APT1 activity is required for spine enlargement caused by miR-138 inhibition

We next explored whether the decrease in dendritic spine volume on overexpression of miR-138 might be causally linked to decreased APT1 expression. First, we monitored spine volume in neurons in which endogenous APT1 levels were decreased by RNAi. As judged by

western blotting, three out of four APT1 small hairpin RNAs (shRNAs) targeting different regions of the *APT1* mRNA effectively decreased endogenous APT1 protein concentration in cortical neurons (Fig. 7a; Supplementary Information, Fig. 4b) and ectopically expressed APT1 in HEK293 cells (Supplementary Information, Fig. 4a). In hippocampal neurons, APT1 knockdown by each of the effective shRNAs (*APT1* shRNA-1, shRNA-3 and shRNA-4) led to a significant decrease in the size of dendritic protrusions compared with control conditions (Fig. 7b, c, and data not shown). Reduced spine volume on APT1 knockdown was accompanied by a significant decrease in the number of spine-associated PSD-95 clusters within dendrites (Supplementary Information, Fig. 4c–e). None of the *APT1* shRNAs had an effect on the total number of dendritic protrusions of hippocampal neurons (Supplementary Information, Fig. 5a) or the dendritic branching index (Supplementary Information, Fig. 5b), indicating a specific effect of APT1 knockdown on spine morphology.

APT1-dependent control of dendritic spine morphology required the depalmitoylating activity of APT1, because inhibition of APT1 enzymatic activity by two different small-molecule inhibitors (FD196 and FD253) similarly led to a decrease in dendritic spine volume (Fig. 7d; Supplementary Information, Fig. 5c), whereas an inactive control compound (RB020) had no effect.

We next tested whether elevated APT1 levels resulting from inhibition of miR-138 are required for the increase in spine volume. A decrease in APT1 levels brought about by *APT1* shRNA-3 in miR-138-depleted cells completely suppressed the spine-growth-promoting effect of miR-138 inhibition by 2′*O*-Me-138 (Fig. 7e) and LNA-138 (Supplementary Information, Fig. 5d). Conversely, transfection of an APT1 expression construct harbouring a mutation in the miR-138-binding site (APT1 mut), but not a wild-type APT1 construct, efficiently rescued spine shrinkage caused by elevated miR-138 levels (Fig. 7f). Taken together, these two lines of evidence strongly suggest that APT1 is a critical downstream effector of miR-138 in the regulation of spine morphogenesis.

Membrane localization of the APT1 substrate G protein α_{13} ($G\alpha_{13}$) counteracts spine enlargement caused by miR-138 inhibition

We investigated the molecular mechanism that underlies dendritic spine enlargement caused by increased APT1 protein levels on inhibition of miR-138. APT1 depalmitoylates several substrates implicated in synaptic plasticity, including endothelial nitric oxide synthase (eNOS), H-Ras and G-protein α subunits, namely $G\alpha_{13}$ (ref. 27). Because $G\alpha_{13}$ palmitoylation is required for plasma membrane localization and Rho-dependent signalling[41], we focused on this subunit. We found that a significant fraction of overexpressed Myc-$G\alpha_{13}$ redistributes from the cytosol to the membrane on shRNA-mediated knockdown of endogenous human APT1 (hAPT1) in HEK293 cells (Fig. 8a–c). In contrast, transfection of an APT1 expression construct (CFP–APT1) had the opposite effect. Thus, APT1 is necessary and sufficient for proper $G\alpha_{13}$ membrane localization in HEK293 cells, presumably by regulating $G\alpha_{13}$ depalmitoylation. More importantly, the introduction of synthetic miR-138 duplex RNA similarly increases the membrane association of Myc–$G\alpha_{13}$ (Fig. 8d, e). miR-138 had no effect on the subcellular distribution of the cytosolic β-actin or membrane-associated calnexin proteins (Fig. 8d). Redistribution of $G\alpha_{13}$ coincides with a decrease in endogenous hAPT1 protein levels in miR-138-transfected HEK293 cells (Fig. 8f).

Finally, we investigated the significance of the regulation of $G\alpha_{13}$ subcellular localization by miR-138 for the control of spine size. In a similar manner to APT1 knockdown (Fig. 7f), overexpression of wild-type $G\alpha_{13}$ was able to suppress the spine-growth-promoting effect caused by miR-138 inhibition (Fig. 8g). A palmitoylation-deficient $G\alpha_{13}$ ($G\alpha_{13}$ CCSS) was ineffective in the rescue experiment, demonstrating that $G\alpha_{13}$ palmitoylation is required for miR-138-mediated spine shrinkage. The effects of $G\alpha_{13}$ palmitoylation are probably due to a redistribution of $G\alpha_{13}$ from the cytosol to the membrane, because a constitutively membrane-attached, myristoylated $G\alpha_{13}$ rescues spine morphology in the context of mutated palmitoylation sites (Myr $G\alpha_{13}$ CCSS; Fig. 8g). The different subcellular localization of the $G\alpha_{13}$ variants was confirmed by cellular fractionation (Fig. 8h) and immunostaining (Supplementary Information, Fig. 6a–c).

We conclude that miR-138 might inhibit spine growth, at least in part, by increasing the membrane localization of $G\alpha_{13}$, resulting in elevated activity of the downstream RhoA signalling pathway (Supplementary Information, Fig. 6d).

DISCUSSION

miRNAs have recently emerged as important regulators of nervous system function in vertebrates, for example during neuronal differentiation (miR-9 and miR-124), neuronal outgrowth (miR-132) and dendritic spine morphogenesis (miR-134)[23]. However, a systematic assessment of miRNA function, based on their temporal and subcellular expression in the brain, has not yet been achieved. In this study we generated a comprehensive list of miRNAs residing within the synaptodendritic compartment, and subsequently probed their function in the regulation of dendritic spine morphology. In this manner we identified two neuronal miRNAs (miR-132 and miR-138) that regulate dendritic spine size in an antagonistic manner. Two recent reports suggest that miRNAs beyond those identified here might participate in local translational control in dendrites[42,43]. There is little overlap between those studies and ours, which might be due to the different sample materials (that is, synaptosomes versus cultured neurons, and adult brain versus P15 brain) and methodologies (microarray versus multiplex RT–PCR) used. However, we note that we might have missed low-expressed miRNAs in dendrites as a result of our very stringent selection criteria. In addition, some of the miRNAs that we identified by microarray might have a function in dendrites that we were unable to uncover with our experimental setup. A more in-depth functional analysis of individual miRNAs identified here will improve our understanding of the dendritic miRNA network.

On the basis of multiple lines of evidence, *APT1* mRNA is a genuine miR-138 target in neurons. Studies in other cell systems document a role for APT1 in the depalmitoylation of several signalling proteins, including H-Ras, Gα subunits and eNOS. Although it was known that these APT1 substrates are important in synapse development, our results provide direct evidence for a biological function of APT1-dependent depalmitoylation in neurons during spine development. Using classical epistasis experiments, we found that $G\alpha_{13}$ is one critical APT1 substrate in spine morphogenesis. Although monitoring $G\alpha_{13}$ palmitoylation in neurons proved technically challenging, our results showing that miR-138 controls the membrane localization of $G\alpha_{13}$ in non-neuronal cells (Fig. 8d, e) and that $G\alpha_{13}$ palmitoylation is required for miR-138-dependent regulation of spine size (Fig. 8g) strongly suggest that miR-138 controls the level of $G\alpha_{13}$ palmitoylation by means of APT1. Further

work is needed to elucidate additional substrates of APT1 in neurons, and whether perturbation of miR-138 affects their palmitoylation. Obvious candidates besides $G\alpha_{13}$ subunits include G-protein-coupled receptors, Fyn, Ras, eNOS and PSD-95, all of which are anchored to the spine membrane by means of palmitoylation[40]. Given that miRNAs usually regulate many target mRNAs, miR-138 probably possesses physiologically relevant targets other than APT1. For example, EphrinB3 and RIMS2 contain canonical miR-138 seed matches in their 3′ UTR, but none of them showed a significant downregulation on miR-138 overexpression in neurons. The failure of these mRNAs to respond to miR-138 might be due to a low accessibility of the respective target sites in neurons (G.O., unpublished observation).

A major outcome of our study is that miRNA regulation in dendritic spines seems to converge on the translation of critical components of G-protein signalling pathways that impinge on the actin cytoskeleton (Supplementary Information, Fig. 6d). For example, miR-134 inhibits the expression of Limk1, a kinase that phosphorylates cofilin, an actin-binding protein that has been implicated in the regulation of dendritic spine and growth cone structure[44]. miR-132 has previously been shown to downregulate p250GAP, an important negative regulator of the spine-growth-promoting GTPases Rac and Cdc42 (ref. 32). In this study we provide evidence that miR-138 mediates its effect on spine structure, at least in part, by regulating the depalmitoylation enzyme APT1. Among the known APT1 substrates is $G\alpha_{13}$, an activator of Rho downstream of G-protein-coupled receptors[45]. A miR-138-mediated increase in $G\alpha_{13}$ palmitoylation and membrane localization could result in elevated Rho activity, which in turn could trigger spine shrinkage[46]. This novel miRNA-dependent layer of regulation of critical actin signalling components could help to adapt cytoskeletal changes in individual spines to changes in synaptic activity[6].

Our electrophysiological measurements show that miR-138-mediated spine shrinkage is correlated with decreased postsynaptic function. Although the effects on mEPSC amplitudes are subtle, our results show a significant contribution of a neuronal miRNA to basal excitatory synaptic transmission. The method of regulation of miR-138 activity by stimuli that affect synapse morphology and function is an important topic for future studies. Our preliminary results indicate that, consistent with its spine growth inhibitory effect, miR-138 expression and activity are negatively regulated by calcium influx (Supplementary Information, Fig. 3d, e). It remains to be determined whether activity-dependent regulation of miR-138 occurs at the level of precursor processing, as suggested by our previous results[47], or by a different mechanism. Nevertheless, it is an intriguing possibility that neuronal activity could regulate the expression and/or activity of a variety of synaptic miRNAs. This in turn could contribute to activity-dependent fine-tuning of signalling pathways that coordinate the structural and functional plasticity of spine synapses. □

METHODS

Methods and any associated references are available in the online version of the paper at http://www.nature.com/naturecellbiology

Note: Supplementary Information is available on the Nature Cell Biology website.

ACKNOWLEDGEMENTS

We thank O. Rocks and P. Wedegaertner for providing reagents; R. Heinen for suggestions on the luciferase reporter assays; T. Wüst for technical assistance; and M. Alenius and A. Keene for critically reading the manuscript. This work was supported by the Deutsche Forschungsgemeinschaft (SFB488; to G.M.S.), the Human Frontier Science Program (Career Development Award; to G.M.S.), the National Institute on Drug Abuse (1R21DA025102-01; to G.M.S.), the National Institutes of Health (NS045500; to M.E.G.) the Bioinformatics Initiative (to C.D. and M.R.), the Austrian Academy of Sciences (to J.M. and S.B. (DOC-fFORTE-fellowship)) and the Austrian Government, GEN-AU initiative (to G.O.). C.H. acknowledges the Alexander von Humboldt foundation for a postdoctoral fellowship. F.D. is a recipient of a TALENT-stipendium from the Netherlands Organization for Scientific Research (NWO) and a Marie-Curie fellowship from the European Union.

AUTHOR CONTRIBUTIONS

G.M.S. performed microRNA profiling, M.C. analysed the microarray data, G.O., R.F. and C.J.B. performed *in situ* experiments, G.S., S.B., G.M.S. and C.K. performed and analysed spine measurements, M.O. and A.D. performed and analysed electrophysiology experiments, G.S. and G.M.S. performed and analysed immunostaining, G.S., G.O. and P.J.L. designed and performed the target validation experiments, G.O., C.D. and M.R. carried out bioinformatics, G.S. performed biochemistry, F.D., C.H., B.R. and H.W. were involved in the design and synthesis of specific APT1 inhibitors, R.F. performed sensor assays, G.S, S.B., M.C. and S.Kh. performed RNA expression analysis, K.H. and S.Ka provided reagents, M.E.G. participated in the initial stages of project planning, J.M. and G.M.S. directed the research and G.M.S. coordinated the project and wrote the manuscript.

Published online at http://www.nature.com/naturecellbiology
Reprints and permissions information is available online at http://npg.nature.com/reprintsandpermissions

1. Hering, H. & Sheng, M. Dendritic spines: structure, dynamics and regulation. *Nature Rev. Neurosci.* **2,** 880–888 (2001).
2. Nimchinsky, E. A., Sabatini, B. L. & Svoboda, K. Structure and function of dendritic spines. *Annu. Rev. Physiol.* **64,** 313–353 (2002).
3. Matsuzaki, M., Honkura, N., Ellis-Davies, G. C. & Kasai, H. Structural basis of long-term potentiation in single dendritic spines. *Nature* **429,** 761–766 (2004).
4. Nagerl, U. V., Eberhorn, N., Cambridge, S. B. & Bonhoeffer, T. Bidirectional activity-dependent morphological plasticity in hippocampal neurons. *Neuron* **44,** 759–767 (2004).
5. Bagni, C. & Greenough, W. T. From mRNP trafficking to spine dysmorphogenesis: the roots of fragile X syndrome. *Nature Rev. Neurosci.* **6,** 376–387 (2005).
6. Okamoto, K., Nagai, T., Miyawaki, A. & Hayashi, Y. Rapid and persistent modulation of actin dynamics regulates postsynaptic reorganization underlying bidirectional plasticity. *Nature Neurosci.* **7,** 1104–1112 (2004).
7. Yi, J. J. & Ehlers, M. D. Ubiquitin and protein turnover in synapse function. *Neuron* **47,** 629–632 (2005).
8. Shi, S. H. *et al.* Rapid spine delivery and redistribution of AMPA receptors after synaptic NMDA receptor activation. *Science* **284,** 1811–1816 (1999).
9. Zhou, Z. *et al.* Brain-specific phosphorylation of MeCP2 regulates activity-dependent Bdnf transcription, dendritic growth, and spine maturation. *Neuron* **52,** 255–269 (2006).
10. Bingol, B. & Schuman, E. M. Synaptic protein degradation by the ubiquitin proteasome system. *Curr. Opin. Neurobiol.* **15,** 536–541 (2005).
11. Steward, O. & Schuman, E. M. Protein synthesis at synaptic sites on dendrites. *Annu. Rev. Neurosci.* **24,** 299–325 (2001).
12. Martin, K. C., Barad, M. & Kandel, E. R. Local protein synthesis and its role in synapse-specific plasticity. *Curr. Opin. Neurobiol.* **10,** 587–592 (2000).
13. Eberwine, J., Miyashiro, K., Kacharmina, J. E. & Job, C. Local translation of classes of mRNAs that are targeted to neuronal dendrites. *Proc. Natl Acad. Sci. USA* **98,** 7080–7085 (2001).
14. Ostroff, L. E., Fiala, J. C., Allwardt, B. & Harris, K. M. Polyribosomes redistribute from dendritic shafts into spines with enlarged synapses during LTP in developing rat hippocampal slices. *Neuron* **35,** 535–545 (2002).
15. Wells, D. G., Richter, J. D. & Fallon, J. R. Molecular mechanisms for activity-regulated protein synthesis in the synapto-dendritic compartment. *Curr. Opin. Neurobiol.* **10,** 132–137 (2000).
16. Kiebler, M. A. & Bassell, G. J. Neuronal RNA granules: movers and makers. *Neuron* **51,** 685–690 (2006).
17. Krichevsky, A. M. & Kosik, K. S. Neuronal RNA granules: a link between RNA localization and stimulation-dependent translation. *Neuron* **32,** 683–696 (2001).
18. Ashraf, S. I., McLoon, A. L., Sclarsic, S. M. & Kunes, S. Synaptic protein synthesis associated with memory is regulated by the RISC pathway in *Drosophila*. *Cell* **124,** 191–205 (2006).
19. Schratt, G. M. *et al.* A brain-specific microRNA regulates dendritic spine development. *Nature* **439,** 283–289 (2006).
20. Ambros, V. The functions of animal microRNAs. *Nature* **431,** 350–355 (2004).
21. Bartel, D. P. MicroRNAs: genomics, biogenesis, mechanism, and function. *Cell* **116,** 281–297 (2004).
22. Filipowicz, W., Bhattacharyya, S. N. & Sonenberg, N. Mechanisms of post-transcriptional regulation by microRNAs: are the answers in sight? *Nature Rev. Genet.* **9,** 102–114 (2008).
23. Kosik, K. S. The neuronal microRNA system. *Nature Rev. Neurosci.* **7,** 911–920 (2006).
24. Miska, E. A. *et al.* Microarray analysis of microRNA expression in the developing mammalian brain. *Genome Biol.* **5,** R68 (2004).

25. Sempere, L. F. *et al*. Expression profiling of mammalian microRNAs uncovers a subset of brain-expressed microRNAs with possible roles in murine and human neuronal differentiation. *Genome Biol*. **5,** R13 (2004).
26. Kim, J. *et al*. Identification of many microRNAs that copurify with polyribosomes in mammalian neurons. *Proc. Natl Acad. Sci. USA* **101,** 360–365 (2004).
27. Yeh, D. C., Duncan, J. A., Yamashita, S. & Michel, T. Depalmitoylation of endothelial nitric-oxide synthase by acyl-protein thioesterase 1 is potentiated by Ca^{2+}-calmodulin. *J. Biol. Chem*. **274,** 33148–33154 (1999).
28. Rao, A. & Steward, O. Evidence that protein constituents of postsynaptic membrane specializations are locally synthesized: analysis of proteins synthesized within synaptosomes. *J. Neurosci*. **11,** 2881–2895 (1991).
29. Meister, G., Landthaler, M., Dorsett, Y. & Tuschl, T. Sequence-specific inhibition of microRNA- and siRNA-induced RNA silencing. *RNA* **10,** 544–550 (2004).
30. Zito, K., Knott, G., Shepherd, G. M., Shenolikar, S. & Svoboda, K. Induction of spine growth and synapse formation by regulation of the spine actin cytoskeleton. *Neuron* **44,** 321–334 (2004).
31. Mansfield, J. H. *et al*. MicroRNA-responsive 'sensor' transgenes uncover Hox-like and other developmentally regulated patterns of vertebrate microRNA expression. *Nature Genet*. **36,** 1079–1083 (2004).
32. Vo, N. *et al*. A cAMP-response element binding protein-induced microRNA regulates neuronal morphogenesis. *Proc. Natl Acad. Sci. USA* **102,** 16426–16431 (2005).
33. Rehmsmeier, M., Steffen, P., Hochsmann, M. & Giegerich, R. Fast and effective prediction of microRNA/target duplexes. *RNA* **10,** 1507–1517 (2004).
34. Kruger, J. & Rehmsmeier, M. RNAhybrid: microRNA target prediction easy, fast and flexible. *Nucleic Acids Res*. **34,** W451–W454 (2006).
35. Rodenas-Ruano, A., Perez-Pinzon, M. A., Green, E. J., Henkemeyer, M. & Liebl, D. J. Distinct roles for ephrinB3 in the formation and function of hippocampal synapses. *Dev. Biol*. **292,** 34–45 (2006).
36. Etournay, R. *et al*. PHR1, an integral membrane protein of the inner ear sensory cells, directly interacts with myosin 1c and myosin VIIa. *J. Cell Sci*. **118,** 2891–2899 (2005).
37. Ozaki, N. *et al*. cAMP-GEFII is a direct target of cAMP in regulated exocytosis. *Nature Cell Biol*. **2,** 805–811 (2000).
38. El-Husseini Ael, D. *et al*. Synaptic strength regulated by palmitate cycling on PSD-95. *Cell* **108,** 849–863 (2002).
39. Linder, M. E. & Deschenes, R. J. Palmitoylation: policing protein stability and traffic. *Nature Rev. Mol. Cell Biol*. **8,** 74–84 (2007).
40. Kang, R. *et al*. Neural palmitoyl-proteomics reveals dynamic synaptic palmitoylation. *Nature* **456,** 904–909 (2008).
41. Bhattacharyya, R. & Wedegaertner, P. B. $G\alpha_{13}$ requires palmitoylation for plasma membrane localization, Rho-dependent signaling, and promotion of p115-RhoGEF membrane binding. *J. Biol. Chem*. **275,** 14992–14999 (2000).
42. Kye, M. J. *et al*. Somatodendritic microRNAs identified by laser capture and multiplex RT-PCR. *RNA* **13,** 1224–1234 (2007).
43. Lugli, G., Torvik, V. I., Larson, J. & Smalheiser, N. R. Expression of microRNAs and their precursors in synaptic fractions of adult mouse forebrain. *J. Neurochem*. **106,** 650–661 (2008).
44. Bernard, O. Lim kinases, regulators of actin dynamics. *Int. J. Biochem. Cell Biol*. **39,** 1071–1076 (2007).
45. Kurose, H. $G\alpha_{12}$ and $G\alpha_{13}$ as key regulatory mediator in signal transduction. *Life Sci*. **74,** 155–161 (2003).
46. Tada, T. & Sheng, M. Molecular mechanisms of dendritic spine morphogenesis. *Curr. Opin. Neurobiol*. **16,** 95–101 (2006).
47. Obernosterer, G., Leuschner, P. J., Alenius, M. & Martinez, J. Post-transcriptional regulation of microRNA expression. *RNA* **12,** 1161–1167 (2006).

METHODS

Cell culture and transfection. Cultures of dissociated primary cortical and hippocampal neurons from embryonic day 18 (E18) Sprague–Dawley rats (Charles River Laboratories, Sulzfeld, Germany) were prepared and cultured as described[48]. Neuronal transfections were performed with Lipofectamine 2000 (Invitrogen). For each well of a 24-well plate a total of 1 μg of DNA/RNA was mixed with a 1:50 dilution of Lipofectamine 2000 in neurobasal medium, incubated at room temperature (15–25 °C) for 20 min and then further diluted 1:5 in neurobasal medium. Neurons were incubated with the transfection mix for 2 h. Nucleofections were performed with the Rat Neuron Nucleofector Kit (Lonza) and program O-003. Primary cortical neurons (4×10^6) of rat embryos (E18) were nucleofected with 2–3 μg of total DNA per condition and plated on six-well dishes in DMEM-Glutamax containing 10% fetal bovine serum (FBS; Invitrogen). After 5 h, medium was replaced with standard neuronal culture medium. Cholesterol-modified 2′*O*-Me-oligonucleotides ('antagomirs'; Thermo Scientific) were applied at 13 DIV at 1 μM in conditioned culture medium for 24 h, and cells were lysed at 18 DIV.

HEK293 cells were maintained in DMEM (Invitrogen) plus 10% FBS, 1 mM glutamine, 100 U ml^{-1} penicillin and 100 μg ml^{-1} streptomycin. Transfections were performed with the calcium phosphate method with a final $CaCl_2$ concentration of 0.1 M and an incubation time of 6–16 h.

DNA constructs. The pSUPER RNAi expression system (Oligoengine) was used for siRNA-mediated knockdown of APT1 in cell culture. Four independent pSUPER constructs (*APT1* shRNA-1–4) were generated with the *Bgl*II and *Hin*dIII restriction sites. pSUPER plasmids were used either at 10 ng ml^{-1} (primary neurons) or 200 ng ml^{-1} (HEK293 cells). An expression vector for full-length mouse APT1 cDNA was obtained from OriGene (MC201121). A version with a mutated miR-138-binding site within the *APT1* 3′ UTR (APT1 mutBS) was generated with the QuikChange Site-Directed Mutagenesis Kit (Stratagene). For generation of an expression vector for Myc-tagged $G\alpha_{13}$, the mouse $G\alpha_{13}$ open reading frame was PCR-amplified from the pCIS-$G\alpha_{13}$ expression vector (provided by S. Offermanns) and then cloned into pcDNA 3.1/Myc–His A (Invitrogen) using *Bam*HI and *Xba*I. See Supplementary Methods for primer sequences.

Preparation of synaptoneurosomes. Synaptoneurosomes were prepared from P15 Sprague–Dawley rat pups (Charles River, Sulzfeld, Germany) as described previously[48].

Microarray. See Supplementary Methods for details.

Northern blot analysis. Northern blots to detect neuronal miRNAs and U6 snRNA were performed as described, with radiolabelled DNA oligonucleotides as probes[19].

Western blot analysis. Proteins were separated by SDS–PAGE and blotted onto a poly-vinylidene difluoride (PVDF) membrane. Non-specific bindings were blocked with Tris-buffered saline plus 5% milk powder and 0.2% Tween 20. The following primary antibodies were used: polyclonal rabbit anti-APT1 (1:1,000 dilution; the anti-APT1 antibody was produced in rabbit from BioGenes (Berlin, Germany) by using purified hAPT1 (provided by R. Vetter)), mouse anti-PSD95 (1:1,000; MA1-046; Dianova), mouse anti-cMyc (sc40; Santa Cruz), mouse anti-HA (1583816; Roche), mouse anti-β_3-tubulin (1:15,000; MMS-435P; Covance), mouse anti-EEA1 (1:10,000; 610456; Becton Dickinson), rabbit anti-calnexin (SPA-865; Stressgen) and mouse anti-β-actin (A5441; Sigma). Primary antibodies were recognized either by a horseradish peroxidase (HRP)-conjugated goat anti-rabbit antibody (1:20,000; 401315; Calbiochem) or an HRP-conjugated rabbit anti-mouse antibody (1:20,000; 402335; Calbiochem). Secondary antibodies were detected by enhanced chemiluminescence with the ECL Plus Western Blotting Detection System (GE Healthcare).

Image analysis. For image analysis, neurons were transfected at 10 DIV or 14 DIV with indicated miRNAs, miRNA inhibitors or siRNA expression vectors in combination with enhanced GFP and processed for confocal microscopy at 18 DIV.

For spine analysis, high-resolution *z*-stack images of GFP-positive neurons were taken with a confocal laser scanning microscope (Zeiss). Random neurons displaying pyramidal morphology were chosen from data sets that had been blinded to the experimental condition. Spine volumes were subsequently analysed with the ImageJ software. At least 15 individual neurons derived from three independent experiments were measured for each experimental condition. For the functional screen 50 spines per neuron were analysed; for subsequent analyses more than 100 spines per neuron were analysed. For Sholl analysis, low-magnification pictures of GFP-positive neurons were taken and dendritic complexity was analysed with ImageJ software. At least ten individual neurons for each experimental condition of a total of three independent experiments were measured. For details on spine analysis and Sholl analysis see ref. 19. The determination of synapse density was performed by the method of ref. 49. The size of GluR2 surface clusters was determined with the Analyze Particle function of ImageJ, using thresholded images. Particles smaller than 0.1 μm^2 were excluded from the analysis.

Luciferase assay. Cortical or hippocampal neurons were transfected at 4 DIV or 14–16 DIV, and luciferase assays were performed one or two days later with the Dual-Luciferase Reporter Assay System (Promega).

***In situ* hybridization.** *In situ* hybridization for APT1 was performed as described in ref. 50 with a specific digoxigenin-labelled RNA riboprobe (992 nucleotides) sub-cloned into pBluescript II Sk^+ (Stratagene) vector for transcription.

For detection of endogenous miRNAs in dissociated neurons we basically followed the *in situ* hybridization protocol described in ref. 48. Fluorescein isothiocyanate (FITC)-conjugated complementary LNA probes (Exiqon) were hybridized overnight with miRNAs at 50 °C. The signal intensity of the FITC probe was amplified with the Alexa Fluor 488 Signal Amplification Kit (Molecular Probes). MAP2 immunostaining (mouse monoclonal; Sigma) was used to reveal dendrites.

Quantitative real-time PCR. Quantitative real-time PCR was performed with the 7300 Real Time PCR System (Applied Biosystems), using the iTaq SybrGreen Supermix with ROX (Bio-Rad) for the detection of mRNAs and the specific TaqMan MicroRNA Assay kits (Applied Biosystems) for the detection of small RNAs (PE Applied Biosystems).

Immunocytochemistry. Hippocampal neurons (17–18 DIV) were fixed in 4% paraformaldehyde for 15 min, permeabilized with PBS plus 0.2% Triton X-100 and blocked in PBS containing 10% normal goat serum. We used a mouse monoclonal anti-PSD95 antibody (1:500; MA1-046; Dianova), a rabbit polyclonal anti-synapsin-1 antibody (1:500; Chemicon), a rabbit polyclonal anti-APT1 antibody (1:50; produced by BioGenes) or a rabbit anti-haemagglutinin antibody (1:2,000; ab9110; Abcam) together with Cy3/Cy5-conjugated anti-mouse/rabbit antibodies (1:400; Jackson Immuno Research). GluR2 surface staining was performed as described[49].

Cell fractionation. Cells were scraped into ice-cold hypotonic buffer (5 mM Tris-HCl pH 7.5, 1 mM $MgCl_2$, 1 mM EGTA, 0.1 mM EDTA) containing protease inhibitors (Complete Mini EDTA-free; Roche). After incubation for 30 min on ice, the lysate was passed ten times through a 20-gauge needle and centrifuged at 3,000*g* for 15 min to remove nuclear debris. The lysate was centrifuged again for 1 h at 150,000*g*. The supernatant (cytosolic fraction) was collected and the pellet (membrane fraction) was resuspended in lysis buffer (50 mM Tris-HCl pH 7.5, 150 mM NaCl, 0.1% Triton-X-100, 0.2% SDS) containing protease inhibitors.

Application of APT1 inhibitors. Small-molecule APT1 inhibitors (FD196, FD253 and RB020) were diluted and stored in DMSO at 10 mM. Inhibitors were pre-diluted in medium and subsequently added to the cells at a final concentration of 10 μM. The treatment was repeated every 60 min because of the high hydrolysis rate of the inhibitors. As control we added equivalent volumes of DMSO. A detailed characterization of the APT1 inhibitors will be published elsewhere.

Electrophysiology. mEPSCs were recorded in visually identified cultured neurons at DIV 18–20. Coverslips with transfected cells were constantly superfused at room temperature with bath solution containing (in mM) NaCl 156, KCl 2, $CaCl_2$ 2, $MgCl_2$ 1, glucose 16.5, HEPES 10; pH 7.3, 330 mOsM). Pipette solution for whole cell recording contained (in mM) KCl 100, NaCl 10, $CaCl_2$ 0.25, EGTA 5, HEPES 10, glucose 40, MgATP 4, NaGTP 0.1; pH 7.3, 310 mOsM. During recording, the bath solution contained gabazine (5 μM) and tetrodotoxin (0.5 μM). See Supplementary Methods for further details.

48. Schratt, G. M., Nigh, E. A., Chen, W. G., Hu, L. & Greenberg, M. E. BDNF regulates the translation of a select group of mRNAs by a mammalian target of rapamycin-phosphatidylinositol 3-kinase-dependent pathway during neuronal development. *J. Neurosci.* **24,** 9366–9377 (2004).
49. Paradis, S. *et al.* An RNAi-based approach identifies molecules required for glutamatergic and GABAergic synapse development. *Neuron* **53,** 217–232 (2007).
50. Obernosterer, G., Martinez, J. & Alenius, M. Locked nucleic acid-based *in situ* detection of microRNAs in mouse tissue sections. *Nature Protocols* **2,** 1508–1514 (2007).

nature cell biology

DOI: 10.1038/ncb1876

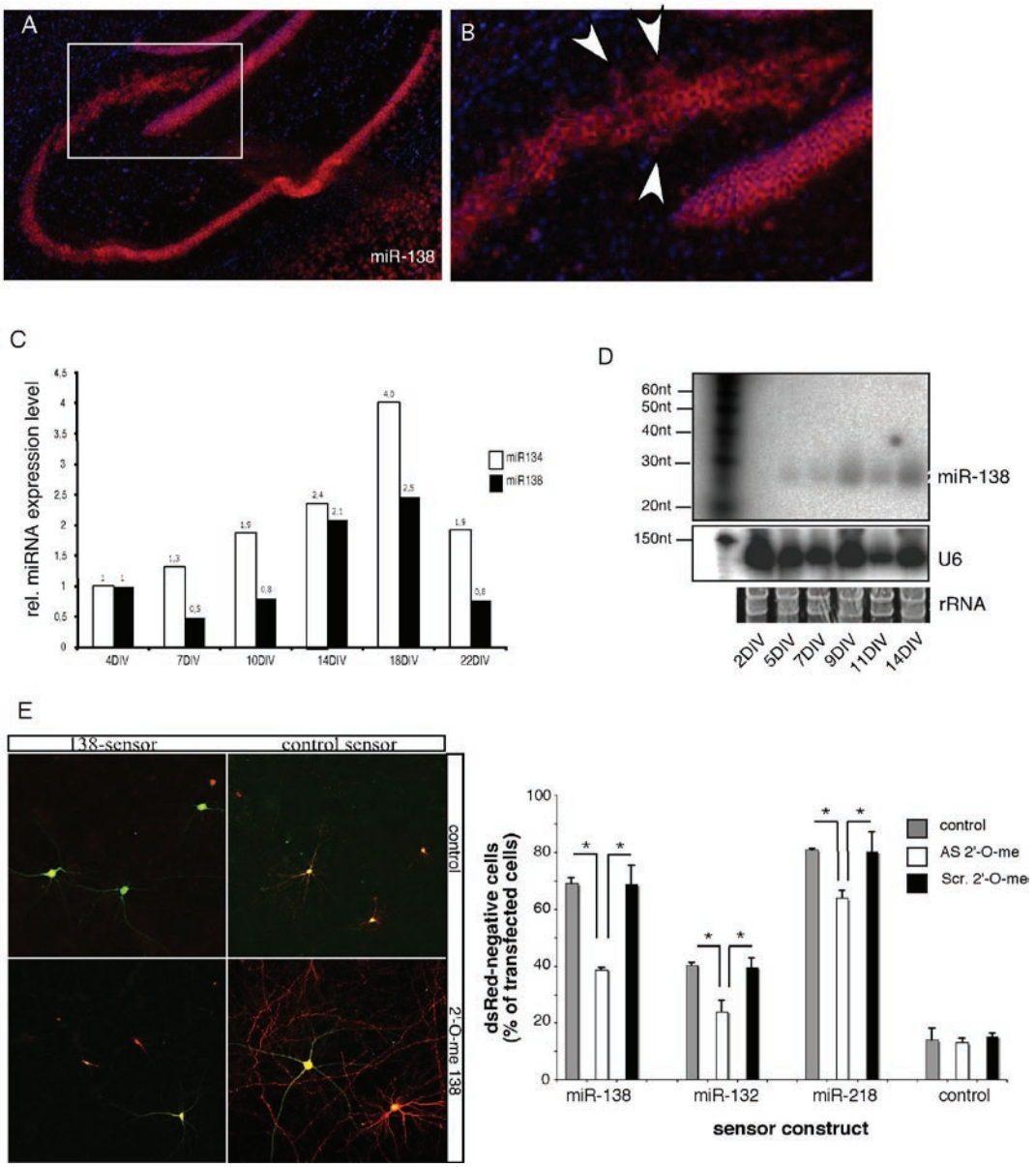

Figure S1 miR-138 is expressed in neurons at times of synapse development. (A) miR-138 expression in adult mouse brain *in vivo*. *In situ* hybridization (red) using an LNA/DNA-oligonucleotide directed against miR-138 reveals strong expression of miR-138 in the CA1/CA3 region of the hippocampus and the dentate gyrus. Boxed inset at higher magnification (B) illustrates miR-138 staining extending into the proximal dendritic layer (marked by arrowheads). Cell nuclei were counterstained with Hoechst dye. (C) miR-138 expression in primary cortical neurons as detected by quantitative real-time stem-loop PCR. Relative expression levels of mature miR-134 and miR-138 microRNA were determined at the indicated time points relative to the endogenous control U6 snRNA. Expression at 4DIV was set to one for each individual microRNA. (D) miR-138 expression in primary hippocampal neurons as detected by Northern blotting. RNA was prepared from cortical neurons between 2-14 DIV, resolved on 15% PAGE/urea and probed for miR-138 and U6 snRNA. Ethidium bromide staining for rRNA before blotting confirms equal loading. (E) miR-138 expression in primary hippocampal neurons as detected by a GFP/RFP-based sensor assay. Hippocampal neurons at 13-17 DIV were transfected with a reporter plasmid containing an RFP expression cassette with a perfect microRNA binding site in its 3'UTR to monitor the activity of miR-138, miR-132 and miR-218. Expression from a GFP expression cassette was used as internal transfection control. Left panel: Representative images of neurons transfected with control sensor (no miR-138 binding site) or miR-138 sensor with or without 2'O-me-antisense oligonucleotide to inhibit endogenous miR-138. Right panel: Statistical analysis of sensor assays for miR-138, miR-132 and miR-218. The percentage of all transfected cells (GFP positive) that were negative for the miRNA sensor dsRed was used as a measure for the activity of each individual miRNA. Note that addition of AS 2'O-me oligonucleotides significantly reduced the activity of all three miRNAs tested. The experiment was repeated twice, counting at least one hundred cells per condition (except for transfections with scrambled 2'O-me, where only 30 cells could be counted per condition due to the low transfection efficiency obtained with this oligonucleotide). *p<0.05.

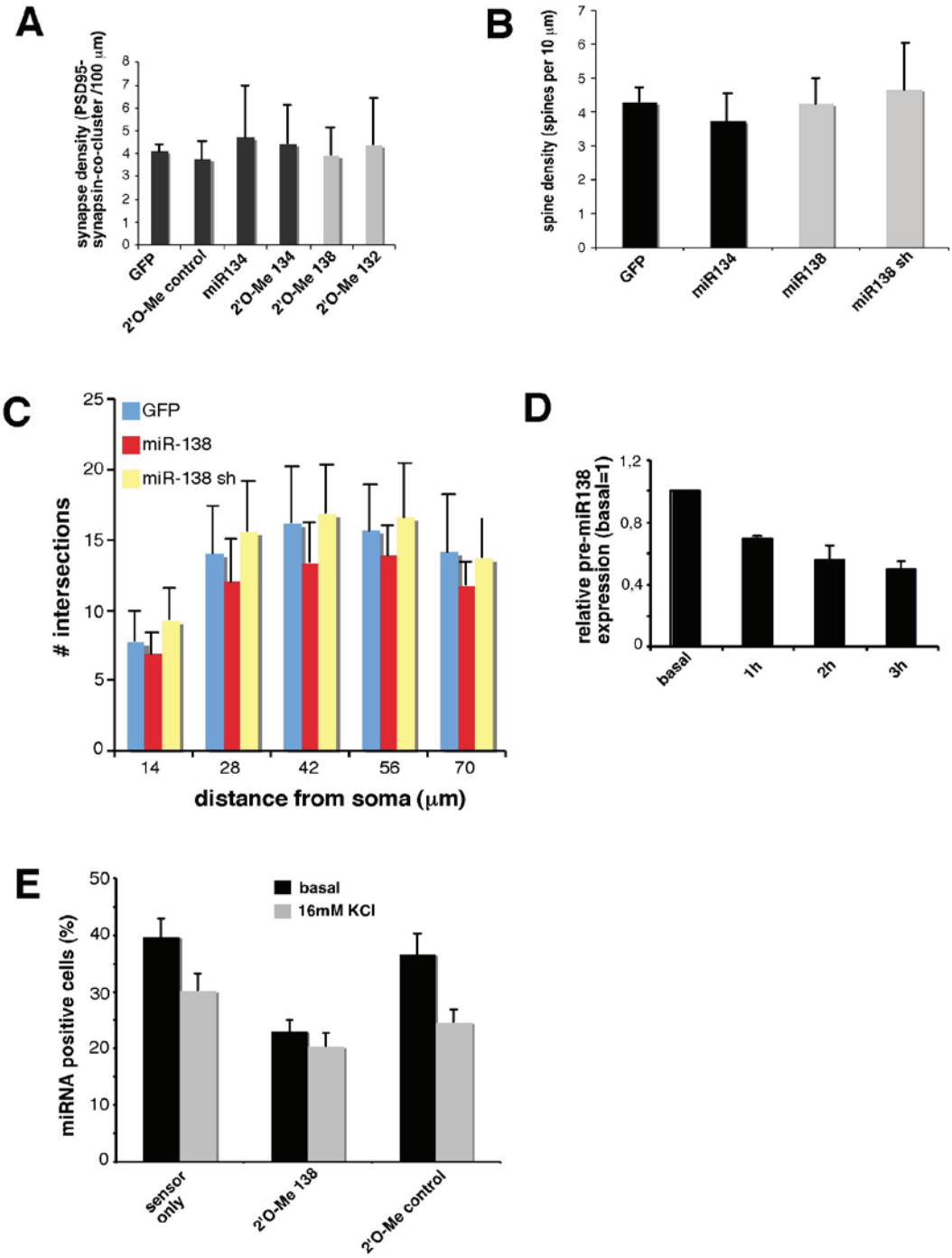

Figure S2 Perturbation of miR-138 activity does not alter synapse density or dendritic complexity. (A) Synapse density of neurons transfected with GFP and the indicated oligonucleotides as determined by the frequency of GFP positive PSD-95/synapsin co-clusters. None of the experimental conditions displayed a significant difference compared to the GFP and 2'O-methyl control conditions. A total of 15 neurons from three independent experiments were analyzed. (B) Overexpression of miR-138 in hippocampal neurons had no effect on dendritic spine density. Quantification of dendritic spine density in hippocampal neurons at 18 DIV transfected as in D. Results represent the average of three independent experiments + STDV. For each experiment, a total of eight neurons grown on two replicate coverslips were analyzed. (C) Expression of miR-138 duplex RNA does not significantly alter the branching index of primary hippocampal neurons at 18 DIV. Hippocampal neurons were transfected with the indicated synthetic duplex RNAs and eGFP, and Sholl analysis was performed at 14 µm intervals from the cell body. At least eight neurons per condition were measured in each experiment. Results represent the mean of two independent experiments + STDV. (D) Regulation of pre-miR-138 expression by neuronal activity. Cortical neurons were membrane depolarized (55 mM Kcl) for up to three hours and relative pre-miR-138 expression levels (normalized to U6 snRNA) were assessed by quantitative real-time RT-PCR. Values were normalized to the untreated condition and represent the mean + STDV of three independent experiments (pre-miR-138).

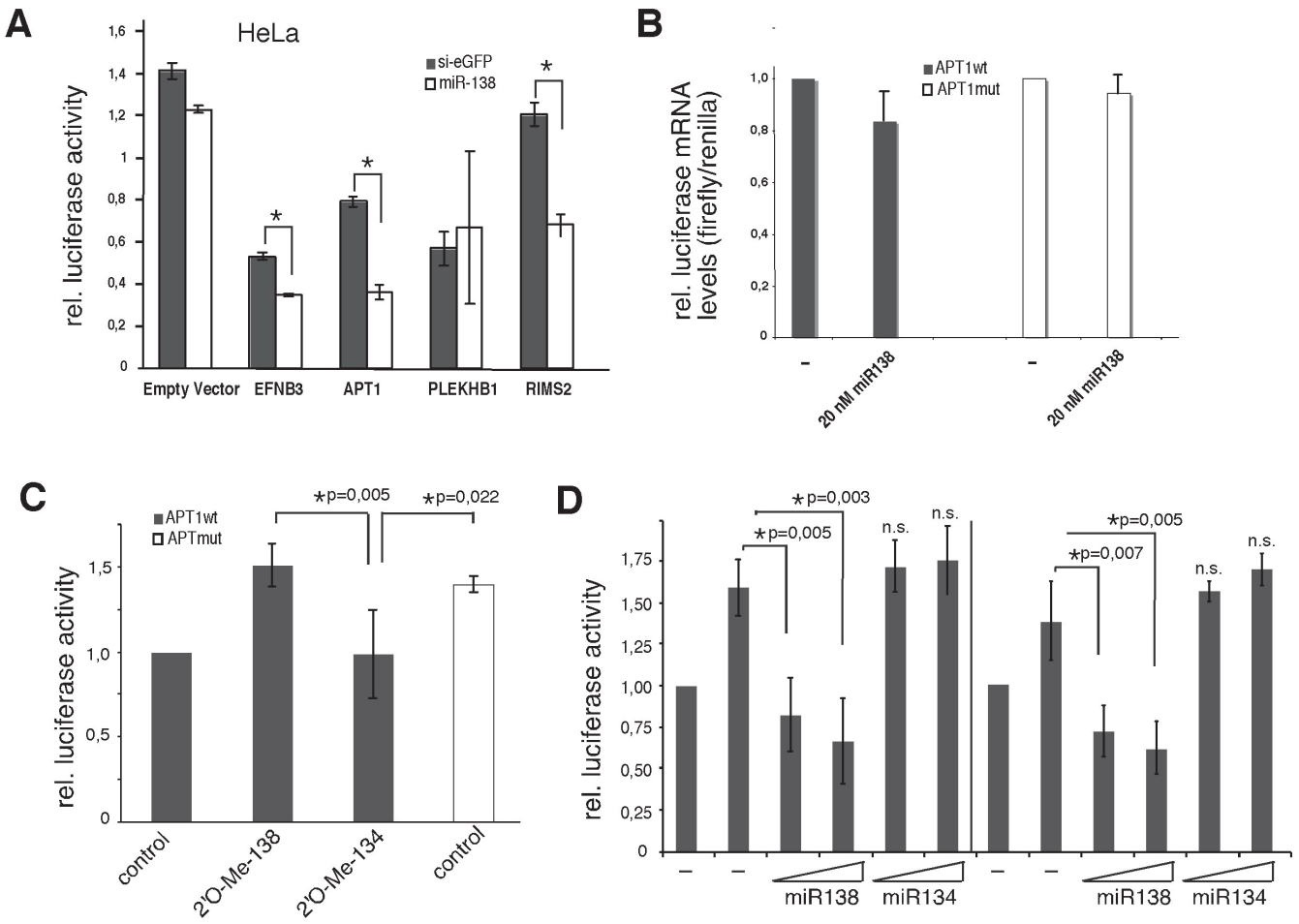

Figure S3 miR-138 inhibits expression of an APT1-luciferase reporter gene. (A) Validation of predicted miR-138 target mRNAs by dual-luciferase reporter assay in HeLa cells. 3'UTR regions of the indicated genes were cloned downstream of the firefly luciferase coding region within pGL3, and the resulting vectors were transfected into HeLa cells along with either miR-138 or si-eGFP duplex RNA (100 nM) as a control. The measured firefly luciferase activity is expressed relative to the internal Renilla luciferase control. Normalized luciferase activity of miR-138 expressing cells compared to control-transfected cells is given for each individual reporter construct. Error bars represent the mean of three replicate measurements. * p<0.05 (pairwise Student's t-test). (B) Introduction of miR-138 into primary neurons does not substantially decrease steady-state APT1 mRNA levels. Cortical neurons at 4 DIV were transfected with APT1 luciferase reporter genes along with 20 nM miR-138 synthetic duplex RNA, and luciferase RNA levels were determined 24 hours later by quantitative real-time PCR analysis. Results represent the mean of three independent transfections + STDV. Values were normalized to Renilla luciferase mRNA levels, and the relative luciferase mRNA level of the APT1 wt reporter without exogenous miR-138 was set to one. (C) Luciferase assay was performed on miR-138 expressing cortical neurons (16 DIV) with a wildtype or mutant APT1-luciferase reporter gene together with 2'O-methyl miR-138 inhibitor or 2'O-methyl miR-134 inhibitor as a control (200 nM). Values are normalized to the internal Renilla luciferase activity. Bars represent the mean ± STDV of at least three independent experiments. *p<0.05 (pairwise Student's t-test; individual p-values are indicated above each bar). (D) 2'O-me-138 effect on APT1 luciferase expression can be specifically antagonized by miR-138 duplex RNA. Hippocampal neurons (16DIV) were transfected with the indicated amounts of 2'O-me-138 together with either miR-134 or miR-138 duplex RNA (5-10nM). Luciferase activity was measured two days later. Results represent the average of three independent experiments ± STDV. * p<0.01 (pairwise Student's t-test; individual p-values are indicated above each bar).

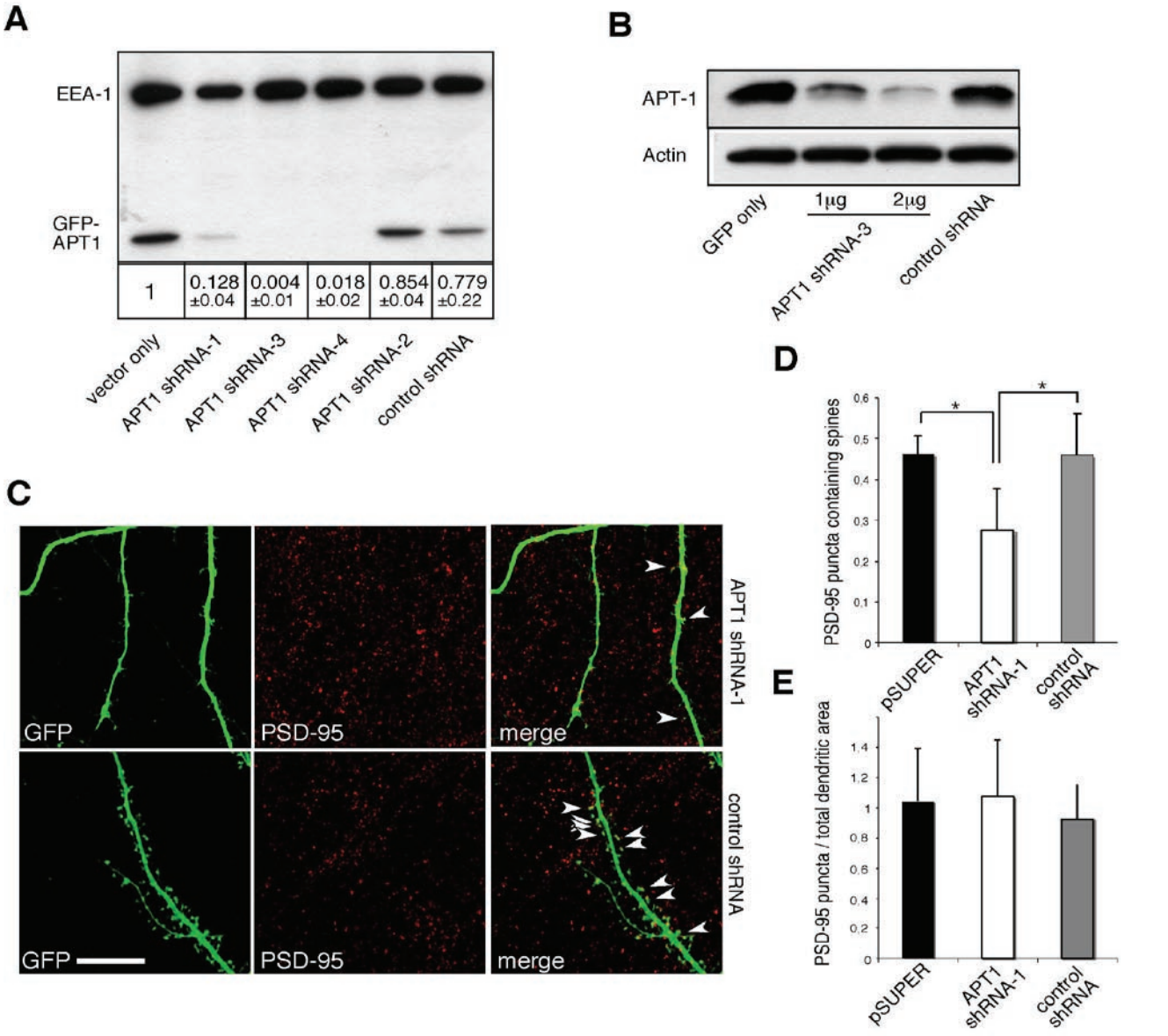

Figure S4 Reduced spine-associated PSD-95 upon APT1 knockdown. (A) Knockdown of APT1 protein levels in HEK293 cells expressing rat APT1 and different pSuper-shRNA constructs. 100 ng/ml of a cDNA expression vector for rat APT1-GFP was transfected together with the indicated shRNAs targeting either APT1 (shRNA 1-4) or an unrelated control sequence (control shRNA). Western blots were probed with both a polyclonal anti-APT1 antiserum or a monoclonal anti-EAA-1 antibody as a loading control. Quantification of three blots based on independent experiments is shown at the bottom (vector only control = 1). (B) Dose-dependent knockdown of endogenous APT1 protein in neurons. Cortical neurons were nucleofected with 2 µg of GFP, 1-2 µg of APT1 shRNA-3 or 2 µg of a control shRNA. Western blot was probed with a polyclonal anti-APT1 antiserum or anti-β-Actin as a loading control. (C) Hippocampal neurons transfected as in Figure 5B were stained at 18 DIV for the post-synaptic density marker protein PSD-95 (red). Representative dendritic segments illustrate that mushroom spines in control shRNA transfected neurons are vastly PSD-95 positive (arrowheads in lower panels), whereas the majority of protrusions in APT1-shRNA-1 transfected neurons lack PSD-95. Instead, PSD-95 puncta accumulate on the dendritic shaft (arrowheads in upper panel). Scale bar = 10 µm. (D, E) Quantification of results obtained with neurons treated as in (C). Bars in (D) represent the ratio of spines containing PSD-95 puncta to the total number of dendritic protrusions for each experimental condition. Bars in (E) represent the overall density of PSD-95 puncta within a defined dendritic area (1 μm^2) for each experimental condition. For each experiment, a total of eight neurons grown on two replicate coverslips were analyzed. *p<0.05 (t-test).

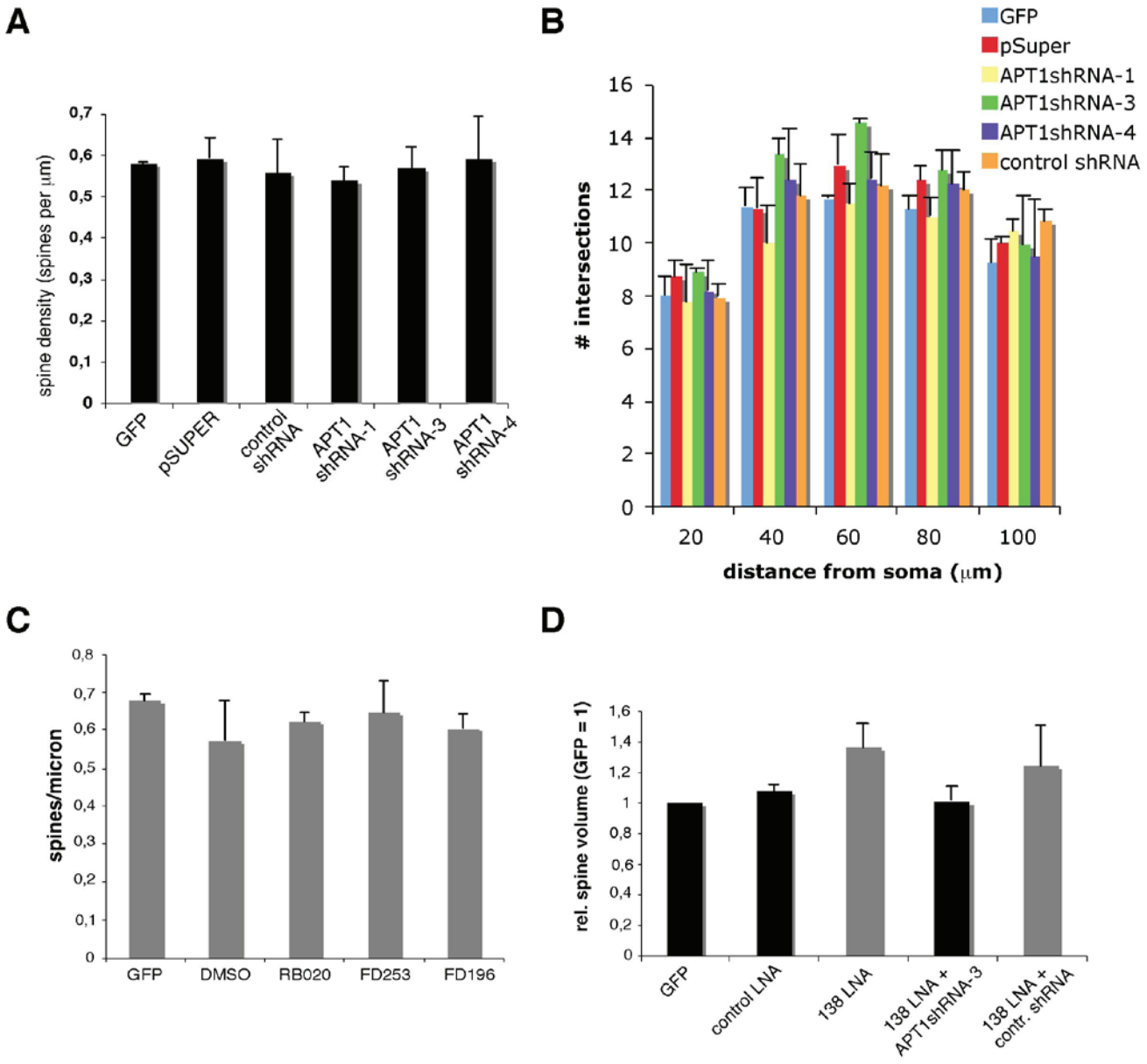

Figure S5 APT1 inhibition does not significantly alter spine density or the dendritic branching index of primary hippocampal neurons at 18 DIV. (A) Hippocampal neurons were transfected with the indicated shRNA expression vectors and eGFP before determining spine density of a total of eight neurons grown on two replicate coverslips per experiment. (B) Sholl analysis was performed in neurons transfected as in (A) at 20 µm intervals from the cell body. At least eight neurons per condition grown on two replicate coverslips were measured in each experiment. For both assays, results represent the mean of three independent experiments + STDV. (C) Neurons (18 DIV) were treated with the indicated inhibitors or DMSO only for 6 hours, and the number of dendritic protrusions per dendritic length was determined. At least eight neurons per condition grown on two replicate coverslips were measured in each experiment. Results represent the mean of three independent experiments + STDV. (D) shRNA-mediated knockdown of APT1 suppresses the increase in spine volume caused by LNA-miR-138. Rat hippocampal neurons (14 DIV) were transfected with the indicated LNA oligonucleotides (100 nM) in combination with APT1 shRNA-3 or control shRNA (5ng each). Bar diagram represents the average of two independent experiments, measuring at least 600 spines of 6 individual neurons each at 18 DIV.

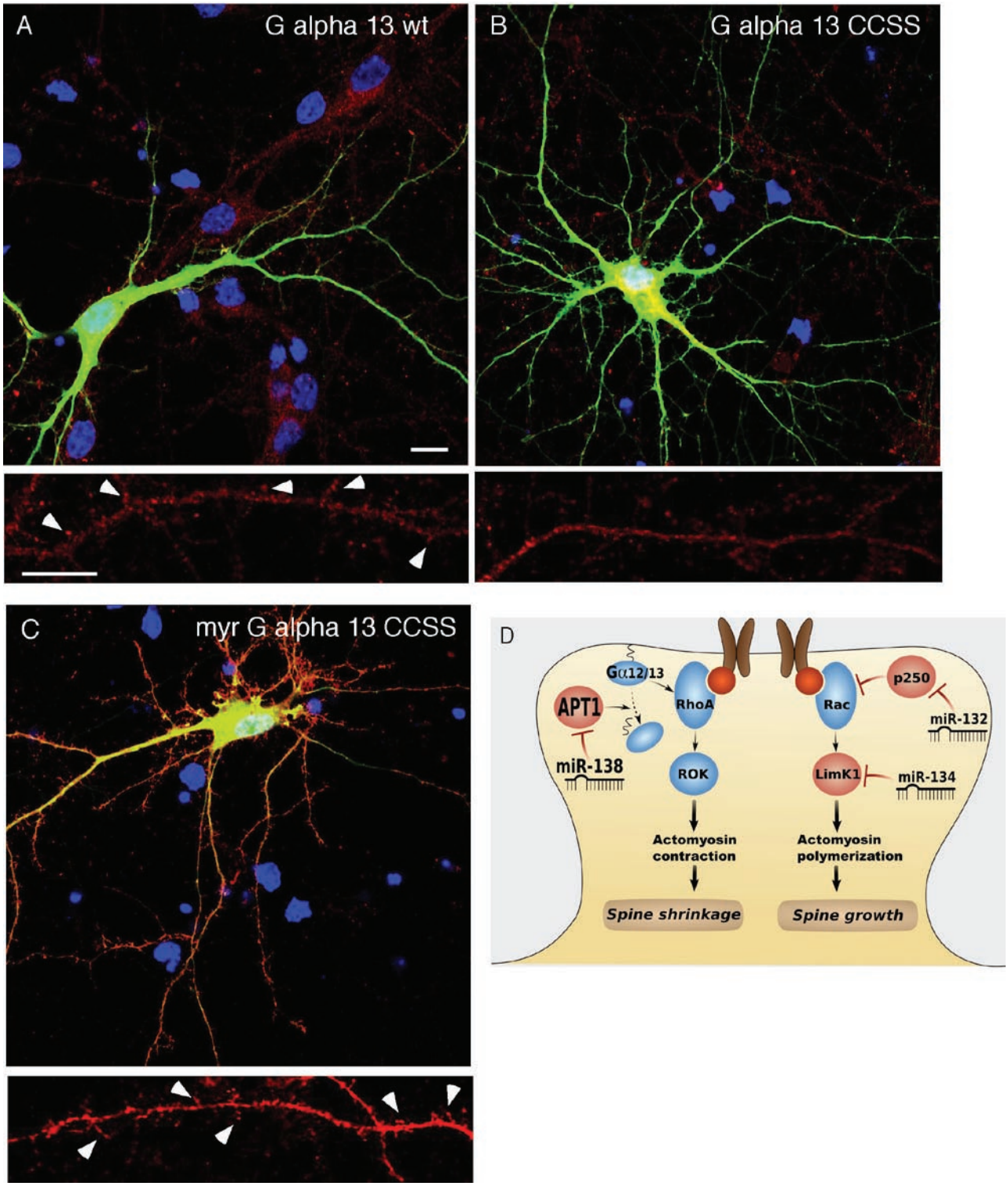

Figure S6 (A-C) Subcellular localization of Gα13 subunits in neurons. Primary hippocampal neurons were transfected with GFP together with constructs expressing HA-tagged wt Gα13 (A), the palmitoylation-defective Gα13 CCSS mutant (B) or the constitutively membrane-attached myr Gα13 CCSS mutant (C). Anti-HA staining (red, 18DIV) reveals Gα13 localization in dendritic protrusions (arrowheads) only for wt Gα13 and myr Gα13 CCSS. Cell nuclei were visualized by DAPI counterstain (blue). Scale bar = 10 μm. (D) Model for the role of miRNAs in the regulation of G protein signaling and dendritic spine morphogenesis. As previously shown, miR-132 and miR-134 antagonistically regulate the activity of the spine growth promoting Rac signaling pathway. In addition, miR-138 might activate the Rho signaling pathway implicated in spine shrinkage by promoting membrane-association of Gα12/13. ROK: Rho-associated kinase. Limk1: Lim-domain containing protein kinase 1.

Supplementary Methods

RNA and DNA oligonucleotides

Synthetic RNA oligos:

let-7c sense: 5'Phospho-ugagguaguagguuguaugguu

let-7c as: 5'-Phospho-ccauacaaccuacuacuuuaaa

miR-134 sense: 5'Phospho-ugugacugguugaccagaggga

miR-134 as: 5'Phospho-ccucuggucaaccaguuauacu

miR-138sh (short)* sense: 5'Phospho-agcugguguugugaauc

miR-138 sense: 5'Phospho- agcugguguugugaaucaggccg

miR-138 as: 5'Phospho – GCCUGAUUCACAACACCAGAUUU

* A truncated version of miR-138 as it appeared in miRBase 7.1.

2'O-methylated oligos:

2'OMe134: ucucucccucuggucaaccagucacaaggcu

2'OMe 138: gauucacaacaccagcu

Antagomirs:

miR138: mG.mA.mU.mU.mC.mA,mC.mA.mA.mC.mA.mC.mC.mA.mG.mC.mU.3'-Chl

control: mC.mA.mU.mC.mA.mC.mG.mU.mA.mC.mG.mC.mG.mG.mA.mA.mU.3'-Chl

Real-time PCR:

APT1 fw (Rn) : tctgaacggtttctttcctgct

APT1 bw (Rn): acaccaaatgaccccacatca

Beta-3-tubulin fw (Rn): ccccagggctcaagatgtc

Beta-3-tubulin bw (Rn): cgcttgaacagctcctggat

Firefly Luc (pGL3) fw: tgaccgcctgaagtctctga

Firefly Luc (pGL3) bw: tggagcaagatggattccaat

GAPDH fw (Rn): gccttctcttgtgacaaagtgga

GAPDH bw (Rn): ccgtgggtagagtcatactggaa

Renilla Luc (pGL4.74) fw: ctgggacgagtggcctgacatc

Renilla Luc (pGL4.74) bw: agcaccattttctcgccctcttc

Pre-miR138 fw: tgcagctggtgttgtgaatca

Pre-miR138 bw: gtgaaatagccgggtaagaggat

Cloning and Mutagenesis:

pGL3-constructs

APT-1: fwd 5' – GGCGCGCCCATCACTAAGAGGCCTTGAGTAGAAGTTCA – 3';
APT-1: rev 5' – GAATTCAGCCAAAATTAAATTTTATTTCACATTGATAGAAACTGTGA – 3';
APT-1mut: fwd 5' – TTGAGTAGAAGTTCA*A*A*C*ACATCACAGTAGTAGAG – 3'
APT-1mut: rev 5' – ACTACTGTGATG*T*G*T*TTGAACTTCTACTCAAGGCC – 3'
EFNB3: fwd 5' – TCTAGAGGGCTCCTCCCACCTGGCT 3';
EFNB3: rev 5' – GGCGCGCCTTGTTCAAATTTCCCTTTTACAATAAAACTATCGAGGTGA – 3';
PLEKHB1: fwd 5' – GGCGCGCCGCCCTGGGGCTCTGACTTCTG – 3';
PLEKHB1 rev 5' – GAATTCGGGGCCAATCATGTCTTTATTAGTGTCTGT – 3';
RIMS2 fwd 5' – GGCGCGCCCAACTATAAAACTGTTGTCACAACAACCAGC – 3';
RIMS2 rev 5' – GAATTCCCTTTGCTAGGGCACAATGTGTACGA – 3.

pSUPER constructs

APT1-siRNA(1) fw:

GATCCCCTTATGCCAGTCACACTAAATTCAAGAGATTTAG

TGTGACTGGCATAATTTTTGGAAA

APT1-siRNA(1) bw:

AGCTTTTCCAAAAATTATGCCAGTCACACTAAATCTCTTG

AATTTAGTGTGACTGGCATAAGGG

APT1-siRNA(2) fw:

GATCCCCGGAGGCGCCTTATCTTTATTTCAAGAGAATAAA

GATAAGGCGCCTCCTTTTTGGAAA

APT1-siRNA(2) bw:

AGCTTTTCCAAAAAGGAGGCGCCTTATCTTTATTCTCTTG

AAATAAAGATAAGGCGCCTCCGGG

APT1-siRNA(3) fw:

GATCCCCAGGAAATGATGGATGTCAATTCAAGAGATTGAC

ATCCATCATTTCCTTTTTTGGAAA

APT1-siRNA(3) bw:

AGCTTTTCCAAAAAAGGAAATGATGGATGTCAATCTCTTGAATTGACATCC

ATCATTTCCTGGG

APT1-siRNA(4) fw:

GATCCCCCAATAGTGCTAATCGAGATTTCAAGAGAATCTC G

ATTAGCACTATTGTTTTTGGAAA

APT1-siRNA(4) bw:

AGCTTTTCCAAAAACAATAGTGCTAATCGAGATTCTCTTG

AAATCTCGATTAGCACTATTGGGG

Control siRNA fw:

GATCCCCAAACCTTGTGGTCCTTAGGTTCAAGAGACCTAAGGACCACAA

GGTTTTTTTTA

Control-siRNA bw:

AGCTTAAAAAAAACCTTGTGGTCCTTAGGTCTCTTGAACCTAAGGACCAC

AAGGTTTGGG

CFP-APT1

Sense: 5'-CTT GAA TTC ATG TGC GGC AAT AAC ATG TCA ACC-3'

Antisense: 5'-AAG GAT CCG GAT CAA TTG GAG GTA GGA GTT TAT CAA TGA ATT G-3'

Mutagenesis: 5'-CCA CTT CGG GCT TCC TTT CCA CAG GGT CCT ATC-3'.

Microarray analysis

Total RNA extracted from rat P15 whole brain and fractionated P15 synaptosomes was Cy3- and Cy5-labeled, respectively, and hybridized to a miRNA microarray (LC Sciences, Austin, USA) comprising three replica of DNA probes for all annotated miRNAs from mouse (*Mus musculus*) and rat (*Rattus norvegicus*) in the miRBase Release 7.0 as well as a set of non experimentally verified probes, assigned S, corresponding to the miRNA* strand of the annotated mature miRNA sequences. Fluorochrome-labeled RNA samples from three independent experiments were hybridized to the microarray and the array data was analyzed using the TIGR MIDAS software package (www.tm4.org). Scanned array images were imported into TIGR Spotfinder version 3.1 for the extraction of integrated Cy3 and Cy5 intensities. Ratios of log-transformed integrated intensities were Lowess (LocFit) normalized using TIGR MIDAS version 2.19. Intensities of replica probes were averaged using Microsoft Excel excluding probes displaying a coefficient of

variance > 100% from further analysis. Only probes with average intensities above the average global background plus four standard deviations were further analyzed. The Cy5/Cy3 ratios were log2-transformed and statistical analysis was carried out using TIGR Multi Experiment Viewer by performing a one-class t-test ($p < 0.1$) with the hypothesized mean of 0. Only probes with an average log2-ratio above 1 or below -1 were considered. Samples with dye bias as indicated by the manufacturer were omitted from the analysis.

miRNA-138 *in situ* hybridization (brain slices)

All mice were maintained at the IMBA mouse house facility, under pathogen-free conditions. C57BL/6 mice were mated to generate embryos for analyses and the morning of the vaginal plug was considered as E0.5. Brains were post-fixed in 4% para-formaldehyde, cryo-protected (30% sucrose in PBS), embedded in Tissue-Tek OCT compound, and cryo-sectioned. Ten-micron cryo-sections were pretreated, hybridized with LNA digoxygenin-labeled probes (Exiqon), and washed according to (Schaeren-Wiemers and Gerfin-Moser, 1993) with some modifications. The miRNA-138 probe sequence was as follows: 5'-CGGCCTGATTCACAACACCAGCT-3'.. Briefly, sections were fixed in 4% paraformaldehyde for 10 min, acetylated, and treated with 5 μg/mL proteinase K (Roche) in PBS for 5 min, washed, and prehybridized for 4 h at room temperature. Hybridization with 22-nt LNA probes (Tm ~ 80°C) was performed at 55°C overnight. Slides were then washed at 60°C and incubated with alkaline phophatase-conjugated goat anti-DIG Fab fragments (1:2000 [Roche]) at 4°C overnight. Fluorescent detection was performed using a Fast Red reaction (Dako Cytomation) for 1 h at room temperature. Sections were analyzed with a with a Zeiss Axioplan-2 microscope and photographed with a digital camera (Coolsnap HQ, Photometrics). A subset of images was adjusted for levels, brightness, contrast, hue, and saturation with Adobe Acrobat 7.0 imaging software to optimally visualize the expression patterns. A detailed description of the above outlined *in situ* hybridization protocol for miRNAs was previously described in (Obernosterer et al., 2007).

microRNA sensor assay

The 138-dsred-sensor was produced by cloning a NotI/XbaI flanked oligo consisting of perfectly complementary mir-138 binding site, together with a EcorI/Not I fragment spanning the dsRED coding sequence, into the EcoRI/XbaI site of the polylinker of ptracer-CMV2 (Invitrogen). A control sensor was cloned by inserting the dsRED alone into ptracer-CMV2. 300 ng of 138-dsRED-sensor or control sensor were transfected into DIV9 rat hippocampal neurons, and the cells were fixed at different time points (DIV13 to DIV17) and scored for GFP/dsRED positive cells (e.g.: mir-138 negative cells) GFP positive cells (e.g.: mir-138 positive cells). A minimum of 80 cells for condition were counted. In order to validate the assay, 30 pmol of mir-138 antagomir or control antagomir were co-transfected with the sensors.

APT1 small molecule inhibitor

Palmostatin B is a recently developed small molecule inhibitor of APT1 (IC_50 = 0.56 ± 0.13μM) with activity in cells (H. Waldmann et al, to be published elsewhere). Samples of Palmostatin B are available from H. Waldmann upon request. Hippocampal neurons were transfected with GFP at 14DIV. At 18DIV APT1-inhibitors (dissolved in DMSO) or an equal volume of DMSO were added to the cell´s medium, so that a final concentration of 10μM was achieved. During incubation time fresh APT1-inhibitors or DMSO was added every 60min. After 6h neurons were fixed in 4% PFA and processed for imaging.

Electrophysiology

Recoring solution was according to Hamill et al. Spontaneous synaptic currents were recorded for 100 s after 10 to 15 minutes of equilibration in whole cell configuration. Experiments were performed blindly with respect to the transfection (miR-138, control duplex RNA, GFP). Currents were recorded in voltage clamp at -70 mV using borosilicate glass pipettes (2- 4 MΩ) and an EPC-7 amplifier (HEKA, Lambrecht, Germany), filtered at 3 kHz and digitized with a CED 1401 interface (CED, Cambridge, UK; sample frequency 20 kHz). Series resistance was controlled every minute and cells were excluded from further analysis if the resistance exceeded 20 MΩ. Data was evaluated off-line with Spike5 and Signal3 software (CED, Cambridge, UK) using custom made routines. After testing for normality of distributions, statistical significance of results was tested by Student's two-tailed t-test using GraphPad InStat Software (GraphPad Software, San Diego, USA). Cumulative amplitude distributions were tested with Kolmogorov-Smirnov test. P-values < 0.05 were considered statistically significant.

References:

Obernosterer, G., Martinez, J., and Alenius, M. (2007). Locked nucleic acid-based in situ detection of microRNAs in mouse tissue sections. Nat Protoc *2*, 1508-1514.

Schaeren-Wiemers, N., and Gerfin-Moser, A. (1993). A single protocol to detect transcripts of various types and expression levels in neural tissue and cultured cells: in situ hybridization using digoxigenin-labelled cRNA probes. Histochemistry *100*, 431-440.

Hamill OP, Marty A, Neher E, Sakmann B, Sigworth FJ (1981) Improved patch-clamp techniques for high-resolution current recording from cells and cell-free membrane patches. Pflugers Arch 391:85-100.

nature cell biology

The mitotic kinesin-14 Ncd drives directional microtubule–microtubule sliding

Gero Fink[1,5], Lukasz Hajdo[2,3,5], Krzysztof J. Skowronek[2,4], Cordula Reuther[1], Andrzej A. Kasprzak[2] and Stefan Diez[1,6]

During mitosis and meiosis, the bipolar spindle facilitates chromosome segregation through microtubule sliding as well as microtubule growth and shrinkage[1]. Kinesin-14, one of the motors involved, causes spindle collapse in the absence of kinesin-5 (refs 2, 3), participates in spindle assembly[4] and modulates spindle length[5]. However, the molecular mechanisms underlying these activities are not known. Here, we report that *Drosophila melanogaster* kinesin-14 (Ncd) alone causes sliding of anti-parallel microtubules but locks together (that is, statically crosslinks) those that are parallel. Using single molecule imaging we show that Ncd diffuses along microtubules in a tail-dependent manner and switches its orientation between sliding microtubules. Our results show that kinesin-14 causes sliding and expansion of an anti-parallel microtubule array by dynamic interactions through the motor domain on the one side and the tail domain on the other. This mechanism accounts for the roles of kinesin-14 in spindle organization.

The mitotic spindle is a molecular machine composed of a bipolar array of microtubules whose minus ends are focused at the spindle poles and whose plus ends demarcate a midzone of overlapping microtubules with opposite polarity. This complex organization is achieved by the activity of molecular motors that generate forces directed towards the minus and plus ends of microtubules[6,7]. In particular, minus-end-directed motor proteins of the kinesin-14 family, which consist of a carboxy-terminal ATP-hydrolysing motor domain and an amino-terminal ATP-independent microtubule binding site[8–11], have been shown to have essential roles in spindle organization during meiosis[12–14] and mitosis[15–17]. Kinesin-14, whose function is highly conserved, specifically enriches at the spindle poles, but also localizes to spindle microtubules[4,17,18]. Malfunctioning of kinesin-14 during mitosis results in splayed multipolar spindles and unfocused spindle poles[4,18,19]. These defects are assumed to result from the microtubule crosslinking activity of kinesin-14, by which the motors form stable contacts between parallel-oriented microtubules near the spindle poles but cause sliding between anti-parallel microtubules in the midzone[4,17,19].

When kinesin-14 is depleted, slightly longer spindles[20] are observed at metaphase–anaphase A transition[21], suggesting an involvement of kinesin-14 in the modulation of spindle length. Conversely, cells lacking kinesin-5, a plus-end-directed microtubule motor capable of sliding microtubules relative to each other[22], have collapsed spindles[2,17,23]. In these studies, simultaneous inhibition of kinesin-14 restored centrosome separation and the formation of bipolar spindles. This antagonistic behaviour suggests that kinesin-14 counteracts kinesin-5 by an oppositely directed microtubule–microtubule sliding mechanism. Consistent with this prediction, recent experiments in which Ncd was overexpressed showed an increase in motility of microtubule bundles[24].

To elucidate the interaction of Ncd motors with microtubules on the single molecule level, we developed an *in vitro* assay that reduces non-specific adhesion of motor proteins to the substrate surface (Fig. 1). Given that Ncd translocates on microtubules in a non-processive manner[25,26], we expected that the motors would interact predominantly with the 'template' microtubules through their N-terminal microtubule binding sites (Fig. 1a). Using total internal reflection fluorescence (TIRF) microscopy we observed that GFP-labelled Ncd (full-length GFP–Ncd) indeed colocalized with the template microtubules (Fig. 1b, c). To investigate whether tail-mediated interaction of Ncd with microtubules involved static binding (as suggested by a recent *in vitro* study[27]) or was dynamic, we performed single-molecule experiments (Fig. 1d). Surprisingly, a high proportion of the full-length motor (identified as dimeric molecules; Supplementary Information, Figs S1, S2) diffused along the microtubule. To test which parts of the protein were required for the diffusional motion, we constructed truncated, dimeric Ncd motors, which lacked either the second microtubule binding site (tailless, GFP–Ncd^{195}) or the motor domain (headless Ncd^{349}–GFP). We observed only very short events of transient binding for the tailless GFP–Ncd^{195}. Diffusion of this protein construct was never observed, indicating that neither the head nor the stalk or GFP alone mediate diffusion. Interestingly, we did not observe any stationary binding of headless Ncd^{349}–GFP. Instead, this construct diffused robustly along the microtubule. When repeating these experiments in the presence of AMP–PNP (adenyl-5′-yl imidodiphosphate; Supplementary

[1]Max Planck Institute of Molecular Cell Biology and Genetics, Pfotenhauerstraβe 108, 01307 Dresden, Germany. [2]Nencki Institute of Experimental Biology, 3 Pasteur St., 02-093 Warsaw, Poland. [3]Department of General Biophysics, University of Lodz, 12/16 Banacha St., 90-237 Lodz,Poland. [4]International Institute of Molecular and Cell Biology, 4 Trojdena St., 02-093 Warsaw, Poland.
[5]These authors contributed equally to this work.
[6]Correspondence should be addressed to S.D. (e-mail: diez@mpi-cbg.de)

Received 3 December 2008; accepted 23 February 2009; published online 10 May 2009; DOI: 10.1038/ncb1877

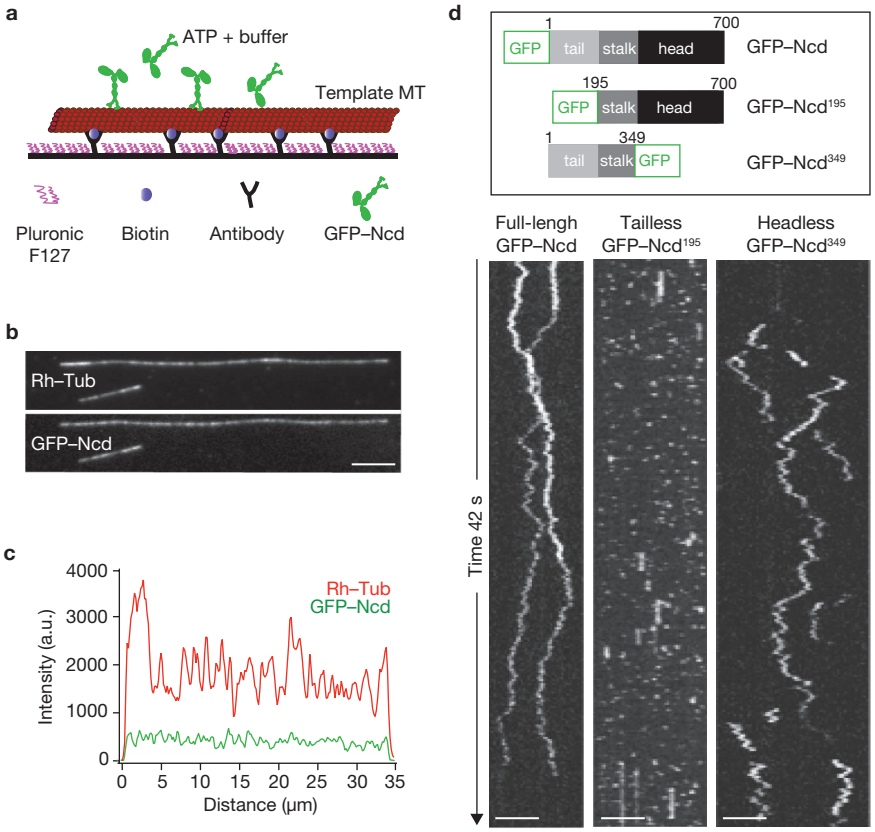

Figure 1 Ncd interaction with microtubules in the presence of ATP. (**a**) Diagram of the experimental setup. 'Template' microtubules (MT; dimly rhodamine-labelled) were tagged with biotin and immobilized to the glass surface by α-biotin antibodies. To block non-specific surface binding of Ncd motors, the surface was coated with Pluronic F127. These template microtubules were then incubated with Ncd motors. (**b**) Epifluorescence and TIRF microscopy images of rhodamine-labelled template microtubules (Rh–Tub) and interacting GFP-labelled full-length Ncd motors (GFP–Ncd). Scale bar, 5 μm. (**c**) Line scan analysis showing the fluorescence intensity profiles of the long template microtubule in B (red) with the corresponding GFP–Ncd signal (green). (**d**) Kymographs of different, single-molecule GFP-labelled Ncd constructs imaged by TIRF microscopy in the presence of 1 mM ATP. Full-length GFP–Ncd diffused along the microtubule. Tailless GFP–Ncd^{195} revealed short-lived binding events (characteristic for head–microtubule interactions of a non-processive motor) but never diffused along the microtubule lattice. Occasional events of short-term stationary binding were probably related to degraded motors with impaired ATP hydrolysis. Headless Ncd^{349}–GFP also diffused along the microtubules. We note, that any potential interaction between the Ncd tail and the GFP in the N-terminal region of the protein can be ruled out as the origin for the diffusive interaction because the GFP is attached on the C-terminal side in Ncd^{349}–GFP. Our high ionic strength experiments complement earlier studies[27]. There, the tail domains of Ncd were suggested to be responsible for static binding, as well as directed motility, of full-length Ncd at low ionic strength. However, no headless constructs were tested and no experiments with full-length Ncd at high ionic strength were conducted in their study. Scale bars, 3 μm. (Supplementary Information, Movies 1–3)

Information, Fig. S3), the diffusion of the headless Ncd^{349}–GFP was not affected. In contrast, full-length Ncd and tailless GFP–Ncd^{195} both showed extended periods of stationary binding. From these observations, we conclude that tailless GFP–Ncd^{195} interacts predominantly with the microtubule through its motor heads in an ATP-dependent manner, and that the Ncd tail alone is capable of mediating diffusion along the microtubule. This tail-dependent diffusion makes the protein a highly dynamic microtubule crosslinker and raises the question of whether Ncd can indeed induce microtubule–microtubule sliding.

To investigate Ncd-induced microtubule–microtubule interactions we again used the assay described in Fig. 1. Individual 'transport' microtubules then landed on the Ncd-covered template microtubules (Fig. 2a). Of the microtubule–microtubule interaction events ($n = 209$), 52.2% of the transport microtubules showed robust sliding (Fig. 2b, c, arrowheads), 37.8% showed only short motility and slowed down exponentially before stopping (Supplementary Information, Fig. S4) and 10% statically crosslinked to the template microtubules immediately after landing (Fig. 2c, arrow). Robust sliding always occurred in the opposite direction along the template microtubules, compared with the short motility events. Additional support for this phenomenon was provided by a number of transport microtubules sliding robustly to the end of the template microtubule, where they performed nodal-end swivelling and crosslinked statically after reorientation (Fig. 2c, asterisk). This suggests a directional sliding mechanism, where oppositely oriented transport microtubules behave differently in their interaction with an individual template microtubule. By contrast, tailless GFP–Ncd^{195} and headless Ncd^{349}–GFP did not induce any specific microtubule–microtubule interactions, indicating that both, Ncd motor and tail domains are compulsory for microtubule–microtubule sliding and crosslinking.

To determine the polarity of the interacting microtubules, we first determined the orientation of the transport microtubules by polarity-marking (Fig. 2a–c; Supplementary Information, Fig. S5). Next we determined the orientation of the template microtubules by imaging

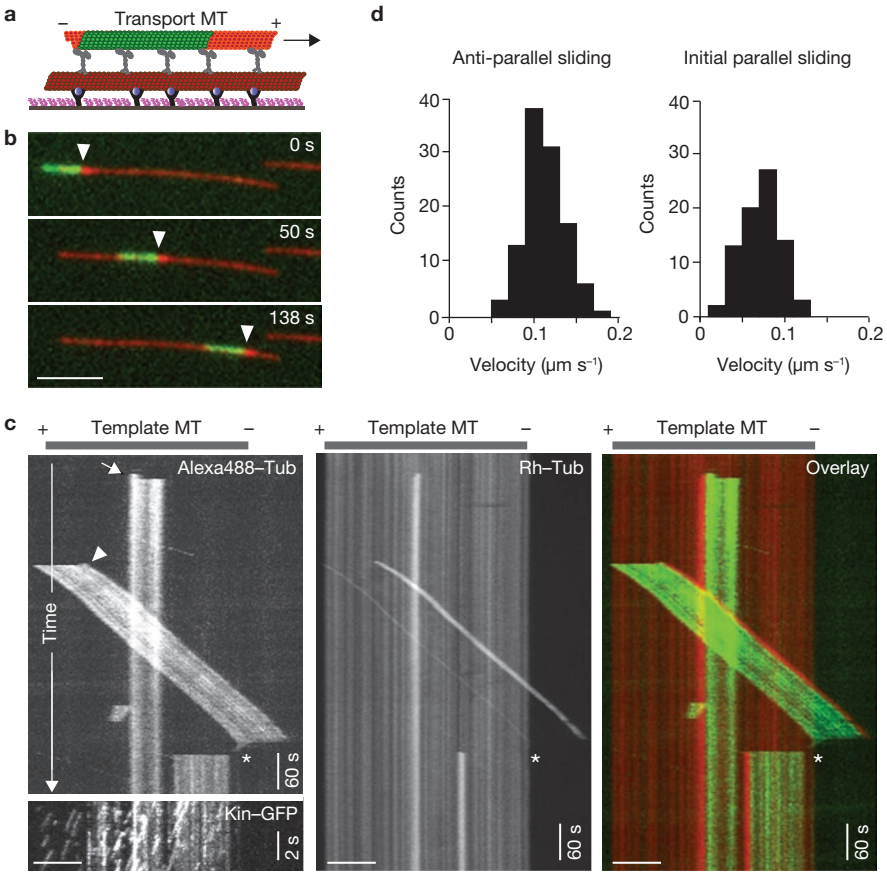

Figure 2 Ncd induces directional microtubule–microtubule sliding and static crosslinking. (**a**) Diagram of a polarity-marked 'transport' microtubule (MT) interacting with a Ncd-decorated template microtubule. After incubation of the dimly-labelled template microtubules with full-length Ncd (GFP–Ncd or unlabelled Ncd), we extensively washed the flowcell to remove free Ncd motor from solution and added non-biotinylated, either polarity-marked or non-marked (brightly-labelled with rhodamine) transport microtubules in ATP-containing motility buffer. Polarity-marked microtubules were composed of Alexa488–tubulin seeds (Alexa488–Tub; green) and rhodamine–tubulin extensions (Rh–Tub; red), with the longer extension marking the plus end of the microtubule. (**b**) Time-lapse fluorescence micrographs of a polarity-marked transport microtubule (arrowheads) robustly sliding along a rhodamine-labelled (dim red) template microtubule. (**c**) Multi-channel kymographs illustrating the dynamic interactions of polarity-marked transport microtubules with a template microtubule (schematically depicted above the kymographs). The polarity of the template microtubule was determined by GFP-labelled kinesin-1 molecules, moving towards the microtubule plus ends (lower left panel, horizontal scale bar for all kymographs, 5 μm). Robust sliding of transport microtubules occurred exclusively with their plus ends leading towards the minus ends of the template microtubules (arrowhead). After reaching the microtubule end, the transport microtubule shown swivelled for a short time, reoriented and was stuck (asterisk). Transport microtubules that were oriented in the opposite direction showed only short motility or statically crosslinked immediately after landing (arrow). (Supplementary Information, Movie 4). (**d**) Histograms of sliding velocities for anti-parallel (0.11 ± 0.02 μm s^{-1}, mean ± s.d., $n = 109$) and parallel (0.07 ± 0.02 μm s^{-1}, mean ± s.d., $n = 79$) microtubule arrangements. For the parallel microtubule arrangement, sliding velocities were averaged during the first 10 s after landing of the transport microtubule.

the plus-end-directed motion of single GFP-labelled kinesin-1 molecules (Fig. 2c; Supplementary Information, Fig. S5) after the Ncd-mediated microtubule–microtubule sliding experiments. From these experiments, we conclude that the events of robust sliding always corresponded to an anti-parallel arrangement of template and transport microtubules, whereas parallel microtubule arrangements led to only short (or no) motility. Quantitative analysis revealed a sliding velocity of 0.11 ± 0.02 μm s^{-1} (mean ± s.d., $n = 109$ microtubules) for anti-parallel microtubules (Fig. 2d). Parallel sliding, during the first 10 s after landing of the transport microtubule, revealed a sliding velocity of 0.07 ± 0.02 μm s^{-1} (mean ± s.d., $n = 79$ microtubules). However, after 100 s, 69% of the parallel transport microtubules (which did not reach a microtubule end, or interacted with other transport microtubules) had stopped. To determine whether single motor molecules continue diffusing during microtubule–microtubule sliding, we performed spiking experiments, where GFP–Ncd was mixed with unlabelled (full-length) Ncd. We never observed any obvious conversion from diffusion to directional motion or from diffusion to static binding (Supplementary Information, Fig. S6).

To understand the role of Ncd in the difference between robust sliding of anti-parallel microtubules and the slowing down of parallel microtubules, we performed dual-colour TIRF microscopy and imaged GFP–Ncd simultaneously with the fluorescent signals of the interacting microtubules (Fig. 3). As expected, the template microtubules were well-decorated with GFP–Ncd; however, we were surprised to find that the transport microtubules also carried a pronounced GFP–Ncd signal during anti-parallel sliding (Fig. 3a, b). In our experiments we aimed at removing free GFP–Ncd in the flowcell before perfusion of the transport microtubules; this raises the question of how motors accumulate on the transport microtubule. We therefore analysed the landing of transport microtubules on template microtubules and found that in 52.6% ($n = 38$

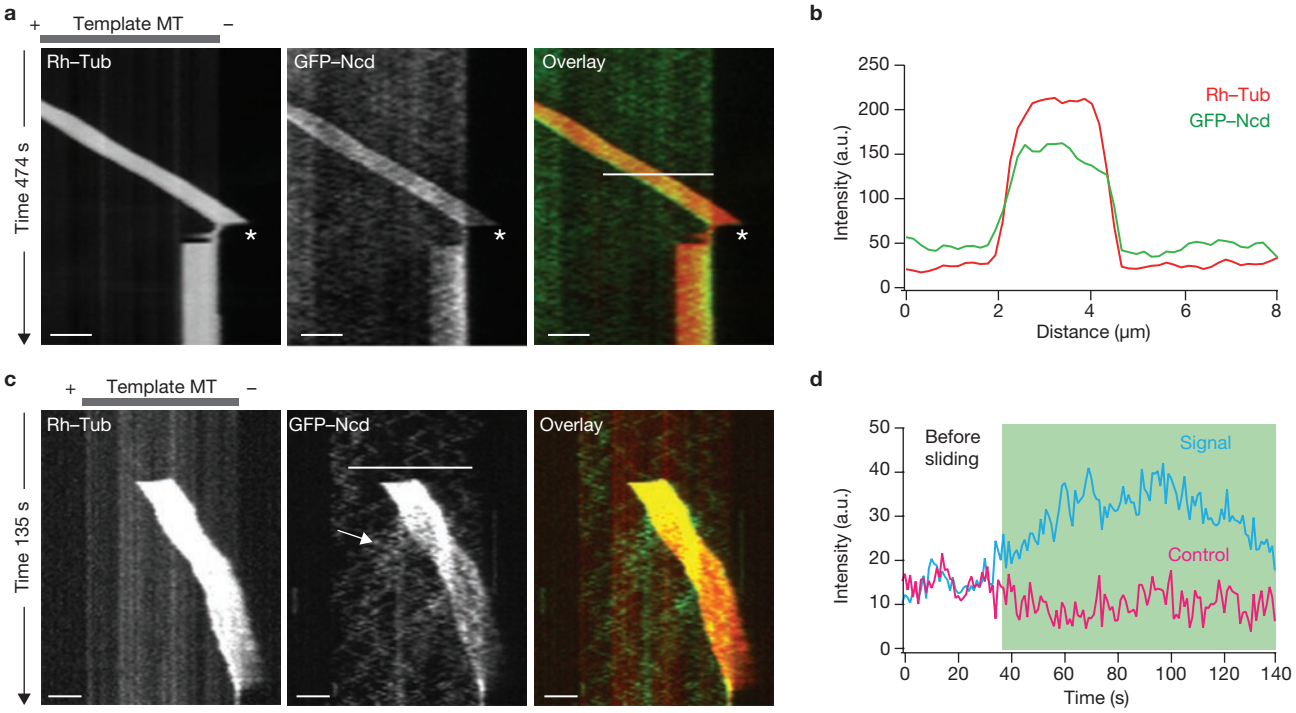

Figure 3 Transport and switching of Ncd during sliding. (**a**) Dual-colour kymographs of an anti-parallel sliding event where transport microtubules (MT) without Ncd were subjected to Ncd-decorated template microtubules. The transport microtubule reorients and statically crosslinks after nodal end swivelling (asterisk). GFP–Ncd is clearly associated with the transport microtubule during sliding and static crosslinking. Scale bars, 3 μm. (**b**) Fluorescence intensity profiles of the sliding transport microtubule (red) with the corresponding GFP–Ncd signal (green). GFP–Ncd is evenly distributed over the whole length of the microtubule. The regions from which the intensity values were taken are indicated by a white line in **a**. (**c**) Dual-colour kymographs of a sliding event where transport microtubules (decorated with GFP–Ncd) were subjected to template microtubules that had not been decorated with GFP–Ncd before. In this way, we reduced the otherwise high GFP–Ncd background along the template microtubules. During sliding, GFP–Ncd switches from the transport microtubule to the template microtubule (arrow). The faint GFP signal already present on the template microtubule before the sliding event is attributed to the earlier landing of residual GFP–Ncd out of solution. In some cases, anti-parallel sliding did not occur as a continuous smooth movement and periods of slightly changing velocities were observed. The origin of these effects remain speculative: in principle a transient slow-down in the movement could arise from the involvement of an increased number of dead (or less active) motors, or from motor hindering (crowding) effects under conditions of high Ncd concentrations. Scale bars, 3 μm. (Supplementary Information, Movie 5). (**d**) Averaged GFP–Ncd fluorescence intensities as a function of time along a template microtubule where a GFP–Ncd-decorated transport microtubule had landed (blue, averaged signal along the white line in **c** and along the two nearest control microtubules without landing events (red). The strong GFP–Ncd signal associated with the transport microtubule during sliding was not considered in the averaging process. The signal increase during microtubule–microtubule sliding (blue curve in the shaded time interval) indicates the transfer of GFP–Ncd from the transport microtubule to the template microtubule.

anti-parallel transport microtubules) of the events, the transport microtubules carried no motors. However, the motor signal along the transport microtubule then rapidly increased, suggesting that Ncd is picked up from the template microtubule during sliding. We confirmed the pickup of motors by the transport microtubule from the template microtubule by single molecule experiments (Supplementary Information, Fig. S7). In 47.4% of the landing events, transport microtubules were already weakly decorated with motors. This decoration presumably originated from residual motors in solution or from the pickup of motors from other template microtubules during previous sliding events.

To further investigate the transfer of motors between sliding microtubules, we mixed transport microtubules with GFP–Ncd in ATP-containing motility solution and added them to non-decorated template microtubules. Analysis of the GFP–Ncd signal after the landing of individual transport microtubules revealed that GFP–Ncd was left behind on the template microtubule during anti-parallel sliding (Fig. 3c, d). The fact that the transferred GFP–Ncd did not remain localized in the areas passed by the transport microtubule can be explained by the diffusive interaction of GFP–Ncd with the template microtubule. We confirmed the described transfer behaviour by single-molecule experiments. We found, moreover, that transfer did not depend on the relative orientation of the microtubules to each other. However, transfer ceased when Ncd interacted more permanently with the microtubules through their motor domains in the presence of AMP–PNP (Supplementary Information, Fig. S7).

Although we did not observe any motor accumulations at either end of the transport microtubule during anti-parallel sliding, GFP–Ncd accumulated at the minus ends of parallel microtubules after reorientation and static parallel crosslinking (Fig. 3a), as well as during the slow-down after landing (Fig. 4a). In the latter, end-accumulation was not observed immediately but rather, developed over time (Fig. 4b). Overall, such accumulations were detected in 28 of 29 parallel, statically crosslinked microtubule bundles. Moreover, the end accumulation shifted to the new minus end of the microtubule-bundle when a second microtubule overlapped with an existing microtubule bundle in a parallel manner (Fig. 4c). Because this end accumulation was never observed on single or anti-parallel microtubules, we conclude that Ncd accumulations are specific for parallel microtubule bundles.

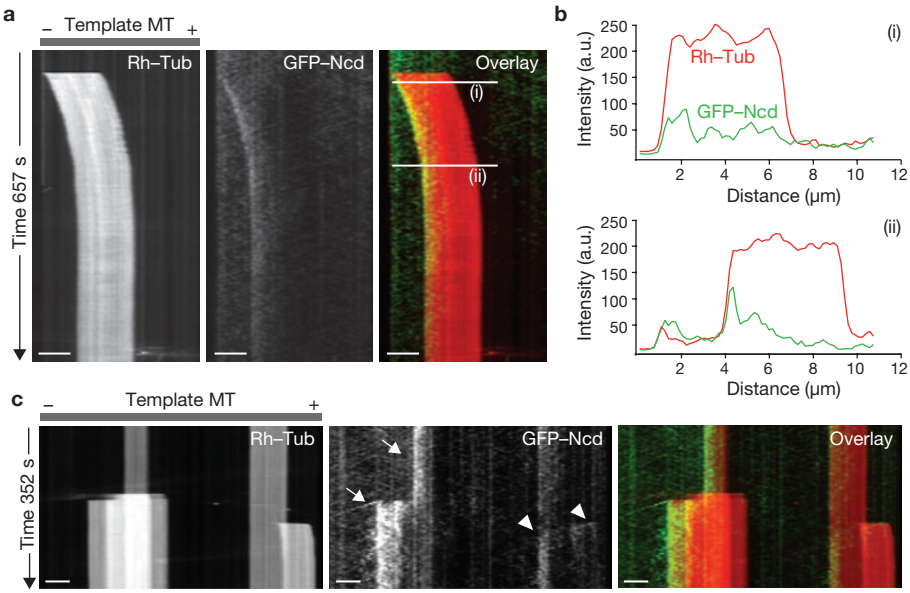

Figure 4 Accumulation of Ncd at the minus ends of parallel microtubule-bundles. (**a**) Dual-colour kymographs of a parallel sliding event where transport microtubules (MT) without Ncd were subjected to GFP–Ncd-decorated template microtubules. Shortly after landing, the GFP–Ncd signal was evenly distributed over the length of the transport microtubule (i), and during and after slow-down a pronounced minus end accumulation was observed (ii). Scale bars, 3 μm. (Supplementary Information, Movie 6). (**b**) Fluorescence intensity profiles (along the white lines in **a**) of the transport microtubule (red) and the corresponding GFP–Ncd signal (green). (**c**) Dual-colour kymographs of microtubule landing events on statically crosslinked, parallel microtubules. Additional GFP–Ncd was shuttled to the minus end of a parallel microtubule-bundle upon the binding of another (spatially overlapping) parallel microtubule (arrowheads). An already existing GFP–Ncd minus end accumulation shifts to the new, peripheral minus-end of the total bundle (arrows). The faint line of GFP–Ncd signal appearing as processive movement towards the minus end of the template microtubule was presumably related to the formation of occasional GFP–Ncd clusters emerging from the motor accumulations at minus ends of the parallel microtubule-bundles.

In our experiments, we directly showed that Ncd alone facilitates robust anti-parallel microtubule–microtubule sliding, whereas it statically crosslinks parallel microtubules. In the case of anti-parallel microtubules, the motors linked through their tail domains to the transport microtubule ('transport motors') push the transport microtubule in the same direction as the motors bound to the template microtubule ('template motors'). Conversely, static crosslinking of parallel microtubules is caused by a tug-of-war where motors work against each other (Fig. 5). Thus, our results suggest that Ncd can mediate spindle collapse in the absence of kinesin-5 by a microtubule–microtubule sliding mechanism. In addition, the motor characteristics described explain how kinesin-14 and kinesin-5 modulate spindle length at a metaphase–anaphase transition[21] and that motor activity is needed to organize microtubules into a parallel array near the spindle poles[28].

The directional sliding mechanism described here is accomplished by the cumulative recruitment of motors from one microtubule to the other. We showed that switching of motors between microtubules is facilitated by their rather loose, diffusive tail–microtubule interactions. *In vivo*, the dynamic switching of motors between microtubules might help to equilibrate the motor number on interacting kinetochore and spindle microtubules with initially asymmetric motor distributions. Such a mechanism would ensure that only parallel microtubules are statically crosslinked. In line with our work Braun and colleagues demonstrated *in vitro* that the kinesin-14 klp2 has the capability to organize microtubules into a parallel array (published in this issue; *Nature Cell Biol.* **11,** 724–730; 2009).

Our observation that Ncd molecules diffused in the microtubule overlap region during sliding shows that a diffusing motor can exert sliding forces. This is probably because the duration of the powerstroke is much shorter than tail-mediated diffusion. Moreover, diffusion of individual motors might be cancelled if multiple motors are simultaneously involved in transport. Using the same argument of collective but uncoordinated diffusion, static crosslinking between parallel microtubules can be explained. However, because it is difficult to determine which of the imaged motors are in fact actively involved in the microtubule–microtubule sliding process, we cannot rule out the possibility that the state of interaction differs for Ncd molecules involved in sliding from those that are not. It could be possible that Ncd is activated by microtubule crosslinking, similarly to kinesin-5 (ref. 29), leading to a different interaction mode during sliding.

Although the effect of Ncd in driving microtubule sliding seems similar to that seen with kinesin-5, the sliding mechanism is different. Kinesin-5 motors move processively on both microtubules at the same time and crosslink microtubules preferentially in an anti-parallel manner[22,30]. Accordingly, in *Drosophila* embryos and *Xenopus leavis* egg extract spindles, kinesin-5 molecules were observed to bind in a stationary manner between interpolar spindle microtubules during spindle elongation[31,32]. By contrast, Ncd diffuses along microtubules with its tail domain, but generates directed force with its head domain. Stationary localization of Ncd molecules in the spindle midzone is therefore not expected. Rather, Ncd is thought to be co-translocated with the sliding microtubules.

Consistent with previous studies[25,26], our single-molecule experiments did not indicate processivity of Ncd. However, Ncd accumulated at the minus ends between statically crosslinked parallel microtubules, consistent with the localization and function of Ncd at spindle poles and

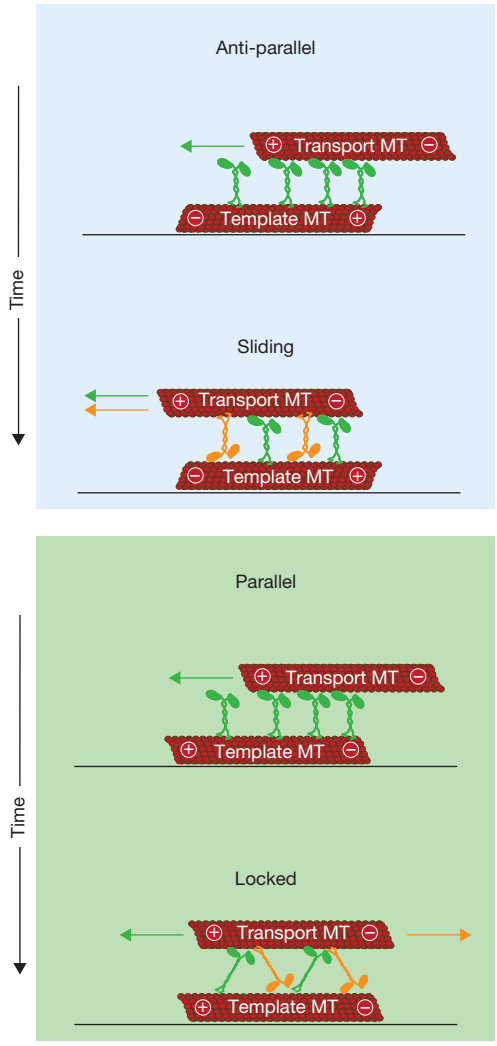

Figure 5 Model for directional sliding and static crosslinking of microtubules by Ncd. For both, parallel and anti-parallel microtubules (MT), motors linked to the template microtubule (green motors) through their tail domains will be able to propel transport microtubules with their plus ends leading. Due to the loose binding of the motors, part of the Ncd molecules will switch with their tail to the transport microtubules (orange motors). Coloured arrows represent the forces on the transport microtubules generated by the respective motors. For anti-parallel sliding, motors pull (orange motors) and push (green motors) the transport microtubule in the same direction. Thus their action is assisting and facilitates sliding. For parallel sliding, motors pull (orange motors) and push (green motors) the transport microtubule in opposite directions. Thus the motors engage in a tug-of-war. Over time, switching of motors from template to transport microtubules leads to an increasing number of counteracting motors and causes slow-down of initially sliding parallel microtubules. Events of immediate static crosslinking after landing were presumably related to transport microtubules that had already picked up a sufficiently high number of Ncd molecules from solution or during previous sliding events.

centrosomes[18]. But how does Ncd reach the microtubule minus end and stay there? Obviously, the existence of a parallel microtubule bundle is a prerequisite for end-accumulation. Recently it has been suggested (using truncated constructs) that Ncd could become weakly processive when simultaneously interacting with multiple microtubules[27]; however, we did not observe such behaviour. Rather, we favour the idea that full-length Ncd could undergo a kind of biased diffusion between parallel microtubules. Moreover, internal strain built up in the Ncd molecules during the tug-of-war could influence crucial motor parameters, such as binding and unbinding rates of the motor head or tail domains.

In recent *in vivo* FRAP experiments, recovery of Ncd on kinetochore microtubules along with a prominent microtubule plus-end localization was reported[18]. We hypothesize that the dynamic interactions observed in our experiments might provide an explanation for the fast recovery. Moreover, Ncd might use one-dimensional diffusion to reach the microtubule plus end, which is similar to the end-targeting mechanism of kinesin-13 (ref. 33). In summary, we believe that the tail-dependent diffusion of motors, which are also able to exert directed force through their head domains, could be a general mechanism by which motors organize cellular structures. □

Note added in proof: a related manuscript by Braun et al. *(*Nature Cell Biol. ***11,*** *724–730; 2009) is also published in this issue.*

METHODS

Methods and any associated references are available in the online version of the paper at http://www.nature.com/naturecellbiology/

Note: Supplementary Information is available on the Nature Cell Biology website.

ACKNOWLEDGEMENTS

We acknowledge the members of the Kasprzak and the Diez labs for comments on the manuscript as well as C. Bräuer and D. Naumburger for technical support. We thank C. Leduc, B. Nitzsche, C. Gell and J. Howard for fruitful discussion, F. Ruhnow for help with the microtubule tracking, as well as S. Bajer and E. Kocik for help with FPLC experiments. This work was supported by the German Federal Ministry of Education and Research (Grant 03 N 8712), the Polish Network for Mechanisms of Cell Motility, the Grant 2 P04C 131 29 and the Max-Planck-Society. G. Fink was supported by a fellowship from the Boehringer Ingelheim Foundation

AUTHOR CONTRIBUTIONS

G.F., L.H., C.R., A.A.K. and S.D. designed the experiments; L.H. and C.R. performed initial experiments; G.F. performed the presented experiments and analysed the data; L.H. and K.J.S. generated the Ncd proteins; G.F and S.D. wrote the manuscript; A.A.K. and S.D. initiated the research and supervised the work. All authors discussed the results and commented on the manuscript.

COMPETING FINANCIAL INTERESTS

The authors declare no competing financial interests.

Published online at http://www.nature.com/naturecellbiology/
Reprints and permissions information is available online at http://npg.nature.com/reprintsandpermissions/

1. Gadde, S. & Heald, R. Mechanisms and molecules of the mitotic spindle. *Curr. Biol.* **14,** 797–805 (2004).
2. Sharp, D. J., Yu, K. R., Sisson, J. C., Sullivan, W. & Scholey, J. M. Antagonistic microtubule-sliding motors position mitotic centrosomes in *Drosophila* early embryos. *Nature Cell Biol.* **1,** 51–54 (1999).
3. Hoyt, M. A., He, L., Loo, K. K. & Saunders, W. S. Two *Saccharomyces cerevisiae* kinesin-related gene products required for mitotic spindle assembly. *J. Cell Biol.* **118,** 109–120 (1992).
4. Walczak, C. E., Verma, S. & Mitchison, T. J. XCTK2: a kinesin-related protein that promotes mitotic spindle assembly in *Xenopus laevis* egg extracts. *J. Cell Biol.* **136,** 859–870 (1997).
5. Sharp, D. J. *et al.* Functional coordination of three mitotic motors in *Drosophila* embryos. *Mol. Biol. Cell* **11,** 241–253 (2000).
6. Hildebrandt, E. R. & Hoyt, M. A. Mitotic motors in *Saccharomyces cerevisiae*. *Biochim. Biophys. Acta* **1496,** 99–116 (2000).
7. Sharp, D. J., Rogers, G. C. & Scholey, J. M. Microtubule motors in mitosis. *Nature* **407,** 41–47 (2000).
8. Chandra, R., Salmon, E. D., Erickson, H. P., Lockhart, A. & Endow, S. A. Structural and functional domains of the *Drosophila* ncd microtubule motor protein. *J. Biol. Chem.* **268,** 9005–9013 (1993).
9. McDonald, H. B. & Goldstein, L. S. Identification and characterization of a gene encoding a kinesin-like protein in *Drosophila*. *Cell* **61,** 991–1000 (1990).
10. McDonald, H. B., Stewart, R. J. & Goldstein, L. S. The kinesin-like ncd protein of *Drosophila* is a minus end-directed microtubule motor. *Cell* **63,** 1159–1165 (1990).

11. Karabay, A. & Walker, R. A. Identification of microtubule binding sites in the Ncd tail domain. *Biochemistry* **38,** 1838–1849 (1999).
12. Matthies, H. J., McDonald, H. B., Goldstein, L. S. & Theurkauf, W. E. Anastral meiotic spindle morphogenesis: role of the non-claret disjunctional kinesin-like protein. *J. Cell Biol.* **134,** 455–464 (1996).
13. Kimble, M. & Church, K. Meiosis and early cleavage in *Drosophila melanogaster* eggs: effects of the claret-non-disjunctional mutation. *J. Cell Sci.* **62,** 301–318 (1983).
14. Segbert, C. *et al.* KLP-18, a Klp2 kinesin, is required for assembly of acentrosomal meiotic spindles in *Caenorhabditis elegans*. *Mol. Biol. Cell* **14,** 4458–4469 (2003).
15. Hatsumi, M. & Endow, S. A. Mutants of the microtubule motor protein, nonclaret disjunctional, affect spindle structure and chromosome movement in meiosis and mitosis. *J. Cell Sci.* **101,** 547–559 (1992).
16. Saunders, W. S. & Hoyt, M. A. Kinesin-related proteins required for structural integrity of the mitotic spindle. *Cell* **70,** 451–458 (1992).
17. Mountain, V. *et al.* The kinesin-related protein, HSET, opposes the activity of Eg5 and cross-links microtubules in the mammalian mitotic spindle. *J. Cell Biol.* **147,** 351–366 (1999).
18. Goshima, G., Nedelec, F. & Vale, R. D. Mechanisms for focusing mitotic spindle poles by minus end-directed motor proteins.[see comment]. *J. Cell Biol.* **171,** 229–240 (2005).
19. Endow, S. A., Chandra, R., Komma, D. J., Yamamoto, A. H. & Salmon, E. D. Mutants of the *Drosophila* ncd microtubule motor protein cause centrosomal and spindle pole defects in mitosis. *J. Cell Sci.* **107,** 859–867 (1994).
20. Troxell, C. L. *et al.* pkl1^{+}and klp2^{+}: Two kinesins of the Kar3 subfamily in fission yeast perform different functions in both mitosis and meiosis. *Mol. Biol. Cell* **12,** 3476–3488 (2001).
21. Brust-Mascher, I. & Scholey, J. M. Microtubule flux and sliding in mitotic spindles of *Drosophila* embryos. *Mol. Biol. Cell* **13,** 3967–3975 (2002).
22. Kapitein, L. C. *et al.* The bipolar mitotic kinesin Eg5 moves on both microtubules that it crosslinks. *Nature* **435,** 114–118 (2005).
23. Hoyt, M. A., He, L., Totis, L. & Saunders, W. S. Loss of function of *Saccharomyces cerevisiae* kinesin-related CIN8 and KIP1 is suppressed by KAR3 motor domain mutations. *Genetics* **135,** 35–44 (1993).
24. Oladipo, A., Cowan, A. & Rodionov, V. Microtubule motor Ncd induces sliding of microtubules *in vivo*. *Mol. Biol. Cell* **18,** 3601–3606 (2007).
25. Foster, K. A. & Gilbert, S. P. Kinetic studies of dimeric Ncd: evidence that Ncd is not processive. *Biochemistry* **39,** 1784–1791 (2000).
26. Case, R. B., Pierce, D. W., Hom-Booher, N., Hart, C. L. & Vale, R. D. The directional preference of kinesin motors is specified by an element outside of the motor catalytic domain. *Cell* **90,** 959–966 (1997).
27. Furuta, K. & Toyoshima, Y. Y. Minus-end-directed motor Ncd exhibits processive movement that is enhanced by microtubule bundling *in vitro*. *Curr. Biol.* **18,** 152–157 (2008).
28. Walczak, C. E., Vernos, I., Mitchison, T. J., Karsenti, E. & Heald, R. A model for the proposed roles of different microtubule-based motor proteins in establishing spindle bipolarity. *Curr. Biol.* **8,** 903–913 (1998).
29. Kapitein, L. C. *et al.* Microtubule cross-linking triggers the directional motility of kinesin-5. *J. Cell Biol.***182,** 421–428 (2008).
30. van den Wildenberg, S. M. *et al.* The homotetrameric kinesin-5 KLP61F preferentially crosslinks microtubules into antiparallel orientations. *Curr. Biol.* **18,** 1860–1864 (2008).
31. Cheerambathur, D. K., Brust-Mascher, I., Civelekoglu-Scholey, G. & Scholey, J. M. Dynamic partitioning of mitotic kinesin-5 cross-linkers between microtubule-bound and freely diffusing states. *J. Cell Biol.* **182,** 429–436 (2008).
32. Uteng, M., Hentrich, C., Miura, K., Bieling, P. & Surrey, T. Poleward transport of Eg5 by dynein-dynactin in *Xenopus laevis* egg extract spindles. *J. Cell Biol.* **182,** 715–726 (2008).
33. Helenius, J., Brouhard, G., Kalaidzidis, Y., Diez, S. & Howard, J. The depolymerizing kinesin MCAK uses lattice diffusion to rapidly target microtubule ends. *Nature* **441,** 115–119 (2006).

METHODS

Microtubules. Microtubules were grown for 30 min at 37 °C from a 6.25 µl BRB80 solution (80 mM Pipes/KOH pH6.9, 1 mM $MgCl_2$, 1 mM EGTA) supplemented by 40 µM bovine tubulin (transport-microtubules: 25% rhodamine-labelled, 75% unlabelled; template-microtubules: 6.4% unlabelled biotinylated, 4.2% rhodamine-labelled and 89.4% unlabelled, Cytoskeleton), 1 mM Mg–GTP (Roche), 4 mM $MgCl_2$ and 5% DMSO. The mix was then resolved in 200 µl BRB80T (BRB80 containing 10 µM Taxol (Sigma)). Assembled microtubules were centrifuged in a Beckman airfuge at 100,000*g* for 5 min. The pellet was resuspended in 200 µl BRB80T. Polarity-marked microtubules were grown as described previously[33] using Alexa488-labelled tubulin for the seeds and bright rhodamine-labelled tubulin for elongation.

***In vitro* single molecule and sliding motility assays.** Microscope chambers were constructed of silanized coverslips using parafilm as spacer, such that channels of 0.1-mm thickness, 3-mm width and 18-mm length were formed. Silanization was performed as described previously[34]. To immobilize microtubules on the glass surface, channels were washed with a series of buffers. First a biotin antibody (Sigma) 1% in PBS was incubated for 5–10 min followed by 15 min incubation of 1% Pluronic F127 (Sigma) in PBS. Finally, biotinylated microtubules in BRB80T were allowed to bind to the surface for 15 min. Channels were rinsed once with BRB80T before the motility solutions were added. Motility solutions consisted of 20 mM Hepes/KOH pH 7.2, 1 mM $MgCl_2$, 0.1 mM EDTA, 0.1 mM EGTA and 5% sucrose freshly supplemented by 75 mM KCl, 0.1% Tween20, 1 mM ATP, 0.5 mg ml^{-1} casein and anti-fade (40 mM glucose, 40 µg ml^{-1} glucose oxidase, 16 µg ml^{-1} catalase, 1 mM DTT). Motors at concentrations below 0.5 nM for single-molecule motor experiments or above 5 nM for microtubule–microtubule sliding experiments (all in motility solution) were injected to the channel and allowed to bind to the template microtubules. To verify that Ncd molecules were present as dimeric motor constructs under our buffer conditions, we performed fluorescence bleaching and gel filtration experiments (Supplementary Information, Fig. S1). For the sliding experiments, channels were washed with 60 µl motility solution after two minutes to remove unbound motors. Finally non-biotinylated transport microtubules in motility solution were added. The polarity of the template microtubules was determined using truncated GFP-labelled rat kinesin-1 (kinesin–GFP) that was purified according to published protocols[35]. Kinesin–GFP in BRB80 supplemented by anti-fade and ATP (1 mM) was added after recording sliding microtubule motility in the same field of view.

Imaging. Microtubules and GFP–Ncd molecules were visualized using an inverted fluorescence microscope (Zeiss Axiovert 200M, Carl Zeiss) with a Zeiss ×100 oil immersion 1.46 NA TIRF objective in combination with an Andor Ixon DV 897 (Andor Technology) EMCCD camera controlled by Metamorph (Molecular Devices Corporation). A Lumen 200 metal arc lamp (Prior Scientific Instruments) for excitation in epi-fluorescence mode and an argon-krypton mixed gas laser at 488 nm (Innova 70 Spectrum, Coherent) for TIRF-illumination were used. For dual-colour experiments, images were acquired either sequentially by switching between GFP and TRITC filters (Chroma Technology) or by dual-colour separation using a spectral beam splitter (W-view A8509, Hamamatsu) equipped with GFP and RFP filters (Chroma Technology). In the latter, the signals of the two colour channels were simultaneously recorded on two different halves of the same CCD camera chip. To align the dual-colour images with respect to each other, multi-fluorescent tetraspeck beads (0.2 µm diameter, Mo Bi Tec), diluted 200-fold in PBS, were imaged before the Ncd experiments. Image acquisition rates ranged from up to 10 frames per second in continuous acquisition mode (in the single molecule experiments) to 0.3 frames per second for sequential dual-colour imaging (in the sliding experiments). For image analysis, kymographs were generated and used for velocity analysis using Metamorph. Trajectories of parallel sliding transport-microtubules were obtained by a custom-made software based on MatLab (Mathworks).

Protein expression and purification. The following recombinant expression constructs were used: 1) pHis–NcF expressing unlabelled, N-terminal His-tagged full-length Ncd from pBS-ncd[9,10] and pET28a (Novagen) 2) pHis–GFP–NcF expressing GFP–Ncd, fusion of His-tag from pET30a (Novagen) up to *Nco*I site, EGFP from pEGFP–C1 (Clontech) and full-length Ncd from pBS-ncd; 2) pHis–GFP–Ncd^{195} expressing GFP–Ncd^{195}, GFP–Ncd with deletion of Ncd amino acids 1–195; 3) pNcS–GFP–His expressing Ncd^{349}–GFP, fusion of Ncd fragment 1–349 with EGFP from pEGFP–C1 (Clonetech) and His_6-tag. pHis–GFP–NcF and pNcS–GFP–His were constructed in pET28a and pET30a vectors, respectively (Novagen). A detailed description of DNA manipulations used in the recombinant plasmids construction is provided in the Supplementary Information. The expression of Ncd proteins was carried out in *Escherichia coli* BL21 (DE3) strain (Novagen). The bacteria were induced with 0.5 mM isopropyl β-D-thiogalactopyranoside for 4 h at 25 °C, collected by centrifugation and resuspended in buffer A (20 mM Hepes/Na, pH 7.2, 1 mM $MgCl_2$, 20 mM 2-mercaptoethanol, 5 µM ADP, 0.1% Tween 20) + 300 mM NaCl and 20 mM imidazole. The culture was centrifuged again and frozen at –80°C. Frozen bacterial cells were thawed, resuspended in buffer A with 300 mM NaCl and 20 mM imidazole and disrupted using French Press (Thermo Spectronic) at 1380 bar in the presence of protease inhibitors. Clarified lysate was loaded on a Talon cobalt-affinity resin (Clontech) equilibrated with lysis buffer. After washing the column, the concentration of NaCl was linearly reduced to 100 mM using buffer A containing100 mM NaCl and 20 mM imidazole. Protein was eluted in buffer A containing 100 mM NaCl and 300 mM imidazole. Next, the peak fractions were purified on an FPLC Superdex 200 10/300 GL column equilibrated with the cobalt elution buffer. The eluted protein was supplemented with 10% w/v of sucrose, frozen in liquid nitrogen and stored at –80°C.

34. Hyman, A. A. Preparation of marked microtubules for the assay of the polarity of microtubule-based motors by fluorescence. *J. Cell Sci. Suppl.* **14,** 125–127 (1991).
35. Rogers, K. R. *et al.* KIF1D is a fast non-processive kinesin that demonstrates novel K-loop-dependent mechanochemistry. *EMBO J.* **20,** 5101–5113 (2001).

nature cell biology

DOI: 10.1038/ncb1877

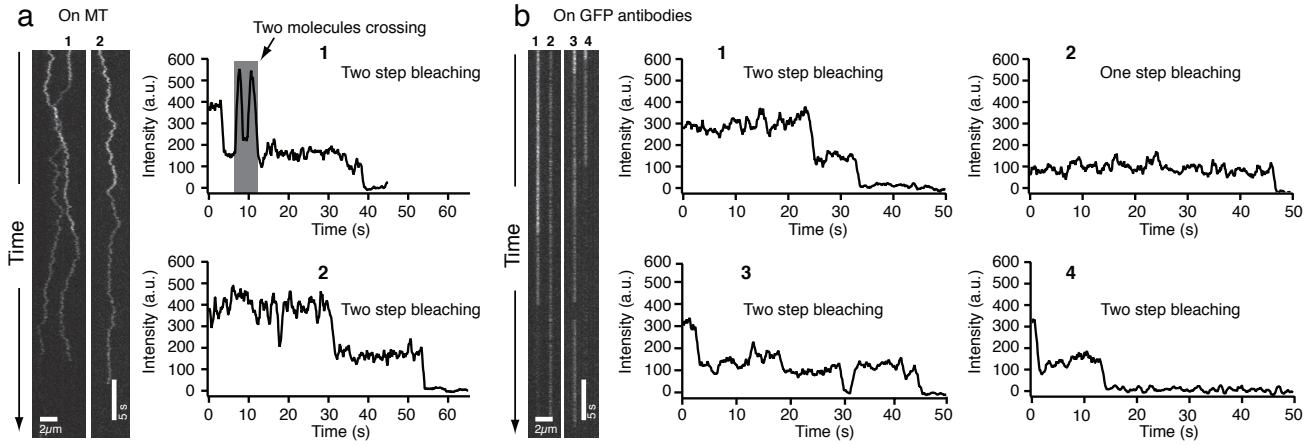

Figure S1 Oligomeric state of Ncd motors as determined from single molecule fluorescence bleaching experiments. **a** Typical kymographs and tracked intensities of GFPNcd diffusing on template MTs in motility buffer (1 mM ATP). Bleaching in two distinct steps - indicative of GFPNcd dimers - was clearly observed in most of the cases. While the noise on the curves was mainly due to GFP-blinking, additional intensity fluctuations arose from the crossings (i.e. transient spatial overlaps) of Ncd molecules (see for example the left kymograph and trace 1, which correspond to the data of Fig. 1d in the main text). **b** Kymographs and tracked intensities of GFPNcd fixed to the surface via GFP antibodies in motility buffer (1 mM ATP). From a total of 789 randomly picked molecules, 43% exhibited two-step bleaching indicative of GFPNcd dimers. In 38% of the events, the molecules bleached in one step probably due to the previous inactivation or non-functionality of one of the GFPs. Moreover, part of these events might have originated from the rapid (and with our time resolution non-resolvable) bleaching of two GFPs after each other. In 5% of the events, bleaching appeared to occur in more than two steps. This behaviour is not speaking against the hypothesis of GFPNcd being dimeric molecules, because the spatially coinciding binding of more than one GFPNcd molecule to the same surface spot (via the same or close-by antibodies) can not be ruled out. In 14% of the events, no clear bleaching steps were detectable. In summary, the presented GFPNcd bleaching experiments verify that Ncd molecules were present as dimeric motor constructs under our buffer conditions.

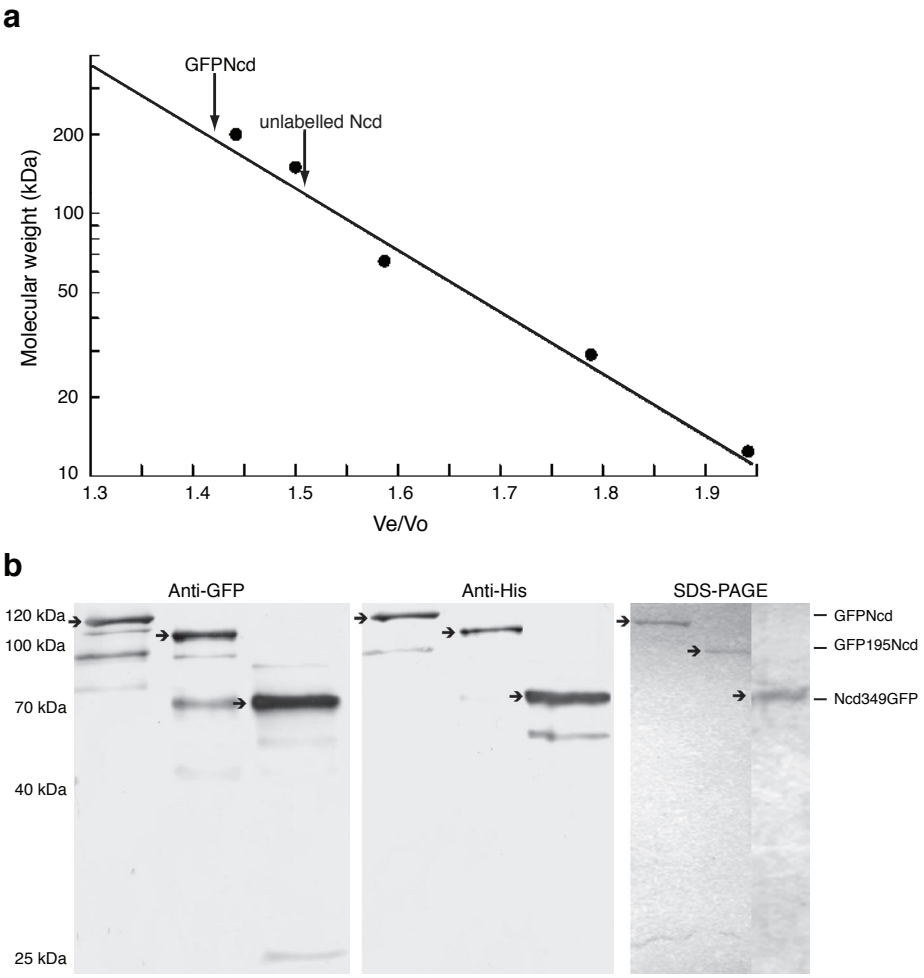

Figure S2 Gel filtration and SDS PAGE of Ncd proteins. **a** Size exclusion chromatography: The calibration graph (points and linear fit) shows the ratio of elution volume to void volume for the used standard proteins (Supplementary Information Methods section) plotted against their logarithmic molecular weight. The arrows show the obtained ratios for GFPNcd and unlabelled full length Ncd. Each investigated protein did elute within a single peak indicating that the used protein was not composed of several populations of monomers, dimers and multimers. Relating the elution volume to the void volume yielded an approximate molecular weight of 195 kDa for the full length GFPNcd (expected molecular weight of 224 kDa for dimers and 112 kDa for monomers). Unlabelled full length Ncd yielded a molecular weight of about 120 kDa (expected molecular weight of 158 kDa for dimers and 79 kDa for monomers). All obtained molecular weights were about 30 kDa lower than the expected molecular weights. This, most likely, resulted from the fact that Ncd exhibits a more elongated structure rather than being completely globular. Nevertheless, the obtained data does indicate that the used proteins had neither formed multimers nor existed as monomers. **b** Western blots using anti-GFP polyclonal antibody (*left*), monoclonal anti-His antibody (*middle*) and Coomassie stained gel (*right*). Numbers on the left correspond to the molecular weights of some of the standards used. Arrows indicate purified proteins corresponding to GFPNcd, GFP195Ncd and Ncd349GFP (from left to right).

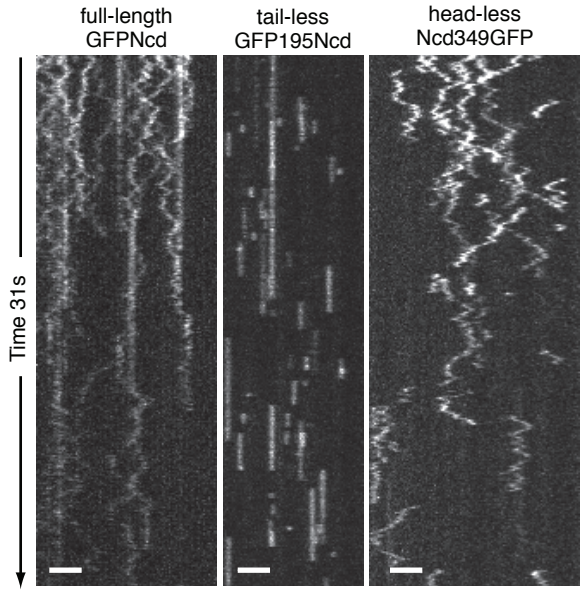

Figure S3 Ncd interaction with MTs in AMPPNP. Typical kymographs of different, single molecule GFP-labelled Ncd constructs imaged by TIRF microscopy in the presence of 1 mM AMPPNP show that: (i) GFPNcd diffuses but also exhibits long periods of static binding, (ii) GFP195Ncd exclusively shows static binding, and (iii) Ncd349GFP diffuses in a very similar manner to the ATP condition. Occasional events of short-termed stationary binding were most likely related to degraded motors with impaired ATP hydrolysis. Scale bars: 3 μm.

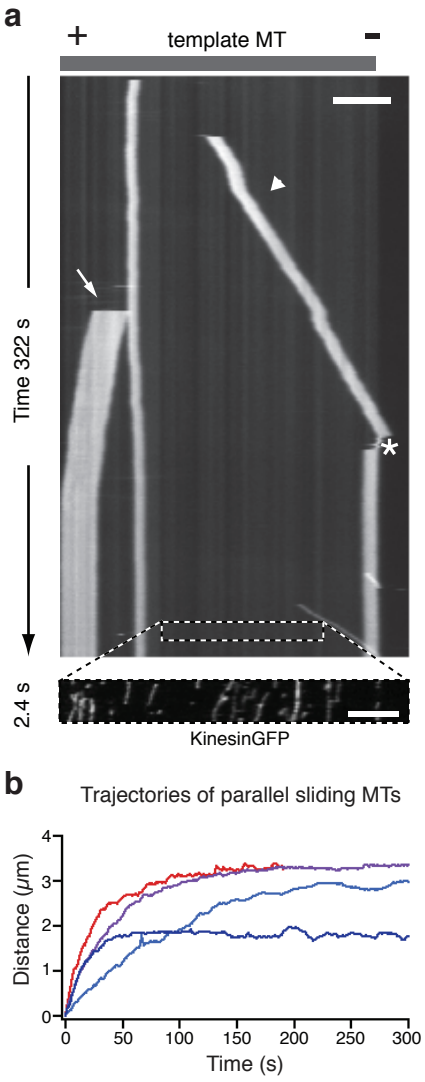

Figure S4 Slow-down of transport MTs during parallel sliding events. **a** Typical kymograph illustrating the dynamic interactions of several transport MTs with a template MT (schematically depicted above the kymograph, scale bar: 5 μm). Robust sliding of transport MTs exclusively occurred towards the minus end of the template MT (arrowhead). After reaching the MT end, the transport MT swivelled for a short time, reoriented and got stuck (asterisk). Transport MTs that moved in opposite direction, towards the plus-ends of the template MT, showed only short motility before they statically crosslinked (arrow). The thin trajectories on the lower right correspond to additional, robustly sliding transport MTs of short lengths (Supplementary Information Movie M7). The polarity of the template MT was determined by the kymograph of GFP-labelled kinesin-1 molecules, moving towards the MT plus ends (dotted box in the lower panel, scale bar: 2 μm). **b** Quantitative analysis of MT translocation during four parallel sliding events showed a gradual decrease of the sliding velocity over time (*Time* = 0 indicates the landing of the transport MTs). After about 100s of interaction most of the transport MTs had stopped to move

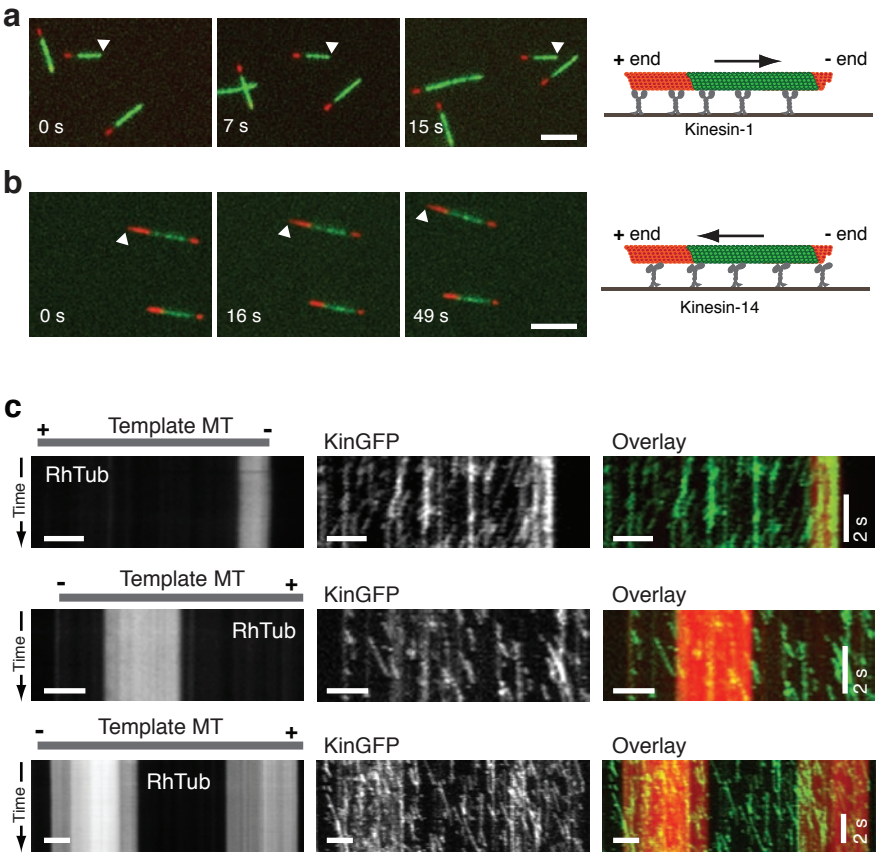

Figure S5 Polarities of transport- and template MTs. **a** We verified the goodness of the polarity-marked MTs by gliding assays on kinesin-1 surfaces. Polarity-marked MTs were gliding with the short red extensions (i.e. their minus ends) leading (arrowheads). Note, that - because the fluorescence images in the red and the green channel were acquired with a short temporal delay - the green seed overlaps with the short red extension on the leading MT minus end. From a total of 221 observed MTs, 194 MTs (88%) clearly showed a short red extension on one side of the green seed and a longer red extension on the other side. All of these MTs were gliding with the short extension (i.e. their minus ends) leading. Scale bar: 5 µm. **b** Gliding motility experiments on Ncd-coated (kinesin-14) surfaces: MTs were gliding with their plus ends leading (arrowheads). 92% of 130 observed MTs clearly showed a short red extension on one side of the green seed and a longer red extension on the other side. 94% of these MTs were gliding with the long extensions (i.e. their plus ends) leading. The small number of MTs (6%) apparently moving into the other direction was most likely caused by MT breakage, after which the originally long red extension finally became the shorter one. Similarly, when performing Ncd MT-MT sliding experiments with polarity-marked transport MTs on Ncd-decorated template MTs (see Fig. 2a-c and Movie M4), 81% of 26 observed transport MTs clearly showed a short red extension on one side of the green seed and a longer red extension on the other side. 95% of these MTs were sliding with the long extensions (i.e. their plus ends) leading. It was therefore not necessary to perform all experiments with polarity-marked MTs, as the leading ends of the transport MTs sliding on Ncd-decorated template MTs (similar to gliding on an Ncd-coated surface) reliably marked the MT plus ends. Scale bar: 5 µm. **c** Kinesin-1 directions (KinGFP) together with the final parts of the MT kymographs from the main text: top panel corresponds to Fig. 3a, middle panel corresponds to Fig. 4a, bottom panel corresponds to Fig. 4b. Horizontal scale bars: 3 µm.

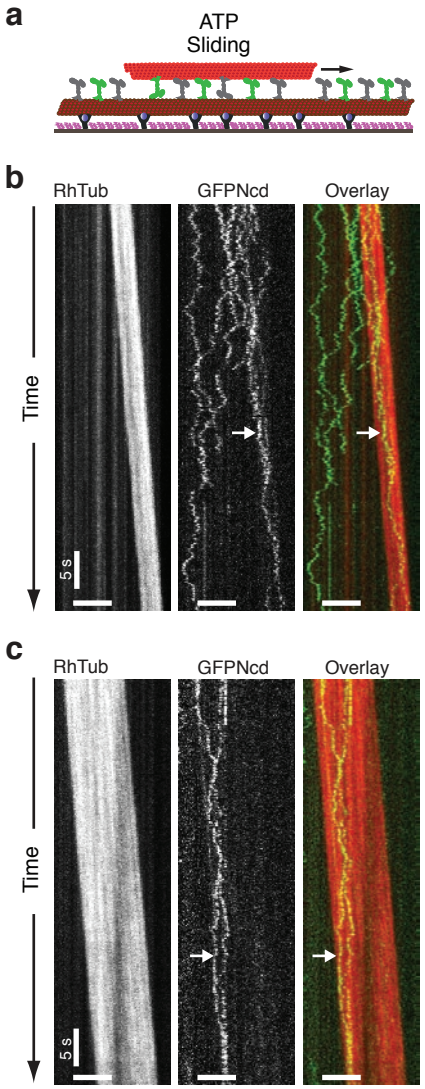

Figure S6 Diffusion of individual GFPNcd motors in the overlap region between sliding MTs. **a** Schematic diagram of the spiking assay. Template MTs (dim red) were preincubated with a mixture of GFPNcd and unlabelled Ncd. Then, non-decorated transport MTs (bright red) were added. **b and c** Typical dual-colour kymographs of sliding transport MTs with the corresponding GFPNcd signal. Both, inside and outside the MT overlap regions we found GFP-Ncd molecules to diffuse and we never observed any directed motion or static fixation in the overlap region. Interestingly, a number of GFPNcd molecules appeared to be either cotransported with the sliding transport MT (arrow in b) or mainly interacting with the template MT (arrow in c). Horizontal scale bars: 5 µm.

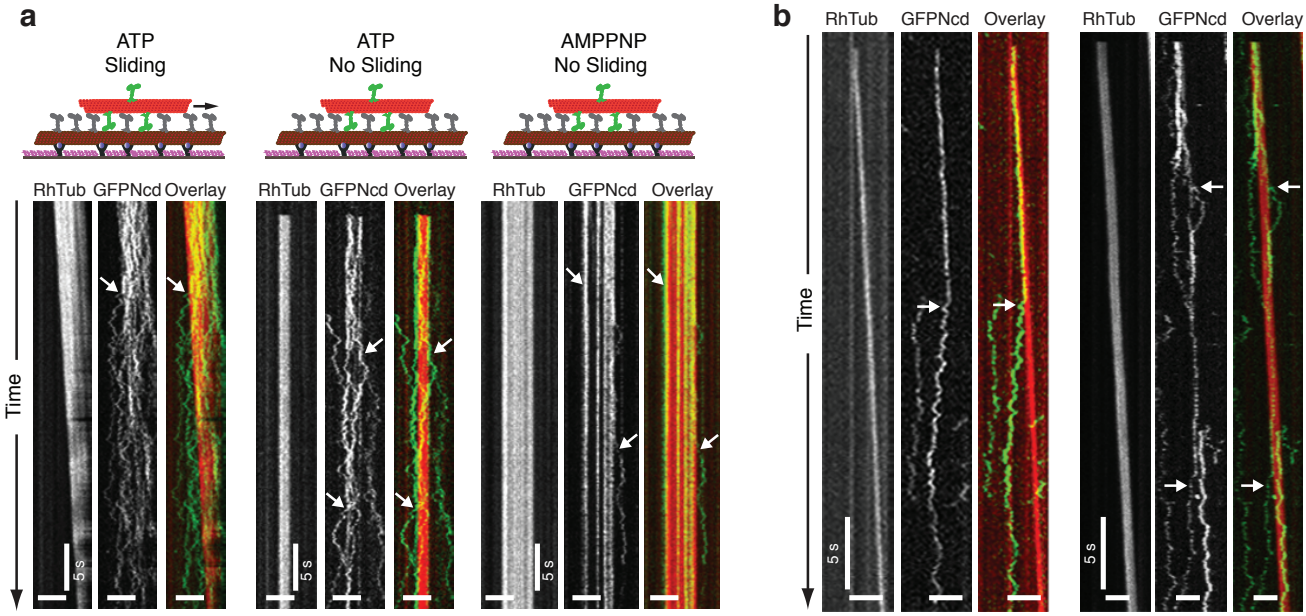

Figure S7 Transfer of individual GFPNcd molecules between transport and template MTs in the presence of ATP and AMPPNP. In order to analyse if single motors have the capability to switch between interacting MTs, brightly-labelled rhodamine transport MTs were decorated with GFPNcd. The template MTs (dim red) were preincubated with unlabelled Ncd in order to increase the landing rates of transport MTs. Using dual colour TIRF microscopy we were able to follow single motors switching between MTs. **a** Typical dual-colour kymographs of Ncd mediated MT-MT interactions in ATP and AMPPNP. **Left panel:** In the presence of ATP, similar to the spiking experiments described in Fig. S6, GFPNcd molecules diffused in the overlap region between sliding MTs. With progressing time, GFPNcd transfered to the template MT and diffused away from the overlap region (arrow). **Middle panel:** In the presence of ATP, GFPNcd molecules diffused in the overlap region between statically crosslinked MTs. Similar to the results in the left panel, GFPNcd molecules were capable of transfer to the template MT and diffusion away from the overlap region (arrow). This indicates that MT sliding is not required for motor switching. **Right panel:** In order to elucidate if ATP hydrolysis was necessary for motor transfer we preformed the same experiments in the presence of 1 mM AMPPNP. Here, MT sliding was never observed. Moreover, Ncd was mainly linked stationary to the MTs in the overlap region and the capability to diffuse on either MT was greatly reduced most likely due to the static binding of the motor domains (heads). Horizontal scale bars: 5 µm. **b** Additional dual-colour kymographs of sliding transport MTs and interacting single GFPNcd molecules in the presence of ATP. Single GFPNcd molecules were clearly able to interact via their tails with the transport MTs as indicated by the cotransportation. However, these molecules often switched their interaction from the transport to the template MT, frequently diffusing away from the overlap region (arrows). Interestingly, after transfer to and diffusion on the template MT, a number of motors were observed to repeatedly return into the overlap region. Horizontal scale bars: 3 µm

Supplementary Movie Legends

Movie S1 GFPNcd single molecules (green) interacting with MTs (red) (scale bar: 3 µm, total time 25 s, real time playback).

Movie S2 GFP195Ncd single molecules (green) interacting with MTs (red) (scale bar: 3 µm, total time 25 s, real time playback).

Movie S3 349NcdGFP single molecules (green) interacting with MTs (red) (scale bar: 3 µm, total time 25 s, real time playback).

Movie S4 Sliding of polarity-marked transport MTs (green seeds and red extension, where the longer extensions mark the MT plus ends) on template MTs (dimly labelled in red) (scale bar: 5 µm, total time 588s, 75x sped-up playback).

Movie S5 GFPNcd (middle panel and green signal in lower panel) switches between transport (bright) template (dim) MTs (upper panel and red signal in lower panel). (scale bar: 3 µm, total time 138s, 10x sped-up playback).

Movie S6 GFPNcd (green) accumulates at the minus ends of parallel, statically crosslinked MTs (red). Moreover, the movie shows another example of anti-parallel sliding and parallel static crosslinking.(scale bar: 5 µm, total time 508s, 35x sped-up playback).

Movie S7 Sliding of transport MTs (bright) on template MTs (dim) (scale bar: 5 µm, total time 347s, 10x sped-up playback).

Supplementary Methods

DNA manipulations: Recombinant plasmid for expression of the full length Ncd in E. coli was constructed by amplification of the full length Ncd coding sequence from plasmid pBS-ncd with primers Ncdf: ATGCATATGGAATCC CGGCTACC and Ncdr: AGCTCGAGTTAT TTATCGAAACTGCCGCTGT adding NdeI and XhoI sites respectively (underlined). PCR product cut with NdeI and XhoI was ligated into pET28a vector (Novagen) digested with the same enzymes producing plasmid pHisNcF expressing full length Ncd protein with N-terminal His-tag. N-terminal fusion of GFP with Ncd was constructed by replacement of NcoI-NdeI fragment of pHisNcF with NcoI-BfaI fragment from pEGFP-C1 plasmid (Clontech) resulting in plasmid pGFPNcF expressing Ncd with N-terminal EGFP fusion but without His-tag. To add N-terminal His-tag preceding the EGFP sequence KspI-NcoI fragment of pGFPNcF was replaced with KspI-NcoI fragment from pET30a vector (Novagen). This construct (pHisGFPNcF) expresses the fusion protein containing His-tag, GFP and Ncd (GFPNcd). The plasmid pHisGFP195Ncd expressing GFP195Ncd (N-terminal fusion of His-tag and EGFP to Ncd fragment 196-700) was constructed by “inside-out” PCR of pHisGFPNcF with primers NcF195f: TGTTCAAGGCCCGCTTC and NcF195r: TATGAGATCCGGTGGATCCC. The reaction product was phosphorylated with T4 Polynucleotide kinase and circularized by ligation. The first step of Ncd349GFP construction was cloning the EGFP coding sequence as a NcoI-SalI fragment from pEGFP-C1 into the pET30a vector resulting in plasmid pET30EGFP. Then the Ncd coding sequence (aa 1-349) was amplified from pHisGFPNcF with primers NcFSzfNde: TATCATATGGAATCCC GGCTACCGAAACC and NcFSzrNco: ATCCATGGCGATGTTGCCGCGCAGGTCC adding NdeI and NcoI sites respectively (underlined). PCR product cut with NdeI and NcoI was ligated into pET30EGFP digested with the same enzymes producing plasmid pNcSGFPHis. Correctness of all DNA manipulations described above was confirmed by DNA sequencing.

Size exclusion chromatography*:* The dimeric structure of the Ncd proteins was confirmed by size exclusion chromatography. Protein samples were run in motility buffer on Superdex 200 PC 3.2/30 columns on an AKTA Purifier system (GE Healthcare). The column was calibrated with a gel filtration molecular weight marker set (Sigma) containing cytochrome c from horse heart (12.4 kDa), carbonic anhydrase from bovine erythrocytes (29 kDa), bovine serum albumin (66 kDa), alcohol dehydrogenase from yeast (150 kDa), β-amylase from sweet potato (200 kDa) and Blue Dextran (2000 kDa, used to measuring column void volume). The apparent molecular weights of the analysed Ncd samples were calculated by comparing their V_e/V_0 values to the calibration curve.

Gliding motility assays: Flowcells were prepared as described in the main text, however using non-silanized glass. Surfaces were blocked by 5 min incubation with casein (0.5 mg/ml). After 5 min either a kinesin-1 (in 1 mM ATP [Roche], 0.2 mg/ml casein in BRB80) or Ncd (in motility buffer used for the sliding assay, main text) was flown in. Another 5 min later polarity-marked MTs were applied in motility buffer.

GFPNcd photobleaching: Flowcells were prepared as described in the main text. Single GFPNcd molecules were immobilized to the surface using anti-GFP antibodies. Imaging was performed in motility buffer. Taking intensities from GFPNcd signals and subtracting the background using Metamorph revealed the photobleaching behaviour. Obtained intensities were smoothened by a moving average (box width of 9 points) and plotted using Igor (WaveMetrics, Lake Oswego, Oregon 97035 USA).

nature cell biology

The kinesin-14 Klp2 organizes microtubules into parallel bundles by an ATP-dependent sorting mechanism

Marcus Braun[1], Douglas R. Drummond[2], Robert A. Cross[2] and Andrew D. McAinsh[1,3]

The dynamic organization of microtubules into parallel arrays allows interphase cells to set up multi-lane highways for intracellular transport and M-phase cells to build the mitotic and meiotic spindles. Here we show that a minimally reconstituted system composed of Klp2, a kinesin-14 from the fission yeast *Schizosaccharomyces pombe*, together with microtubules assembled from purified *S. pombe* tubulin, autonomously assembles bundles of parallel microtubules. Bundles form by an ATP-dependent sorting mechanism that requires the full-length Klp2 motor. By this mechanism, antiparallel-overlapped microtubules slide over one another until they dissociate from the bundles, whereas parallel-overlapped microtubules are selectively trapped by an energy-dissipating force-balance mechanism. Klp2-driven microtubule sorting provides a robust pathway for the organization of microtubules into parallel arrays. *In vivo* evidence indicates that Klp2 is required for the proper organization of *S. pombe* interphase microtubules into bipolar arrays of parallel-overlapped microtubules[1–4], suggesting that kinesin-14-dependent microtubule sorting may have wide biological importance.

In eukaryotic mitosis and meiosis, the interlocking half-spindles are each composed of parallel microtubules[5], while in interphase, cells use parallel arrays of microtubules both as stable tracks for motorized intracellular transport and as a guidance system for cell growth and motility[6]. The mechanisms by which cells organize microtubules into parallel arrays are unclear. In principle, parallel arrays might form either by the crosslinking of a set of parallel microtubules emanating from a common organizing centre, or by the capture, orientation and linking-in of individual free microtubules by microtubule-associated proteins and microtubule-attached molecular motors, independently of microtubule dynamics[7–9]. A useful model system for studying the formation of higher-order microtubule-based structures is the interphase microtubule array (IMA) in the fission yeast *S. pombe*. The IMA, which is involved in determining and maintaining cell polarity in fission yeast[10,11], consists of several bundles of parallel microtubules lying parallel to the long axis of the cell. These parallel bundles are linked to one another in a narrow zone of anti-parallel overlap in the centre of the cell[12,13], so that in each half of the cell, dynamic microtubule plus ends grow outwards towards the cell ends. *In vivo,* the IMA grows either from interphase microtubule nucleation centres that are associated with the nucleus, or from secondary nucleation sites in the cytoplasm or on the side of existing microtubules[2,3]. Microtubules that originate from these secondary sites are subsequently recruited into the IMA. These studies demonstrate that a combination of cytoplasmic nucleation factors, stabilizing factors and the Klp2 motor, are required for self-organization of the IMA[1–4]. Here we show that purified, full-length Klp2 alone is sufficient to drive ATP-dependent *in vitro* self-organization of *S. pombe* microtubules into parallel arrays.

Purified, recombinant full-length Klp2 (Fig. 1b) is present in solution at physiological ionic strength (PEM100 buffer (100 mM Pipes pH 6.9, 1 mM $MgCl_2$, 2 mM EGTA) plus 100 mM NaCl) as a single elongated homodimeric species (Fig. 1d, e), consistent with the carboxy-terminal motor domain and amino-terminal flexible tail region being connected by a predicted coiled coil (Fig. 1c). In microtubule gliding assays using microtubules assembled from pig brain tubulin (Fig. 1f), Klp2 drove minus-end-directed motility, as expected for a kinesin-14 family member (Supplementary Information, Movie 1). Gliding velocities were slightly faster with pig brain microtubules (65 ± 1.0 nm s^{-1}; mean ± s.e.m., $n = 50$), compared with microtubules that were assembled from tubulin purified from *S. pombe* (42 ± 0.8 nm s^{-1}; mean ± s.e.m., $n = 50$; Fig. 1h). This slightly slower rate compared with measurements made in *S. pombe* cells (92 nm s^{-1}; ref. 4) probably reflects the involvement of additional regulatory factors *in vivo*. The solution Klp2 ATPase was activated 15-fold more effectively by *S. pombe* microtubules (V_{max} 3.8 ± 0.3 s^{-1}) than by pig brain microtubules (V_{max} 0.25 ± 0.03 s^{-1}) although the apparent affinities for the two microtubule species were similar (K_m for *S. pombe* microtubules = 0.77 ± 0.2 μM and for pig-brain microtubules = 0.55 ± 0.2 μM; Fig. 1i). The origins of the low V_{max} measured for activation of the Klp2 ATPase by pig brain microtubules are currently unclear. Pig brain and *S. pombe* tubulin both caused a modest activation of the Klp2 ATPase (Fig. 1i)[14]. Overall, these experiments demonstrate that our purified full-length Klp2 is an active molecular motor protein.

[1]Chromosome Segregation Laboratory and [2]Molecular Motors Laboratory, Marie Curie Research Institute, The Chart, Oxted, RH8 0TL, Surrey, UK.
[3]Correspondence should be addressed to A.D.M (e-mail: a.mcainsh@mcri.ac.uk)

Received 20 January 2009; accepted 24 February 2009; published online 10 May 2009; DOI: 10.1038/ncb1878

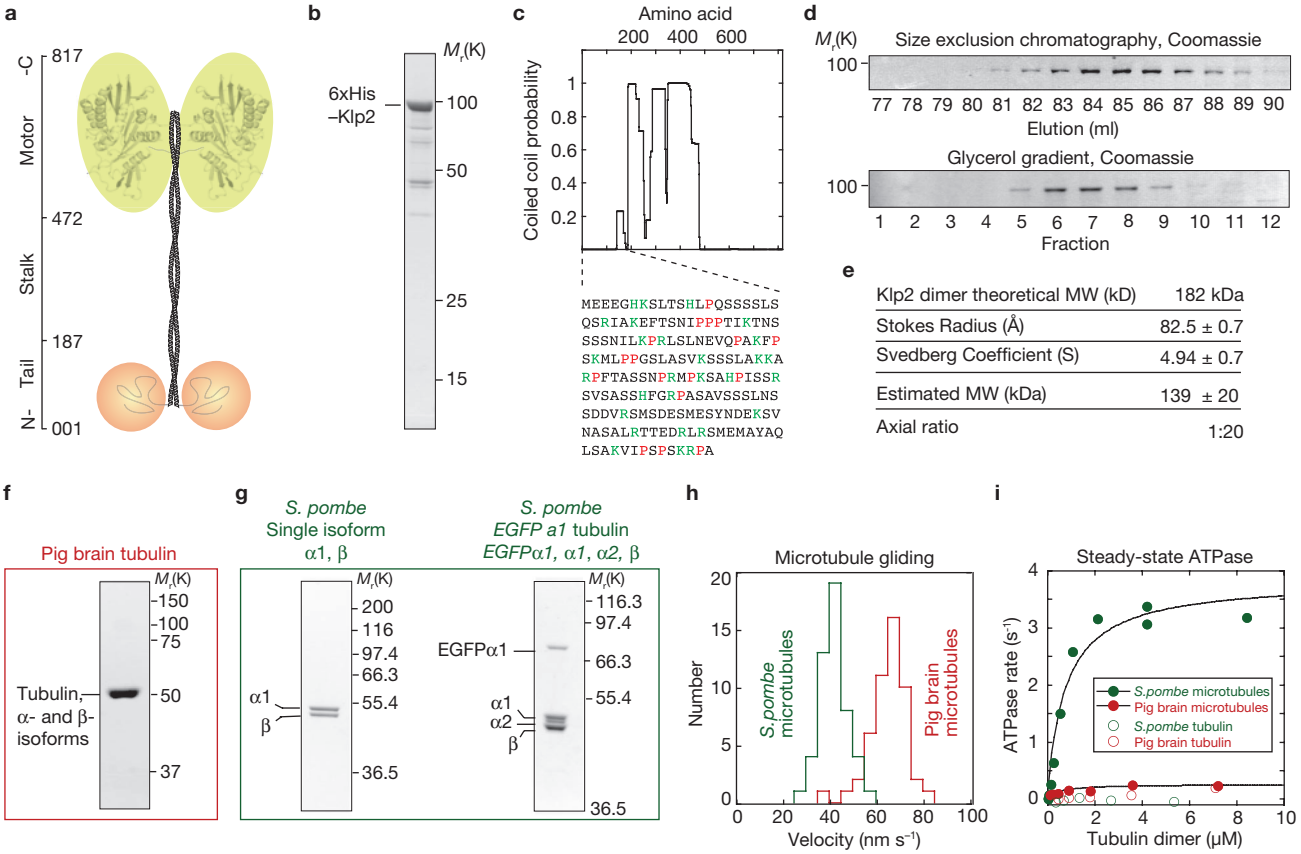

Figure 1 Purified full-length *S. pombe* kinesin-14 Klp2 is a microtubule-minus-end directed motor. (**a**) Schematic of the Klp2 domain structure indicating the motor domain position (based on crystal structure of the Kar3 motor domain[20], coiled-coil and flexible tail region. (**b**) Coomassie-stained SDS–PAGE of purified, recombinant full-length Klp2 protein expressed in *Escherichia coli*. (**c**) Coiled coil prediction of the full-length Klp2 protein using the COILS program[21]. (**d**) Hydrodynamic analysis of the purified full-length Klp2 protein performed in PEM100 buffer plus 100 mM NaCl. The upper panel shows fractions from size exclusion chromatography column and the lower panel fractions from a 5–40% glycerol gradient (**e**) Calculation of hydrodynamic parameters based on the experimentally derived stokes radius and Svedberg coefficients for full-length Klp2. (**f**, **g**) SDS–PAGE and Coomassie staining of purified pig brain tubulin (**f**), single isoform *S. pombe* tubulin (**g**, left panel) and EGFP–α1-tubulin (**g**, right panel). (**h**) Microtubule gliding velocities promoted by Klp2 at 25 °C in 100 mM PIPES buffer containing 100 mM NaCl, 1 mM ATP, 20 μM paclitaxel and 1 mM GMP–CPP, using microtubules polymerized from *S. pombe* EGFP–tubulin (green) and rhodamine labelled pig-brain tubulin (red). (**i**) Steady-state ATPase activity of Klp2 at 25 °C in PEM100, 100 mM NaCl, 1 mM ATP, 20 μM paclitaxel and 1 mM GMP–CPP using non-labelled microtubules polymerized from *S. pombe* tubulin (solid green circles; V_{max} 3.8 ± 0.3 s^{-1}, K_m 0.8 ± 0.2 μM) and pig brain tubulin (solid red circles; V_{max} 0.25 ± 0.03 s^{-1}, K_m 0.5 ± 0.2 μM). The V_{max}/K_m values of 4.75 μM s^{-1} for *S. pombe* and 8.3 μM s^{-1} for pig brain microtubules indicate strongly that Klp2 is a non-processive kinesin[22]. Measurements for non-polymerized *S. pombe* (open green circles) and pig brain tubulin (open red circles) show that the Klp2 kinesin is activated by polymerized microtubules exclusively. Full scans of the SDS–PAGE gels are provided in Supplementary Information, Figs S2, S3.

On the basis of previous experiments with *Drosophila melanogaster* kinesin-14 (Ncd)[15,16], we predicted that the flexible, proline-rich, basic N-terminal tail of Klp2 (theoretical pI 10.0; Fig. 1c) might act as a second microtubule-binding site. To investigate this possibility, we expressed and purified a Klp2 protein lacking the motor domain (Klp2-tail) and a Klp2 protein containing only the motor domain and a short coiled coil to mediate dimerization (Klp2-motor) which was confirmed to exist as a single homodimeric species by size exclusion chromatography, Fig. 2a; Supplementary Information, Fig. S1a). We first demonstrated that full-length Klp2 bound *S. pombe* microtubules in a pelleting assay in the presence of ATP using PEM100 plus 100 mM NaCl buffer (Fig. 2c). This binding was reduced when the experiment was performed using pig brain microtubules (Fig. 2c, compare lanes 2 and 4). Klp2-motor, which lacks the tail domain did not pellet with pig brain microtubules (Fig. 2d, lane 4), indicating that the Klp2 tail greatly increases the microtubule affinity of the motor, and suggesting that the tail contributes a second microtubule binding site. To confirm this, we carried out microtubule pelleting assays with Klp2-tail, which was found to bind both *S. pombe* and pig brain microtubules (Fig. 2e, compare lanes 4 and 10). Thus, only full-length Klp2, with intact tail and motor domains, shows selective binding of *S. pombe* versus pig brain microtubules. Binding of Klp2-tail, to both *S. pombe* and pig brain microtubules, was probably mediated through electrostatic interactions, as pelleting decreased as the ionic strength was increased (Fig. 2e, f). We next determined the stoichiometry of Klp2-tail:*S. pombe* microtubule binding by titration of Klp2-tail using a constant microtubule concentration. This showed stoichiometric binding to the lattice, with saturation at a ratio of about 1:1 Klp2-tail:tubulin heterodimer and a fitted K_d of 1.2 ± 0.1 μM (Fig. 2g, h). These binding data confirm that full-length Klp2 has two independent microtubule-binding sites, one in its head and one in its tail. The specific 1:1 binding of the isolated Klp2-tail domain to microtubules

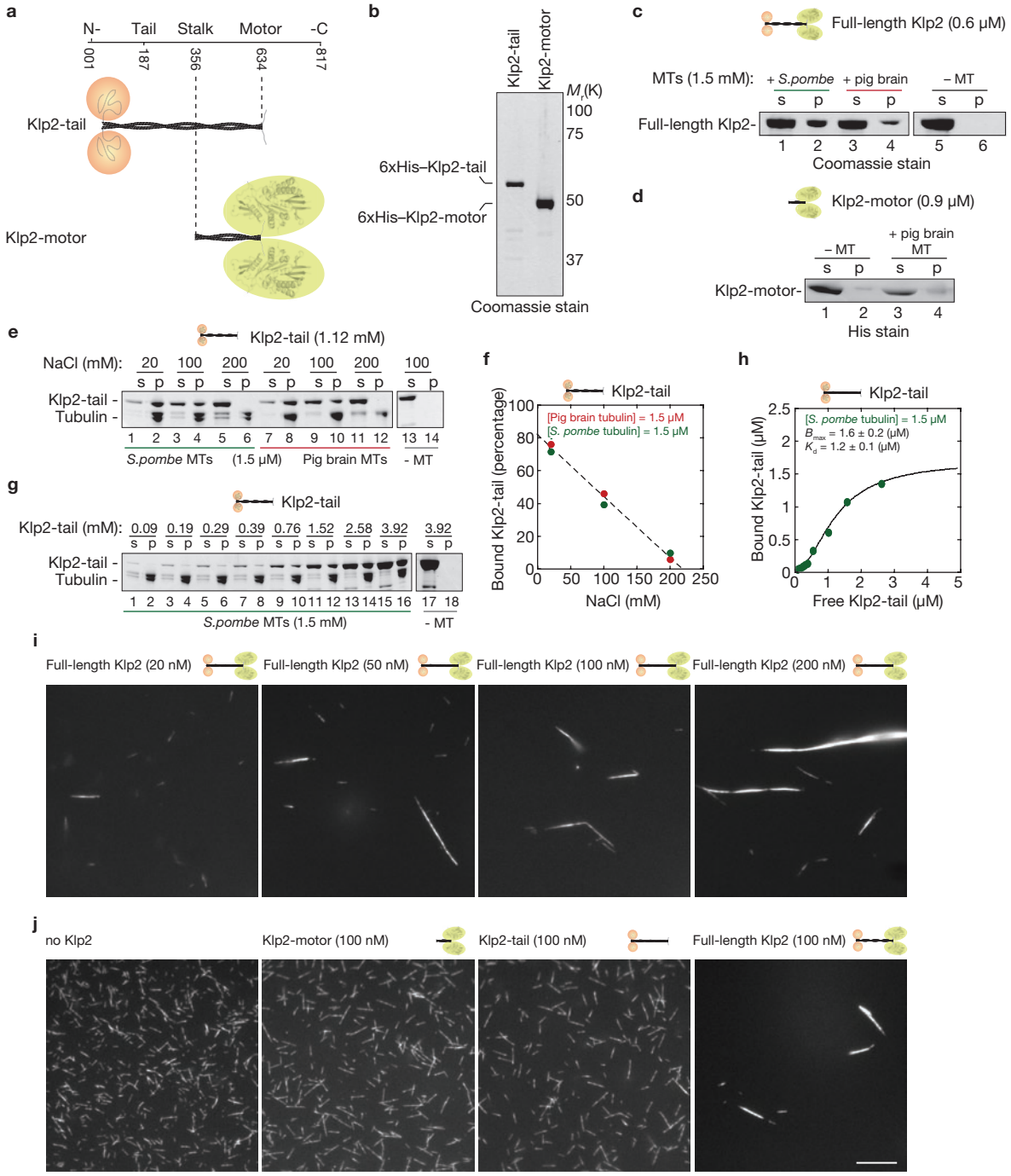

Figure 2 Microtubule bundling requires both the motor-domain and the N-terminal tail region of Klp2. (**a**) Schematic of the Klp2-tail and Klp2-motor constructs. (**b**) Coomassie-stained SDS–PAGE of purified, recombinant Klp2-tail and Klp2-motor proteins expressed in *E. coli*. (**c**, **d**) Microtubule (MT) co-pelleting assay performed in PEM100, 100 mM NaCl, 10 mM β-mercaptoethanol buffer, 1 mM GMP–CPP 1 mM ATP using 0.6 μM of Klp2 and 1.5 μM of non-labelled *S. pombe* (**c**, lanes 1 and 2) or pig brain (**c**, lanes 3 and 4) microtubules, or 0.9 μM Klp2-motor and 1.5 μM pig-brain microtubules. Supernatant (S) and pellet (P) fractions are indicated. (**e**) Binding of Klp2-tail (1.12 μM) to 1.5 μM of *S. pombe* (lanes 1-6) or 1.5 μM of pig brain (lanes 7-12) microtubules in PEM100 plus 20, 100 or 200 mM NaCl. (**f**) Quantification of binding shown in **e**. (**g**) Binding of Klp2-tail (concentrations, 0.1–3.9 μM) to 1.5 μM of *S. pombe* in PEM100 plus 100 mM NaCl. (**h**) Quantification of binding shown in **g**. (**i**) Full-length Klp2 (20–200 nM) was mixed with 200 nM of *S. pombe* EGFP–microtubules (PEM100 plus 100 mM NaCl, pH6.8) and the mixture added to a flow cell. Representative images of the microtubule-motor structures that formed after 20 min are shown. Scale bar, 10 μm. (**j**) Full-length Klp2, Klp2-motor or Klp2-tail (all at 100 nM) were mixed with 200 nM of *S. pombe* EGFP–microtubules and the mixture added to a flow cell. Representative images of the microtubule-motor structures that formed after 20 min are shown. We note that surface binding is mediated by the population of Klp2 that was not microtubule-bound (see pelleting assay, **c**, lane 1), in addition to motors attached to the bundles. For the no motor control and Klp2-tail experiments, *Drosophila* kinesin-1 was pre-bound to the glass surface in the flow cell to allow microtubules to be visualized. Scale bar, 10 μm. Full scans of the SDS–PAGE gels are provided in Supplementary Information, Figs S3, S4.

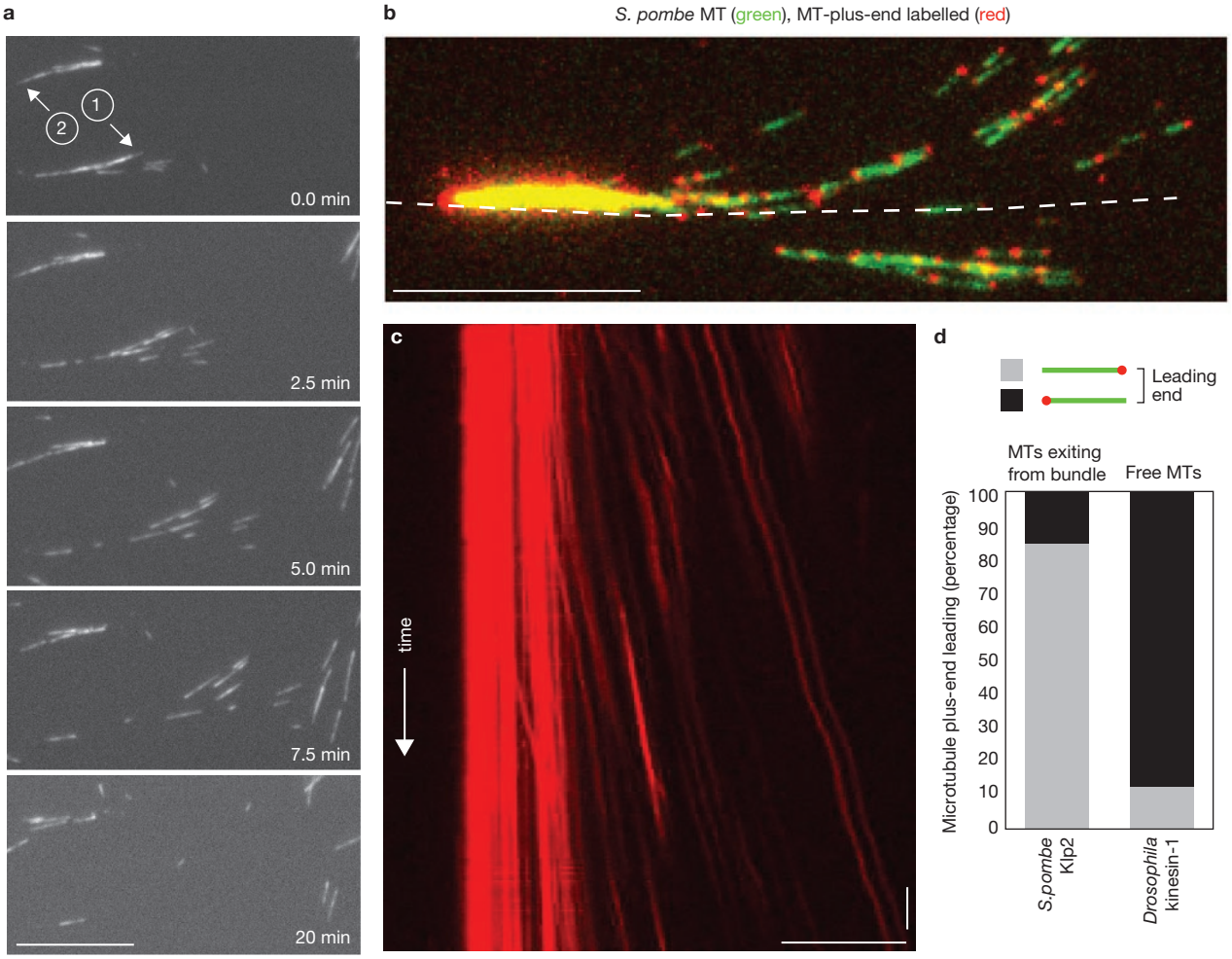

Figure 3 Full-length Klp2 organizes *S. pombe* microtubules into parallel bundles. (**a**) Microtubule gliding assay using microtubules assembled from *S. pombe* EGFP–tubulin (green) in PEM100 plus 100 mM NaCl. We note that surface binding is mediated by the population of Klp2 that was not microtubule-bound (see pelleting assay Fig. 2c, lane 1), in addition to motors attached to the bundles. Two bundles are shown (1 and 2) dispersing. Note that $t = 0$ is the time-point 20 min after motors and microtubules were mixed together. Scale bar, 10 μm. (**b**) Microtubule gliding assay using polarity-marked *S. pombe* microtubules (MT, 200 nM) which were premixed with 100 nM full-length Klp2 in solution (PEM100 plus 42 mM NaCl) and then added to the flow cell. The image shows the position of microtubules at the first time-point. Scale bar, 10 μm. (**c**) Kymograph analysis based on the dotted white line in **b**. Time is on the *y* axis with the vertical bar indicating 1 min and horizontal scale bar, 10 μm. (**d**) Quantification of microtubule gliding events using full-length Klp2 (minus-end directed motor; $n = 32$) or *Drosophila* kinesin-1 (plus-end-directed motor; $n = 38$). Shown are the percentages of gliding microtubules with a single leading (grey) or lagging (black) rhodamine-labelled end.

indicates that there is a specific binding site for the tail on each tubulin heterodimer or possibly between adjacent heterodimers.

We next asked whether the two microtubule binding sites in full-length Klp2 (motor domain and tail region) could support the formation of lateral contacts between microtubules and, in turn, microtubule bundling. We therefore mixed 100 nM full-length Klp2 with 200 nM *S. pombe* EGFP-labelled microtubules in solution (PEM100 plus 100mM NaCl) and incubated them for 20 min. This mixture was then added to a flow cell and bundles visualized as the motor–microtubule complexes bound to the glass surface. This experiment revealed that full-length Klp2 promoted the formation of *S. pombe* microtubule bundles (Fig. 2i, third panel). The extent of bundle formation depended on the Klp2 concentration: reducing the Klp2 protein concentration (20–50 nM) produced a reduction in bundles and an increase in free microtubules, whereas increasing the concentration to 200 nM produced larger bundle structures (Fig. 2i). When these experiments were carried out with a mixture of pig brain and *S. pombe* microtubules (both at 200 nM) and full-length Klp2 (100 nM), we also observed combined *S. pombe*/pig brain microtubule bundles (Supplementary Information, Fig. S1b). Crucially, neither Klp2-tail or Klp2-motor domain proteins (both at 100 nM) were able to drive bundle formation (Fig. 2j, second and third panels). These data demonstrate that the formation of microtubule bundles requires microtubule binding by both the motor-head and the tail domain of Klp2.

To investigate the organization of the microtubule bundles we took advantage of the classic microtubule-gliding assay. We mixed 100 nM full-length Klp2 with 200 nM EGFP-labelled *S. pombe* microtubules in solution and after 20 min added the mixture to a flow cell. We observed that in the presence of ATP, single microtubules were pulled out of those bundles that landed on the surface-attached Klp2 kinesins, demonstrating that the bundles could be 'unlocked' by an imbalance of Klp2-generated force. All microtubules moved uni-directionally, initially sliding in parallel, and subsequently tending to splay apart until

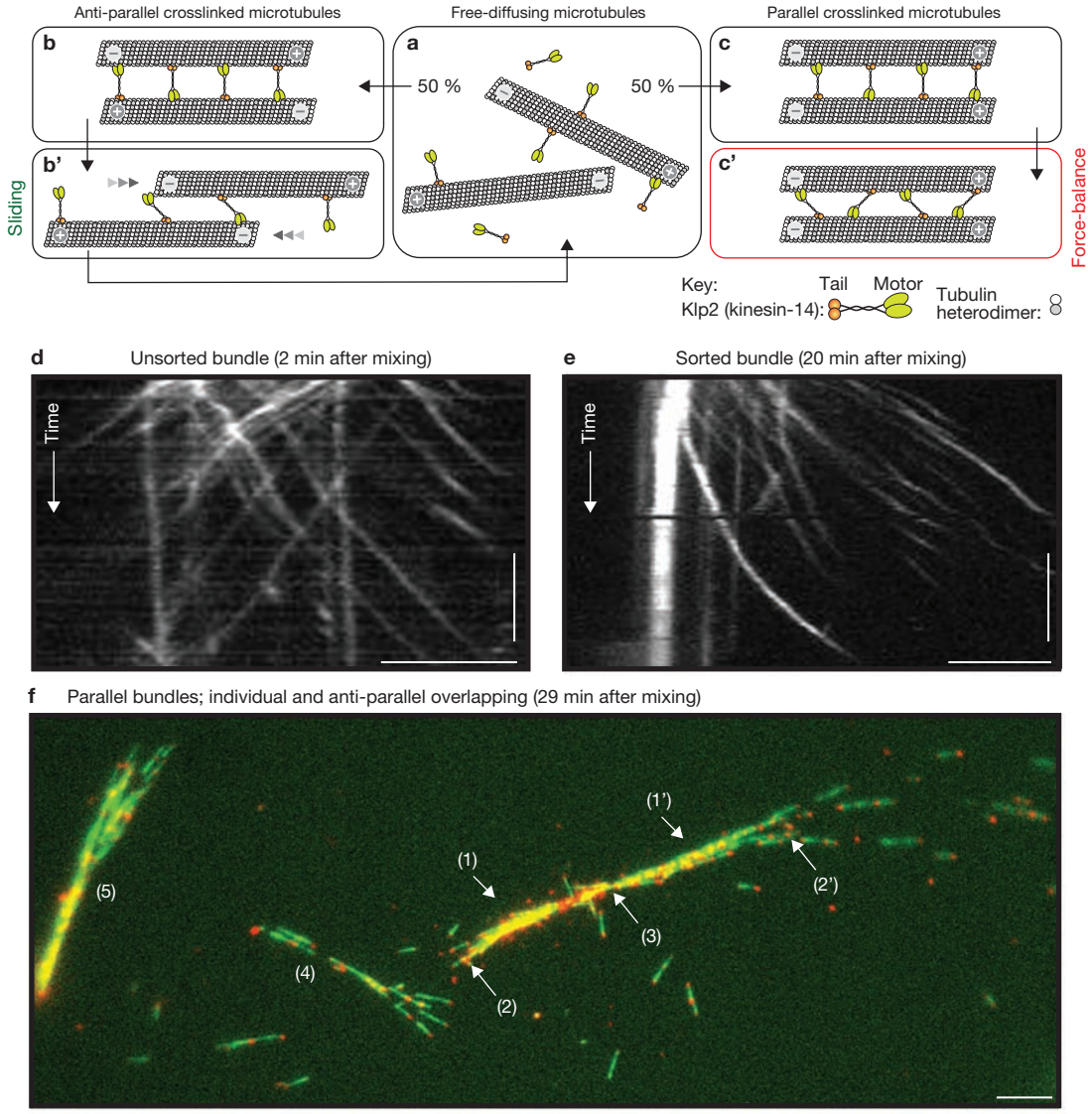

Figure 4 Force-balance model for motorized microtubule sorting. (**a**–**c**) Klp2 motors freely diffusing in solution bind to microtubules through interactions with the motor (yellow ovals) and tail (orange circles) domain (**a**). Klp2 motors thus establish lateral crosslinks between diffusing microtubules at random, leading to a mixture of anti-parallel (**b**) and parallel (**c**) overlapping microtubules. (**b**′) Klp2 causes anti-parallel overlapped microtubules to slide apart, leading to a full dissociation of the microtubules (direction of sliding microtubules is indicated by arrowheads) (**c**′) Parallel-overlapped microtubules are selectively trapped by the force-balance of the oppositely attached sets of Klp2 motors. (**d**, **e**) Kymographs from microtubule gliding assay using polarity-marked *S. pombe* microtubules (200 nM), which were premixed with 100 nM full-length Klp2 in solution (PEM100 plus 100 mM NaCl) and then added to the flow cell after 2 min (**d**) or 20 min (**e**). Time is on the *y* axis with the vertical bar indicating 5 min. Horizontal scale bar, 5 μm. (**f**) Image of a microtubule array at t = 9 min (29 min after mixing microtubules and motors in PEM100 plus 42 mM NaCl) from Supplementary Information, Movie 6, which is composed from two parallel microtubule bundles (1 and 1′). Each bundle contains microtubules with their plus-ends exclusively orientated towards the distal ends of the array (2 and 2′), and overlap in an antiparallel zone (3). Also visible are two parallel bundles (4 and 5). Scale bar, 10 μm.

the entire bundle disassembled (Fig. 3a; Supplementary Information, Movie 2). To further confirm this, we generated polarity-marked *S. pombe* microtubules. To do this, microtubules were first polymerized from GFP-labelled *S. pombe* tubulin and then capped with rhodamine-labelled pig brain tubulin. This resulted in a microtubule population in which about 30% had a single red mark at one end (the rest had multiple marks, presumably resulting from fusion events between microtubules, and were removed from any analysis). In a gliding assay with the plus-end directed *Drosophila* kinesin-1, more than 85% of these microtubules moved with the non-labelled end leading as expected when the rhodamine-cap marks the microtubule plus-ends (Fig. 3d). We then mixed 100 nM Klp2 with 200 nM polarity-marked *S. pombe* microtubules in solution, incubated for 20 min and added the mixture to a flow cell. As expected, we observed bundles that landed on the surface with microtubules exiting the bundle uni-directionally (Fig. 3b; Supplementary Information, Movie 3). Of these microtubules pulled out of the bundle, 87.5% had the rhodamine-cap leading (Fig. 3d), confirming their parallel configuration. Kymograph analysis of the rhodamine caps from this movie again clearly shows microtubules exiting the bundle from the right-hand side, but not the left-hand side (Fig. 3c). This uni-directional sliding of microtubules out of the bundle unequivocally demonstrates that the bundles are composed exclusively of parallel microtubules.

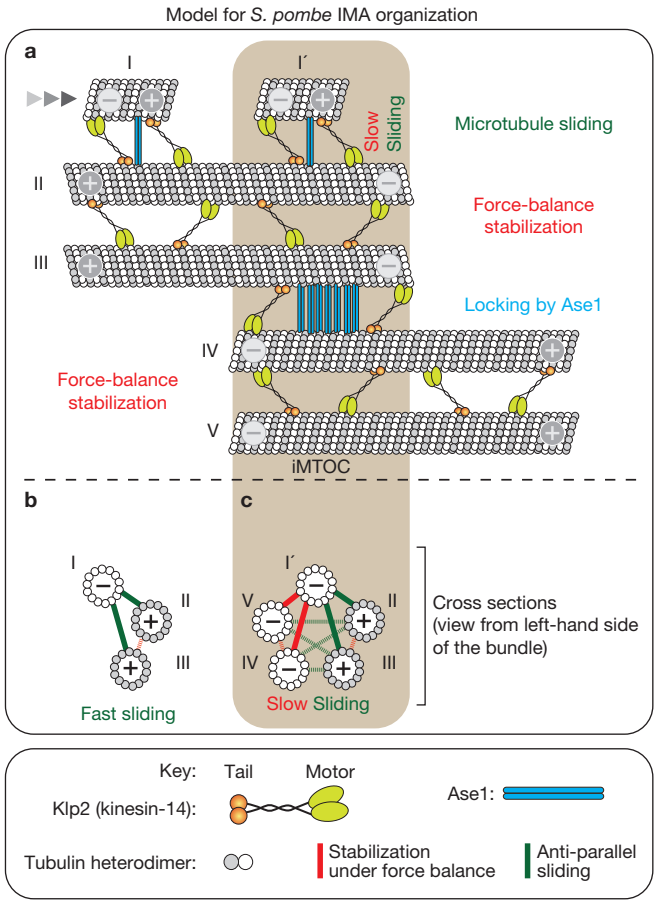

Figure 5 Model for the *S. pombe* interphase IMA organization. During dynamic IMA maintenance *in vivo,* assembled microtubules are incorporated into existing microtubule arrays. (**a**) We propose that microtubules (for example, II and III), which are in a parallel configuration, will be locked under force balance by Klp2. By contrast, a short microtubule (for example, I), which binds in an anti-parallel configuration with the IMA (for example, II and III), will slide to the centre of the cell. The force of the Klp2 motor is able to overcome the effect of Ase1 (blue bar), which has been shown to localize to these short microtubules *in vivo* and crosslink anti-parallel microtubules *in vitro.* (**b**) Cross-section of interactions between microtubule I, II and III: green lines indicate sliding and red lines stabilization under force balance. As microtubule I (now designated as microtubule I´) arrives at the antiparallel overlap zone within the IMA (iMTOC), Klp2 molecules can also now interact with parallel microtubules (for example, V and IV) and cause sliding to slow down. (**c**) Cross-section of interactions between microtubule I´, II, III, IV and V. At this point, the Ase1 molecules are able to overcome the reduced Klp2 sliding force and stabilize the iMTOC.

To explain our data we propose that Klp2 drives the formation of parallel bundles of *S. pombe* microtubules by a motorized sorting mechanism. In our model, free microtubules in solution (Fig. 4a) are first captured and crosslinked by Klp2 motor and tail domains. This initial capture phase results in an equal proportion of anti-parallel or parallel microtubule overlaps (Fig. 4b, c). In the presence of ATP, the motor activity of Klp2 then resolves these initial mixed-polarity bundles into a purely parallel arrangement: In the case of anti-parallel crosslinked microtubules, the Klp2 motor domains drive relative sliding apart of the crosslinked microtubules until they eventually dissociate (Fig. 4b´). By contrast, in the parallel geometry, all Klp2 kinesins attempt to move to the minus-end of the bundle, which causes the motors to stall under load. The forces produced by the two opposing sets of Klp2 motors balance and effectively cancel each other out (Fig. 4c´), stabilizing the structure in force-balance. Our data show that the parallel microtubule bundles generated *in vitro* are self-organized, energy dissipating structures (because of the requirement for ATP), which are stable under force-balance, yet can be readily destabilized through the application of external force, or by an imbalance of internal forces.

One prediction of our model is that repeated rounds of microtubule sliding, dissociation, and recapture are required for Klp2-dependent sorting to reach completion. To test this, we mixed Klp2-full length protein with *S. pombe* microtubules in solution and observed the formation of organized bundles by removing a sample at 2 min and then at 20 min. As predicted, we observed anti-parallel microtubules within the evolving bundle structure at the 2 min time-point: the kymograph of rhodamine caps clearly shows the movement of microtubules in both directions within the bundle structure, indicating an unsorted bundle (Fig. 4d; Supplementary Information, Movie 4). After 20 min incubation, we observed parallel structures, with microtubules all moving in the same direction as they exit the bundle (Fig. 4e; Supplementary Information, Movie 5). At the same time we also observed the presence of structures composed of two parallel bundles that were joined by a short overlap zone (Fig. 4f; Supplementary Information, Movie 6). We propose that such structures are intermediates between unsorted and sorted bundles. These data support our model that Klp2 actively sorts microtubules into organized parallel bundles.

What inferences can we draw about the *in vivo* role of Klp2? Current models for IMA formation in *S. pombe* propose that Klp2 is required for the sliding of short microtubules into the overlap zone, and in controlling the proportion of anti-parallel overlaps, compared with parallel overlaps within the IMA[1,4]. Models from Tran, Nedelec, Nurse and colleagues postulate a role for plus-tip-bound Klp2 in sliding short anti-parallel microtubules along an IMA arm and into the mid-zone of the cell where they are locked in place by Ase1, a protein that recognizes and specifically stabilizes anti-parallel overlaps[4]. Our new data are consistent with, and complimentary to, this proposal. Our *in vitro* data show that Klp2 binds along the lattice of *S. pombe* microtubules, where it drives antiparallel-overlapped microtubules to slide apart, while stabilizing parallel overlaps. Consistent with this model, we could observe that Klp2–GFP is localized to both microtubule plus-ends and the microtubule lattice in *S. pombe* cells (Supplementary Information, Movie 7). We now propose a synthesis of these two models, in which lattice-bound Klp2 slides short anti-parallel-overlapped microtubules into the mid-zone, where their anti-parallel overlap with the opposing IMA arm is stabilized by Ase1, and the parallel overlap of the newly arrived microtubule with the opposing IMA arm is stabilized by Klp2 (Fig. 5). This new model is consistent with observations that deletion of *ASE1* still allows microtubule bundling to take place, but overlapping regions are unstable[3,17].

What are the general implications of our results? Our data identify a robust mechanism for the motor-driven self-organization of microtubules into parallel bundles. Consistent with this, work from Diez and colleagues have directly demonstrated using a microtubule–microtubule sliding assay that another kinesin-14 (*Drosophila* Ncd), can slide apart pairs of anti-parallel microtubules but locks together parallel ones (see Fink *et al.,* this issue of *Nature Cell Biology*). Eg5, the *Xenopus* homotetrameric microtubule plus-end-directed kinesin-5, has previously been reported to slide antiparallel- but lock parallel microtubules[18,19]. This suggests the possibility that

a sorting mechanism similar to that described here may be conserved in both kinesin-14 and kinesin-5. We therefore expect that the mechanisms defined in our force-balance model will have a fundamental role in the establishment of complex cellular microtubule-based structures such as the IMA and bipolar spindles. The dynamic organization of microtubule arrays driven by molecular motors, in contrast to passive crosslinking of microtubules by MAPs (microtubule associated proteins), has the advantage that microtubule-based structures can be rapidly readjusted, as we have shown, by tipping of the force-balance. To fully test the implications of these ideas it will be crucial to develop an *in vitro* reconstitution assay that faithfully recapitulates the combination of microtubule dynamics, modulated by MAPs and molecular motors, and the self-organization of assembled microtubules mediated by MAPs, and sliding driven by molecular motors, these being distinct but complementary strategies that eukaryotic cells use to control and adjust the structure of their microtubule cytoskeleton. □

Note added in proof: a related manuscript by Fink et al. *(*Nature Cell Biol. ***11,*** *717–723; 2009) is also published in this issue.*

METHODS

Methods and any associated references are available in the online version of the paper at http://www.nature.com/naturecellbiology/

Note: Supplementary Information is available on the Nature Cell Biology website.

ACKNOWLEDGEMENTS

We thank Joe Howard for the full-length *Drosophila* kinesin-1 construct and Michael Osei for purification of *S. pombe* tubulin and EGFP–tubulin. This work was supported by Marie Curie Cancer Care (A.D.M. and R.A.C.) and the Medical Research Council (R.A.C.).

AUTHOR CONTRIBUTIONS

M.B. conceived, designed and performed the experiments, and contributed to the writing of this study; D.R.D. created *S. pombe* strains, developed the methodology for purification of *S. pombe* tubulin and helped write the manuscript; A.D.M. and R.A.C. designed experiments and wrote the manuscript.

COMPETING FINANCIAL INTERESTS

The authors declare no competing financial interests.

Published online at http://www.nature.com/naturecellbiology/
Reprints and permissions information is available online at http://npg.nature.com/reprintsandpermissions/

1. Carazo-Salas, R. E., Antony, C. & Nurse, P. The kinesin Klp2 mediates polarization of interphase microtubules in fission yeast. *Science* **309,** 297–300 (2005).
2. Carazo-Salas, R. E. & Nurse, P. Self-organization of interphase microtubule arrays in fission yeast. *Nature Cell Biol.* **8,** 1102–1107 (2006).
3. Daga, R. R., Lee, K. G., Bratman, S., Salas-Pino, S. & Chang, F. Self-organization of microtubule bundles in anucleate fission yeast cells. *Nature Cell Biol.* **8,** 1108–1113 (2006).
4. Janson, M. E. *et al.* Crosslinkers and motors organize dynamic microtubules to form stable bipolar arrays in fission yeast. *Cell* **128,** 357–368 (2007).
5. Gadde, S. & Heald, R. Mechanisms and molecules of the mitotic spindle. *Curr. Biol.* **14,** 797–805 (2004).
6. Broussard, J. A., Webb, D. J. & Kaverina, I. Asymmetric focal adhesion disassembly in motile cells. *Curr. Opin. Cell Biol.* **20,** 85–90 (2008).
7. Nedelec, F. J., Surrey, T. & Karsenti, E. Self-organisation and forces in the microtubule cytoskeleton. *Curr. Opin. Cell Biol.* **15,** 118–124 (2003).
8. Ehrhardt, D. W. Straighten up and fly right: microtubule dynamics and organization of non-centrosomal arrays in higher plants. *Curr. Opin. Cell Biol.* **20,** 107–116 (2008).
9. Surrey, T., Nedelec, F. J., Leibler, S. & Karsenti, E. Physical properties determining self-organization of motors and microtubules. *Science* **292,** 1167–1171 (2001).
10. Hagan, I. M. The fission yeast microtubule cytoskeleton. *J. Cell Sci.* **111,** 1603–1612 (1998).
11. Brunner, D. & Nurse, P. New concepts in fission yeast morphogenesis. *Philos. Trans. R. Soc. Lond. B. Biol. Sci.* **355,** 873–877 (2000).
12. Drummond, D. R. & Cross, R. A. Dynamics of interphase microtubules in *Schizosaccharomyces pombe*. *Curr. Biol.* **10,** 766–775 (2000).
13. Hoog, J. L. *et al.* Organization of interphase microtubules in fission yeast analyzed by electron tomography. *Dev. Cell* **12,** 349–361 (2007).
14. Alonso, M. C. *et al.* An ATP gate controls tubulin binding by the tethered head of kinesin-1. *Science* **316,** 120–123 (2007).
15. Karabay, A. & Walker, R. A. Identification of microtubule binding sites in the Ncd tail domain. *Biochemistry* **38,** 1838–1849 (1999).
16. Wendt, T. *et al.* A structural analysis of the interaction between ncd tail and tubulin protofilaments. *J. Mol. Biol.* **333,** 541–552 (2003).
17. Loiodice, I. *et al.* Ase1p organizes antiparallel microtubule arrays during interphase and mitosis in fission yeast. *Mol. Biol. Cell* **16,** 1756–1768 (2005).
18. Kapitein, L. C. *et al.* The bipolar mitotic kinesin Eg5 moves on both microtubules that it crosslinks. *Nature* **435,** 114–118 (2005).
19. Uteng, M., Hentrich, C., Miura, K., Bieling, P. & Surrey, T. Poleward transport of Eg5 by dynein–dynactin in *Xenopus laevis* egg extract spindles. *J. Cell Biol.* **182,** 715–726 (2008).
20. Gulick, A. M., Song, H., Endow, S. A. & Rayment, I. X-ray crystal structure of the yeast Kar3 motor domain complexed with Mg.ADP to 2.3 A resolution. *Biochemistry* **37,** 1769–1776 (1998).
21. Lupas, A., Van Dyke, M. & Stock, J. Predicting coiled coils from protein sequences. *Science* **252,** 1162–1164 (1991).
22. Hackney, D. D. Implications of diffusion-controlled limit for processivity of dimeric kinesin head domains. *Biophys. J.* **68,** 267S–270S (1995).

METHODS

Protein purification. The 6xHis-tagged full-length Klp2 (amino acids 1–817), Klp2 motor domain (Klp2-motor; amino acids 356–817) and Klp2 coiled coil plus tail domain (Klp2-tail; amino acids 1–634) were generated as described in the Supplementary Information, Methods. The full-length *Drosophila* kinesin-1 heavy chain was expressed and purified as described in the Supplementary Information, Methods.

***S. pombe* tubulin.** We created an *S. pombe* strain mmsp174 (*h⁻ura4.d18 arg3.D4 atb2⁻::nda2⁺*) containing only α1- and β-tubulin protein isoforms by replacing the *atb2* (α2) gene protein-encoding region with the protein-encoding region of the α1 gene *nda2*, using a DNA fragment PCR-amplified from genomic DNA and a previously described method for gene replacement in yeast[23]. Single isoform *S. pombe* α1 and β-tubulin was prepared from an 80 l culture of cells grown in a fermenter, collected by centrifugation and frozen in liquid nitrogen (Large Scale Laboratory, NIMR, London). The cell pellet was processed as described previously[24] with the addition of a polymerization and depolymerization cycle then gel filtration on Superdex 200 before the purified tubulins were desalted into PEMICO buffer[25] (100 mM PIPES, 1 mM $MgSO_4$ and 2 mM EGTA adjusted to pH 6.9 with KOH) containing 20 μM GDP, concentrated in a spin concentrator and stored in liquid nitrogen. Protein concentrations were determined by UV-absorption scan of protein samples dissolved in guanidine hydrochloride (6 M), assuming full nucleotide occupancy and ε of 108,390 M^{-1} cm^{-1}. GFP-labelled tubulin was prepared by the same method from the *S. pombe* strain mmsp33 (ref. 12), which contains α1β, α2β and EGFP–α1β tubulin heterodimers. The EGFP–α1β tubulin forms 13% of the total purified tubulin heterodimers. Both *S. pombe* tubulin preparations had a purity of 98%, as determined by Sypro Red fluorescence dye staining of SDS–PAGE gels loaded with 10ug of tubulin. Gels were imaged using an FX ProPlus Molecular Imager (Bio-Rad) and quantified using Quantity One software (Bio-Rad).

Protein biochemistry. Size exclusion chromatography and glycerol gradients were performed as described previously[26], except that we used PEM100 (100 mM Pipes pH 6.9, 2 mM EGTA, 1 mM $MgCl_2$) plus 100 mM NaCl and 10 mM β-mercaptoethanol.

Biochemical assays. The steady-state ATPase assay was performed as described previously[18] except that we used PEM100, 100 mM NaCl, 10 mM β-mercaptoethanol buffer. Microtubule pelleting assays were performed as described previously[27] and quantified using the Sypro Red fluorescence dye staining method described above. All assays, including microtubule gliding, were carried out at 25 °C.

***S. pombe* microtubules.** *S. pombe* microtubules were assembled from *S. pombe* tubulin (5 μM) in PEM100, 1 mM GMP–CPP for 1 h at 4 °C and then 1.5 h at 30 °C. Note that *S. pombe* microtubules cannot be stabilized with paclitaxel; therefore GMP–CPP was used which leads to more nucleation events, and subsequently more numerous but shorter microtubules at a given tubulin concentration. To generate plus-end labels, EGFP–*S. pombe* microtubules polymerized from 5 μM tubulin were incubated with 0.4 μM N-ethylmaleimide-modified pig-brain tubulin and 0.8 μM rhodamine-labelled bovine brain tubulin (Cytoskeleton) in PEM100, 1 mM GMP–CPP for 30 min at 30 °C. The capped microtubules were pelleted, resuspended in PEM100, 1 mM GMP-CPP, 20 μM paclitaxel, and stored at 30 °C. Pig-brain microtubule polymerization is described in the Supplementary Information, Methods.

Microtubule gliding assay. Microtubules and Klp2 proteins were premixed and incubated at 25 °C in PEM100, 100 mM NaCl, 10 mM β-mercaptoethanol, 10 mg ml^{-1} BSA and 20 μM paclitaxel, 1 mM GMP-CPP, 4 mM ATP, Oxygen scavenger (20 mM glucose, 0.2 mg ml^{-1} catalase, 0.4 mg ml^{-1} glucose oxidase) and an ATP regeneration system (10 mM phosphocreatine, 50 μg ml^{-1} creatine phosphate-kinase). The assay mix was then flowed into the chamber and frames acquired every 3 s using a ×60 oil NA 1.4 objective on a Olympus DeltaVision RT (API) equipped with a DAPI-FITC-Rhod/TR-Cy5 filter set (Chroma) and a Coolsnap HQ camera.

23. Erdeniz, N., Mortensen, U. H. & Rothstein, R. Cloning-free PCR-based allele replacement methods. *Genome Res.* **7,** 1174–1183 (1997).
24. Davis, A., Sage, C. R., Wilson, L. & Farrell, K. W. Purification and biochemical characterization of tubulin from the budding yeast *Saccharomyces cerevisiae*. *Biochemistry* **32,** 8823–8835 (1993).
25. Walker, R. A. *et al.* Dynamic instability of individual microtubules analyzed by video light microscopy: rate constants and transition frequencies. *J. Cell Biol.* **107,** 1437–1448 (1988).
26. McClelland, S. E. *et al.* The CENP-A NAC/CAD kinetochore complex controls chromosome congression and spindle bipolarity. *EMBO J.* **26,** 5033–5047 (2007).
27. Lockhart, A. & Cross, R. A. Origins of reversed directionality in the ncd molecular motor. *EMBO J.* **13,** 751–757 (1994).

nature cell biology

DOI: 10.1038/ncb1878

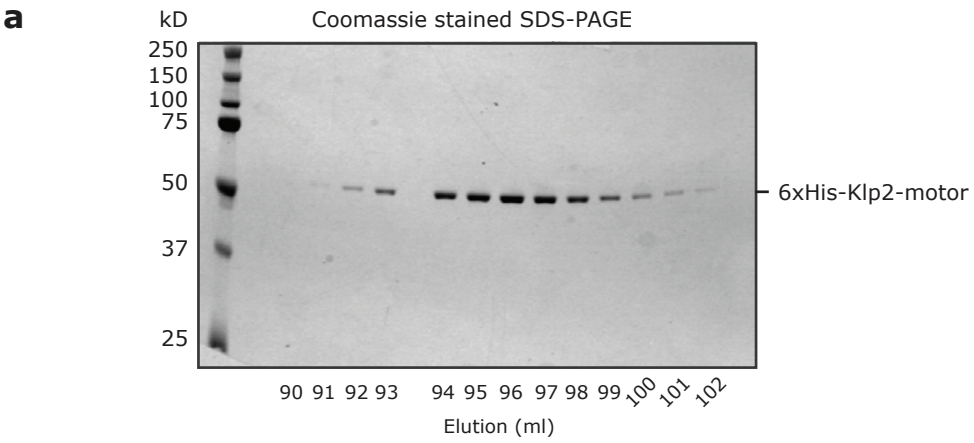

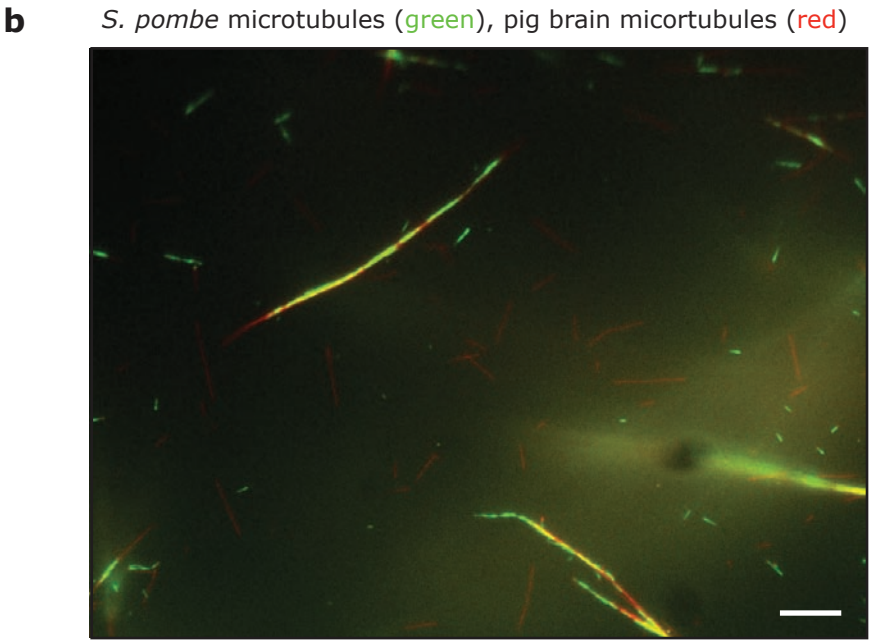

Figure S1 a, Fractions of the single-peak elution from the size exclusion chromatography of the purified Klp2-motor protein performed in PEM100 plus 100 mM NaCl. Note that the A_{280} trace showed no proteins eluting at any other positions on the column. The measured stokes radius for the Klp2-motor was 47Å, consistent with a homodimeric species. **b,** Representative images of the microtubule-motor structures that formed after 20 mins when Klp2-full length (100 nM) was mixed with 200 nM of *S. pombe* EGFP-microtubules and 200 nM Rhodamine-labelled pig-brain microtubules (PEM100 plus 100 mM NaCl, pH6.8) and the mixture added to a flow cell. Scale bar = 10 μm.

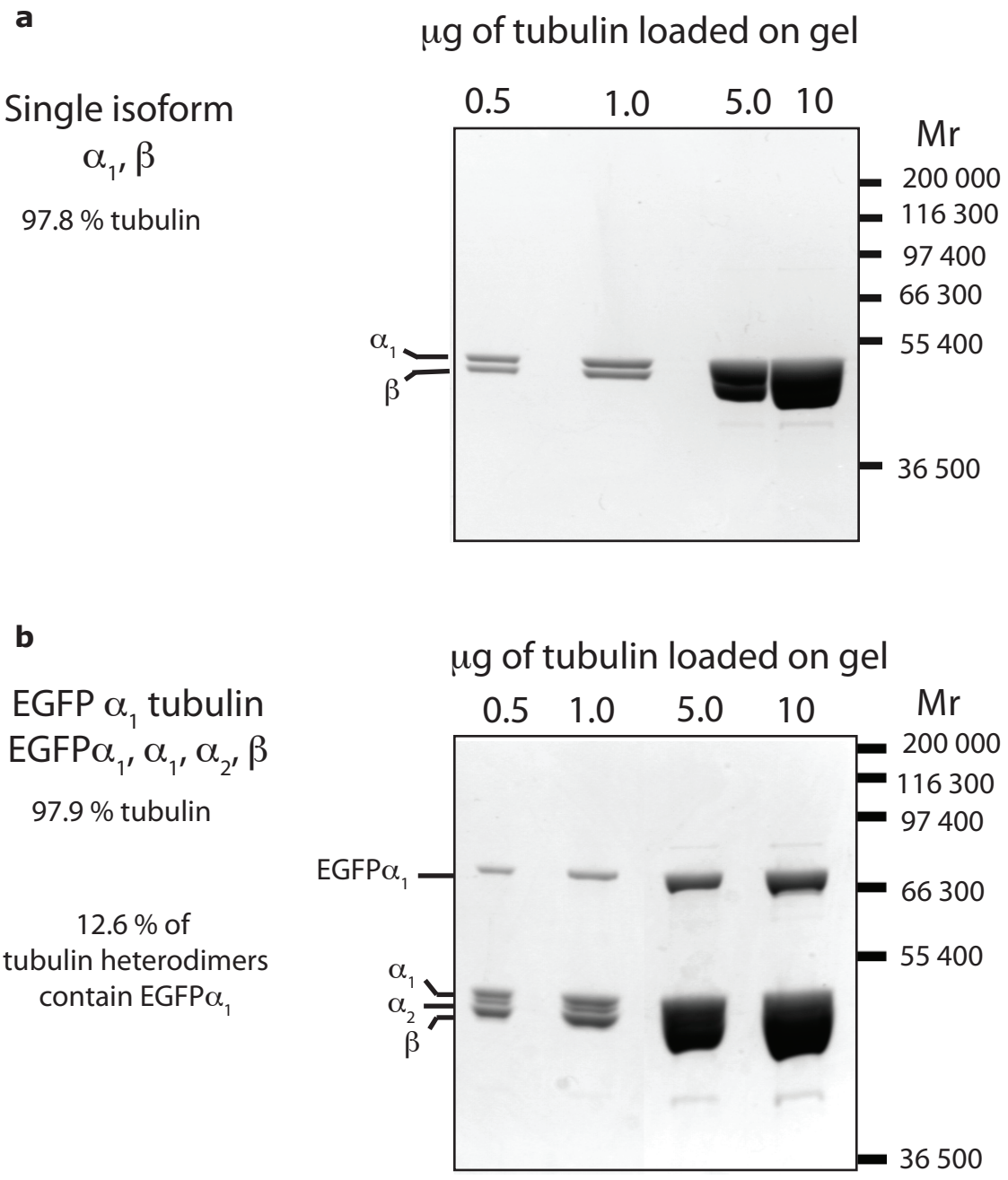

Figure S2 Coomassie stained SDS-PAGE of purified *S. pombe* tubulin **a,** Single isoform *S. pombe* tubulin and **b,** EGFPα_1 tubulin. This corresponds to Fig. 2b.

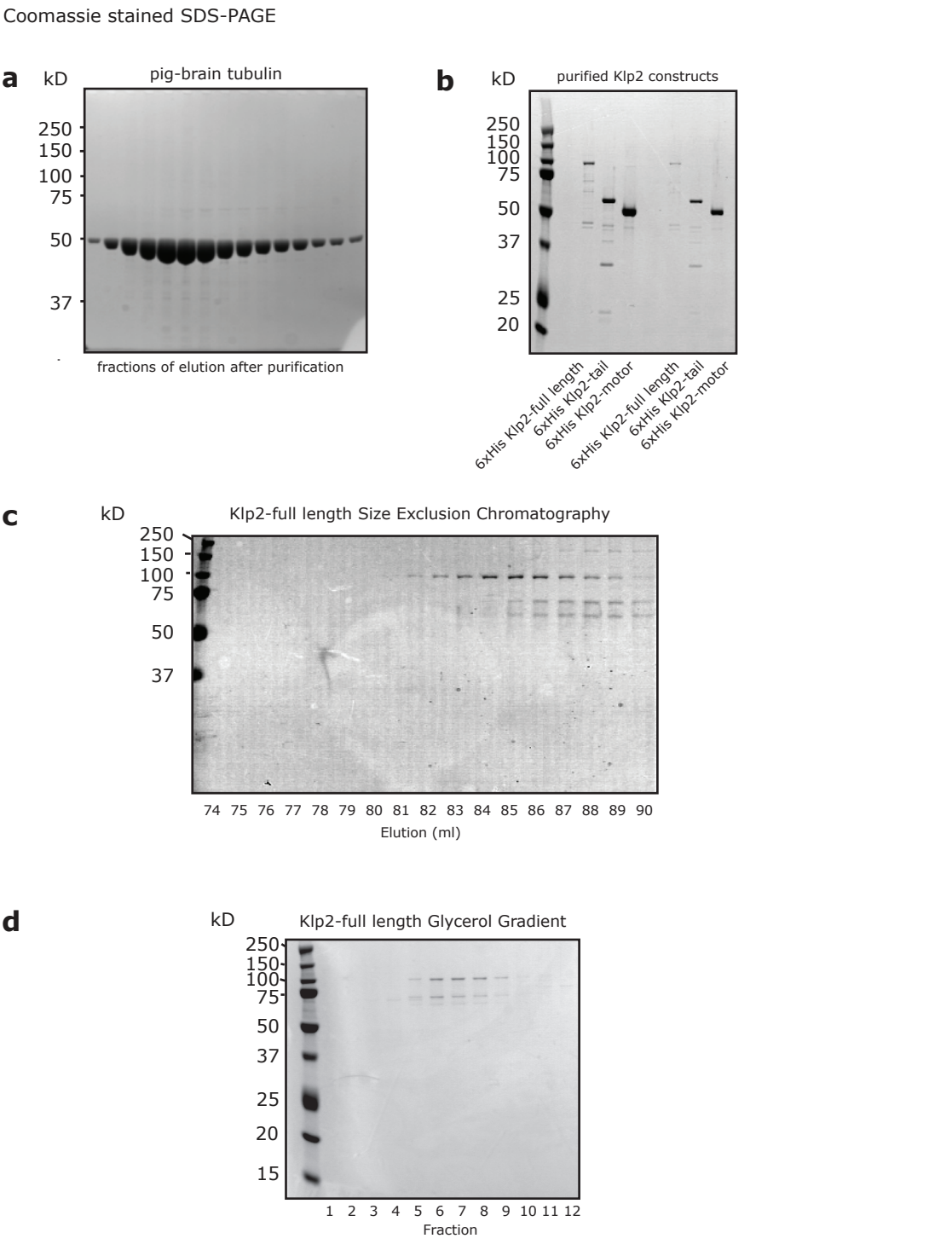

Figure S3 Coomassie stained SDS-PAGE of **a,** Purified pig-brain tubulin (corresponds to Fig. 1f) **b,** Purified Klp2 recombinant protein constructs (corresponds to Fig. 2b) **c,** Full-length Klp2 size exclusion chromatography (corresponds to Fig. 1d, upper panel) and **d,** Full-length Klp2 glycerol gradient (corresponds to Fig. 1d, lower panel).

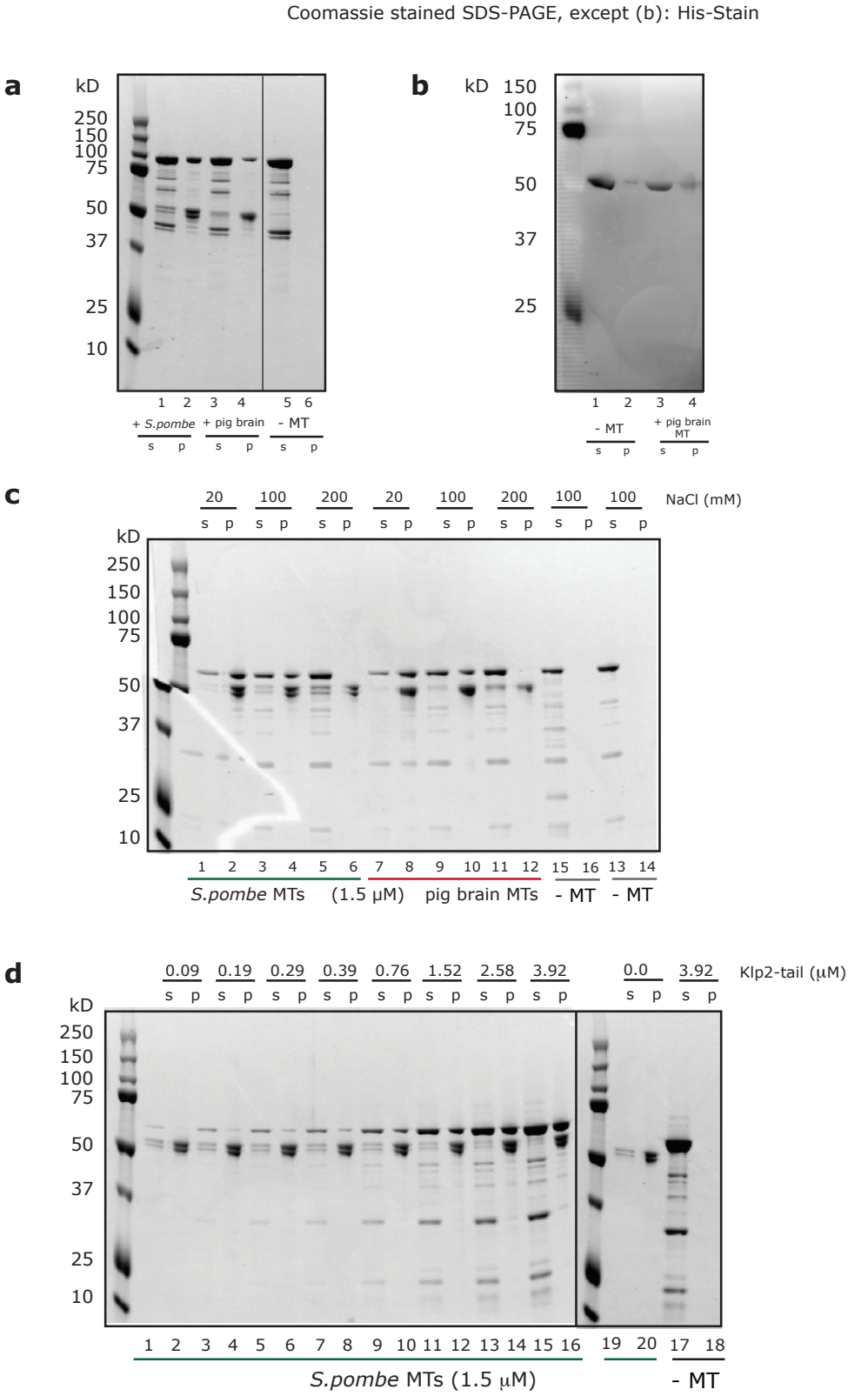

Figure S4 Microtubule co-pelleting assays, SDS-PAGE stained with His-stain **b,** Klp2-motor (corresponds to Fig. 2d), or Coomassie **a,** Full-length Klp2 (corresponds to Fig. 2c), **c,** Klp2-tail, ionic strength dependent binding, (corresponds to Fig. 2e) and **d,** Klp2-tail titration (corresponds to Fig. 2g).

Supplementary Movie Legends
Time-lapse and scale as indicated in the movies.

Movie S1 Microtubule gliding assay using polarity-marked rhodamine-labaled pig brain microtubules showing that full length Klp2 is a minus-end directed molecular motor protein.

Movie S2 Microtubule gliding assay using polarity-marked *S. pombe* EGFP microtubules (only the green, EGFP channel is shown). The dispersion of two parallel microtubule bundles is shown. Note that the microtubules all move uni-directionaly out of the bundle structure, which fully disperses during the course of the movie showing that all microtubules were parallel. This movie corresponds to Fig. 3a.

Movie S3 Microtubule gliding assay using polarity-marked *S. pombe* EGFP microtubules showing the dispersion of a parallel microtubule bundle. Both the EGFP channel (microtubules) and Rhodamine channel (Paclitaxel stabilized Rhodamine-labelled pig brain tubulin – microtubule plus-end caps) are shown. Note that the microtubules all move uni-directionaly out of the bundle structure. This movie corresponds to Fig. 3b.

Movie S4 Microtubule gliding assay using polarity-marked *S. pombe* EGFP microtubules showing the dispersion of a non-parallel unsorted microtubule bundle. Both the EGFP channel (microtubules) and Rhodamine channel (taxol stabilized Rhodamine-labelled pig brain tubulin) are shown. Note that the microtubules move in both directions within the bundle structure. This movie corresponds to Fig. 4d.

Movie S5 Microtubule gliding assay using polarity-marked *S. pombe* EGFP microtubules showing the dispersion of a parallel microtubule bundle. Both the EGFP channel (microtubules) and Rhodamine channel (taxol stabilized Rhodamine-labelled pig brain tubulin) are shown. Note that the microtubules all move uni-directionaly out of the bundle structure. This movie corresponds to Fig. 3e.

Movie S6 Microtubule gliding assay using polarity-marked *S. pombe* EGFP microtubules showing the dispersion of a parallel microtubule bundle. Microtubules and Klp2 motors were mixed in solution and then added to a flow cell at T=9 min. At the start the movie a microtubule array composed of two parallel microtubule bundles is visible in the centre of the field. Each bundle contains microtubules with their plus-ends exclusively orientated towards the distal ends of the array. After 2 min, and then 3 min, additional bundles land on the surface. These are both parallel bundles (now to the left of the large array) that disperse during the course of the movie. This movie corresponds to Fig. 4f and both the EGFP channel (microtubules; green) and Rhodamine channel (Paclitaxel stabilized Rhodamine-labelled pig brain tubulin; red) are shown.

Movie S7 Representative movie of Klp2-GFP (green) localization in living *S. pombe* cells. Movie showing stack of frames through the z-axis (step size = 0.2 μm). Note the localization of Klp2-GFP to bright foci as previously described (Janson et al., 2007) which represent the microtubule plus-ends. In addition, Klp2-GFP signal is clearly visible along the microtubule demonstrating that Klp2 is not restricted to only plus-ends, but also binds the microtubule lattice in *S. pombe* cells.

Supplementary Methods

Klp2 purification. Full-length *KLP2* cDNA was PCR amplified from a *S. pombe* cDNA library and cloned into the pET-28a(+) expression vector (Novagen). Deletion constructs were subcloned from that vector. The recombinant N-terminal hexa-histidine tagged fusion proteins were expressed in *E. coli* BL21-CodonPlus®(DE3)-RIPL Competent Cells (Stratagene) induced with 0.5 mM IPTG for 16 h at 15 °C. Harvested cells were resuspended in buffer A (50 mM sodium phosphate buffer pH 7.4, 2 mM $MgCl_2$, 10 mM 2-Mercaptoethanol, 0.1 mM ATP containing 50 mM NaCl and protease inhibitors (Roche), and lysed in 0.05 % vol/vol Triton X-100 (Sigma) and 0.1 mg/ml Lysozyme (Sigma) for 30 min at 4 °C. Cleared lysates were precipitated by adding 0.404 g/ml Ammonium sulfate (Sigma) and incubating for 1 h at 4 °C. The spun down pellet was resuspended in buffer A containing 300 mM NaCl, 10 mM ATP, 10 mM $MgCl_2$, 1 % vol/vol CHAPS (Sigma and protease inhibitors (Roche) and loaded onto a HisTrapHP column (GE Healthcare). The column was washed with buffer A containing 300 mM NaCl and 20 mM imidazole. Proteins were eluted in buffer A containing 300 mM NaCl and 85 mM imidazole; then desalted into PEM100, 100 mM NaCl, 10 mM β-mercaptoethanol, and snap-frozen in liquid nitrogen. Drosophila kinesin-1 was purified using the same method.

Rhodamine labeled pig-brain microtubules. Microtubules were either polymerized at 5 μM pig-brain tubulin, 0.6 μM rhodamin-labeled bovine-brain tubulin in PEM100, 1 mM GMP-CPP for 1.5 h at 30 °C or at 38 μM pig-brain tubulin in PEM100, 1 mM GTP for 20 min at 37 °C and then stabilized with 20 μM paclitaxel. Minus-end labeled pig-brain microtubules were generated by first polymerizing microtubule seeds from 20 μM pig-brain tubulin and 40 μM rhodamine-labeled bovine tubulin in PEM100, 1 mM GMP-CPP for 10 min at 37 °C. Then the seeds were diluted and microtubules polymerized at 23 μM pig-brain tubulin, 14 μM N-ethylmaleimide-modified pig-brain tubulin, 3.3 μM rhodamine-labeled bovine-brain tubulin in PEM100, 1 mM GTP and stabilized by the addition of 20 μM paclitaxel.

Flow chamber preparation. Coverslips were incubated in 10 M NaOH for ½ h and repeatedly sonicated together with slides (both Menzel Gläser) in detergent solution (2.8 ml/l Neutracon, Decon), followed each time by extensive rinsing with ddH_2O.

Flow chambers were assembled with < 0.5 mm grease as spacer resulting in 3 to 5 μl volume.

Gliding assay analysis. Raw data was processed by ImageJ software, microtubule movements were analyzed with the "MultipleKymograph' plug-in for ImageJ (http://www.embl.de/eamnet/html/body_kymograph.html). Average microtubule gliding velocities and standard deviations were obtained from velocity histograms generated from at least 50 microtubules.

Live cell imaging of *S. pombe* cells. *S. pombe* strain McI322 (*h- leu1 ura4 his-D1 ade6-210 klp2+-GFP-ura4+;* gift of Richard McIntosh) was grown under standard conditions. Cells were imaged at 26ºC on a Deltavision RT microscope using a 100x oil NA1.4 objective and an FITC filter set (API). Images were deconvoved using softworx software.

nature cell biology

The Patched dependence receptor triggers apoptosis through a DRAL–caspase-9 complex

Frédéric Mille[1,3], Chantal Thibert[1,3], Joanna Fombonne[1], Nicolas Rama[1], Catherine Guix[1], Hideki Hayashi[2], Véronique Corset[1], John C. Reed[2] and Patrick Mehlen[1,4]

Sonic hedgehog (Shh) and its main receptor, Patched (Ptc), are implicated in both neural development and tumorigenesis[1,2]. Besides its classic morphogenic activity, Shh is also a survival factor[3,4]. Along this line, Ptc has been shown to function as a dependence receptor; it induces apoptosis in the absence of Shh, whereas its pro-apoptotic activity is blocked in the presence of Shh[5]. Here we show that, in the absence of its ligand, Ptc interacts with the adaptor protein DRAL (downregulated in rhabdomyosarcoma LIM-domain protein; also known as FHL2). DRAL is required for the pro-apoptotic activity of Ptc both in immortalized cells and during neural tube development in chick embryos. We demonstrate that, in the absence of Shh, Ptc recruits a protein complex that includes DRAL, one of the caspase recruitment (CARD)-domain containing proteins TUCAN (family member, 8) or NALP1 (NLR family, pyrin domain containing 1) and apical caspase-9. Ptc triggers caspase-9 activation and enhances cell death through a caspase-9-dependent mechanism. Thus, we propose that in the absence of its ligand Shh the dependence receptor Ptc serves as the anchor for a caspase-activating complex that includes DRAL, and caspase-9.

There are now more than a dozen identified dependence receptors, which include DCC[6] (deleted in colorectal cancer), UNC5H (uncoordinated 5 homologue), some integrins, neogenin, p75NTR (p75 neurotrophin receptor), RET (rearranged during transfection), ALK (anaplastic lymphoma kinase), EphA4 (ephrin type A receptor 4) and TrkC (tyrosine kinase receptor C)[7–10]. They share several features in common (see reviews)[7,8]: (i) these receptors create cellular states of dependence on their respective ligands as they induce programmed cell death in the absence of their ligands and this pro-apoptotic activity is inhibited in the presence of their ligands; (ii) these receptors are typically involved in both neural development and neoplasia; (iii) apoptosis induction requires a caspase-cleavage site in the intracytoplasmic domain.

Ptc fulfills all of these criteria as a candidate dependence receptor. The expression of Ptc induces apoptosis, which is suppressed by its ligand, Shh. Besides its key role during development, Ptc is a tumour suppressor and mutations of Ptc are associated with neoplasia, especially basal cell carcinomas[11] and medulloblastomas[12]. Moreover, apoptosis induction by Ptc requires the caspase-cleavage site at Asp 1392 (ref. 5).

However, the mechanism by which the withdrawal of trophic ligands from their respective dependence receptors leads to apoptosis is largely unknown. Previous studies on DCC have suggested that some of these dependence receptors may recruit a caspase-activating complex[13]. This complex, comprising the initiator apical caspase-9, is independent of the two main apoptosis-related caspase-activating complexes, the DISC (death-induced signalling complex) and the apoptosome[14]. Yet, the precise identification of such an apoptosis-inducing dependence receptor complex has been unsuccessful so far.

In an attempt to identify pro-apoptotic signalling components downstream of Ptc, a two-hybrid screen was performed using the pro-apoptotic domain of Ptc (residues 1165–1392; ref. 5) as bait and a human embryonic brain cDNA library as prey (Fig 1a). Of the seven putative Ptc interactors (Supplementary Information, Fig S1a), we focused our attention on DRAL. Indeed, DRAL is a multifunctional protein that consists of four and a half LIM protein–protein interaction domains[15]. DRAL participates in cellular processes that include regulation of gene expression, cytoarchitecture, cell adhesion, cell mobility, signal transduction and cell survival[15]. Interestingly, DRAL overexpression seems to be pro-apoptotic in a variety of cells, however, the mechanism for DRAL-induced apoptosis is unknown[16]. DRAL has also been shown to interact with TUCAN[17], which was proposed to function as an adaptor protein for caspase-1 (ref. 18) or caspase-9 (ref. 19).

To further confirm the interaction between the Ptc pro-apoptotic domain and DRAL, a targeted two-hybrid screen was performed. As shown in Fig. 1b, residues 1165–1392 of Ptc and DRAL interact in yeast. To monitor whether this interaction could be observed in mammalian cells, co-immunoprecipitation studies were performed on

[1]Apoptosis, Cancer and Development Laboratory, Equipe labellisée 'La Ligue', CNRS UMR5238, Université de Lyon. Centre Leon Bérard, 69008 Lyon, France.
[2]Burnham Institute for Medical Research, 10901 North Torrey Pines Road, La Jolla, CA 92037, USA.
[3]These authors contributed equally to this work.
[4]Correspondence should be addressed to P.M. (e-mail: mehlen@lyon.fnclcc.fr)

Received 12 December 2008; accepted 2 March 2009; published online 24 May 2009; DOI: 10.1038/ncb1880

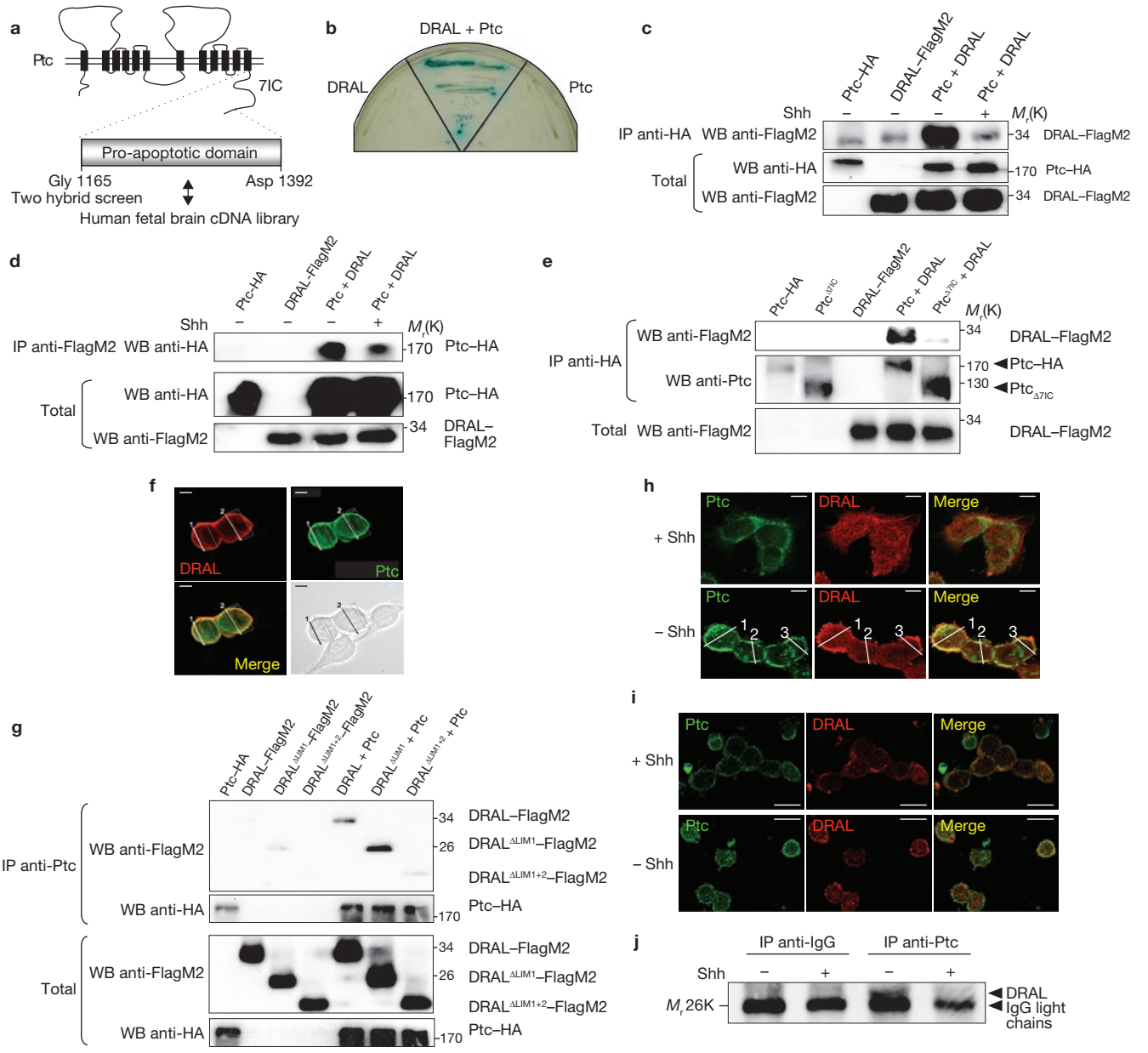

Figure 1 The pro-apoptotic domain of Ptc interacts with DRAL. (**a**) A two-hybrid screen with the pro-apoptotic domain of Ptc-1. 7IC refers to the seventh intracellular domain. (**b**) The Ptc–DRAL interaction was confirmed by a direct two-hybrid screen. AH109 yeasts were transformed with a mock Gal4BD plasmid and a Gal4AD plasmid fused with DRAL (DRAL), a mock Gal4AD plasmid and a Gal4BD plasmid fused with the Ptc pro-apoptotic domain (Ptc) or a Gal4AD plasmid fused with DRAL and a Gal4BD plasmid fused with Ptc (DRAL + Ptc). (**c**) Co-immunoprecipitations were performed on HEK293T cells transiently expressing Ptc–HA (Ptc) or DRAL–FlagM2 (DRAL) or Ptc–HA and DRAL–FlagM2 (Ptc + DRAL) in the absence (–) or presence (+) of Shh (300 ng ml^{-1}). Pulldown with an anti-HA antibody was used to immunoprecipitate (IP) Ptc and DRAL was revealed by western blotting (WB) using an anti-FlagM2 antibody. Western blotting on lysates before pulldown are shown (Total). (**d**) The same experiment as in **c** was performed, except DRAL pulldown was performed with an anti-FlagM2 antibody and specific Ptc binding was revealed using an anti-HA antibody. See Supplementary Information, Fig. S7a for full blots. (**e**) DRAL co-immunoprecipitates with Ptc, but not with Ptc lacking its seventh intracellular domain (Ptc$^{\Delta 7IC}$). Pulldown results of Ptc in lysates from cells expressing DRAL–FlagM2 (DRAL) and Ptc–HA (Ptc) or Ptc$^{\Delta 7IC}$ are shown. DRAL was revealed by western blotting using an anti-FlagM2 antibody. (**f**) Co-localization of Ptc and DRAL in transiently transfected HEK293T cells. Cells were stained with anti-Ptc (Ptc, green) and anti-DRAL (DRAL, red) antibodies. A representative field from three independent experiments is shown. See Supplementary Information, Fig. S1c for merge fluorescence analysis at the plasma membrane at positions 1 and 2. Phase contrast of transfected cells is shown (bottom right). (**g**) Co-immunoprecipitation of Ptc with DRAL deletion mutants was performed as described in **c** on cells expressing Ptc–HA and DRAL–FlagM2, DRAL$^{\Delta Lim1}$–FlagM2 or DRAL$^{\Delta LIM1+2}$–FlagM2. The presence of DRAL was revealed using an anti-FlagM2 antibody. (**h**, **i**) Co-localization of endogenous Ptc and DRAL in Daoy medulloblastoma cells (**h**) or in primary cultured cerebellar granule neurons (**i**), in the presence or absence of Shh. Cells were stained as described in **f**. See Supplementary Information, Fig. S1e for merge fluorescence analysis at positions 1, 2 and 3 in **h**. (**j**) Immunoprecipitation on mice cortex of E16.5 embryos incubated in absence (–) or presence (+) of Shh was performed using an anti-Ptc antibody (or IgG as a control) and DRAL was detected by immunoblotting using an anti-DRAL antibody. Scale bars, 5 μm in **f**, **h** and **i**.

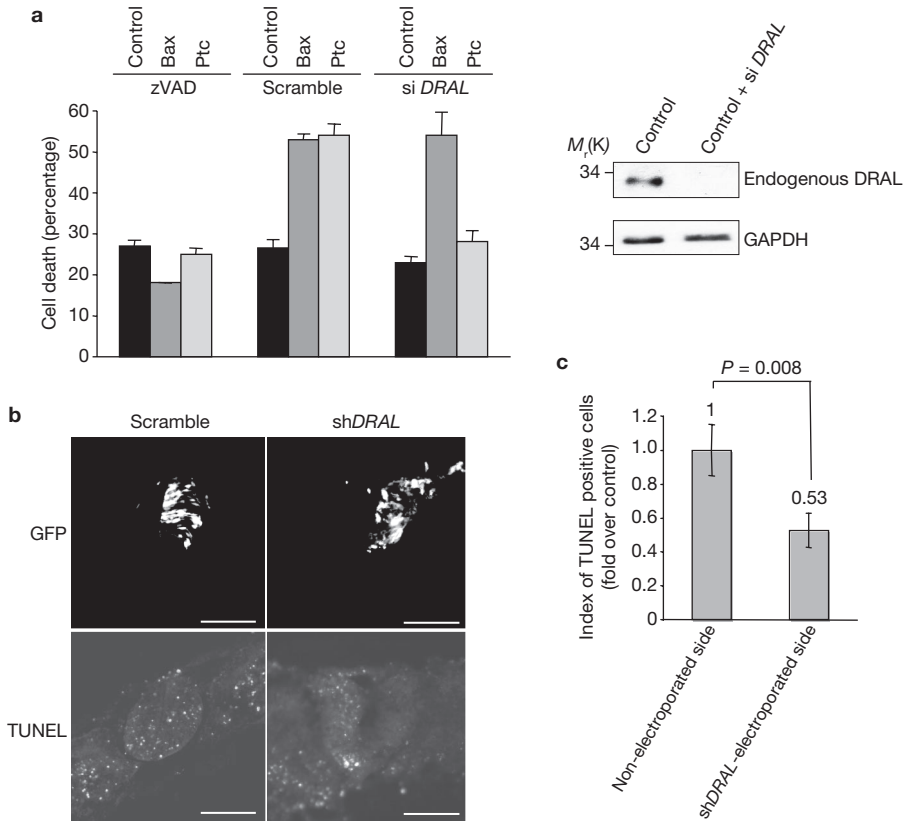

Figure 2. DRAL is required for Ptc pro-apoptotic activity. (**a**) HEK293T cells were transiently transfected with an empty vector, scrambled siRNA (scramble) or *DRAL* siRNA (si *DRAL*). At 48 h after siRNA transfection, cells were transfected a second time with an empty vector (control), a Bax encoding vector (Bax) or a Ptc encoding vector (Ptc) in the absence or presence of caspase inhibitor zVAD-fmk (zVAD). Cell death was analysed 24 h after the second transfection using trypan blue exclusion as described peviously[5] (data are mean ± s.d.). *DRAL* siRNA efficiency in reducing endogenous DRAL expression was shown by western blotting using an anti-DRAL antibody. An anti-GAPDH immunoblot is shown as a control of specificity and loading. (**b**) DRAL function in Ptc-induced apoptosis was also addressed *in vivo* in the absence of Shh, as achieved in chick embryos *in ovo* at E1.5 by removal of the caudal part of the Hensen node by microsurgery. Before the microsurgery, the left side of the neural tube was electroporated with GFP and *DRAL* shRNA or scrambled shRNA. Electroporation efficiency is shown (top; GFP) as is TUNEL staining of the same section (bottom; TUNEL). Scale bar, 100 μm. (**c**) The index of TUNEL-positive cells is represented as the ratio between the number of cells stained under the *DRAL* shRNA condition (sh*DRAL*-electroporated side) to the number of cells stained under the control condition (Non-electroporated side) counted over 15 sections. Data are mean ± s.e.m., $P = 0.008$ as determined by U test. Note that *DRAL* shRNA electroporation alone or forced expression of DRAL had no significant effect on cell death (Supplementary Information,. Fig. 2e, f).

HEK293T cells co-transfected with tagged Ptc and DRAL. As shown in Fig. 1c, full-length DRAL was pulled down by full-length Ptc. When Shh was added to the culture medium, the Ptc–DRAL interaction was strongly decreased (Fig. 1c). Similar interaction data were observed when the reverse immunoprecipitation was performed (Fig. 1d). Moreover, as expected from the two-hybrid screen, the seventh intracellular region of Ptc, which includes the pro-apoptotic domain, was sufficient to interact with DRAL (Supplementary Information, Fig. S1b), whereas deletion of this region prevented the Ptc– DRAL interaction (Fig. 1e).

Confocal analysis of the two co-expressed full-length proteins showed co-localization of Ptc and DRAL in HEK293T cells (Fig. 1f; Supplementary Information, Fig. S1c). In an attempt to define the region of DRAL important for the Ptc–DRAL interaction, we tested whether DRAL lacking LIM domains 1 and 2 could be pulled down by Ptc. While deletion of the LIM1 domain had no effect on the Ptc–DRAL interaction, deletion of both LIM1 and LIM2 domains, or deletion of the LIM2 domain only, strongly decreased the ability of DRAL to interact with Ptc (Fig. 1g; Supplementary Information, Fig. S1d). Thus, both in yeast and in mammalian cells, Ptc interacts through its seventh intracellular domain with a region of DRAL that includes the LIM2 domain.

To address whether this interaction may be observed not only with ectopically expressed proteins but also with endogenous proteins, Ptc–DRAL co-localization was analysed in the Daoy medulloblastoma cell line in the absence or presence of Shh. In the presence of Shh, DRAL was mainly cytoplasmic and failed to co-localize with Ptc, in the absence of Shh, DRAL and Ptc clearly co-localized at the membrane of these cells (Fig. 1h; Supplementary Information, Fig. S1e). Similar results were obtained with primary cultured cerebellar granule cells (CGN; Fig. 1i; Supplementary Information, Fig. S1f). We then addressed the *in vivo* interaction of Ptc and DRAL using co-immunoprecipitation in mouse developing brain extract. Semi-dissociated embryonic day (E) 16.5 brains were either left untreated or exposed to Shh, and then further processed for Ptc immunoprecipitation. In the absence of Shh treatment, an anti-Ptc antibody pulled down DRAL, whereas Ptc–DRAL association was not observed with an unrelated isotypic antibody, confirming the specificity of the interaction. Addition of Shh inhibited

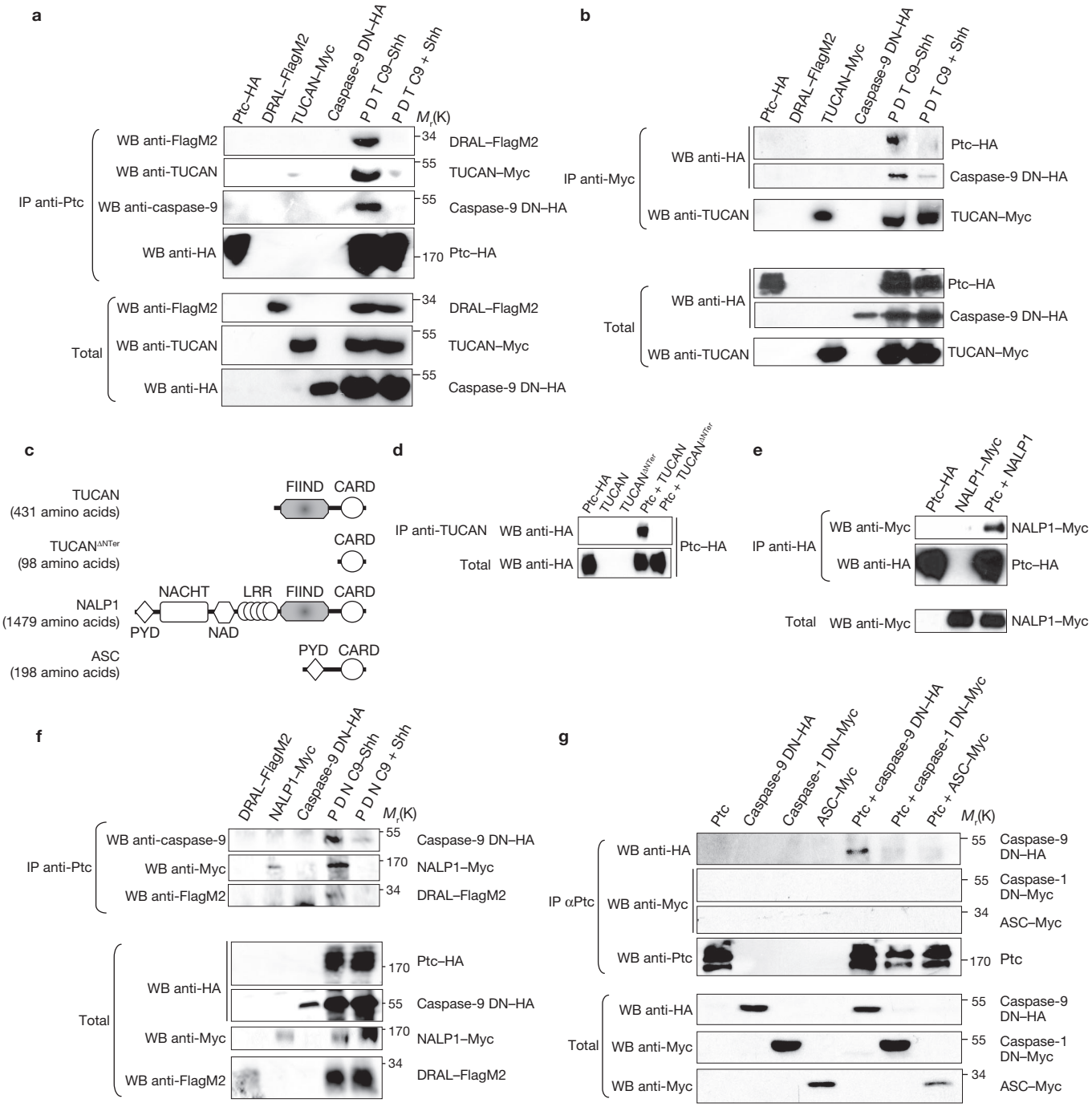

Figure 3 Ptc–DRAL serves as a platform to recruit TUCAN or NALP1 and caspase-9. (**a**) Ptc pulldown in HEK293-EcrShh cells transfected with either Ptc (Ptc–HA), DRAL (DRAL–FlagM2), TUCAN (TUCAN–Myc) or caspase-9 dominant negative (caspase-9 DN–HA) alone or the four constructs together in the absence (P D T C9 – Shh) or presence (P D T C9 + Shh) of Shh. DRAL, TUCAN and caspase-9 interaction with Ptc were revealed by anti-FlagM2, anti-Myc or anti-caspase-9 immunoblots, respectively (IP, immunoprecipitation; WB, western blotting). See Supplementary Information, Fig. S7b for full blots. (**b**) TUCAN immunoprecipitation from HEK293T cells transfected with Ptc–HA, DRAL–FlagM2, TUCAN–Myc or caspase-9 DN–HA alone or the four constructs together in the absence (P D T C9 – Shh) or presence (P D T C9 + Shh) of Shh. Ptc and caspase-9 were revealed after pulldown with an anti-HA immunoblot and TUCAN was revealed with an anti-TUCAN antibody (Total: immunoblots on lysate before pull-down). (**c**) Schematic representations of TUCAN, the TUCAN mutant deleted of its N-terminal domain (TUCAN$^{\Delta NTer}$), NALP1 and ASC. Note the FIIND domain homology between TUCAN and NALP1 in their N-terminal region. (**d**) TUCAN immunoprecipitation (using an anti-TUCAN antibody with an epitope in the CARD domain) in HEK293T cells transfected with an empty vector and Ptc (Ptc–HA), TUCAN (TUCAN), N-terminal-deleted TUCAN (TUCAN$^{\Delta Nter}$) or Ptc with either TUCAN (Ptc + TUCAN) or N-terminal-deleted TUCAN (Ptc + TUCAN$^{\Delta Nter}$). Ptc was revealed in pulldown experiments by anti-HA immunoblotting. (**e**) Ptc pulldown experiments in HEK293T cells transfected with an empty vector and Ptc (Ptc–HA) or NALP1 (NALP1–Myc) or Ptc and NALP1 (Ptc + NALP1). NALP1 pull-down with Ptc was revealed by immunoblotting using anti-Myc. (**f**) Co-immunoprecipitations were performed as in **a** except that TUCAN was replaced by NALP1 (NALP1–Myc). (**g**) Ptc pulldown experiments were performed on HEK293T cells transfected with Ptc (Ptc), caspase-9 DN (caspase-9 DN–HA), caspase-1 DN (caspase-1 DN–Myc) or ASC (ASC–Myc) alone or in combination with Ptc (Ptc + caspase-9 DN–HA; Ptc + caspase-1 DN–Myc; Ptc + ASC–Myc). Caspase-9, caspase-1 or ASC pulled down by Ptc were detected using anti-HA or anti-Myc antibodies. See Supplementary Information, Fig. S7c for full blots.

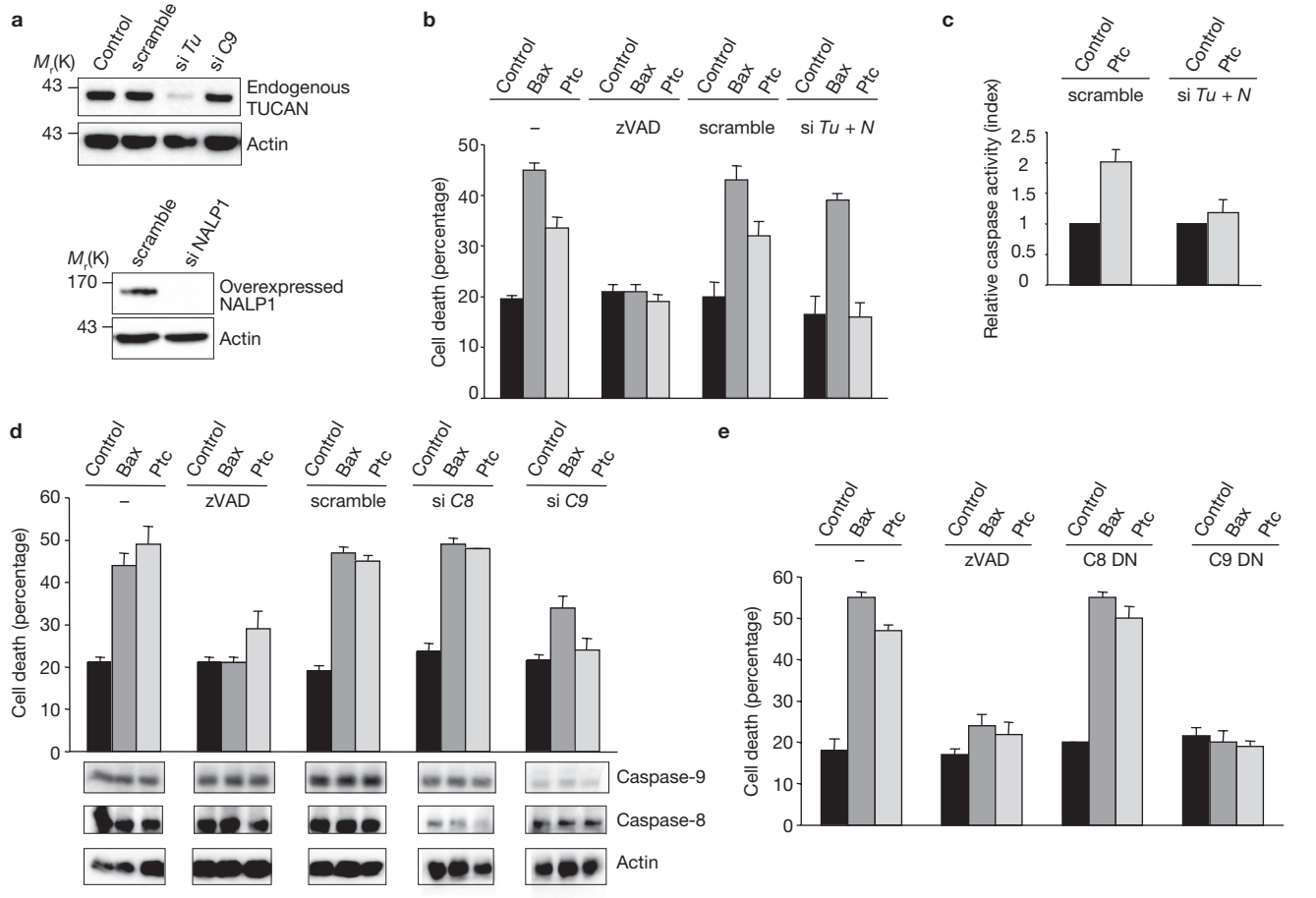

Figure 4 TUCAN/NALP1 and caspase-9 are required for Ptc-induced apoptosis. (**a**) *TUCAN* siRNA efficiency and specificity is shown by western blotting of endogenous TUCAN protein in HEK293T cells expressing scrambled siRNA (scramble), *TUCAN* siRNA (si *Tu*) or *caspase-9* siRNA (si *C9*). The same was done with NALP1, but *NALP1* siRNA efficiency was assessed in HEK293T cells overexpressing NALP1. An anti-actin immunoblot is shown as a control of specificity and loading. See Supplementary Information, Fig. S7d for full blots. (**b**) HEK293T cells were transfected with an empty vector (control), Bax or Ptc either without treatment (–) or in the presence of caspase inhibitor zVAD-fmk (zVAD), scrambled siRNA (scramble) or *TUCAN* siRNA plus *NALP1* siRNA (si *Tu* + *N*) and cell death was analysed using a trypan blue exclusion assay. (**c**) Ptc-induced caspase activation is inhibited by a combination of *TUCAN* siRNA plus *NALP1* siRNA as measured by relative caspase-3 activity. HEK293T cells were transfected with mock vector pcDNA3 (control) or with Ptc in the presence of scrambled siRNA (scramble) or *TUCAN* siRNA plus *NALP1* siRNA (si *Tu* + *N*). The index of relative caspase activity is presented as the ratio of the caspase activity of the sample to that measured in the control. Cell death was also compared in primary cultured cerebellar granule neurons from either a CBA/J or a C57Bl/6J genetic background when deprived of Shh. Whereas death of primary neurons was detected in the CBA/J culture, no cell death was detected in the C57Bl/6J culture (Supplementary Information, Fig. S3). (**d**) HEK293T cells were transfected with an empty vector (control), Bax or Ptc either without treatment (–) or in the presence of zVAD-fmk (zVAD), scrambled siRNA (scramble), *caspase-8* siRNA (si C8) or *caspase-9* siRNA (si C9) and cell death was analysed using a trypan blue exclusion assay. *Caspase-8* and *9* siRNA efficiencies are shown by western blotting using anti-caspase-8 and 9 antibodies. An anti-actin western blot is shown as a control of specificity and loading. (**e**) HEK293T cells were co-transfected with an empty vector (control), Bax or Ptc plus either an empty vector (–), caspase-8 dominant-negative (C8 DN) or caspase-9 dominant-negative (C9 DN). Cell death was analysed as in **d**. In **b**–**e**, data are mean ± s.d., $n = 3$.

the association of DRAL with Ptc (Fig. 1j). Thus, Ptc directly interacts with DRAL both in cell culture and in the developing brain, and this interaction is prevented by Shh.

As a first assay to monitor the functional role of the Ptc–DRAL interaction, Ptc-induced cell death was assessed by Ptc transient expression in HEK293T cells[5] after DRAL gene silencing by short interfering RNA (siRNA). *DRAL* siRNA dramatically reduced endogenous DRAL expression in HEK293T cells, whereas the control siRNA did not (inset, Fig. 2a). Ptc-induced cell death was reduced when DRAL was downregulated by siRNA (Fig. 2a). In contrast to Ptc, overexpression of the classic cell-death inducer Bax triggered HEK293T cell death to a similar extent irrespective of *DRAL* siRNA expression. Thus, in immortalized cells, Ptc requires DRAL to trigger cell death.

We next analysed whether Ptc-induced cell death requires DRAL *in vivo*. Whereas it has been extensively demonstrated that Shh acts as a morphogen during nervous system development[1], several studies have shown that Shh may also act as a survival factor[4,20]. Consistently, it has been shown that the experimental withdrawal of Shh in chick embryos leads to massive death of neuroepithelial cells in the developing neural tube[3,20]. We have demonstrated that this survival activity is due to Shh-induced inhibition of Ptc pro-apoptotic activity[5]. In initial studies, we and others used surgical procedures to prevent Shh production by the notochord and floor plate. We investigated whether a similar effect could be observed by the ectopic expression of HHIP1 (hedgehog-interacting protein 1), a protein known to inhibit Shh signalling through direct interaction[21]. The left side of the developing

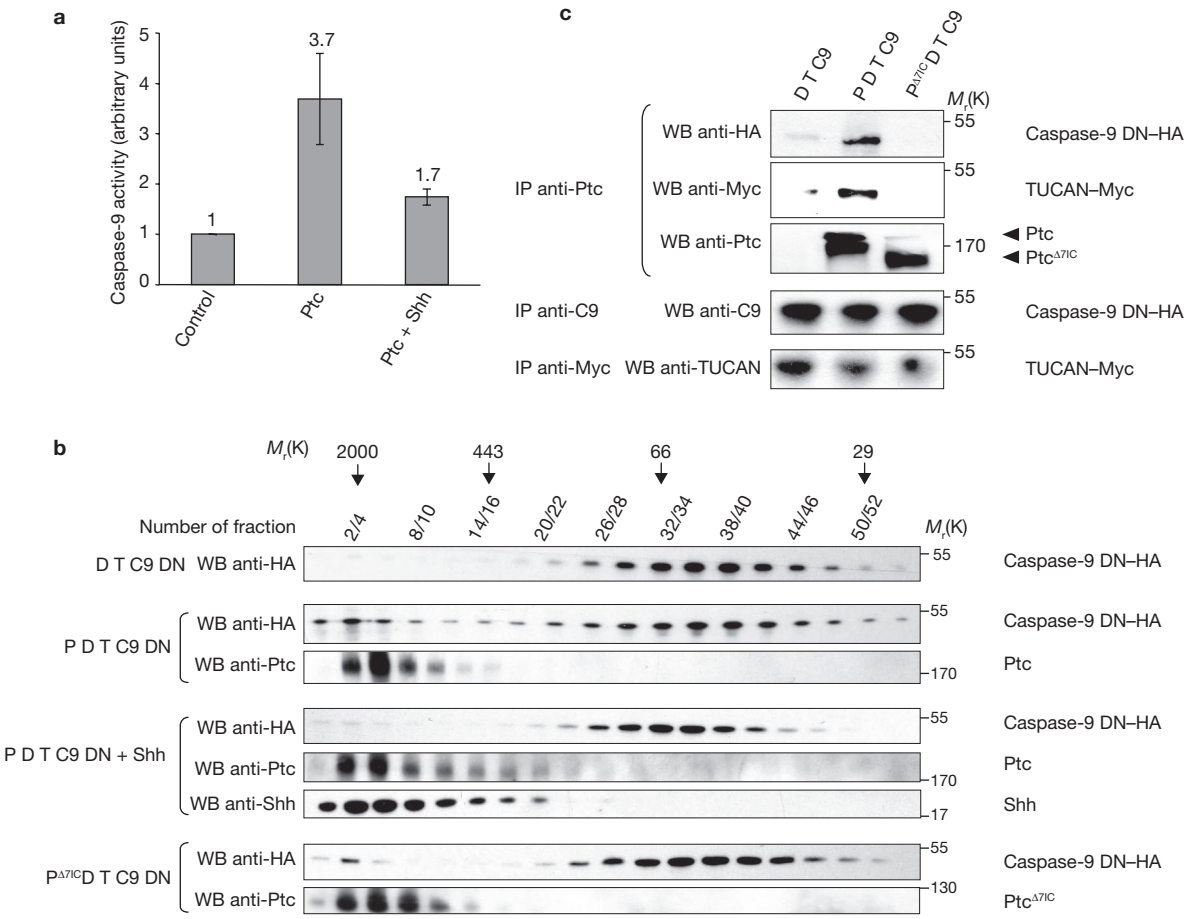

Figure 5 Ptc pro-apoptotic complex recruits and activates caspase-9. (**a**) HEK293-EcRShh cells were transfected with either an empty vector (control) or Ptc encoding vector in the absence (Ptc) or in the presence (Ptc + Shh) of Shh (induction with Muristerone A plus addition of 300 ng ml^{-1} of recombinant Shh). The cell lysates were subjected to a caspase-9 activity assay over time using the LEHD-AFC substrate of caspase-9. Data are mean ± s.d., $n = 4$. (**b**) HEK293-EcRShh cells were transfected with DRAL–FlagM2, TUCAN–Myc and caspase-9 dominant negative (DN)–HA vectors plus an empty vector (D T C9), Ptc vector in the absence of Shh (P D T C9) or in the presence of Shh (P D T C9 + Shh; induction by Muristerone A plus recombinant Shh), or Ptc deleted of its seventh intracellular domain (P$^{\Delta 7IC}$ D T C9). Cell lysates were separated by gel filtration chromatography. Fractions were then analysed by western blotting for caspase-9, Ptc and Shh. The numbers of the fractions and the fractions in which the molecular mass markers were eluted are shown. (**c**) The 20 first fractions were pooled and Ptc pulldown experiments were performed. Anti-HA and anti-Myc immunoblots showed that caspase-9 and TUCAN interact with Ptc in these high molecular weight fractions. The relative quantity of proteins of interest (caspase-9 and TUCAN) in cell lysates of each condition was checked by immunoprecipitation and western blotting with anti-caspase-9 and anti-TUCAN antibodies, respectively.

neural tube of HH11-13 chick embryos was co-electroporated *in ovo* with green fluorescent protein (GFP) and either a control or HHIP1 expression construct. Whereas GFP was detected after electroporation, a significant increase in apoptosis, measured by TUNEL (TdT-mediated dUTP nick end labelling) staining, was observed in HHIP1 electroporated neural tubes compared with mock electroporated embryos (as shown in Supplementary Information, Fig. S2a, b). To further confirm that this HHIP1-dependent cell death was related to the loss of Shh inhibition of Ptc-induced apoptosis, a dominant-negative mutant of Ptc[5] was co-electroporated with HHIP1. Consistent with our previous data[5], the Ptc dominant-negative mutant inhibited HHIP1-induced apoptosis (Supplementary Information, Fig. S2a, b). Thus, HHIP1 electroporation triggers Ptc-induced apoptosis *in vivo*. We then assessed the importance of DRAL in Ptc-induced cell death by co-electroporating HHIP1 with a DRAL short hairpin RNA (shRNA)-expressing construct that is effective at inhibiting chick DRAL expression (Supplementary Information, Fig. S2c). Whereas scrambled shRNA failed to suppress HHIP1-induced apoptosis, *DRAL* shRNA significantly inhibited HHIP1-induced apoptosis (Supplementary Information, Fig. S2a, b). Moreover, similar inhibition by *DRAL* shRNA was observed when electroporation of HHIP1 was performed more ventrally through the use of an electrode located below the neural tube (Supplementary Information, Fig. S2d). It is, however, intriguing to note that HHIP1-electroporations were associated with cell death occurring mainly in the middle third and the dorsal third of the neural tube, but only modestly in the third ventral neural tube. The discrepancy between this apparent dorsal cell death and the higher Shh level detected ventrally, raised the possible limitation of Shh titration by HHIP1. However, similar cell-death inhibition after *DRAL* shRNA electroporation was observed when Shh production was reduced using a surgical procedure[3,5] (Fig. 2bc). Thus, together these data support the view that cell death induced after inhibition of Shh in the developing neural tube requires DRAL.

DRAL has been shown to interact with TUCAN, a protein initially thought to bind to caspase-9 (ref. 19). Because caspase-9 has been

implicated in the pro-apoptotic activity of many dependence receptors[9,13], we explored whether TUCAN might be part of a Ptc–DRAL complex that could allow the recruitment of caspase-9, using co-immunoprecipitation experiments with HEK293 cells. As shown in Fig. 3a, Ptc immunoprecipitation resulted in the pulldown of DRAL, TUCAN and caspase-9. Similarly, TUCAN immunoprecipitation pulled down Ptc and caspase-9 (Fig.3b). Interestingly, the presence of Shh strongly inhibited the interaction between TUCAN and Ptc, while also decreasing the interaction between TUCAN and caspase-9 (Fig. 3ab). Thus, in the absence of the dependence ligand Shh, Ptc allows the recruitment of a complex that includes DRAL, TUCAN and caspase-9.

TUCAN is composed of two main domains: a FIIND domain located in the amino-terminal region and a CARD domain at the carboxyl terminus which is known to interact with caspases (see scheme, Fig. 3c). Interestingly, deletion of the N-terminal region of TUCAN is sufficient to abrogate the interaction of Ptc–DRAL with TUCAN (Fig. 3d). This N-terminal domain is closely related to a domain found in NALP1 (NLR family, pyrin domain containing 1; 66% homology in human), another CARD domain-containing protein known to recruit caspases that has been implicated in both cell death regulation and inflammation[22,23] (Fig. 3c). Using a similar co-immunoprecipitation approach, NALP1 was also pulled down with Ptc, but this interaction was strongly reduced in the presence of Shh (Fig. 3e, f). A control for specificity, ASC (apoptosis speck protein) a protein related to NALP1, failed to interact with Ptc (Fig. 3c, g). Interestingly, whereas TUCAN-knockdown by *TUCAN* siRNA expression (Fig. 4a), was not sufficient to fully and reproducibly inhibit Ptc-induced cell death (data not shown), *TUCAN* and *NALP1* siRNA co-expression completely inhibited the cell death observed after Ptc transfection in HEK293T cells (Fig. 4bc). Thus, NALP1 or TUCAN behave as adaptor proteins of the Ptc–DRAL complex, which includes caspase-9 and seems to be required for Ptc-induced cell death. Even though TUCAN and NALPs have been implicated in the classic survival pathway NF–κB (nuclear factor kappa-light-chain-enhancer of activated B cells) regulation[22,24] we were able to exclude a putative link between the NF-κB pathway and the regulation of Ptc pro-apoptotic activity (Supplementary Information, Fig. S4a–c). Moreover, because TUCAN and NALP1 have been shown to also interact with caspase-1 (refs 18, 22, 25), we next investigated the specificity of caspase-9 recruitment to Ptc. Although Ptc interacted with caspase-9 after expression in HEK293T cells, Ptc failed to pulldown caspase-1 (Fig. 3g). Thus, the Ptc–DRAL interaction represents an anchor for a specific TUCAN/NALP1-caspase-9-containing complex.

To assess the importance of this DRAL–TUCAN/NALP1–caspase-9 complex in Ptc-mediated cell apoptosis, we next assessed whether Ptc-induced apoptosis requires caspase-9. As shown in Fig. 4d, whereas Ptc-induced cell death in HEK293T cells (and Bax-induced cell death as a control) was not modulated by siRNA-induced caspase-8 knockdown, it was strongly inhibited by siRNA-induced caspase-9 knockdown (Fig.4d inset). Similar results were obtained when dominant-negative mutants for caspase-8 and caspase-9 were used instead of siRNAs (Fig. 4e) or when using chemical caspase inhibitors (data not shown). To further address the requirement of caspase-9 in a biological system where endogenous Ptc induces apoptosis after Shh deprivation, developing neural tubes of HH11-13 chick embryos were co-electroporated *in ovo* by GFP and a HHIP1 expression construct together with a dominant-negative mutant for caspase-9. While HHIP1 electroporation triggered apoptosis, co-electroporation with the mutant strongly inhibited Ptc-mediated apoptosis (Supplementary Information, Fig. S5a, b).

Given that Ptc interacts with caspase-9 (through a DRAL–TUCAN/NALP1 complex) and that Ptc requires caspase-9 to trigger apoptosis both in immortalized cells in culture and in the developing neural tube *in vivo*, we hypothesized that ligand-free Ptc activates caspase-9. To investigate this possibility, we analysed the activity of caspase-9 by measurement of LEHD–AFC substrate cleavage in HEK293 cells transfected with Ptc. As shown in Fig. 5a, Ptc triggered caspase-9 activity whereas the presence of Shh strongly decreased this Ptc-induced effect. We next analysed whether this activation is associated with the formation of large caspase-9-containing complexes, by analogy to other initiator caspase-activating complexes[26]. To this end, gel-exclusion chromatography analysis of caspase-9 was performed using lysates from control and Ptc-expressing HEK293 cells. Although in the absence of Ptc, caspase-9 was detected at a small exclusion size (relative molecular mass, M_r, 50,000–100,000, 50K–100K), the presence of Ptc triggered a shift of caspase-9 toward the higher molecular weight fractions, such that caspase-9 was also detected to have M_r in the 1000K-2000K size fraction (Fig. 5b). As a negative control, Ptc deleted of its pro-apoptotic domain (seventh intracellular domain) failed to trigger this shift toward larger fractions (Fig. 5b). Moreover, the presence of caspase-9 in higher fractions observed on Ptc expression was inhibited in the presence of Shh (Fig.5b). Interestingly, in the absence of Shh, when caspase-9 was detected in the high molecular weight fractions, caspase-9 was present in a complex containing Ptc and TUCAN, as shown by co-immunoprecipitation experiments (Fig. 5c). When endogenous caspase-9 was pulled down by Ptc, the caspase-9 recruited in the Ptc complex was proteolytically processed (Supplementary Information, Fig. S6), further confirming that, in the absence of Shh, Ptc induces a complex of high molecular mass that includes DRAL and TUCAN (and/or NALP1), which results in caspase-9 activation.

Our data support the view that cell-death initiation by the Ptc dependence receptor occurs through the recruitment of a protein complex that results in the activation of caspase-9. In this regard, caspase-9 is an initiator or apical protease involved in the control of a downstream cascade of caspase activation that leads to apoptosis. Initiator caspases are typically activated through formation of large multi-protein complexes (see review)[27]. Among the known caspase-activating complexes of mammals are the apoptosome (comprising Apaf-1, cytochrome c and caspase-9), the DISC (comprising Fas, FADD and caspase-8; ref. 14), the PIDDosome (comprising PIDD, RAIDD and caspase-2; ref. 28) and the inflammasome (comprising NALPs, ASC, caspase-1 and caspase-5; ref. 22). Here we report the existence of a fifth caspase-activating complex that signals downstream of the dependence receptor Ptc. Future work will aim to define whether this 'dependosome' is a common platform for dependence-receptor death signalling, as suggested by the interaction of DCC with caspase-9 and the requirement of caspase-9 for DCC to trigger cell death[13].

In addition to the adaptor protein DRAL, the Ptc-based activating complex also requires either TUCAN or NALP1. Whereas TUCAN directly binds to pro-caspase-9 through their CARD-domains, NALP1 has been reported to indirectly bind through association with the pro-caspase-9-binding protein Apaf-1 (ref. 29). Whether Apaf-1 can also be recruited to the Ptc-dependence receptor complex remains to be investigated. Similarly, it will be interesting to determine the stoichiometry of the Ptc complex that activates caspase-9, as the observation that caspase-9

is detected in a complex of M_r 1000K–2000K in Ptc-expressing cells suggests the formation of a multimeric complex, similar to other caspase-activating platforms.

METHODS

Methods and any associated references are available in the online version of the paper at http://www.nature.com/naturecellbiology

Note: Supplementary Information is available on the Nature Cell Biology website.

ACKNOWLEDGEMENTS

We thank J. Briscoe and N. Le Douarin for advice and reagents, B. W. Schafer, C. Sardet and R. Sadoul for reagents, K. Cywinska for technical work on immunoprecipitation experiments and L. Kremer for the 5e1 hybridoma cell line (protein tools service at the Centro Nacional de Biotecnologia of Madrid). This work was supported by the Ligue Contre le Cancer, the Agence Nationale de la Recherche, the Institut National du Cancer, the Rhône-Alpes Region, the Centre National de la Recherche Scientifique, the EU grants Hermione and APO-SYS, NIH grants to P.M. (NS45093) and J.C.R. (AI56324), and a Rhône-Alpes Region fellowship and an Association pour la Recherche sur le Cancer fellowship to F.M.

AUTHOR CONTRIBUTIONS

F.M., C.T., J.F., N.R., H.H. and V.C. performed experiments and analysed data; C.G. performed experiments; J.C.R. provided materials; C.T planned the project and P.M. planned the project, analysed data and wrote the manuscript.

COMPETING FINANCIAL INTERESTS

The authors declare no competing financial interests.

Published online at http://www.nature.com/naturecellbiology/
Reprints and permissions information is available online at http://npg.nature.com/reprintsandpermissions/

1. Jessell, T. M. Neuronal specification in the spinal cord: inductive signals and transcriptional codes. *Nature Rev. Genet.* **1,** 20–29 (2000).
2. Murone, M., Rosenthal, A. & de Sauvage, F. J. Sonic hedgehog signaling by the patched-smoothened receptor complex. *Curr. Biol.* **9,** 76–84 (1999).
3. Charrier, J. B., Lapointe, F., Le Douarin, N. M. & Teillet, M. A. Anti-apoptotic role of Sonic hedgehog protein at the early stages of nervous system organogenesis. *Development* **128,** 4011–4020 (2001).
4. Litingtung, Y. & Chiang, C. Specification of ventral neuron types is mediated by an antagonistic interaction between Shh and Gli3. *Nature Neurosci.* **3,** 979–985 (2000).
5. Thibert, C. *et al.* Inhibition of neuroepithelial patched-induced apoptosis by sonic hedgehog. *Science* **301,** 843–846 (2003).
6. Mehlen, P. *et al.* The DCC gene product induces apoptosis by a mechanism requiring receptor proteolysis. *Nature* **395,** 801–804 (1998).
7. Bredesen, D. E., Mehlen, P. & Rabizadeh, S. Apoptosis and dependence receptors: a molecular basis for cellular addiction. *Physiol. Rev.* **84,** 411–430 (2004).
8. Mehlen, P. & Bredesen, D. E. The dependence receptor hypothesis. *Apoptosis* **9,** 37–49 (2004).
9. Tauszig-Delamasure, S. *et al.* The TrkC receptor induces apoptosis when the dependence receptor notion meets the neurotrophin paradigm. *Proc. Natl Acad. Sci. USA* **104,** 13361–13366 (2007).
10. Furne, C. *et al.* EphrinB3 is an Anti-apoptotic Ligand that Inhibits the Dependence Receptor Functions of EphA4 Receptors during adult neurogenesis *Biochem. Biophys. Acta* **1793 (2),** 231–238 (2009).
11. Hahn, H. *et al.* Mutations of the human homolog of *Drosophila* patched in the nevoid basal cell carcinoma syndrome. *Cell* **85,** 841–851 (1996).
12. Goodrich, L. V., Milenkovic, L., Higgins, K. M. & Scott, M. P. Altered neural cell fates and medulloblastoma in mouse patched mutants. *Science* **277,** 1109–1113 (1997).
13. Forcet, C. *et al.* The dependence receptor DCC (deleted in colorectal cancer) defines an alternative mechanism for caspase activation. *Proc. Natl Acad. Sci. USA* **98,** 3416–3421 (2001).
14. Zimmermann, K. C. & Green, D. R. How cells die: apoptosis pathways. *J. Allergy Clin. Immunol.* **108,** S99–103 (2001).
15. Johannessen, M., Moller, S., Hansen, T., Moens, U. & Van Ghelue, M. The multifunctional roles of the four-and-a-half-LIM only protein FHL2. *Cell. Mol. Life Sci.* **63,** 268–284 (2006).
16. Scholl, F. A., McLoughlin, P., Ehler, E., de Giovanni, C. & Schafer, B. W. *DRAL* is a p53-responsive gene whose four and a half LIM domain protein product induces apoptosis. *J. Cell Biol.* **151,** 495–506 (2000).
17. Stilo, R. *et al.* TUCAN/CARDINAL and DRAL participate in a common pathway for modulation of NF-kappaB activation. *FEBS Lett.* **521,** 165–169 (2002).
18. Razmara, M. *et al.* CARD-8 protein, a new CARD family member that regulates caspase-1 activation and apoptosis. *J. Biol. Chem.* **277,** 13952–13958 (2002).
19. Pathan, N. *et al.* TUCAN, an antiapoptotic caspase-associated recruitment domain family protein overexpressed in cancer. *J. Biol. Chem.* **276,** 32220–32229 (2001).
20. Charrier, J. B., Teillet, M. A., Lapointe, F. & Le Douarin, N. M. Defining subregions of Hensen's node essential for caudalward movement, midline development and cell survival. *Development* **126,** 4771–4783 (1999).
21. Stamataki, D., Ulloa, F., Tsoni, S. V., Mynett, A. & Briscoe, J. A gradient of Gli activity mediates graded Sonic Hedgehog signaling in the neural tube. *Genes Dev.* **19,** 626–641 (2005).
22. Tschopp, J., Martinon, F. & Burns, K. NALPs: a novel protein family involved in inflammation. *Nature Rev. Mol. Cell Biol.* **4,** 95–104 (2003).
23. Liu, F. *et al.* Expression of NALP1 in cerebellar granule neurons stimulates apoptosis. *Cell Signal* **16,** 1013–1021 (2004).
24. Kinoshita, T., Wang, Y., Hasegawa, M., Imamura, R. & Suda, T. PYPAF3, a PYRIN-containing APAF-1-like protein, is a feedback regulator of caspase-1-dependent interleukin-1 β secretion. *J. Biol. Chem.* **280,** 21720–21725 (2005).
25. Faustin, B. *et al.* Reconstituted NALP1 inflammasome reveals two-step mechanism of caspase-1 activation. *Mol. Cell* **25,** 713–724 (2007).
26. Boatright, K. M. *et al.* A unified model for apical caspase activation. *Mol. Cell* **11,** 529–541 (2003).
27. Riedl, S. J. & Salvesen, G. S. The apoptosome: signalling platform of cell death. *Nature Rev. Mol. Cell Biol.* **8,** 405–413 (2007).
28. Tinel, A. & Tschopp, J. The PIDDosome, a protein complex implicated in activation of caspase-2 in response to genotoxic stress. *Science* **304,** 843–846 (2004).
29. Chu, Z. L. et al. A novel enhancer of the Apaf1 apoptosome involved in cytochrome c-dependent caspase activation and apoptosis. *J. Biol. Chem.* **276,** 9239–9245 (2001).

METHODS

Site directed mutagenesis and plasmid constructs. The different constructs used in this study are detailed in Supplementary Information, Methods. The pcDNA3-Ptc-7ICmyr construct was obtained by polymerase chain reaction (PCR) on the pcDNA3-Ptc-7IC plasmid with the primers Ptc-myr7IC-F and Ptc-7IC-HA-R. The Ptc mutant with the deletion of its seventh intracellular domain (7IC; pRK5–PtcΔ7IC) was obtained by directed mutagenesis through Quikchange strategy (Stratagene) on pRK5-Ptc with mPtc1-Δ7IC-F and mPtc1-Δ7IC-R. For two-hybrid screening, the coding sequence of Ptc-7IC from pcDNA3-Ptc-7IC was amplified by PCR using the primers mPtc1-Eco-7IC-F and mPtc1-Pst-7IC-R and then inserted into pGBKT7 plasmid by digestion through EcoRI-PstI. By directed mutagenesis using Quikchange strategy on the resulting plasmid, a stop amino acid was generated in position 1393, to obtain the pGBKT7-GAL4 DNA-binding domain–Ptc 1165–1392 fusion plasmid (for primers sequence mPtc1-1393StopQC-F and mPtc1-1393StopQC-R, see Supplementary Information, Table S1). The construct pcDNA3-DRAL-3×FlagM2ΔLIM2 deleted only of its LIM2 domain was obtained by directed mutagenesis with Quikchange strategy using the primers DralΔLim2-F and DralΔLim2-R on the plasmid pcDNA3-DRAL-3×FlagM2 as matrix. A pcDNA3 plasmid encoding haemagglutinin (HA)-tagged DRAL from chicken was generated by PCR on cDNAs of one-day-old chick embryos by using the primers Chick-DRAL-F and Chick-DRAL-R. This plasmid was used as matrix to be amplified by PCR DRAL-encoding sequence using the primers pCAGGS-Chick-DRAL-XhoI-F and pCAGGS-Chick-DRAL-BglII-R. The PCR product was inserted into a pCAGGS vector. The pcDNA3-TUCANΔNTer plasmid was obtained by PCR using the primers TUCANΔNTerm-F and TUCANΔNTerm-Myc-R on the pcDNA3-TUCAN-Myc plasmid. For the *in ovo* chick electroporation, most constructs were based in pCAGGS which was also used as empty vector. pCAGGS-caspase-9 dominant negative was constructed by subcloning from pcDNA3-caspase-9 dominant negative[13] into a pCAGGS vector. Primers to construct pSilencer1.0-U6 containing small interfering hairpins of *DRAL* mRNA were designed with siRNA Target Designer program (Promega). See Supplementary Information, Table S1 for primers.

Cell cultures, transfection procedures, reagents and immunoblotting. Transient transfection of HEK293T cells and HEK293 cells expressing Muristerone A-inducible Shh (HEK293-EcRShh) was performed as described previously[5]. Daoy cells (ATCC, #HTB-186) were grown in 10% DMEM media on poly-L-lysine (Sigma)-coated round coverslips. Primary cultured cerebellar granule neurons (CGNs) were prepared from P6-aged mice (NMRI). 5e1 hybridoma cells producing a Shh-blocking antibody (Developmental Studies Hybridoma Bank), were maintained in 20% DMEM. Immunoblotting was performed as described previously[6], except antibodies were obtained from different sources and different dilutions were used (Supplementary Information, Methods). Recombinant Shh-N was from R&D systems. To induce Shh production in HEK293-EcRShh cells, Muristerone A (A.G. Scientific Inc.) was used (1 μM).

Yeast two-hybrid screen and co-immunoprecipitation. Matchmaker two-hybrid system III (Clontech) was used according to the manufacturer's instructions, using the DNA-binding domain GAL4 fused to Ptc residues 1165–1392 as a bait and the GAL4 transcriptional activation domain AD fused to a human fetal brain cDNA library (Clontech) as prey. *In vitro* co-immunoprecipitation were carried out on HEK293T or HEK293-EcRShh cells transfected with various tagged constructs as described previously[13]. For experiments requiring Shh, after plating and at the time of transfection cells were untreated or treated with Muristerone A, and recombinant Shh was added (to a final concentration of 300 ng ml^{-1}) 24 h before collecting the cells. *In vivo* immunoprecipitations were performed in OF-1 mice cortex embryos. Two cortices were dissected from embryonic day (E) 16.5 embryos, cut in small species and triturated. Shh-treated cortices were incubated for 40 min at 37 °C in conditioned supernatant of HEK293-EcRShh-induced cells in which recombinant Shh-N (R&D systems) was added (900 ng per cortex). Non-treated cortices were incubated in the same condition in supernatant of non-induced HEK293-EcRShh cells and without addition of recombinant Shh-N. Dissociated cortices were further processed for immunoprecipitation using μMACS Protein G MicroBeads system (Miltenyi Biotec).

Co-localization studies. After transfection or treatment as described in Supplementary Information, Materials, HEK293T, Daoy or CGNs cells were fixed in 4% paraformaldehyde for 30 min, washed and permeabilized with 0.2% Triton X-100 in PBS for 30 min. The coverslips were mounted in crystal/mount (Biomeda) and photographed with a Zeiss Axioplan2 LSM510 confocal microscope. Profiles were created using Axiovision 4.0V4.6.1.0 program.

Gel filtration. Gel filtrations were performed as described in Supplementary Information, Materials, using size-exclusion chromatography on High Prep Sephacryl S300 (HR 16/60) columns using an FPLC protein purification system (Biologic HR, Biorad). Proteins were separated with the lysis buffer. Columns were calibrated with protein standards (29K–2000K) according to the manufacturer's instructions (Sigma). Aliquots of the fractions were analysed on Criterion XT Precast gels (Bis-Tris 4–12%; Biorad) and western blotting. Aliquots of the twentieth first fractions were also pooled and used for co-immunoprecipitation experiments as described for *in vitro* co-immunoprecipitation.

Cell death analysis and caspase assays. Cell death was analysed 24 h after transfection using trypan blue staining procedures as described previously[5]. Cell death was also analysed using Toxilight assay (Lonza) according to the manufacturer's instructions. For caspase-9 activity fluorometric assay, HEK293-EcRShh cells were treated twice (when seeded and when transfected) with Muristerone A for the condition with Shh, and recombinant Shh-N (300 ng ml^{-1}) was added 1 h before collecting the cells. Caspase-9 activity was then measured by using the caspase-9 fluorometric assay kit (BioVision). Caspase-3 activity was measured by using the caspase-3 fluorometric assay kit (BioVision) as described previously[5].

Chick *in ovo* experiments and TUNEL staining on chick embryos. Cell-death analysis in the developing chick neural tube was performed using fertilized chicken eggs obtained from a local farm and incubated at 38 °C. Embryos were staged according to Hamburger and Hamilton (HH). Chick embryos were electroporated with purified plasmid DNA (4.5 μg μl^{-1}; Sigma). For floor plate electroporation, chick embryos of stage HH10-11 were injected with plasmid DNA into the lumen of the neural tube and electroporated with specifically designed electrodes. In each condition, GFP was co-electroporated to check the electroporation efficiency. Chick microsurgery was done as described in previously[5], except that the electroporation performed before microsurgery was performed in only one side of the neural tube. Detection and quantification of apoptosis by TUNEL was performed using the *In Situ* Cell Death Detection Kit (Roche) as described previously[3]. For each embryo, GFP and TUNEL double-positive cells of the electroporated and non-electroporated sides of the neural tube were counted in more than six sections. The ratio of the number of TUNEL-positive cells from the electroporated side to that of the non-electroporated side was then calculated. For each condition, results from at least five embryos were used to calculate a mean of the ratio. A U test was done to evaluate if the difference between various conditions was significant. Fluorescent TUNEL was performed as described previously[30].

NF-*k*B luciferase reporter assays. Analysis of NF-*k*B activation was performed according standard luciferase reporter assays as described in Supplementary Information, Methods.

30. Furne, C., Rama, N., Corset, V., Chedotal, A. & Mehlen, P. Netrin-1 is a survival factor during commissural neuron navigation. *Proc. Natl Acad. Sci. USA* **105,** 14465–14470 (2008).

nature cell biology

DOI: 10.1038/ncb1880

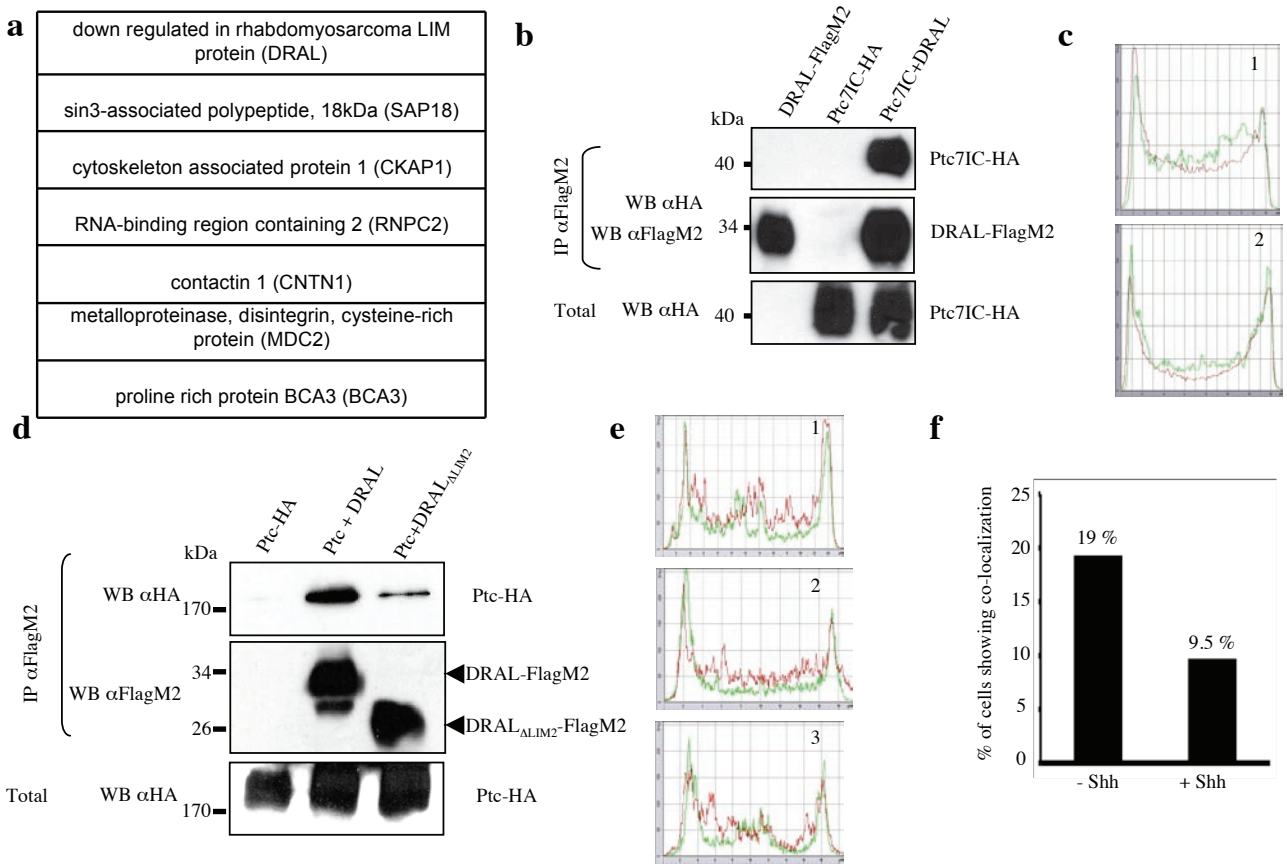

Figure S1 Mapping of Ptc and DRAL domains of interaction. (**a**) The putative seven Ptc partners found by two hybrid screen are shown. (**b**) Co-immunoprecipitations were performed on HEK293T cells transiently transfected with empty vector and either Ptc-7ICmyr (Ptc-7IC-HA) or DRAL vectors (DRAL-FlagM2) or transfected with Ptc-7ICmyr and DRAL vectors (Ptc-7IC + DRAL). Anti-FlagM2 antibody was used to immunoprecipitate DRAL (IP αFlagM2) and specific binding of Ptc-7ICmyr was revealed by Western blot by using anti-HA antibody. Western blot on lysates before pull down is shown (Total). (**c**) Ptc and DRAL in HEK293T cells co-localize at the plasma membrane. Profiles 1 and 2 correspond to Merge fluorescence analysis of the two positive transfected cells from the pictures shown in Fig1f. These profiles show that Ptc and DRAL fluorescence detection superimpose at the plasma membrane. (**d**) Co-immunoprecipitations were performed on HEK293T cells transiently transfected with empty vector and Ptc vector (Ptc-HA) or transfected with Ptc and either DRAL (Ptc + DRAL) or DRAL deleted of its LIM2 domain vectors (Ptc + $DRAL_{\Delta LIM2}$). Anti-FlagM2 antibody was used to immunoprecipitate DRAL (IP αFlagM2) and specific binding of Ptc was revealed by Western blot by using anti-HA antibody. Western blot on lysates before pull down is shown (Total). (**e**) Ptc and DRAL in Daoy cells co-localized at the plasma membrane mainly in the absence of Shh. Profiles 1, 2 and 3 correspond to Merge fluorescence analysis of three positive cells from the pictures shown Fig1h. These profiles show that Ptc and DRAL fluorescence detection superimposes at the plasma membrane. (**f**) Ptc and DRAL co-localization in cerebellar granular neurons is twice greater in the absence of Shh than in the presence of Shh. Total and yellow cells of five large fields were counted. The graphic is the representation of the % of the sum of yellow cells over the total number of cells counted on 5 randomly chosen fields (137 cells total were counted for the condition with Shh and 189 cells total were counted for the condition without Shh).

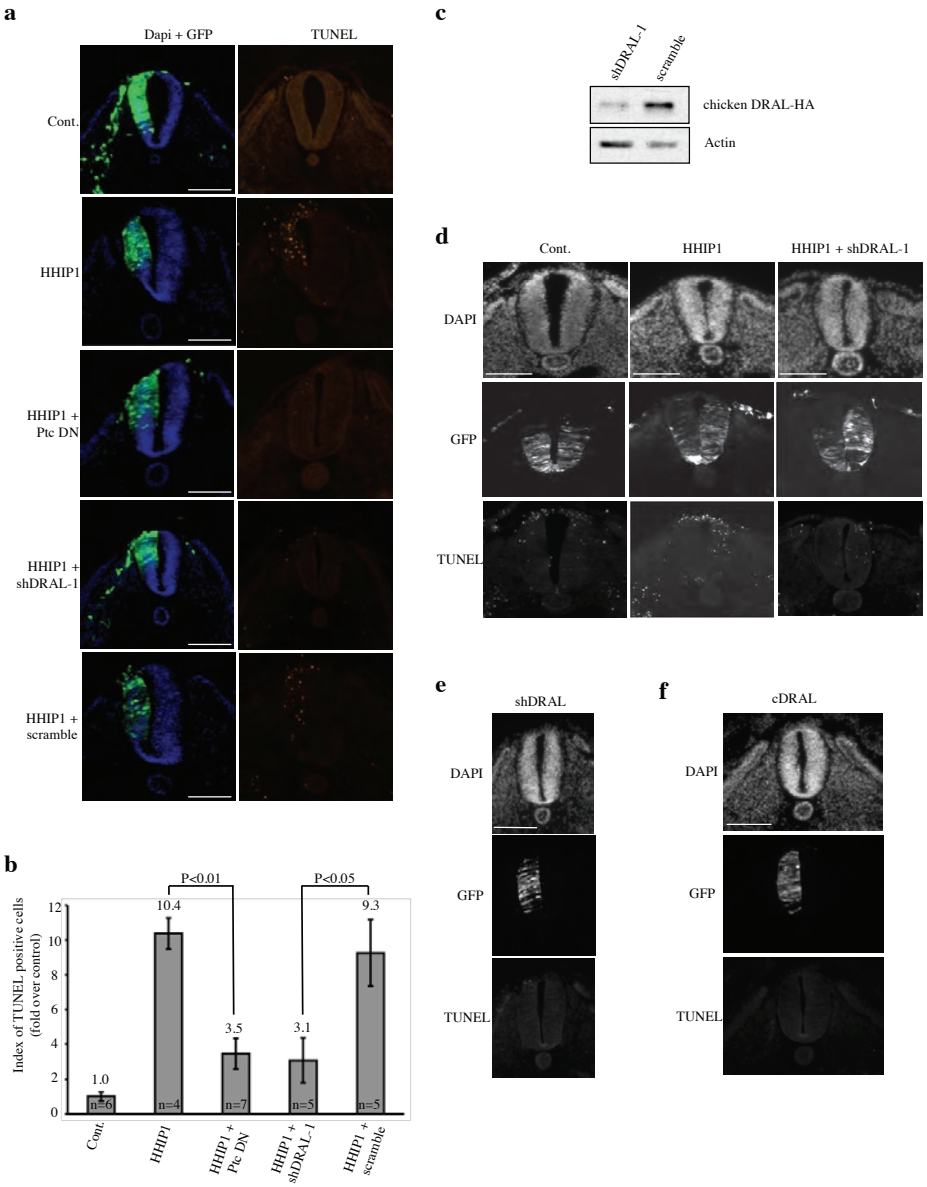

Figure S2 DRAL is required for Ptc-induced apoptosis *in vivo* during neural tube development. (**a**) DRAL function in Ptc-induced apoptosis was addressed *in vivo* by lateral electroporation of HHIP1 with or without shDRAL-1. In control condition (Cont.), HH 11-13 stage chick embryos were electroporated *in ovo* with GFP and empty vector. In all other conditions, embryos were co-electroporated with GFP and HHIP1 with either control vector (HHIP1) or Ptc dominant-negative (HHIP1 + Ptc DN) or shDRAL-1 (HHIP1 + shDRAL-1) or scramble (HHIP1 + scramble). A representative image of each condition is presented. Electroporated side of the neural tube is on the left side of the figures. Nuclei of cells and electroporation efficiency are shown on the left pictures (Dapi + GFP) and fluorescent TUNEL staining of the same sections are shown on the right pictures (TUNEL). The number of TUNEL positive cells is increased in the HHIP1-electroporated side of the neural tube. When co-electroporated with Ptc DN and shDRAL-1, HHIP1-induced apoptosis is inhibited. (**b**) Graphic representation of the TUNEL positive cells quantification as the mean of at least four embryos per condition (the exact number of embryo per each condition is indicated in the graphic). For each condition, the number of TUNEL positive cells in the ¾ ventral of the neural tube was quantified with respect to the electroporated area (GFP volume). Index of TUNEL positive cells is the ratio between the value of each condition and the value in the control condition (GFP). Error bars indicate SEM. U test was performed and p values are indicated. (**c**) A pcDNA3 plasmid encoding chicken DRAL HA-tagged was co-transfected with scramble or shDRAL-1 in HEK293T cells. Cell lysates were analyzed by Western blotting by using anti-HA antibody. Anti-Actin Western blot is shown as a control of loading. (**d**) Floor plate electroporation was performed *in ovo* in HH10-11 stage chick embryos. Conditions Cont., HHIP1 and HHIP1 + shDRAL-1 are same as described in (**a**). Fluorescent TUNEL staining was performed. A representative image of each condition is shown. (**e**) HH 11-13 stage chick embryos were electroporated with GFP and shDRAL-1 vectors. A representative image is presented. Electroporated side of the neural tube is to the left side of the figures. The section of the embryo is shown on top (DAPI). Electroporation efficiency is shown in the picture in the middle (GFP) and TUNEL staining of the corresponding section is shown in the bottom picture (TUNEL). The number of TUNEL positive cells is not modified in the shDRAL-electroporated side of the neural tube. (**f**) Same as in (**e**) but HH 11-13 stage chick embryos were electroporated *in ovo* with GFP and a vector encoding DRAL of chicken (cDRAL). A representative image is presented. Electroporated side of the neural tube is to the left side of the figures. The section of the embryo is shown on top (DAPI). Electroporation efficiency is shown in the picture in the middle (GFP) and TUNEL staining of the corresponding section is shown in the bottom picture (TUNEL). The number of TUNEL positive cells is not modified in the cDRAL-electroporated side of the neural tube. Scale bars : 50 μm.

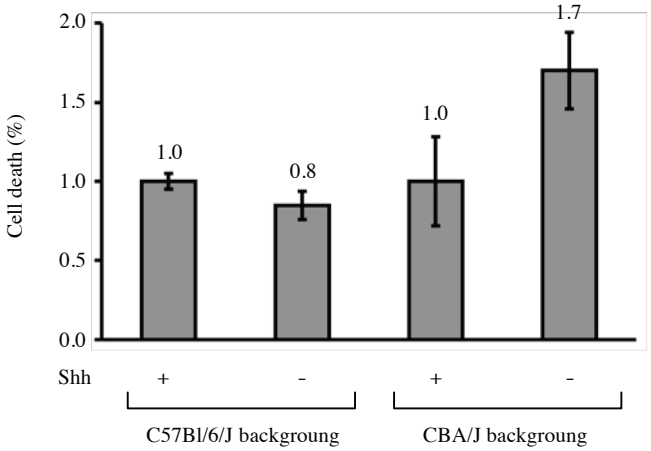

Figure S3 Effect of mice genetic background on Shh survival of primary cerebellum granular neurons. Primary culture of cerebellum granular neurons were prepared from C56Bl/6/J and CBA/J background mice. After 4 days of culture, cells were incubated during 24 hours in the presence of purified 5e1 antibodies (4 μg/ml) for a condition without Shh (Shh -) or with the antibody purification's buffer for a condition with Shh (Shh +). Cell death in each condition for the two genetic backgrounds was then assayed by Toxilight assay. Shh inhibition triggers cell death only in the CBA/J background.

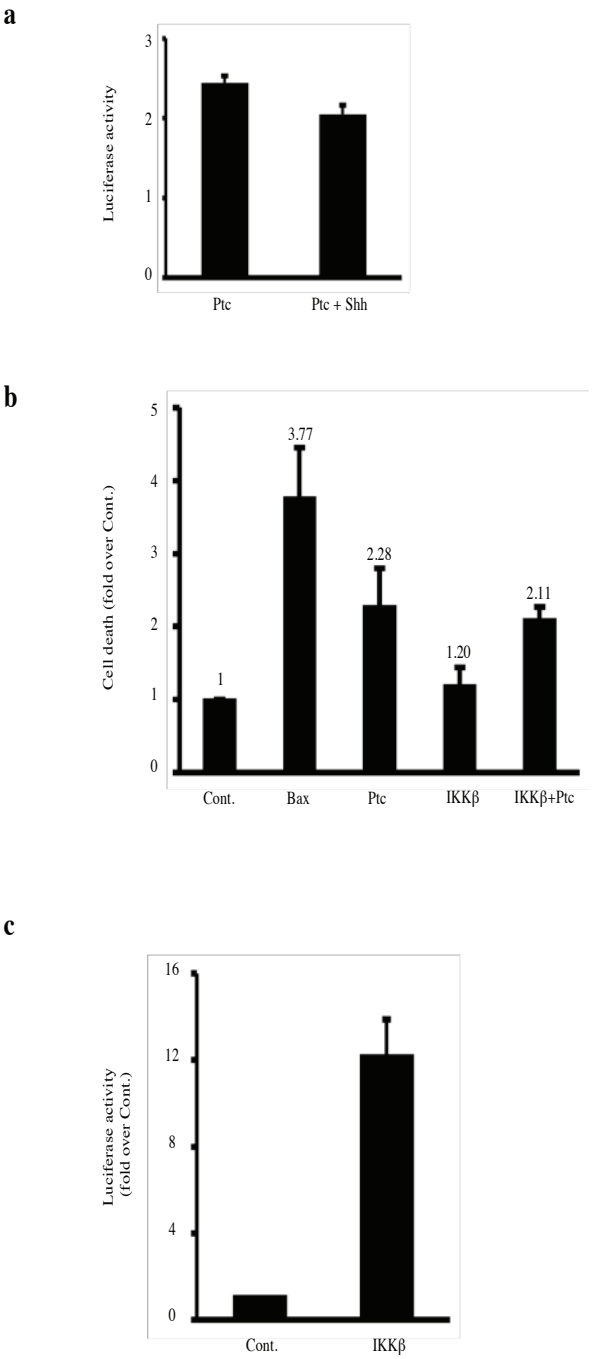

Figure S4 NF-κB pathway in Ptc-induced cell death. (**a**) HEK293-EcRShh cells were transiently co-transfected with *Renilla* luciferase expressing construct, a pFLRG-luciferase reporter and a Ptc-encoding vector in the absence of Shh (Ptc) or in the presence of Shh (Ptc + Shh) following both Muristerone A treatment plus addition of recombinant Shh. Cell lysates were prepared and luciferase activity associated with NF-κB activation and consequently with pFLRG driven luciferase reporter was measured in triplicate. Luciferase activity values were normalized to *Renilla* luciferase activity values to correct for variability in transfection efficiency between wells. Results are representative of at least six separate experiments. (**b**) HEK293T cells were transiently transfected with empty vector (Cont.), Bax encoding vector (Bax), Ptc encoding vector (Ptc), NF-κB pathway activator IKKβ encoding vector (IKKβ) or Ptc encoding vector plus IKKβ encoding vector (IKKβ + Ptc) and cell death was measured by Toxilight assay. The presence of IKKβ does not modify Ptc-induced cell death (n=5). (**c**) The efficiency of IKKβ as an activator of NF-κB pathway was checked by NF-κB Luciferase assay on HEK293T cells as described in (**a**). Results are representative of at least six separate experiments.

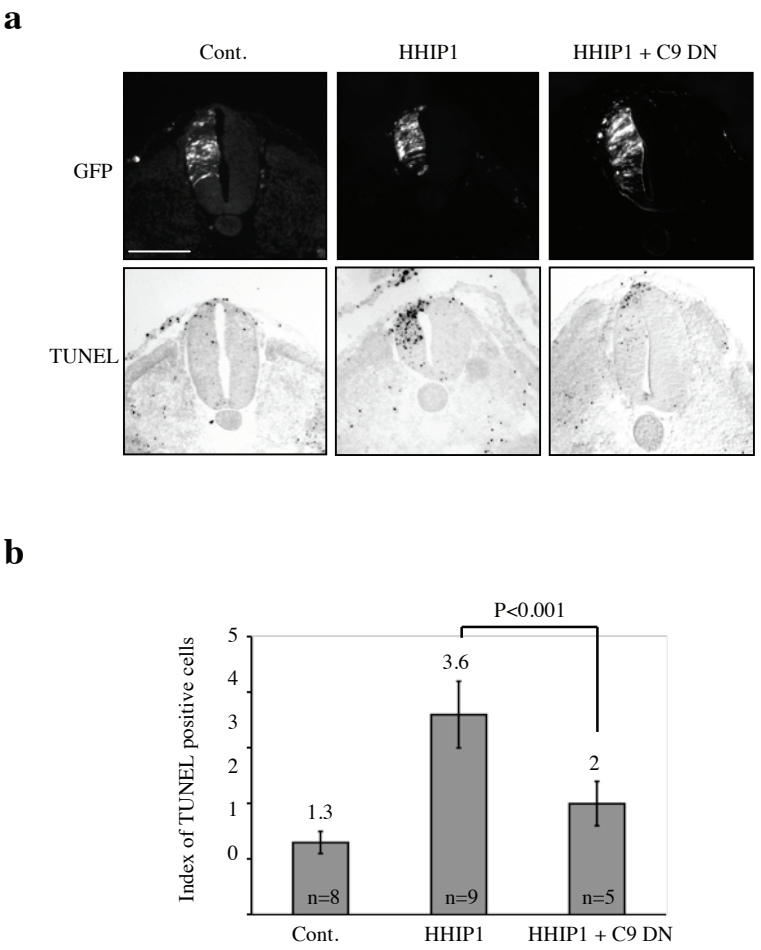

Figure S5 Requirement of caspase-9 in Ptc-induced apoptosis *in vivo*. (**a**) HH 11-13 stage chick embryos neural tube were electroporated as described Supp.Fig.2a with GFP and empty vector (Cont.), HHIP1 with empty vector (HHIP1) or HHIP1 with caspase-9 dominant negative (HHIP1 + C9 DN). A representative image of each condition is shown. Electroporated side of the neural tube is to the left side of the figures. Electroporation efficiency is shown in the upper pictures (GFP) and TUNEL staining of the corresponding sections are shown in the lower pictures (TUNEL). The number of TUNEL positive cells is increased in the HHIP1-electroporated side of the neural tube. HHIP1-induced apoptosis is blocked by co-electroporation with caspase-9 dominant negative. Scale bar : 50 μm. (**b**) TUNEL quantification as the mean of at least five embryos per condition. Error bars indicate s.d. U test was performed ($p<0.001$). The exact number of analyzed embryos is indicated in the graphic.

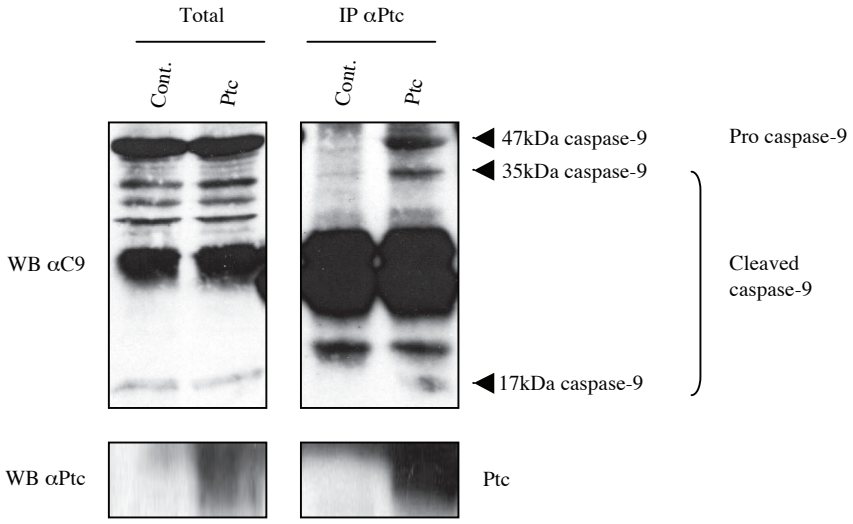

Figure S6 Full length and cleaved caspase-9 interact with Ptc. Co-immunoprecipitations between Ptc and endogenous caspase-9 were performed on HEK293T cells lysates transiently transfected with either empty vector (Cont.) or Ptc-encoding vector (Ptc) using anti-Ptc antibody (IP αPtc). Caspase-9 was detected by Western blotting using anti-caspase-9 antibody which recognizes both the full length and cleaved forms of caspase-9. Full length caspase-9 (Pro-caspase-9) and cleaved forms of caspase-9 (cleaved caspase-9) were co-immunoprecipitated by Ptc pull-down. The molecular weight of each form of caspase-9 is indicated.

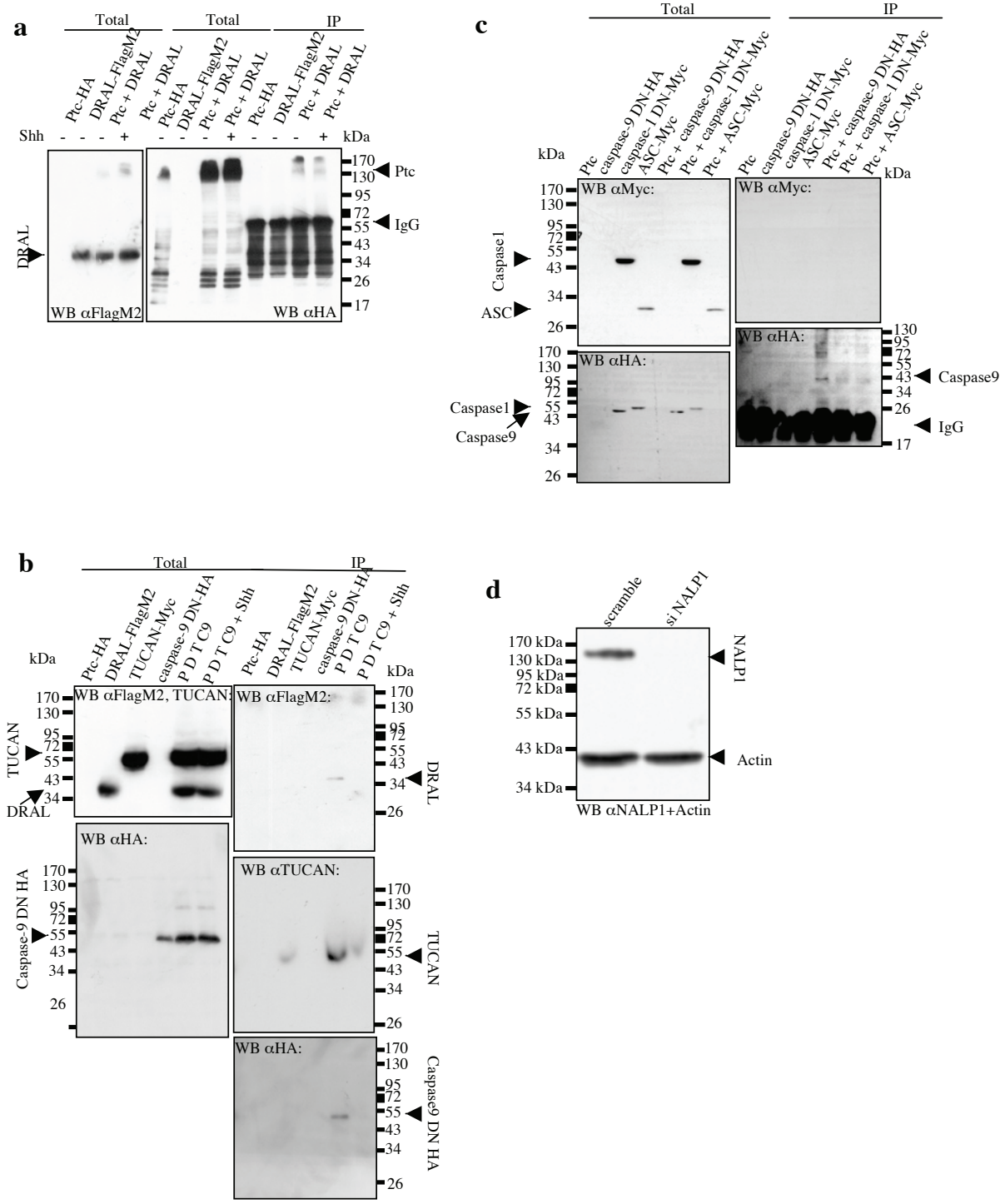

Figure S7 Full blots of key experiments. (**a**) Selected full blots for Fig.1d. (**b**) Selected full blots for Fig.3a. (**c**) Selected full blots for Fig.3g. (**d**) Selected full blots for Fig.4a.

Supplementary Table 1 Oligonucleotides used for cloning. The oligonucleotides used for all the cloning required for this study are shown.

mPtc1-Δ7IC-F	5'-GTCCTCTTATCCTTCTTTTAACCGTGTCCTGAG-3'
mPtc1-Δ7IC-R	5'-CTCAGGACACGGTTAAAAGAAGGATAAGAGGAC-3'
mPtc1-Eco-7IC-F	5'-GAGGCCGAATTCGGACCGTGTCCTGAGGTG-3'
mPtc1-Pst-7IC-R	5'-TAGCTTGGCTGCAGGTCAGTTGGAGCTGCT-3'
mPtc1-1393StopQC-F	5-AGCTACCCTGAGACTGATTAAGGGGTATTTGAG-3
mPtc1-1393StopQC-R	5-CTCAAATACCCCTTAATCAGTCTCAGGGTAGCT-3
Ptc-myr7IC-F	5'-GCACCATGGGGAGTAGCAAGAGCAAGCCTAAGGACCCCAGCCAGCGCGGACCGTGTCCTG-3'
Ptc-7IC-HA-R	5'-AAGGAAATGCGGCCGCTTAAGCGTAATCTGGAACATCGTATGGGTAGTTGGAGCTGCTCCC-3'
DralΔLim2-F	5'-CCAACGAGTACTCATCCAAGTATGAGAAACAACATGCCATG-3'
DralΔLim2-R	5'-CATGGCATGTTGTTTCTCATACTTGGATGAGTACTCGTTGG-3'
Chick-DRAL-F	5'-CACCATGACTGAGCGTTTCGACTGCCAC-3'
Chick-DRAL-R	5'-TTAAGCGTAATCTGGAACATCGTATGGGTAGATATCCTTTCCACATTCAGG-3'
pCAGGS-Chick-DRAL-XhoI-F	5'-AATTCTCGAGATGACTGAGCGTTTCGACTGCCAC-3'
pCAGGS-Chick-DRAL-BglII-R	5'-AATTAGATCTTTAGATATCCTTTCCACATTCAGG-3'
shDRAL1-F	5'-GGCACAATGATTGCTTTAATTCAAGAGATTAAAGCAATCATTGTGCCTTTTTT-3'
shDRAL1-R	5'-AATTAAAAAAGGCACAATGATTGCTTTAATCTCTTGAATTAAAGCAATCATTGTGCCGGCC-3'
scramble DRAL1-F	5'-GATGCCTGCATATGTAAATTTCAAGAGAATTTACATATGCAGGCATCTTTTTT-3'
scramble DRAL1-R	5'-AATTAAAAAAGATGCCTGCATATGTAAATTCTCTTGAAATTTACATATGCAGGCATCGGCC-3'
TUCANΔNterm-F	5'-CACCATGGTAGCTGCATCAGCCCCTCCT-3'
TUCANΔNterm-Myc-R	5'-TTACAGATCCTCTTCAGAGATGAGTTTCTGTTCCAAATTCTGCTGTCTAAGATAG-3'

Supplementary Methods

Site directed mutagenesis and plasmid constructs.

Plasmids encoding either entire mouse *ptc-1* gene (pRK5-Ptc) or mutant *ptc-1* gene (pRK5-Ptc-D1392N) or domains of mouse *ptc-1* gene (pcDNA3-Ptc-7IC, pcDNA3-Ptc-7IC-D1392N -Ptc dominant negative-, pcDNA3-Ptc 1165-1392) were described previously [1]. The pcDNA3-Ptc-7ICmyr construct was obtained by PCR on the pcDNA3-Ptc-7IC plasmid with the primers Ptc-myr7IC-F and Ptc-7IC-HA-R (given in Suppl. Table1). All these plasmids encode HA-tagged Ptc proteins. pRK5-Ptc plasmid encoding Ptc without tag has been described in [1]. Ptc mutant with the deletion of its last intracellular domain (pRK5-$Ptc_{\Delta 7IC}$) was obtained by directed mutagenesis *via* Quikchange strategy (Stratagene) on pRK5-Ptc with the primers given in Suppl. Table1 (mPtc1-Δ7IC-F and mPtc1-Δ7IC-R). For two-hybrid screen, the coding sequence of Ptc-7IC from pcDNA3-Ptc-7IC was amplified by PCR using the primers mPtc1-Eco-7IC-F and mPtc1-Pst-7IC-R (given in Suppl. Table1) which introduced EcoRI and PstI restriction sites. The digested PCR product was then inserted into pGBKT7 plasmid by digestion through EcoRI-PstI restriction sites. By directed mutagenesis *via* Quikchange strategy (Stratagene) on the resulting plasmid, a stop amino acid was generated in position 1393, in order to obtain the pGBKT7-GAL4 DNA binding domain/Ptc 1165-1392 fusion plasmid (for primers sequence mPtc1-1393StopQC-F and mPtc1-1393StopQC-R, see Suppl. Table1).

The human DRAL/FHL2 gene containing plasmid pcDNA3-DRAL-FlagM2 was obtained from B.W. Schäfer [2]. The constructs pcDNA3-DRAL-3xFlagM2 either wild type or with deletion of LIM1/2+1 (pcDNA3-DRAL-3xFlagM2$_{\Delta Lim1}$) or deletion of LIM1/2+1+2 (pcDNA3-DRAL-3xFlagM2$_{\Delta Lim1+2}$) were obtained from C. Sardet laboratory [3]. The construct pcDNA3-DRAL-3xFlagM2$_{\Delta LIM2}$ -deleted only of its LIM2 domain- was obtained by directed mutagenesis *via* Quikchange strategy (Stratagene) using the primers DralΔLim2-F and DralΔLim2-R (see Suppl. Table1) on the plasmid pcDNA3-DRAL-3xFlagM2 as matrix. A pcDNA3 plasmid encoding HA-tagged DRAL from chicken was generated by PCR on cDNAs of one day chick embryo by using the primers Chick-DRAL-F and Chick-DRAL-R given in Suppl. Table1. This plasmid was used as matrix to amplify by PCR DRAL-encoding sequence from chicken using the primers pCAGGS-Chick-FRAL-XhoI-F and pCAGGS-Chick-FRAL-BglII-R (see Supp. Table1). The PCR product was digested by XhoI and BglII and inserted into pCAGGS vector.

Human TUCAN (pcDNA3-TUCAN-Myc), NALP1 (pcDNA3-NALP1-Myc) and ASC cDNAs (pcDNA3-ASC-Myc) were previously described [4] [5] [6]. The pcDNA3-TUCAN$_{\Delta NTer}$ plasmid was obtained by PCR using the primers TUCAN ΔNTerm-F and TUCAN ΔNTerm-Myc-R (see Suppl. Table1) on the pcDNA3-TUCAN-Myc plasmid. pcDNA3-Bax was described before [7]. PcDNA3 encoding the dominant-negative caspase-9-HA and caspase-1-Myc with the mutation in the catalytic sites C287A or C285G respectively have been previously described [8] [9] [10]. For the *in ovo* chick electroporation, most constructs were based in pCAGGS which was

also used as empty vector. Empty pCAGGS was a kind gift from R. Sadoul [11]. pCAGGS-GFP has been described in [12]. pCAGGS-HHIP1 was a kind gift from J. Briscoe [13]. pCAGGS-caspase-9 dominant negative has been constructed by subcloning from pcDNA3-caspase-9 dominant negative [9] into pCAGGS vector by digestion through KpnI and NotI restriction sites. Primers to construct pSilencer1.0-U6 containing small interfering hairpins of DRAL mRNA were designed thanks to Promega siRNA Designer program. Primers (shDRAL1-F, shDRAL1-R, scrambleDRAL1-F, scrambleDRAL1-R, see Suppl. Table1) were hybridized by incubation in 500 mM NaCl, 60 mM TrisHCl pH 7.5, 10 mM DTT 3 minutes at 90°C and 1 hour at 37°C (final concentration of oligonucleotides was 40 ng/ml in 50 μl total). Hybridized oligonucleotides (8 ng) were ligated in linearized pSilencer 1.0-U6 (100 ng) with Roche T4 ligase DNA according to the manufacturer's instructions.

Cell cultures, transfection procedures, reagents and immunoblots.

Transient transfection of Human Embryonic Kidney 293T cells (HEK293T) and Human Embryonic Kidney 293 cells expressing Muristerone A-inducible Shh (HEK293-EcRShh [14]) were performed as previously described [1] according to a modified calcium phosphate procedure or using Lipofectamine according to the manufacturer's instructions (Invitrogen). Daoy cells (ATCC, #HTB-186) were grown in 10% DMEM media on poly-L-lysine (Sigma) coated round coverslip. Primary cultured cerebellar granule neurons (CGNs) were prepared from P6-

aged mice (NMRI) as described in [15]. Primary cells were cultured on round coverslips previously coated with poly-D-lysin. 5e1 hybridoma cells producing a Shh blocking antibody (Developmental Studies Hybridoma Bank), a generous gift from the Centro Nacional de Biotecnologia (Madrid), were maintained in 20% DMEM media. Immunoblots were performed as described previously [16] using anti-Myc (Sigma, 1/1000) anti-FlagM2 (Sigma, 1/5000), anti-HA (Sigma, 1/10000), anti-Ptc-1 (Santa Cruz Biotechnology, 1/1000), anti-DRAL (Abcam, 1/1000), anti-TUCAN (Abcam, 1/1000), anti-NALP1 (Abcam, 1/300), anti-caspase-8 (BD Biosciences, 1/500), anti-caspase-9 (Cell signaling, 1/1000), anti-GAPDH (Sigma, 1/5000), anti-Actin (Chemicon, 1/1000) or anti-Shh (R&D systems, 1/1000). Recombinant Shh-N was from R&D systems. To induce Shh production by HEK293-EcRShh cells, Muristerone A (A.G. Scientific, inc) was used (1 μM).

siRNA transfection.

For siRNA experiments, cells were transfected by Lipofectamine 2000 according to the manufacturer's instructions (Invitrogen) with 60 pmols siRNA total for a single siRNA transfection, or with 120 pmols siRNA total for double siRNA transfection. DRAL, caspase-8, caspase-9, NALP1, scramble siRNAs were from Santa Cruz Biotechnology; TUCAN siRNA was from Dharmacon. For DRAL, caspase-8 and -9 siRNA assays, 48 hours after Lipofectamine 2000 transfection of siRNA, cells were transfected with either empty vector (pcDNA3), Bax vector

as controls and Ptc vector by Lipofectamine Plus (Invitrogen). For TUCAN and NALP1 siRNA assays, the cells were transfected at the same time with siRNA and plasmids using Lipofectamine 2000.

Yeast two-hybrid screen.

Matchmaker two-hybrid system III (Clontech) was used according to the manufacturer's instructions. As a bait, the pGBKT7 plasmid harboring the DNA binding domain GAL4 fused to Ptc 1165-1392 was used to transform AH109 strain. The yeasts were further transformed with plasmids containing the GAL4 transcriptional activation domain AD fused to a human fetal brain cDNA library (Clontech). Cells were grown in the absence of leucine, tryptophane, adenine and histidine and in the presence of 30 mM 3-amino-1,2,4-triazole and X-α-Gal. For direct two-hybrid, the matchmaker two-hybrid system III (Clontech) was used with pGBKT7-Ptc 1165-1392 and pACT2-DRAL. As a negative control, yeast cells were co-transformed with Ptc 1165-1392 and empty Gal4AD vector, or with DRAL and empty Gal4BD vector. Cells were allowed to grow in the absence of leucine, tryptophane, adenine, histidine and in the presence of 30 mM 3-amino-1,2,4-triazole and X-α-Gal.

Co-immunoprecipitation assays.

In cellulo co-immunoprecipitation were carried out on HEK293T or HEK293-EcRShh cells (for experiments requiring Shh) transfected with various tagged

constructs as described previously [8]. For experiment requiring Shh, cells were treated or not with Muristerone A when plated and at the time of transfection, and recombinant Shh was added at a final concentration of 300 ng/ml 24 hours before harvesting the cells. Then, HEK293T or HEK293-EcRShh cells were lysed in 50 mM HEPES pH 7.6, 150 mM NaCl, 5 mM EDTA and 1% NP-40 in the presence of protease inhibitor cocktail (Roche), and further incubated with anti-HA (Sigma, 2.4 μg/ml), anti-FlagM2 (Sigma, 2.4 μg/ml), anti-Myc antibody (Sigma, 2.4 μg/ml), anti-Ptc-1 (Santa Cruz Biotechnology, 0.8 μg/ml), anti-TUCAN (Abcam, 4 μg/ml) or anti-caspase-9 (Cell Signaling, 4 μg/ml) and protein-A (Sigma) or protein-G Sepharose (GE Healthcare). Washes were done in 50 mM HEPES pH 7.6, 150 mM NaCl, 5 mM EDTA (4 washes) plus one extra wash in 50 mM HEPES pH 7.6, 500 mM NaCl, 5 mM EDTA. *In vivo* immunoprecipitation were performed in OF-1 mice cortex embryos. Two cortices from E16.5 embryos were dissected out, cut in small species and triturated. Shh-treated cortices were incubated 40 minutes at 37°C in conditioned supernatant of HEK293-EcRShh-induced cells in which recombinant Shh-N (R&D systems) was also added at 900 ng per cortex. Non-treated cortices were incubated in the same condition in supernatant of non-induced HEK293-EcRShh cells and without addition of recombinant Shh-N. Dissociated cortices were further incubated in lysate buffer (50 mM HEPES pH 7.6, 150 mM NaCl, 5 mM EDTA, inhibitor protease cocktail (Roche), 0.15% NP40) and subjected to potterisation. Immunoprecipitation was performed overnight at 4°C in lysis buffer 1% BSA

using 4 μg/ml of anti-Ptc-1 antibodies (Santa Cruz Biotechnology) or Normal goat IgG as control (R&D systems) and then purified with μMACS Protein G MicroBeads system (Miltenyi Biotec). Immunoprecipitates were immunoblotted using anti-DRAL polyclonal antibody (Abcam).

Co-localization studies.

HEK293T cells were plated on 24 well-plate round coverslips and transfected for 24 hours either with empty vector or with pRK5-Ptc plus pcDNA3-DRAL-FlagM2. A day after seeding, Daoy cells were incubated for 4 hours either with medium enriched in recombinant Shh (900ng/ml) or with supernatant of 5e1 hybridoma cells producing a Shh blocking antibody, supplemented with purified Shh blocking antibody (10 μg/ml). For CGNs, 24h after platting, cells were treated with 10 μM of Cytosin-β-D- arabinofuranoside (Sigma) and kept 4 days in culture. Cells were then incubated for 5 hours either with supernatant of Muristerone A-induced HEK293-EcRShh enriched with recombinant Shh (900ng/ml) or with supernatant of 5e1 hybridoma cells, supplemented with purified Shh blocking antibody (5 μg/ml). Both medium were supplemented with 25 mM KCl and 10 mM HEPES. After transfection or treatment, 293T, Daoy or CGNs cells were fixed in 4% paraformaldehyde for 30 minutes, washed and permeabilized with Triton 0.2 % in PBS 30 minutes. Permeabilized cells were washed 3 times in PBS and then saturated for 1 hour with 2 % BSA and 2 % Normal Donkey Serum in PBS. After a PBS wash, cells were incubated for 1 hour at room temperature simultaneously

with the combination of the appropriate first antibodies diluted in PBS. After rinsing the cells 3 times with PBS, the Ptc-1 antibody at 0.44 μg/ml diluted in PBS (Santa Cruz Biotechnology) and the DRAL antibody at 2.2 μg/ml diluted in PBS (Abcam) were detected respectively using Alexa Fluor 488 monoclonal Donkey anti-Goat antibody (Invitrogen) and Alexa Fluor 647 monoclonal Donkey anti-Rabbit (Invitrogen) in combination at 4.4 μg/ml each one during 1 hour at room temperature. After three washes in PBS, the coverslips were mounted in crystal/mount (Biomeda) and photographed with a Zeiss Axioplan2 LSM510 confocal microscope. Profiles were created using Axiovision 4.0V4.6.1.0 program.

Gel filtration.

For the condition with Shh treatment, HEK293-EcRShh cells were treated twice with Muristerone A (24 hours before transfection and at the time of transfection) and recombinant Shh (300 ng/ml) was added 1 hour before harvesting the cells. HEK293-EcRShh cells transfected by pcDNA3-DRAL-FlagM2, pcDNA3-TUCAN-Myc and pcDNA3-caspase-9-DN with or without pRK5-Ptc-HA or pRK5-Ptc$_{\Delta 7IC}$ were lysed in 50 mM HEPES pH 7.6, 150 mM NaCl, 5 mM EDTA and 0.1% NP-40 in the presence of protease inhibitors and sonicated 2 times 2 seconds per condition. The supernatant lysates were fractionated by size-exclusion chromatography on High Prep ^{TM} Sephacryl ^{TM} S300 (HR 16/60) columns using an FPLC protein purification system (Biologic HR, Biorad). Proteins were separated

with the lysis buffer. Columns were calibrated with protein standards (29 kDa-2000 kDa) according to the manufacturer's instructions (Sigma). Aliquots of the fractions were analyzed on Criterion XT Precast gels (Bis-Tris 4-12%; Biorad) and Western blotting. Aliquots of the 20th first fractions were also pooled and used for co-immunoprecipitation experiments as described for *in cellulo* co-immunoprecipitation.

Cell death analysis and caspase assays.

Cell death was analyzed 24h after transfection using trypan blue staining procedures as described previously [1]. Cell death was also analyzed using Toxilight assay according to the manufacturer's instructions (Lonza). Briefly, HEK293T were seeded at 50 000 cells/well in 24-well plates. The following day, cells were transfected using Lipofectamine Plus (Invitrogen) with 1 μg total DNA per well (0.7 μg pRK5-Ptc1-HA plus 0.3 μg IKKβ; Total DNA was kept constant using empty pcDNA3-3xFlag plasmid). 24 hours after transfection, the release of adenylate kinase by cells was measured from the supernatant and normalized to total adenylate kinase from cell lysate by luminometer (Infinite-F500, Tecan). For caspase-9 activity fluorometric assay, HEK293-EcRShh cells were treated twice (when seeded and when transfected) with Muristerone A for the condition with Shh, and recombinant Shh-N was added (300 ng/ml) 1 hour before harvesting the cells. Caspase-9 activity was then measured by using the caspase-9 fluorometric assay kit (BioVision). This assay uses the LEHD-AFC substrate. The

activity was measured every 30 minutes during 2 hours according to the manufacturer's instructions. For each condition, caspase-9 activation was calculated with the following way: we first calculated the average of the slopes of the affine regression curves representing the number of fluorescent units in terms of minutes; we then made the ratio between the caspase activity of the sample and that measured in 293T cells transfected with empty vector. The background level of the fluorescence (with lysis buffer only) has been substracted for each condition. Samples were also incubated with caspase-9 inhibitor zLEHD-fmk (20 μM) in order to eliminate the non-apoptotic background of fluorescence. Caspase-3 activity was measured by using the caspase-3 fluorometric assay kit (BioVision) as described previously [1].

Chick *in ovo* experiments and TUNEL staining on chick embryos.

Cell death analysis in the developing chick neural tube was performed using fertilized chicken eggs obtained from a local farm and incubated at 38°C. Embryos were staged according to Hamburger and Hamilton (HH). Chick embryos were electroporated with Sigma purified plasmid DNA (4.5 μg/μl) with 50 ng/ml Fast Green. For floor plate electroporation, chick embryos of stage HH10-11 were injected with plasmid DNA into the lumen of the neural tube and electroporated with specifically designed electrodes. These electrodes allowed us to fit the anode under the embryo and to lay the cathode on the embryo with 3 mm spacing. We carried out electroporation with 4 pulses of 50 ms duration at 20

V. The embryos were collected 24 hours after electroporation. For classical lateral electroporation of one side of the neural tube, plasmid DNA was injected into the lumen of HH stage 11-13 neural tubes and electrodes (CUY 613P3 standard electrodes; NEPA Gene) were placed either side of the neural tube (with 4 mm spacing) and electroporation carried out using CUY21 electroporator (NEPA Gene) delivering three 50 ms square pulses of 18 V with interval of 500 ms. In each condition, Green Fluorescent Protein (GFP) was co-electroporated (pCAGGS-GFP; 0.5 μg/μl) to check the electroporation efficiency. In the control condition, GFP was electroporated with empty vector alone (pCAGGS, 4 μg/μl). In all other conditions, GFP was co-electroporated with HHIP1 (pCAGGS-HHIP1, 2.5 μg/μl) with either empty vector or Ptc dominant negative (pcDNA3-Ptc-7IC D1392N) or shDRAL (pSilencer1.0-U6shDRAL1) or scramble DRAL (pSilencer1.0-U6-scrambleDRAL) or caspase-9 dominant negative (pCAGGS-caspase-9 DN), each then at 1.5 μg/μl. Chick microsurgery was done as described in [9], except that the electroporation performed before microsurgery was done in only one side of the neural tube. Transfected embryos were allowed to develop for 24 hours, then dissected, fixed 12 hours at 4°C in 4% paraformaldehyde in PBS, rinsed, sunk in 30% sucrose in PBS solution, embedded in gelatine 7.5%/sucrose 10% and sectioned in a MICROM cryostat (HM560). Detection and quantification of apoptosis by TUNEL was performed using the *in situ* cell TUNEL detection kit from Roche, following manufacturer's instructions and as previously described [17]. For each embryo, TUNEL-positive

cells of electroporated and non-electroporated side of the neural tube were added for more than six sections with adequate GFP expression. The ratio between the number of TUNEL-positive cells from the electroporated side to the non-electroporated side was then calculated. For each condition, results of at least five embryos were used to calculate a mean of the ratio. A U test was done to evaluate if the difference between various conditions was significant. Fluorescent TUNEL was done as described in [18].

NF-*k*B luciferase reporter assays.

HEK293-EcRShh or HEK293T cells were seeded respectively at 600 000 cells/well and 120 000 cells/well in 12-well plates. The following day, cells were transfected using Lipofectamine Plus (Invitrogen) with 10 ng of *Renilla* luciferase expressing construct (pRL-Rluc, Promega), 250 ng of reporter pFLRG-*Firefly* luciferase [19] and various expression plasmids (1.2 μg pRK5-Ptc1 0.5 μg pcDNA3-IKKβ) per well. Total DNA was kept constant using empty pcDNA3-3xFlag plasmid. After 24 hours, cells were lysed and activity from *Firefly* and *Renilla* luciferases was measured using a Dual-Luciferase Reporter System (Promega) by a luminometer.

Methods Reference.

1. Thibert, C. *et al.* Inhibition of neuroepithelial patched-induced apoptosis by sonic hedgehog. *Science* **301**, 843-846 (2003).
2. Scholl, F.A., McLoughlin, P., Ehler, E., de Giovanni, C. & Schafer, B.W. DRAL is a p53-responsive gene whose four and a half LIM domain protein product induces apoptosis. *J Cell Biol* **151**, 495-506 (2000).
3. Paul, C. *et al.* The LIM-only protein FHL2 is a negative regulator of E4F1. *Oncogene* **25**, 5475-5484 (2006).
4. Pathan, N. *et al.* TUCAN, an antiapoptotic caspase-associated recruitment domain family protein overexpressed in cancer. *J Biol Chem* **276**, 32220-32229 (2001).
5. Chu, Z.L. *et al.* A novel enhancer of the Apaf1 apoptosome involved in cytochrome c-dependent caspase activation and apoptosis. *J Biol Chem* **276**, 9239-9245 (2001).
6. Stehlik, C. *et al.* The PAAD/PYRIN-only protein POP1/ASC2 is a modulator of ASC-mediated nuclear-factor-kappa B and pro-caspase-1 regulation. *Biochem J* **373**, 101-113 (2003).
7. Llambi, F. *et al.* The dependence receptor UNC5H2 mediates apoptosis through DAP-kinase. *Embo J* **24**, 1192-1201 (2005).
8. Forcet, C. *et al.* The dependence receptor DCC (deleted in colorectal cancer) defines an alternative mechanism for caspase activation. *Proc Natl Acad Sci U S A* **98**, 3416-3421 (2001).
9. Furne, C. *et al.* The dependence receptor DCC requires lipid raft localization for cell death signaling. *Proc Natl Acad Sci U S A* **103**, 4128-4133 (2006).
10. Faustin, B. *et al.* Reconstituted NALP1 inflammasome reveals two-step mechanism of caspase-1 activation. *Mol Cell* **25**, 713-724 (2007).

11. Mahul-Mellier, A.L., Hemming, F.J., Blot, B., Fraboulet, S. & Sadoul, R. Alix, making a link between apoptosis-linked gene-2, the endosomal sorting complexes required for transport, and neuronal death in vivo. *J Neurosci* **26**, 542-549 (2006).
12. Momose, T. *et al.* Efficient targeting of gene expression in chick embryos by microelectroporation. *Dev Growth Differ* **41**, 335-344 (1999).
13. Stamataki, D., Ulloa, F., Tsoni, S.V., Mynett, A. & Briscoe, J. A gradient of Gli activity mediates graded Sonic Hedgehog signaling in the neural tube. *Genes Dev* **19**, 626-641 (2005).
14. Cooper, M.K., Porter, J.A., Young, K.E. & Beachy, P.A. Teratogen-mediated inhibition of target tissue response to Shh signaling. *Science* **280**, 1603-1607 (1998).
15. Trioulier, Y. *et al.* Alix, a protein regulating endosomal trafficking, is involved in neuronal death. *J Biol Chem* **279**, 2046-2052 (2004).
16. Mehlen, P. *et al.* The DCC gene product induces apoptosis by a mechanism requiring receptor proteolysis. *Nature* **395**, 801-804 (1998).
17. Charrier, J.B., Lapointe, F., Le Douarin, N.M. & Teillet, M.A. Anti-apoptotic role of Sonic hedgehog protein at the early stages of nervous system organogenesis. *Development* **128**, 4011-4020 (2001).
18. Furne, C., Rama, N., Corset, V., Chedotal, A. & Mehlen, P. Netrin-1 is a survival factor during commissural neuron navigation. *Proc Natl Acad Sci U S A* **105**, 14465-14470 (2008).
19. Bartholin, L., Guindon, S., Martel, S., Corbo, L. & Rimokh, R. Identification of NF-kappaB responsive elements in follistatin related gene (FLRG) promoter. *Gene* **393**, 153-162 (2007).

nature cell biology

The bioenergetic and antioxidant status of neurons is controlled by continuous degradation of a key glycolytic enzyme by APC/C–Cdh1

Angel Herrero-Mendez[1], Angeles Almeida[1,2], Emilio Fernández[1], Carolina Maestre[1,2], Salvador Moncada[3,4] and Juan P. Bolaños[1,4]

Neurons are known to have a lower glycolytic rate than astrocytes and when stressed they are unable to upregulate glycolysis[1] because of low Pfkfb3 (6-phosphofructo-2-kinase/fructose-2, 6-bisphosphatase-3) activity[2]. This enzyme generates fructose-2,6-bisphosphate ($F2,6P_2$)[3], the most potent activator of 6-phosphofructo-1-kinase (Pfk1; ref. 4), a master regulator of glycolysis[5]. Here, we show that Pfkfb3 is absent from neurons in the brain cortex and that Pfkfb3 in neurons is constantly subject to proteasomal degradation by the action of the E3 ubiquitin ligase[6], anaphase-promoting complex/cyclosome (APC/C)–Cdh1. By contrast, astrocytes have low APC/C–Cdh1 activity and therefore Pfkfb3 is present in these cells. Upregulation of Pfkfb3 by either inhibition of Cdh1 or overexpression of Pfkfb3 in neurons resulted in the activation of glycolysis. This, however, was accompanied by a marked decrease in the oxidation of glucose through the pentose phosphate pathway (a metabolic route involved in the regeneration of reduced glutathione[7]) resulting in oxidative stress and apoptotic death. Thus, by actively downregulating glycolysis by APC/C–Cdh1, neurons use glucose to maintain their antioxidant status at the expense of its utilization for bioenergetic purposes.

Using reverse-transcriptase polymerase-chain reaction (RT–PCR) in RNA extracts from terminally differentiated rat cortical neurons and astrocytes, we established that *Pfkfb* mRNA is expressed in neurons and that isoform 3 (*Pfkfb3*) mRNA is the most abundant in both cell types (Supplementary Information, Fig. S1a). This was confirmed by northern blotting (Fig. 1a, upper panel). Having demonstrated by RT–PCR that K6 was the most abundant splice variant of *Pfkfb3* mRNA, we raised an antibody against its carboxy-terminal domain (Supplementary Information, Fig. S1b, c) and used it to assess the expression of Pfkfb3 protein in neurons and astrocytes. Pfkfb3 was undetectable by western blotting in neurons, whereas it was present in astrocytes (Fig. 1a, lower panels; Supplementary Information, Fig. S1d, e). Immunohistochemistry in coronal sections of rat brain cortex showed that Pfkfb3 did not colocalize with the neuronal nuclear marker NeuN but it did colocalize with the astrocyte marker GFAP (Fig. 1b). Thus, although *Pfkfb3* mRNA is present in neurons, Pfkfb3 protein is absent, suggesting that the enzyme is downregulated post-transcriptionally in these cells.

Incubation of neurons with the proteosome inhibitors MG132 or lactacystine for 1 h resulted in accumulation of Pfkfb3 protein (Fig. 1c, upper panel). Furthermore, immunoprecipitation of Pfkfb3 in either MG132- or lactacystine-treated neurons, followed by western blotting using an anti-ubiquitin antibody, revealed an increase in Pfkfb3 ubiquitylation (Fig. 1c, lower panel). These results indicate that in neurons Pfkfb3 is degraded through the ubiquitin–proteosome pathway, which has been described in myogenic cells during differentiation[8]. We then investigated possible motifs targeting Pfkfb3 for ubiquitylation and found that Pfkfb3, but not the 1, 2 or 4 isomers, contains a KEN box at position 142 (Supplementary Information, Fig. S1f). A KEN box targets proteins for ubiquitylation by the APC/C[9]. Activation of APC/C requires the formation of a complex with Cdc20 or Cdh1 (ref. 10); however, Cdh1 is the only possible activator of APC/C in the terminally differentiated neurons used in this study[11]. Cdh1 was knocked down in neurons using short interfering RNA (siRNA) and Pfkfb3 protein was found to accumulate (Fig. 1d). Cdh1 protein abundance (Fig. 1d) and APC/C activity (Fig. 1e) were lower in astrocytes than in neurons, and overexpression of Cdh1 in astrocytes decreased Pfkfb3 protein (Fig. 1f). Transfection of neurons with wild-type Pfkfb3 or a mutant form in which the KEN box was altered to AAA by site-directed mutagenesis, followed by flow cytometry sorting (using green fluorescent protein $(GFP)^+$ labelling) revealed greater accumulation of the mutant Pfkfb3 form than of the wild-type (Fig. 1g). These results demonstrate that although Pfkfb3

[1]Departamento de Bioquimica y Biologia Molecular, Universidad de Salamanca, Instituto de Neurociencias de Castilla y Leon, 37007 Salamanca, Spain. [2]Unidad de Investigacion, Hospital Universitario de Salamanca, Instituto de Estudios de Ciencias de la Salud de Castilla y Leon, 37007 Salamanca, Spain. [3]Wolfson Institute for Biomedical Research, University College London, Gower Street, London WC1E 6BT, UK.
[4]Correspondence should be addressed either to J.P.B. or S.M. (e-mail: jbolanos@usal.es; s.moncada@ucl.ac.uk)

Received 12 December 2008; accepted 17 February 2009; published online 17 May 2009; DOI: 10.1038/ncb1881

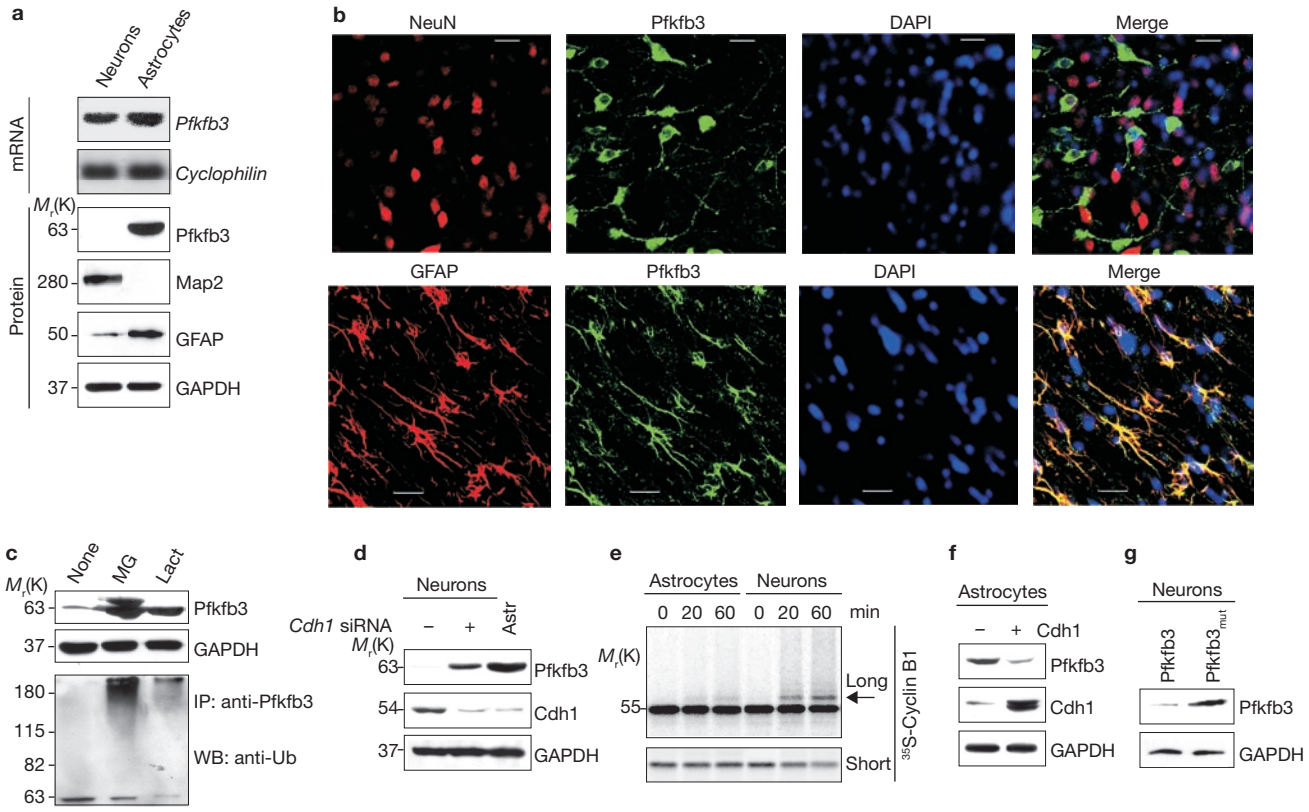

Figure 1 Pfkfb3 protein is degraded through the ubiquitin–proteasome pathway mediated by APC/C–Cdh1 in rat cortical neurons but not in astrocytes. (**a**) Upper panel: northern blotting of total RNA extracts from terminally differentiated rat cortical neurons and astrocytes showed that similar amounts of *Pfkfb3* mRNA were expressed in each cell type. *Cyclophilin* was used as an mRNA loading marker. Lower panel: western blotting using an anti-Pfkfb3 antibody revealed the absence of Pfkfb3 protein expression in neurons, whereas Pfkfb3 was expressed abundantly in astrocytes. Map2 was used as a neuronal marker, GFAP as a glial marker and GADPH as a loading control. (**b**) Fluorescence microphotographs of coronal sections of rat brain cortex show immunohistochemically the absence of Pfkfb3 in neurons and its presence in astrocytes. Neurons and glial cells were identified using the specific markers NeuN and GFAP, respectively. Nuclei were identified using DAPI. Scale bars, 20 μm. (**c**) Incubation of neurons with the proteasome inhibitors lactacystine or MG132 for 1 h resulted in Pfkfb3 accumulation, shown by western blotting. Immunoprecipitation of protein extracts with an anti-Pfkfb3 antibody, followed by western blotting against ubiquitin (Ub) showed increased Pfkfb3 protein ubiquitylation in the lactacystine- and MG132-treated neurons. (**d**) Silencing *Cdh1* in neurons at 3 days *in vitro* resulted in significant knockdown of Cdh1 protein and accumulation of Pfkfb3 (after 3 days) to approximately 50% of the level found in astrocytes, as assessed by densitometry; astrocytes express very little Cdh1 protein. (**e**) APC/C activity, measured as the ability to ubiquitylate ^{35}S-cyclin B1, is lower in astrocytes than in neurons (the arrow indicates the most abundant ubiquitylated form of cyclin B1; 'long' and 'short' indicate the exposure time of the film: short exposure allows visualization of the corresponding decrease in ^{35}S-cyclin B1). (**f**) Overexpression of Cdh1 in astrocytes decreases Pfkfb3 protein. (**g**) Wild-type Pfkfb3, but not a site-directed mutant form (^{142}KEN to ^{142}AAA, Pfkfb3$_{mut}$), is degraded when expressed in neurons using low amounts of cDNA.

is subject to degradation by the action of APC/C–Cdh1 in neurons, Pfkfb3 protein is stable in astrocytes as a result of their low APC/C–Cdh1 activity. The results also indicate that post-transcriptional repression of Pfkfb1, 2 and 4 in neurons, if it occurs, is through a mechanism that is independent of APC/C–Cdh1.

We then investigated whether Cdh1 regulates glycolysis in neurons. Silencing Cdh1 increased both the glycolytic flux (Fig. 2a; Supplementary Information, Fig. S2a) and the concentration of intracellular lactate (Fig. 2b; Supplementary Information, Fig. S2b). These effects were abolished by co-silencing phosphoglucose isomerase (PGI), the glycolytic enzyme responsible for the formation of fructose-6-phosphate (F6P), which is the substrate of Pfk1 (Fig. 2a; Supplementary Information, Fig. S2c,d). The increase in the glycolytic flux induced by silencing Cdh1 was also abolished by co-silencing Pfkfb3 (Fig. 2a). Thus the low glycolytic rate in neurons can be accounted for by APC/C–Cdh1-mediated degradation of Pfkfb3.

Next we investigated whether an increase in the basal glycolytic rate would render neurons more resistant to stress. Glycolysis was increased initially by silencing Cdh1; however, this treatment enhanced neuronal apoptotic death, as assessed by flow cytometry of annexin V$^+$/7-AAD$^-$ cells (Fig. 2c; Supplementary Information, Fig. S2e). The apoptosis caused by silencing Cdh1 was partially prevented by silencing PGI (Fig. 2c) or Pfkfb3 (Fig. 2d). Cyclin B1 also mediates, in part, apoptosis induced by silencing Cdh1 in neurons[11] (Fig. 2d), but co-silencing cyclin B1 and Pfkfb3 fully abolished apoptosis in *Cdh1* siRNA neurons (Fig. 2d). Thus, silencing Cdh1 in these cells triggers apoptosis through both cyclin B1 (ref. 11) and Pfkfb3. Neurons were then transfected with the full-length *Pfkfb3* cDNA and sorted by flow cytometry using GFP (Supplementary Information, Fig. S2f, g). This resulted in an increase in glycolytic flux (Fig. 2a) and an accumulation of lactate, which was prevented by silencing *PGI* (Fig. 2e). Expression of Pfkfb3 increased apoptosis in neurons in a concentration- (Fig. 2f) and time- (Fig. 2g) dependent

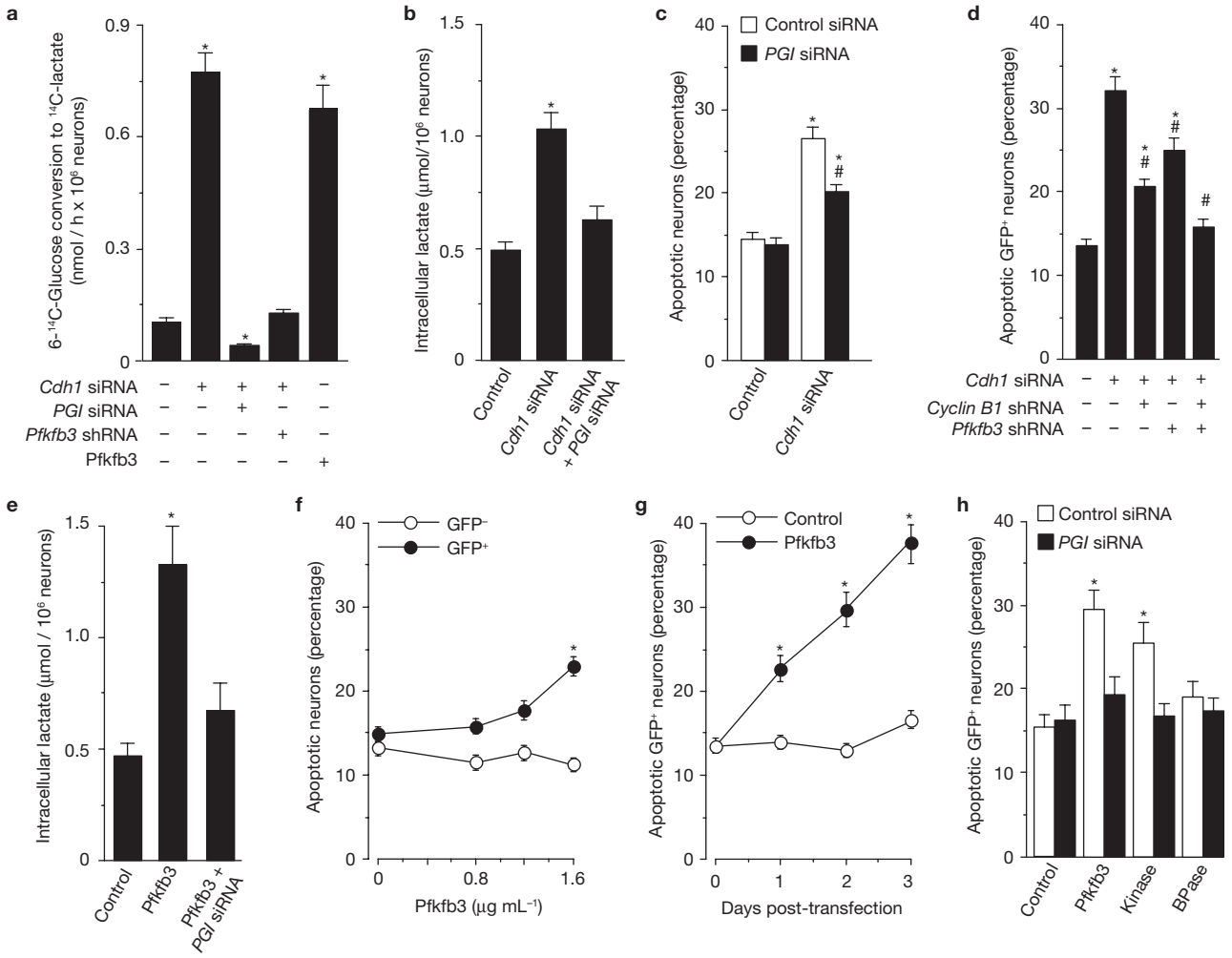

Figure 2 Cdh1 downregulates glycolysis and protects against apoptotic death through Pfkfb3 degradation in neurons. (**a**) Transfection with *Cdh1* siRNA in neurons significantly increased the rate of glycolysis, measured as the rate of 6-^{14}C-glucose conversion to ^{14}C-lactate; this effect was prevented by co-silencing *PGI* or *Pfkfb3*, and was mimicked by overexpression of Pfkfb3. Left histogram bar corresponds to control (luciferase) siRNA/shRNA. (**b**) Silencing *Cdh1* increased intracellular lactate concentrations, an effect that was prevented by co-silencing *PGI*. (**c**) *Cdh1* siRNA increased the proportion of apoptotic (annexin V$^+$/7-AAD$^-$) neurons, an effect that was partially prevented by co-silencing *PGI*. (**d**) Apoptotic death in *Cdh1*-silenced neurons was partially prevented by co-silencing either *cyclin B1* or *Pfkfb3* and was abolished by silencing both. Left histogram bar corresponds to control (luciferase) siRNA/shRNA. (**e**) Transfection of full-length *Pfkfb3* cDNA in neurons significantly increased intracellular lactate concentrations, as assessed in GFP$^+$ neurons after sorting by flow cytometry; this effect was prevented by *PGI* siRNA. (**f**, **g**) Transfection of neurons with *Pfkfb3* induced apoptotic death in a concentration- (**f**) and time- (**g**) dependent manner. Apoptosis was assessed by the presence of annexin V$^+$/7-AAD$^-$ cells measured by flow cytometry within the GFP$^+$ population. (**h**) Apoptotic death was also observed following transfection of *Pfkfb3* and of a truncated form of *Pfkfb3* containing the kinase domain. Transfection of the bisphosphatase Pfkfb3 domain did not affect apoptosis. The increase in apoptotic death in neurons caused by *Pfkfb3* or the kinase domain was prevented by silencing *PGI*. Results are mean ± s.e.m. ($n = 3$). *$P < 0.05$ versus the corresponding control; $^{\#}P < 0.05$ *versus Cdh1* siRNA (**d**).

manner, but had no effect on apoptosis in astrocytes (Supplementary Information, Fig. S3a). Expression of the kinase, but not the bisphosphatase domain of Pfkfb3 mimicked its effect on apoptosis in neurons (Fig. 2h). Silencing *PGI* abolished the apoptosis triggered by expression of either the full-length or the kinase domain of Pfkfb3 (Fig. 2h). The apoptosis in neurons resulting from expression of Pfkfb3 was caused by activation of the intrinsic apoptotic pathway, as demonstrated by the use of selective inhibitors of caspases (Supplementary Information, Fig. S3b). Thus, although overexpression of Pfkfb3 in neurons activates glycolysis, it concomitantly triggers apoptotic death.

To understand the reason(s) for apoptotic death of neurons following Pfkfb3-mediated activation of glycolysis, we decided to investigate whether such activation affected the rate of glucose utilization by the pentose-phosphate pathway (PPP), which is metabolically linked to glycolysis through the common intermediate glucose-6-phosphate (G6P)[12]. To establish whether modulation of glycolysis in neurons affects the rate of G6P oxidation through the PPP, neurons were transfected with *Pfkfb3* and GFP$^+$ cells were sorted by flow cytometry to assess PPP activity[13,14]. In control neurons the rate of glucose consumption through the PPP (Fig. 3a) was double that through glycolysis (Supplementary Information, Fig. S2a). *Pfkfb3* transfection inhibited glucose consumption through the PPP in neurons by about 50% (Fig. 3a); this effect was abolished by silencing *PGI*, indicating that such inhibition was a consequence of the activation of glycolysis (Fig. 3a). Overexpression of the full-length cDNA coding for glucose-6-phosphate dehydrogenase (G6PD; the rate-limiting step of the

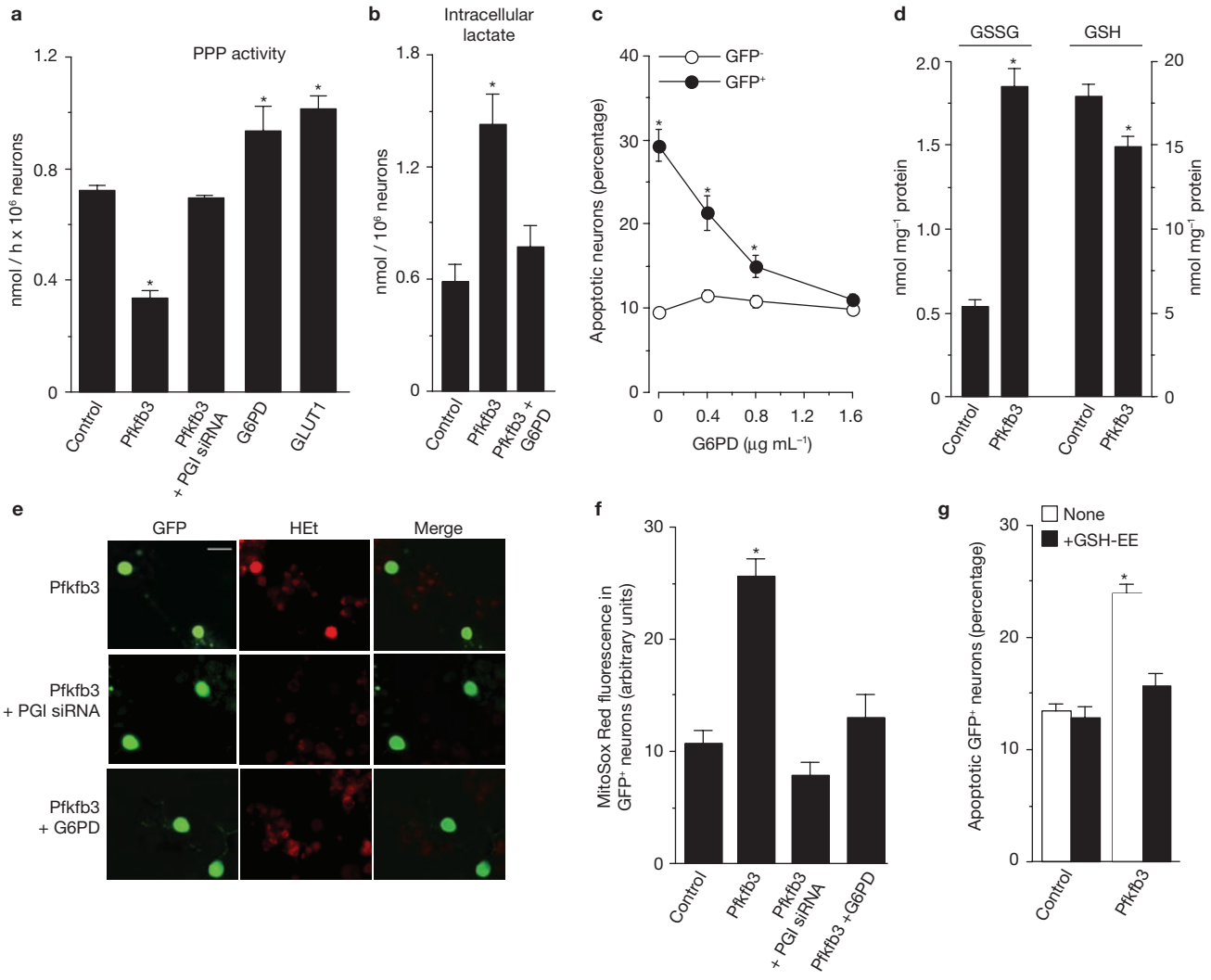

Figure 3 Pfkfb3 expression in neurons triggers a decrease in glucose oxidation through the PPP, causing oxidative stress. (**a**) The rate of PPP activity, measured as the difference in the rates of oxidation of 1-^{14}C- and 6-^{14}C-glucose, was reduced in neurons transfected with *Pfkfb3*; this effect was prevented by *PGI* siRNA. Expression of a plasmid vector encoding the full-length cDNA of G6PD, or the glucose transporter GLUT1 increased the rate of 1-^{14}C-glucose oxidation. These measurements were performed in GFP$^+$ cells sorted by flow cytometry. (**b**) Transfection of *Pfkfb3* in neurons resulted in increased intracellular lactate concentrations, an effect that was prevented by co-expressing G6PD. These measurements were performed in GFP$^+$ cells sorted by flow cytometry. (**c**) Neuronal apoptotic death (annexin V$^+$/7-AAD$^-$) caused by Pfkfb3 expression was prevented by co-expression of G6PD. GFP$^+$ neurons indicate those efficiently transfected with the *Pfkfb3* cDNA construct, whereas GFP$^-$ neurons represent those that were not transfected. (**d**) Pfkfb3 expression in neurons followed by flow cytometric sorting of the GFP$^+$ neurons revealed an increase of about 4-fold in the intracellular concentration of GSSG and a corresponding decrease in reduced glutathione (GSH). (**e**) Pfkfb3 expression in neurons increased the intensity of hydroethidine (HEt) fluorescence in the GFP$^+$ population, but not in the GFP$^-$ cells. Increased HEt fluorescence was abolished either by silencing *PGI* (*PGI* siRNA) or by G6PD expression. Scale bars, 20 μm. (**f**) Pfkfb3 expression in neurons increased the intensity of MitoSox fluorescence in the GFP$^+$ population, but not in the GFP$^-$ cells; this effect was abolished either by silencing *PGI* (*PGI* siRNA) or by G6PD expression. (**g**) Incubation of neurons with a plasma-permeable form of glutathione (glutathione ethyl ester, GSH-EE) prevented apoptotic death caused by Pfkfb3 expression. Results are means ± s.e.m. ($n = 3$). *$P < 0.05$ versus the corresponding control.

PPP) significantly increased PPP activity, as did overexpression of the glucose transporter GLUT1 (Fig. 3a). Furthermore, the increase in lactate accumulation and the apoptosis induced by *Pfkfb3* transfection could be prevented by co-expression of G6PD (Fig. 3b, c). These results suggest that in neurons a significant proportion of G6P is directed towards the PPP and that Pfkfb3 upregulation diverts it towards glycolysis. In astrocytes, however, despite considerable PPP activity[14], there is substantial metabolism of glucose by glycolysis (Supplementary Information, Fig. S3c), consistent with the observed higher expression of both G6PD (Supplementary Information, Fig. S3d) and Pfkfb3 (Fig. 1a) when compared with neurons.

A major function of the PPP is the regeneration of reduced glutathione at the expense of NADPH(H$^+$)[7,13] to provide neuroprotection[14–16]. We found that *Pfkfb3* transfection increased the oxidation of glutathione (Fig. 3d), indicating oxidative stress. We therefore measured the formation of reactive oxygen species (ROS). Pfkfb3 expression enhanced the formation of ROS in neurons, an effect that was prevented either by silencing *PGI* or by co-expressing G6PD (Figs 3e, f; Supplementary Information, Fig. S3e). Moreover, incubation of neurons with a plasma-membrane-permeable form of glutathione (glutathione ethyl ester) prevented apoptosis caused by Pfkfb3 expression (Fig. 3g). These results indicate that production of ROS in neurons

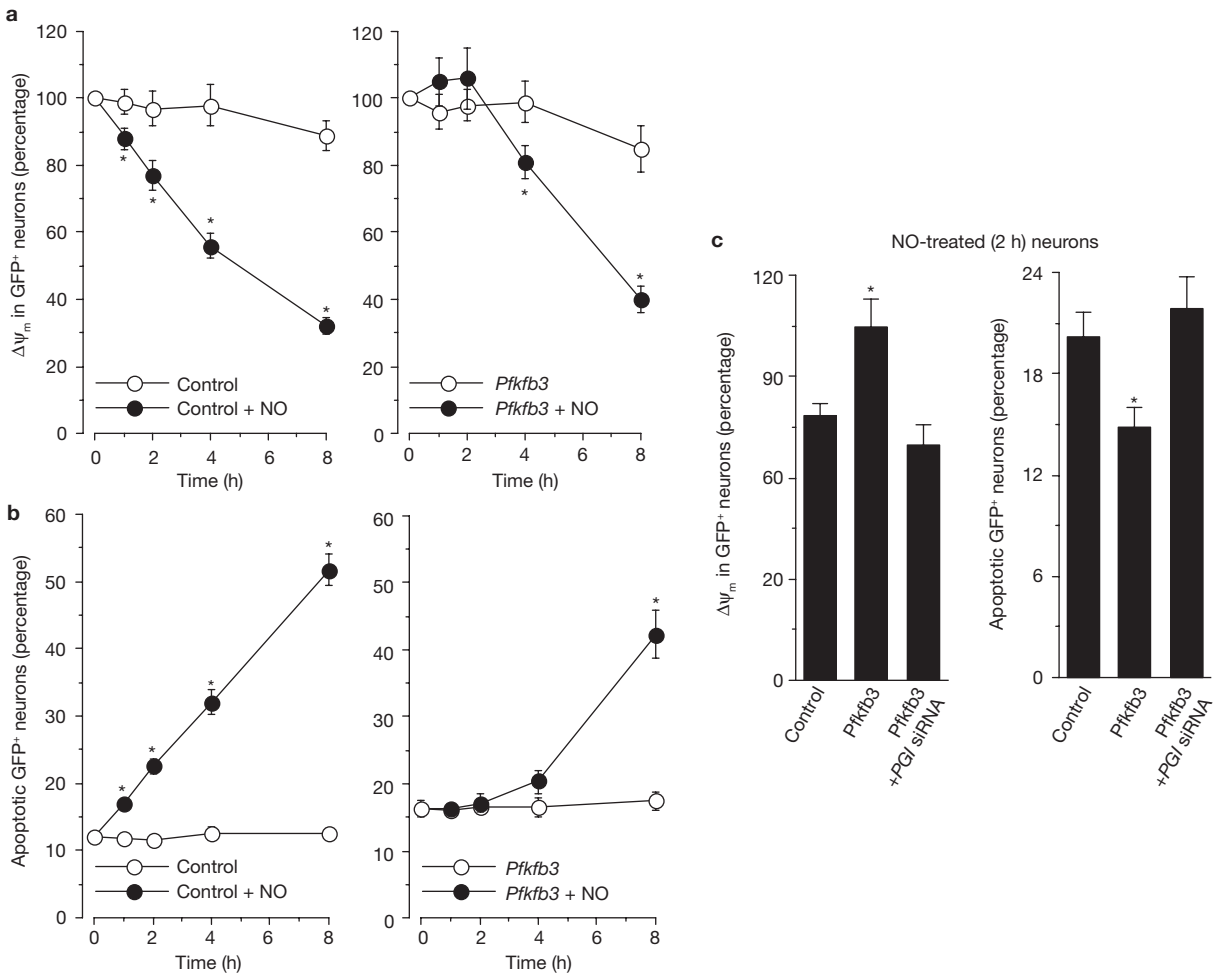

Figure 4 Expression of Pfkfb3 transiently protects neurons from loss of mitochondrial membrane potential ($\Delta\psi_m$) and apoptotic death triggered by nitric oxide (NO). (**a**) Primary neurons were transfected with control plasmid vector (left panel) or *Pfkfb3* (right panel) and then exposed to NO (released from the NO donor DETA–NONOate, 0.5 mM). NO triggered a rapid loss of $\Delta\psi_m$, which was initially prevented in neurons transfected with *Pfkfb3*. (**b**) Apoptotic death was assessed in neurons treated as in **a**. NO triggered apoptotic death of neurons transfected with control plasmid vector (left panel). However, in neurons transfected with *Pfkfb3*, the effect of NO was delayed for 4 h (right panel). (**c**) The protective effect of Pfkfb3 against NO-mediated loss of $\Delta\psi_m$ (left panel) and apoptotic death (right panel) was prevented by *PGI* siRNA. Results are means ± s.e.m. ($n = 3$). $^*P < 0.05$ versus the corresponding control.

transfected with *Pfkfb3* is consequent to the diversion of G6P from the PPP to glycolysis.

Treatment of neurons with the cytochrome *c* oxidase inhibitor nitric oxide (NO) is known to cause a marked drop in mitochondrial membrane potential ($\Delta\psi_m$), which is associated with an increase in apoptosis[1]. This does not occur in astrocytes because they are able to upregulate glycolysis and can use glycolytically generated ATP to maintain their $\Delta\psi_m$. We therefore investigated the effect of Pfkfb3 expression (at a concentration that did not itself cause apoptosis) on the response of neurons to inhibition of mitochondrial respiration. Treatment with NO, administered as DETA–NONOate, resulted in a marked drop in $\Delta\psi_m$ (Fig. 4a, left panel) and an increase in apoptosis (Fig. 4b, left panel). Transfection with *Pfkfb3* transiently delayed, but did not prevent the onset of the NO-induced fall in $\Delta\psi_m$ (Fig. 4a, right panel) and apoptosis (Fig. 4b, right panel), an effect that could be abolished by silencing *PGI* (Fig. 4c). Similar results were obtained when antimycin A was used to inhibit the electron transport chain (Supplementary Information, Fig. S3f–h). Thus, following cellular stress induced by inhibition of mitochondrial respiration, transfection of neurons with *Pfkfb3* activates glycolysis; however this produces only limited protection, as glycolysis diverts glucose away from the PPP, resulting in oxidative stress and death.

Thus, Pfkfb3 is degraded by an active mechanism that seems to be physiological as the enzyme is absent in neurons in the normal rat brain. This explains the lower rate of glycolytic metabolism in neurons than in astrocytes[1]. Furthermore, under stress conditions, this mechanism prevents upregulation of glycolysis, which is normally observed in astrocytes as part of their defence response[2]. Indeed, we show that enhancement of glycolysis in neurons leads to their apoptotic death from oxidative stress, consequent to a decrease in the regeneration of reduced glutathione.

Our results also suggest that neuronal consumption of glucose by the PPP to maintain their antioxidant status may take priority over the use of glucose to fulfill their bioenergetic requirements, which can be met by other sources. Increasing evidence indicates that neurons can use lactate generated by astrocytes to produce energy[17] and that this is not a uniform process but varies as a result of glutamatergic activation[18]. The fact that Pfkfb3 is subject to proteasomal degradation suggests that this mechanism is amenable to modulation, under conditions that now

require investigation. Indeed, it is likely that the increased use of lactate by neurons is coupled to an increase in their regeneration of reduced glutathione from glucose. Regulation of Pfkfb3 stability by the APC/C–Cdh1 pathway that we now describe might underlie this process. □

METHODS

Methods and any associated references are available in the online version of the paper at http://www.nature.com/naturecellbiology

Note: Supplementary Information is available on the Nature Cell Biology website.

ACKNOWLEDGEMENTS

This work was supported by Ministerio de Ciencia e Innovación (SAF2007-61492 and Consolider-Ingenio CSD2007-00020, Spain), Instituto de Salud Carlos-III (FIS06/0794 and Renevas), and Junta de Castilla y León (SA066A07 and Red de Terapia Celular y Medicina Regenerativa). We would like to thank H. Yamano for valuable help with the APC/C–Cdh1 activity assays, Carmela Gómez-Rodríguez for immunohistochemistry experiments, M. Resch for technical assistance and A. Higgs for critical evaluation of this paper.

AUTHOR CONTRIBUTIONS

A.H.M., E.F. and C.M. performed the experiments; A.A. and J.P.B. analysed the data; A.A., S.M. and J.P.B. planned the experiments and wrote the paper.

COMPETING INTERESTS

The authors declare that they have no competing financial interest.

Published online at http://www.nature.com/naturecellbiology/
Reprints and permissions information is available online at http://npg.nature.com/reprintsandpermissions/

1. Almeida, A., Almeida, J., Bolaños, J. P. & Moncada, S. Different responses of astrocytes and neurons to nitric oxide: the role of glycolytically-generated ATP in astrocyte protection. *Proc. Natl Acad. Sci. USA* **98,** 15294–15299 (2001).
2. Almeida, A., Moncada, S. & Bolaños, J. P. Nitric oxide switches on glycolysis through the AMP protein kinase and 6-phosphofructo-2-kinase pathway. *Nature Cell Biol.* **6,** 45–51 (2004).
3. Hue, L. & Rider, M. H. Role of fructose 2, 6-bisphosphate in the control of glycolysis in mammalian tissues. *Biochem. J.* **245,** 313–324 (1987).
4. Van Schaftingen, E., Lederer, B., Bartrons, R. & Hers, H. G. A kinetic study of pyrophosphate: fructose-6-phosphate phosphotransferase from potato tubers. Application to a microassay of fructose 2, 6-bisphosphate. *Eur. J. Biochem.* **129,** 191–195 (1982).
5. Uyeda, K. Phosphofructokinase. *Adv. Enzymol. Relat. Areas Mol. Biol.* **48,** 193–244 (1979).
6. Sudakin, V. *et al.* The cyclosome, a large complex containing cyclin-selective ubiquitin ligase activity, targets cyclins for destruction at the end of mitosis. *Mol. Biol. Cell* **6,** 185–197 (1995).
7. Kletzien, R. F., Harris, P. K. W. & Foellmi, L. A. Glucose-6-phosphate dehydrogenase: a housekeeping enzyme subject to tissue-specific regulation by hormones, nutrients, and oxidant stress. *FASEB J.* **8,** 174–181 (1994).
8. Riera, L. *et al.* Regulation of ubiquitous 6-phosphofructo-2-kinase by the ubiquitin-proteasome proteolytic pathway during myogenic C2C12 cell differentiation. *FEBS Lett.* **550,** 23–29 (2003).
9. Pfleger, C. M. & Kirschner, M. W. The KEN box: an APC recognition signal distinct from the D box targeted by Cdh1. *Genes Dev.* **14,** 655–65 (2000).
10. Visintin, R., Prinz, S. & Amon, A. CDC20 and CDH1: a family of substrate-specific activators of APC-dependent proteolysis. *Science* **278,** 460–463 (1997).
11. Almeida, A., Bolanos, J. P. & Moreno, S. Cdh1/Hct1-APC is essential for the survival of postmitotic neurons. *J. Neurosci.* **25,** 8115–8121 (2005).
12. Cohen, S. S. Studies on the distribution of the oxidative pathway of glucose-6-phosphate utilization. *Biol. Bull.* **99,** 369 (1950).
13. Hothersall, J. S., Baquer, N. Z., Greenbaum, A. L. & McLean, P. Alternative pathways of glucose utilization in brain. Changes in the pattern of glucose utilization in brain during development and the effect of phenazine methosulphate on the integration of metabolic routes. *Arch. Biochem. Biophys.* **198,** 478–492 (1979).
14. Garcia Nogales, P., Almeida, A. & Bolaños, J. P. Peroxynitrite protects neurons against nitric oxide-mediated apoptosis. A key role for glucose-6-phosphate dehydrogenase activity in neuroprotection. *J. Biol. Chem.* **278,** 864–874 (2003).
15. Ben-Yoseph, O., Boxer, P. A. & Ross, B. D. Assessment of the role of the glutathione and pentose phosphate pathways in the protection of primary cerebrocortical cultures from oxidative stress. *J. Neurochem.* **66,** 2329–2337 (1996).
16. Vaughn, A. E. & Deshmukh, M. Glucose metabolism inhibits apoptosis in neurons and cancer cells by redox inactivation of cytochrome c. *Nature Cell Biol.* **10,** 1477–1483 (2008).
17. Tsacopoulos, M. & Magistretti, P. J. Metabolic coupling between glia and neurons. *J. Neurosci.* **16,** 877–885 (1996).
18. Pellerin, L. *et al.* Activity-dependent regulation of energy metabolism by astrocytes: an update. *Glia* **55,** 1251–1262 (2007).

METHODS

Cell culture. Cortical neurons or astrocytes in primary culture were prepared from fetal (E16) and neonatal (P0) Wistar rats, respectively. Cells were seeded (2.5×10^5 cells/cm^2) in DMEM (Sigma) supplemented with 10% (v/v) fetal calf serum (FCS, Roche Diagnostics) and incubated at 37 °C in a humidified 5% CO_2-containing atmosphere. For neuronal cultures, 48 h after plating the medium was replaced with DMEM supplemented with 5% horse serum (Sigma) and with 20 mM D-glucose. On day 4 cytosine arabinoside (10 μM) was added to prevent non-neuronal proliferation. Cells were used by day 6 (neurons) or 12 (astrocytes). Enrichment was about 99% (neurofilament) or about 85% (glial-fibrillary acidic protein) in neurons and astrocytes, respectively. Most other cells in astrocytic cultures were microglia and progenitor cells[11].

Plasmid constructions. The full-length *Pfkfb3* cDNA (1563 bp; accession number BAA21754) was obtained by RT–PCR using total RNA from rat astrocytes as the template. The sense and antisense oligonucleotides and RT–PCR conditions are described in Supplementary Information Methods. Full-length rat *G6PD* cDNA[14], rat *GLUT1* cDNA[19] and human *Cdh1* cDNA[11] were also used. For small hairpin RNA (shRNA) expression, pSuper-based vectors were used[20].

Site-directed mutagenesis. To mutate the KEN-box to AAA in *Pfkfb3* cDNA, we used the QuikChange XL site-directed mutagenesis kit (Stratagene) using the following forward and reverse primers, respectively: 5′-ATCCTTCATTTTGCCGCAGCAGCTGACTTCAAGGC-3′ and 5′-ATGCCTTGAAGTCAGCTGCTGCGGCAAAATGAAGG-3′ (mutated nucleotides underlined).

Anti-Pfkfb3 antibody. This was generated by immunization of rabbits with the synthetic peptide ^{508}MRSPRSGAESSQKH^{521}-C, as described in the Supplementary Information Methods.

RT–PCR. To identify the Pfkfb isoforms and Pfkfb3 splice variants expressed in neurons, total RNA samples were amplified using the oligonucleotides and conditions described in the Supplementary Information Methods.

RNA interference. Using previously reported criteria[21,22], two sequences, 5′-CCTTACCAGACGTAGTGTT-3′ (nucleotides 1248–1266) and 5′-GCAAAGCTATCACGGACAT-3′ (nucleotides 503–521), were designed to target *PGI* by small interfering RNA (siRNA). However, the former was most effective at decreasing PGI protein in preliminary experiments (data not shown). Previously reported siRNA/ shRNA sequences for *Cdh1* (5′-TGAGAAGTCTCCCAGTCAG-3′, nucleotides 235-253; ref. 20), *cyclin B1* (5′-GATGGAGCTGATCCAAACC-3′, nucleotides 478–496; ref. 11) and *Pfkfb3* (5′-AAAGCCTCGCATCAACAGC-3′, nucleotides 1908–1926; ref. 2) were used. In all cases, a siRNA or shRNA against luciferase (5′-CTGACGCGGAATACTTCGATT-3′) was used as a control[3].

Cell treatments. Preliminary experiments using 20–100 nM of the siRNAs (Thermo Fisher Scientific) showed a concentration-dependent effect, and only the results using 100 nM are shown. Transfection of cells with plasmid vectors was carried out using 0.4–1.6 μg ml^{-1} of the plasmids. All transfections were performed using lipofectamine 2000 (Invitrogen) according to the manufacturer's instructions. After 6 h, the medium was removed and cells were further incubated for the indicated times in the presence of culture medium. Neuronal siRNA transfections were performed at day 3 *in vitro*, although experiments were performed at days 5 or 6; plasmid transfections were performed at day 5 *in vitro*. Experiments with the proteasome inhibitors MG-132 and lactacystine (10 μM; Calbiochem) were performed at day 6 *in vitro* and cells collected after 1 h. Glutathione ethyl ester (5 mM; Sigma), or the caspase inhibitors Z-VAD-FMK, Z-DEVD-FMK, Z-IETD-FMK, Z-VDVAD-FMK and Z-LEHD-FMK (50 μM; Calbiochem) was added to the cell medium 6 h after transfection. To expose the cells to controlled amounts of NO, cells were incubated in DMEM containing DETA–NO ((Z)-1-[2-aminoethyl-N-(2-ammonioethyl)amino] diazen-1-ium-1,2-diolate; Alexis Corporation) at 0.5 mM, which is the concentration seen to release about 1.4 μM of NO continuously for about 18 h at 37 °C, as measured by an NO-sensitive electrode (World Precision Instruments). To ensure immediate exposure of the cells to NO, all DETA–NO-containing solutions were always pre-incubated in DMEM at 37 °C for 30 min before addition to the cells[1]. Antimycin A was used at 5 μM for 30 min, neurons were washed and further incubated in DMEM for the indicated times.

Flow cytometric analysis of apoptotic cell death. APC-conjugated annexin-V and 7-amino-actinomycin D (7-AAD) (Becton Dickinson Biosciences) were used to determine quantitatively the percentage of apoptotic neurons by flow cytometry. Cells were stained with annexin V-APC and 7-AAD, according to the manufacturer's instructions, and were analysed on a FACScalibur flow cytometer (15 mW argon ion laser tuned at 488 nm; CellQuest software, Becton Dickinson Biosciences). GFP$^+$ and GFP$^-$ cells were analysed separately, and the annexin V–APC-stained cells that were 7-AAD-negative were considered to be apoptotic[2].

Cell sorting. Neurons were transfected and, at the indicated time-points, carefully detached from the plates using 1 mM tetrasodium EDTA in PBS. Cell sorting was performed by flow cytometry in a FACScalibur flow cytometer (Becton Dickinson Biosciences). Distinction between the two cells subsets was based on expression of the GFP protein or the annexin V/7-AAD staining. The purity of the sorted fraction was 98% ± 1.6% (range, 95%–99.5%).

Flow cytometric analysis of mitochondrial membrane potential ($\Delta\psi_m$). This was assessed in the GFP$^+$-stained cells using a MitoProbe DiC1(5) assay kit for flow cytometry (Molecular Probes Europe BV) according to the manufacturer's instructions. We used the FL1 and FL4 channels of a FACScalibur flow cytometer (15 mW argon ion laser tuned at 488 nm; CellQuest software, Becton Dickinson Biosciences). $\Delta\psi_m$ values were expressed as percentages, and the mitochondrial uncoupler oligomycin (10 μM, 10 min; Sigma) was used to define the 0% $\Delta\psi_m$ values.

Detection of reactive oxygen species (ROS). This was carried out using both the dihydroethidine and MitoSox-Red methods (Invitrogen). Neurons were incubated in PBS containing dihydroethidine (10 μM; Molecular Probes) at 37 °C in the dark for 45 min; excess dihydroethidine was removed and the amount of oxidized product (ethidium) was determined by fluorescence (510–560 nm) microscopy. For the MitoSox-Red method, neurons were incubated with MitoSox-Red (2 μM) for 30 min, washed with PBS and fluorescence assessed by flow cytometry.

Determination of the glycolytic flux. This was measured by two different methods, namely the rate of 6-^{14}C-glucose conversion to ^{14}C-lactate and the rate of ^3H_2O production from 3-^{3}H-glucose, as described in the Supplementary Information Methods.

Determination of activity of the pentose-phosphate pathway (PPP). This was measured in flow cytometric GFP$^+$-sorted neurons, prepared as indicated in the Supplementary Information Methods, by assessing the difference between $^{14}CO_2$ production from 1-^{14}C-glucose, which decarboxylates through the 6-phosphogluconate dehydrogenase-catalysed reaction, and that of 6-^{14}C-glucose, which decarboxylates through the tricarboxylic acid cycle[13,23].

Metabolite determinations. Glucose G6P, F6P, F1,6P_2, F2,6P_2, lactate and total and oxidized glutathione concentrations were measured as described in the Supplementary Information Methods.

APC/C ubiquitin ligase activity, northern blotting, western blotting and immunohistochemistry. These procedures were carried out as described in the Supplementary Information Methods.

Protein determinations. Protein concentrations were determined in the cell suspensions, lysates or in parallel cell culture incubations after solubilization with 0.1 M NaOH. Protein concentrations were determined as described[24] using bovine serum albumin as a standard.

Statistical analysis. Measurements from individual cultures were always carried out in triplicate. The results are expressed as mean ± s.e.m. for three different culture preparations. Statistical analysis of the results was performed by one-way analysis of variance, followed by the least significant difference multiple range test. In all cases, $P < 0.05$ was considered significant.

19. Cidad, P., Almeida, A. & Bolaños, J. P. Inhibition of mitochondrial respiration by nitric oxide rapidly stimulates cytoprotective GLUT3-mediated glucose uptake through5′-AMP-activated protein kinase. *Biochem. J.* **384,** 629–636 (2004).
20. Brummelkamp, T. R., Bernards, R. & Agami, R. A system for stable expression of short interfering RNAs in mammalian cells. *Science* **296,** 550–553 (2002).

DOI: 10.1038/ncb1881

21. Reynolds, A. *et al.* Rational siRNA design for RNA interference. *Nature Biotechnol.* **22,** 326–330 (2004).
22. Ui-Tei, K. *et al.* Guidelines for the selection of highly effective siRNA sequences for mammalian and chick RNA interference. *Nucleic Acids Res.* **32,** 936–948 (2004).
23. Larrabee, M. G. Evaluation of the pentose phosphate pathway from $^{14}CO_2$ data. Fallibility of a classic equation when applied to non-homogeneous tissues. *Biochem. J.* **272,** 127–132 (1990).
24. Lowry, O. H., Rosebrough, N. J., Lewis-Farr, A. & Randall, R. J. Protein measurement with the Folin phenol reagent. *J. Biol. Chem.* **193,** 265–275 (1951).

nature cell biology

DOI: 10.1038/ncb1881

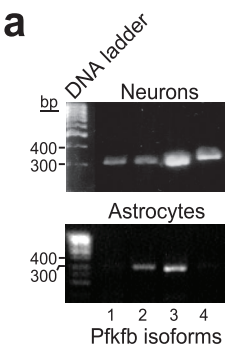

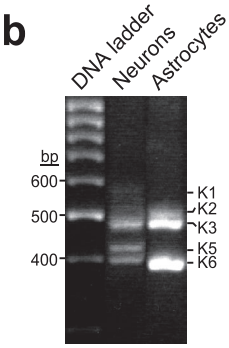

c

Pfkfb3 splice variant	Swiss Prot Entry	447 ·
RB2K1	O35552-1	EAVKIQHFASVVRPSSYTELDFLSVESAKQDAKKGPNPLMRRNSVTPLASPEP
RB2K2	O35552-2	EAVKIQHFASVVRPSSYTELDFLSVESAKQDAKKGPNPLMRRNSVTPLASPEP
RB2K3	O35552-3	EAVKIQHFASVVRPSSYTELDFLSVESAKQDAKKGPNPLMRRNSVTPLASPEP
RB2K4	O35552-4	E----------DAKKGPNPLMRRNSVTPLASPEP
RB2K5	O35552-5	E----------DAKKGPNPLMRRNSVTPLASPEP
RB2K6	O35552-6	E----------DAKKGPNPLMRRNSVTPLASPEP
RB2K7	O35552-7	EAVKIQHFASVVRPSSYTELDFLSVESAKQDAKKGPNPLMRRNSVTPLASPEP
RB2K8	O35552-8	E----------DAKKGPNPLMRRNSVTPLASPEP
		501 · 550 ·
RB2K1		TKKPRINSFEEHVASTSAALPSCLPPEVPTQLPGQPLLGKACLRTVCHIFSKFSPY
RB2K2		TKKPRINSFEEHVASTSAALPSCLPPEVPTQLPGQPLLGKACLT
RB2K3		TKKPRINSFEEHVASTSAALPSCLPPEVPTQLPGQNMRSPRSGAESSQKH
RB2K4		TKKPRINSFEEHVASTSAALPSCLPPEVPTQLPGQPLLGKACLRTVCHIFSKFSPY
RB2K5		TKKPRINSFEEHVASTSAALPSCLPPEVPTQLPGQPLLGKACLT
RB2K6		TKKPRINSFEEHVASTSAALPSCLPPEVPTQLPGQNMRSPRSGAESSQKH
RB2K7		TKKPRINSFEEHVASTSAALPSCLPPEVPTQLPGQPLLGKACL
RB2K8		TKKPRINSFEEHVASTSAALPSCLPPEVPTQLPGQPLLGKACL

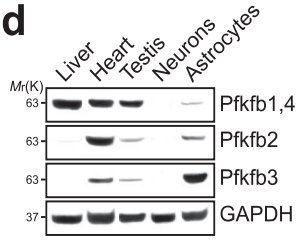

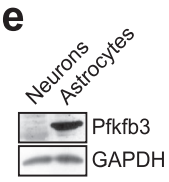

f

Pfkfb isoform	Swiss Prot Entry	140 · 147 ·
Pfkfb1	P07953	FAKEHGYK
Pfkfb2	Q9JJH5	FAKQNAFK
Pfkfb3	O35552-6	FAKENDFK
Pfkfb4	P25114	FGEQNGYK

Figure S1 (a) Reverse-transcriptase polymerase-chain reaction (rtPCR) was carried out in total RNA samples from rat cortical neurons and astrocytes to identify the four different Pfkfb isoforms. Isoform 3 (Pfkfb3) was found to be the most abundant in both cell types. **(b)** rtPCR was performed in total RNA samples obtained from rat cortical neurons or astrocytes to identify the most abundant mRNA splice variants (K1 to K8) expressed. In neurons, the expression of K3, K5 and K6 was comparable, whereas in astrocytes K6, followed by K3 was expressed the most. K7 and K8 were not detectable in either cell type (not shown). **(c)** Aminoacid sequences of the C-terminal domains of the eight splice variants described for the rat Pfkfb3. The epitope used for antibody production is highlighted. **(d)** Neurons do not express any Pfkfb isoform, whereas astrocytes express Pfkfb3, Pfkfb2 and Pfkfb1,4. **(e)** Western blotting against Pfkfb3 using a commercial antibody that does not distinguish among different splice variants (catalogue number sc-10091, Santa Cruz Biotechnologies; see Supplementary Methods) confirms the lack of Pfkfb3 protein in neurons. **(f)** 140-147 aminoacid sequence of Pfkfb isoforms showing the presence of a KEN box in Pfkfb3 but not in the other isoforms.

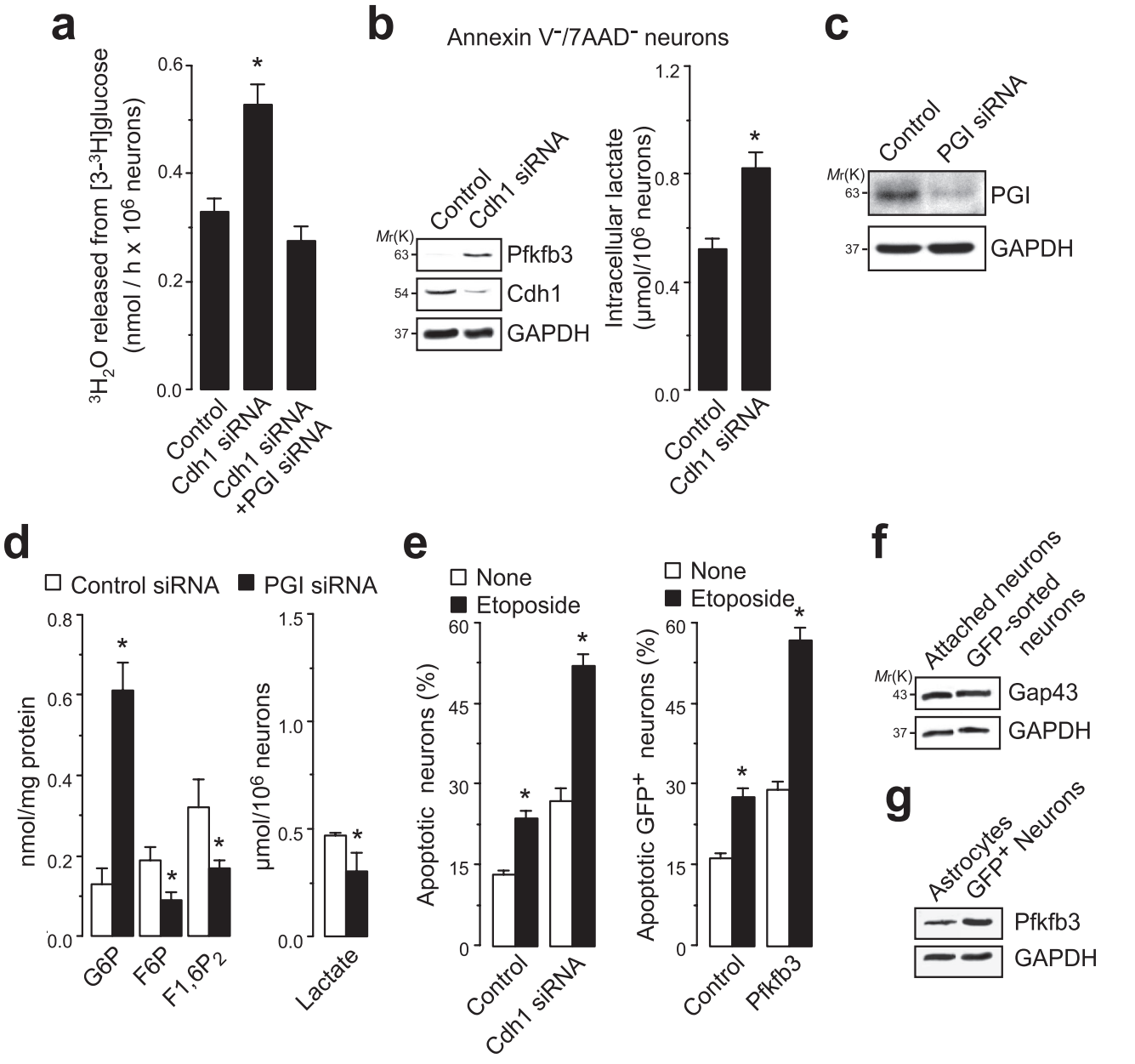

Figure S2 (a) Knockdown of Cdh1 increased the rate of ^3H_2O released from [3-^{3}H]glucose, an index of glucose utilization through Pfk1; this effect was prevented by co-silencing PGI. **(b)** Cdh1 silencing increased Pfkfb3 protein and lactate in the surviving subpopulation of neurons (annexin V$^-$/7-AAD$^-$). **(c)** Primary cortical neurons were transfected with PGI siRNA at 3 days *in vitro*. Three days later, western blotting showed that PGI was knocked down by the siRNA procedure. **(d)** To further validate the effectiveness of the PGI siRNA procedure, both PGI substrate (glucose-6-phosphate; G6P) and product (fructose-6-phosphate; F6P), as well as the Pfk1 product fructose-1,6-bisphosphate (F1,6P_2), and lactate, were measured in primary cortical neurons transfected with PGI siRNA under the conditions described in the legend to panel (c). PGI siRNA resulted in accumulation of G6P and a decrease in F6P, thus confirming inhibition of the PGI-catalyzed reaction by PGI siRNA. The decrease in F1,6P_2 and lactate concentrations observed after PGI siRNA treatment also suggests that glycolysis in neurons is not supported by redirection of G6P through the non-oxidative branch of the PPP. **(e)** Cdh1 silencing (left panel) or over-expression of Pfkfb3 (right panel) increased neuronal apoptosis triggered by etoposide. **(f)** To test whether detachment of neurons from the plates resulted in a loss of neurites and/or axons, western blotting against the synaptic protein Gap43 was performed in neurons lysed on plates or lysed after cell sorting. The presence of equivalent amounts of Gap43 in the attached and the cell-sorted neurons shows that collection of the neurons followed by flow cytometric sorting does not cause a loss of the neurites/axons. **(g)** Moderate over-expression of Pfkfb3 cDNA in neurons followed by cell sorting revealed the accumulation of Pfkfb3 in amounts approximately 1-5-fold higher than those found in astrocytes, as assessed by densitometry. Results are means ± S.E.M (n=3). *p<0.05 *versus* the corresponding control.

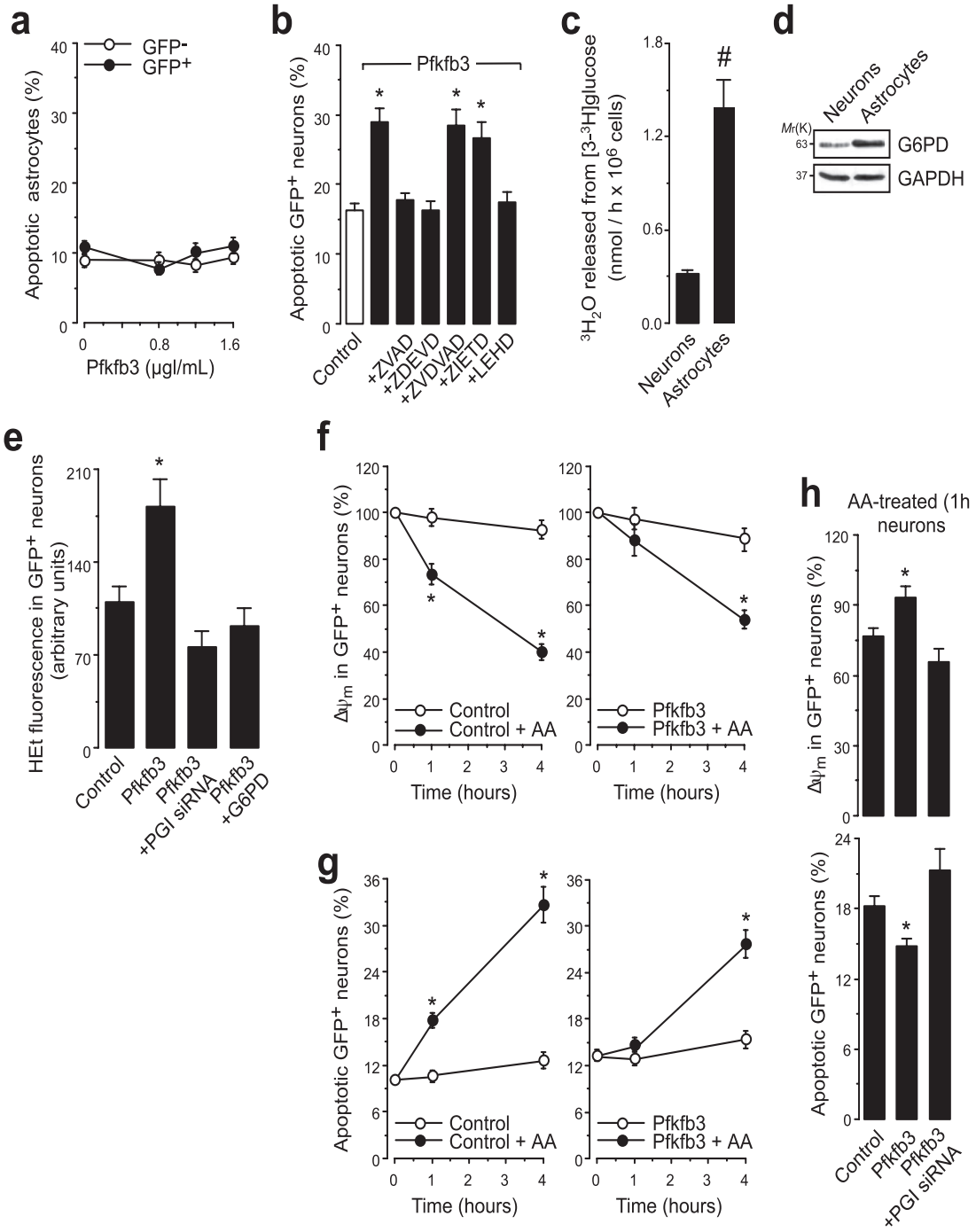

Figure S3 (a) Over-expression of Pfkfb3 does not cause apoptotic cell death in astrocytes. **(b)** The apoptotic death of primary neurons caused by Pfkfb3 expression was prevented by inhibitors of caspases (ZVAD), caspase-3 (ZDEVD) and caspase-9 (LEHD), but not by inhibitors of caspase-8 (ZVDVAD) or caspase-2 (ZIETD). **(c)** The rate of ^3H_2O released from [3-^{3}H]glucose (an index of glucose consumption through Pfk1) was about 4.5-times higher in astrocytes than in neurons. The rate of conversion of [3-^{3}H]glucose into ^3H_2O was expressed per 10^6 cells in order to facilitate comparison of glucose consumed through Pfk1 (this panel) with that consumed through the PPP (see Fig. 3a); 10^6 astrocytes contained 0.80 mg of protein, and 10^6 neurons contained 0.70 mg of protein. **(d)** Endogenous levels of glucose-6-phosphate dehydrogenase (G6PD) are approximately 2.5-fold higher in astrocytes than in neurons, as assessed by densitometry. **(e)** Quantitation of HEt fluorescence (see Fig. 3e) after Pfkfb3 expression in neurons, showing that the increased HEt fluorescence was abolished either by PGI silencing (PGI siRNA) or G6PD expression. **(f)** Primary neurons were transfected with control plasmid vector (left panel) or Pfkfb3 (right panel) and then exposed to antimycin A (AA). AA triggered a rapid loss of $\Delta\psi_m$, which was initially prevented in neurons transfected with Pfkfb3. **(g)** Apoptotic death was assessed in neurons treated as in **(f)**. AA triggered apoptotic death of neurons transfected with control plasmid vector (left panel). However, in neurons transfected with Pfkfb3 the effect of AA was delayed (right panel). **(h)** The protective effect of Pfkfb3 against AA-mediated loss of $\Delta\psi_m$ (upper panel) and apoptotic death (lower panel) was prevented by GPI siRNA. Results are means ± S.E.M (n=3). *p<0.05 *versus* the corresponding control; #p<0.05 *versus* neurons.

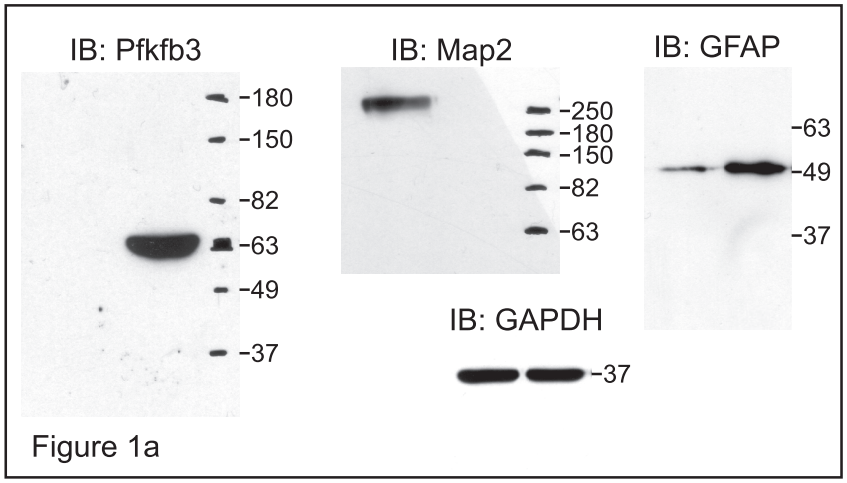

Figure 1a

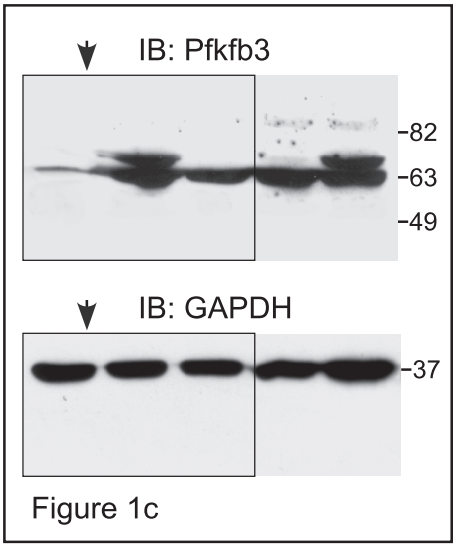

Figure 1c

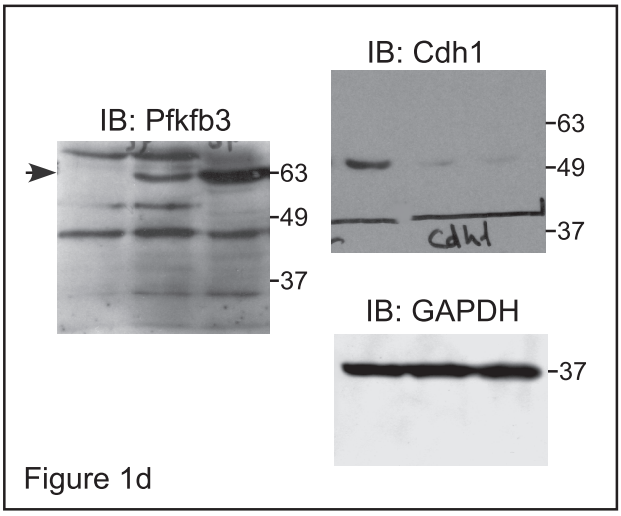

Figure 1d

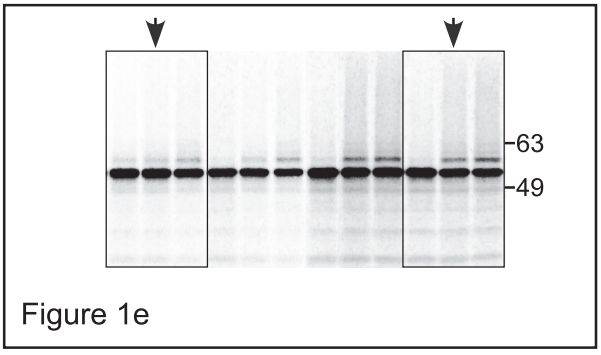

Figure 1e

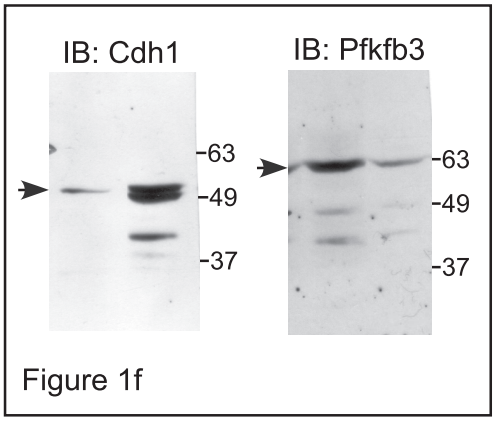

Figure 1f

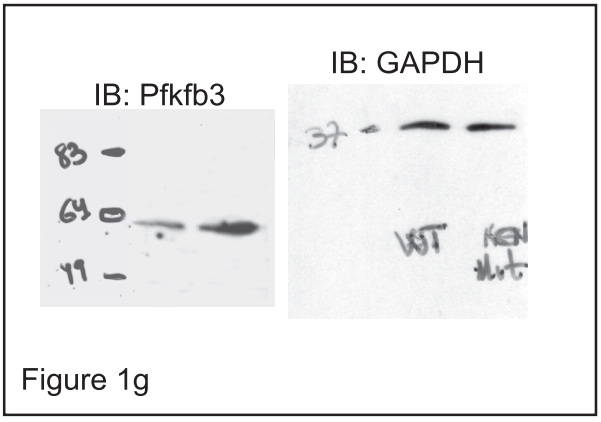

Figure 1g

Figure S4 Full scan of key western data shown in Fig. 1a, 1c, 1d, 1e, 1f, 1g; Fig S1b, S1d. S1e; Fig S2c, S2g.

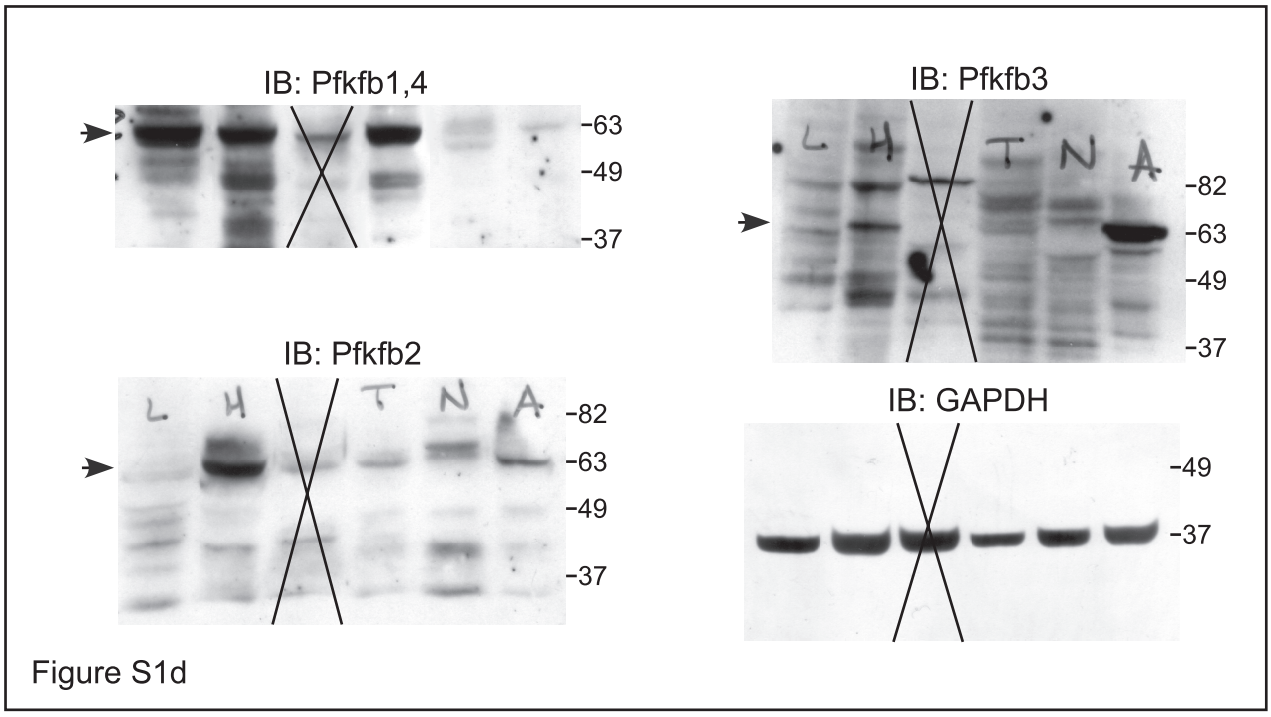

Figure S1d

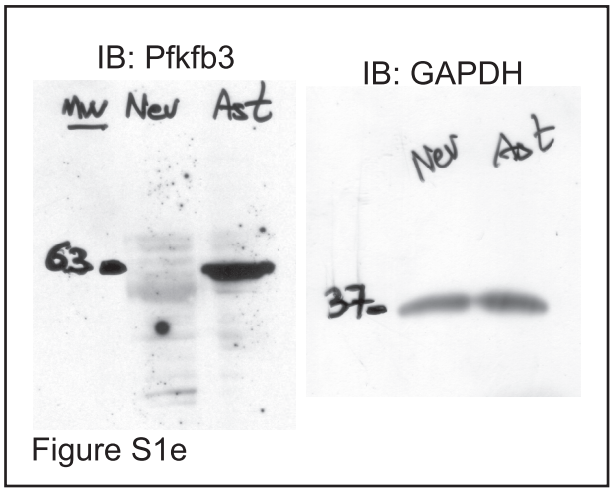

Figure S1e

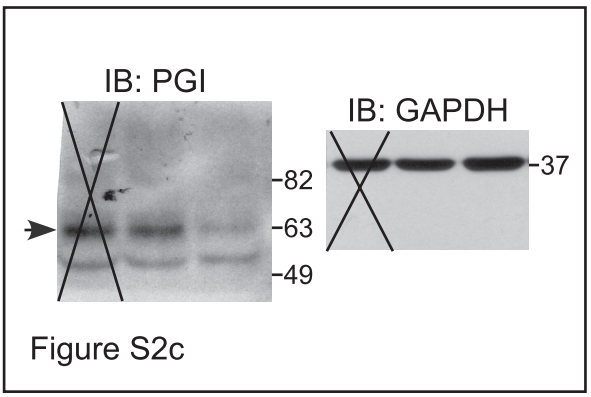

Figure S2c

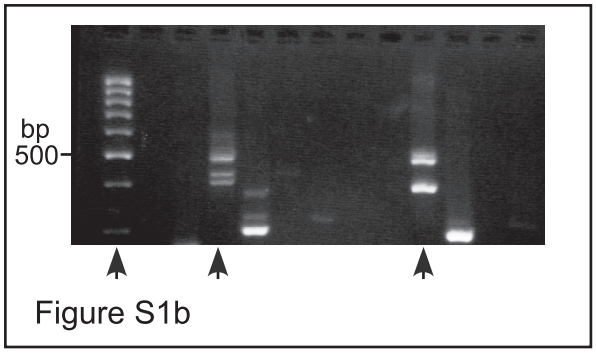

Figure S1b

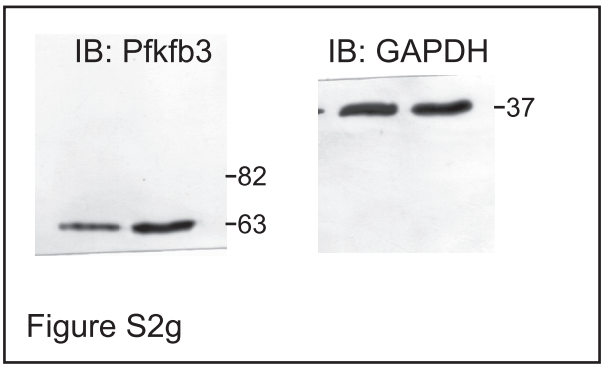

Figure S2g

Figure S4 continued

Supplementary Methods

Oligonucleotides and rtPCR conditions to amplify Pfkfb3. The sense and antisense oligonucleotides used to amplify the Pfkfb3 full length cDNA were 5'-GTCGCCGAATACAGCAACGAAGATG-3' and 5'-GAACCCCTACTTCAGCATCAGTG-3', respectively. To obtain the Pfkfb3 kinase domain (735 bp) we used the following forward and reverse oligonucleotides, respectively: 5'-GTCGCCGAATACAGCAACGAAGATG-3' and 5'-TCCGGGGGAAATCCGGCTACTGCACGTGGATGTTCA-3'. To obtain the Pfkfb3 bisphosphatase domain (828 bp) we used 5'-CCCCGGACCATCTACCTGTGT and 5'-GAACCCCTACTTCAGCATCAGTG-3'. Reverse transcription was performed at 48 ºC for 50 min, and PCR conditions were 10 min at 94 ºC, 1 min at 94 °C (35 cycles), 1 min at 59,7 ºC, and 2 min at 68 °C. Final extension was carried out for 10 min at 68 °C. The cDNA products were purified, inserted in the *EcoRI* site of pIRES2-EGFP mammalian expression vector (Invitrogen) and sequenced. This construction was functional, as judged by the increased $F2,6P_2$ concentrations obtained in HEK293T cells (in nmol/mg protein, control, 80±5; Pfkfb3, 130±11; n=3). HEK293T cells were incubated in DMEM containing 10% FCS and seeded at 10^5 cells/cm^2 24 h before the experiments were carried out.

Antibodies against Pfkfb3. A polyclonal antibody against Pfkfb3 was obtained by rabbit immunization with 100 ng of the Keyhole Limpet haemocyanin-coupled synthetic peptide (Thermo Fisher Scientific, Waltham, MA, USA) ^{508}MRSPRSGAESSQKH^{521}-C, which is common to the translational products of the Pfkfb3 mRNA splice variants K3 and K6. Antisera were purified by affinity chromatography using columns of cyanogen-bromide-activated sepharose coupled to the peptide. The specificity of the antibody was tested by dot blotting against the peptides at a dilution of 1:20,000. Since this antibody does not recognise the other translational products of the rat Pfkfb3, we also used a commercial anti-Pfkfb3 antibody raised against a C-terminal region of the human Pfkfb3 (Protein Accession Q16875; catalogue number sc-10091, Santa Cruz Biotechnology, Santa Cruz, CA. U.S.A.). This antibody cross-reacts with human and rat Pfkfb3 (http://www.scbt.com/datasheet-10091-pfk-2-br-pl-l-13-antibody.html) and therefore recognizes a region that is shared by all translational products of the rat K1 to K8 Pfkfb3 mRNA splice variants.

Reverse transcription-polymerase chain reaction (rtPCR). To identify the Pfkfb isoforms expressed in neurons, total RNA samples from rat cultured neurons were amplified using the following forward and reverse oligonucleotides, respectively: 5'-CAGATGAGCTGCCCTATCTCAAGT-3' and 5'-AGGTAGGGCACTCTCAGGCCATAG-3' for Pfkfb1; 5'-CGTCCTCGTTATCTCTCACC-3' and 5'-CCCAACACTGTAATTTCTTGGAC-3' for Pfkfb2; 5'-CCAGCCTCTTGACCCTGATAAATG-3' and 5'-TCCACACGCGGAGGTCCTTCAGAT-3' for Pfkfb3, and 5'-ACCACTACCCGCTGGAGTTTG-3' and 5'-GTCTGTCTCGGTGTGTGTTCA-3' for Pfkfb4. RT-PCR conditions were 50 min at 48 ºC for reverse transcription; 10 min at 94 ºC; 35 cycles of 1 min at 94 °C, 1 min at 58 ºC, and 30 seconds at 68 °C; final extension was carried out for 10 min at 68 °C. To identify the eight Pfkfb3 alternative splice variants[1] in rat neurons and astrocytes, total RNA samples of these cells were amplified using the following forward and reverse oligonucleotides, respectively: 5'-CTAGCCTACTTCCTTGACAAG-3' and 5'-GTGACAGACAGTTCGTAGACAGG-

3' (for both K1 and K4); 5'-CTAGCCTACTTCCTTGACAAG-3' and 5'-GAACCCCTACTTCAGCATCAGTG-3' (for K1 to K6); 5'-CTAGCCTACTTCCTTGACAAG-3' and 5'-GGAGACCAAAAGGGCCAACAAGC-3' (for K7 and K8). Reverse transcription was carried out at 48 ºC for 50 min, and PCR conditions were 10 min at 94 ºC; 1 min at 94 °C (35 cycles); 45 seconds at 56.8 ºC and 45 seconds at 68 °C; final extension was carried out for 10 min at 68 °C.

Preparations of cells for the measurement of PPP and glycolytic fluxes. Suspensions of known amounts of cells (~1-2 x 10^5 cells) obtained from sorting or culture were incubated in sealed vials containing a central well, which was used for $^{14}CO_2$ or ^3H_2O trapping, in the presence of 1 μCi of D-[1-^{14}C]glucose (for PPP determinations), D-[6-^{14}C]glucose (1 μCi for glycolytic flux determinations; 5 μCi for PPP determinations) or 5 μCi of D-[3-^{3}H]glucose (for glycolytic flux determinations) in a Krebs-Henseleit buffer (11 mM Na_2HPO_4, 122 mM NaCl, 3.1 mM KCl, 0.4 mM KH_2PO_4, 1.2 mM $MgSO_4$, 1.3 mM $CaCl_2$; pH 7.4) containing 5 mM D-glucose at 37 ºC. We used this buffer instead of the culture medium because of its simpler composition. In addition, we used suspended, rather than plated cells because cell-sorted neurons do not attach when re-plated, and also because most $^{14}CO_2$ or ^3H_2O released from cells would be lost from the non-hermetically-sealed Petri dishes. In order to ensure an adequate O_2 supply for oxidative metabolism by the cells throughout the 90 minute incubation period, the gas phase in the vials containing the cells was supplied with extra O_2 before the vials were sealed.

Determination of the glycolytic flux. Cells were incubated as indicated in the previous section, and the reaction was stopped after 90 min with either NaOH (0.06 M) (for ^{14}C-lactate determinations) or $HClO_4$ (3%, v/v) (for ^3H_2O determinations). To quantify ^{14}C-lactate, cell extracts were neutralized with 1% (w/v) $ZnSO_4$, centrifuged at 16,000 x *g* and 0.5 ml of the supernatant passed through 0.5 x 5 cm Dowex AG 1x8 borate and Dowex AG 1x8 formate tandem columns (BioRad Laboratories)[2,3]. Lactate and glucose elution coefficients were calculated by loading columns with 0.4 ml of a mixture of either 5 mM glucose and 5 mM lactate (standard mixture A), or 2 μCi ml^{-1} of [3-^{3}H]glucose and 0.5 μCi ml^{-1} of [U-^{14}C]lactate (standard mixture B). Once loaded with samples or standards, tandem columns were washed with 8 ml of water and separately eluted with 8 ml of 4 M formic acid. Aliquots of 1 ml of the eluates were used to determine spectrophotometrically lactate and glucose concentrations (for standard mixture A) or ^{3}H and ^{14}C radioactivity (for eluates of standard mixture B and samples). Using this method, >95% of the radioactivity from glucose and >98% of radioactivity from lactate (from standard mixture B) was recovered from the borate and formate columns at fractions 3-6 and 2-4 of formic acid, respectively. In preliminary experiments, solutions of [3-^{3}H]glucose or [U-^{14}C]lactate were passed through borate and formate columns in tandem. This was followed by elution of each column separately with formic acid. No ^{3}H radioactivity was found in any of the ten formic acid fractions collected from the formate columns or ^{14}C radioactivity in any of the ten formic acid fractions collected from the borate columns. In addition, we found that the ^{3}H to ^{14}C ratios delivered by the scintillation counter were 0.007948 (dpm ^{3}H/dpm ^{14}C ratio, in channel B) and 0.003650 (dpm ^{14}C /dpm ^{3}H ratio, in channel A), indicating almost complete separation of both radioisotopes. These experiments indicate that there was no cross-contamination between [3-^{3}H]glucose and [U-^{14}C]lactate in the collected fractions. The retention indices (RI) for organic acids are inversely correlated with the pKa using formic acid as eluent in the Dowex AG1x8 formate column [4]. Thus, acidic metabolites of the cellular oxidative metabolism with a lower pKa than lactate (pKa,

3.08), such as pyruvate (pKa, 2.25), aspartate (pKa, 2.1), glutamate (pK, 2.2), or 2-oxoglutarate (pKa, 2.47) have higher RI values than lactate and are retained in the column or eluted after lactate. Other acidic metabolites of the Krebs cycle, such as succinate (pKa, 4.19), malate (pKa, 3.4) and isocitrate (pKa, 3.29), with lower RI values than lactate are eluted with the first few fractions. Thus, the possible contribution of metabolites with pool sizes of the order of those of lactate in the lactate fractions is likely to be insignificant. Citrate (pKa, 3.13) or fumarate (pKa, 3.03), which might co-elute with lactate because of their similar pKa values, could contribute to the lactate fraction only negligibly because of their much lower pool sizes than those to lactate. To quantify ^3H_2O, vials were left to equilibrate for 48 h with 1 ml of water, which was used to quantify the ^3H content by liquid scintillation counting[5,6]. Sufficient counts were collected to achieve a coefficient of variation of the counting rates for ^{14}C and ^3H not greater than 2%. Both ^{14}C-lactate and ^3H_2O formation was linear over time for at least 90 min.

Metabolite determinations. D-Glucose, D-glucose-6-phosphate (G6P), D-fructose-6-phosphate (F6P) and D-fructose-1,6-bisphosphate ($F1,6P_2$) were measured in neutralized perchloric extracts obtained from approximately 15 x 10^6 cells. For D-glucose, the increments in absorbance of the samples were measured at 340 nm in a reaction mixture containing 3.8 mM $MgCl_2$, 0.38 mM $NADP^+$, 0.38 mM ATP, 1 U ml^{-1} of G6PD and 2 U ml^{-1} of hexokinase in 38.5 mM Tris-HCl buffer at pH 8 (Ref. [7]). G6P and F6P were measured as the increments in absorbance at 340 nm of the samples in two consecutive coupled reactions, catalyzed by G6PD (0.17 U ml^{-1}) and PGI (0.7 U ml^{-1}), respectively, in a reaction mixture containing 5 mM $MgCl_2$ and 0.2 mM $NADP^+$ in 0.2 M triethanolamine buffer at pH 7.6 (Ref. [8]). For $F1,6P_2$, the decrease in absorbance of the samples was measured at 340 nm in a reaction mixture containing 0.017 mM $NADH(H^+)$, 0.13 U ml^{-1} glycerol-3-phosphate dehydrogenase, 0.83 U ml^{-1} triosephosphate isomerase and 0.04 U ml^{-1} aldolase in a 0.2 M triethanolamine/20 mM EDTA buffer at pH 7.6 (Ref. [9]). For lactate, the increments in absorbance of the samples were measured at 340 nm in a mixture containing 1 mM NAD^+ and 22.5 U ml^{-1} lactate dehydrogenase in 0.25 M glycine/0.5 M hydrazine/1 mM EDTA at pH 9.5 (Ref. [10]). For fructose-2,6-bisphosphate ($F2,6P_2$) determinations, cell extracts were lysed in 0.1 M NaOH and centrifuged (20,000 *g* for 20 min). An aliquot of the homogenate was used for protein determination and the remaining sample was heated at 80ºC (5 min), centrifuged (20,000 *g* for 20 min) and the resulting supernatant used for determination of $F2,6P_2$ concentrations[11]. For glutathione determinations, cell sorted-neurons were treated with 1% (w/v) sulfosalicylic acid and centrifuged at 13,000 x *g* for 5 min at 4°C. Total (GSx, i.e. the amount of GSH plus 2 times the amount of GSSG) and oxidized glutathione concentrations were measured in the supernatants using the enzymatic method of Tietze[12]. GSSG was quantified after derivatization of GSH in the samples with 2-vinylpyridine. Data were extrapolated to those obtained with GSSG standards (0-5 µM for GSSG; 0-50 µM for GSx). GSH concentrations were calculated as the difference between GSx and 2 x GSSG.

APC/C ubiquitin ligase activity. Active APC/C was immunoprecipitated from neurons or astrocytes using monoclonal α-APC3 antibody (Becton Dickinson Biosciences) and immobilized on Dynabeads Protein A (Invitrogen). For ubiquitination, reactions were performed as described[13] at 37 ºC in 10 µl of buffer (0.1 M KCl, 2.5 mM $MgCl_2$, 2 mM ATP, 7.5 µg ubiquitin, 0.3 mM dithiothreitol, 135 mM MG132, 1 mM ubiquitin aldehyde, 2.5 mM His-UbcH10 and 2.5 µM UbcH5a in 20 mM Tris-HCl, pH 7.5)

containing 2.5 µl of APC/C beads and 1 µl of [^{35}S]cyclin B1. Reactions were stopped at the indicated time points with SDS sample buffer, mixtures resolved by SDS-polyacrylamide gel electrophoresis and visualized by phosphorimaging.

Northern blotting. Purified (Genelute mammalian total RNA miniprep kit, Sigma) total RNA samples were electrophoresed (15 µg of RNA/line) on a 1% (w/v) agarose-formaldehyde gel. After transfer to a GeneScreen Plus membrane (NEN Life Sci., Boston, MA) and cross-linking by ultraviolet irradiation, membranes were hybridised for 18 h at 65 °C in the presence of random-primed [α-^{32}P]dCTP-radiolabelled (Amersham Biosciences, Buckinghamshire, U.K.) cDNA probes for the Pfkfb3 kinase domain and a 0.7 kb cDNA fragment of the rat cyclophilin, used as a loading control. Membranes were then exposed to Kodak XAR-5 film.

Western Blotting. Aliquots (100 µg of protein) of neuron lysates (in 2% sodium dodecylsufate, 2 mM EDTA, 2 mM EGTA, 5 mM Tris, 100 µM phenylmethylsulfonyl fluoride, 50 µg ml^{-1} pepstatin, 50 µg ml^{-1} amastatin, 50 µg ml^{-1} leupeptin, 50 µg ml^{-1} bestatin and 50 µg ml^{-1} soybean trypsin inhibitor) were centrifuged (14,000 *g*, 10 min) and electrophoresed in an 8% SDS acrylamide gel. Proteins were transferred electrophoretically to nitrocellulose membranes, which were blocked in 5% (w/v) low-fat milk in 20 mM Tris, 500 mM sodium chloride, 0,1% (w/v) Tween 20 (at pH 7.5) for 1h, and further incubated with antibodies against Pfkfb3 (described in Methods), commercial Pfkfb3 (PFK-2 brain/placental, catalogue number sc-10091; Santa Cruz Biotechnology) PGI (Santa Cruz Biotechnology), Cdh1 (AR38, J. Gannon, Clare Hall Laboratories, Cancer Research UK), Gap43 (Abcam plc, Cambridge, UK), G6PD (J. M. Bautista, Universidad Complutense, Madrid, Spain), Pfkfb2 (C. MacIntosh, University of Dundee, UK), Pfk1/4 (Santa Cruz Biotechnology) or GAPDH (Sigma) overnight at 4 ºC. Signal detection was performed with an enhanced chemiluminescence kit (Pierce, Thermo Scientific, Waltham, MA, USA).

Inmunohistochemistry. Wistar rats were deeply anaesthetized with a mixture (3:4) of ketamine hydrochloride (Ketolar; Parke-Davis, Barcelona, Spain) and tiacine hydrochloride (Rompún; Bayer, Leverkusen, Germany) using 1 mL of the mixture per kg body weight, and then perfused intra-aortically with 0.9% NaCl, followed by Somogy's fixative without glutaraldehyde (5 mL/g per body weight). After perfusion, brains were dissected out and postfixed with the same fixative for 24 h at 4 ºC. Brain blocks were then rinsed for 2 h with 0.1 M phosphate buffer (PB), pH 7.4, and immersed in 30% (w/v) sucrose PB until they sank. After cryoprotection, 30 µm-thick coronal sections were obtained with a freezing-sliding microtome (Leica Frigomobil, Jung SM 2000, Leica, Nussloch, Germany). The sections were collected in 0.05% sodium azide (w/v) in PB at 4 ºC. Coronal sections were rinsed in 0.1 M PB, pH 7,4 three times each for 10 minutes, and then incubated sequentially in: (i) 1% sodium borohydride for 20 minutes to remove aldehyde autofluorescence; (ii) 0,2% Triton X-100 and 5% normal donkey serum in PB for 1h at room temperature; (iii) 1:100 goat anti-Pfkfb3 (PFK2 br/pl Santa Cruz Biotechnology sc-10091), 1:5,000 mouse anti-NeuN (No.MAB377, Chemicon international. Temecula, CA, USA), 1:1,000 mouse anti-glial fibrillary acidic protein (GFAP; No.G-3893, Sigma) in 0.2% Triton X-100 and 5% normal donkey serum for 72 h at 4 ºC in PB; (iv) 0.1 µg/mL DAPI in PB for 10 minutes at room temperature and; (v) 1:400 Cy2-conjugated donkey anti-goat, 1:400 Cy3-conjugated donkey anti-mouse (all the secondary antibodies are from Jackson Immunoresearch, Pennsylvania, U.S.A.) in PB for 2 h at room temperature. Between

each step, the sections were carefully rinsed three times each for 10 minutes in PB. After rinsing, sections were mounted with an antifading medium. Sections were examined using both a microscope (Provis AX70; Olympus, Tokyo, Japan) equipped with epifluorescence and appropriated filters sets, and a confocal microscope (TCS SP2; Leica, Mannheim, Germany).

Accession numbers. Pfkfb1 (NM_012621), Pfkfb2 (NM_080477), Pfkfb3 (NM_057135), Pfkfb4 (NM_019333), PGI (NM_207192), Cdh1 (NM_016263), and cyclin B1 (AY338491).

References

1. Watanabe, F., Sakai, A. & Furuya, E. Novel isoforms of rat brain fructose 6-phosphate 2-kinase/fructose 2,6-bisphosphatase are generated by tissue-specific alternative splicing. *J Neurochem* **69**, 1-9 (1997).
2. Hammerstedt, R. H. The use of Dowex-1-borate to separate 3HOH from 2-3H-glucose. *Anal Biochem* **56**, 292-3 (1973).
3. Huang, M. & Veech, R. L. The quantitative determination of the in vivo dephosphorylation of glucose 6-phosphate in rat brain. *J Biol Chem* **257**, 11358-63 (1982).
4. Thauer, R. K., Rupprecht, E. & Jungermann, K. Separation of 14C-formate from CO2 fixation metabolites by isoionic-exchange chromatography. *Anal Biochem* **38**, 461-8 (1970).
5. Katz, J., Rognstad, R. & Kemp, R. G. Isotope Discrimination Effects in the Metabolism of Tritiated Glucose. *J Biol Chem* **240**, PC1484-6 (1965).
6. Hughes, S. D., Quaade, C., Johnson, J. H., Ferber, S. & Newgard, C. B. Transfection of AtT-20ins cells with GLUT-2 but not GLUT-1 confers glucose-stimulated insulin secretion. Relationship to glucose metabolism. *J Biol Chem* **268**, 15205-12 (1993).
7. Bergmeyer, H. U., Bernt, E., Schmidt, F. & Stork, H. in *Methods of Enzymatic Analysis* (ed. Bergmeyer, H. U.) 1196-1201 (Verlag Chemie GmbH, Weinheim, 1974).
8. Michal, G. in *Methods of Enzymatic Analysis* (eds. Bergmeyer, J. & Graßl, M.) 191-198 (Verlag Chemie, Weinheim, Deerfield Beach (FL), Basel, 1985).
9. Michal, G. in *Methods of Enzymatic Analysis* (eds. Bergmeyer, J. & Graßl, M.) 342-350 (Verlag Chemie, Weinheim, Deerfield Beach (FL), Basel, 1985).
10. Gutmann, I. & Wahlefeld, A. W. in *Methods of Enzymatic Analysis* (ed. Bergmeyer, H. U.) 1464-1468 (Verlag Chemie GmbH, Weinheim, 1974).
11. Van Schaftingen, E., Lederer, B., Bartrons, R. & Hers, H. G. A kinetic study of pyrophosphate: fructose-6-phosphate phosphotransferase from potato tubers. Application to a microassay of fructose 2,6-bisphosphate. *Eur J Biochem* **129**, 191-195 (1982).
12. Tietze, F. Enzyme method for quantitative determination of nanogram amounts of total and oxidized glutathione: application to mammalian blood and other tissues. *Anal. Biochem.* **27**, 502-522 (1969).
13. Kimata, Y. et al. A mutual inhibition between APC/C and its substrate Mes1 required for meiotic progression in fission yeast. *Dev Cell* **14**, 446-54 (2008).

nature cell biology

Replication stress induces sister-chromatid bridging at fragile site loci in mitosis

Kok Lung Chan[1,2], Timea Palmai-Pallag[1], Songmin Ying[1] and Ian D. Hickson[1,3]

Several inherited syndromes in humans are associated with cancer predisposition. The gene products defective in two of these disorders, BLM (a helicase defective in Bloom's syndrome)[1] and FANC A–N (defective in Fanconi anaemia)[2], associate in a multienzyme complex called BRAFT[3]. How these proteins suppress tumorigenesis remains unclear, although both conditions are associated with chromosome instability. Here we show that the Fanconi anaemia proteins FANCD2 and FANCI specifically associate with common fragile site loci irrespective of whether the chromosome is broken. Unexpectedly, these loci are frequently interlinked through BLM-associated ultra-fine DNA bridges[4] (UFBs) even as cells traverse mitosis. Similarly to fragile site expression[5], fragile site bridging is induced after partial inhibition of DNA replication. We propose that, after replication stress, sister chromatids are interlinked by replication intermediates primarily at genetic loci with intrinsic replication difficulties, such as fragile sites. In Bloom's syndrome cells, inefficient resolution of DNA linkages at fragile sites gives rise to increased numbers of anaphase UFBs and micronuclei containing fragile site DNA. Our data have general implications concerning the contribution of fragile site loci to chromosomal instability and tumorigenesis.

Maintenance of chromosome stability requires several DNA repair factors, including a protein complex comprising BLM, topoisomerase IIIα and RMI1 (RecQ-mediated genome instability 1)[1,6]. BLM is defective in Bloom's syndrome, a disorder associated with growth retardation, sunlight sensitivity and cancer predisposition[7]. Bloom's syndrome cells show both an elevated frequency of micronuclei and dysregulated homologous recombination[4,6,7]. BLM functions primarily at DNA replication forks disrupted by chemical adducts or by DNA synthesis inhibitors such as aphidicolin (APH)[6]. Another set of proteins required for S phase DNA damage responses are those defective in Fanconi anaemia, a disorder with similarities to Bloom's syndrome including genomic instability and cancer predisposition[2]. Fanconi anaemia is caused by defects in any one of 13 genes. Eight of the Fanconi anaemia gene products comprise the Fanconi anaemia core complex, which promotes the monoubiquitylation of FANCD2 and FANCI[2]. Although the BLM and Fanconi anaemia core complex proteins have been detected in the BRAFT complex[3], it is unclear whether there is functional crosstalk between their respective pathways in the suppression of tumorigenesis.

Recently, immunofluorescence microscopy staining for BLM revealed the existence of UFBs in anaphase that had escaped detection previously because they do not stain with conventional DNA dyes[4]. These structures are surprisingly prevalent; indeed, normal human cells undergoing anaphase generally contain several UFBs, many of which originate from centromeres[4,8]. It has long been speculated that, in addition to sister chromatid cohesion, sister centromeres are held together by DNA catenanes. The identification of UFBs in normal anaphase cells provides direct evidence that DNA linkages exist between centromeres. The only proteins known to colocalize with BLM to these bridges are topoisomerase IIIα, RMI1 (ref. 4) and an SNF2-family protein, PICH (Plk-interacting checkpoint helicase)[8]. The predominance of UFBs at centromeres and their induction by topoisomerase II inhibitors[4,8] strongly suggests that most UFBs represent fully replicated, double-stranded DNA catenanes. However, previous studies could not exclude the possibility that some UFBs derive from recombination or replication intermediates.

Although most UFBs derive from centromeric regions[4,8], we found that some arise from regions near telomeric ends (data not shown). During a search for other DNA replication or repair factors that might localize to UFBs, we identified an intriguing staining pattern for FANCD2 that formed a focus at each terminus of a subset of the bridges (Fig. 1a, top). FANCD2 foci were also evident in Bloom's syndrome cells, where they marked the extremities of bridges (as revealed by PICH staining). Occasionally, a faintly stained FANCD2 'thread' was seen to connect the strongly stained pair of FANCD2 foci (Fig. 1a, bottom).

We investigated possible reasons for the localization of FANCD2 to the termini of UFBs. One possibility was that FANCD2 might mark regions of the genome not processed adequately during S/G2 phase, which then generate UFBs in mitosis. Thus, we analysed FANCD2 localization before anaphase. FANCD2 formed tightly linked, paired foci as early as G2 phase (data not shown). These paired foci remained throughout prophase and metaphase (Fig. 1b) before segregating symmetrically in a manner

[1]Weatherall Institute of Molecular Medicine, University of Oxford, John Radcliffe Hospital, Oxford, OX3 9DS, UK. [2]Current address: Department of Biochemistry, University of Oxford, South Parks Road, Oxford OX1 3QU, UK.
[3]Correspondence should be addressed to I.D.H. (e-mail: ian.hickson@imm.ox.ac.uk)

Received 19 November 2008; accepted 9 February 2009; published online 24 May 2009; DOI: 10.1038/ncb1882

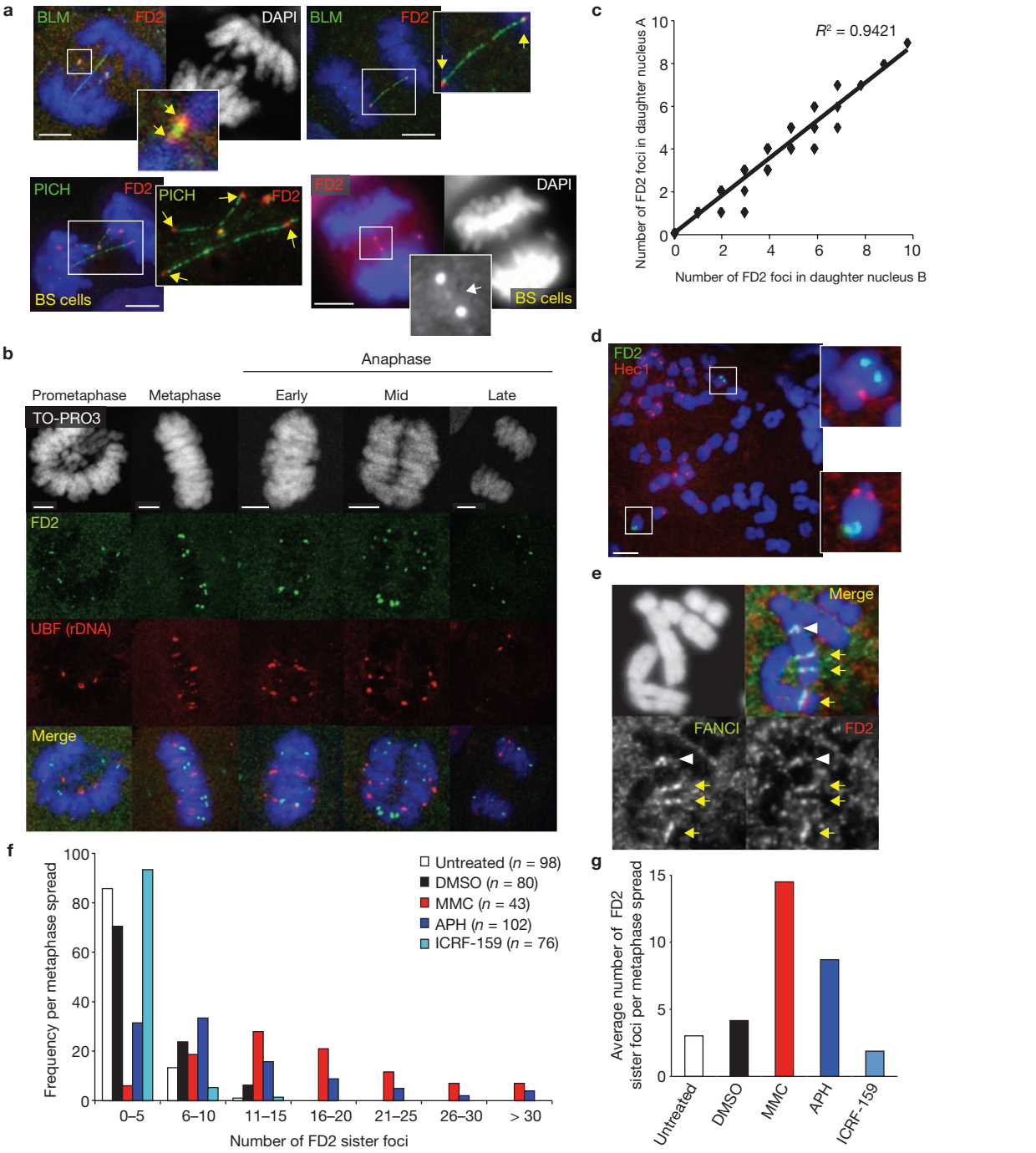

Figure 1 Replication perturbation induces formation of paired FANCD2/I foci at sister genetic loci. (**a**) Deconvoluted images showing pairs of FANCD2 (FD2) foci (yellow arrows) linked by a short (top left) or long (top right) UFB in GM00637 anaphase cells (top). Images show FANCD2 foci at the extremities (yellow arrows, bottom) of PICH-coated UFBs in PSNG13 Bloom's syndrome cells (bottom left). FANCD2 forms a short 'thread' (white arrow) between two FANCD2 foci in PSNG13 Bloom's syndrome (BS) cells (bottom, right). Boxed regions are enlarged. (**b**) Confocal microscopy images of prometaphase, metaphase and anaphase MRC5 primary fibroblasts showing pairs of FANCD2 foci (green) that separate in a symmetrical manner during chromosome segregation in anaphase. UBF (RNA polymerase transcription factor; red) marks rDNA loci. (**c**) The ratio of FANCD2 foci in one MRC5 daughter nucleus to those in the other is shown in **b** (n = 76 anaphase cells). (**d**) FANCD2 (blue) forms foci at the same genetic locus on each sister chromatid on metaphase spreads of HS68 diploid cells. Kinetochores were labelled using an anti-Hec1 antibody (red). **(e)** Colocalization of FANCI and FANCD2 sister-foci (yellow arrows) on HeLa metaphase chromosomes. A 'triple-focus' located at a broken region of chromatin is shown by white arrowheads. (**f**) The effect of MMC, APH and ICRF-159 on the formation of FANCD2 sister foci on mitotic chromosomes. GM00637 cells were untreated, treated with DMSO (0.1%), APH (0.4 μM) or ICRF-159 (10 μM) for 24 h, or with MMC (1 μM) for 8 h, and were then released for 17 h. (**g**) Average number of FANCD2 sister foci per metaphase spread in GM00637 cells after treatments shown in **f**. Scale bars, 5 μm in **a**, **b** and **d**.

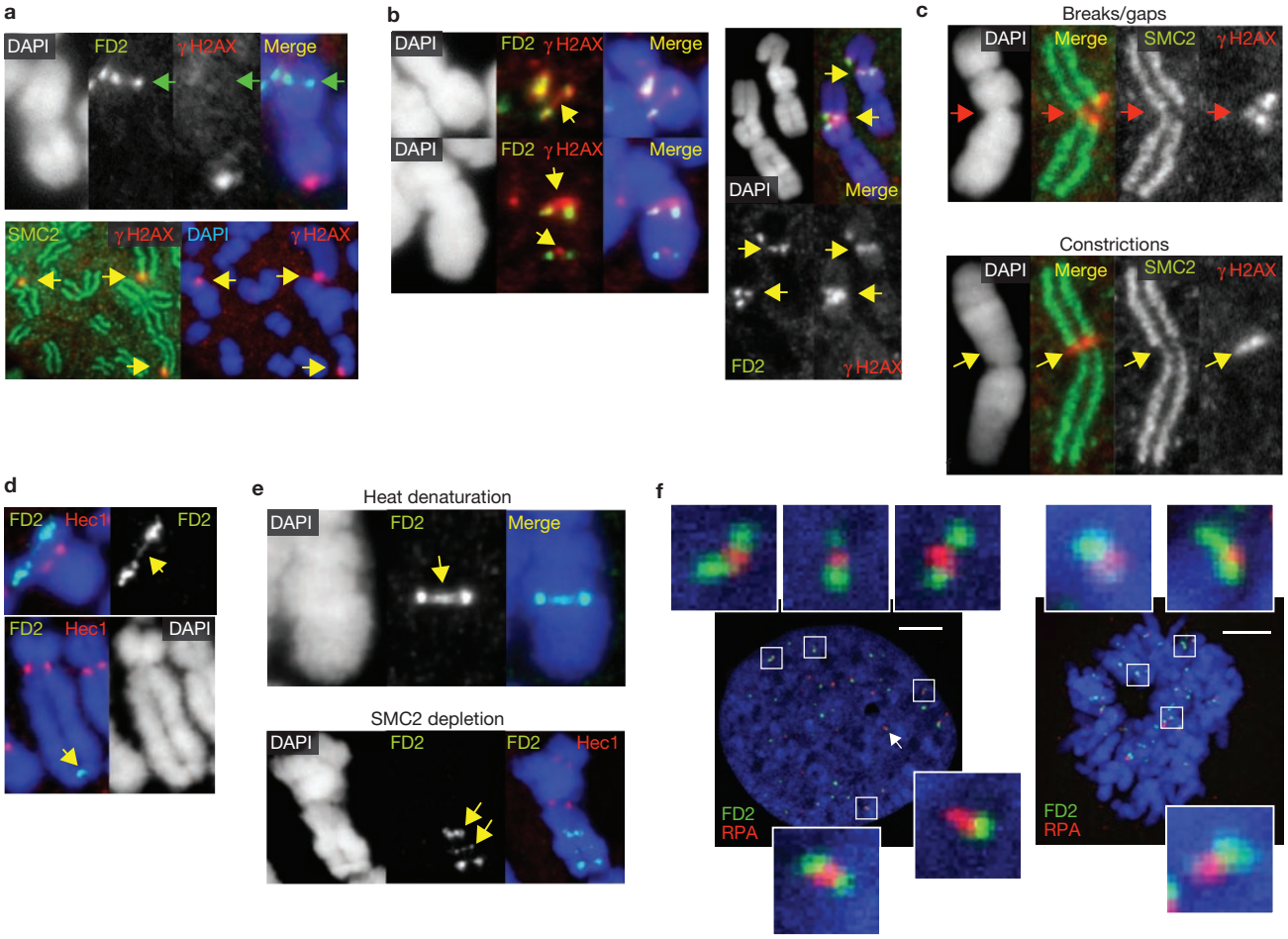

Figure 2 FANCD2 foci on sister genetic loci show aberrant sister chromatid constrictions and DNA interlinkage. HeLa cells were treated with APH (0.4 μM) before being subjected to immuofluorescence analysis. (**a**) A metaphase chromosome shows FANCD2 (FD2) sister foci without activation of γH2AX (green arrows, top) and a telomeric site positive for γH2AX but negative for FANCD2 (yellow arrows, bottom). Each chromosomal axis was labelled using an anti-SMC2 antibody. Of the FANCD2 sister foci 34% were γH2AX-negative, and of the telomeric γH2AX-positive sister foci 1% were also positive for FANCD2 foci. (**b**) FANCD2 sister foci colocalize with and/or flank γH2AX on intact sister chromatids stained with DAPI (left). Triple-foci of FANCD2 and γH2AX are shown on sister-chromatids with breaks/gaps (right). Arrows denote the formation of FANCD2/γH2AX foci at the corresponding locus of the intact sister chromatid opposite the breaks/gaps. (**c**) Activation of γH2AX (red) at chromatid breaks/gaps and corresponding intact sister regions (red arrows), as well as at constricted regions of intact sister chromatids (yellow arrows). Of the breaks/gaps and constrictions 97% were positive for FANCD2 foci ($n = 40$ metaphase cells; total number of FANCD2 sister/triple foci = 577; total number of γH2AX foci = 392). (**d**) Representative images showing a short thread (arrow, top) and a single focus (arrow, bottom) connecting sister chromatids. (**e**) Formamide heat denaturation (top) or partial depletion of SMC2 by RNAi (bottom) was used to disrupt chromosome architecture and show the direct connection between the FANCD2 sister foci. Arrows denote FANCD2-stained threads connecting the sister foci. (**f**) RPA foci located between (boxes) or adjacent to (arrow) FANCD2 sister foci in G2 phase (left) and early mitotic (right) GM00637 cells after treatment with APH. Scale bars, 5μm in **f**.

identical to that of sister ribosomal DNA (rDNA) loci (Fig. 1b, c). Moreover, immunofluorescence microscopy staining on metaphase spreads showed FANCD2 foci localized in pairs on the sister chromatids, one on each sister locus (FANCD2 sister foci; Fig. 1d). The FANCD2 partner protein, FANCI, was similarly localized (Fig. 1e). Consistent with previous analysis of the Fanconi anaemia pathway[2], FANCD2/I sister foci were absent from both FANCI- and FANCD2-deficient cells, and their formation was dependent on an intact Fanconi anaemia core complex (data not shown) and monoubiquitylation of FANCD2 (Supplementary Information, Fig. S1). In contrast, FANCD2/I sister focus formation was independent of other proposed downstream Fanconi anaemia factors, including FANCJ and FANCD1 (also known as BRCA2), and of the ATM (ataxia telangiectasia mutated) and ATR (ATM and Rad3-related) checkpoint kinases (Supplementary Information, Fig. S1).

Replication inhibitors such as mitomycin C (MMC), hydroxyurea and APH induce FANCD2 foci in interphase nuclei[2]. We found that APH and MMC also induced the formation of FANCD2 sister foci (Fig. 1f, g). In contrast, inhibition of topoisomerase II using ICRF-159 (a bis-dioxopiperazine) had no effect on focus formation (Fig. 1f, g), although this agent does increase the frequency of UFBs[4,8]. Notably, all of the FANCD2/I sister foci were located on chromosome arms in normal fibroblasts, and not at centromeres. These data indicate that FANCD2 sister foci are established during S phase and persist into mitosis. We excluded the possibility that FANCD2 foci simply marked sites of DNA double-strand breaks, although some FANCD2 sister foci did colocalize with γ-H2AX (a phosphorylated histone and marker of DNA double-strand breaks; Fig. 2a–c; Supplementary Information, Text and Fig. S2).

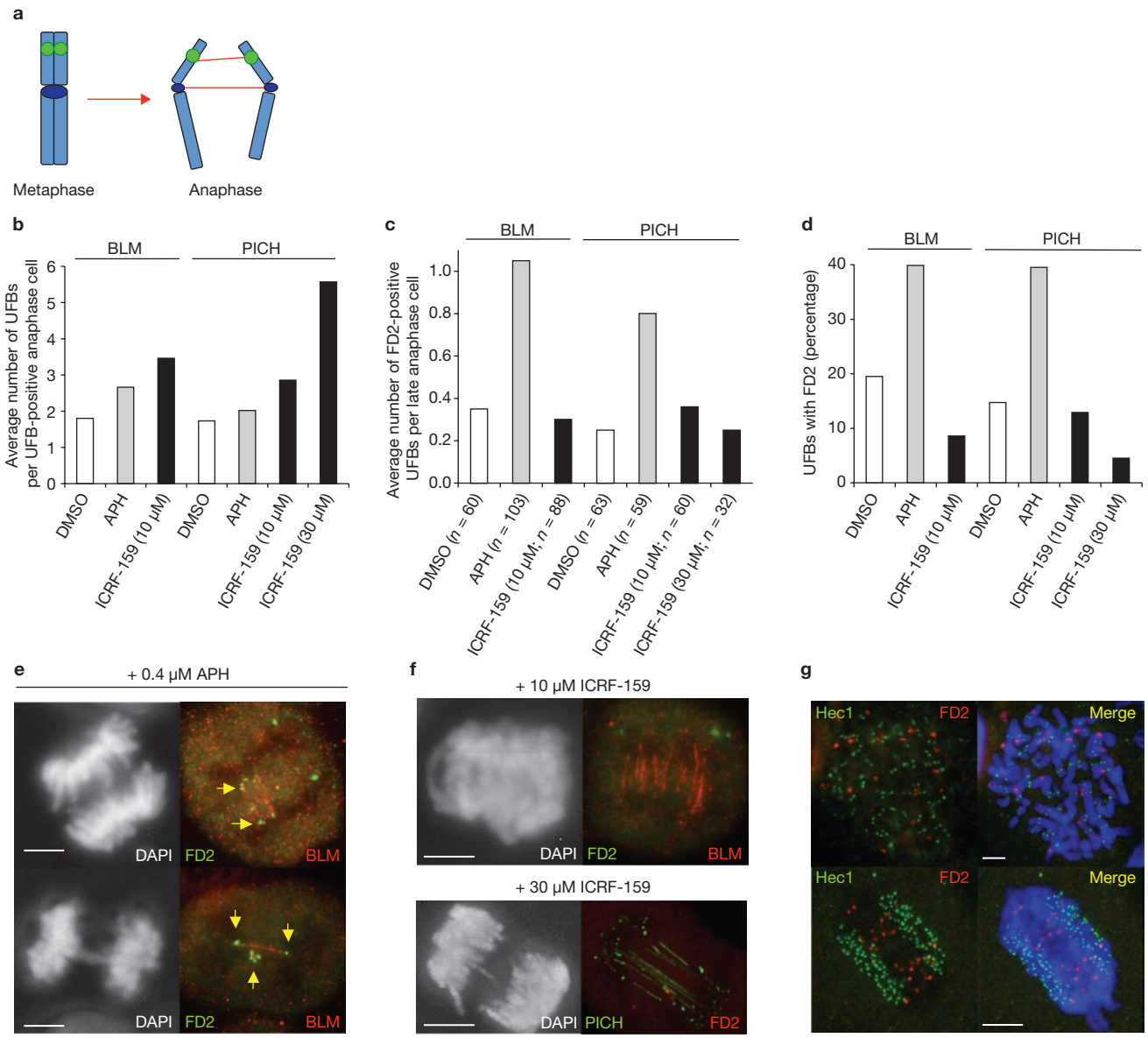

Figure 3 APH specifically induces the formation of FANCD2-associated UFBs in anaphase cells. (**a**) The diagram depicts centromeric (dark blue) or non-centromeric (FANCD2-associated; green) loci. UFBs (red) linking the segregating sister chromatids (light blue) are shown in anaphase. (**b**) GM00637 cells were treated with either APH (0.4 μM) or ICRF-159 (10 μM or 30 μM) for 24 h. DMSO was used as a control. Anaphase DNA bridges were revealed using either anti-BLM or anti-PICH antibodies, and the average number of UFBs per UBF-positive anaphase cell was quantified. (**c**) GM00637 cells were treated as in **b** and the average number of FANCD2-specific UFBs per late anaphase cell was quantified. (**d**) GM00637 cells were treated as in **b**. APH significantly and specifically increases the proportion of UFBss marked by paired FANCD2 foci, whereas ICRF-159 has the opposite effect ($n = 32–103$ anaphase cells). (**e**) Representative, deconvoluted *z*-projection images showing the association of FANCD2 (FD2; arrows) with the termini of APH-induced UFBs. (**f**) Representative, deconvoluted *z*-projection images showing the lack of FANCD2 foci associated with ICRF-159-induced UFBs (10 μM, top; 30 μM, bottom). (**g**) Images showing the lack of centromeric localization of APH-induced FANCD2 foci (red) in mitotic cells. Kinetochores were labelled using a Hec1 antibody (green). Scale bars, 5μm in **e**–**g**.

Next, we addressed whether any physical interlinkage could be detected between the FANCD2 sister foci. Indeed, some sister foci seemed to be connected by a fine 'thread' of FANCD2 (Fig. 2d, top). Moreover, in cases where the arms of sister chromatids had not fully separated in metaphase and appeared fused at a defined point, a single focus of FANCD2 staining was found at the connection point (Fig. 2d, bottom). To analyse this further, we either subjected the metaphase chromosome preparations to mild denaturation or to partial depletion of SMC2, a subunit of the condensin complex required for chromosome condensation[9]. In both cases, the presence of a clear, thread-like structure connecting the FANCD2 sister foci was observed (Fig. 2e). These observations indicate that the FANCD2 sister foci are physically linked, possibly by some form of replication or repair intermediate arising during S phase. This proposal is consistent with the finding that replication protein A (RPA) was also found 'sandwiched' between FANCD2 sister foci in early mitotic cells (Fig. 2f). We therefore analysed whether FANCD2 foci define DNA replication and/or recombination structures. We found that homologous recombination is not required for the formation of FANCD2-associated

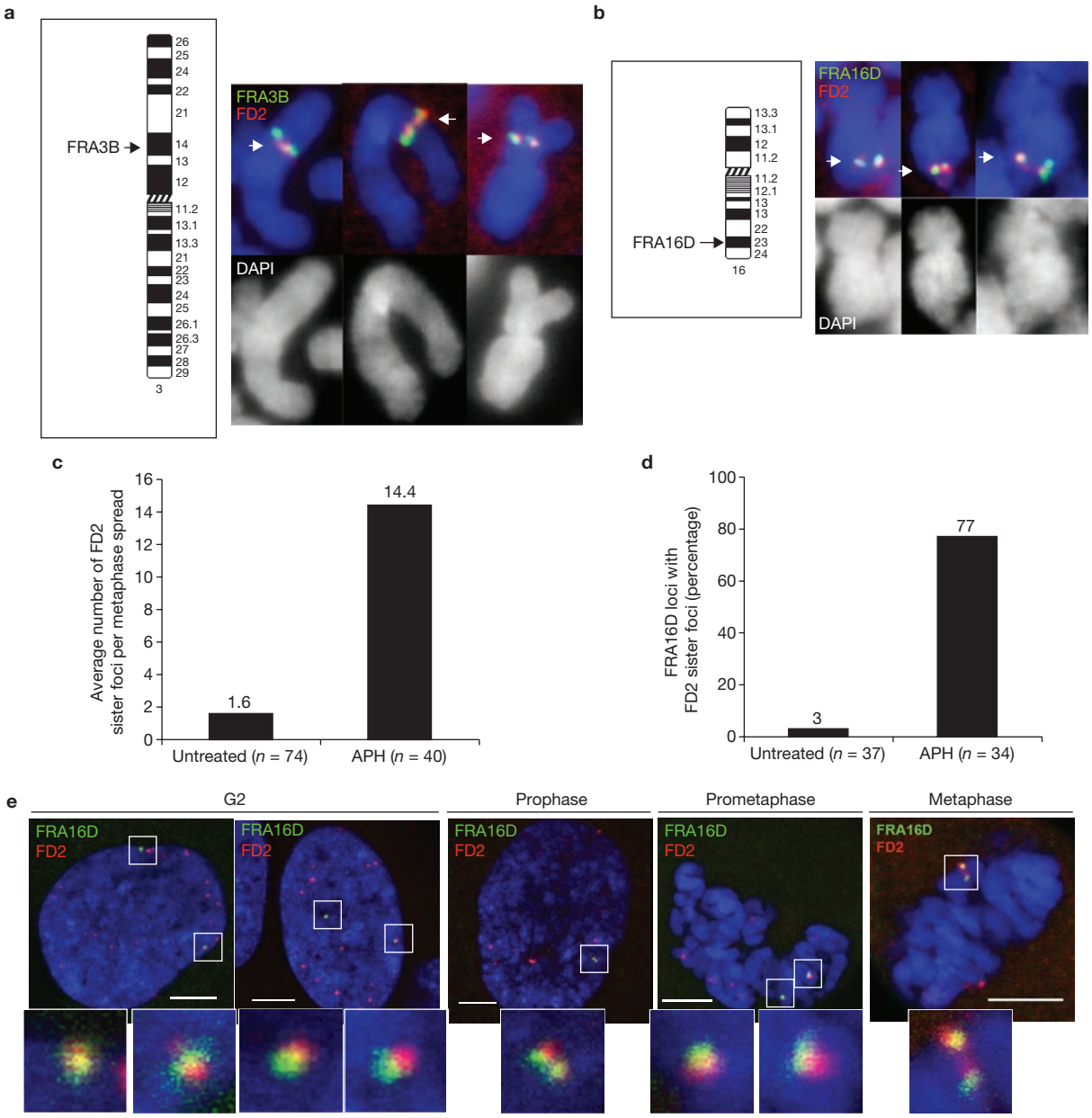

Figure 4 Replication stress induces localization of FANCD2 sister foci to common fragile sites. HeLa or HS68 cells were exposed to a low dose of APH (0.4 μM) for 24 h before analysis. (**a**, **b**) Representative images showing that FANCD2 (FD2) sister-foci specifically localize to the FRA3B (**a**) or FRA16D (**b**) common fragile sites on HeLa metaphase chromosomes. FRA3B, $n = 66$, 21.2% were positive for FANCD2 foci ; FRA16D, $n = 34$, 76.5% were positive for FANCD2 foci. (**c**) Quantification of FANCD2 sister foci on HeLa metaphase spreads under untreated and low dose APH-treated conditions. (**d**) Percentage of FRA16D loci showing associated FANCD2 sister foci after low dose APH treatment of HeLa cells. (**e**) Confocal microscopy images showing the localization of FANCD2 foci to the FRA16D locus from G2 phase to metaphase in HS68 fibroblasts. Enlarged images of the boxes are shown. Scale bars, 5 μm in **e**.

sister chromatid interlinkages, but is instead required for their prevention (Supplementary Information, Text and Fig. S3).

These data imply that perturbation of replication should induce UFBs that arise specifically from FANCD2 sister foci (Fig. 3a). Indeed, APH, MMC and hydroxyurea treatment strongly increased both the percentage of anaphase cells that contained UFBs and the average number of UFBs per anaphase cell (Fig. 3b and data not shown). These drugs also increased the number of FANCD2-associated UFBs (Fig. 3c and data not shown). Importantly, the UFBs induced by APH were not identical to those induced by ICRF-159. After treatment with APH, the proportion of FANCD2 sister foci-associated UFBs increased sharply (Fig. 3d, e), whereas UFBs induced after decatenation-inhibition by ICRF-159 lacked FANCD2 staining at their termini (Fig. 3d, f). These ICRF-159-induced UFBs have been shown previously to be derived primarily from centromeres[4,8]. Notably, FANCD2 sister foci and their associated UFBs did not arise from centromeric regions, irrespective of whether cells were treated with APH (Fig. 3g). Our data indicate that mitotic FANCD2/I sister foci represent sites of sister chromatid linkage, which probably derive from unresolved replication intermediates. However, it should be noted that we could detect UFBs arising from only approximately 10%

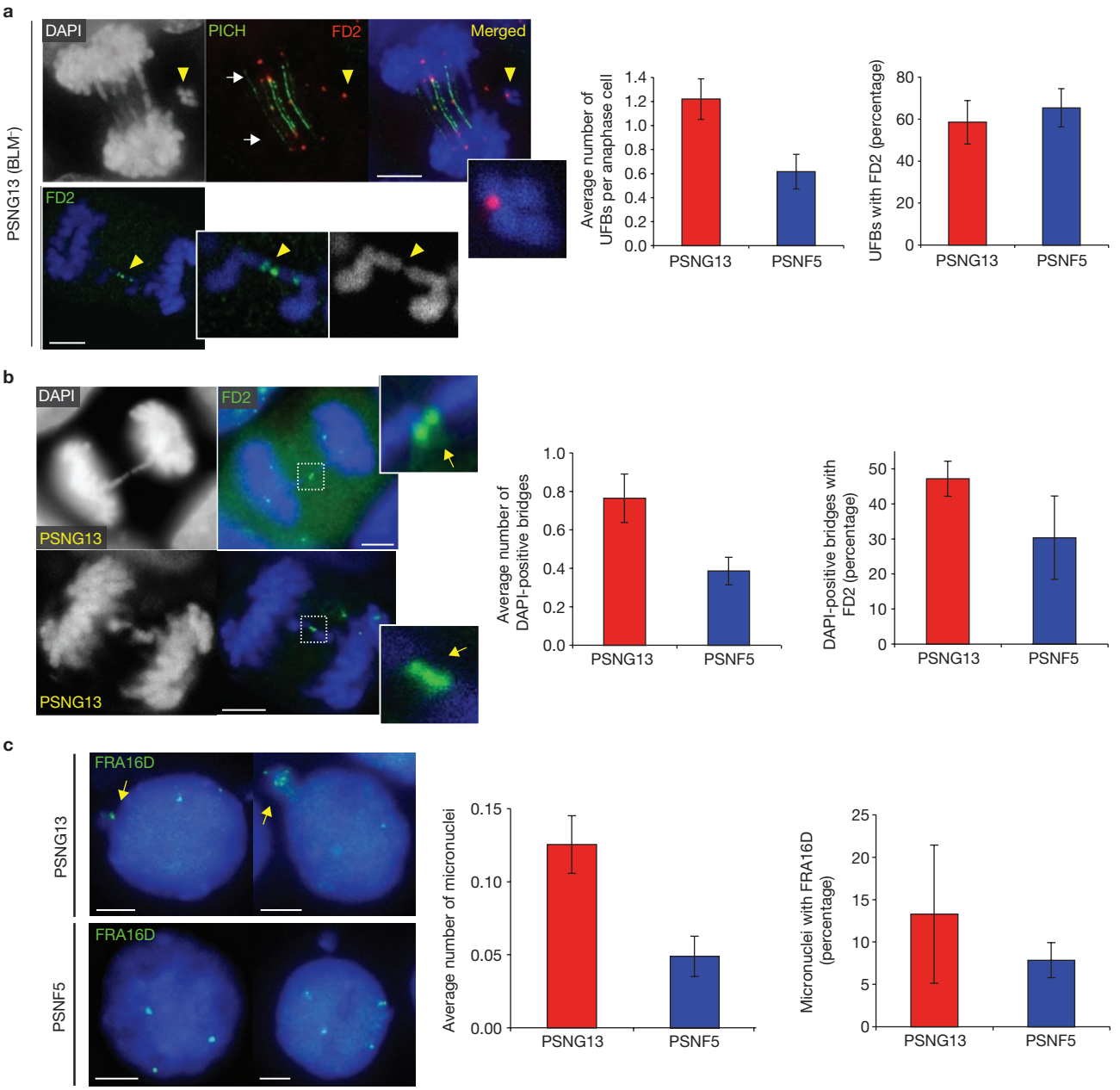

Figure 5 BLM is required for the resolution of DNA linkages that arise from common fragile sites. (**a**–**c**) Isogenic Bloom's syndrome cells, PSNG13 (BLM⁻) and PSNF5 (BLM⁺), were analysed for FANCD2 (FD2)-associated UFBs (**a**, **b**) and FRA16D-associated micronuclei (**c**). (**a**) The average number of UFBs per anaphase cell (left graph) and the proportion of those UFBs associated with FANCD2 (right graph) are shown. Representative images show the formation of FANCD2-associated UFBs (white arrows) and lagging chromatin (yellow arrowheads) in PSNG13 cells. Error bars represent mean ± s.d. from three independent experiments (a total of > 120 anaphase cells). (**b**) Detection of FANCD2 sister foci in the central region of DAPI-positive anaphase bridges (arrows) in PSNG13 cells. The average number of FANCD2-associated DAPI-positive bridges (left graph) and the proportion of these associated with FANCD2 (right graph) are shown. Error bars represent mean ± s.d. from four independent experiments (a total of > 120 anaphase cells). (**c**) Identification of FRA16D sequences (arrows) using FISH in micronuclei from PSNG13 cells (left). Quantification of total micronuclei (left graph) and proportion of micronuclei with FRA16D sequences (right graph) in isogenic Bloom's syndrome cells. Error bars represent mean ± s.d. from three independent experiments (a total of > 1900 cells). Scale bars, 5μm in **a**–**c**.

of the FANCD2 sister foci seen in metaphase, regardless of whether cells had undergone APH treatment. This suggests that the DNA structure recruiting FANCD2 is usually efficiently resolved at, or soon after, the initiation of anaphase.

Non-toxic doses of replication inhibitors (classically APH) can induce chromosome fragility; in particular, at loci defined as common fragile sites[5,10]. We analysed the location of FANCD2 foci on metaphase chromosome spreads. Significantly, all FANCD2 sister foci examined on chromosomes 3, 6, 13, 16 and X seemed to lie at known common fragile site loci (Supplementary Information, Text and Figs S4 and S5). Therefore, we analysed more directly and with higher resolution the location of FANCD2 foci with respect to the chromosomal location of three of the most common fragile site loci, FRA3B, FRA16D and FRA7H. We found that APH-induced FANCD2 sister foci localized specifically to these fragile sites (Fig. 4a, b;

Supplementary Information, Fig. S4f). The rare chromosome 7-specific foci that did not localize to FRA7H were found in regions corresponding to other common fragile sites: FRA7J, FRA7G, FRA7F, FRA7B and FRA7I (Supplementary Information, Fig. S4f). Because of the marked prevalence of localization to FRA16D, we focused on this locus. Similarly to fragile site expression, APH considerably elevated the frequency of FANCD2 sister foci localization to FRA16D in both HeLa (from 3% to 77%) and HS68 (from 2% to 63%; Fig. 4c, d; Supplementary Information, Fig. S5) cells. FANCD2 localization to FRA16D was evident as early as G2 phase, and remained throughout mitosis (Fig. 4e). On average, 6–8 FANCD2 sister foci per metaphase cell were detected in APH-treated HS68 fibroblasts, compared with an average of less than one focus in untreated cells (Supplementary Information, Fig. S5b). Remarkably, more than 20% of these foci were found at the FRA16D locus (Supplementary Information, Fig. S5c). Other commonly observed sites (each at a frequency of approximately 2–4% of the total) were FRA3B, FRA13D, FRA6E and FRA6F (Supplementary Information, Fig. S5c). In the 40 metaphase cells analysed, we did not find any FANCD2 foci on dispersed rDNA loci or on chromosomes 14, 15, 21 or 22 (Supplementary Information, Fig. S5c, d), which rarely express or are devoid of common fragile sites[5] (Supplementary Information,Text).

Interestingly, the percentage of FRA16D loci with a FANCD2 signal (76%; Fig. 4b, d) is much higher than the observed frequency of fragile site expression at this locus (4–20%; data from our laboratory and others)[11,12]; we propose that this is because FANCD2 is recruited not only to broken fragile sites, but also to abnormal linkage or constriction at sites of intact fragile loci. Consistently, we also detected a higher frequency of FANCD2 foci at fragile site loci that were shown previously to have a relatively low rate of breakage, such as FRA13D.

Next, we addressed the functional consequences of forming FANCD2 (fragile site)-associated UFBs. The ability of a low APH doses to induce large genomic deletions and rearrangements is controversial. However, a recent report showed that APH could induce tumour-like microdeletions at the FRA3B locus in human–mouse chromosome 3 somatic cell hybrids[13]. Our discovery of fragile site-associated UFBs (which are estimated to contain hundreds of kilobases of DNA) provides a reasonable explanation for the APH-induced microdeletions, if the UFBs are inefficiently or aberrantly resolved. It has been shown that Bloom's syndrome cells have a higher number of UFBs[4] than normal cells; therefore, we analysed whether Bloom's syndrome cells show chromosome missegregation specifically at fragile site loci. Using the isogenic Bloom's syndrome cell-line pair, PSNG13 (BLM–) and PSNF5 (BLM$^+$; ref. 4), we found that Bloom's syndrome cells had elevated levels of both FANCD2 (fragile site)-associated and non-FANCD2-associated UFBs (Fig. 5a, left graph), although the proportion of FANCD2-associated UFBs was similar to that in BLM$^+$ cells (Fig. 5a, right graph). There was also no significant difference in the frequency of FANCD2 sister foci scored on metaphase chromosomes (data not shown), consistent with the finding that Bloom's syndrome cells do not show an elevation in fragile site expression[10]. Therefore, our results strongly indicate that BLM is required for the resolution of fragile site-associated UFBs rather than for preventing their formation before mitosis. In contrast, Fanconi anaemia cells do not show an elevation in UFBs (data not shown; Supplementary Information, Text)

We next considered whether the FANCD2-associated bridging that persists in Bloom's syndrome cells might impede the dynamics of chromosome segregation. We consistently observed FANCD2 foci at connection points on pairs of lagging chromosomes in these cells (Fig. 5a, bottom left). More importantly, we also detected a higher level of bulky (DAPI-positive) anaphase bridges associated with FANCD2 sister foci in Bloom's syndrome cells. Similarly to the foci seen on lagging chromosomes, FANCD2 was always located in the central connection point of the bridges (Fig. 5b). These results strongly suggest that there is inefficient resolution of DNA linkages at fragile site loci in Bloom's syndrome cells, leading to formation of UFBs and bulky anaphase bridges. One detrimental consequence of an unresolved anaphase bridge is chromosome breakage, which can then generate micronuclei. Therefore, we investigated the DNA content of micronuclei in PSNG13 and PSNF5 cells. Consistent with the finding of increased FANCD2-associated bridges in BLM-deficient cells (PSNG13), a higher proportion of micronuclei in these cells contained FRA16D sequences (Fig. 5c). Several tumour suppressor genes have been mapped to fragile site loci, including *WWOX* at FRA16D (ref. 5). We propose that one possible explanation for the cancer predisposition in Bloom's syndrome patients is the accumulated loss of tumour suppressor function of genes residing at fragile site loci. At present, the scarcity of tumour biopsy samples from Bloom's syndrome patients makes the testing of this hypothesis impossible.

One intriguing aspect of centromeric UFBs is the possibility that lack of resolution before early anaphase allows them to contribute to the process whereby tension applied by mitotic spindle forces is sensed in metaphase[8,14]. However, our discovery of UFBs located at fragile sites strongly indicates that this class of bridges (at least) represents pathological, not physiological, structures. Our data imply that while Fanconi anaemia proteins are required to prevent the replication-associated disturbance that precedes fragile-site breakage (the disturbance probably being due to a failure to overcome replication fork stalling or breakdown), BLM is involved later in this pathway, in the resolution of intertwined DNA structures that, if not resolved, give rise to UFBs in anaphase (Supplementary Information, Fig. S6).

Our findings have wide significance in providing new insights into how fragile loci may be hotspots for viral integration, gene amplification and breakpoints in cancers. We suggest that aberrant bridge resolution generates non-programmed DNA breakage that can lead to illegitimate repair and genome rearrangements. Our data also lead us to question previous assumptions concerning both the existence of a checkpoint for preventing cells with an incompletely replicated genome entering mitosis and the source of many anaphase bridges. We propose that unresolved replication structures might be a far more important source of bridges than, for example, chromosome end-to-end fusions. □

*Note added in proof: a related manuscript by Naim & Roselli (*Nature Cell Biol. ***11,*** *761–768; 2009) is published in this issue.*

METHODS

Methods and any associated references are available in the online version of the paper at http://www.nature.com/naturecellbiology/

Note: Supplementary Information is available on the Nature Cell Biology website.

ACKNOWLEDGEMENTS

We thank members of the Hickson laboratory for helpful discussions, P. McHugh and L. Wu for helpful comments on the manuscript, and P. White for preparation of the manuscript. B. Lopes, P. Jeggo, F. Esashi, A. D'Andrea, G. Brown, E. Nigg and S. Elledge kindly supplied reagents. This work was supported by Cancer Research UK. K.L.C. was supported by the Croucher Foundation (Hong Kong).

AUTHOR CONTRIBUTIONS

K.L.C., T.P.P. and S.Y. performed experiments and, together with I.D.H., analysed data. K.L.C. and I.D.H. planned experiments and wrote the manuscript.

COMPETING FINANCIAL INTERESTS

The authors declare no competing financial interests.

Published online at http://www.nature.com/naturecellbiology/
Reprints and permissions information is available online at http://npg.nature.com/reprintsandpermissions/

1. Ellis, N. A. *et al.* The Bloom's syndrome gene product is homologous to RecQ helicases. *Cell* 83, 655–666 (1995).
2. Wang, W. Emergence of a DNA-damage response network consisting of Fanconi anaemia and BRCA proteins. *Nature Rev. Genet.* 8, 735–748 (2007).
3. Meetei, A. R. *et al.* A multiprotein nuclear complex connects Fanconi anemia and Bloom syndrome. *Mol. Cell. Biol.* 23, 3417–3426 (2003).
4. Chan, K. L., North, P. S. & Hickson, I. D. BLM is required for faithful chromosome segregation and its localization defines a class of ultrafine anaphase bridges. *EMBO J.* 26, 3397–3409 (2007).
5. Durkin, S. G. & Glover, T. W. Chromosome fragile sites. *Annu. Rev. Genet.* 41, 169–192 (2007).
6. Mankouri, H. W. & Hickson, I. D. The RecQ helicase–topoisomerase III–Rmi1 complex: a DNA structure-specific 'dissolvasome'? *Trends Biochem. Sci.* 32, 538–546 (2007).
7. German, J. Bloom syndrome: a mendelian prototype of somatic mutational disease. *Medicine (Baltimore)* 72, 393–406 (1993).
8. Baumann, C., Korner, R., Hofmann, K. & Nigg, E. A. PICH, a centromere-associated SNF2 family ATPase, is regulated by Plk1 and required for the spindle checkpoint. *Cell* 128, 101–114 (2007).
9. Losada, A. & Hirano, T. Dynamic molecular linkers of the genome: the first decade of SMC proteins. *Genes Dev.* 19, 1269–1287 (2005).
10. Arlt, M. F., Casper, A. M. & Glover, T. W. Common fragile sites. *Cytogenet. Genome Res.* 100, 92–100 (2003).
11. Casper, A.M, Nghiem, P, Arlt M.F & Glover T. W. ATR regulates fragile site stability. *Cell* 13, 779–789 (2002).
12. Schwartz, M. *et al.* Homologous recombination and nonhomologous end-joining repair pathways regulate fragile site stability. *Genes Dev.* 19, 2715–2726 (2005).
13. Durkin, S. G. *et al.* Replication stress induces tumor-like microdeletions in FHIT/FRA3B. *Proc. Natl Acad. Sci. USA.* 8, 246–251 (2007).
14. Wang, L. H., Schwarzbraun, T., Speicher, M. R. & Nigg, E. A. Persistence of DNA threads in human anaphase cells suggests late completion of sister chromatid decatenation. *Chromosoma* 117, 123–135 (2008).

METHODS

Cell lines. PSNF5 is a stable Bloom's syndrome cell line constitutively expressing the BLM protein, whereas PSNG13 is an isogenic control containing the pcDNA3 vector only. These cells, together with normal human fibroblast cells GM00637; FANCJ-deficient fibroblasts; FANCA-deficient cells, PD220i; FANCA-complemented cells, PD220+A; FANCD2-deficient fibroblasts, PD20i; FANCD2-complemented cells, PD20i+D2; FAND2-deficient cells expressing a form of FANCD2 that cannot be mono-ubiquitylated, PD20i + FANCD2-K561R (ref. 15); ATM-deficient fibroblasts, AT5 BIVA and untransformed MRC5 diploid cells were maintained in MEM-α (α-minimal essential media). Human telomerase reverse transcriptase (hTERT)-immortalized normal human diploid fibroblasts HS68, and HeLa cells were grown in Dulbecco's modified Eagle's medium. Seckel cells were provided by P. Jeggo (University of Sussex, UK) and were maintained in MEM-α with fetal calf serum (15%, FCS). P185 (FANCI-deficient) and P177 (FANCI-complemented) cells were a gift from S. J. Elledge (Harvard University, MA). CAPAN-1 cells were provided by F. Esashi, and were maintained in RPMI1640. All media were supplemented with FCS (10%, except the media for Seckel cells), glutamine (4 mM), penicillin (100 U ml^{-1}) and streptomycin (100 μg ml^{-1}).

Antibodies and immunofluorescence microscopy. Primary antibodies and dilutions used were: rabbit anti-FANCD2, 1:400 (NB100-82; Novusbio); goat anti-FANCD2, 1:50 (E-19; Santa Cruz); rabbit anti-FANCI, 1:150 (ab15344; Abcam); goat anti-BLM, 1:150 (C-18; Santa Cruz); rabbit anti-BLM, 1:300 (IHIC34; Cancer Research UK, Biological Resources); mouse anti-γH2AX, 1:400 (JBW-301; Upstate); rabbit anti-hRMI1, 1:300 (a gift from G. Brown, University of Toronto); mouse anti-UBF, 1:50 (SC-1125; Santa Cruz); rabbit anti-RAD51, 1:200 (AP-1; Oncogene); rabbit anti-SMC2 1:200 (A300-058A; Bethyl laboratories); mouse anti-Hec1, 1:200 (G93; Abcam); rat anti-PICH, 1:600 (a gift from E. A. Nigg, University of Basel, Switzerland); mouse anti-RPA2, 1:200 (9H8; ab2175; Abcam) and mouse anti-RPA, 1:70 (RPA34-19; CalbioChem). Secondary antibodies and dilutions used were: chicken anti-mouse Alexa Fluor 488, 1:600; donkey anti-goat Alexa Fluor 488 or 555, 1:600; donkey anti-rabbit Alexa Fluor 488, 1:400; donkey anti-rat Alexa Fluor 488, 1:500; sheep anti-rabbit Cy3, 1:800 and sheep anti-mouse Cy3, 1:600. Immunofluorescence staining was performed according to previously described protocols[4]. Nuclear DNA was detected using DAPI (1.5 μg ml^{-1}) or TO-PRO3 (200 nM) and cells were mounted in ProLong Gold antifade reagent (Invitrogen). Images were captured using either a Nikon Eclipse 80i fluorescence microscope equipped with a Plan Apo ×100/1.4 objective or a Zeiss LSM510 META confocal imaging system. Deconvolution was performed using Lucia G/F software (Laboratory Imaging). *z*-stack images were acquired at 0.2–0.3-μm intervals.

Preparation of metaphase spreads. Mitotic cells were collected by mitotic shake-off and were swollen in hypotonic solution (10 mM Tris-HCl at pH7.5, 10 mM NaCl and 5 mM $MgCl_2$) at 37 °C for 10 min. Mitotic cells (8,000) were spun onto coverslips using a cytospin apparatus (Cytospin2). Metaphase spreads were then fixed and subjected to immunofluorescence staining and/or FISH (fluorescence *in situ* hybridization). For analysis of FRA16D in micronuclei, cells were fixed using 3:1 methanol/acetic acid and subjected to standard FISH.

Combined immunofluorescence staining and FISH. Cells or metaphase spreads were fixed and subjected to immunofluorescence staining as described above. After washing, samples were refixed in paraformaldehyde (8%) at 4 °C for 20 min. Following ethanol dehydration, samples were denatured along with the Cy3-conjugated centromere-specific (Cytocell) or DIG-labelled fragile site-specific probes (BAC clones: 264L1 for FRA16D and 36B6 for FRA7H; mixed clones: 149J4, 48E21 and 94D19 for FRA3B) at 90–93 °C for 3 min. Slides were then incubated in a humidified chamber at 37 °C for 16 h. For telomeric FISH, a telomere PNA FISH kit (DakoCytomation) was used. DIG-label FISH probes were detected using a FITC-conjugated sheep anti-digoxigenin antibody (1:100; Roche).

Depletion of nuclear proteins by RNA interference (RNAi). SMC2 was partially depleted by transfecting HeLa cells with *SMC2* short interfering RNA (siRNA) duplexes[16] (5′-UGCUAUCACUGGCUUAAAUTT-3′; Qiagen) for 24 h using Oligofectamine (Invitrogen). RAD51 was depleted by transfection with siRNA duplexes (*RAD51* stealth siRNA; Invitrogen) for 48 h. A control siRNA (Invitrogen) was used. Cell extracts were subjected to western blotting for RAD51 using an anti-RAD51 antibody (ab1837; Abcam). Metaphase spreads were prepared as described above.

15. Taniguchi, T. *et al.* Convergence of the Fanconi anemia and ataxia telangiectasia signaling pathways. *Cell* **109,** 459–472 (2002).
16. Hirota, T., Gerlich, D., Koch, B., Ellenberg, J. & Peters, J. M. Distinct functions of condensin I and II in mitotic chromosome assembly. *J. Cell Sci.* **15,** 6435–6445 (2004).

nature cell biology

DOI: 10.1038/ncb1882

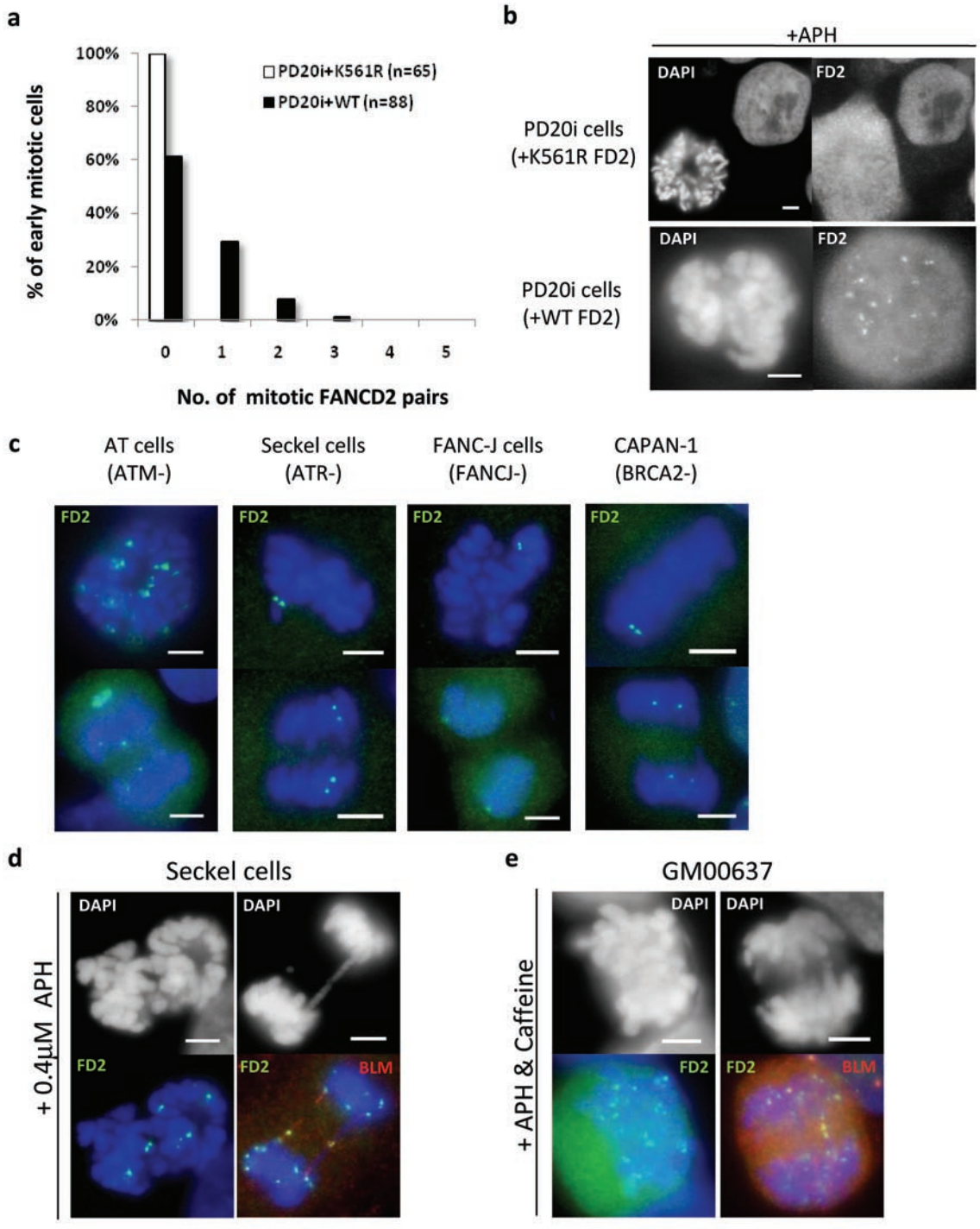

Figure S1 The formation of mitotic FANCD2 sister foci depends on FANCD2 mono-ubiquitination, but is not dependent on several DNA damage response proteins. **(a)** Quantification of mitotic FANCD2 paired foci in PD20i fibroblasts stably expressing a FANCD2-mutant K561R mono-ubiquitination or wild-type FANCD2. **(b)** The K561R FANCD2 mutant protein fails to form foci in both interphase and mitotic cells following low dose aphidicolin treatment. **(c)** Representative images showing mitotic FANCD2 sister foci (green) in cells deficient in ATM, ATR, FANCJ or BRCA2. **(d)** Low dose APH treatment induces FANCD2 foci (green) and its associated UFBs (marked by BLM; red) in Seckel (ATR-deficient) cells. **(e)** Representative images showing FANCD2 foci (green) in mitotic cells after combined 0.4μM APH and 5mM caffeine treatment for 24 hours. Scale bars, 5μm.

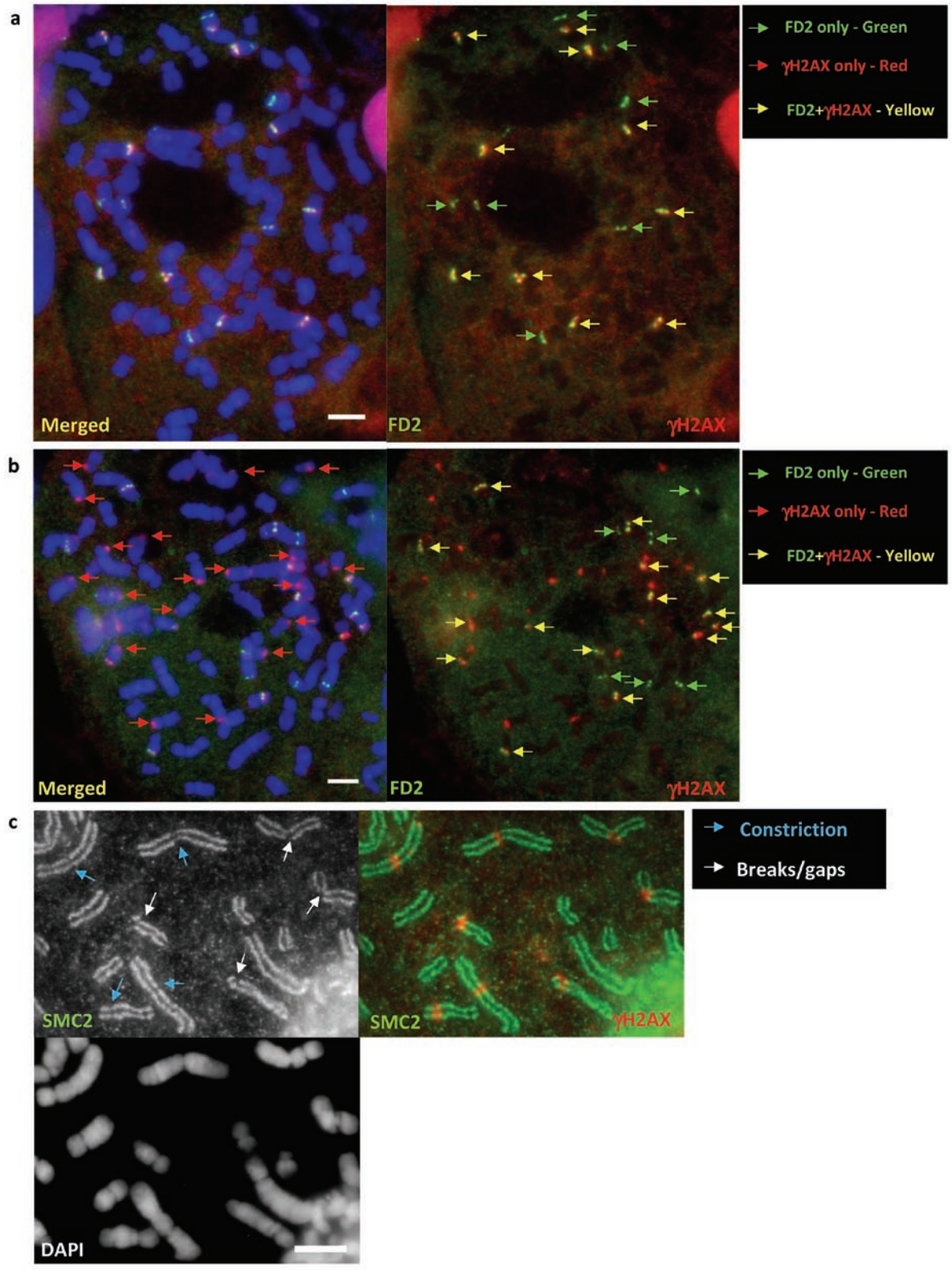

Figure S2 Co-localization of FANCD2 and γH2AX at chromosomal breaks/gaps and at regions of constriction on intact sister-chromatids. HeLa cells were treated with 0.4mM APH prior to analysis. **(a)** A representative image showing FANCD2 sister foci that are positive (yellow arrows) or negative (green arrows) for γH2AX. **(b)** Examples of telomeres positive for γH2AX, but negative for FANCD2 (red arrows). **(c)** Activation of γH2AX (red) across genetic loci showing breaks/gaps or a constriction, as revealed by SMC2 staining (green). The DAP1 image is also shown for comparison. Scale bars, 5μm.

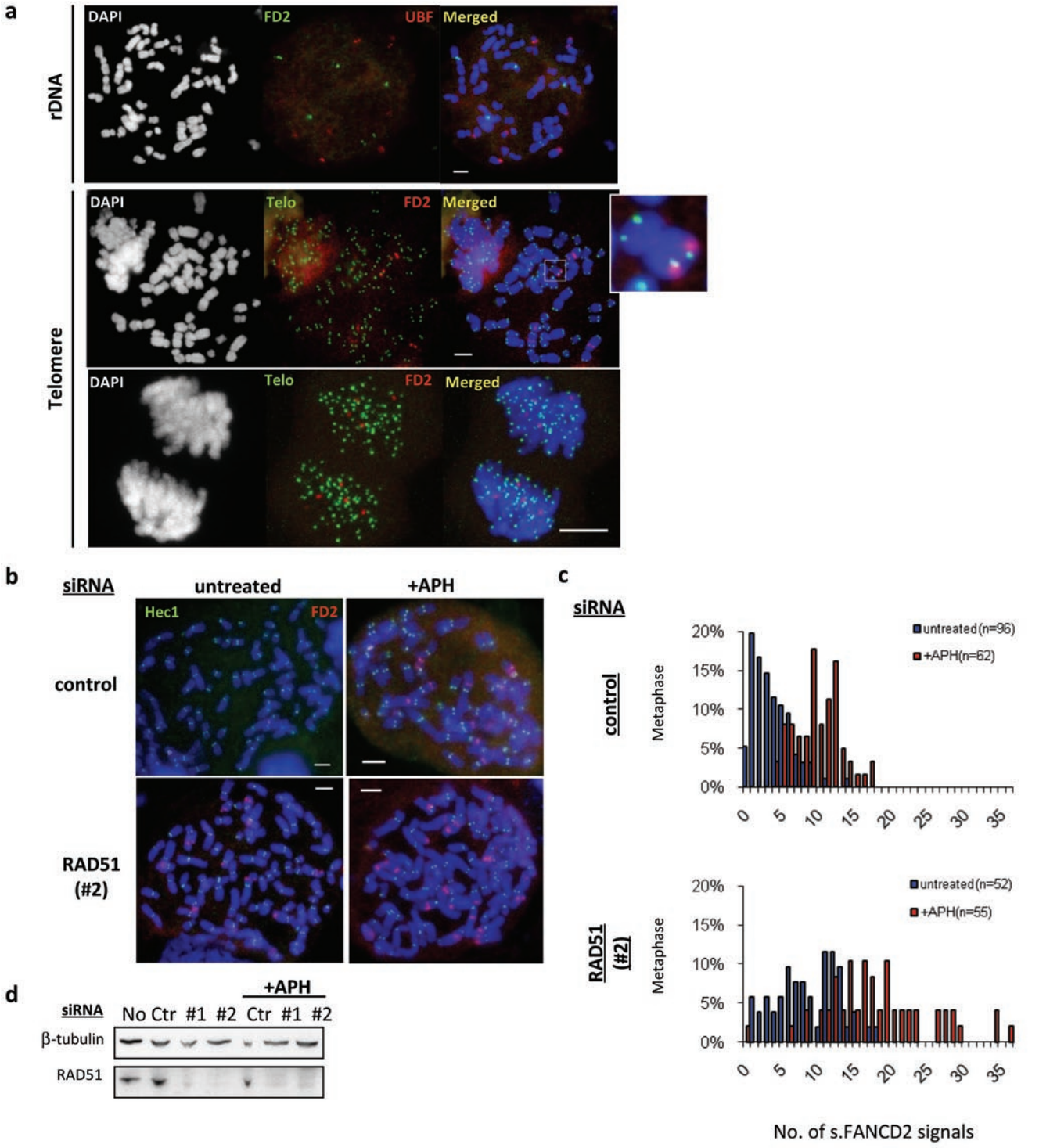

Figure S3 FANCD2 sister-foci are not associated with hyper-recombinogenic genomic regions, and are not dependent upon RAD51. **(a)** Lack of FANCD2 sister foci at ribosomal DNA loci (upper panels) and telomeres (lower panels) in mitotic cells of HS68 diploid fibroblasts after treatment with 0.4μM APH. An enlarged image of a rare case showing a pair of FANCD2 sister-foci adjacent to a telomere. **(b)** Depletion of human RAD51 significantly induces the formation of FANCD2 sister-foci on metaphase chromosomes. HeLa cells were transfected with control oligo or either of two validated siRNA oligos targeting RAD51. The transfected cells were either mock treated or treated with 0.4μM APH for 24 hours before quantification of FANCD2 sister-foci. Representative examples showing the formation of FANCD2 sister-foci on metaphase chromosomes in HeLa cells treated with control or RAD51 siRNA (oligo #2) in the presence or absence of APH. Scale bars, 5μm. **(c)** Quantification of FANCD2 sister-foci in HeLa metaphase spreads shown in (b). **(d)** Western blotting showing the protein level of RAD51 after siRNA depletion (lower). No, untreated; Ctr, control siRNA; #1 and #2, validated RAD51 siRNAs. β-tubulin was used as a loading control. Scale bars, 5μm.

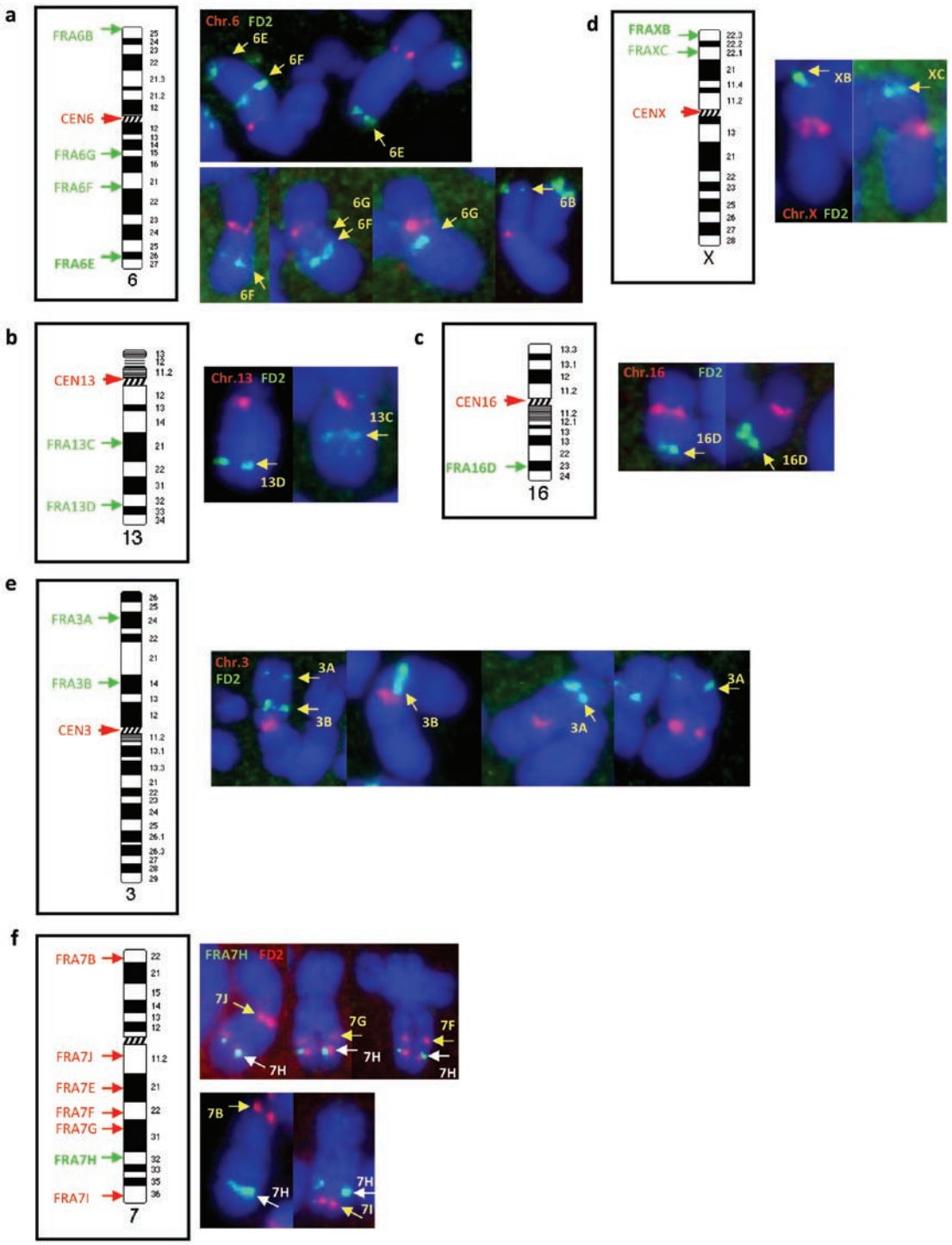

Figure S4 FANCD2 sister-foci localize with chromosomal regions containing common fragile sites. Combined FISH with chromosome-specific probes (red) and immunofluorescence staining for FANCD2 (green) performed on HS68 normal diploid fibroblasts after treatment with 0.4μM APH for 24 hours. **(a)** A representative example showing FANCD2 sister-foci formed in the region of the FRA6E genetic locus on both copies of chromosome 6, in a single metaphase, and to FRA6F on one chromosome 6 (upper panel). The sister-foci also form at loci corresponding to other common fragile sites on chromosome 6; FRA6G and FRA6B (lower panel). **(b)** FANCD2 sister-foci localize to the FRA13C and FRA13D loci on chromosome 13. **(c)** A single site for FANCD2 sister-foci was observed on chromosome 16, at the FRA16D locus. **(d)** Two FANCD2 binding sites were found on chromosome X, at the FRAXB and FRAXC loci. **(e)** Two common fragile sites, FRA3A and FRA3B loci, were shown to be positive for FANCD2 sister foci. **(f)** Representative images showing the localization of FANCD2 sister-foci (red) at the FRA7H fragile locus (green) (upper panel). Other binding sites of FANCD2 sister-foci were matched to common fragile sites on chromosome 7; FRA7B, FRA7F, FRA7I and FRA7J (upper and lower panels). At least 20 metaphase spreads were analysed in each case.

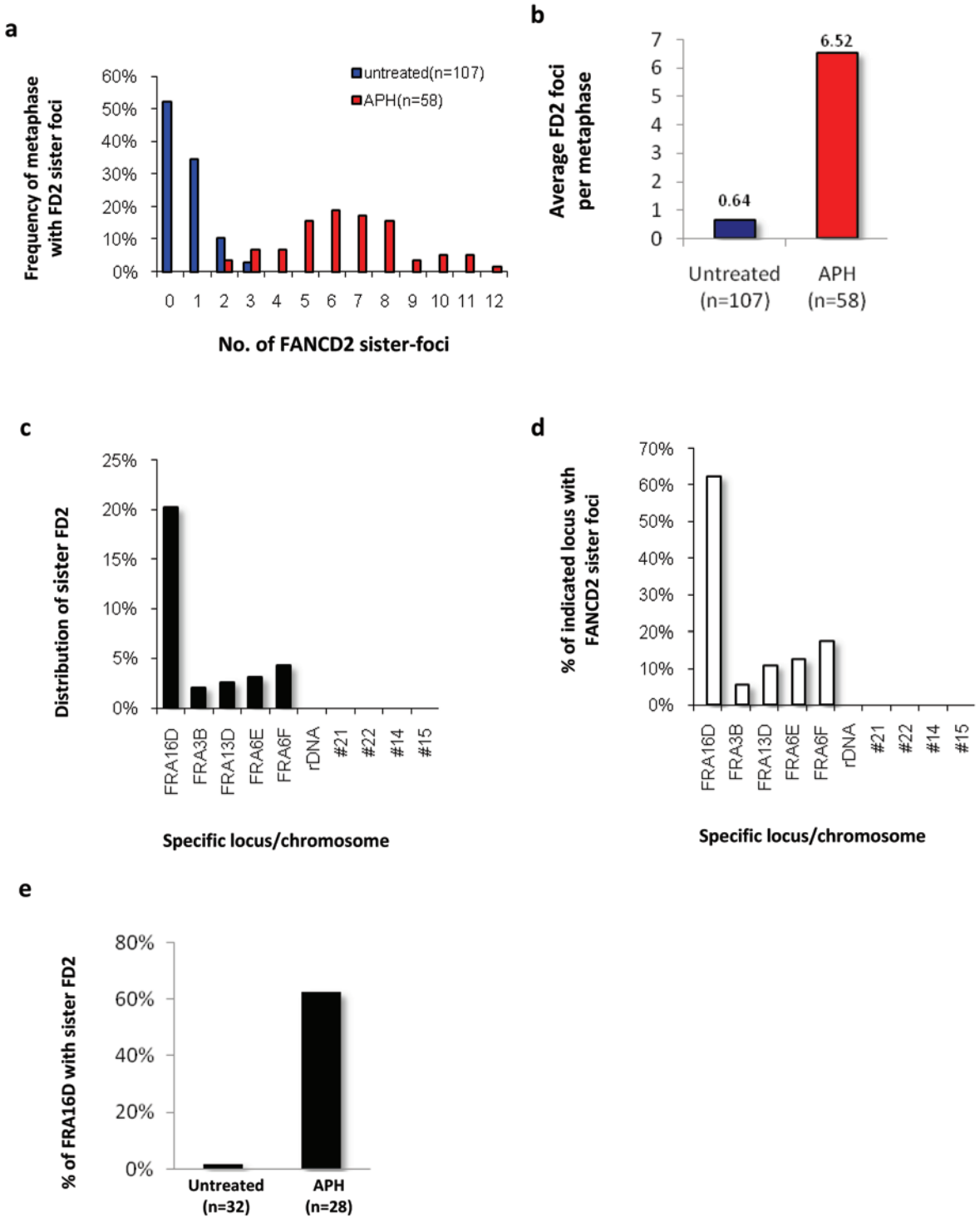

Figure S5 Distribution of FANCD2 sister-foci and their frequency of co-localization to specific genetic loci. Frequency **(a)** and average number **(b)** of FANCD2 sister-foci in HS68 metaphases untreated or treated with 0.4μM APH for 24 hours. **(c)** Percent distribution of FANCD2 sister-foci on common fragile sites, rDNA, and selected whole chromosomes. **(d)** Frequency of particular fragile sites, rDNA and selected whole chromosomes displaying FANCD2 sister-foci. **(e)** Low dose APH treatment for 24 hours significantly induces the formation of FANCD2 sister-foci at FRA16D loci. At least 20 HS68 metaphase spreads were analyzed for each genomic region (an average of 6-8 FANCD2 sister foci/metaphase was detected after APH treatment).

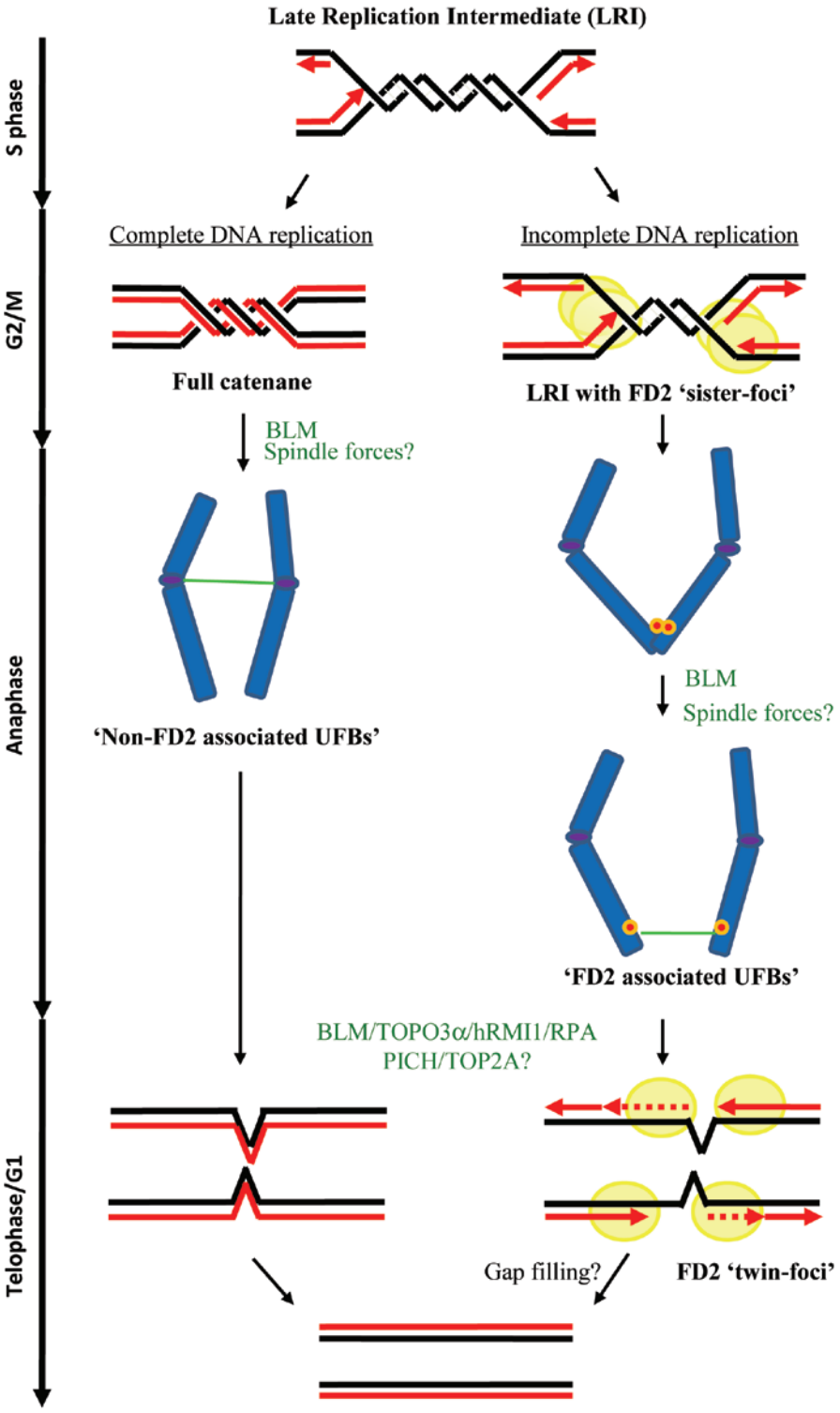

Figure S6 A proposed model for the formation of ultra-fine anaphase bridges. Regions of the genome where replication forks converge or where replication is slow may fail to complete replication prior to mitosis. If replication is completed (left) 'full' (dsDNA) catenanes can be produced. If replication is incomplete, a late-replication intermediate (LRI) with ssDNA catenanes may be generated preferentially at fragile site loci under replication stress (right). We propose that FANCD2 enhances the stability and/or 'rescue' of stalled replication forks throughout lateS/G2 and potentially into mitosis. The non-FANCD2-associated (largely centromeric) bridges arise from full catenanes and require TOPO2 for decatenation, perhaps with an involvement of BLM/TOPO3α/RMI1(left), whereas FANCD2-associated bridges represent hemi-catenated LRIs that are decatenated by the BLM/TOPO3α/RMI1 complex (right). The role of PICH in either pathway remains unclear. In telophase/G1 the FANCD2 foci can still be detected as 'twin-foci'. Completion of replication will require ssDNA gap filling.

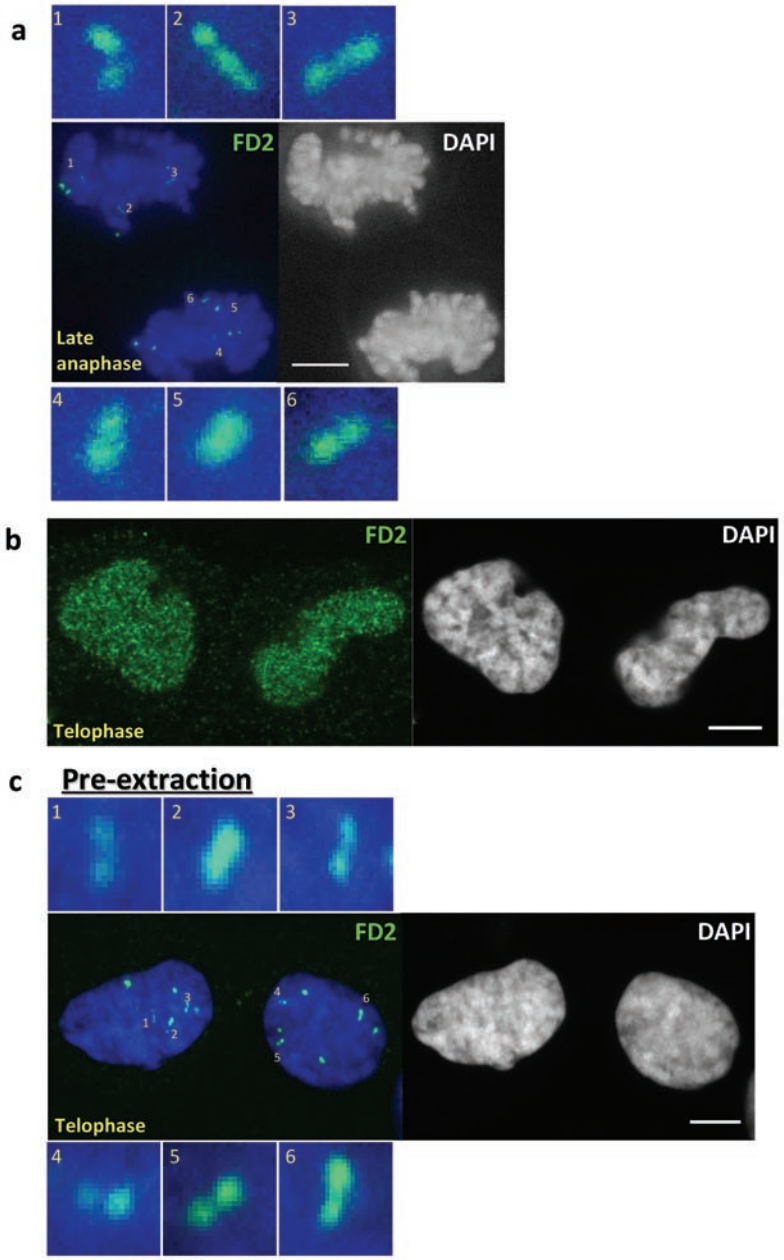

Figure S7 Formation of FANCD2 'twin-foci' in telophase cells. **(a)** A representative image showing splitting of FANCD2 foci ('twin-foci') in each daughter nucleus of a GM00637 late anaphase cell. Detection of FANCD2 'twin-foci' in HS68 telophase cells without **(b)** or with **(c)** nuclear pre-extraction. Scale bars, 5μm.

Supporting Online Material

FANCD2 foci and DNA double strand breaks

We considered the possibility that the existence of FANCD2 sister foci might be marking sites of DNA double-stranded breaks (DSBs) on both sister-chromatids. Although the vast majority (97%) of γ-H2AX (a marker of DSBs) foci found on chromosome arms were positive for FANCD2, approximately one-third of FANCD2 sister foci were found on intact chromatids where no break/gap was evident, and no γ-H2AX staining was detected (Fig. 2a, upper panels; 2c & Fig. S2a). Almost all γ-H2AX foci found at telomeric regions were also negative for FANCD2 (Fig. 2a, lower panels & Fig. S2b). γ-H2AX staining was found generally either in a zone between and around the FANCD2 foci, or as a discrete focus 'sandwiched' between the FANCD2 sister foci (Fig. 2b, left panels). Interestingly, we also found that FANCD2 and γ-H2AX appeared as a 'triple-focus' at sites of chromatid breaks/gaps where only one sister chromatid was visibly broken (as per classical fragile site identification). In these cases, the broken sister displayed a pair of FANCD2/γ-H2AX foci flanking the break. However, more significantly, the corresponding intact sister also had a single FANCD2/γ-H2AX focus located opposite the break site (Fig. 2b, right; arrows). Apart from 'triple-foci' associated with breaks/gaps, we frequently also detected an abnormal constriction of intact chromatids at sites where FANCD2/γ-H2AX sister foci were evident (Fig. 2c & Fig. S2c, arrowed). These data further support our proposal that aberrant DNA structures exist on both sister DNA molecules that may be still inter-linked even in mitotic cells.

Are FANCD2 foci marking sites of DNA replication and/or recombination structures?

To delineate the relative contributions of DNA replication and HR structures to the formation of FANCD2 sister foci, we performed three sets of analysis. First, we determined whether key HR factors such as RAD51, BRCA1 and FANCJ (BACH1) co-localize with FANCD2 sister foci. Although co-localization of these proteins with FANCD2 was evident in interphase and prophase cells, foci either of RAD51, or of BRCA1 and FANCJ, disappeared after DNA condensation and nuclear envelope breakdown, respectively (data not shown), in contrast to FANCD2 foci. Second, we analyzed whether ribosomal DNA (rDNA) loci, telomeres and centromeres might be hotspots for formation of FANCD2 sister foci, because perturbation of replication leads to increased HR especially at these loci[1,2]. However, in normal fibroblasts, we could not detect any FANCD2 sister foci at any of the dispersed rDNA loci and centromeres, and only very few foci localized close to, but not coincident with, telomeres (Figs. 3f, S3a & S5d). Third, we analyzed more directly whether the frequency of FANCD2 sister foci was influenced by modulating HR. For this, we depleted RAD51 to partially disable the initial steps in HR. RAD51 depletion did not lead to a reduction in FANCD2 focus numbers, but instead led to a marked increase in the number of FANCD2 foci in both untreated and APH-treated cells (Fig. S3b-d).

FANCD2 sister foci appear to define common fragile site loci

Deficiency in ATR is known to strongly induce fragile site formation. We found that mitotic FANCD2 foci are abundant in Seckel cells (ATR-hypomorphic mutant), both

in untreated cells and following low dose APH treatment (Fig. S1 & data not shown). Moreover, caffeine treatment, which inhibits the ATM and ATR kinases, and induces fragile site expression[3,4], significantly elevated the frequency of FANCD2 sister foci (Fig. S1e & data not shown). Taken together with the findings that replication stress induces FANCD2 sister foci, that FANCD2 forms 'triple foci' at chromatid breaks/gaps (see main text) and that deficiency in ATR, RAD51, or FA proteins increases fragile site expression[3,5,6], our data suggest that FANCD2 sister foci in metaphase might define specific genomic loci prone to breakage; most likely, common fragile sites. MMC also strongly induced FANCD2 sister foci, but we currently do not know if these foci localize specifically to fragile site loci. Given that MMC-induced DNA inter-strand cross-links represent a complete physical block to the replication machinery, we predict that these foci will arise throughout the genome and not in a site-specific manner. Further work is needed to confirm if this prediction is correct.

Based on the published chromosome locations of common fragile sites, we examined 10 individual chromosomes that either have no common fragile sites or have one or more well defined fragile sites in HS68 normal diploid fibroblasts (Fig. S4 & S5). On chromosome 6, four specific sites were observed, but all of these positions match published common fragile sites (FRA6B, 6G, 6F and 6E). On chromosome 13, only two sites were consistently seen, which again mapped to known fragile site loci (FRA13C and 13D), with the vast majority co-localizing with FRA13D. On chromosome 16, only the FRA16D locus was positive for FANCD2 sister foci. On the X chromosome, two loci near the tip of the p arm were evident, matching the locations of FRAXB and FRAXC, and only two positions on the p arm

of chromosome 3 were positive for FANCD2 sister foci, which again matched to the FRA3A and FRA3B loci.

FRA16D is a hotspot for FANCD2 sister foci

Perhaps unexpectedly, the FRA16D locus showed a higher frequency of FANCD2 sister foci than did FRA3B in both HeLa and HS68 cells (Fig. 4a/b and Fig. S5), whereas FRA3B has been reported to have a higher rate of fragile site expression in lymphocytes and some cell lines[4]**.** This might represent a cell type difference, but also might be indicative of differences between fragile loci in terms of their propensity to undergo replication fork stalling/disruption (where FANCD2 foci would be present, but the locus would not necessarily be broken; suggested to be a common event at FRA16D) versus the likelihood of overt chromatid breakage (more common at FRA3B). Moreover, the notably higher frequency of FANCD2/I focus formation than of fragile site breakage at FRA16D (and probably other fragile sites) suggests that there has previously been a significant under-estimation of the extent to which aberrant replication occurs at many of the common fragile sites. To our knowledge, FANCD2/I is the first protein complex to show this persistent and specific localization to fragile site loci, and we propose that FANCD2 may be a more sensitive marker than studying chromatid breakage that will likely have broader applications in chromosome abnormality studies in the future. In particular, FANCD2 sister foci could serve as a diagnostic marker in early pre-malignant lesions to reveal replication stress that would be a prelude to chromosomal breakage/rearrangements.

No obvious role for FA proteins in preventing UFB formation

It was shown previously that cells deficient in FANCD2 show an increase in fragile site expression[6]. We asked, therefore, whether FANCD2 deficient cells also have an elevated level of UFBs in anaphase. However, we found no significant increase in DNA bridges in FANCD2-deficient cells compared to that of isogenic FANCD2 'corrected' cells (data not shown). One possible explanation is that FANCD2 localizes to stalled replication forks that arise at common fragile site loci, where it acts to stabilize the intertwined sister-loci at the unreplicated site. These sites have the potential, if unresolved, to generate a bridge visible in anaphase. Without FANCD2 stabilization, the linked sister loci are very prone to rupture, which manifests as a break/gap on the metaphase chromosome before cells enter anaphase. This breakage eliminates the potential for a bridge to form at that locus.

We infer that the selective sensitivity to DNA cross-linking agents in FA cells reflects the fact that these agents are uniquely effective amongst drugs that can generate DNA adducts in causing fork stalling. We have shown that the cross-linking agent, MMC, is able to efficiently induce FANCD2/I sister foci, suggesting the possibility that fragile site loci may be the 'Achilles' heel' of the cell with respect to the cytotoxicity of MMC. Further work will be required to address this issue.

Different roles for BLM and FA proteins at fragile loci

This work reveals a hitherto unanticipated mechanism by which replication intermediates at fragile loci might generate chromosomal instability through the aberrant inter-linkage of sister DNA and/or failed resolution of anaphase bridges. Our findings also raise the possibility that the cancer predisposition in BS and FA may have at least one common source via aberrant processing of replication structures that

persist in mitosis at fragile sites. While BS is associated with a broad spectrum of cancers[7], tumorigenesis in FA is seemingly more restricted to leukemia[8], although the dramatic reduction in life expectancy in FA (median 16 years) likely obscures most solid cancer development that might otherwise occur prematurely. Nevertheless, deficiency in BLM or FA proteins does not give identical outcomes in terms of fragile site expression. FA cells show excessive fragile site formation[6], as measured conventionally on metaphase chromosomes, while BS cells do not[4]. Moreover, although BS cells do not display excessive FANCD2 sister-foci in metaphase, there is an increase in FANCD2 (fragile site)-associated DNA bridges in BS anaphases.

Fate of FANCD2 foci in late anaphase/telophase

If, as we propose, FANCD2-associated UFBs arise due to the persistence of an incompletely replicated region flanked by two stalled forks, it seemed possible that, after chromosome segregation/bridge resolution of the unreplicated DNA region followed by chromosome de-condensation, we ought to be able to visualize a scission of a single FANCD2 focus on each sister-DNA in the daughter nuclei (see model in Fig. S6). Consistent with this prediction, we could detect 'twin-foci' of FANCD2 in each individual daughter nucleus after chromosome segregation in late anaphase and telophase (Fig. S7).

Supplementary References

1. Paques, F. & Haber, J. E. Multiple pathways of recombination induced by double-strand breaks in Saccharomyces cerevisiae. *Microbiol. Mol. Biol. Rev.* **63**, 349-404 (1999).
2. Jaco, I,, Canela, A,, Vera, E, & Blasco, M.A. Centromere mitotic recombination in mammalian cells. *J. Cell Biol.* ***181****, 885-92 (2008).*

3 Casper, A.M., Nghiem, P., Arlt, M.F, & Glover, T.W. ATR regulates fragile site stability. *Cell*. **13**, 779-789 (2002).
4. Arlt, M. F., Casper, A. M. & Glover, T. W. Common fragile sites. *Cytogenet. Genome Res*. **100**, 92-100 (2003).
5. Schwartz, M. et al. Homologous recombination and nonhomologous end-joining repair pathways regulate fragile site stability. *Genes Dev*. **19**, 2715-2726 (2005).
6. Howlett, N. G., Taniguchi, T., Durkin, S. G., D'Andrea, A. D. & Glover, T. W. The Fanconi anemia pathway is required for the DNA replication stress response and for the regulation of common fragile site stability. *Hum. Mol. Genet*. **14**, 693-701 (2005).
7. German, J. Bloom syndrome: a mendelian prototype of somatic mutational disease. *Medicine (Baltimore)* **72**, 393-406 (1993).
8. Wang, W. Emergence of a DNA-damage response network consisting of Fanconi anaemia and BRCA proteins. *Nat. Rev. Genet*.**8**, 735-748 (2007).

nature cell biology

The FANC pathway and BLM collaborate during mitosis to prevent micro-nucleation and chromosome abnormalities

Valeria Naim[1] and Filippo Rosselli[1,2]

Loss-of-function of caretaker genes characterizes a group of cancer predisposition diseases that feature cellular hypersensitivity to DNA damage and chromosome fragility; this group includes Fanconi anaemia and Bloom syndrome[1–3]. The products of the 13 *FANC* genes[4] (mutated in Fanconi anaemia), which constitute the 'FANC' pathway, and BLM (the RecQ helicase mutated in Bloom syndrome) are thought to collaborate during the S phase of the cell cycle, preventing chromosome instability. Recently, BLM has been implicated in the completion of sister chromatid separation during mitosis, a complex process in which precise regulation and execution is crucial to preserve genomic stability. Here we show for the first time a role for the FANC pathway in chromosome segregation during mitotic cell division. FANCD2, a key component of the pathway, localizes to discrete spots on mitotic chromosomes. FANCD2 chromosomal localization is responsive to replicative stress and specifically targets aphidicolin (APH)-induced chromatid gaps and breaks. Our data indicate that the FANC pathway is involved in rescuing abnormal anaphase and telophase (ana-telophase) cells, limiting aneuploidy and reducing chromosome instability in daughter cells. We further address a cooperative role for the FANC pathway and BLM in preventing micronucleation, through FANC-dependent targeting of BLM to non-centromeric abnormal structures induced by replicative stress. We reveal new crosstalk between FANC and BLM proteins, extending their interaction beyond the S-phase rescue of damaged DNA[5–6] to the safeguarding of chromosome stability during mitosis.

The 13 FANC proteins (FANCA, B, C, D1, D2, E, F, G, I, J, L, M and N) have been subdivided into 3 groups according to their function[4]. The first group comprises eight FANC proteins that associate to form the FANCcore, a nuclear complex with E3 ubiquitin ligase activity[7], responsible for DNA damage-induced monoubiquitylation of both FANCD2 and FANCI components of the second group[4]. FANCD2 monoubiquitylation requires the joint intervention of FANCcore complex and proteins involved in cell-cycle checkpoints and DNA repair, including RPA (replication protein A), ATR (ataxia telangiectasia mutated and Rad3 related), CHK1 (checkpoint kinase 1) and BRCA1 (breast cancer 1, early onset; ref. 8–12). In the presence of phosphorylated histone H2AX (γ-H2AX)[13], monoubiquitylated FANCD2 forms nuclear foci, where it colocalizes with several proteins, including BLM[3]. The FANCcore complex was retrieved in a supramolecular complex with RPA and BLM[5], and is necessary for DNA interstrand crosslink-induced BLM phosphorylation[6]. The third FANC protein group, which comprises the breast cancer-associated proteins FANCD1–BRCA2 (breast cancer associated gene 2), FANCN–PALB2 (partner and localizer for BRCA2) and FANCJ–BRIP1 (BRCA1-interacting protein 1), is dispensable for FANCD2 monoubiquitylation and is thought to function downstream to promote DNA repair[4].

Interestingly, BRCA2 and the FANC pathway partners BRCA1 and BLM have been implicated in mitotic events such as chromosome segregation, spindle assembly, cytokinesis and sister chromatid decatenation at anaphase[14–17]. These observations prompted us to determine whether chromosome abnormalities in Fanconi anaemia cells are solely the consequence of altered DNA repair or whether they could be also ascribed to an unknown role of the FANC pathway during mitosis.

To characterize the mitotic process in Fanconi anaemia cells, we compared FANC-deficient cells with their corrected counterparts and with FANC-proficient human fibroblasts (Fig. 1). Both FANC-proficient and -deficient cells form bipolar spindles at metaphase that elongate and organize the central spindle and midbody at ana-telophase. In contrast, Fanconi anaemia cells show various types of chromosome segregation defects, including anaphase bridges, lagging chromosomes/fragments at ana-telophase and unequal chromosome partitioning (Fig. 1a and data not shown). Indeed, the frequency of these irregular ana-telophase figures (that is the appearance of mitotic chromosomes) is significantly higher in FANC-deficient cell lines (Fig. 1b), whereas the relative proportion of pro-metaphase and ana-telophase figures is similar in FANC-deficient and -proficient cells (Fig. 1c). These data suggest that,

[1]Université *Paris-Sud,* CNRS FRE2939, CEA LRC43V, Institut Gustave Roussy 39, Rue Camille Desmoulins, 94805, Villejuif Cedex, France.
[2]Correspondence should be addressed to F.R. (e-mail: rosselli@igr.fr)

Received 16 February 2009; accepted 5 May 2009; published online 24 May 2009; DOI: 10.1038/ncb1883

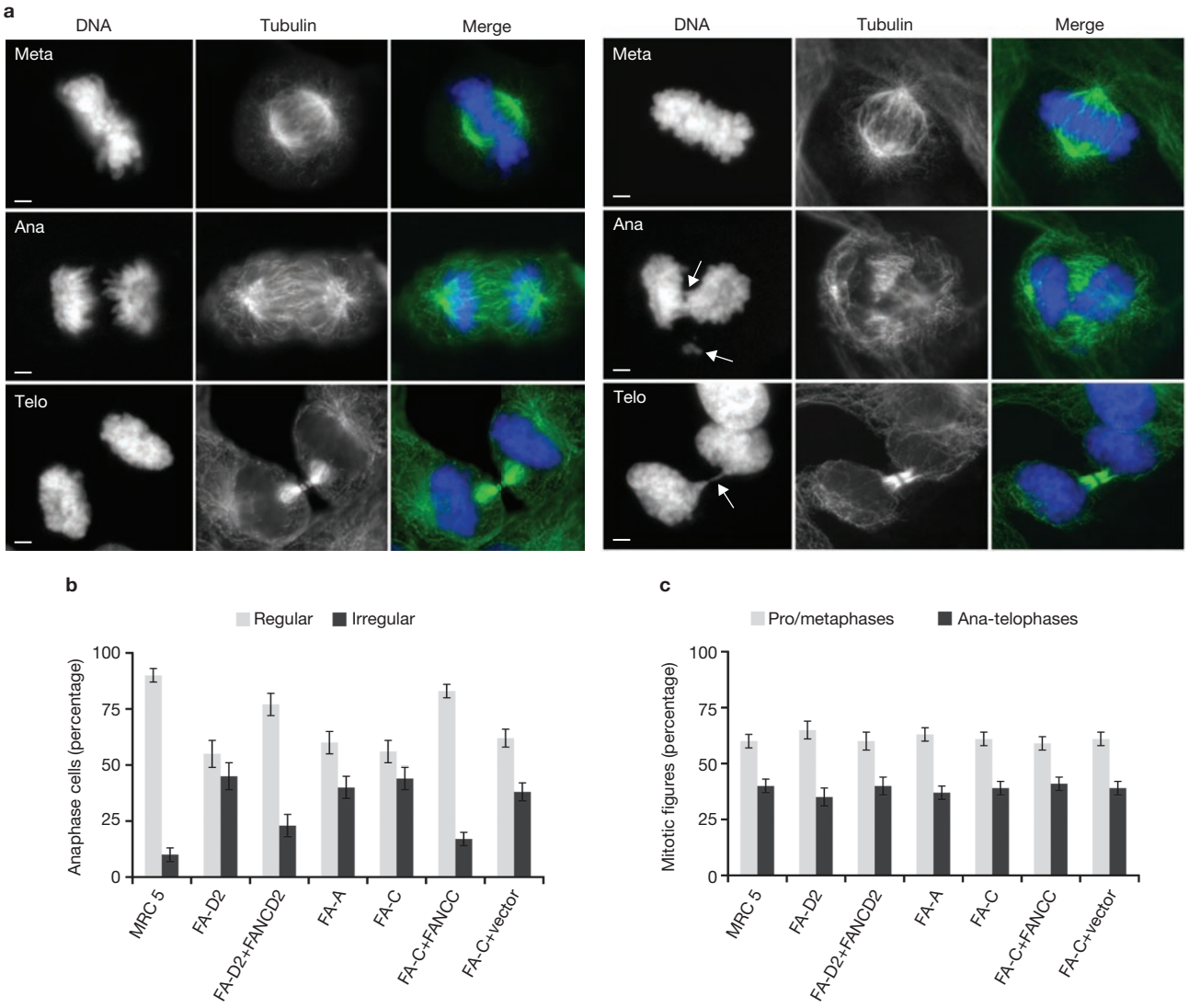

Figure 1 Mitotic characterization of FANC-proficient and deficient cells. (**a**) Defective chromosome segregation in FANC-deficient cells. Mitotic cells were identified by immunostaining for DNA (using DAPI) and α-tubulin (using specific antibodies) to visualize chromosomes and the mitotic spindle. In the merged images DNA is blue and α-tubulin is green. Representative images of metaphase (meta), anaphase (ana) and telophase (telo) figures of MRC5 cells (left) and FA-A fibroblasts (right). Arrows point to chromosome bridges and lagging chromatin. Scale bars, 5 μM. (**b**) Frequency of chromosome segregation defects in FANC-deficient and -proficient cell lines. Anaphase and telophase cells with bridges, lagging chromatin or unequal chromosome segregation were considered irregular. (**c**) Distribution of mitotic figures in the same cells as **b**. The relative proportion of prometaphase and metaphase figures (pro/metaphases) with respect to anaphase and telophase figures (ana-telophases) was calculated. In **b** and **c**, data are mean ± s.e.m. from three independent experiments, 173–307 mitotic figures were counted for each cell line. MRC5, wild-type; FA-D2, FANCD2$^{-/-}$ mutant; FA-D2+FANCD2, FANCD2$^{-/-}$ mutant corrected by introducing wild-type FANCD2 allele; FA-A, FANCA$^{-/-}$ mutant; FA-C, FANCC$^{-/-}$ mutant; FA-C+FANCC, FANCC$^{-/-}$ mutant corrected by ectopic expression of wild-type FANCC cDNA; FA-C + Vector, FANCC$^{-/-}$ transduced with an empty vector.

in Fanconi anaemia cells, overall progression through mitosis is not impaired but chromosome segregation is severely affected.

To investigate a possible function of the FANC proteins in chromosome segregation, we analysed the localization of FANCD2, a key component for assessing normal FANC pathway activation, during mitotic cell division. FANCD2 showed dynamic localization (Fig. 2a): at the onset of mitosis, FANCD2 is excluded from chromosomes and diffuses into the cytoplasm, returning to the nucleus at the end of cell division. During this analysis, we observed that some cells had a few FANCD2 spots localized on mitotic chromosomes (Fig. 2a, b). These spots were often present as couples and they tended to be segregated with the chromosomes at anaphase (Fig. 2b; Supplementary Information, Fig. S1A). FANCD2 spots were completely absent in FANCcore-mutated cells, unable to monoubiquitylate FANCD2 (Table 1). Consistent with previous observations showing that FANCD2 mutations are hypomorphic[18] and that residual protein can be monoubiquitylated, spots were only rarely present in FA-D2 cells (FANCD2$^{-/-}$ mutant cells). These data can only be accounted for if these spots represent the assembly of monoubiquitylated FANCD2. Similar results were also obtained in primary, untransformed fibroblasts from healthy donors and Fanconi anaemia patients (Supplementary Information, Fig. S1A and data not shown). Since chromosome missegregation can be a consequence of spindle checkpoint dysfunction, we set out to determine whether the FANCD2 foci on mitotic chromosomes arose from mitotic checkpoint

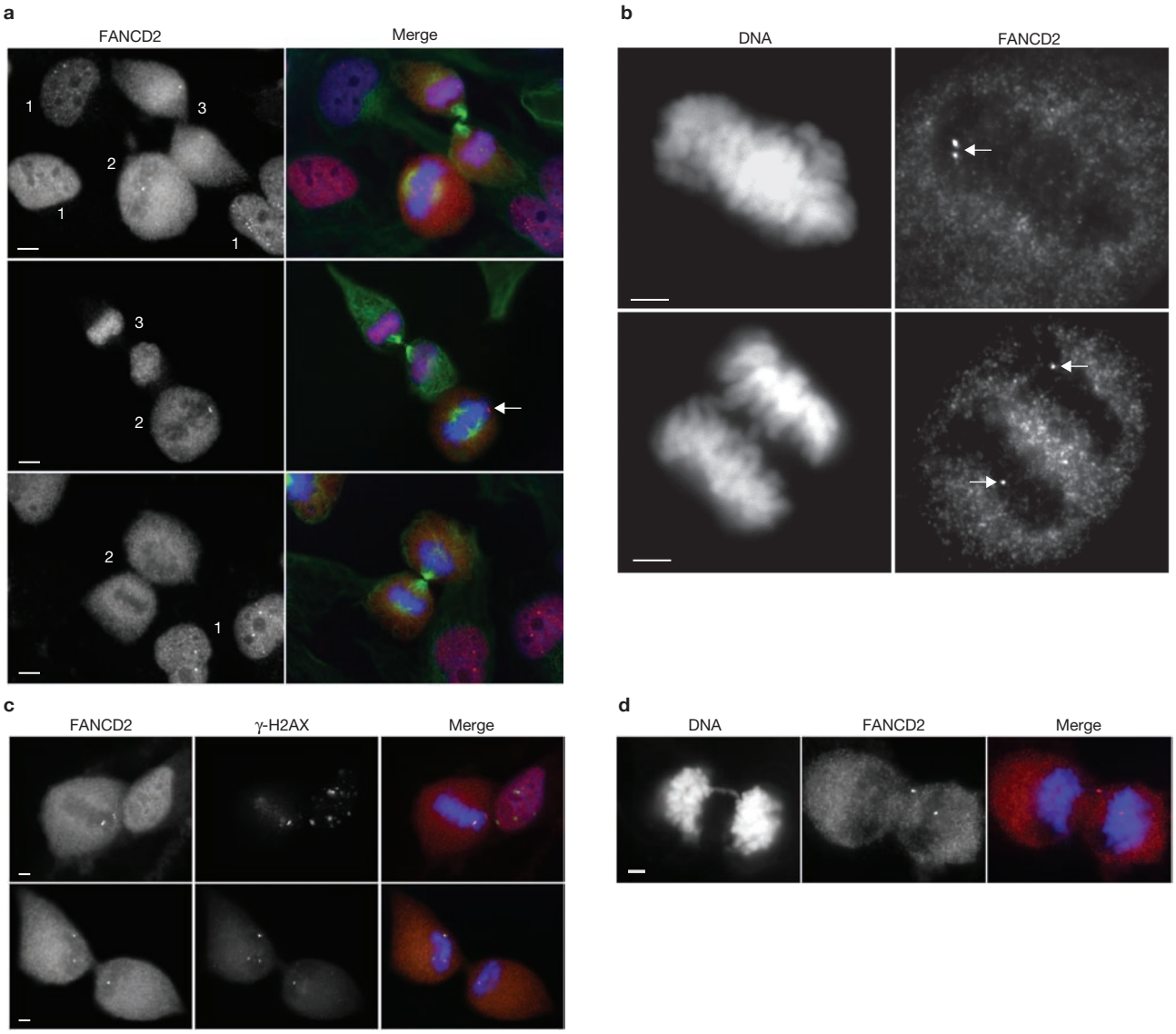

Figure 2 FANCD2 localization at mitosis. (**a**) FANCD2 localizes as spots on mitotic chromosomes. MRC5 fibroblasts were immunostained for FANCD2 (left; red in the merge, right), DNA (blue in the merge) and α-tubulin (green in the merge). FANCD2 staining is nuclear in interphase (1; the punctuate stain of FANCD2 in some cells, reflects the presence of the classical S/G2 phase FANCD2 sub-nuclear foci) and exhibits a diffuse pattern throughout mitosis (2) until the end of cell division (3). The arrow indicates brilliant FANCD2 spots on mitotic chromosomes. Scale bars, 10 μM. (**b**) Examples of MRC5 mitotic cells stained for DNA (left) and FANCD2 (right), showing a couple of FANCD2 spots at metaphase (top arrow) and two spots (bottom arrows) segregating with the chromosomes at anaphase (bottom). Scale bars, 5 μM. (**c**) FANCD2 colocalizes with γ-H2AX on mitotic chromosomes. MRC5 cells were stained for FANCD2 (left; red in the merge, right) and γ-H2AX (middle; green in the merge, right). The FANCD2 spots almost completely overlap with the γ-H2AX foci on mitotic chromosomes, both at metaphase (top) and anaphase (bottom). Scale bars, 5 μM. (**d**) FANCD2 marked sites can undergo defective anaphase separation. Images show a representative irregular anaphase cell stained for DNA (left; blue in the merge, right) and FANCD2 (middle; red in the merge, right), showing a FANCD2 spot on a chromosome bridge. Scale bar, 5 μM.

activation at kinetochores. Consequently, we performed double immunostaining of cells at prometaphase for FANCD2 and BubR1, a spindle checkpoint protein specifically localized to kinetochores[19]. We did not observe colocalization of FANCD2 and BubR1, suggesting that FANCD2 spots do not mark kinetochores (Supplementary Information, Fig. S1B). This was confirmed by the lack of colocalization of FANCD2 with Hec1, a constituent of the kinetochore outer plate[20] (Supplementary Information, Fig. S1C). Moreover, accumulation of cells in M phase following nocodazole or taxol treatment as well as kinetochore recruitment of BubR1 in pro-metaphase-arrested cells is comparable in FANC-proficient and deficient cells, suggesting that the spindle checkpoint function is not compromised by FANC loss-of-function (Supplementary Information, Fig. S1D, E and data not shown).

Localization of γ-H2AX to mitotic chromosomes has been reported in unperturbed cells as well as in response to DNA damage; it is thought to be either evidence of a still altered DNA structure or the memory of a previously repaired lesion[21,22]. Since the assembly of FANCD2 foci in the S and G2 phases requires the presence of γ-H2AX foci[13], we asked whether FANCD2 spots on mitotic chromosomes associate with γ-H2AX-targeted structures. By using a double immunostaining approach, we found that 75% of FANCD2 spots colocalize with γ-H2AX foci on mitotic chromosomes (Fig. 2c), whereas less than 20%

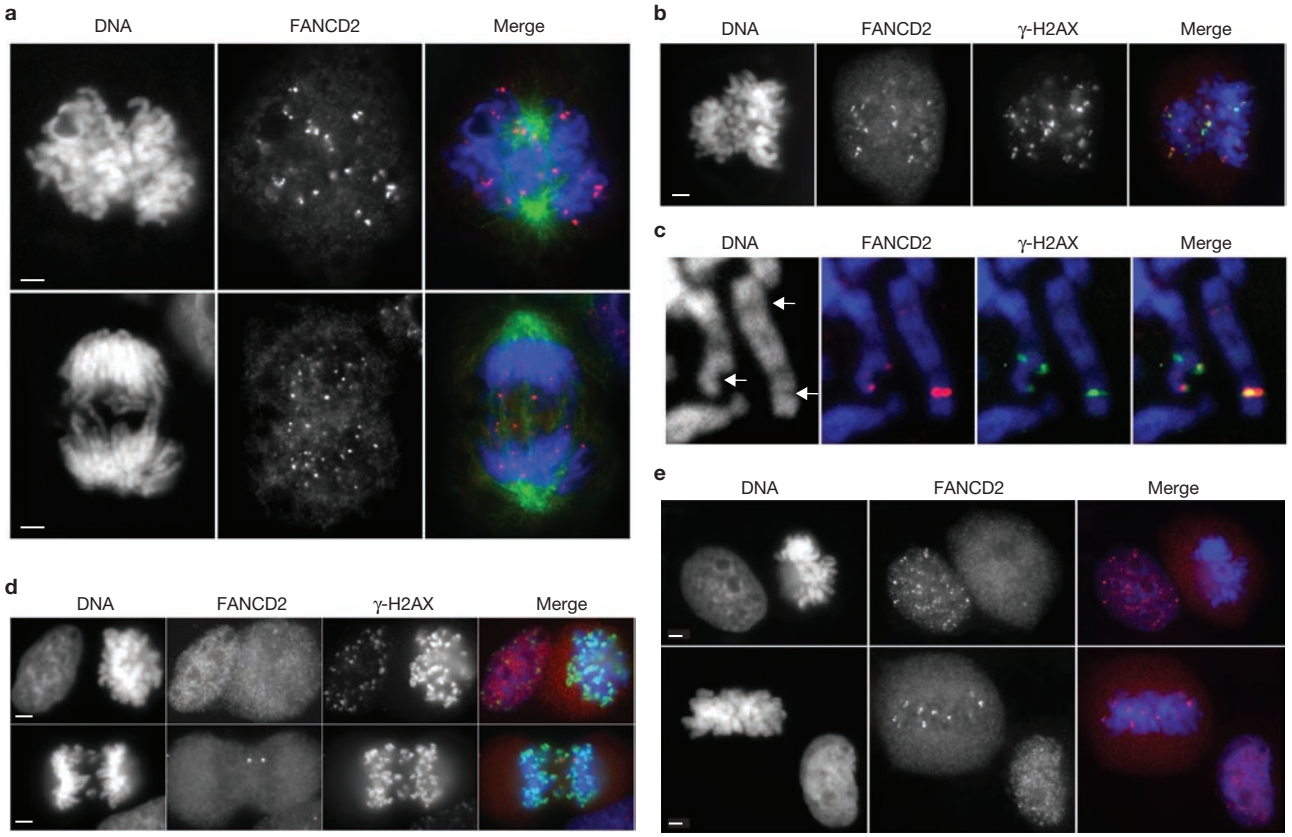

Figure 3 APH induces FANCD2 spots on mitotic chromosomes. (**a**) MRC5 cells treated with APH (0.3 μM) for 24 h were stained for DNA (left; blue in the merge, right), FANCD2 (middle; red in the merge, right) and α-tubulin (green in the merge). Representative pro-metaphase (top) and anaphase (bottom) figures exhibit an increased number of FANCD2 mitotic spots. Note that some of the spots are located on lagging chromosomes and bridges. Scale bar, 5 μM. (**b**) APH treatment increases the number of both FANCD2 and γ-H2AX foci on mitotic chromosomes. The images show an example of an APH-treated MRC5 mitotic cell stained for DNA (left; blue in the merge, right), FANCD2 (second panel; red in the merge, right) and γ-H2AX (third panel; green in the merge, right), with a large overlap between the two protein signals. Scale bar, 5 μM. (**c**) FANCD2 targets APH-induced chromatid discontinuities (arrows). Images are of a metaphase spread from APH-treated MRC5 cells, showing DNA (grayscale, left and blue in the other panels), FANCD2 (red) and γ-H2AX (green). (**d**) Neocarzinostatin (3 nM, 10 min exposure, 1 h recovery time)-induced DNA damage, visualized as γ-H2AX foci, does not induce FANCD2 spots on chromosomes. Images show examples of interphase, pro-metaphase (top) and anaphase (bottom) cells. Scale bars, 5 μM. (**e**) Mitomycin C-induced FANCD2 foci only appear in interphase nuclei soon after treatment (1μg ml^{-1}, 2 h after treatment, top), whereas in mitotic cells they are evident at later times (25 ng ml^{-1}, 24 h after treatment, bottom). Scale bars, 5 μM.

of γ-H2AX foci colocalize with FANCD2. Co-localization was confirmed by confocal microscopic analysis (Supplementary Information, Fig. S2A). These data suggest that only a subset of DNA lesions induce co-localization of FANCD2 and γ-H2AX. Moreover, FANCD2 was found to be associated with chromatid sites undergoing defective separation, raising the possibility that FANCD2 spots reflect abnormal chromatin conformations (Fig. 2d).

Recently, a role for the FANC pathway in the maintenance of chromosome stability at fragile sites has been proposed[23]. To investigate the possible connection between chromosome stability and segregation at mitosis, we treated MRC5 cells with a low dose of APH, known to induce fragile site expression. Strikingly, the number and frequency of FANCD2 spots were greatly enhanced after this treatment, providing evidence that FANCD2 localization on mitotic chromosomes is responsive to perturbation of DNA replication (Fig. 3a; Supplementary Information, Fig. S4). APH treatment also increased γ-H2AX foci on mitotic chromosomes (Fig. 3b). Similarly to localization in untreated cells, about 75% of FANCD2 spots colocalized with γ-H2AX foci. We further analysed metaphase spreads from APH-treated cells and found that FANCD2 localized to chromatid gaps and breaks, suggesting that these spots specifically mark sites of chromosome fragility (Fig. 3c). Cells committed to mitosis following exposure to low doses of APH are still able to divide and we observed a consistent number of ana-telophase figures showing FANCD2 spots on lagging chromosomes and anaphase bridges, supporting a link between APH-induced chromosome anomalies and mitotic defects. To determine whether DNA breakage in mitosis is sufficient for FANCD2 chromosome localization, we treated cells with neocarzinostatin, a radiomimetic drug that produces single- and double-strand breaks and examined mitotic cells 1 h later. Despite the induction of extensive DNA damage as visualized from γ-H2AX staining of chromosomes, FANCD2 did not relocalize with γ-H2AX (Fig. 3d). We also analysed FANCD2 response to the crosslinking agent mitomycin C (MMC). At 2 h post-treatment, FANCD2 foci had only increased in interphase nuclei and not in mitotic cells (Fig. 3e). In contrast, FANCD2 spots appeared on mitotic chromosomes at later times, suggesting that FANCD2 spots on mitotic chromosomes represent unresolved foci induced by fork stalling during the previous S phase (Fig. 3e).

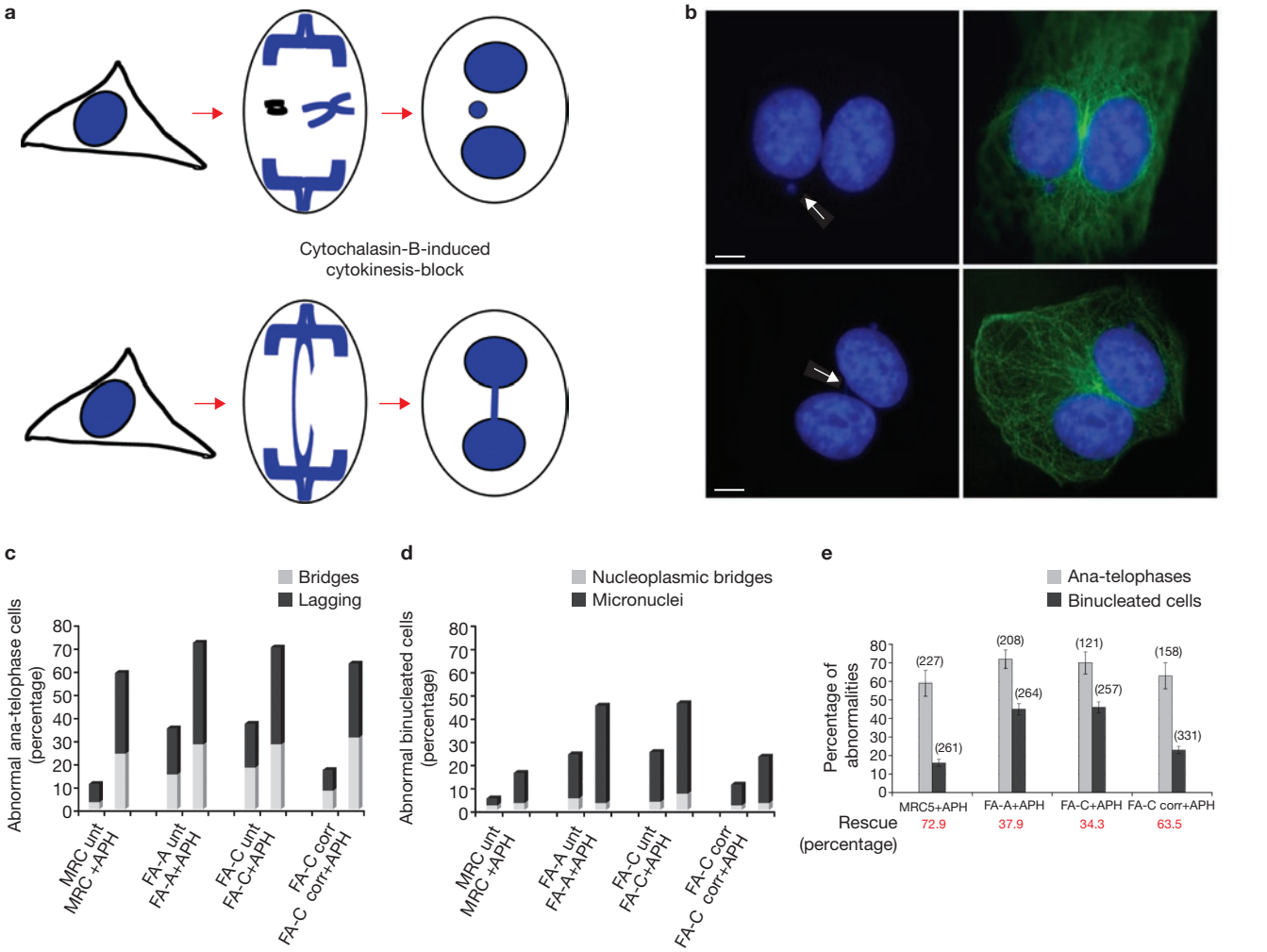

Figure 4 Fanconi anaemia cells fail to recover from APH-induced chromosome missegregation. (**a**) A diagram of a cytokinesis block assay[24]: abnormal chromosome segregation events during mitosis can be identified in daughter cells recognized by their binucleated status after cytochalasin B-induced cytokinesis block: lagging chromosomes or acentric fragments give rise to micronuclei (top) and anaphase bridges to nucleoplasmic bridges (bottom). (**b**) Examples of binucleated cells as scored in the cytokinesis-block assay. Cells were stained for DNA (blue) and α-tubulin (green). Arrows indicate a micronucleus (top) and a thin nucleoplasmic bridge (bottom). Scale bars, 10 μm. (**c**) Cells were left untreated or were treated with APH and fixed and stained for DNA and tubulin to visualize mitotic cells. Chromosome segregation defects were counted as the percentage of anaphase and telophase figures displaying lagging chromatin (lagging) or chromosome bridges in FANC-proficient or deficient cell lines. In each case at least 100 cells were counted. (**d**) Cells untreated or treated with APH were exposed to cytochalasin B (at the same time as the APH treatment) to block cytokinesis. Binucleated cells with well-separated nuclei were counted and those presenting micronuclei or nucleoplasmic bridges were scored as positive. In each case at least 250 cells were counted. (**e**) Percentage of ana-telophase abnormalities in APH-treated cells and their outcome as binucleated cells. The percentages of regular binucleated cells rescued from irregular ana-telophases are in red. Raw data are reported in **c** and **d**. In **c**–**e** data are mean ± s.e.m. based on the number of ana-telophase figures from at least three independent experiments (provided above the bars in brackets in **e**). MRC5, wild-type cells; unt, untreated; +APH, aphidicolin-treated; FA-A, FANCA$^{-/-}$ mutant; FA-C, FANCC$^{-/-}$; FA-C corr, FANCC$^{-/-}$ cells corrected by the ectopic expression of wild-type FANCC cDNA.

We next tested for a mitotic role of the FANC pathway. For this purpose, two parameters were taken into account in untreated and APH-treated FANC-proficient and -deficient cells: chromosome segregation defects (bridges and lagging chromatin) and the outcome of the following mitotic division as measured by scoring micronuclei and nucleoplasmic bridges in cytochalasin B-induced binucleated cells (Fig. 4a, b)[24]. APH treatment induced missegregation by nearly the same amount in wild-type and Fanconi anaemia cells (Fig. 4c). Nevertheless, APH-treated wild-type cells were still able to recover during the later steps of cell division and they only had a few binucleated cells with micronuclei. In contrast, micronucleation was a clear outcome in APH-treated Fanconi anaemia cells (Fig. 4d, e). Collectively, these data suggest that the FANC pathway is required to support proper chromatid separation and/or to avoid chromosome breakage of entangled chromatids at the end of cell division. We scored micronuclei in binucleated cells for the presence of the centromeric protein CENPA. We found that 9.6% of micronuclei in FANC-deficient and 6.1% in FANC-proficient cells stained positive for CENPA (Supplementary Information, Fig. S3A, B). Accordingly, metaphase chromosome counting revealed a slight but consistent and significant increase in aneuploidy in Fanconi anaemia primary fibroblasts in response to APH treatment (Supplementary Information, Fig. S3C, E). Together, these data indicate that although chromosome breakage is the major outcome of ana-telophase abnormalities the

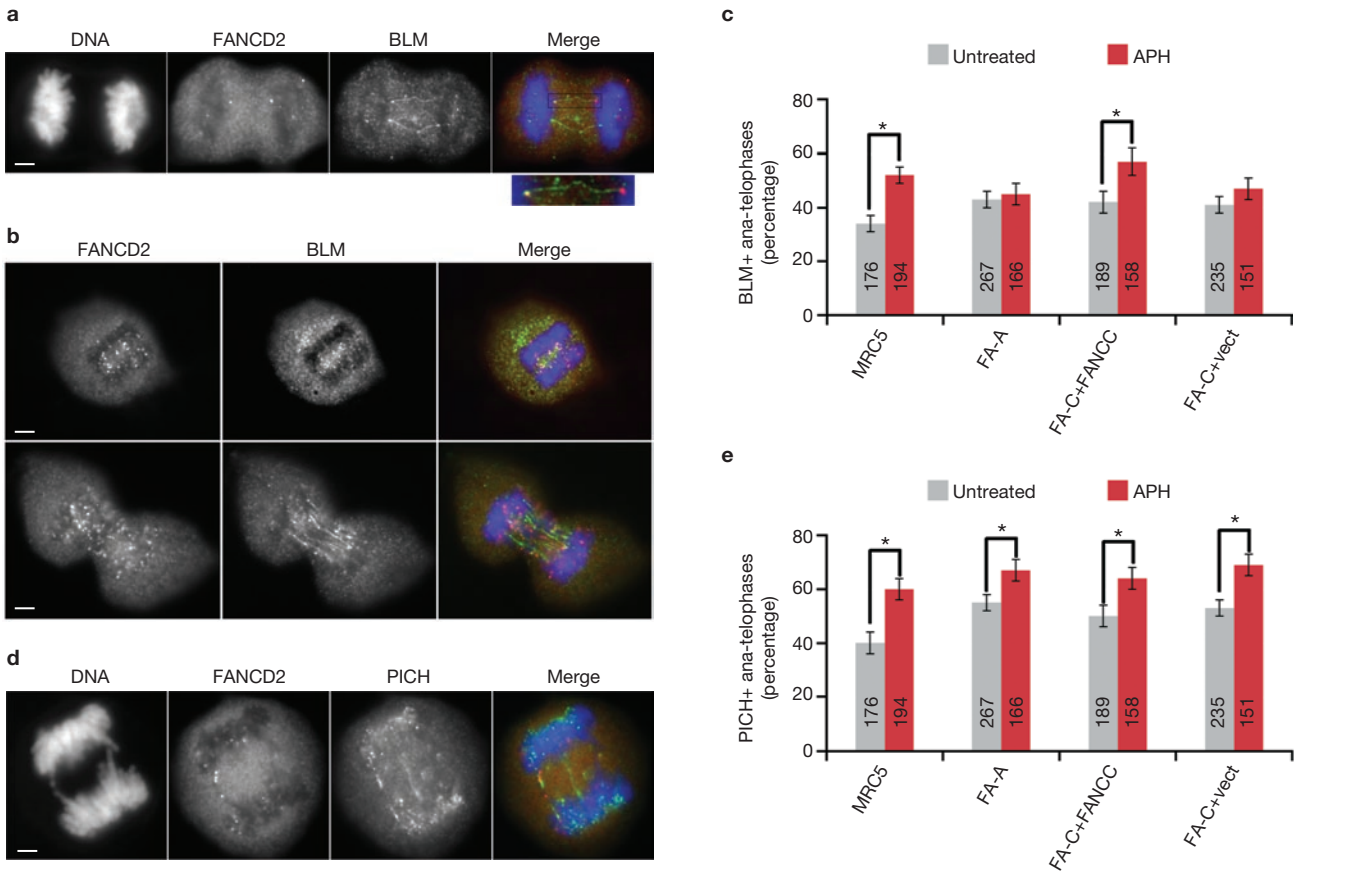

Figure 5 Localization of FANCD2, BLM and PICH during mitosis. (**a**) A subset of BLM-stained bridges connects FANCD2 spots on separating chromosome sets at anaphase. Scale bar, 5 μM. (**b**) APH-treated MRC5 cells were immunostained for FANCD2 (left; red in the merge, right) and BLM (middle; green in the merge, right). Some FANCD2 spots colocalize with BLM foci at early anaphase (top), whereas they are connected by BLM bridges at ana-telophase (bottom). Scale bars, 5 μM. (**c**) Frequency of BLM-positive ana-telophases in FANC-proficient and deficient cells. Cells were left untreated or treated with APH (0.3 μM for 24 h), and ana-telophase figures were scored for the presence of BLM-positive (BLM^+) bridges. Data are mean ± s.e.m. of pooled data of at least 150 anaphases from three independent experiments. Differences were considered statically significant when $^*P < 0.05$ as determined using the $\chi 2$ contingency test. The bars show the total number of scored cells. (**d**) PICH stained bridges link FANCD2 spots in APH-treated cells. Scale bar, 5 μM. (**e**) The frequency of PICH-positive anaphases and telophases in Fanc-proficient and -deficient cells. Cells were left untreated or treated with APH (0.3 μM for 24 h) and ana-telophase figures were scored for the presence of PICH-positive ($PICH^+$) bridges. Data are mean ± s.e.m. of pooled data of at least 150 anaphases from three independent experiments. Differences were considered statically significant when $^*P < 0.05$ as determined using the $\chi 2$ contingency test. The bars show the total number of scored cells. MRC5, wild-type cells; FA-A (cells belonging to the Fanconi anaemia complementation group A), $FANCA^{-/-}$ mutant cells; FA-C+FANCC, $FANCC^{-/-}$ mutant cells corrected by the ectopic expression of wild-type cDNA; FA-C+vect, $FANCC^{-/-}$ cells transduced with an empty vector.

risk of aneuploidy for chromosomes is significantly more important in the absence of a functional FANC pathway.

Clear crosstalk has been described between the FANC pathway and the BLM helicase[5,6]. Importantly, Bloom syndrome cells also show a higher than normal frequency of micronuclei[25], anaphase bridges and lagging chromosomes[17], and BLM was shown to localize to ultrafine anaphase bridges[17]. To determine the relationship between FANCD2 and BLM during mitosis, we examined the localization pattern of the two proteins in normal untreated cells and found that a subset of BLM bridges connect FANCD2 spots on separating chromosome sets (Fig. 5a). The number of BLM bridges linking FANCD2 spots on segregating chromosomes increased as a consequence of exposure to either APH (Fig. 5b) or MMC (Supplementary Information, Fig. S4A). Next, we compared the frequency of BLM-positive ana-telophase figures in untreated and APH-treated normal and Fanconi anaemia fibroblasts. In response to APH, the frequency of BLM-positive ana-telophases was significantly enhanced in FANC-proficient cells, whereas no significant increase was observed in Fanconi anaemia cells (Fig. 5c). The tension sensor protein PICH colocalizes with BLM[17,26] and, consistently, was also found associated with FANCD2 spots (Fig. 5d). However, we did not detect significant differences between the behaviour of PICH-positive ana-telophases in FANC-deficient and -proficient cells, indicating that only BLM localization is affected by loss-of-function of the FANC pathway (Fig. 5e; Supplementary Information, Fig. S4B). These data suggest that replication stress induces a FANCcore complex-dependent response involving FANCD2 and BLM, which prevents chromosome segregation failures.

It has been reported that BLM associates with both centromeric and non-centromeric bridges[17]. Consequently, we sought to determine if a FANC pathway deficiency affects localization of BLM on both kinds of bridges. To do this, we compared the frequency of centromeric (Hec1 positive) and non-centromeric (Hec1 negative) BLM- or PICH-positive

Table 1 Quantification of mitotic cells with FANCD2 spots

Cell line	Pro/metaphase	Ana-telophase
MRC5		
Cells with spots	63%	40%
Spots per cell	2.4	0.8
FA-D2		
Cells with spots	47%	30%
Spots per cell	0.7	0.5
FA-D2+*FANCD2*		
Cells with spots	62%	43%
Spots per cell	2.6	0.8
FA-C		
Cells with spots	0	0
Spots per cell	0	0
FA-C+*FANCC*		
Cells with spots	58%	34%
Spots per cell	1.9	0.9

A total of at least 150 mitotic figures from three independent experiments for each examined cell line were scored for the presence of FANCD2 spots and the number of spots per cell.

bridges in FANC-deficient and -proficient cells as a function of APH treatment. In response to APH, the frequency of centromeric BLM and PICH bridges slightly increased in both FANC-proficient and -deficient cells. Interestingly, while the frequency of non-centromeric PICH-positive bridges showed a similar increase in FANC-proficient and -deficient cells, the frequency of non-centromeric BLM positive bridges increased only in FANC-proficient cells (Supplementary Information, Fig. S4C, E). These data strongly suggest that the FANC pathway is required for proper assembly of BLM only on non-centromeric bridges.

To strengthen the relationship between BLM and FANC proteins we downregulated BLM in FANC-proficient and -deficient cells and scored nucleoplasmic bridges and micronuclei in binucleated cells after APH exposure (Supplementary Information, Fig. S5A, B). Compared to BLM and FANC pathway-proficient cells, BLM-deficient cells showed an increase in both nucleoplasmic bridges (19.9% versus 2.3%) and micronuclei (29.6% versus 15.0%), whereas FANC deficiency resulted mainly in micronucleation (33.0%). Interestingly, the BLM and FANC pathway double-deficient cells showed the same levels of micronuclei observed in cells deficient in either BLM or the FANC pathway, indicating the lack of an additive or synergistic effect. Finally, in BLM and FANC pathway double-deficient cells, the frequency of nucleoplasmic bridges was the same as that observed in the BLM-only deficient cells. Together with previously reported data[17], these results suggest that the BLM and FANC pathways are epistatic with respect to the micronucleation phenotype and that BLM and the FANC pathway work together to resolve non-centromeric bridges. In contrast, centromeric bridge resolution only depends on BLM.

The FANC pathway is currently considered to have a key role in maintaining chromosome stability through its emerging role in DNA replication stress and DNA damage response[4]. Here we show that the FANC pathway is also required to prevent chromosome instability and aneuploidy during mitosis. Proper chromosome segregation is impaired in Fanconi anaemia cells and replicative stress induced by APH is able to raise chromosome instability in these cells by different mechanisms. Increased chromosome breakage at fragile sites have been described in Fanconi anaemia[23,27,28]. Here we show that FANCD2 localizes on mitotic chromosomes during unperturbed cell cycles and to APH-induced chromosome gaps and breaks, suggesting that it targets fragile sites (this has also been shown by Chen *et al.* published in this issue; *Nature Cell Biol.* **11,** 753–760; 2009). While we could not directly deduce which specific sites were targeted by FANCD2 during unperturbed conditions, we hypothesized that they could be sites of replication fork stalling. Our characterization allowed us to establish that these sites underlie abnormal chromatin structure, as marked by γ-H2AX, and are prone to defective segregation at anaphase. We also inferred that FANCD2 spots in mitosis represent FANCD2 unresolved foci assembled during the previous S/G2 phases of the cell cycle. Micronucleation in Fanconi anaemia cells has already been reported[29,30]. Our data indicate a role of the FANC pathway, not only in preventing formation of aberrant chromosome structures, but also in preventing breakage and loss of missegregating chromatin at the end of cell division, particularly after replication stress. We found that FANC-proficient cells were able to rescue around 70% of the APH-induced anaphase abnormalities, whereas Fanconi anaemia cells failed to recover properly, leading to massive micronucleation (Fig. 4e). A similar phenotype, involving anaphase bridging and lagging chromatin, has been described for Bloom syndrome cells[17]. BLM helicase is targeted to chromatin and DNA bridges where it colocalizes with PICH and has been suggested to function in the resolution of intertwined DNA structures due to not fully replicated chromosomal regions or aberrant replication intermediates (as at the centromeres)[17]. Our data, showing a significant increase of BLM bridges after replication stress, further support this model. Moreover, we show that in the absence of an intact FANC pathway, BLM recruitment to APH-induced non-centromeric anaphase bridges is less efficient. We propose that the FANC pathway is required to target BLM or to stabilize it on DNA replication or recombination intermediates, fostering their resolution (Supplementary Information, Fig. S5C). It is noteworthy that FANCD2 has been found associated with BRCA1 in both interphase foci and synaptonemal complexes on meiotic chromosomes[9]. Moreover, both localization of BLM to synaptonemal complexes and a possible function in homologous chromosome disjunction have also been reported[31]. Thus it is conceivable that sites of FANCD2 localization on mitotic chromosomes represent structurally related chromatin regions. However, we did not observe colocalization of FANCD2 with BRCA1 on mitotic chromosomes, as would be expected if these sites were not undergoing recombination (Supplementary Information, Fig. S5D). It could also be argued that FANCD2 foci persist on unresolved structures promoting their stabilization and resolution while other foci-associated proteins like BRCA1 are released from chromatin. Moreover, the reported function for BRCA1 in spindle formation and chromosome segregation[16] seems unrelated to the role of the FANC pathway in mitosis. Although we cannot rule out the possibility that different DNA intermediates are generated in response to replication stress in wild-type and Fanconi anaemia cells, the increase of PICH stained structures in both cell types suggests that the FANC pathway is specifically required for BLM localization and/or stabilization on the APH-induced non-centromeric structures. Future investigations will be directed towards defining both the underlying nature of FANCD2-associated chromosome structures and the role of the FANC pathway in the management of DNA alterations during mitotic cell division. Finally, it would be interesting to determine if the described role of BRCA2 in cell division[15] is dependent on the upstream components of the FANC pathway.

Note added in proof: a related manuscript by Chen et al. *(*Nature Cell Biol. ***11,*** *753–760; 2009) is published in this issue.*

METHODS

Methods and any associated references are available in the online version of the paper at http://www.nature.com/naturecellbiology/

Note: Supplementary Information is available on the Nature Cell Biology website.

ACKNOWLEDGEMENTS

We thank all the past and present members of F. Rosselli's team for technical support and helpful discussions, J. Soulier and D. Briot for the FA-C complemented cell lines, E. Nigg for the anti-PICH antibody, Y. Lecluse for FACS analysis, A. Jalil for help with confocal microscopy and P. Kannouche for providing materials and technical advice. This work was supported by grants from La Ligue Contre le Cancer (Equipe Labellisée 2006 and 2009), Electricité de France (EDF) and Institut Nationale pour le Cancer (INCa) to F.R., and a fellowship from INCa-Lilly to V.N.

AUTHOR CONTRIBUTIONS

V.N. performed experiments and V.N. and F.R. conceived and designed research, performed data analysis and wrote the manuscript.

COMPETING FINANCIAL INTERESTS

The authors declare no competing financial interests.

Published online at http://www.nature.com/naturecellbiology/
Reprints and permissions information is available online at http://npg.nature.com/reprintsandpermissions/

1. D'Andrea, A. D. & Grompe, M. The Fanconi anaemia/BRCA pathway. *Nature Rev. Cancer* **3,** 23–34 (2003).
2. Kinzler, K. W. & Vogelstein, B. Cancer-susceptibility genes. Gatekeepers and caretakers. *Nature* **386,** 761–763 (1997).
3. Ellis, N. A. *et al.* The Bloom's syndrome gene product is homologous to RecQ helicases. *Cell* **83,** 655–666 (1995).
4. Wang, W. Emergence of a DNA-damage response network consisting of Fanconi anaemia and BRCA proteins. *Nature Rev. Genet.* **8,** 735–748 (2007).
5. Meetei, A. R. *et al.* A multiprotein nuclear complex connects Fanconi anemia and Bloom syndrome. *Mol. Cell Biol.* **23,** 3417–3426 (2003).
6. Pichierri, P., Franchitto, A. & Rosselli, F. BLM and the FANC proteins collaborate in a common pathway in response to stalled replication forks. *EMBO J.* **23,** 3154–3163 (2004).
7. Meetei, A. R., Yan, Z. & Wang, W. FANCL replaces BRCA1 as the likely ubiquitin ligase responsible for FANCD2 monoubiquitination. *Cell Cycle* **3,** 179–181 (2004).
8. Andreassen, P. R., D'Andrea, A. D. & Taniguchi, T. ATR couples FANCD2 monoubiquitination to the DNA-damage response. *Genes Dev.* **18,** 1958–1963 (2004).
9. Garcia-Higuera, I. *et al.* Interaction of the Fanconi anemia proteins and BRCA1 in a common pathway. *Mol. Cell* **7,** 249–262 (2001).
10. Pichierri, P. & Rosselli, F. The DNA crosslink-induced S-phase checkpoint depends on ATR-CHK1 and ATR-NBS1-FANCD2 pathways. *EMBO J.* **23,** 1178–1187 (2004).
11. Guervilly, J. H., Mace-Aime, G. & Rosselli, F. Loss of CHK1 function impedes DNA damage-induced FANCD2 monoubiquitination but normalizes the abnormal G2 arrest in Fanconi anemia. *Hum. Mol. Genet.* **17,** 679–689 (2008).
12. Wang, X. *et al.* Chk1-mediated phosphorylation of FANCE is required for the Fanconi anemia/BRCA pathway. *Mol. Cell Biol.* **27,** 3098–3108 (2007).
13. Bogliolo, M. *et al.* Histone H2AX and Fanconi anemia FANCD2 function in the same pathway to maintain chromosome stability. *EMBO J.* **26,** 1340–1351 (2007).
14. Tutt, A. *et al.* Absence of Brca2 causes genome instability by chromosome breakage and loss associated with centrosome amplification. *Curr. Biol.* **9,** 1107–1110 (1999).
15. Daniels, M. J., Wang, Y., Lee, M. & Venkitaraman, A. R. Abnormal cytokinesis in cells deficient in the breast cancer susceptibility protein BRCA2. *Science* **306,** 876–879 (2004).
16. Joukov, V. *et al.* The BRCA1/BARD1 heterodimer modulates ran-dependent mitotic spindle assembly. *Cell* **127,** 539–552 (2006).
17. Chan, K. L., North, P. S. & Hickson, I. D. BLM is required for faithful chromosome segregation and its localization defines a class of ultrafine anaphase bridges. *EMBO J.* **26,** 3397–3409 (2007).
18. Kalb, R. *et al.* Hypomorphic mutations in the gene encoding a key Fanconi anemia protein, FANCD2, sustain a significant group of FA-D2 patients with severe phenotype. *Am. J. Hum. Genet.* **80,** 895–910 (2007).
19. Chan, G. K., Jablonski, S. A., Sudakin, V., Hittle, J. C. & Yen, T. J. Human BUBR1 is a mitotic checkpoint kinase that monitors CENP-E functions at kinetochores and binds the cyclosome/APC. *J. Cell Biol.* **146,** 941–954 (1999).
20. Ciferri, C. *et al.* Architecture of the human ndc80-hec1 complex, a critical constituent of the outer kinetochore. *J. Biol. Chem.* **280,** 29088–29095 (2005).
21. Ichijima, Y. *et al.* Phosphorylation of histone H2AX at M phase in human cells without DNA damage response. *Biochem. Biophys. Res. Commun.* **336,** 807–812 (2005).
22. Suzuki, M., Suzuki, K., Kodama, S. & Watanabe, M. Phosphorylated histone H2AX foci persist on rejoined mitotic chromosomes in normal human diploid cells exposed to ionizing radiation. *Radiat. Res.* **165,** 269–276 (2006).
23. Howlett, N. G., Taniguchi, T., Durkin, S. G., D'Andrea, A. D. & Glover, T. W. The Fanconi anemia pathway is required for the DNA replication stress response and for the regulation of common fragile site stability. *Hum. Mol. Genet.* **14,** 693–701 (2005).
24. Fenech, M. Cytokinesis-block micronucleus cytome assay. *Nature Protoc.* **2,** 1084–1104 (2007).
25. Rosin, M. P. & German, J. Evidence for chromosome instability *in vivo* in Bloom syndrome: increased numbers of micronuclei in exfoliated cells. *Hum. Genet.* **71,** 187–191 (1985).
26. Baumann, C., Korner, R., Hofmann, K. & Nigg, E. A. PICH, a centromere-associated SNF2 family ATPase, is regulated by Plk1 and required for the spindle checkpoint. *Cell* **128,** 101–114 (2007).
27. Porfirio, B. *et al.* Fragile sites and chromosome instability: the distribution of breaks induced by cis-diamine-dichloro-platinum (II) in Fanconi anemia lymphocyte cultures. *Hum. Genet.* **86,** 256–260 (1991).
28. Fundia, A., Gorla, N. & Larripa, I. Spontaneous chromosome aberrations in Fanconi's anemia patients are located at fragile sites and acute myeloid leukemia breakpoints. *Hereditas* **120,** 47–50 (1994).
29. Maluf, S. W. & Erdtmann, B. Genomic instability in Down syndrome and Fanconi anemia assessed by micronucleus analysis and single-cell gel electrophoresis. *Cancer Genet. Cytogenet.* **124,** 71–75 (2001).
30. Willingale-Theune, J. *et al.* Ultrastructure of Fanconi anemia fibroblasts. *J. Cell Sci.* **93 (Pt 4)**, 651–665 (1989).
31. Walpita, D., Plug, A. W., Neff, N. F., German, J. & Ashley, T. Bloom's syndrome protein, BLM, colocalizes with replication protein A in meiotic prophase nuclei of mammalian spermatocytes. *Proc. Natl Acad. Sci. USA* **96,** 5622–5627 (1999).

METHODS

Cell lines and culture conditions. Human SV-40-immortalized MRC5 (wild type), PD20 (FA-D2) and the complemented counterpart corrected by microcell-mediated chromosome transfer (PD20-3.15), PD220 (FA-A), and PD331 (FA-C), fibroblasts were grown in DMEM (Dulbecco's modified Eagle's medium; Gibco) supplemented with 12% fetal bovine serum (FBS; PAA GmbH) in a 5% CO_2 incubator at 37 °C. The FANCC-corrected (FA-C+FANCC) and vector transduced (FA-C+vector) FA-C cell lines (from J. Soulier, Hôpital Saint-Louis, Paris) were maintained in DMEM supplemented with 12% FBS and puromycin (0.5 μg ml^{-1}).
The human FHSL01 and FHSL02 (Fanconi pathway proficients), and Fanconi patients EGF031 (FA-G), EGF088 (FA-A) and EGF050 (FA-D2) primary fibroblasts (provided by J. Soulier) were cultured in DMEM supplemented with 20% FBS.

Cell treatments. To analyse the effects of perturbation of DNA replication in mitosis, asynchronous cells were exposed to APH (0.3 μM; Sigma) for 24 h before cell fixation or metaphase chromosome preparations. For the detection of micronuclei and nucleoplasmic bridges in the cytokinesis-block assay, cells were either untreated or treated with APH (0.3 μM) while being incubated with cytochalasin-B (2 μg ml^{-1}; Sigma) for 24 h before fixation.

To induce DNA breaks cells were exposed to neocarzinostatin (3 nM; Sigma) for 10 min, then washed with PBS and incubated with normal medium for 1 h before cell fixation. To examine the effects of a DNA crosslinking agent, cells were exposed to MMC (1 μg ml^{-1} or 25 ng ml^{-1} Sigma). To accumulate cells in mitosis, cells were treated with nocodazole (100 ng ml^{-1}; Sigma) or taxol (10 μM; Sigma) for 24 h and then processed for immunofluorescence or FACS (fluorescence-activated cell sorting) analysis.

Immunocytochemistry and microscopy Immunofluorescence staining was performed using standard methods. Essentially cells grown on glass coverslides in 6-well plates were fixed with 4% paraformaldehyde in PBS for 15 min at room temperature, permeabilized in either Triton Buffer (0.5% Triton X-100, 20 mM Hepes at pH 7.9, 50 mM NaCl, 3 mM $MgCl_2$ and 300 mM sucrose) or 0.5% Triton X-100 in PBS for 10 min and blocked with 3% BSA in PBS containing 0.05% Tween-20 for 20 min. In some cases cells were pre-extracted with 0.1% Triton X-100 in PBS for 3 min before fixation. For metaphase chromosome staining, cells were incubated with colcemid (0.1 μg ml^{-1}; Roche) for 4 h at 37 °C, then hypotonically swollen in 0.075 M KCl solution for 15 min at 37 °C and finally processed for immunostaining.

For indirect immunofluorescence experiments the following primary antibodies were used: rabbit anti FANCD2 (1:1000; ab2187, Abcam), mouse anti-BubR1 (1:100; 8G1, Abcam), mouse anti-γH2AX (1:5000; Upstate), goat anti-BLM (1:150; C-18, Santa Cruz), mouse anti-α-tubulin (1:500; DM1A, Abcam), rat anti-PICH (1:500; a gift from E. Nigg, Max Planck Institute, Germany), mouse anti-Hec1 (1:200; 9G3, Abcam) and mouse anti-CENPA (1:500; Ab13939, Abcam). Unless otherwise specified, all the incubations with primary antibodies were performed overnight at 4 °C.

Incubations with secondary antibodies (Alexa 488- or Alexa 592-conjugated; Molecular Probes, Invitrogen) were performed at room temperature for 1 h in the dark. Slides were air-dried and mounted in Vectashield (Vector Laboratories) with DAPI.

Images were captured using an ORCA-ER digital camera (Hamamatsu) connected to an Olympus A×70 fluorescence microscope with a × 100 / 1.3 oil immersion objective. Acquisitions were made using the Simple PCI software (Compix, Imaging Systems). The images were then imported in Photoshop (Adobe Photoshop CS 8.0.1, Adobe Systems), pseudocoloured and merged using the same software.

Colocalization analysis was performed using a confocal laser scanning system (LSM 510, Carl Zeiss) equipped with an Axiovert 200M microscope that had a × 63 / 1.4 NA oil immersion objective. Images were acquired with an AxioCam MR camera (Zeiss) using the LSM 5 Image Browser (Zeiss).

Flow cytometry. For FACS analysis, cells were trypsinized, washed with PBS, fixed in chilled, 80% ethanol and stored overnight at –20 °C. Fixed cells were then washed in PBS and resuspended in PBS containing propidium iodide (30 μg ml^{-1}; Sigma) and RNAse (100 μg ml^{-1}; Roche). Data were collected using a Becton Dickinson FACS machine and analysed with Cell Quest software.

Metaphase chromosome preparations. For chromosome counting, primary fibroblasts were left untreated or treated with APH (0.3 μM) for 24 h and collected after 24 h recovery. Cells were incubated with colcemid (0.1 μg ml^{-1}) and metaphase spreads obtained using standard procedures. Briefly, cells were incubated in hypotonic solution (0.075 M KCl) for 15 min at 37 °C, and the reaction was stopped by adding freshly prepared fixative solution (3:1 methanol/glacial acetic acid). Cells were then subjected to several rounds of fixative changes before making slides. Air-dried preparations were Giemsa stained, dried at room temperature for 48 h and mounted in Eukitt medium.

RNA interference and western blotting. Corrected (+FANCC) or vector-transduced (+vector) FA-C fibroblasts were transfected with control (si*LacZ*) or BLM (si*BLM*) siRNA duplex oligonucleotides (Eurogentec), using Oligofectamine (Invitrogen). The following sense sequences were used: 5′-GUCGACGGAAUACUUCGA-3′ (si*LacZ*), 5′-AGCAGCGAUGUGAUUUGCA-3′ (si*BLM1*) and 5′-AUCAGCUAGAGGCGAUCAA-3′ (si*BLM2*). After 48 h cells were untreated or treated with APH and cytochalasin-B for 24 h and processed either for immunostaining, as described above, or western blotting. For western blotting, cells were lysed in RIPA buffer containing a protease inhibitor cocktail (Roche), lysates were separated on 8% SDS-polyacrilamide gels and transferred to nitrocellulose membranes. The following primary antibodies were used: goat anti-actin (1:1000; I-19, Santa Cruz), rabbit anti-BLM (1:1000; Calbiochem) and rabbit anti-FANCC (1:1000; R9098, provided by the Fanconi Anemia Research Fund). Membranes were then incubated with HRP (horseradish peroxidase)-conjugated secondary antibodies (Santa Cruz) before undergoing a chemiluminescence HRP substrate reaction (Immobilon, Millipore). Signals were detected using the Gene Gnome system (Syngene Bio Imaging).

nature cell biology

DOI: 10.1038/ncb1883

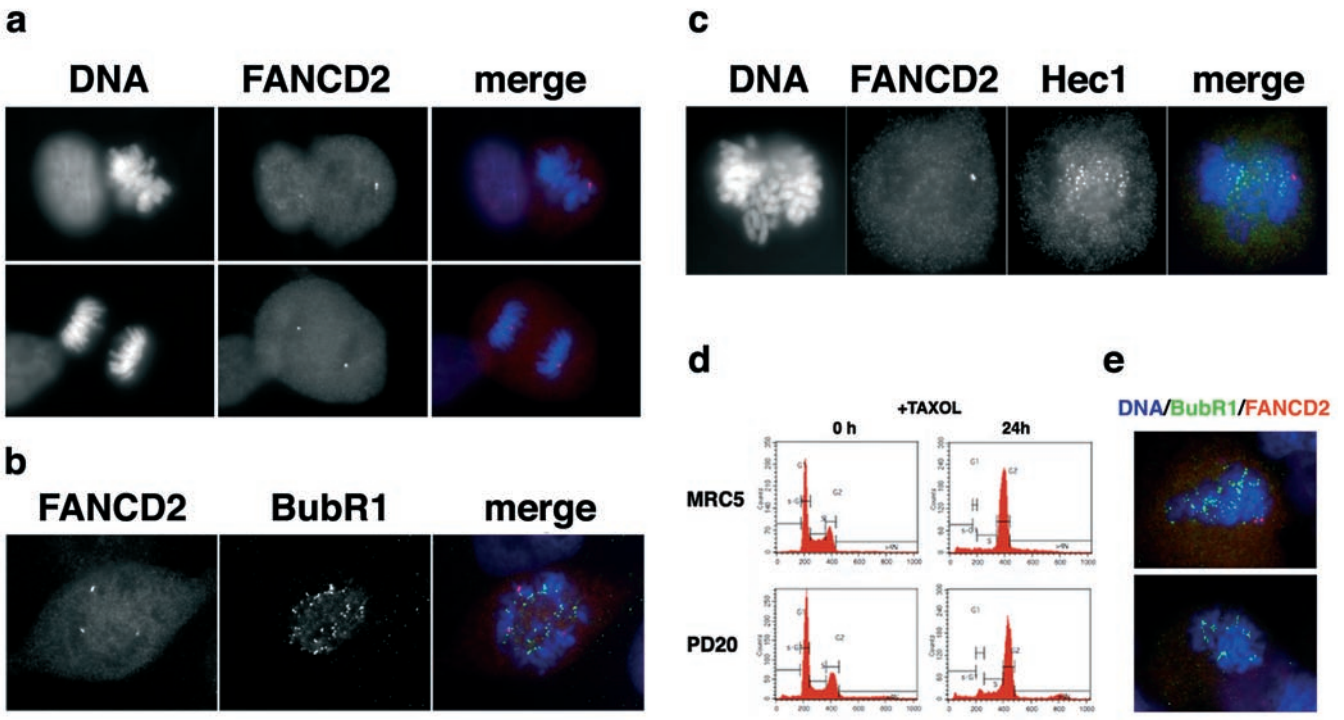

Figure S1 A. FANCD2 localization in untransformed primary fibroblasts from a FANC-proficient individual. Primary cells were immunostained for DNA (left panels, blue in the merge) and FANCD2 (middle panels, red in the merge). Representative images of cells at metaphase (upper panel) and anaphase (bottom) showing FANCD2 spots on mitotic chromosomes. Note the two spots segregating with the chromosome at anaphase. **B.** FANCD2 does not co-localize with BubR1. A prometaphase figure stained for FANCD2 (left panel, red in the merge) and BubR1 (middle, green in the merge). FANCD2 spots do not overlap with BubR1-stained kinetochores. **C.** FANCD2 spots do not localize at kinetochores. A mitotic cell stained (left to right) for DNA (blue in the merge), FANCD2 (red in the merge), Hec1 (green in the merge). **D.** Accumulation of cells with a 4N DNA content is similar in MRC5 and PD20 (FA-D2) cells exposed to a 24h treatment with taxol (10μM) and analyzed by FACS. **E.** Nocodazole-treated cells (100 ng/ml) immunostained for BubR1 (green) and FANCD2 (red). In the merged images the DNA is blue. BubR1 accumulates at kinetochores of both PD20 3.15 (FA-D2+FANCD2) (upper panel) and PD20 (FA-D2) (bottom) pro-metaphase-arrested cells. Note also that the FANCD2 spots in FA-D2 corrected cells do not co-localize with BubR1.

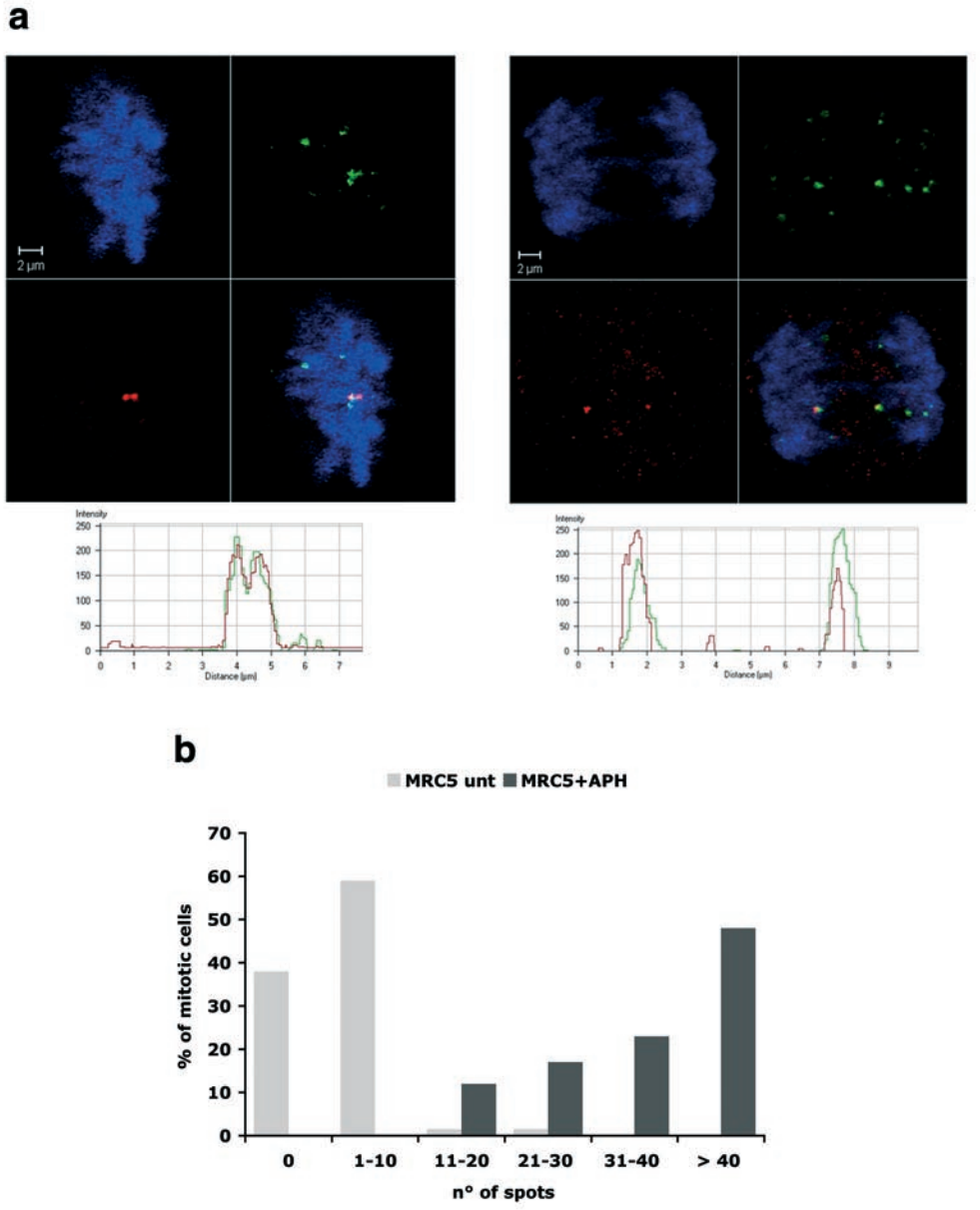

Figure S2 A. Confocal microscopy analysis of FANCD2 and γH2AX co-localization on mitotic chromosomes. Upper panels show confocal data sets relative to DNA (blue), FANCD2 (red), γH2AX (green), and merged signals. Lower panels represent the corresponding peak intensity profiles relative to FANCD2 (red) and γH2AX (green), showing the large overlapping between the two signals. **B.** Distribution of FANCD2 spots in mitotic cells. MRC5 mitotic cells untreated or treated with APH were scored for the presence and the number of FANCD2 spots on mitotic chromosomes. A total of at least 60 cells were counted. Note that after the APH treatment a strong increase both in the number and in the frequency of FANCD2 spots is induced.

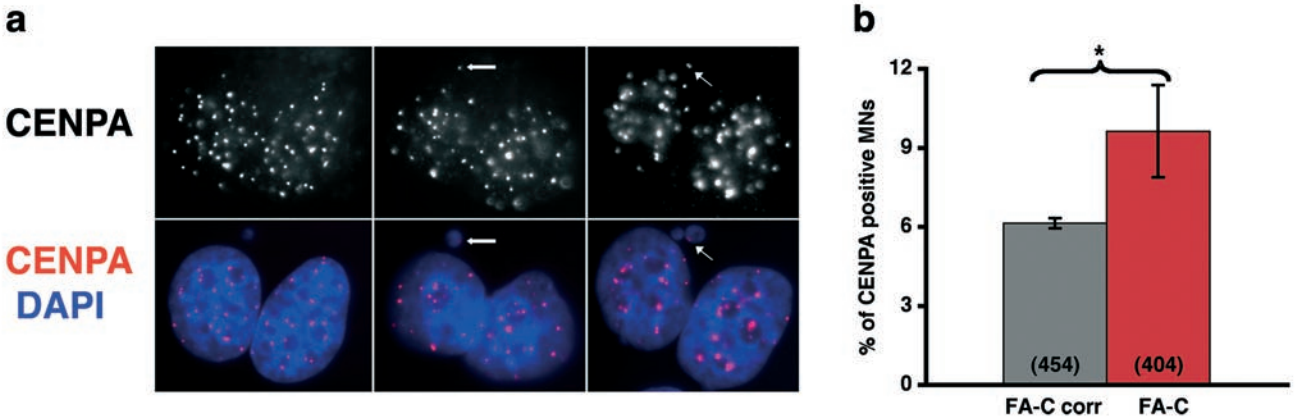

c

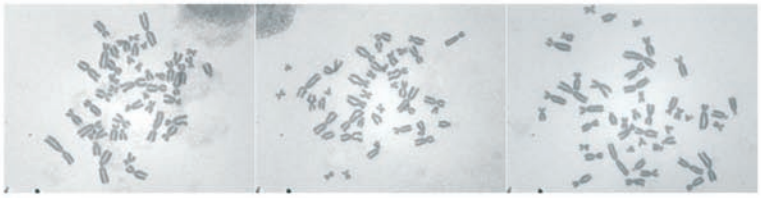

d

		Chromosome number <46	46	>46	Aneuploidy increment (%) in APH treated vs untreated cells
WT	Untreated	5,4 %	93,2 %	1,4 %	
	APH	7,2 %	92,8 %	0 %	0,32% *
FA-A	Untreated	7,7 %	91,0 %	1,3 %	
	APH	14,5 %	85,5 %	0 %	5,47% **
FA-G	Untreated	8,6 %	90,0 %	1,4 %	
	APH	10,8 %	84,6 %	4,6 %	5,95%

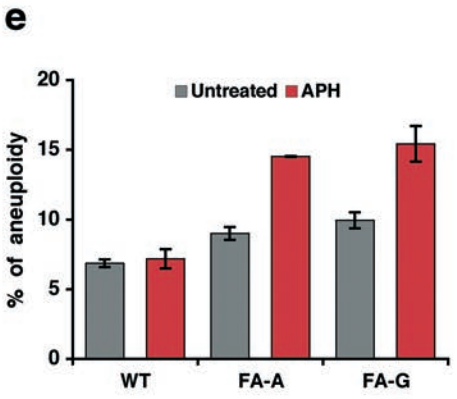

Figure S3 Examples of micronucleated binucleated cells after APH exposure showing CENPA staining (upper panels; red in the merge, bottom panels) in nuclei and MNs. Binucleated cells were obtained by cyt-B treatment, as previously described. Wheat germ agglutinin (WGA, Molecular Probes) was used to stain plasma membranes (not shown). Quantification of CENPA positive MNs in APH-treated FA-C and FA-C corrected binucleated cells. Numbers in parenthesis represent the scored MNs from four independent experiments. For each experiment at least 100 MNs were scored. Standard deviation is presented for each cell line. The difference between FA-C and FA-C corrected cells is statistically significant as calculated using *t*-student test ($p<0,05$ (*)). Examples of metaphase plates from human primary fibroblasts. A wild-type diploid metaphase and two hypodiploid metaphases (41 and 45 chromosomes, respectively) from FANC-deficient fibroblasts are shown left to right. Table representing the frequency of metaphases with the indicated chromosome content from untreated and APH-treated wt, FA-A and FA-G primary fibroblasts. Only good quality metaphases (presenting 40 to 52 chromosomes) were included in the count. At least 50 metaphases from two independent experiments for each genotype and condition were scored in a blinded fashion. The difference in aneuploidy increment between FANC-proficient and deficient cells is statistically significant with the *t*-student test ($p<0,05$ (*) and $p<0,01$ (**)). Diagram showing the frequency of aneuploid cells in untreated and APH-treated wt, FA-A and FA-G human primary fibroblasts, summarizing data presented in D. Error bars correspond to the maximum variance between the experiments.

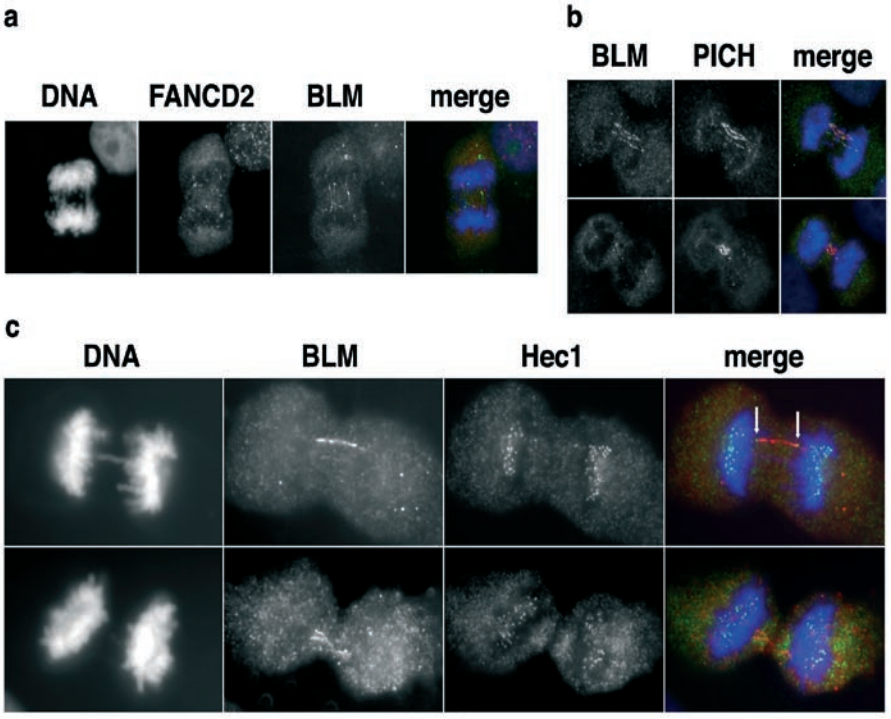

d

		Frequency of BLM^+ HEC^+ bridges/anaphase	Frequency of BLM^+ HEC^- bridges/anaphase	Total BLM^+
FANCCcorr	Untreated (134)	0,4	0,2	0,6
	APH (65)	0,6	0,5	1,1
FANCC	Untreated (153)	0,5	0,2	0,7
	APH (106)	0,7	0,2	0,9
		Frequency of $PICH^+$ HEC^+ bridges/anaphase	Frequency of $PICH^+$ HEC^- bridges/anaphase	Total $PICH^+$
FANCCcorr	Untreated (77)	0,6	0,2	0,8
	APH (50)	0,9	0,8	1,7
FANCC	Untreated (57)	0,8	0,2	1,0
	APH (51)	1,1	0,7	1,7

e

% of BLM^+ anaphases			Frequency of BLM^+ HEC^+ bridges/BLM^+ anaphase	Frequency of BLM^+ HEC^- bridges/BLM^+ anaphase	Total BLM^+
47,8	FANCCcorr	Untreated	0,8	0,4	1,2
55,4		APH	1,1	0,9	2,0
47,1	FANCC	Untreated	1,1	0,4	1,5
43,4		APH	1,7	0,4	2,1
% of $PICH^+$ anaphases			Frequency of $PICH^+$ HEC^+ bridges/$PICH^+$ anaphase	Frequency of $PICH^+$ HEC^- bridges/$PICH^+$ anaphase	Total $PICH^+$
48,1	FANCCcorr	Untreated	1,2	0,4	1,6
64,0		APH	1,4	1,3	2,7
57,9	FANCC	Untreated	1,3	0,4	1,7
70,6		APH	1,5	1,0	2,5

Figure S4 A. MMC treatment induces FANCD2 spots and chromosome missegregation. MRC5 cells were exposed to 25 ng/ml MMC for 24h and then fixed and immunostained for FANCD2 (red), BLM (green) and DNA (blue). Note the increase of FANCD2 spots on mitotic chromosomes and the BLM bridges connecting FANCD2-marked sites on missegregating chromosomes. **B.** BLM and PICH co-localization on anaphase bridges. MRC5 and FA cells were treated with APH, and ana-telophase figures were scored for the presence of PICH and BLM positive bridges. Examples of MRC5 (upper panel) and FA (bottom) ana-telophase figures immunostained for BLM (left panels, green in the merge) and PICH (middle panels, red in the merge). Note the lack of BLM and PICH co-staining in the APH-treated FA cell. **C.** Examples of Hec1 positive (upper panels) and Hec1 negative (lower panels) BLM stained bridges. Arrows indicate the Hec1 signals at the tips of the BLM bridge. **D.** The frequency of Hec1 positive and negative BLM or PICH stained bridges per anaphase in untreated or APH-treated FANC proficient and deficient cells. The number of anaphases scored is reported in parenthesis. **E.** The same as in **D,** but in this case the frequency of bridges per BLM or PICH positive anaphase was calculated.

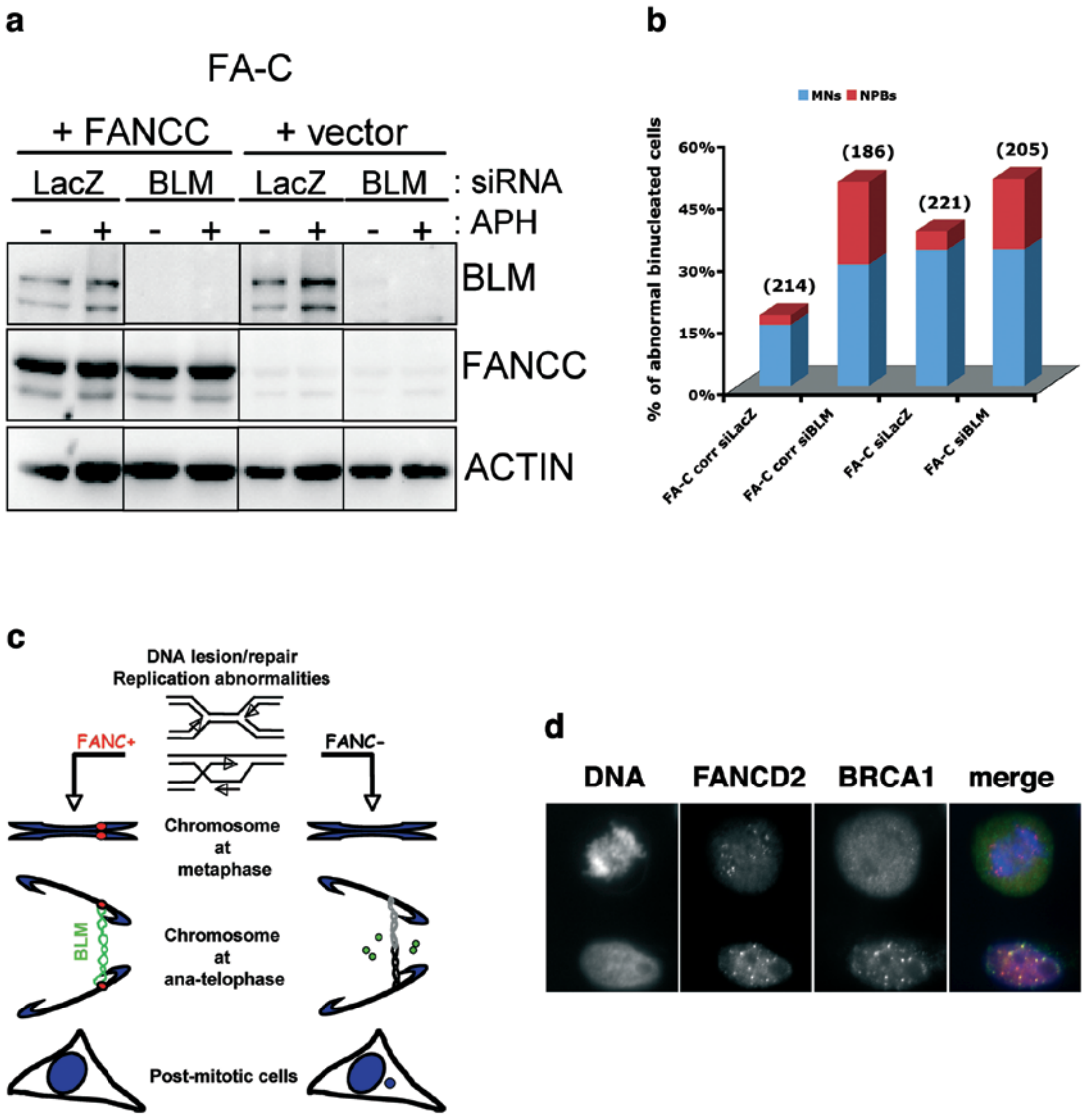

Figure S5 Epistasis analysis of BLM and FANC pathway associated mitotic phenotypes: BLM function was down-regulated by RNA interference in FA-C corrected (+FANCC) and empty vector transduced (+vector) cells. **A.** A Western blot showing effective knock-down of BLM protein (siBLM2 oligo duplex is shown in this blot). Recognition of two bands by BLM antibody has been described (Neff NF et al., Mol Biol Cell, 1999). **B.** Percentage of micronuclei (MNs) and nucleoplasmic bridges (NPBs) in binucleated FA-C corrected or deficient APH-treated cells transfected with the indicated oligo siRNA. Number in parenthesis represents BN cells scored. **C.** A model for the role of FANC pathway during mitosis. Following replication stress, abnormal DNA replication or recombination intermediates are generated. In normal cells, FANC pathway is activated and monoubiquitylated FANCD2 localizes at the level of aberrant chromatin structures on mitotic chromosomes. The presence of activated FANCD2 on these sites could help targeted localization of the BLM helicase at anaphase and resolution of concatenated structures preventing chromosome loss or breakage. In the absence of an intact FANC pathway intertwined chromatid sites are not resolved resulting in micronucleation. **D.** BRCA1 does not co-localize with FANCD2 on mitotic chromosomes. APH-treated MRC5 cells were immunostained for FANCD2 (red) and BRCA1 (green). FANCD2 and BRCA1 co-localize in interphase nuclear foci, whereby mitotic cells display FANCD2 spots on the chromosomes and a diffuse staining of BRCA1.

nature cell biology

Deficiency of MIP/MTMR14 phosphatase induces a muscle disorder by disrupting Ca^{2+} homeostasis

Jinhua Shen[1,6], Wen-Mei Yu[1,6], Marco Brotto[2,6], Joseph A. Scherman[3], Caiying Guo[4], Christopher Stoddard[4], Thomas M. Nosek[5], Héctor H. Valdivia[3] and Cheng-Kui Qu[1,7]

The intracellular Ca^{2+} concentration ($[Ca^{2+}]_i$) in skeletal muscles must be rapidly regulated during the excitation-contraction-relaxation process[1]. However, the signalling components involved in such rapid Ca^{2+} movement are not fully understood. Here we report that mice deficient in the newly identified PtdInsP (phosphatidylinositol phosphate) phosphatase MIP/MTMR14 (muscle-specific inositol phosphatase) show muscle weakness and fatigue. Muscles isolated from *MIP/MTMR14*$^{-/-}$ mice produced less contractile force, had markedly prolonged relaxation and showed exacerbated fatigue relative to normal muscles. Further analyses revealed that MIP/MTMR14 deficiency resulted in spontaneous Ca^{2+} leakage from the internal store — the sarcoplasmic reticulum. This was attributed to decreased metabolism (dephosphorylation) and the subsequent accumulation of MIP/MTMR14 substrates, especially PtdIns(3,5)P_2 and PtdIns (3,4)P_2. Furthermore, we found that PtdIns(3,5)P_2 and PtdIns(3,4)P_2 bound to, and directly activated, the Ca^{2+} release channel (ryanodine receptor 1, RyR1) of the sarcoplasmic reticulum. These studies provide the first evidence that finely controlled PtdInsP levels in muscle cells are essential for maintaining Ca^{2+} homeostasis and muscle performance.

During a systematic genome-wide survey for tyrosine and dual specificity phosphatases (Supplementary Information, Methods), we discovered a new phosphatase by hidden Markov database mining using the conserved catalytic motif (V/I)(V/I)HCXXGXXR(T/S) as the bait sequence. We identified both human (NCBI accession number BC035690) and mouse (NCBI accession number BC018294) homologues, which had a 90% amino-acid sequence homology (Supplementary Information, Fig. S1). Northern blotting analysis showed that this phosphatase is predominantly expressed in skeletal and heart muscle (Fig. 1a). Immunostaining indicated that it is primarily localized in the cytoplasm (data not shown). To verify its phosphatase property, we generated a glutathione *S*-transferase (GST) fusion protein and tested its catalytic activity using p-nitrophenyl phosphate (pNPP), a widely used non-specific substrate for tyrosine and dual specificity phosphatases. This new phosphatase did not significantly hydrolyze pNPP (Fig. 1b). Instead, it dephosphorylated a variety of PtdInsPs, especially PtdIns(3,5)P_2 (Fig. 1c), similarly to PTEN (phosphatase and tensin homologue) and MTMR (myotubularin and myopathy related) phosphatases, which also favour PtdInsP substrates, despite containing tyrosine phosphatase domains[2]. As this new phosphatase is mainly expressed in skeletal and heart muscle, we named it MIP (muscle-specific inositol phosphatase). While our gene-knockout work on *MIP/MTMR14* was continuing, another group also identified this phosphatase (NCBI accession number FLJ20133) in their comprehensive collection of tyrosine phosphatases from the human genome. They listed it as the fourteenth member of the MTMR family (MTMR14) based on the homology of its catalytic motif to myotubularin[3]. More recently, inactivating mutations in this phosphatase were identified in two cases of human autosomal centronuclear myopathy[4]. However, it has not yet been determined whether these mutations have a causal role in this disease.

To characterize the physiological function of MIP, we generated MIP-deficient mice through gene targeting (Supplementary Information, Fig. S2). *MIP*$^{-/-}$ mice were born at the Mendelian ratio and showed no obvious deficiencies during their first 12 months. It seems that heart development and basal functions of *MIP*$^{-/-}$ mice under resting conditions were not significantly affected (Supplementary Information, Tables S1, S2). Interestingly, animal behaviour tests revealed a decreased motor function in *MIP*$^{-/-}$ mice (Supplementary Information, Fig. S3). We reasoned that a muscle-specific phenotype might manifest itself more evidently during or after a stress response. Thus, untrained 16–24-week-old female wild-type and *MIP*$^{-/-}$ mice were run in a rodent treadmill until exhausted according to a protocol reported previously[5]. The running time of the knockout

[1]Department of Medicine, Center for Stem Cell and Regenerative Medicine, Case Comprehensive Cancer Center, Case Western Reserve University, Cleveland, OH 44106, USA. [2]Schools of Nursing and Medicine, University of Missouri, Kansas City, MO 64108, USA. [3]Department of Physiology, University of Wisconsin Medical School, Madison, WI 53706, USA. [4]Gene Targeting and Transgenic Facility, University of Connecticut Health Center, Farmington, CT 06030, USA. [5]Department of Physiology and Biophysics, Case Western Reserve University, Cleveland, OH 44106, USA.
[6]These authors contributed equally to this work.
[7]Correspondence should be addressed to: C.K.Q. (e-mail: cxq6@case.edu)

Received 10 October 2008; accepted 9 March 2009; published online 24 May 2009; DOI: 10.1038/ncb1884

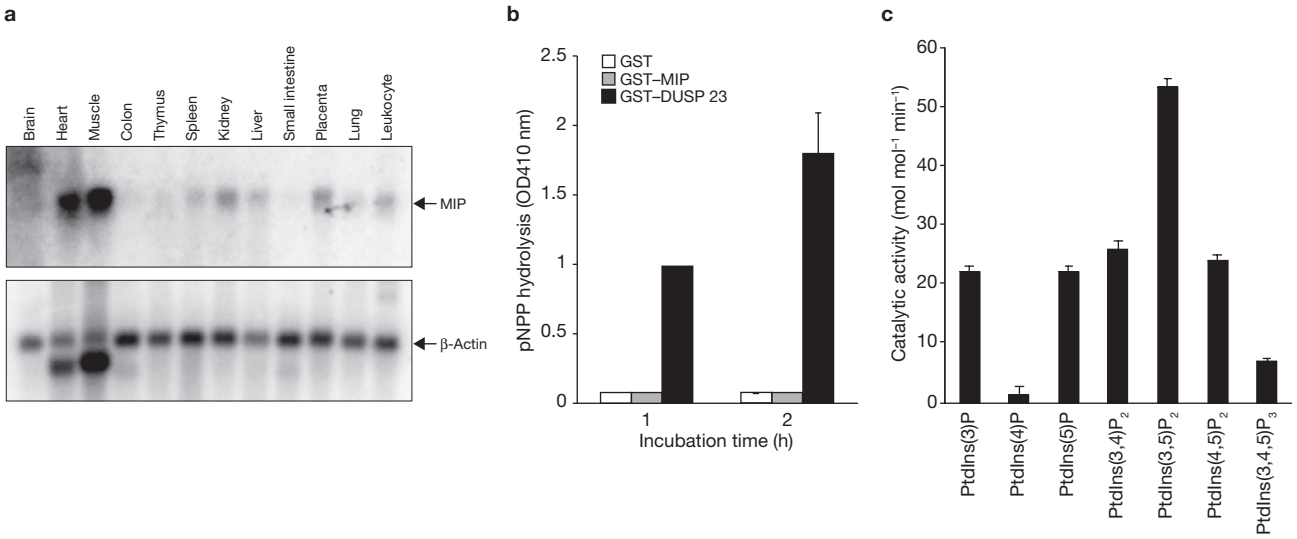

Figure 1 Characterization of human MIP. (**a**) A human tissue RNA blot (Clontech) was hybridized with a dCTP (α-^{32}P-deoxycytidine triphosphate)-labelled human MIP cDNA probe according to the standard protocol. The blot was then stripped and re-probed with a β-actin-positive control probe to monitor RNA loading. See Supplementary Information, Fig. S6 for full scans. (**b**) Purified GST–MIP fusion protein (1 μM) or GST alone protein (1 μM) was incubated with pNPP as described in Supplementary Information, Methods. The reaction was stopped with NaOH (0.1 M) and pNPP hydrolysis was determined by measuring absorbance at 410 nm (OD 410 nm). Dual specificity phosphatase 23 (GST-DUSP 23) was included as the positive control. (**c**) GST–MIP (1 μg) was tested for its dephosphorylating activity using the indicated PtdInsPs (di-C8, an eight carbon-long fatty acid on a glycerol backbone; Echelon Biosciences Inc.) as substrates. In **b** and **c**, three independent experiments were performed and similar results were obtained in each, data are mean ± s.d. of triplicates from one experiment.

mice was considerably decreased compared to that of the wild-type mice (Fig. 2a). These strenuous-exercise results indicate that *MIP*$^{-/-}$ mice are prone to greater skeletal muscle fatigue. However, treadmill performance does not necessarily reflect intrinsic changes within the essential contractile features of intact skeletal muscles and may be related to other systemic changes. To directly measure muscle function, extensor digitorum longus (EDL, a fast-twitch muscle) was isolated from the animals used in the treadmill experiments 1–2 weeks after the fatigue tests and was assessed for contractility and fatigability characteristics. As shown in Fig. 2b, the force-generating capacity (magnitude of the maximal fused isometric tetanic contraction, T_{max}) of EDL muscles from the *MIP*$^{-/-}$ mice was reduced by ~60% compared with that of the control muscles. In addition, the relaxation profile of *MIP*$^{-/-}$ muscles was substantially prolonged. To further investigate the performance of isolated muscles, the *in vitro* intermittent fatigue of the muscles[6,7] was studied. When compared with wild-type controls, on exposure to repeated electrical stimulations the resting baseline force of MIP mutant muscles increased, the maximum tetanic force quickly decreased and the muscles became non-responsive to subsequent stimulations (Fig. 2c).

To systematically compare fatigability and fatigue recovery in wild-type and *MIP*$^{-/-}$ muscles, we tested the effects of *in vitro* fatigue stimulation on slow-twitch, fatigue-resistant soleus muscle. We found that soleus muscles from *MIP*$^{-/-}$ mice fatigued to a greater extent and recovered significantly less than wild-type muscles (Fig. 2d, e). In addition, the kinetics of single tetanic contractions were altered in *MIP*$^{-/-}$ muscles and the plateau phase of the contraction was not well maintained (Fig. 2f). We next determined T_{max} of soleus muscles from *MIP*$^{-/-}$ mice and found that it was reduced by ~15% from that of wild-type muscles (Fig. 2g). Finally, the normalized force versus frequency relationship was shifted to the right in *MIP*$^{-/-}$ muscles (Fig. 2g), that is, at any given frequency of stimulation less force was generated. These results, obtained from isolated intact muscles, reaffirmed that the contractility and relaxation defects of *MIP*$^{-/-}$ muscles are muscle-cell autonomous. Remarkably, the muscle phenotypes appear to be exacerbated in aged mutant mice. About 30% of *MIP*$^{-/-}$ mice older than 18 months displayed accelerated muscle wasting compared with wild-type littermates (Fig. 2h).

The poor performance of *MIP*$^{-/-}$ muscles may indicate a defect in the regulation of $[Ca^{2+}]_i$, because rapid cycling of $[Ca^{2+}]_i$ is critical for force production, relaxation and recovery from fatigue[1]. As $[Ca^{2+}]_i$ control in muscle cells primarily takes place in a highly specialized junctional structure (triad junction) that is formed from the transverse tubule invagination of the plasma membrane and the terminal cisternae of the sarcoplasmic reticulum[8], we surveyed the morphology of this anatomic structure in mutant muscle cells. Electron microscopic examination revealed that the terminal cisternae of sarcoplasmic reticulum were slightly swollen (Fig. 3a). Ultrastructures of mutant cells otherwise seemed normal.

To functionally test whether *MIP*$^{-/-}$ muscle cells might have impaired Ca^{2+} signalling, we prepared primary myotubes and assessed $[Ca^{2+}]_i$ by the ratiometric fluorescence technique. The basal fluorescence ratio (the ratio of Fura-2 fluorescence at excitation wavelength 340 nm to that at 380 nm, F340/F380) in *MIP*$^{-/-}$ myotubes was higher than that in wild-type cells (Fig. 3b, c), indicating elevated resting $[Ca^{2+}]_i$. We changed the extracellular buffer (ECB) from one that was Ca^{2+}-containing (1.5 mM) to one that was Ca^{2+}-free and added caffeine and ryanodine (these induce sustained opening of the RyR1 channel; Fig. 3b)[9,10] or thapsigargin (a potent inhibitor of the sarcoplasmic or endoplasmic reticulum Ca^{2+}-ATPase pump), which inhibits the reuptake of Ca^{2+} into the sarcoplasmic reticulum[11] (Fig. 3c). This resulted in a rapid and transient elevation of $[Ca^{2+}]_i$ before loss of Ca^{2+} from the myotubes. Under these conditions, the magnitude of the initial transient $[Ca^{2+}]_i$ was reduced in *MIP*$^{-/-}$ cells compared with that of wild-type cells (Fig. 3b, c), suggesting a decreased Ca^{2+} content in the mutant sarcoplasmic reticulum. Moreover, the duration of the decaying phase was markedly increased in the mutant cells, indicating a prolonged release or a defective clearance of $[Ca^{2+}]_i$.

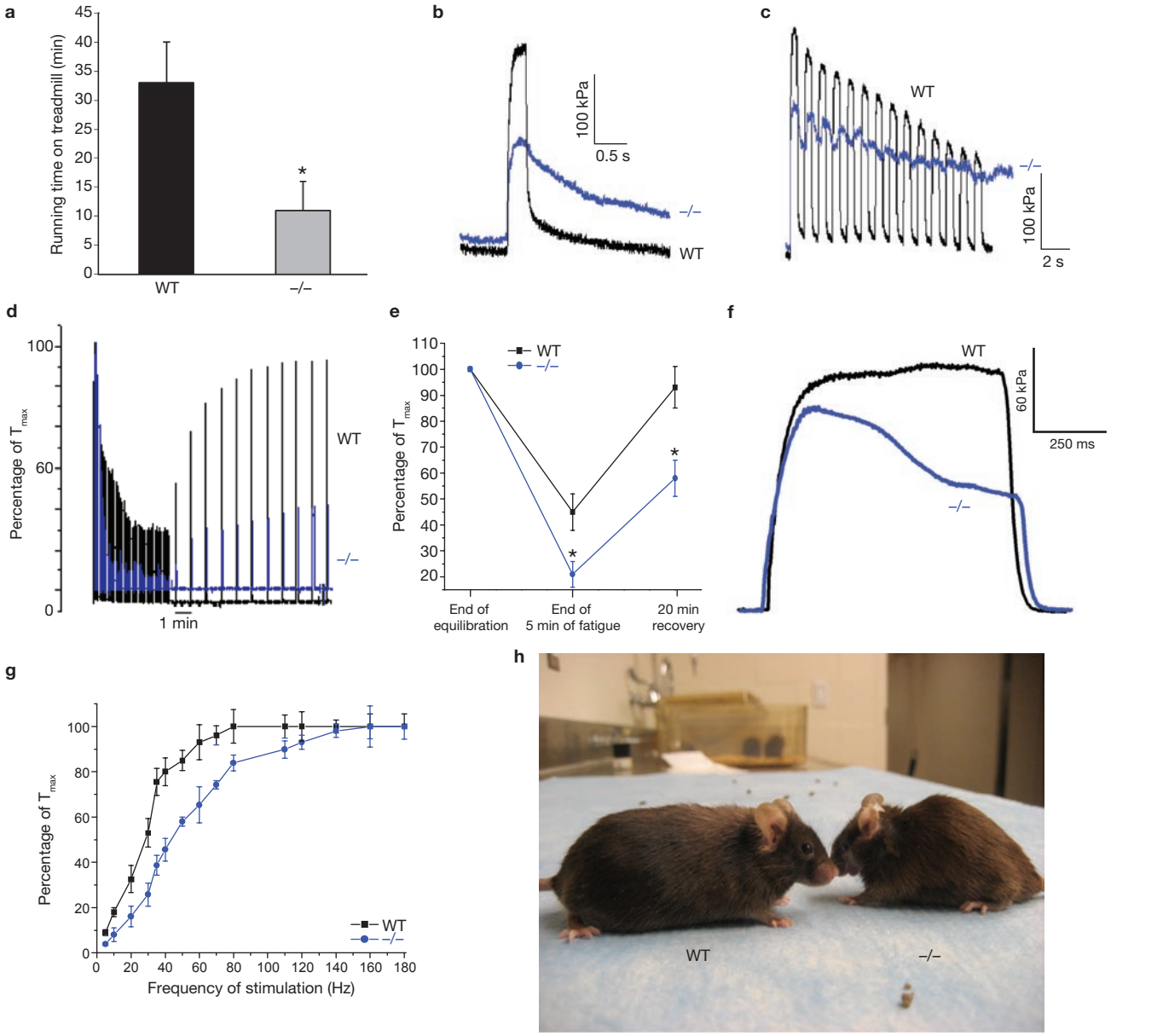

Figure 2 Decreased force production, prolonged relaxation and exacerbated fatigue in *MIP*$^{-/-}$ muscles. (**a**) 16–24-week-old female wild-type (WT) and *MIP*$^{-/-}$ (–/–) mice were run in a rodent treadmill until exhausted (see Supplementary Information, Methods). Three trials were conducted on each animal and the average running times were obtained. Data are mean ± s.e.m., $n = 7$, $^*P < 0.003$ as determined by one-way ANOVA followed by Tukey's post hoc test. (**b**) One to two weeks after the treadmill tests, EDL muscles isolated from wild-type and *MIP*$^{-/-}$ mice were subjected to contractility measurements. The cross-sectional area-normalized T_{max} (magnitude of the maximal fused isometric tetanic contraction) of *MIP*$^{-/-}$ ($n = 8$) and wild-type ($n = 12$) EDL muscles were 130 ± 28 kPa and 280 ± 32 kPa, respectively. Data are mean ± s.e.m., $P < 0.001$ as determined by Kruskal-Wallis one-way ANOVA on ranks test, representative results are shown. (**c**) EDL muscles isolated from wild-type and *MIP*$^{-/-}$ mice were subjected to *in vitro* muscle fatigue tests using repeated electrical stimulations ($n = 7$–8). (**d**) Soleus muscles dissected from wild-type and *MIP*$^{-/-}$ mice were subjected to 5 min of fatiguing stimulation (80 Hz, 500 ms) followed by 10 min of fatigue recovery. Contractile forces were normalized to T_{max} (100%). (**e**) Summary data of the response of soleus muscles to fatiguing stimulation and recovery from fatigue. Data are mean ± s.e.m., $n = 8$, $^*P < 0.001$ as determined by one-way ANOVA followed by Tukey's post hoc test. (**f**) Kinetic profile of a single tetanic contraction in soleus muscles following stimulation with a tetanic stimulation train (80 Hz, 1000 ms). (**g**) Wild-type and *MIP*$^{-/-}$ soleus muscles were subjected to force-frequency relationship tests using stimulation frequencies in the range of 1–180 Hz. Data are mean ± s.e.m. from eight preparations, $P < 0.02$ as determined by one-way ANOVA followed by Tukey's post hoc test. T_{max} of *MIP*$^{-/-}$ soleus was reduced by ~15% from that of wild-type muscle (180 ± 22 kPa in wild-type versus 153 ± 18 kPa in *MIP*$^{-/-}$). (**h**) Of aged *MIP*$^{-/-}$ mice, 30% showed accelerated muscle wasting ($n = 10$). Images are of an 18-month-old wild-type mouse and a *MIP*$^{-/-}$ mouse with muscle wasting. The horizontal scale bar indicates time and the vertical scale bar, absolute force in **b**, **c** and **f**.

Store operated Ca^{2+} entry (SOCE), capacitative Ca^{2+} entry through store-operated Ca^{2+} channels on the plasma membrane after the depletion or decrease of Ca^{2+} from internal stores, is a universal mechanism that provides a direct way of refilling intracellular Ca^{2+} stores[12]. As *MIP*$^{-/-}$ muscles had lower levels of Ca^{2+} in their sarcoplasmic reticulum, we reasoned that a compromised SOCE could have contributed to their

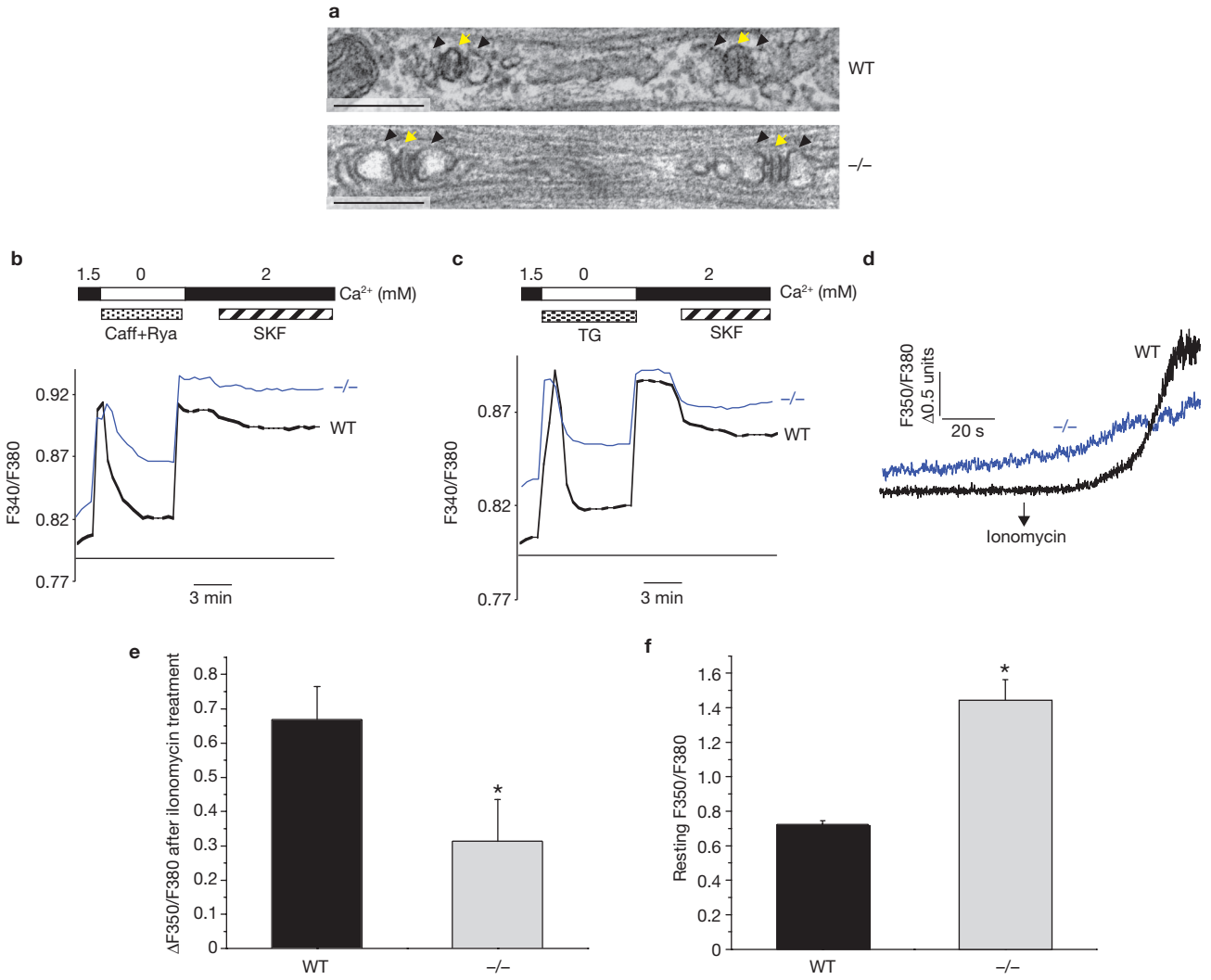

Figure 3 Compromised store-operated Ca^{2+} signalling in *MIP*$^{-/-}$ muscle cells. (**a**) Soleus muscles dissected from 4-week-old wild-type (WT) and *MIP*$^{-/-}$ (–/–) mice were processed for examination by transmission electron microscopy. Myofibers of the longitudinal ultrathin sections were photographed at a magnification of × 20,000. Yellow arrows indicate transverse tubules and black arrowheads indicate the terminal cisternae of the sarcoplasmic reticulum. Scale bars, 200 nm. (**b, c**) Myotubes were prepared (see Methods) and subjected to ratiometric Ca^{2+} analysis. Myotubes were loaded with Fura-2-AM (5 μM) in ECB containing $CaCl_2$ (1.5 mM). The ECB was replaced sequentially with Ca^{2+}-free ECB containing caffeine (Caff; 10 mM) and ryanodine (Rya; 1 μM; **b**) or thapsigargin (TG; 10 μM; **c**), Ca^{2+} (2 mM)-containing ECB or Ca^{2+} (2 mM)-containing ECB supplemented with SKF-96365 (50 μM, **b** or 100 μM, **c**). Kinetic changes in $[Ca^{2+}]_i$ were continuously monitored based on F340/F380 readings from all cells (4–5 cells) in the field. Note that the basal levels of $[Ca^{2+}]_i$ in *MIP*$^{-/-}$ cells were significantly increased; basal F340/F380 ratios of *MIP*$^{-/-}$ and wild-type cells were 0.848 ± 0.007 and 0.825 ± 0.009, respectively. Three independent experiments were performed and similar results were obtained in each. Data are mean ± s.d., $n = 26$ preparations, $P < 0.001$ as determined by Student's *t*-test. (**d**) Intact FDB muscle fibers from wild-type and *MIP*$^{-/-}$ mice were prepared (see Methods) before they were loaded with Fura 2, treated with ionomycin (5 μM; arrow indicates time of treatment) and their $[Ca^{2+}]_i$ monitored. The horizontal scale bar indicates time and the vertical, the relative change in the F350/F380 ratio. (**e**) Summary data of $[Ca^{2+}]_i$ response to ionomycin treatment. (**f**) Summary data of the basal levels of $[Ca^{2+}]_i$ in wild-type and *MIP*$^{-/-}$ FDB fibers. In **e** and **f**, data are mean ± s.e.m. from 12–13 preparations, $^*P < 0.03$ as determined by one-way ANOVA followed by Tukey's post hoc test.

reduced Ca^{2+} storage capacity. Consistently, our data showed that SOCE was decreased in the mutant myotubes, as shown by the reduced $[Ca^{2+}]_i$ response to the restoration of extracellular Ca^{2+} (2 mM) to the ECB medium (Fig. 3b, c). Subsequent treatment with SKF-96365 (a known blocker of the store-operated Ca^{2+} channel in the plasma membrane)[13], quickly decreased $[Ca^{2+}]_i$. By comparing $[Ca^{2+}]_i$ traces from wild-type and *MIP*$^{-/-}$ cells (Fig. 3b, c), it is clear that although SOCE is still functional in *MIP*$^{-/-}$ myotubes, this response is significantly blunted.

To further determine whether sarcoplasmic reticulum Ca^{2+} storage is reduced in *MIP*$^{-/-}$ adult muscles, we prepared single intact flexor digitorum brevis (FDB) fibers and exposed them to ionomycin (a Ca^{2+} ionophore), an experimental condition designed to assess total Ca^{2+} storage within the sarcoplasmic reticulum[14,15]. Ionomycin-mobilized Ca^{2+} was greatly decreased in *MIP*$^{-/-}$ muscle fibers (Fig. 3d, e). In addition, we found that the resting $[Ca^{2+}]_i$ was increased in *MIP*$^{-/-}$ fibers (Fig. 3d, f), consistent with earlier observations in myotubes (Fig. 3b, c). Thus, ablation of MIP causes diminished Ca^{2+} storage within the sarcoplasmic reticulum and an elevated $[Ca^{2+}]_i$, findings that are consistent with and supported by the muscle weakness and impairment of muscle relaxation in *MIP*$^{-/-}$ mice (Fig. 2b–d, f).

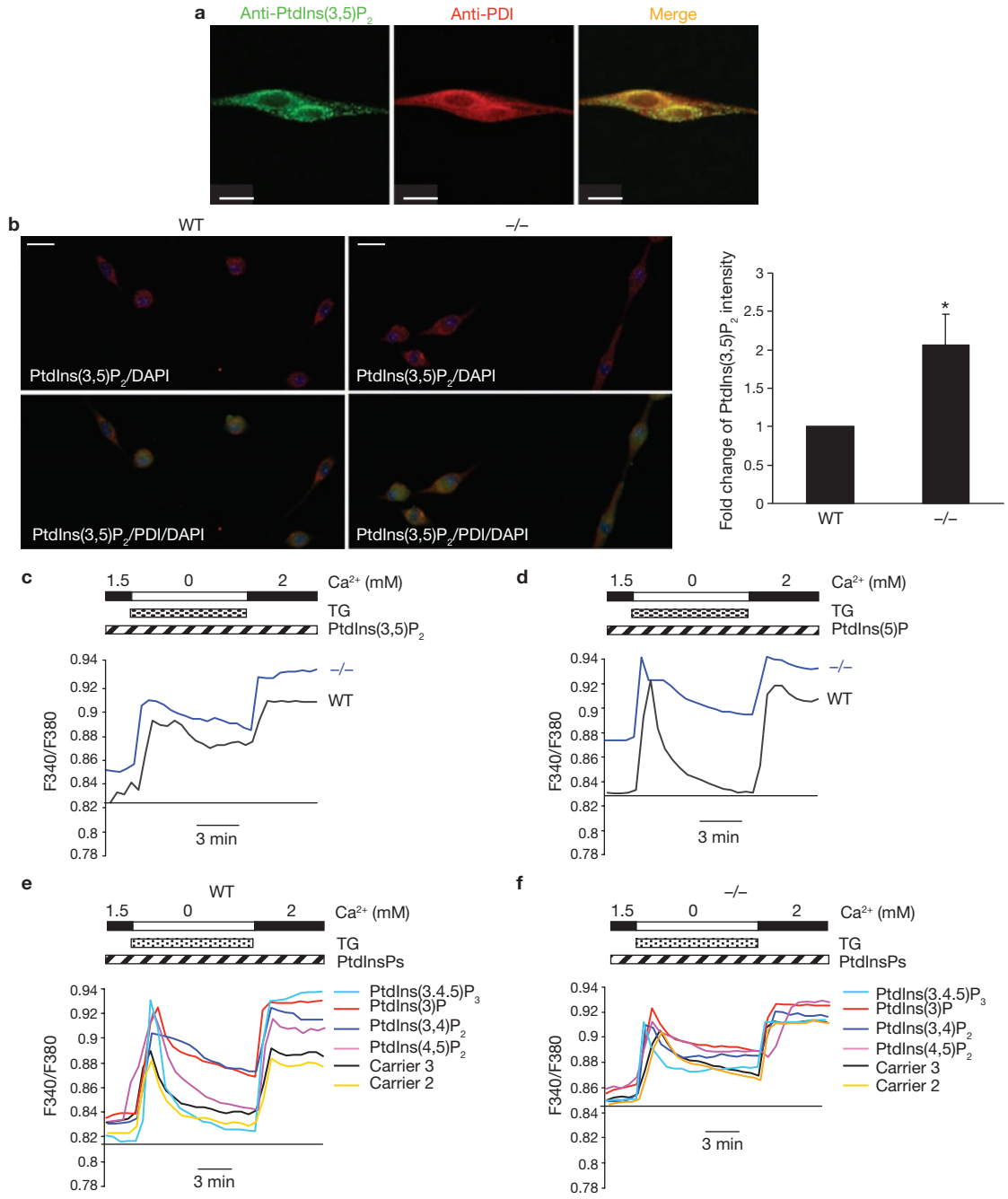

Figure 4 Perfusion of PtdIns(3,5)P_2, PtdIns(3,4)P_2 and PtdIns(3)P (to a lesser extent) into wild-type myotubes results in aberrant Ca^{2+} signalling. (**a**) Differentiated myotubes were double immunostained with anti-PtdIns(3,5)P_2 (Echelon Biosciences Inc.) and anti-PDI (Stressgen) antibodies. PtdIns(3,5)P_2 and PDI were visualized using FITC (fluorescein isothiocyanate)-conjugated anti-mouse and Cy5-conjugated anti-rabbit secondary antibodies (Molecular Probes), respectively. Images were analyzed with a Zeiss laser-scanning microscope LSM510 confocal imaging system. Scale bar, 18 μm. (**b**) Primary wild-type and *MIP*$^{-/-}$ myotubes were immunostained with anti-PtdIns(3,5)P_2 and anti-PDI antibodies followed by laser scanning cytometric analysis as described in Supplementary Information, Methods. The immunofluorescence intensity of PtdIns(3,5)P_2 in PDI-positive areas (sarcoplasmic reticulum) of *MIP*$^{-/-}$ cells was quantified and normalized against the wild-type control. Representative images are shown in the left panel and statistical results are shown in the right panel. Data are mean ± s.d. from three independent experiments, $*P < 0.05$ as determined by Student's *t*-test. Scale bars, 20 μm. (**c**–**f**) PtdIns(3,5)P_2 (di-C_{16}; **c**), PtdIns(5)P (di-C_{16}, a 16 carbon-long fatty acid on a glycerol backbone; **d**), and other PtdInsPs (di-C_{16}) as indicated (**e**, **f**) were delivered into myotubes at a concentration of 200 nM for 20 min, using Shuttle PIP kits following the manufacturer's protocol (Echelon Biosciences Inc.). Carrier 2 was used to deliver PtdIns(3,4)P_2, PtdIns(3,5)P_2, PtdIns(4,5)P_2 and PtdIns(3,4,5)P_3. Carrier 3 was used to deliver PtdIns(3)P and PtdIns(5)P. Ca^{2+} signalling was then analysed as described in Fig. 3c. Representative results of three experiments are shown.

MIP dephosphorylates multiple PtdInsPs (Fig. 1c), especially PtdIns(3,5)P_2, the most recently identified phosphatidylinositol-bisphosphate (PtdInsP_2) isomer whose subcellular localization and function in mammalian cells have not been well characterized[16,17]. To test whether the dysfunction of store-operated Ca^{2+} signalling in MIP-deficient cells is associated with decreased dephosphorylation or metabolism of PtdIns(3,5)P_2, we first

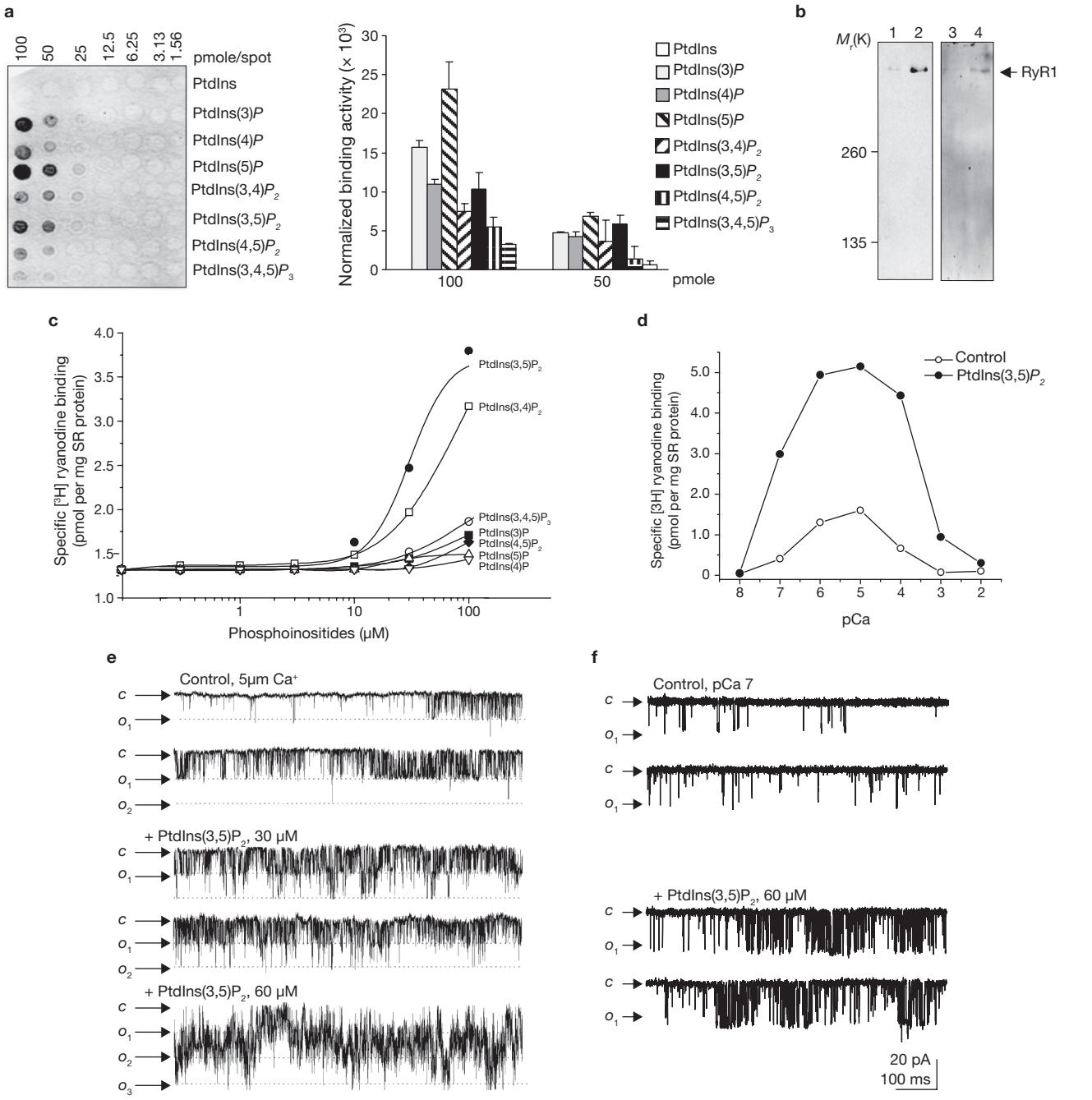

Figure 5 Activation of the skeletal muscle RyR1 Ca^{2+} channel by PtdInsPs. (**a**) PtdInsP array blots (Echelon Biosciences Inc.) were blocked with fatty acid-free BSA (3%) before incubation with RyR1 (2 μg ml^{-1}) purified from rabbit skeletal muscle sarcoplasmic reticulum microsomes. RyR1 bound to the blots was then detected with an anti-RyR1 antibody following standard immunoblotting procedures (left) . The fluorescence intensity of each spot of 100 and 50 pmol groups was quantified using a PhosphoImager (Amersham Biosciences) and normalized against the intensity of PtdIns spot of the same group (right). Data are mean ± s.d. from three independent experiments. (**b**) PtdIns(3,5)P_2-agarose beads (lane 2), control agarose beads (lane 1), anti-PtdIns(3,5)P_2 antibody (lane 4) and IgG control (lane 3) were incubated with lysates prepared from purified rabbit sarcoplasmic reticulum vesicles (425 μg). Proteins bound to the beads or the antibody were detected by immunoblotting with an anti-RyR1 antibody. (**c**) [^{3}H]ryanodine binding to muscle RyR1 in the presence of free Ca^{2+} (10 μM) and PtdIns(3,5)P_2 (di-C_8) or other PtdInsPs (di-C_8) at the indicated concentrations was determined as described (see Methods; SR, sarcoplasmic reticulum). (**d**) The effects of PtdIns(3,5)P_2 (150 μM) on Ca^{2+}-dependent binding of [^{3}H]ryanodine to RyR1 at various concentrations of free Ca^{2+} were determined. Nonspecific binding (~20% of total binding) was detected with ryanodine (20 μM) and subtracted. (**e**, **f**) The effects of PtdIns(3,5)P_2 on Ca^{2+}-release activity of a single RyR1 channel reconstituted in a planar lipid bilayer were determined in the presence of nominally free Ca^{2+} (5 μM; **e**) or pCa 7 (10^{-7} M; **f**). The activity of a reconstituted RyR1 channel was continuously recorded at -30 mV holding potential. Channel openings are presented as downward deflections. Results shown were obtained from the same channels ~1 min after addition of PtdIns(3,5)P_2 (30 or 60 μM) to the *cis* side (*c*, closed channel; *o*, opened channel). In **b**–**f** , results are representative of two to four experiments.

determined the subcellular localization of PI(3,5)P_2 in myotubes. Confocal microscopic examination after immunostaining showed that it resided in the sarcoplasmic reticulum, as confirmed by its co-localization with the endoplasmic reticulum-specific protein disulfide isomerase (PDI; Fig. 4a). We then assessed PtdIns(3,5)P_2 levels in *MIP*$^{-/-}$ sarcoplasmic reticulum by immunostaining myotubes with anti-PtdIns(3,5)P_2 and anti-PDI antibodies and performing laser scanning cytometric analyses[18,19]. As shown in Fig. 4b, immunofluorescence microscopy showed the intensity of PtdIns(3,5)P_2 in *MIP*$^{-/-}$ sarcoplasmic reticulum, defined by PDI-positive areas, to be twice that of wild-type reticulum, confirming excessive accumulation of PtdIns(3,5)P_2 in the mutant sarcoplasmic reticulum. We next dialyzed wild-type and *MIP*$^{-/-}$ myotubes with PtdIns(3,5)P_2 (200 nM) or its hydrolyzed product, PtdIns(5)P (200 nM), and monitored Ca^{2+} signalling. As illustrated in Fig. 4c, perfusion with PtdIns(3,5)P_2 resulted in dysfunction of the sarcoplasmic reticulum in wild-type myotubes, recapitulating the defects of Ca^{2+} signalling in *MIP*$^{-/-}$ cells (Fig. 3b, c). The decaying phase of the $[Ca^{2+}]_i$ transient triggered by thapsigargin was substantially prolonged by PtdIns(3,5)P_2 overloading. In contrast, addition of PtdIns(5)P did not rescue Ca^{2+} signalling in *MIP*$^{-/-}$ cells, nor were the Ca^{2+} profiles in wild-type cells changed (Fig. 4d). Furthermore, we tested other PtdInsPs that can be dephosphorylated by MIP. As shown in Fig. 4e, overloading of PtdIns(3,4)P_2 or PtdIns(3)P (to a lesser extent), but not PtdIns(4,5)P_2 or PtdIns(3,4,5)P_3, also prolonged the decaying phase of thapsigargin-triggered $[Ca^{2+}]_i$ transients in wild-type myotubes. Overloading of these PtdInsPs into *MIP*$^{-/-}$ cells either did not increase, or only slightly increased Ca^{2+} signalling defects (Fig. 4f). Together, these PtdInsP perfusion results support the idea that dysfunction of the Ca^{2+} store (sarcoplasmic reticulum) in MIP-deficient muscle cells is attributable to increased levels of PtdInsP substrates, especially PtdIns(3,5)P_2 and PtdIns(3,4)P_2.

To define the molecular mechanisms underlying the disrupted Ca^{2+} homeostasis in *MIP*$^{-/-}$ cells, we assessed SERCA ATPase activity, which is responsible for reuptake of Ca^{2+} into the sarcoplasmic reticulum, as reported previously[20,21]. To test for the contribution made by a potential functional change in membrane Na^+/Ca^{2+} exchangers to the phenotypes, we treated myotubes with KB-R9743, a selective inhibitor for the reverse mode of the Na^+/Ca^{2+} exchanger[22]. Neither SERCA ATPase nor the Na^+/Ca^{2+} exchanger appeared to be affected in *MIP*$^{-/-}$ cells (Supplementary Information, Fig. S4). Thus, these data led us to the hypothesis that Ca^{2+} stores in *MIP*$^{-/-}$ cells were spontaneously leaky. To test this hypothesis, we focused on potential functional changes in RyR1 (**A002108**), the skeletal muscle Ca^{2+} release channel on the sarcoplasmic reticulum[23,24]. First, we tested for potential physical interactions of MIP PtdInsP substrates with RyR1 protein, using PtdInsP array analyses. As shown in Fig. 5a, PtdIns(3)P, PtdIns(5)P and PtdIns(3,5)P_2 bound to purified RyR1. In addition, PtdIns(4)P and PtdIns(3,4,5)P_2 showed weak binding to RyR1. The direct physical interaction between PtdIns(3,5)P_2 and RyR1 was further verified by a PtdIns(3,5)P_2–agarose bead pulldown assay and anti-PtdIns(3,5)P_2 co-immunoprecipitation analysis (Fig. 5b). We then determined whether the interactions of PtdInsPs with RyR1 in purified sarcoplasmic reticulum microsomes produced functional effects. We used a [^{3}H]ryanodine binding assay to assess RyR1 channel activity, because [^{3}H]ryanodine binds with high affinity to the open conformational state of the channel[25,26]. The dose-response curve conducted at near-optimal (pCa 5, 10^{-5} M) free Ca^{2+} (Fig. 5c) showed that of all the PtdInsPs tested, PtdIns(3,5)P_2 was the most effective at activating RyR1, even though its physical interaction with the RyR1 protein was weaker than that of PtdIns(3)P and PtdIns(5)P (Fig. 5a). In addition, PtdIns(3,4)P_2 also activated RyR1, despite binding very weakly to it. The observation that the RyR1-binding affinity of PtdInsPs does not directly correlate with their effects on RyR1 channel activation suggests that some RyR1–PtdInsP interactions are functionally more productive than others, and that PtdInsPs each elicit distinct re-arrangements of the channel protein that have differing repercussions on channel gating. PtdInsP function in regulating ion channels and transporters is complicated. This is exemplified by PtdIns(4,5)P_2, the best characterized PtdInsP. The effects of PtdIns(4,5)P_2 on various channels and transporters includes activation, inhibition and insensitivity[27]. Clearly, further systemic studies are needed to determine the structure-activity relationship of PtdInsPs on RyR1 channel function.

We next produced Ca^{2+}-dependent [^{3}H]ryanodine binding curves to determine whether PtdIns(3,5)P_2 activates RyR1 at a free Ca^{2+} level comparable with that found in myofibers at rest (pCa 7) or during contraction (pCa 6–5). The Ca^{2+}-dependence of [^{3}H]ryanodine binding to RyR1 has been well established; in the range of pCa 9 (10^{-9} M) to pCa 5 (10^{-5} M), Ca^{2+} has an activating effect and increases [^{3}H]ryanodine binding to RyR1, whereas in the range of pCa 4 to pCa 2, Ca^{2+} has an inactivating effect. This dual effect of Ca^{2+} gives rise to a characteristic bell-shaped curve (Fig. 5d), which is similar to the relationship between Ca^{2+} and the probability of single RyR1 channels being open (P_o)[25,26]. In the presence of PtdIns(3,5)P_2, the binding curve maintained the same bell shape; however, the absolute binding values were dramatically increased, especially between pCa 7 and pCa 4. These results strongly suggest that partial Ca^{2+} depletion in the sarcoplasmic reticulum of *MIP*$^{-/-}$ muscle cells may be caused by direct activation of the RyR1 Ca^{2+} release channel by accumulated MIP PtdInsP substrates.

Finally, we directly tested the functional significance of the interaction between PtdIns(3,5)P_2 and RyR1. PtdIns(3,5)P_2 was added to RyR1 reconstituted lipid bilayers. A nominally free Ca^{2+} solution (~5 μM of contaminant Ca^{2+}) in the *cis* (cytosolic) side served to activate RyR1 (Fig. 5e). Before addition of PtdIns(3,5)P_2, the P_o of the RyR1 channel multiplied by the number of channels in the recording (NP_o), was low (1.15 ± 0.3, n = 3). Addition of PtdIns(3,5)P_2 (30 and 60 μM) induced a significant increase in open events, NP_o to 1.92 ± 0.4 and 2.6 ± 0.6 (n = 3), respectively (Fig. 5e; Supplementary Information, Fig. S5a). The effect of PtdIns(3,5)P_2 on the RyR1 channel was even more dramatic at a low concentration of free Ca^{2+} (pCa7; Fig. 5f), suggesting an enhancement of Ca^{2+} leakage and Ca^{2+}-induced Ca^{2+} release (CICR) activities by PtdIns(3,5)P2. The basal activity of the RyR1 channel was minimal under this condition (P_o = 0.08 ± 0.03, n = 3; Fig. 5f; Supplementary Information, Fig. S5b), but increased to P_o = 0.28 ± 0.04 and 0.51 ± 0.11 (n = 3) immediately after addition of 30 and 60 μM PtdIns(3,5)P_2, respectively (n = 3). Unitary conductance (~700 pS) remained unchanged after addition of PtdIns(3,5)P_2. These electrophysiological analyses demonstrate that PtdIns(3,5)P_2 binds to RyR1 and directly modifies channel activity at contracting (pCa 5) and resting (pCa 7) levels of Ca^{2+}, suggesting that the enhanced CICR and increased Ca^{2+} leakage observed in *MIP*$^{-/-}$ cells may be due, at least in part, to the increased PtdIns(3,5)P_2 levels resulting from MIP absence.

In summary, our studies provide the first evidence that finely controlled PtdInsP levels in the sarcoplasmic reticulum membrane, and possibly the sarcolemmal membrane, are critical for the proper function of the sarcoplasmic reticulum in Ca^{2+} storage and in rapidly regulating intracellular Ca^{2+}. However, the mechanisms that regulate MIP activity and thus PtdInsP levels in normal skeletal muscle physiology remain to be

addressed. As PtdInsPs, especially PtdIns(3,5)P_2, are also the major substrates of other phosphatases of the MTMR family[2], dysregulated metabolism or dephosphorylation of these PtdInsPs may also be responsible for MTMR phosphatase-associated muscle disorders. Further exploration of the PtdInsP pathway involved in intracellular Ca^{2+} homeostasis may provide new therapeutic targets for these muscle diseases. □

METHODS

Methods and any associated references are available in the online version of the paper at http://www.nature.com/naturecellbiology/

Note: Supplementary Information is available on the Nature Cell Biology website.

ACKNOWLEDGEMENTS

We are grateful to D. Chess, M. Chandler, T. Stefan, J. Jacobberger, L. Brotto, N. Wiesleder and J. Ma for technical assistance and helpful discussions. Motor function tests were performed by the Case Western Reserve University Rodent Behavior Core. This work was supported by NIH grants (HL068212 and HL082670) to C.K.Q. and (HL55438) H.H.V., an American Heart Association grant (0535555N) to M.B. and a pilot grant from the Case Center for Transdisciplinary Research on Energetics and Cancer to T.M.N., C.K.Q. and M.B.

AUTHOR CONTRIBUTIONS

J.S., W.M.Y., M.B., J.A.S. and C.S. conducted the research and summarized the data, and C.K.Q., M.B., H.H.V., T.M.N. and C.G. designed the experiments and wrote the manuscript.

COMPETING FINANCIAL INTERESTS

The authors declare no competing financial interests.

Published online at http://www.nature.com/naturecellbiology/.
Reprints and permissions information is available online at http://npg.nature.com/reprintsandpermissions/.

1. MacLennan, D. H. Ca2+ signalling and muscle disease. *Eur. J. Biochem.* **267,** 5291–5297 (2000).
2. Wishart, M. J. & Dixon, J. E. PTEN and myotubularin phosphatases: from 3-phosphoinositide dephosphorylation to disease. *Trends Cell Biol.* **12,** 579–585 (2002).
3. Alonso, A. *et al.* Protein tyrosine phosphatases in the human genome. *Cell* **117,** 699–711 (2004).
4. Tosch, V. *et al.* A novel PtdIns3P and PtdIns(**3,** 5)P2 phosphatase with an inactivating variant in centronuclear myopathy. *Hum. Mol. Genet.* **15,** 3098–3106 (2006).
5. Zhao, X. *et al.* Enhanced resistance to fatigue and altered calcium handling properties of *sarcalumenin* knockout mice. *Physiol. Genomics* **23,** 72–78 (2005).
6. Nagaraj, *R.* Y. *et al.* Increased susceptibility to fatigue of slow- and fast-twitch muscles from mice lacking the *MG29* gene. *Physiol. Genomics* **4,** 43–49 (2000).
7. Nosek, T. M. *et al.* Functional properties of skeletal muscle from transgenic animals with upregulated heat shock protein 70. *Physiol. Genomics* **4,** 25–33 (2000).
8. Takeshima, H. *et al.* Excitation-contraction uncoupling and muscular degeneration in mice lacking functional skeletal muscle ryanodine-receptor gene. *Nature* **369,** 556–559 (1994).
9. Lai, F. A., Erickson, H. P., Rousseau, E., Liu, Q. Y. & Meissner, G. Purification and reconstitution of the calcium release channel from skeletal muscle. *Nature* **331,** 315–319 (1988).
10. Pan, Z. *et al.* Dysfunction of store-operated calcium channel in muscle cells lacking mg29. *Nature Cell Biol.* **4,** 379–383 (2002).
11. Thastrup, O., Cullen, P. J., Drobak, B. K., Hanley, M. R. & Dawson, A. P. Thapsigargin, a tumor promoter, discharges intracellular Ca2+ stores by specific inhibition of the endoplasmic reticulum Ca2(+)-ATPase. *Proc. Natl Acad. Sci. USA* **87,** 2466–2470 (1990).
12. Lewis, R. S. The molecular choreography of a store-operated calcium channel. *Nature* **446,** 284–287 (2007).
13. Merritt, J. E. *et al.* SKF 96365, a novel inhibitor of receptor-mediated calcium entry. *Biochem. J.* **271,** 515–522 (1990).
14. Bhogal, M. S. & Colyer, J. Depletion of sarcoplasmic reticulum calcium prompts phosphorylation of phospholamban to stimulate store refilling. *Ann. NY Acad. Sci.* **853,** 260–263 (1998).
15. Toth, A. *et al.* Quantitative assessment of [Ca2+]i levels in rat skeletal muscle *in vivo*. *Am. J. Physiol.* **275,** H1652–1662 (1998).
16. Michell, R. H., Heath, V. L., Lemmon, M. A. & Dove, S. K. Phosphatidylinositol 3, 5-bisphosphate: metabolism and cellular functions. *Trends Biochem. Sci.* **31,** 52–63 (2006).
17. Di Paolo, G. & De Camilli, P. Phosphoinositides in cell regulation and membrane dynamics. *Nature* **443,** 651–657 (2006).
18. Min., J. *et al.* Forward chemical genetic approach identifies new role for GAPDH in insulin signaling. *Nature Chem. Biol.* **3,** 55–59 (2007).
19. Niswender, K. D. *et al.* Immunocytochemical detection of phosphatidylinositol 3-kinase activation by insulin and leptin. *J. Histochem. Cytochem.* **51,** 275–283 (2003).
20. Ishii, T., Lemas, M. V. & Takeyasu, K. Na(+)-, ouabain-, Ca(2+)-, and thapsigargin-sensitive ATPase activity expressed in chimeras between the calcium and the sodium pump alpha subunits. *Proc. Natl Acad. Sci. USA* **91,** 6103–6107 (1994).
21. Bartolommei, G. *et al.* Clotrimazole inhibits the Ca2+-ATPase (SERCA) by interfering with Ca2+ binding and favoring the E2 conformation. *J. Biol. Chem.* **281,** 9547–9551 (2006).
22. Amran, M. S., Homma, N. & Hashimoto, K. Pharmacology of KB-R7943: a Na+-Ca2+ exchange inhibitor. *Cardiovasc. Drug Rev.* **21,** 255–276 (2003).
23. Treves, S., Jungbluth, H., Muntoni, F. & Zorzato, F. Congenital muscle disorders with cores: the ryanodine receptor calcium channel paradigm. *Curr. Opin. Pharmacol.* **8,** 319–326 (2008).
24. Benkusky, N. A., Farrell, E. F. & Valdivia, H. H. Ryanodine receptor channelopathies. *Biochem. Biophys. Res. Commun.* **322,** 1280–1285 (2004).
25. Zhu, X., Zamudio, F. Z., Olbinski, B. A., Possani, L. D. & Valdivia, H. H. Activation of skeletal ryanodine receptors by two novel scorpion toxins from Buthotus judaicus. *J. Biol. Chem.* **279,** 26588–26596 (2004).
26. Zhu, X., Ghanta, J., Walker, J. W., Allen, P. D. & Valdivia, H. H. The calmodulin binding region of the skeletal ryanodine receptor acts as a self-modulatory domain. *Cell Calcium* **35,** 165–177 (2004).
27. Hilgemann, D. W., Feng, S. & Nasuhoglu, C. The complex and intriguing lives of PIP2 with ion channels and transporters. *Sci. STKE* **2001,** RE19 (2001).

METHODS

Generation of *MIP*$^{-/-}$ mice. The *MIP* allele was targeted by homologous recombination. Exon 3, containing the start codon ATG, to exon 5 was replaced with a neomycin (Neo) cassette. The targeting vector was constructed using the recombineering technique. It was then electroporated into D1 mouse embryonic stem (ES) cells with a 129S6 × C57BL/6J hybrid background. G418-resistant ES cell clones were isolated and screened by PCR genotyping using the primers as shown in Supplementary Information, Fig. S2a. Two ES cell clones containing a correctly targeted *MIP* allele were used to generate chimaeric mice. Three germline transmitted chimaeric mice were obtained and used to cross C57BL6J mice to produce heterozygous (*MIP*$^{+/-}$) mice. *MIP*$^{+/-}$ mice were backcrossed with C57BL6J mice for three generations and the F4 generation of mice were used for studies. No differences in the two lines of mutant mice derived from the original two ES cell clones were detected.

Contractile properties of skeletal muscle. We tested the *in vitro* contractility properties of intact, anatomical muscles from the animals as described previously[5,28]. Wild-type and mutant EDL and soleus muscles were dissected intact and placed into Ca^{2+}-modified (2.5 mM) Ringer solution (142 mM NaCl, 5 mM KCl, 2.5 mM $CaCl_2$, 2 mM $MgCl_2$, 10 mM HEPES and 10 mM glucose at pH 7.4) bubbled with O_2 (100%). We compared the results with those obtained using a bicarbonate buffer system and did not observe any significant differences. After careful dissection, a pair of control and mutant intact muscles were mounted vertically onto 20-ml Radnotti glass chambers with built in platinum stimulating electrodes (Radnoti Products). One tendon of each muscle was attached to a force transducer and the other one to a stationary arm in preparation for *in vitro* fatiguing experiments. A Powerlab computer-interface program (AD Instruments) was used to control the electrical stimulation protocols and to record, digitize and store force output data. Field stimulation (squared-waves electrical currents of 500-msec duration, 300 mA using stimulation frequencies in the range of ~1–180 Hz) was accomplished with the platinum electrodes running on both sides of the muscles. Wild-type and *MIP*$^{-/-}$ muscles were mounted in parallel and their resting lengths were adjusted to produce maximal isometric twitch force. The muscles were then used to obtain the relationship between force and frequency, and the stimulating frequencies that produced T_{max} were determined. Frequencies that produced T_{max} were then used for the remainder of the protocols. After 20 min of equilibration (1-min intervals, 0.83% duty cycle) at a high frequency, muscles were exposed to a fatiguing stimulation protocol (1-sec intervals, 50% duty cycle) using the same frequency of stimulation for 5 min. The fatiguing protocol used in this study was modified from our previous protocol[6,7]. Force output data during fatigue were normalized to T_{max} before the onset of fatigue and analyzed by Origin software (OriginLab Corp.). T_{max} was normalized to the cross-sectional area of each muscle and is reported in kPa. All experiments were conducted at room temperature (23 ± 2 °C).

Ca^{2+} fluorometry. Primary myoblasts were isolated from hind-limb muscles of wild-type and *MIP*$^{-/-}$ neonates, grown and differentiated into myotubes as described previously[29]. Three independent isolates of each genotype were analyzed. Spatial and temporal distribution of $[Ca^{2+}]_i$ in individual myotubes was determined as reported previously[10,30]. After 4–5 days of differentiation, myotubes derived from primary myoblasts were loaded with Fura-2-AM (5 μM) for 45 min at 25°C in ECB (130 mM NaCl, 5 mM KCl, 1.5 mM $CaCl_2$, 1 mM $MgCl_2$, 25 mM HEPES at pH 7.5, 1 mg ml^{-1} bovine serum albumin and 5 mM glucose). The buffer was replaced with fresh ECB and the incubation was continued for 45 min at 25 °C to permit de-esterification. A dual-wavelength spectrofluorometer (excitation at 340 nm and 380 nm) was used to determine the kinetic changes of $[Ca^{2+}]_i$, which is reflected by the average ratio of fluorescence emitted on excitation at 340 nm to that at 380 nm (F340/F380) of all cells (4-5 cells) in the field. Changes in $[Ca^{2+}]_i$ were measured for 8 min after exposure to thapsigargin (10 μM) or caffeine (10 mM) plus ryanodine (1 μM) in the Ca^{2+}-free balanced salt solution (ECB was deficient in Ca^{2+} and supplemented with 0.5 mM EGTA). The extracellular bath solution was then changed to ECB containing Ca^{2+} (2 mM) and the average ratio of F340/F380 was continuously monitored. In some cases, after 3 min the extracellular buffer was changed to ECB containing SKF-96365 (50 μM or 100 μM) and $[Ca^{2+}]_i$ was monitored for an additional 8 min.

For the determination of resting cytosolic Ca^{2+} and total sarcoplasmic reticulum Ca^{2+} content, intact FDB fibers directly dissected from adult mice were used. In brief, FDB fibers were isolated by enzymatic disassociation in type I collagenase (0.2%, Sigma-Aldrich). The mean FDB fiber size was 1 mm × 20 μM. The fibers were loaded with Fura-2 AM (10 μM) for 45 min at room temperature in Tyrode solution. A myosin inhibitor, N-benzyl-p-toluene sulphonamide (20 μM), was applied for 15 min to prevent motion artifacts from muscle contraction[31]. Fibers were also embedded into silicone grease to maintain their position in the culture dish[32]. The ratio of Fura-2 fluorescence at excitation wavelength 350 nm to that at 380 nm was measured on a PTI spectrofluorometer (Photon Technology International) to assess $[Ca^{2+}]_i$. Total sarcoplasmic reticulum Ca^{2+} storage was measured by the addition of ionomycin (5 μM) in the presence of $CaCl_2$ (2 mM) to the bath solution.

[^{3}H]ryanodine binding assay. [^{3}H]ryanodine binding to purified rabbit skeletal muscle sarcoplasmic reticulum was performed as described previously[25,26]. The incubation medium (0.2 M KCl, 40 mM Na-HEPES at pH 7.2, 7 nM [^{3}H] ryanodine, 1 mM EGTA) contained various concentrations of $CaCl_2$ as necessary to set the free Ca^{2+} to 10 nM–10 mM. Mouse skeletal muscle sarcoplasmic reticulum-enriched microsomes (60 μg) were added to the incubation medium together with PtdIns(3,5)P_2 (to the indicated concentrations). Samples (0.1 ml) were incubated at 37 °C for 90 min. Mathematical fitting of data was accomplished with the computer program Origin (version 7.0; Micro-cal Inc.).

Planar lipid bilayer technique. Purified rabbit skeletal muscle RyR1 protein was reconstituted into Muller-Rudin planar lipid bilayers as described previously[25,26]. Single channel data were collected at steady voltages (+35 mV, *cis* chamber grounded) for 2 min in symmetrical cesium methane-sulfonate (300 mM) and Na-HEPES (10 mM at pH 7.2). The recording solution contained ~ 5 μM free Ca^{2+} as assessed by a calibration curve, which was sufficient to activate the RyR1 channel. Various concentrations of PtdIns(3,5)P_2 were added to the *cis* chamber, which corresponded to the cytosolic side of the channel. Signals were digitized at 4 kHz and analyzed after filtering with a low-pass 8-pole Bessel filter at a sampling frequency of 1.5 kHz. Data acquisition and analyses were performed with Axon Instruments software and hardware (pClamp version 8.03; Digidata 200 AD/DA interface). The full- and non-conducting current values were obtained from Gaussian fits to the amplitude histograms, as described previously[24,25].

Accession codes. USCD-Nature Signaling Gateway (http://www.signaling-gateway.org): **A002108**.

28. Brotto, M. A., Nosek, T. M. & Kolbeck, R. C. Influence of ageing on the fatigability of isolated mouse skeletal muscles from mature and aged mice. *Exp. Physiol.* **87,** 77–82 (2002).
29. Frock, R. L. *et al.* Lamin A/C and emerin are critical for skeletal muscle satellite cell differentiation. *Genes Dev.* **20,** 486–500 (2006).
30. Shin, D. W. *et al.* A retrograde signal from calsequestrin for the regulation of store-operated Ca2+ entry in skeletal muscle. *J. Biol. Chem.* **278,** 3286–3292 (2003).
31. Cheung, A. *et al.* A small-molecule inhibitor of skeletal muscle myosin II. *Nature Cell Biol.* **4,** 83–88 (2002).
32. Jacquemond, V. Indo-1 fluorescence signals elicited by membrane depolarization in enzymatically isolated mouse skeletal muscle fibers. *Biophys. J.* **73,** 920–928 (1997).

nature cell biology

DOI: 10.1038/ncb1884

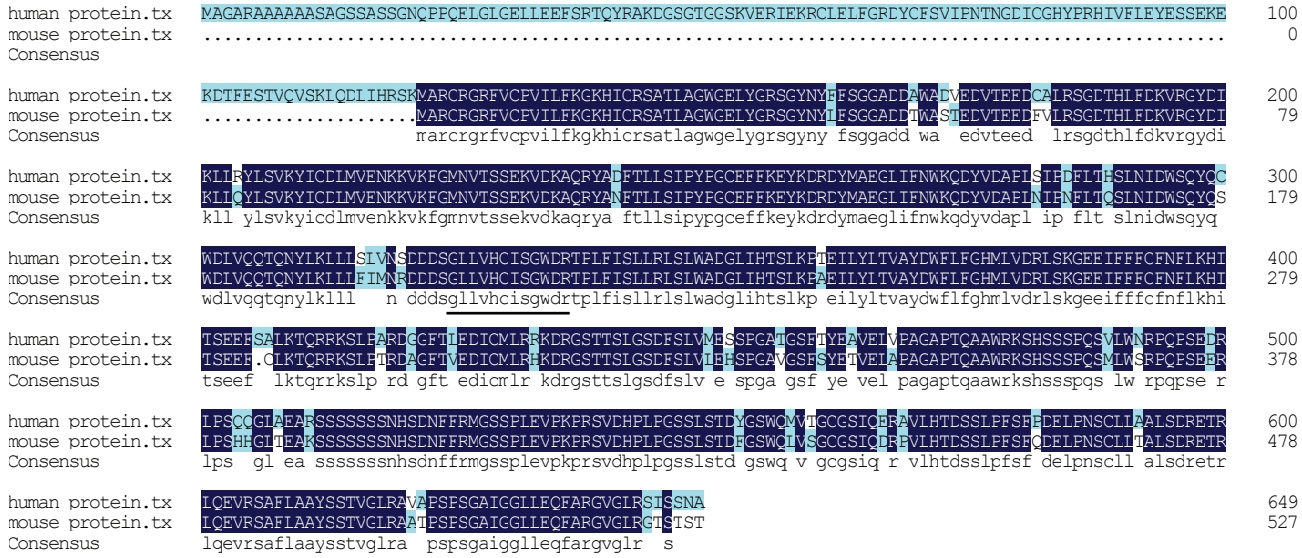

Figure S1 Homology between human and mouse MIP. Amino acid sequences of human and mouse MIP were compared. Shaded areas are consensus sequences. The underlined region is the catalytic site.

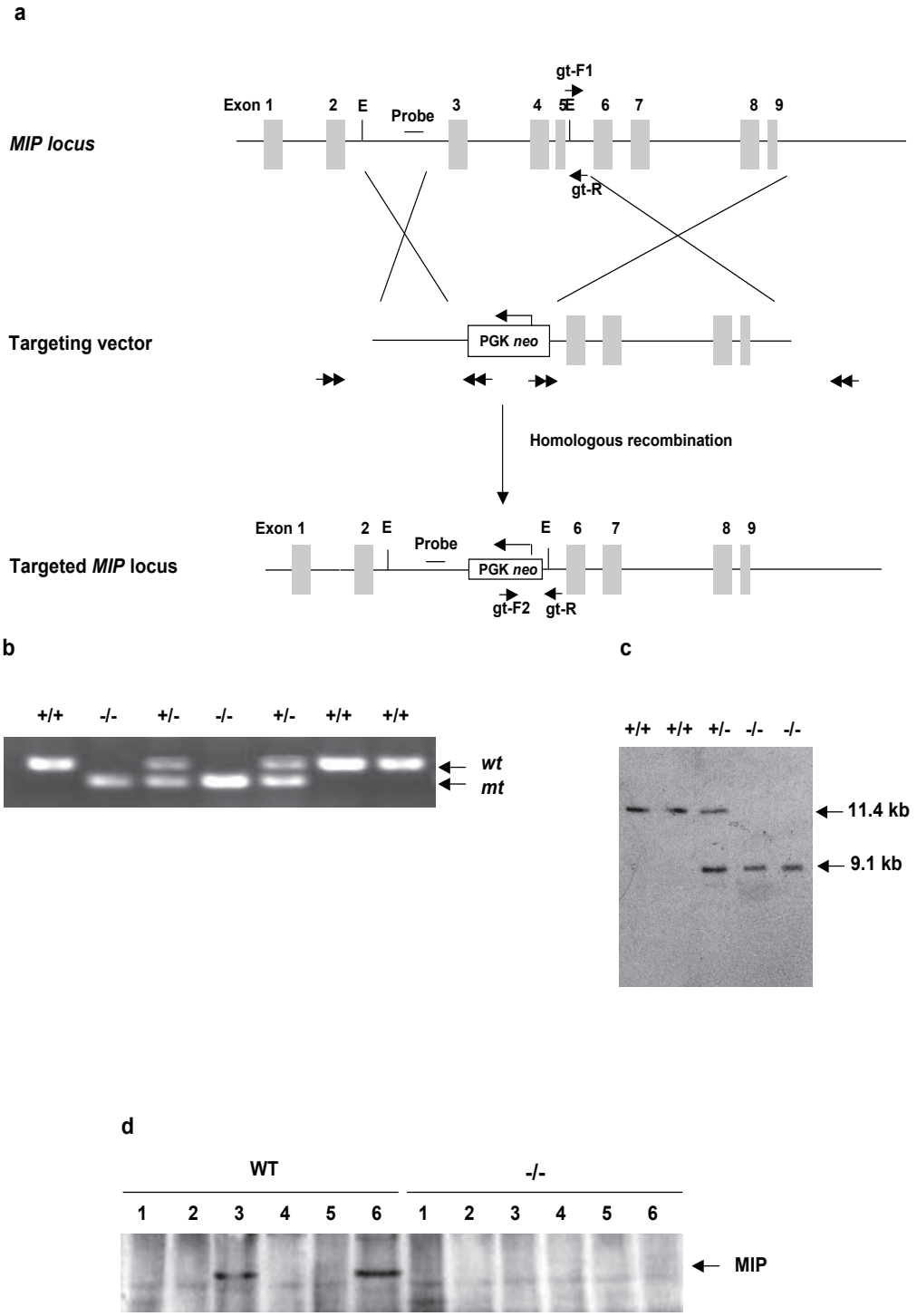

Figure S2 Generation of MIP knockout mice. (**a**) The gene targeting strategy. *Exon 3* containing the start codon ATG to *Exon* 5 was replaced with *Neo* by homologous recombination. PCR primers for ES cell screening are shown in double-head arrows. Genotyping primers are shown in single-head arrows. The probe used for Southern blotting and two flanking EcoRV sites (E) are also indicated. (**b**) PCR genotyping results of young pups produced from the crossing of $MIP^{+/-}$ mice. (**c**) Genomic DNA extracted from tissues from WT, $MIP^{+/-}$, and $MIP^{-/-}$ mice was digested with EcoRV and subjected to Southern blotting using the probe labeled with Digoxigenin-11-dUTP following standard procedures. The WT allele generated a 11.4 Kb band, whereas the targeted allele generated a 9.1 Kb band. (**d**) Tissue lysates prepared from WT and $MIP^{-/-}$ mice were examined for MIP expression by immunoprecipitation followed by immunoblotting with the polyclonal antibody raised in house. Samples in lanes 1, 2, 3, 4, 5, and 6 are liver, lung, heart, kidney, spleen, and skeletal muscle. A full scan of the image is shown in **Fig. S6**.

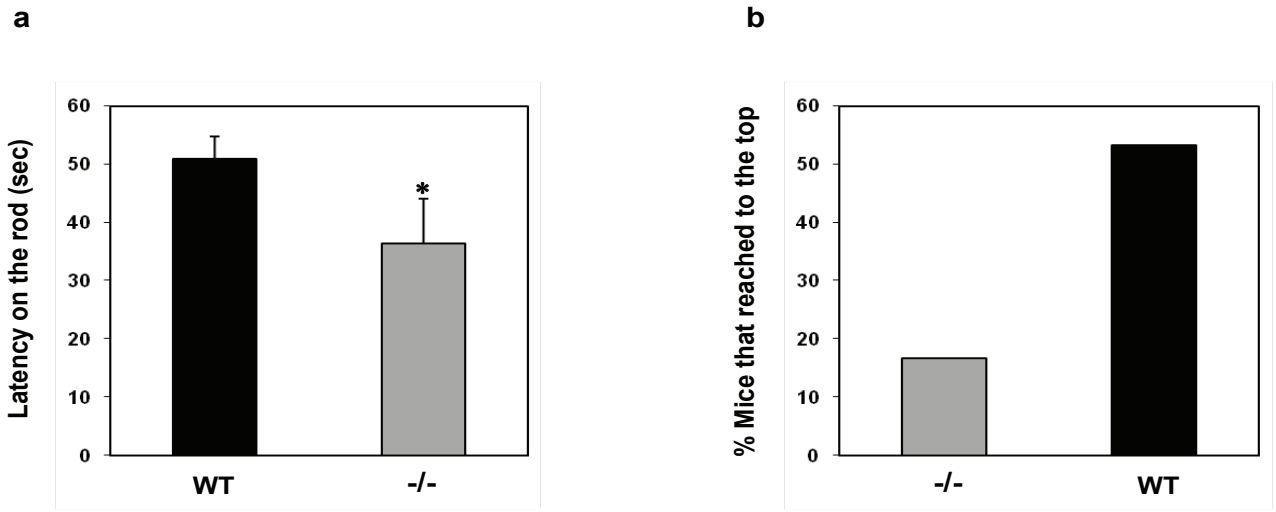

Figure S3 Decreased motor function of MIP knockout mice. Sixteen-week old female MIP$^{-/-}$ (n=9) and WT (n=15) littermates were subjected to rotarod (**a**) and inclined screen (90 degree) (**b**) tests in two independent experiments as described in Supplementary Information, Methods. The latency to fall off the rotarod was recorded. The scores from 3 trials were averaged for each animal (* indicates $p < 0.05$ by *t* test). In the inclined screen tests, the percentages of WT and mutant mice that could reach to the top of the inclined screen were determined.

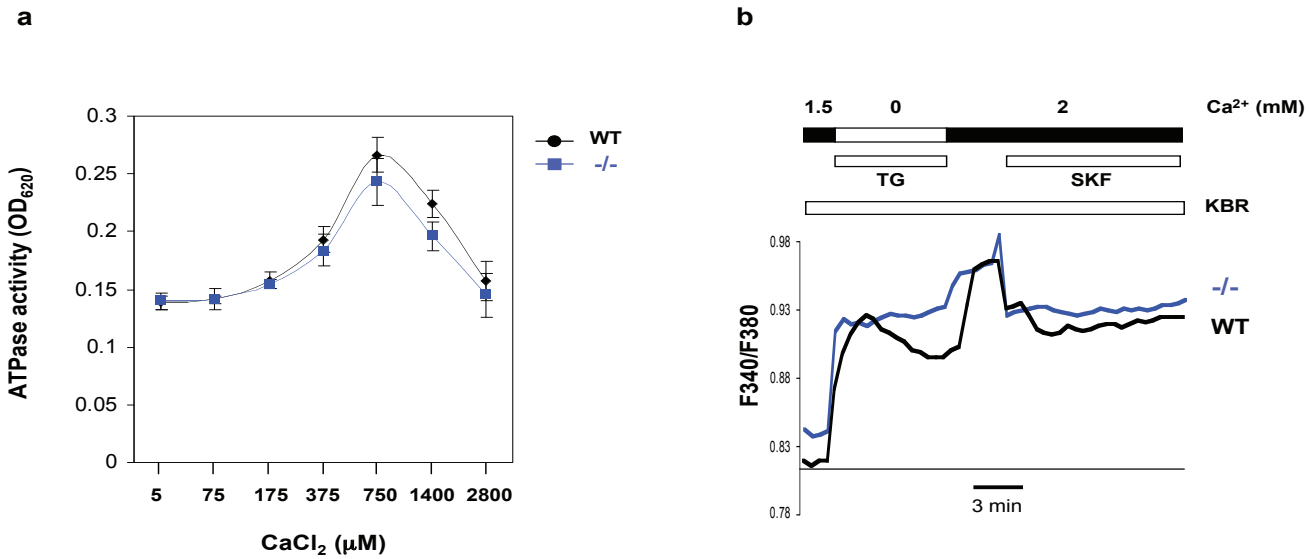

Figure S4 SERCA ATPase (Ca^{2+} pump) and the Na^{+}/Ca^{2+} exchanger functions are not affected in $MIP^{-/-}$ cells. (**a**) Ca^{2+}-dependent ATPase activities of SR microsomes purified from WT and $MIP^{-/-}$ skeletal muscles were determined in the presence of 1 mM EGTA, 2 μM Ca^{2+} ionophore, and various concentrations of $CaCl_2$ as described in Supplementary Information, Methods. Two independent experiments were performed and similar results were obtained in each. Results shown are mean±S.D. of triplicates from one experiment. Note that $MIP^{-/-}$ SR possessed almost identical Ca^{2+}-dependent ATPase activity as WT SR. (**b**) Myotubes were continuously treated with KB-R9743 (KBR, 10 μM), a selective inhibitor for Na^{+}/Ca^{2+} exchangers. Ca^{2+} signaling was then analyzed as described in **Fig. 3c**. Representative results of three experiments are shown. Note that in the presence of KBR, WT and $MIP^{-/-}$ myotubes still showed a large difference in Ca^{2+} handling — The basal level of $[Ca^{2+}]_i$ in $MIP^{-/-}$ cells was higher than that in WT cells and more prominently, the decaying phase of TG-triggered Ca^{2+} transient in $MIP^{-/-}$ cells was completely lost.

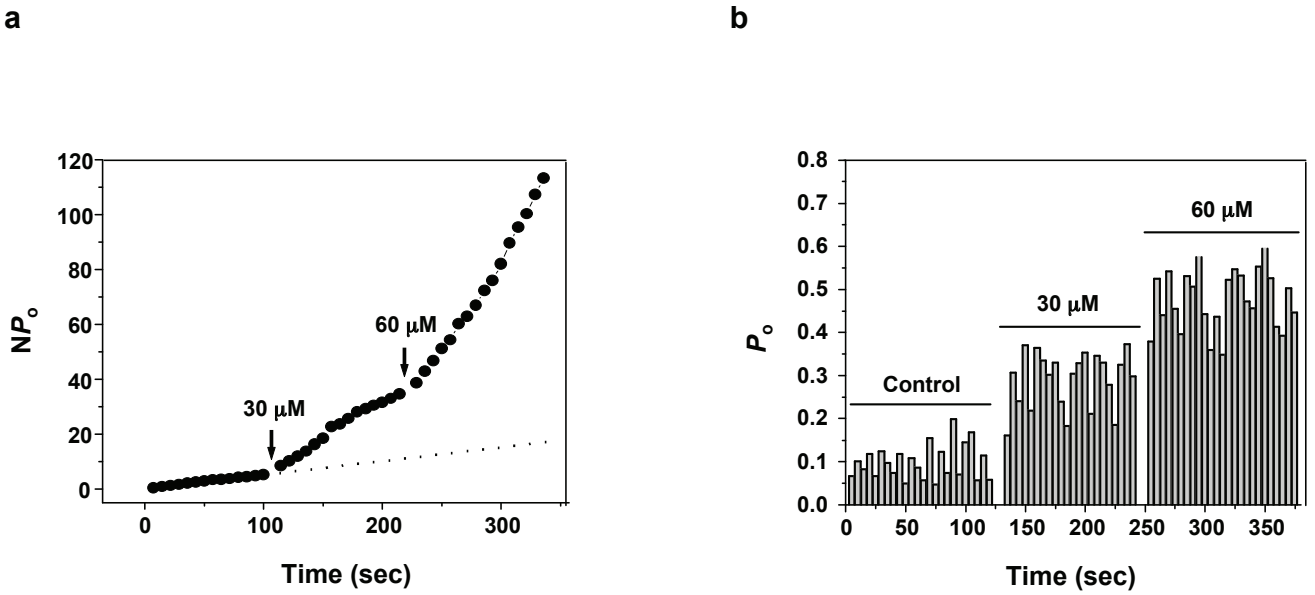

Figure S5 Plots of RyR1 channel activity before and after addition of PI(3,5)P_2 to the cytosolic side of the channel. (**a**) Effects of PI(3,5)P_2 on RyR1 channels activated by 5 μM *cis* (cytosolic) Ca^{2+}. NP_o (open probability of a single channel multiplied by the number of observable channels) of a 10-sec segment of activity was added to the NP_o of the next 10-sec segment to yield the cumulative plot. The dotted line represents the cumulative activity of a control channel in the absence of PI(3,5)P_2. (**b**) Effects of PI(3,5)P_2 on single RyR1 channel activated by 100 nM cytosolic Ca^{2+}. Bars represent the average P_o of RyR1 over a 5-sec segment of activity. The cumulative NP_o (**a**) and bar histogram (**b**) depict the time course of a single experiment, which was repeated 3 times for each condition. Average P_o's are given in the text.

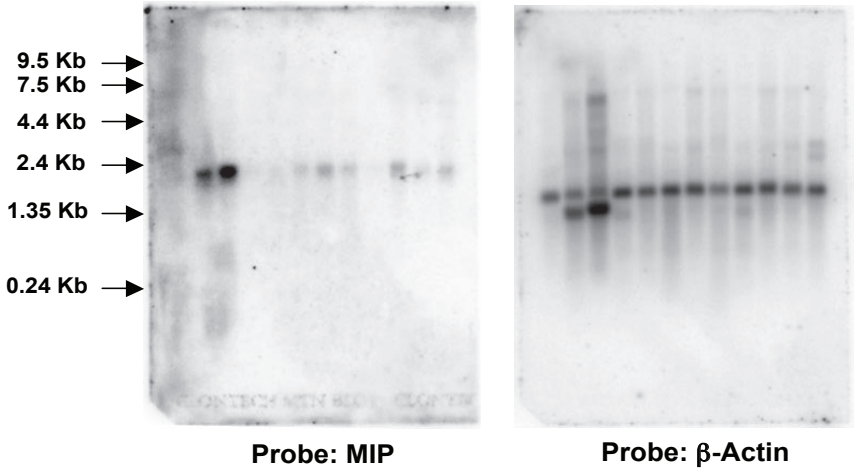

Figure 1a

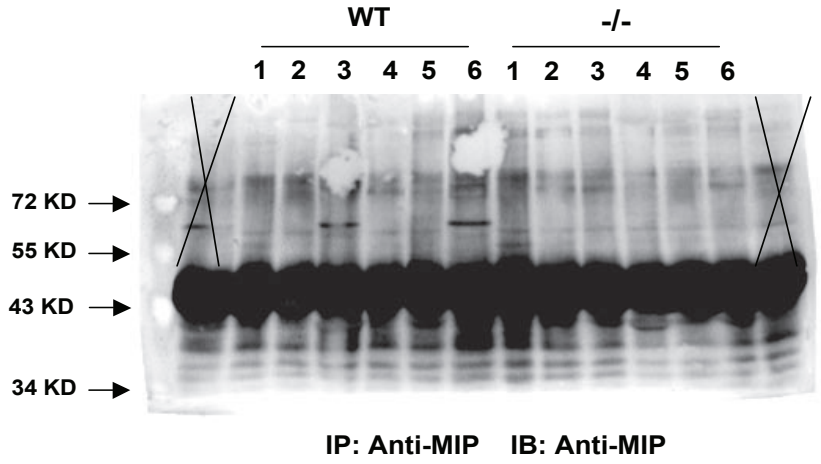

Figure S2d

Figure S6 Full scans of Northern blotting and Western blotting data shown in **Fig. 1a** and **S2d**. Lanes that are not relevant are crossed.

Table S1 and S2 Heart development and basal functions are not significantly disturbed in MIP$^{-/-}$ mice. Twelve week old WT and MIP$^{-/-}$ female mice (**Table S1**, n=3) and male mice (**Table S2**, n=5) were examined by echocardiography as described in Supplementary Information, Methods. Parameters were analyzed by *t* test. Note that no significant differences in echocardiography were found between WT and mutant female mice under resting conditions. In MIP$^{-/-}$ male mice, however, the cardiac index and end diastolic diameter were increased while posterior wall thickness was decreased.

Table S1

Analysis of cardiac sizes and functions by echocardiography (female mice)

	WT (n=3)	-/- (n=3)	p-value
End diastolic diameter (mm)	3.43±0.21	3.51±0.34	0.80
End systolic diameter (mm)	2.35±0.07	2.38±0.45	0.93
Fractional shortening (%)	31±2	32±6	0.84
Area of fractional shortening (%)	49±5	50±5	0.81
Velocity of circumferential shortening	4.27±0.49	4.24±0.75	0.96
Myocardial performance index	0.21±0.01	0.23±0.03	0.39
Cardiac index (ml/min/kg)	465.7±119.9	398.5±13.8	0.48
Relative wall thickness	0.61±0.09	0.61±0.11	0.95
Posterior wall thickness (mm)	0.94±0.10	0.86±0.18	0.64

Table S2

Analysis of cardiac sizes and functions by echocardiography (male mice)

	WT (n=5)	-/- (n=5)	p-value
End diastolic diameter (mm)	3.15±0.21	3.87±0.26	<0.05
End systolic diameter (mm)	2.08±0.27	2.44±0.43	0.19
Fractional shortening (%)	34±5	38±7	0.45
Area of fractional shortening (%)	51±8	53±4	0.54
Velocity of circumferential shortening	4.93±1.07	6.21±1.11	0.14
Myocardial performance index	0.21±0.01	0.24±0.02	0.06
Cardiac index (ml/min/kg)	293.9±64.6	400.5±43.6	<0.05
Relative wall thickness	0.61±0.10	0.51±0.08	0.16
Posterior wall thickness (mm)	1.39±0.17	1.16±0.08	<0.05

Supplementary Methods

Hidden Markov model (HMM) database search. The profiles of the phosphatase catalytic domains/motifs (PTPc, PTPc_motif, PTPc_DSPc, DSPc, and LMWPc) collected by the SMART database (Build May 11, 2002) (http://smart.embl-heidelberg.de) were downloaded. These profiles and the conserved catalytic motif ([V/I][V/I]HCXXGXXR[T/S]) shared by protein tyrosine/dual specificity phosphatases were used as baits for a HMM search. Default parameters were used for the HMM search (http://hmmer.wustl.edu/). All publicly available human protein or cDNA sequences (before Nov. 15, 2003) from the GenPept, RefSeq, PDB, SwissProt, PIR, PRF, ESTs, and UniGene database that partitions GenBank sequences into a non-redundant set of gene-oriented clusters, and human GenomeScan protein sequences (Build. 33) predicted by NCBI (http://www.ncbi.nlm.nih.gov/Ftp/index.html) were downloaded for HMM searches. All sequences hit by the searching were considered as candidate phosphatase genes for further analyses.

Phosphatase assay. To determine the tyrosine phosphatase activity, purified GST-MIP fusion protein or GST alone protein (1 μM) were incubated with pNPP (20 mM) for 1 hour at 37 °C in a reaction buffer containing 50 mM imidazole (pH 7.5) and 5 mM dithiothreitol. The reaction was stopped by the addition of 0.1 N NaOH, and the pNPP hydrolysis was measured by absorbance at 410 nm. To determine the lipid phosphatase activity, Di-C_8 phosphoinositides (Echelon Biosciences Inc., Salt Lake City, UT) and dioleoyl-phosphatidylserine (Sigma, St. Louis, MO) were resuspended

via sonication in the assay buffer (100 mM sodium acetate, 50 mM bis-Tris, 50 mM Tris pH 5.5, and 10 mM dithiothreitol) to final concentrations of 100 and 1000 μM, respectively. Equal volumes of di-C_8 phosphoinositides and dioleoyl-phosphatidylserine were added into microcentrifuge tubes and the mixtures were prewarmed at 37°C for 5 min. Reactions were initiated by the addition of 1 μg of GST-MIP fusion protein diluted in the assay buffer containing 1.0 mg/ml gelatin. Reactions were quenched after 30 min by the addition of 20 μl of 0.1 M *N*-ethylmaleimide and spun to sediment the lipid aggregates. The supernatant (25 μl) was added to a 96-well plate and 100 μl of Malachite green reagent (Echelon Biosciences Inc., Salt Lake City, UT) was added to each well. After incubation at room temperature for 15 min, the color development was measured at 620 nm. Inorganic phosphate release was quantified based on a standard curve generated with KH_2PO_4 in distilled H_2O.

Rotarod and inclined screen tests [1,2]. Motor coordination and function were tested using a RotaRod (Columbus Instruments, Columbus, OH). Each mouse was given 3 trials on the RotaRod which accelerated at a consent rate from 4 to 40 rpm in a 5 min period. When the animals were no longer able to stay on the accelerating wheel, they fell into a waiting chamber and the latency to fall was recorded. The scores from the 3 trials were averaged for each animal. An inclined screen (90 degree) was used to evaluate muscle strength by measuring latency to the top of the screen. Mice were placed in the middle of the screen, facing upward, and were given 60 sec(s) to reach the top of the screen. Each

mouse was given 3 trials to complete the task. The percentage of the animals that could reach the top was determined.

Treadmill performance. MIP$^{-/-}$ and WT female mice of 16-24 weeks old were subjected to a treadmill running test following a protocol modified from that of Zhao et al [3]. Mice were placed on a rodent treadmill equipped with an electric grid at the rear and were allowed to acclimatize for 4 consecutive days. On day 1, they ran at a speed of 38 m/min for 5 min; on day 2, 48 m/min for 5 min; on day 3, 58 m/min for 5 min; and on day 4, 68 m/min for 5 min. On days 5, 7 and 9 WT and MIP$^{-/-}$ mice ran concomitantly at 88 m/min until exhausted (indicated by falling on the electric grid 3 times), and running times were recorded. Three separate trials were conducted and the average running times of WT and MIP$^{-/-}$ mice were obtained.

Echocardiography. Left ventricular function was evaluated by echocardiography using a Sequoia C256 System (Siemens Medical) with a 15-MHz linear array transducer as previously described [4]. Briefly, mice were anesthetized with 1.5-2% isoflurane by mask, the chest was shaved, the animal was situated in the supine position on a warming pad, and ECG limb electrodes were placed. Two-dimensional (2-D), 2-D-guided M-mode, and Doppler echocardiographic studies of aortic and transmitral flows were performed from parasternal and foreshortened apical windows. End-diastolic and end-systolic dimensions were measured by using software resident on the ultrasonograph, and fractional shortening, myocardial performance index, and cardiac index were calculated as previously described [5].

Transmission electron microscopy. Soleus muscles dissected from 4-week old mice were fixed in 3% paraformaldehyde, 2.5% glutaraldehyde, and 0.1 M cacodylate buffer, pH7.4, and later postfixed in 1% OsO_4 and 0.1 M cacodylate buffer, pH 7.4. Microthin sections were double stained with uranyl acetate and lead citrate. These sections were examined under a transmission electron microscope (JEM-1200, JEOL, Japan).

Laser scanning cytometry. Laser scanning cytometry was used to quantitatively assess PI(3,5)P_2 levels in the SR of WT and MIP$^{-/-}$ myotubes as previously reported [6,7]. Primary WT and MIP$^{-/-}$ myotubes were immunostained with anti-PI(3,5)P_2 and anti-PDI antibodies. PI(3,5)P_2 and PDI were visualized using Alexa 647 labeled anti-mouse 2nd antibody and Alexa 488 labeled anti-rabbit 2nd antibody, respectively. DAPI (4',6-diamidino-2-phenylindole) was used as a nuclear counterstain to contour and quantify cells. The slides were analyzed using a laser scanning cytometer (Compucyte iCyte, Cambridge, MA), which allows quantitative fluorescence signal processing of the SR (defined by PDI) in individual cells in a population on a flat surface. The slides were scanned at 40X magnification using argon laser. The SR was contoured based on PDI fluorescence. The laser scanning cytometer recorded the Alexa 647 fluorescence of the SR and counted the total number of the cells. The mean fluorescence intensity of Alexa 647 in the SR of all of the cells in each well was calculated to determine PI(3,5)P_2 levels.

SERCA activity assay [8,9]. Hind leg muscles of WT and MIP$^{-/-}$ mice were homogenized. SR vesicles were isolated by differential centrifugation as described [10]. The SR vesicles

were resuspended in a buffer containing 300 mM Sucrose and 25 mM HEPES (pH 7.2). Ca^{2+}-dependent and basal ATPase activities of SERCA in SR were determined at 37 °C for 30 min by the colorimetric assay of P_i production in the reaction containing 20 mM HEPES (pH 7.2), 300 mM Sucrose, 100 mM KCl, 5 mM $MgCl_2$, 1 mM EGTA, 2 mM NaN_3, 0-2.5 mM $CaCl_2$, 2 μM Ca^{2+} ionophore (ionomycin), 1mM ATP, and 2 μg of SR protein/ml. Ca^{2+}-dependent SERCA ATPase activity was identified as Ca^{2+}- ATPase hydrolytic activity inhibited by 0.1μM thapsigargin (TG).

References:

1. Bogo, V., Hill, T. A. & Young, R. W. Comparison of accelerod and rotarod sensitivity in detecting ethanol- and acrylamide-induced performance decrement in rats: review of experimental considerations of rotating rod systems. *Neurotoxicology* 2, 765-87 (1981).
2. Dean, R. L., 3rd et al. Age-related differences in behavior across the life span of the C57BL/6J mouse. *Exp Aging Res* 7, 427-51 (1981).
3. Zhao, X. et al. Enhanced resistance to fatigue and altered calcium handling properties of sarcalumenin knockout mice. *Physiol Genomics* 23, 72-8 (2005).
4. Morgan, E. E. et al. Effects of chronic activation of peroxisome proliferator-activated receptor-alpha or high-fat feeding in a rat infarct model of heart failure. *Am J Physiol Heart Circ Physiol* 290, H1899-904 (2006).
5. Rennison, J. H. et al. High-fat diet postinfarction enhances mitochondrial function and does not exacerbate left ventricular dysfunction. *Am J Physiol Heart Circ Physiol* 292, H1498-506 (2007).

6. Min, J. et al. Forward chemical genetic approach identifies new role for GAPDH in insulin signaling. *Nat Chem Biol* 3, 55-9 (2007).

7. Niswender, K. D. et al. Immunocytochemical detection of phosphatidylinositol 3-kinase activation by insulin and leptin. *J Histochem Cytochem* 51, 275-83 (2003).

8. Ishii, T., Lemas, M. V. & Takeyasu, K. Na(+)-, ouabain-, Ca(2+)-, and thapsigargin-sensitive ATPase activity expressed in chimeras between the calcium and the sodium pump alpha subunits. *Proc Natl Acad Sci U S A* 91, 6103-7 (1994).

9. Bartolommei, G. et al. Clotrimazole inhibits the Ca2+-ATPase (SERCA) by interfering with Ca2+ binding and favoring the E2 conformation. *J Biol Chem* 281, 9547-51 (2006).

10. Meissner, G. Adenine nucleotide stimulation of Ca2+-induced Ca2+ release in sarcoplasmic reticulum. *J Biol Chem* 259, 2365-74 (1984).

nature cell biology

TGF-β signalling is regulated by Schnurri-2-dependent nuclear translocation of CLIC4 and consequent stabilization of phospho-Smad2 and 3

Anjali Shukla[1], Mariam Malik[1], Christophe Cataisson[1], Yan Ho[1], Travis Friesen[1], Kwang S. Suh[1,2] and Stuart H. Yuspa[1,3]

CLIC4 (chloride intracellular channel 4), a multifunctional protein that traffics between the cytoplasm and nucleus, interacts with Schnurri-2, a transcription factor in the bone morphogenetic protein (BMP) signalling pathway. Here we show that transforming growth factor β (TGF-β) promotes the expression of CLIC4 and Schnurri-2 as well as their association in the cytoplasm and their translocation to the nucleus. In the absence of CLIC4 or Schnurri-2, TGF-β signalling is abrogated. Direct nuclear targeting of CLIC4 enhances TGF-β signalling and removes the requirement for Schnurri-2. Nuclear CLIC4 associates with phospho (p)-Smad2 and p-Smad3, protecting them from dephosphorylation by nuclear phosphatases. An intact TGF-β signalling pathway is essential for CLIC4-mediated growth-arrest. These results newly identify Schnurri-2 and CLIC4 as modifiers of TGF-β signalling through their stabilization of p-Smad2 and 3 in the nucleus.

CLIC4 is a member of the chloride intracellular channel (CLIC) family of proteins, which are ubiquitously expressed in several tissue types[1]. In addition to chloride channel activity in artificial and biological membranes, CLIC family members participate in cell-cycle control, cytoskeletal function, mitosis and differentiation[1], but the pathway(s) through which they function are undefined. Analysis of the molecular structure of CLIC1 and CLIC4 has revealed dimorphic proteins that exist in both soluble and membrane-bound configurations, which are, at least in part, regulated by redox potential[2–4]. CLIC4 is essential for p53- and c-Myc-mediated apoptosis and its promoter is a direct downstream target of these transcription factors[5,6]. Cytoplasmic CLIC4 translocates to the nucleus under conditions of metabolic stress, growth arrest, apoptosis and DNA damage; this is mediated by a functional nuclear localization signal (NLS) on its carboxyl terminus. Nuclear residence is an essential component of CLIC4 pro-apoptotic and growth-arrest activity in keratinocytes[8]. In contrast, CLIC4 is excluded from the nucleus in epithelial cancer cells, but upregulated in tumour stromal cells that are associated with myofibroblast conversion[9]. CLIC4 has been linked to myofibroblast conversion in mammary fibroblasts treated with TGF-β (**A002271**; ref. 10). Thus, although CLIC4 participates in growth control and tissue remodelling, the signalling pathway through which it participates is not known.

We performed yeast two-hybrid assays using six CLIC4 sequences, spanning the entire protein, as baits. The CLIC4 bait comprising amino-acid residues 120–254 interacted with several potential binding proteins one of which was Schnurri-2 (which interacted with residues 814–1167), a zinc finger protein known to function in the TGF-β superfamily —decapentaplegic (Dpp)/BMP — signalling pathway[11–13]. We validated the interaction of CLIC4 and Schnurri-2 using co-immunoprecipitation assays in primary cultures of mouse keratinocytes expressing haemagglutinin (HA)-tagged CLIC4 or an empty vector. Schnurri-2-interacting proteins were co-immunoprecipitated using an anti-Schnurri-2 antibody. Immunoblotting of the SDS–PAGE-separated immunoprecipitates revealed both endogenous and exogenous CLIC4 (Fig. 1a; Supplementary Information, Fig. S1a), confirming the yeast two-hybrid results. CLIC4 and Schnurri-2 did not associate *in vitro*; full-length Schnurri-2 or its interacting domain failed to co-immunoprecipitate with recombinant full-length CLIC4 or the CLIC4 interacting domain (data not shown).

We transfected primary keratinocytes with adenoviral vectors expressing deletion constructs of C-terminal V5-His tagged CLIC4 (Supplementary Information, Fig. S1b). An anti-Schnurri-2 antibody co-precipitated both full-length CLIC4 (residues 1–253) and the region lacking the NLS (residues 1–197), but not the amino-terminal half (residues 1–120) or the region containing the transmembrane domain (residues 1–60; Supplementary Information, Fig. S1c). We did not detect interaction with the regions containing residues 1–120 or 1–60, even at the highest exposures. Thus, Schnurri-2 interacts with a region of CLIC4 between residues 121 and 197, consistent with the bait region attracting Schnurri-2 in the yeast two-hybrid assay.

As CLIC4 causes cell-cycle arrest and Schnurri-2 participates in TGF-β superfamily signalling, we asked whether TGF-β could influence the interaction between CLIC4 and Schnurri-2. Whole-cell protein

[1]Laboratory of Cancer Biology and Genetics, 37 Convent Drive, National Cancer Institute, National Institutes of Health, Bethesda, MD 20892. [2]Current address: Tumor Bank and Genomics Program, Hackensack University Medical Center, Hackensack, NJ 07601.
[3]Correspondence should be addressed to S.H.Y (e-mail: yuspas@mail.nih.gov)

Received 20 November 2008; accepted 12 March 2009; published online 17 May 2009; DOI: 10.1038/ncb1885

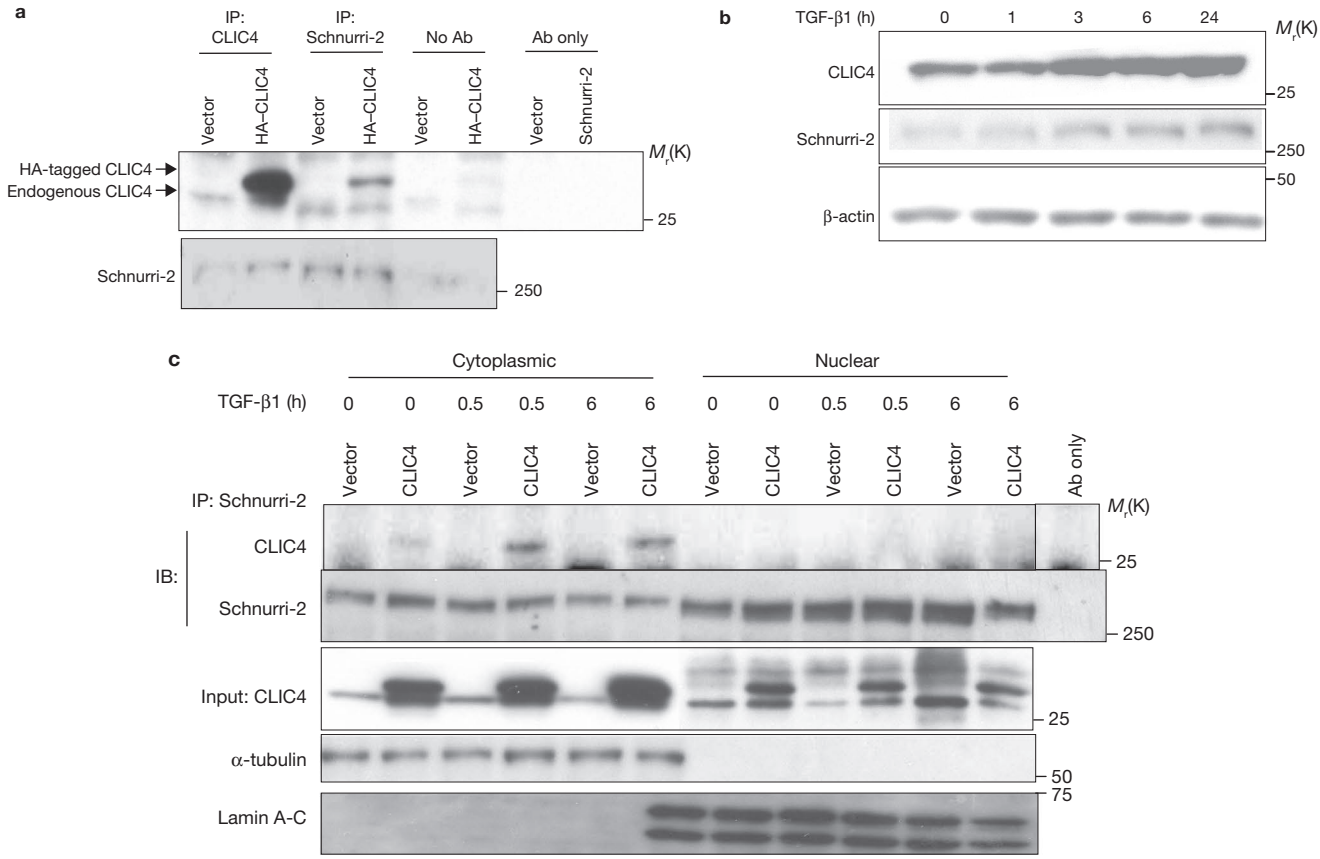

Figure 1 TGF-β enhances the expression and association of CLIC4 and Schnurri-2. (**a**) An empty vector or HA-tagged CLIC4 was expressed in primary Balb/c keratinocytes using adenoviral constructs. Whole-cell lysates were immunoprecipitated (IP) using anti-CLIC4 or anti-Schnurri-2 antibodies and immunoblotted for CLIC4 and Schnurri-2. Antibodies (Ab) without cell lysates or cell lysates without antibodies were subjected to immunoprecipitation as controls. (**b**) Primary keratinocytes were treated with TGF-β1 (1 ng ml^{-1}) for the indicated times. Whole-cell lysates were immunoblotted for CLIC4 and Schnurri-2. β-actin was used as a loading control. (**c**) An empty vector or HA-tagged CLIC4 was expressed in keratinocytes for 16 h and cells were then treated with TGF-β1 (1 ng ml^{-1}) for the indicated times. Cytoplasmic and nuclear fractions were immunoprecipitated using an anti-Schnurri-2 antibody and immunoblotted (IB) for CLIC4 and Schnurri-2. Only exogenous CLIC4 was monitored because endogenous CLIC4 and IgG co-migrate in the presence of cell fractionation buffers. An anti-Schnurri-2 antibody was subjected to immunoprecipitation and immunoblotting without cell lysates as a control. Aliquots of the cytoplasmic and nuclear fractions were used directly as input for immunoblotting of CLIC4, lamin A-C and α-tubulin (α-tubulin and lamin A-C were used as controls for the cytoplasmic and nuclear fraction respectively). The lanes separated by a line are from the same gel. See Supplementary Information, Fig. S11 for uncropped scans.

lysates from keratinocytes that had been treated with TGF-β1 for various times showed a persistent increase in CLIC4 and Schnurri-2 levels for up to 24 h after treatment (Fig. 1b). This increase was transcriptional and sustained (Supplementary Information, Fig. S2a). Furthermore, skin biopsies from single- and double-transgenic mice overexpressing active TGF-β1 in the epidermis in response to doxycycline stimulation[14] showed elevated transcripts for both Schnurri-2 and CLIC4 within 4–5 days of treatment (Supplementary Information, Fig. S2b) . At this point, transcripts for the TGF-β response gene Smad7 are also increased, as reported previously. Thus, CLIC4 and Schnurri-2 respond to TGF-β stimulation similarly, both *in vitro* and *in vivo*. TGF-β also stimulates the interaction of CLIC4 and Schnurri-2. Co-immunoprecipitation experiments in keratinocytes showed an increase in the interaction of both endogenous and exogenous CLIC4 with Schnurri-2 within 30 min of TGF-β1 treatment (Supplementary Information, Fig. S3). The interaction seemed to occur only in the cytoplasmic compartment of subcellular fractions, persisting for at least 6 h (Fig. 1c). We did not detect any interaction of these proteins in the nucleus. The TGF-β-stimulated interaction of CLIC4 and Schnurri-2 is not Smad dependent, as it was not interrupted by short interfering RNA (siRNA)-mediated knockdown of *Smad2*, *Smad3* or *Smad4* (Supplementary Information, Fig. S4).

Expression of exogenous CLIC4 in mouse keratinocytes modestly enhanced the activity of the TGF-β-dependent reporter plasmid p3TP-lux in response to a low dose (50 pg ml^{-1}) of TGF-β1 (Fig. 2a). CLIC4 increased the reporter activity in a TGF-β1-dose-dependent manner (Supplementary Information, Fig. S5a). This enhancement required the presence of Schnurri-2; expression of *Schnurri-2* siRNA prevented CLIC4 from increasing TGF-β reporter activity (Fig. 2a; Supplementary Information, Fig. S5a). Growth inhibition is a major physiological response of keratinocytes to TGF-β. Exogenous CLIC4 alone inhibited keratinocyte DNA synthesis, and together with TGF-β1 inhibited DNA synthesis to a greater extent than TGF-β1 alone (Fig. 2b); this required Schnurri-2. Keratinocyte growth inhibition by CLIC4 and TGF-β also followed a TGF-β1 dose-dependent course (Supplementary Information, Fig. S5b). Schnurri-2 is a Smad binding partner in Dpp and BMP signalling in *Drosophila melanogaster* and mice, respectively,

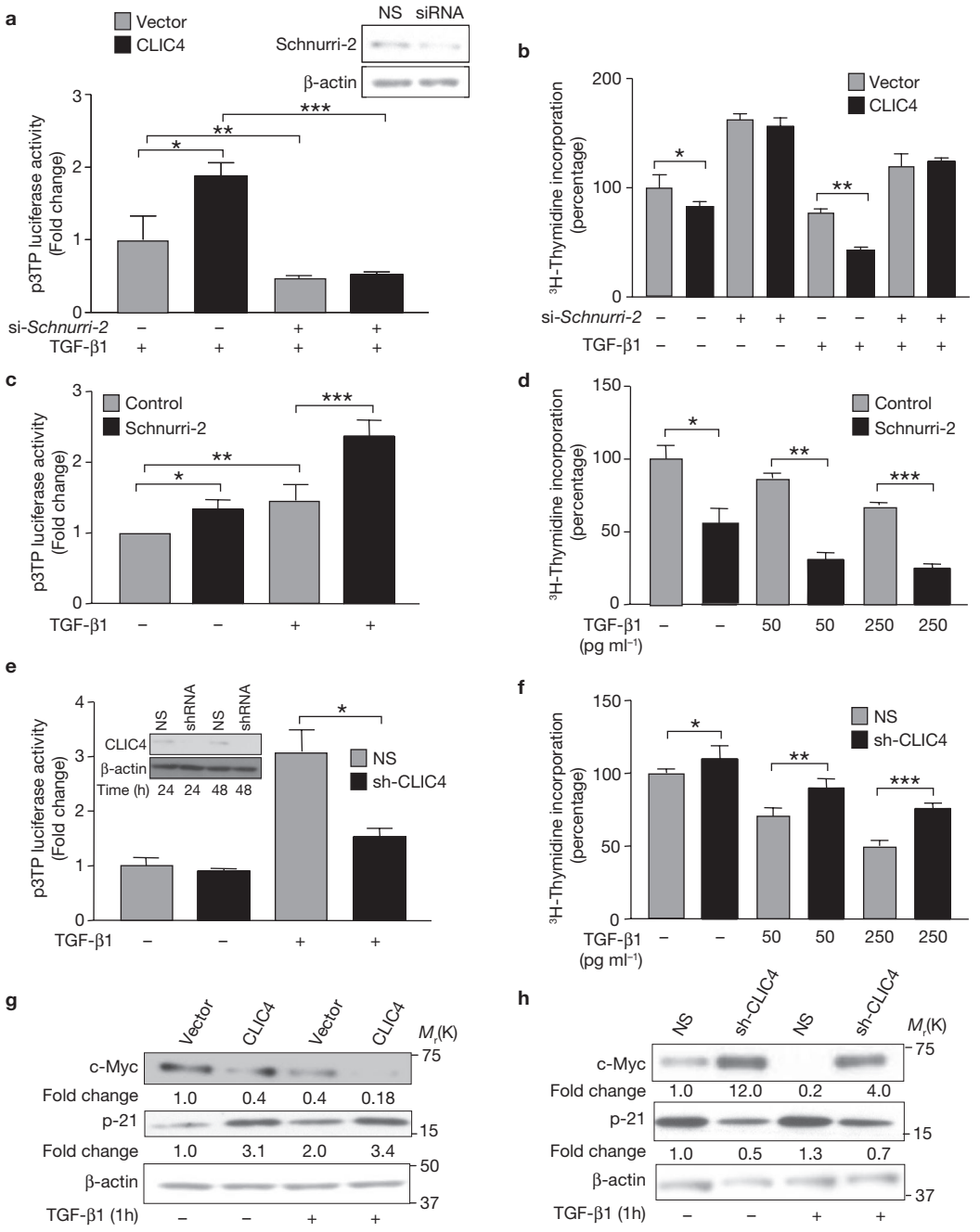

Figure 2 CLIC4 and Schnurri-2 enhance TGF-β signalling. Primary keratinocytes or HEK 293 cells were transfected with a p3TP-lux or pRLTK plasmid. (**a**, **b**) Keratinocytes were transfected with non-silencing (–) or *Schnurri-2* (+) siRNA (si-*Shnurri-2*; inset in panel **a**) for 24 h, before being transduced with an empty vector or CLIC4 using adenoviral constructs. Cells were then treated with TGF-β1 (50 pg ml^{-1}) for 14 h in **a** or 16 h in **b**. P3TP luciferase activity was normalized to pRLTK activity and data presented as fold change relative to that of a sample transduced with an empty vector and non-silencing siRNA (**a**; $*P = 0.0125$, $**P = 0.0155$, $***P = 0.0092$). ^{3}H-thymidine incorporation is presented as a percentage of incorporation observed in an untreated sample transduced with an empty vector and non-silencing siRNA (**b**; $*P = 0.0279$, $**P < 0.0001$) . (**c, d**) HEK293 cells were transfected with pAct-Flag–hShn-2 (Schnurri-2) or transfection reagent alone (control) and treated with TGF-β1 (50 pg ml^{-1}) for 16 h in **c** or 24 h in **d**. Luciferase data is presented as fold change relative to that of the control (**c**; $*P = 0.0253$, $**P = 0.0291$, $***P = 0.0357$). ^{3}H-thymidine incorporation is presented as a percentage of incorporation observed in the control (**d**; $*P = 0.015$, $**P < 0.0001$, $***P = 0.0001$). (**e**) Keratinocytes were transduced with a non-silencing (NS) or *CLIC4* shRNA (sh-*CLIC4*; inset) adenovirus for 24 h before TGF-β1 treatment (50 pg ml^{-1}) for 14 h. Luciferase data is presented as fold change relative to that of an untreated, non-silencing shRNA-transduced sample ($*P = 0.0102$). (**f**) Keratinocytes were transduced with *CLIC4* shRNA as in **e** and treated with TGF-β1 for 16 h. ^{3}H-thymidine incorporation is presented as a percentage of incorporation observed in the untreated, non-silencing shRNA-transduced sample ($*P = 0.0177$, $**P = 0.0005$, $***P < 0.0001$). (**g**, **h**) Keratinocytes were transduced with an empty vector or CLIC4 using adenoviral constructs (**g**) or *CLIC4* knockdown vectors (**h**) for 16 h and then treated with TGF-β1 (1 ng ml^{-1}) for 1 h. ImageJ software was used to quantify c-Myc and p21 bands, which are normalized to their respective β-actin controls and are represented as fold change relative to untreated empty vector-transduced samples. Data are mean ± s.d. in **a**–**f**, $n = 4$ in **a**–**f**. See Supplementary Information, Fig. S11 for uncropped scans.

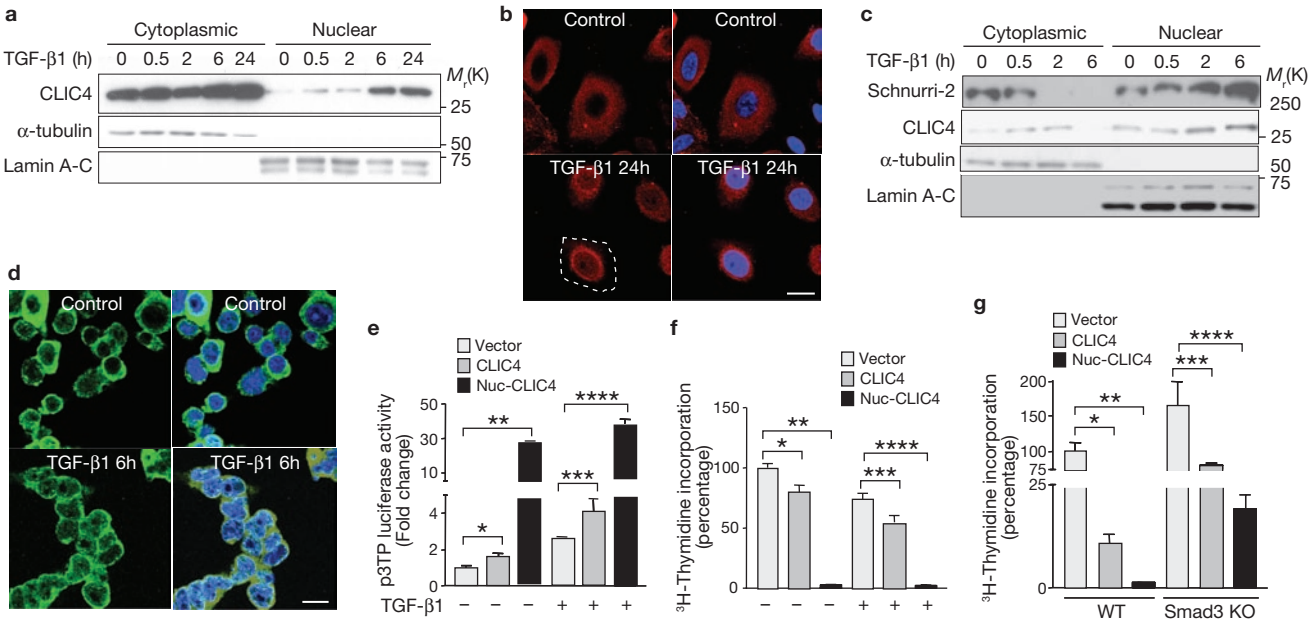

Figure 3 TGF-β induces nuclear translocation of CLIC4, enhancing TGF-β signalling. (**a**, **b**) Primary keratinocytes were treated with TGF-β1 (1 ng ml^{-1}) for the times indicated. Cytoplasmic and nuclear fractions were immunoblotted (**a**) or immunostained (**b**) for CLIC4. In panel **a**, α-tubulin and lamin A-C were used as controls for the cytoplasmic and nuclear fractions respectively. See Supplementary Information, Fig. S11 for the uncropped scan. In **b**, DAPI was used to visualize nuclei. The dotted line defines the cell periphery. (**c**, **d**) HEK293 cells were transfected with the plasmid pAct-Flag–hShn-2 and treated with TGF-β1 for the times indicated. Cytoplasmic and nuclear fractions were immunoblotted for Schnurri-2 and CLIC4 (**c**; α-tubulin and lamin A–C,were used as controls), or immunostained for Flag–Schnurri-2 (green) with anti-Flag primary and fluorescein isothiocyanate (FITC)-labelled secondary antibodies (**d**). DAPI (blue) was used to visualize nuclei in **d** (right). (**e**) Primary keratinocytes were transfected with a p3TP-lux or pRLTK (control) plasmid before being transduced with an empty control vector (vector), wild-type CLIC4 or nuclear-targeted (nuc) CLIC4 using adenoviral constructs, and were then treated with TGF-β1 (50 pg ml^{-1}) for 14 h. Luciferase assays were performed, p3TP activity was normalized to pRLTK activity and data presented as fold change relative to that of an untreated, empty vector-transduced sample (*$P = 0.0074$, **$P < 0.0001$, ***P = 0.0056,****$P < 0.0001$). (**f**) Keratinocytes were transduced as in **e** and treated with TGF-β1 (50 pg ml^{-1}) for 16 h. ^{3}H-thymidine incorporation is presented as a percentage of incorporation observed in the untreated empty vector-transduced sample (*$P = 0.03$, **$P < 0.0001$, ***$P < 0.032$, ****$P < 0.0001$). (**g**) Keratinocytes from *Smad3* knockout (KO) mice or wild-type (WT) littermates were transduced as in **e** and treated with TGF-β1 (50 pg ml^{-1}) for 16 h. ^{3}H-thymidine incorporation is presented as a percentage of incorporation in the wild-type vector-transduced sample (*$P < 0.0005$, **$P < 0.0001$, ***$P = 0.0022$, ****$P = 0.0001$). In **a**, **b** and **c** data are mean ± s.d. from quadruplicates ($n = 4$) of a representative experiment. Scale bar, 20 μm in **b** and **d**.

and it alters downstream signalling[12,13]. We confirmed that Schnurri-2 also modifies TGF-β1 signalling in a mammalian system by introducing a Schnurri-2 expression plasmid, pAct-Flag–hShn-2, into a readily transfectable epithelial cell line, HEK293. Schnurri-2 alone caused CLIC4 to translocate to the nucleus and activated Smad2 (**A002174**) and suppressed c-Myc (Supplementary Information, Fig. S6). Together with TGF-β1, Schnurri-2 increased TGF-β-dependent signal transduction, transcriptional activity and growth inhibition (Fig. 2c, d; Supplementary Information, Fig. S7a). These results indicate that Schnurri-2 is involved in TGF-β signalling in addition to its known function in BMP signalling.

Next we examined the biological significance of CLIC4 in TGF-β responses. *CLIC4* knockdown by short hairpin (sh) RNA-expression in keratinocytes reduced both TGF-β1-induced p3TP-lux activity and inhibition of thymidine incorporation by TGF-β1, further confirming participation of CLIC4 in TGF-β signalling (Fig. 2e, f). Expressing exogenous CLIC4 in keratinocytes also enhanced both TGF-β1-dependent downregulation of c-Myc and upregulation of p21, even in the absence of TGF-β1 (Fig. 2g). These changes are known to be involved in TGF-β-mediated growth inhibition[15,16]. Furthermore, suppression of CLIC4 by shRNA enhanced c-Myc and reduced p21 expression in the absence of TGF-β1 and reduced c-Myc inhibition and p21 induction in the presence of TGF-β1 (Fig. 2h).

TGF-β1 increased total CLIC4 and caused nuclear trafficking of CLIC4 in keratinocytes within 30 min of treatment (Fig. 3a). Nuclear CLIC4 could be detected by confocal microscopy as early as 1 h after exposure to TGF-β1 (data not shown), and was sustained for at least 24 h (Fig. 3b). In TGF-β1-exposed HEK293 cells, exogenous Schnurri-2 (pAct-Flag–hShn2) translocated to the nucleus in a time-course virtually identical to that observed for endogenous CLIC4 (Fig. 3c). Confocal microscopy for Flag staining confirmed nuclear trafficking of Schnurri-2 (Fig. 3d). Together, these results support a mechanism whereby TGF-β1 enhances its activity through stimulating an interaction between CLIC4 and Schnurri-2 and promoting their nuclear translocation.

To confirm that nuclear translocation of CLIC4 by TGF-β1 has functional significance, we introduced a nuclear-targeted CLIC4-expressing adenovirus[7] into keratinocytes, and monitored TGF-β responses. Both wild-type and nuclear CLIC4 enhanced TGF-β1-dependent reporter activity, but nuclear CLIC4 was 10-fold more potent than wild-type CLIC4 (Fig. 3e). TGF-β-dependent inhibition of DNA synthesis in keratinocytes was enhanced by both wild-type and nuclear-targeted CLIC4, but much more so by the latter. Furthermore, nuclear CLIC4 caused marked inhibition of DNA synthesis in the absence of exogenous TGF-β1 (Fig. 3f). To examine whether growth inhibition by nuclear CLIC4 is TGF-β-dependent, we expressed exogenous wild-type and nuclear-targeted CLIC4 in primary keratinocytes from *Smad3*-knockout

mice and wild-type littermates, and treated cells with TGF-β1 for 16 h. Results indicate that the lack of Smad3 (**A002175**) increased thymidine incorporation (Fig. 3g), consistent with a growth inhibitory function of the TGF-β pathway in this cell type. Wild-type CLIC4 and, especially, nuclear CLIC4 enhanced TGF-β-mediated growth inhibition in wild-type keratinocytes but were much less effective in *Smad3*-knockout keratinocytes. Whereas DNA synthesis in wild-type keratinocytes was inhibited 83-fold by overexpression of nuclear CLIC4, it was only inhibited 9-fold in *Smad3*-knockout cells, thus confirming that a completely intact TGF-β signalling pathway is essential for CLIC4-mediated keratinocyte growth inhibition.

To understand the mechanism by which Schnurri-2 facilitates CLIC4 enhancement of TGF-β signalling, we analysed the effect of *Schnurri-2* siRNA expression on TGF-β1-dependent nuclear translocation of CLIC4. Knockdown of *Schnurri-2* prevented CLIC4 from translocating to the nucleus after TGF-β1 treatment of keratinocytes (Fig. 4a, b), indicating that Schnurri-2 is important for CLIC4 nuclear translocation in response to TGF-β1. We found that depletion of Schnurri-2 prevented wild-type CLIC4 from enhancing TGF-β1 transcriptional activation (Fig. 2a), but did not prevent nuclear CLIC4 from enhancing TGF-β reporter activity (Fig. 4c). This result was confirmed in immortalized mouse embryonic fibroblasts (MEFs) from *Schnurri-2*-knockout mice (Supplementary Information, Fig. S7b). However, exogenous expression of Schnurri-2 restored the ability of wild-type CLIC4 to enhance TGF-β signalling in these cells. In contrast, nuclear-targeted CLIC4 enhanced reporter activity in the absence of Schnurri-2. Thus, the primary requirement for Schnurri-2 in this pathway is to facilitate CLIC4 nuclear translocation and not nuclear CLIC4 activity.

Nuclear targeting of CLIC4 enhanced nuclear p-Smad2 and 3 levels, even in the absence of exogenous TGF-β stimulation (Fig. 5a). Expression of *CLIC4* shRNA decreased nuclear p-Smad2 and 3 in both untreated and TGF-β1-treated (1 h) keratinocytes (Supplementary Information, Fig. S8a). The targeting of a non-specific protein to the nucleus (green fluorescent protein, GFP) by an adenoviral vector[7] did not enhance levels of p-Smad2 or 3 (data not shown), indicating that nuclear CLIC4 has a specific effect. P-Smad2 and 3 levels were increased when endogenous or exogenous CLIC4 was targeted to the nucleus by TGF-β1 treatment; exogenous CLIC4 translocation sustained these levels for extended periods (Supplementary Information, Fig. S8b). Smad4 levels were not altered by nuclear-targeted CLIC4 (Fig. 5a). P-Smad2 and 3 are predominantly nuclear proteins, although phosphorylation occurs in the cytoplasm. Nuclear CLIC4 primarily enhanced nuclear p-Smad2 and 3, even in the absence of exogenous TGF-β1 (Fig. 5b). However, nuclear CLIC4 did not enhance translocation of p-Smad2 or 3 from the cytoplasm to the nucleus in the absence or presence of exogenous TGF-β1, as cytoplasmic p-Smad2 or 3 were not reduced in its presence (Fig. 5b). The increase in nuclear p-Smads was not a consequence of enhanced total Smad protein levels, as they remained unchanged (Fig. 5b).When keratinocytes were treated with TGF-β type I receptor inhibitor SB431542, the overall levels of p-Smad2 decreased due to a blockade of basal Smad activation. Nevertheless, p-Smad2 levels were partially sustained by nuclear CLIC4 (Supplementary Information, Fig. S9a). This indicates that CLIC4 does not function through receptor-mediated phosphorylation and that spontaneous dephosphorylation of p-Smads is delayed by nuclear CLIC4.

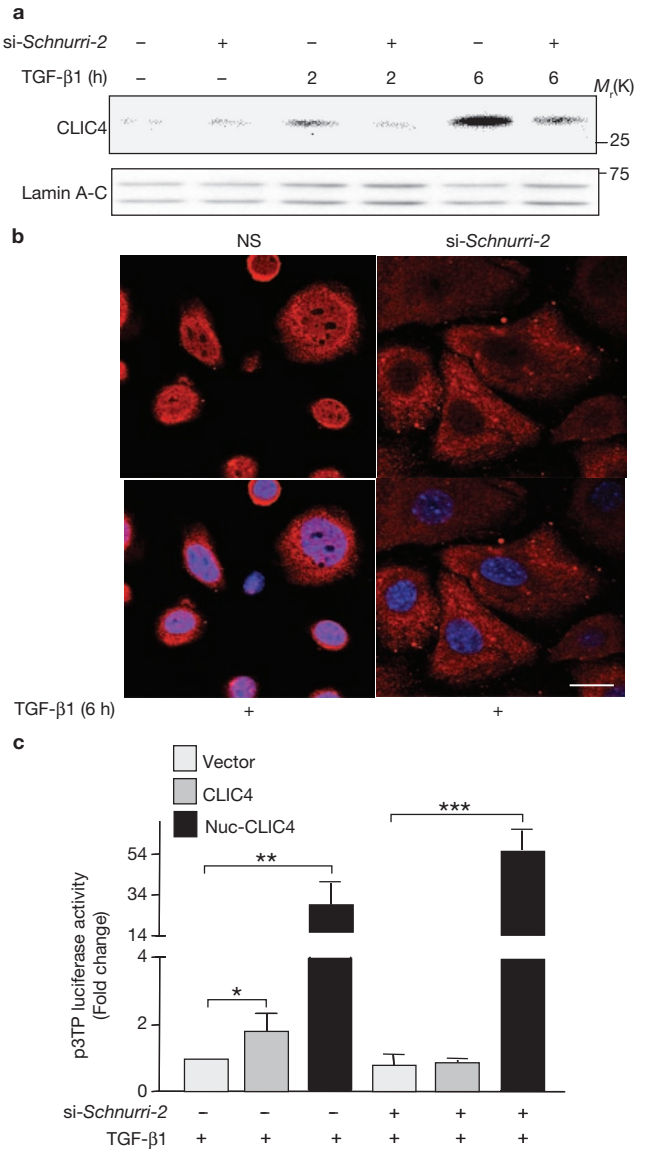

Figure 4 Schnurri-2 is essential for TGF-β-dependent nuclear translocation of CLIC4. (**a**) Primary Balb/c keratinocytes were transfected with non-silencing (–) or *Schnurri-2* (+) siRNA 24 h before treatment with TGF-β1 (1 ng ml^{-1}) for 2 h or 6 h. Nuclear fractions were immunoblotted for CLIC4. Lamin A-C was used as a loading control. See Supplementary Information, Fig. S11 for the uncropped scan. (**b**) Keratinocytes were transfected with non-silencing (NS) or *Schnurri-2* siRNA (si-*Schnurri-2*) 24 h before treatment with TGF-β1 for 6 h. Cells were immunostained with anti-CLIC4 primary and rhodamine-labelled secondary antibodies (red) and visualized by confocal microscopy with or without DAPI (blue) to visualize nuclei. Scale bar, 20 μm. (**c**) Keratinocytes were transfected with a p3TP-lux or pRLTK (control) plasmid and non-silencing (-) or *Schnurri-2* (+) siRNA before transduction with adenoviral constructs expressing empty control vector (vector), wild-type CLIC4 or nuclear-targeted (nuc) CLIC4 and then treatment with TGF-β1 (50 pg ml^{-1}) for 14 h. Luciferase assays were performed and data presented as fold change relative to that of a non-silencing siRNA-transfected sample. Data are mean ± s.d. from quadruplicates ($n = 4$) of a representative experiment (*$P = 0.023$, **$P = 0.0068$, ***$P = 0.0005$).

After short TGF-β1 treatment, endogenous CLIC4 co-immunoprecipitated from keratinocyte nuclear fraction lysates with endogenous p-Smad2 and 3. However, the abundance of p-Smads (hence the level

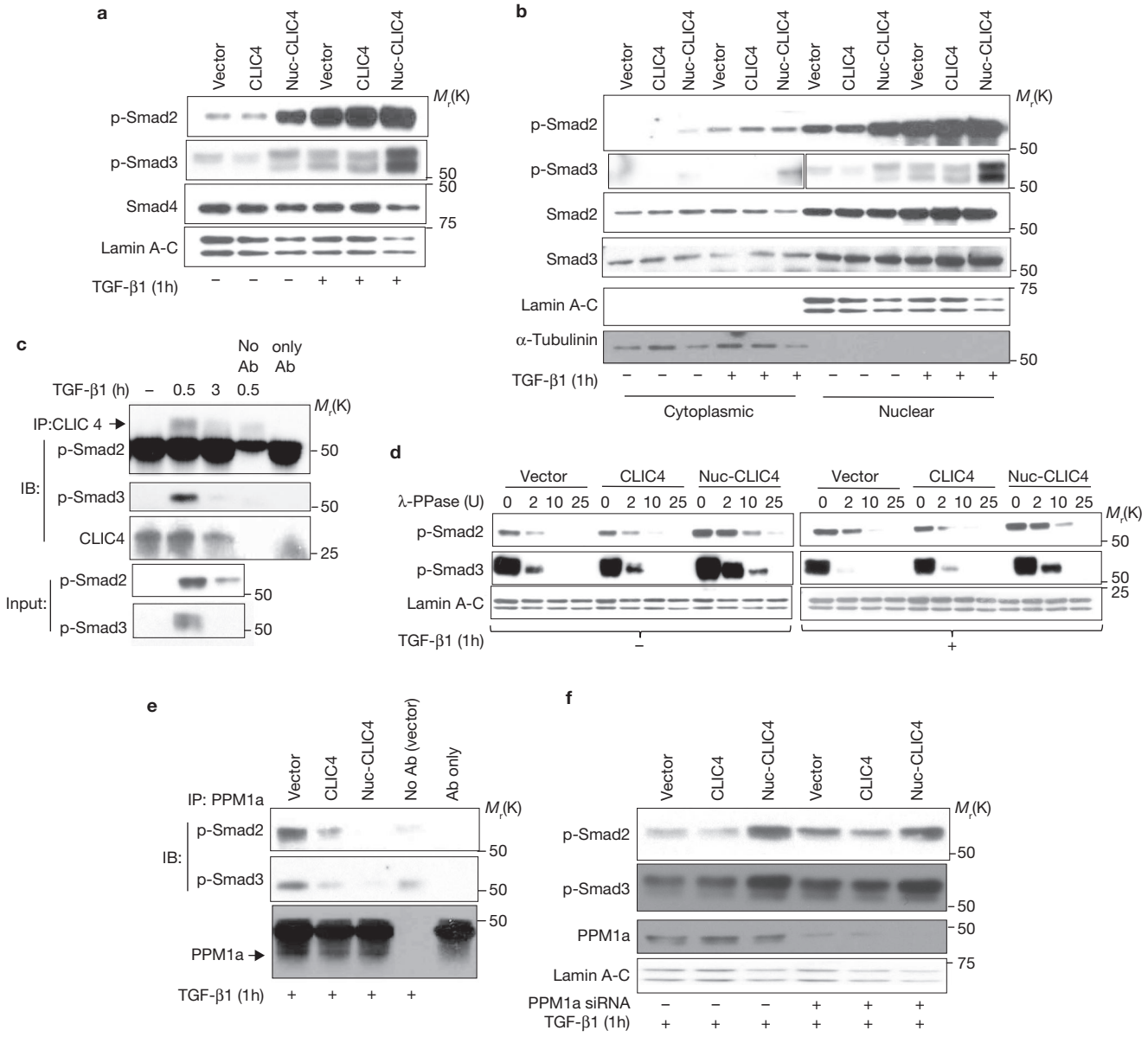

Figure 5 Nuclear CLIC4 associates with and stabilizes p-Smad2 and 3. (**a**) Nuclear lysates from primary keratinocytes transduced with an empty control vector (vector), wild-type CLIC4 or nuclear (nuc)-targeted CLIC4 with adenoviral constructs for 16 h and treated with TGF-β1 for 1 h (1 ng ml^{-1}) were immunoblotted for the indicated proteins. Lamin A-C was used as a loading control. (**b**) Cytoplasmic and nuclear lysates from primary keratinocytes transduced and treated as in panel **a** were immunoblotted for p-Smad2, p-Smad3 and total Smad2 and 3. Lamin A-C and α-tubulin were used as loading and subcellular fraction purity controls. The separated sections of the p-Smad3 blot are from the same gel, but reflect adjusted exposure times for optimal visualization. (**c**) Nuclear lysates of keratinocytes untreated or treated with TGF-β1 for indicated times were immunoprecipitated (IP) with an anti-CLIC4 antibody and immunoblotted (IB) for p-Smad2, p-Smad3 and CLIC4. An anti-CLIC4 antibody (Ab) without cell lysates and cell lysates without antibodies were subjected to immunoprecipitation as controls. An aliquot of lysates used for immunoprecipitation was used as input. (**d**) Primary keratinocytes were transduced and treated as in panel **a**. Nuclear lysates were dephosphorylated using indicated amounts of λ-PPase, and immunoblotted for p-Smad2 and 3. Lamin A-C was used as a loading control. The exposure time for TGF-β1-treated samples was adjusted to compensate for the higher p-Smad2 and 3 levels. ImageJ software was used to quantify p-Smad2 and 3 bands, which are normalized to their respective lamin A-C controls. (**e**) Nuclear lysates of keratinocytes transduced and treated as in panel **a** were immunoprecipitated with an anti-PPM1a antibody and immunoblotted for p-Smad2, p-Smad3 and PPM1a. An anti-PPM1a antibody without cell lysates and lysates without an antibody were subjected to immunoprecipitation and used as controls. (**f**) Primary Balb/c keratinocytes were transfected with non-silencing (–) or *PPM1a* (+) siRNA 48 h before transduction with an empty control vector (vector), wild-type CLIC4 or nuclear targeted CLIC4 for 16 h, followed by treatment with TGF-β1 (1 ng ml^{-1}) for 1 h. Lysates were separated by SDS–PAGE and immunoblotted for p-Smad2, p-Smad3 and PPM1a. Lamin A-C was used as a loading control. See Supplementary Information, Fig. S11 for uncropped scans.

of immunoprecipitated p-Smads) diminished over 3 h, consistent with the reported degradation of nuclear p-Smads after TGF-β1 treatment[17]. These results indicate that CLIC4 directly interacts with p-Smad2 and 3 in keratinocytes. Co-immunoprecipitation analysis demonstrates that CLIC4 also interacts with Smad4 (Supplementary Information, Fig. S9b).

Among the complexities of TGF-β signalling, a dynamic interplay of Smad phosphorylation and dephosphorylation regulates nuclear responses. Ligand stimulation results in Smad phosphorylation and Smad-complex accumulation at the nucleus where Smad is dephosphorylated and exported, thereby terminating the signal[18,19]. To understand whether physical association of CLIC4 with p-Smad2 and 3 could protect them from dephosphorylation, we exposed nuclear lysates of keratinocytes transduced with either an empty vector (control), wild-type or nuclear-targeted CLIC4 adenovirus to lambda protein phosphatase (λ-PPase, a serine threonine phosphatase). P-Smad2 and 3 in lysates containing nuclear CLIC4 were the most resistant to dephosphorylation, regardless of TGF-β treatment (Fig. 5d). Relative to their respective untreated samples, λ-PPase (2 U) dephosphorylated p-Smad2 by ~75% and ~50%, in empty vector- and wild-type CLIC4-expressing samples, respectively, but only by 10% in nuclear-targeted CLIC4-expressing samples. Similarly, p-Smad3 was dephosphorylated by ~80–95% in empty vector-, ~70-80% in wild-type CLIC4- and by only 50% in nuclear CLIC4-expressing samples. Thus, in this assay nuclear CLIC4 and, to a lesser extent, wild-type CLIC4 protected p-Smad2 and 3 from phosphatases. With short TGF-β exposure (1 h), only small amounts of wild-type CLIC4 are expected in the nucleus.

Protein phosphatase 1a (PPM1a) has been identified as a Smad-binding protein and a Smad phosphatase[18]. When nuclear CLIC4 was overexpressed in TGF-β-treated keratinocytes, co-immunoprecipitation of p-Smad2 and 3 with PPM1a was inhibited (Fig. 5e). Notably, wild-type CLIC4 also inhibited the interaction of p-Smad2 and 3 with PPM1a, consistent with CLIC4 translocation to the nucleus after TGF-β treatment. siRNA-mediated knockdown of *PPM1a* increased levels of p-Smad2 and 3 in keratinocytes transduced with an empty vector or wild-type CLIC4, but did not enhance levels in samples with nuclear-targeted CLIC4 (Fig. 5f). This indicates that at least part of the nuclear CLIC4 effect on p-Smad2 and 3 stabilization is due to its inhibition of PPM1a interaction with p-Smads. That the levels of p-Smad2 and 3 in empty vector- and wild-type CLIC4-expressing cells did not rise to the levels of those in nuclear-targeted CLIC4-expressing cells after *PPM1a* knockdown might indicate that other, yet to be described, Smad phosphatases are also inhibited by nuclear CLIC4 (or perhaps the knockdown of *PPM1a* was incomplete).

These results indicate a new mechanism for enhancement of TGF-β signalling: TGF-β stimulates the association of Schnurri-2 and CLIC4 in the cytoplasm, leading to Schnurri-2-dependent nuclear translocation of the complex where it dissociates. Nuclear CLIC4 stabilizes nuclear p-Smad2 and 3 levels by associating with these proteins and protecting them from dephosphorylation by PPM1a, and possibly other Smad phosphatases; thus enhancing and sustaining TGF-β nuclear signalling (Supplementary Information, Fig. S10). The protection of nuclear p-Smads by CLIC4 increases both early (c-Myc downregulation and p21 upregulation) and later (growth inhibition) functions of TGF-β signalling, while also prolonging responses. A positive feedback loop may also be established, as a consequence of TGF-β signalling is to increase both Schnurri-2 and CLIC4 expression.

Previous data have indicated that the CLIC4 NLS is required for nuclear translocation in response to cell stress[7], suggesting that, apart from TGF-β stimulation, there are other mechanisms regulating CLIC4 nuclear translocation independent of Schnurri-2. Nevertheless, TGF-β signalling could be downstream from CLIC4 nuclear translocation (in response to stress and cell-cycle arrest) as well as from the participation of CLIC4 in myofibroblast conversion. CLIC4 loss in tumours could contribute to tumour resistance to TGF-β signalling. Schnurri-2 and CLIC4 now join a panoply of Smad signalling regulators in the nucleus, reflecting the need for precise TGF-β signalling control. In addition to p-Smad dephosphorylation by PPM1a, there is the Arkadia-mediated degradation of the co-repressor SnoN (Ski-related novel protein N)[20], the direct action of Arkadia on both activation and degradation of p-Smads[17] and retention of Smad proteins in the nucleus by TAZ (transcriptional co-activator with PDZ binding motif)[21]. Together, the combination of Schnurri-2 and CLIC4 present a unique duo of new players in a critical pathway that controls diverse aspects of cell behaviour. Schnurri-2 and CLIC4 may serve as targets for modifying TGF-β signalling under conditions where this pathway is involved in pathological changes. □

METHODS

Methods and any associated references are available in the online version of the paper at http://www.nature.com/naturecellbiology/

Note: Supplementary Information is available on the Nature Cell Biology website.

ACKNOWLEDGEMENTS

The authors thank L. Wakefield for critically reading the manuscript, M. Anzano for help with genotyping, C. Cheng for help with immunoprecipitation assays and colleagues for providing constructive criticism throughout the study. This work was supported by the Intramural Research Program of the Center for Cancer Research, National Cancer Institute, NIH.

AUTHOR CONTRIBUTIONS

A.S. designed and carried out studies, analysed data and wrote the manuscript; C.C. performed the analysis of *in vivo* samples and contributed to writing the manuscript; Y.H. and T.F. performed immunoblotting, immunofluorescence and luciferase assays; M.M. designed the yeast two-hybrid study;, K.S.H. provided essential reagents; S.H.Y. designed experiments, analysed and organized the data and wrote the manuscript. All authors proofread the manuscript.

COMPETING FINANCIAL INTERESTS

The authors declare no competing financial interests.

Published online at http://www.nature.com/naturecellbiology/
Reprints and permissions information is available online at http://npg.nature.com/reprintsandpermissions/

1. Suh, K. S. & Yuspa, S. H. Intracellular chloride channels: critical mediators of cell viability and potential targets for cancer therapy. *Curr. Pharm. Des.* **11,** 2753–2764 (2005).
2. Littler, D. R. *et al.* The intracellular chloride ion channel protein CLIC1 undergoes a redox-controlled structural transition. *J. Biol. Chem.* **279,** 9298–9305 (2004).
3. Littler, D. R. *et al.* Crystal structure of the soluble form of the redox-regulated chloride ion channel protein CLIC4. *FEBS J.* **272,** 4996–5007 (2005).
4. Shorning, B. Y., Wilson, D. B., Meehan, R. R. & Ashley, R. H. Molecular cloning and developmental expression of two chloride intracellular channel (CLIC) genes in *Xenopus laevis*. *Dev. Genes Evol.* **213,** 514–518 (2003).
5. Fernandez-Salas, E. *et al.* mtCLIC/CLIC4, an organellular chloride channel protein, is increased by DNA damage and participates in the apoptotic response to p53. *Mol. Cell. Biol.* **22,** 3610–3620 (2002).
6. Shiio, Y. *et al.* Quantitative proteomic analysis of Myc-induced apoptosis: a direct role for Myc induction of the mitochondrial chloride ion channel, mtCLIC/CLIC4. *J. Biol. Chem.* **281,** 2750–2756 (2006).
7. Suh, K. S. *et al.* The organellular chloride channel protein CLIC4/mtCLIC translocates to the nucleus in response to cellular stress and accelerates apoptosis. *J. Biol. Chem.* **279,** 4632–4641 (2004).
8. Suh, K. S. *et al.* CLIC4 mediates and is required for Ca2+-induced keratinocyte differentiation. *J. Cell Sci.* **120,** 2631–2640 (2007).
9. Suh, K. S. *et al.* Reciprocal modifications of CLIC4 in tumor epithelium and stroma mark malignant progression of multiple human cancers. *Clin. Cancer Res.* **13,** 121–131 (2007).
10. Ronnov-Jessen, L., Villadsen, R., Edwards, J. C. & Petersen, O. W. Differential expression of a chloride intracellular channel gene, CLIC4, in transforming growth factor-β1-mediated conversion of fibroblasts to myofibroblasts. *Am. J. Pathol.* **161,** 471–480 (2002).

11. Dai, H. *et al.* The zinc finger protein schnurri acts as a Smad partner in mediating the transcriptional response to decapentaplegic. *Dev. Biol.* **227,** 373–387 (2000).
12. Jin, W. *et al.* Schnurri-2 controls BMP-dependent adipogenesis via interaction with Smad proteins. *Dev. Cell* **10,** 461–471 (2006).
13. Udagawa, Y. *et al.* Schnurri interacts with Mad in a Dpp-dependent manner. *Genes Cells* **5,** 359–369 (2000).
14. Liu, X. *et al.* Conditional epidermal expression of TGFβ 1 blocks neonatal lethality but causes a reversible hyperplasia and alopecia. *Proc. Natl Acad. Sci. USA* **98,** 9139–9144 (2001).
15. Pietenpol, J. A. *et al.* TGF-β1 inhibition of *c-myc* transcription and growth in keratinocytes is abrogated by viral transforming proteins with pRB binding domains. *Cell* **61,** 777–785 (1990).
16. Datto, M. B. *et al.* Transforming growth factor β induces the cyclin-dependent kinase inhibitor p21 through a p53-independent mechanism. *Proc. Natl Acad. Sci. USA* **92,** 5545–5549 (1995).
17. Mavrakis, K. J. *et al.* Arkadia enhances Nodal/TGF-β signaling by coupling phospho-Smad2/3 activity and turnover. *PLoS Biol.* **5,** e67 (2007).
18. Lin, X. *et al.* PPM1A functions as a Smad phosphatase to terminate TGFβ signaling. *Cell* **125,** 915–928 (2006).
19. Hill, C. S. Nucleocytoplasmic shuttling of Smad proteins. *Cell Res.* **19,** 36–46 (2009).
20. Levy, L. *et al.* Arkadia activates Smad3/Smad4-dependent transcription by triggering signal-induced SnoN degradation. *Mol. Cell. Biol.* **27,** 6068–6083 (2007).
21. Varelas, X. *et al.* TAZ controls Smad nucleocytoplasmic shuttling and regulates human embryonic stem-cell self-renewal. *Nature Cell Biol.* **10,** 837–848 (2008).

METHODS

Cell culture, expression vectors and transfection. Primary keratinocytes from newborn Balb/c mice and *Smad3* knockout mice (provided by L. Wakefield, National Cancer Institute, MD) were prepared and cultured according to established methods[22]. Readily transfectable epithelial HEK293 cells were cultured in Dulbecco's Modified Eagles Medium (DMEM) supplemented with newborn calf serum (10%). Adenoviral Smad4 was provided by A. Glick (Pennsylvania State University, PA). A Schnurri-2 expression plasmid, pAct-Flag–hShn-2, was provided by S. Ishii (RIKEN Tsukuba Institute, Japan). Primary MEFs from *Schnurri-2* knockout mice (provided by S. Ishii)[23] were immortalized by pRSV-T and cultured in DMEM with newborn calf serum (10%). Transfections were performed using Lipofectamine 2000 (Invitrogen). Generation of HA–CLIC4, nuclear targeted CLIC4, V5–His tagged full length CLIC4 and deletion constructs lacking the NLS and the C-terminal half were as described previously[7]. The deletion mutant construct expressing CLIC4 amino-terminal amino-acid residues 1–60 was generated similarly. Cells were transduced with CLIC4 expression vectors for 16 h before TGF-β1 treatment.

Construction of adenovirus expressing *CLIC4* shRNA. CLIC4 sequence 5′-gggctgaaggaggaggacaaagag-3′ was sequentially cloned into pENTR/H1/TO and pLenti4/Block iT/Dest vectors (Invitrogen) to produce pLenti6/ Block iT-GW/U6 as the final vector. The inducible portion of this vector was subcloned into Ad5 RNAi adenovirus (ABM) and amplified by the Adenovirus Core Facility (Frederick National Cancer Institute, MD). *CLIC4* shRNA is constitutively active without requiring the TetR transactivator expression system and is homologous to both human and mouse *CLIC4*, allowing it to be used for both species. For nonspecific shRNA, 5′-gttctccgagagtgtcacgt-3′ was used (Cellogenetics).

Schnurri-2, *Smad2*, *Smad3*, *Smad4* and *PPM1a* siRNA. Schnurri-2 siRNA (5′-uuaggauauaaagcccuuc-3′), *Smad2* siRNA (5′-uaguaugcgauugaacacc-3′), *Smad3* siRNA (5'-cgaguguaaauuauuucaa-3'), *Smad4* siRNA (5'-agaugaauuggauucuuua-3′), *PPM1a* siRNA (5′-uuggaauucuuccuaaucg-3′) and non-silencing siRNA (5′-uucuccgaacgugucacgudtdt-3′) were obtained from Qiagen and transfected using HiPerfect (20 nM; Qiagen). At 24 h post-transfection with *Schnurri-2* siRNA and 48 h post transfection with *Smad2* and *PPM1a* siRNAs, cells were treated with TGF-β1 or infected with a control, CLIC4 or nuclear CLIC4 adenovirus.

Yeast two-hybrid assay. The CLIC4 yeast two-hybrid screen was conducted by Myriad Genetics, based on established methodology[24]. *CLIC4* cDNA fragments were cloned into pGBT.superB, a GAL4 DNA-binding domain (residues 1–441) plasmid, and used as bait to screen a mouse embryo cDNA library cloned into a pGAD.PN2 plasmid containing a GAL4 activation domain (residues 2301–2643). Bait-transformed PYN200 cells were mated with prey-transformed BK100 cells and plated on selective media. Interactions were confirmed by transforming naive yeast cells with purified bait and prey constructs and assaying for β-galactosidase using a chemiluminescent assay. Although multiple bait constructs spanning the entire CLIC4 open reading frame were screened separately, only residues 120–254 successfully recruited prey.

Antibody generation, subcellular fractionation, co-immunoprecipitation and immunoblotting. A monospecific polyclonal antibody was generated against the N-terminal peptide of CLIC4 as described previously[25]. The polyclonal serum was purified through a protein A column (Pharmacia) and dialyzed in borate buffer. The following antibodies were used: anti-c-Myc and anti-p-Smad2 (1:1000 dilution; Cell Signalling Technologies), anti-p21 (1:1000 dilution; BD Biosciences), anti-Smad4 (1:1000 dilution), anti-Schnurri-2 (1:500 dilution) and anti-Lamin A-C (1:500 dilution; Santa Cruz Biotechnologies), anti-PPM1a (1: 1000 dilution; Abcam), anti-α-tubulin (1:1000 dilution; Bethyl Laboratories) and anti-p-Smad3 (1:5000 dilution; a gift from E. Leof, Mayo Clinic, MN). Keratinocytes or HEK293 cells were washed and scraped into a lysis buffer (Cell Signalling Technologies). Nuclear and cytoplasmic extracts were produced using NE-PER (Thermo Fischer Scientific). Protein (25 μg) was subjected to immunoblotting and then visualized using enhanced chemiluminescence (Thermo Fischer Scientific).

For immunoprecipitation, cells were washed with cold phosphate-buffered saline (PBS) and lysed in M-PER (Thermo Fischer Scientific) containing protease and phosphatase inhibitors. Lysates were precleared with protein A-G PLUS agarose beads and then incubated overnight with the antibody of interest and protein A/G PLUS agarose beads at 4 °C. Beads were washed and boiled before electrophoresis of the eluate. Co-immunoprecipitation from nuclear fractions was performed using the Nuclear Complex Co-IP kit (Active Motif).

Luciferase assay. TGF-β-responsive p3TP luciferase reporter (p3TP-lux) was used in a luciferase assay. Keratinocytes plated in 12-well culture plates were transfected with p3TP-lux (2.0 μg per well) and pRLTK (0.2 μg per well). Cells were transduced in quadruplicate with a wild-type CLIC4-, nuclear targeted CLIC4-, empty vector-, *CLIC4* shRNA- or non-silencing shRNA-expressing adenovirus. At 3 h after infection they were treated with TGF-β1 (50 pg per well) for 14 h. Luciferase activity was determined in cell extracts using the Dual Luciferase Reporter assay system (Promega) and normalized to *Renilla* luciferase activity. To determine Schnurri-2-mediated changes in p3TP-lux-luciferase activity, the procedure described above was followed, except that HEK293 cells were transfected with the Schnurri-2 expression plasmid for 24 h before exposure to TGF-β1.

^{3}H-thymidine incorporation assay. Keratinocytes or HEK293 cells were plated in 24-well plates and siRNAs, where required, were transfected into cells 24 h before transduction with control, wild-type or nuclear-targeted CLIC4 viruses for 16 h or transfected with a Schnurri-2 expression plasmid for 24 h. At 2 h after transduction or 8h after transfection cells were treated with TGF-β1 (25 pg per well) for 24 h. ^{3}H-thymidine (1 μCi per well) was added for 3 h before the end of the TGF-β1 treatment. Cells were fixed using methanol and acetic acid (3:1 ratio), solubilized in NaOH (5 normal) and incorporated counts were measured using a scintillation counter.

Confocal microscopy. Cells were fixed in 2% paraformaldehyde/PBS (phosphate buffered saline) for 30 min, washed with PBS, permeabilized with cold methanol for 6 min and dried briefly. Samples were then re-hydrated and washed with PBS, treated with glycine (100 mM) for 30 min, equilibrated with Triton X-100 (0.2%) for 10 min, washed with PBS and blocked in 0.5% bovine serum albumin (BSA)/PBS for 1 h. This was followed by overnight incubation with a primary antibody (anti-CLIC4 or anti-Schnurri-2) at 4 °C, washing with PBS and incubation in the dark with a fluorescence-labelled secondary antibody for 1 h. The plates were washed again, Vectashield mounting medium with DAPI (Vector Laboratories) was added for nuclear staining and cells were analysed by confocal microscopy (Zeiss-NLO microscope).

Dephosphorylation of nuclear extracts using lambda protein phosphatase. Nuclear extracts of keratinocytes transduced with control, wild-type or nuclear targeted CLIC4 adenovirus with or without treatment with TGF-β for 1 h were dephosphorylated using lambda protein phosphatase (New England Biolabs) at 30 °C for 30 min. Reactions were stopped by adding 2× SDS–PAGE sample buffer and heating for 5 min at 100 °C.

Reverse transcription (RT)-PCR. TGF-β1-treated total RNA from keratinocytes was isolated using Tri zol (Invitrogen), subjected to DNAse I (Ambion) treatment and reverse transcribed using SuperScript II Reverse Transcriptase (Invitrogen). PCR amplification of CLIC4 and Schnurri-2 was carried out using Platinum Supermix (Invitrogen). Sequences for Schnurri-2 primers were 5′-GGAAAGAGGGAAAGGAGAGATTCACGGAGAT-3′ and 5′-ATCTGAGTGTCATCACAAGAGTCACTGGGT-3′. CLIC4 primers were from Superarray (PPH08576A) and GAPDH primers were from Gene Link (40-1005-10). For *in vivo* analysis, cDNA (provided by A. Glick) was reverse transcribed from RNA isolated from the skin of single- (control) or double-transgenic mice engineered to express active TGF-β1 from skin keratinocytes after induction by doxycycline[14]. For real-time PCR analysis, predesigned Quantitect primers (Qiagen), BioRad iQ iCycler and Gene Expression Macro were used.

Accession numbers. The Genbank accession numbers for TGF-β1, Smad2 and Smad3 are A002271, A002174 and A002175, respectively.

Statistical analysis. All luciferase and ^{3}H-thymidine incorporation assays were repeated at least three times in quadruplicate. Statistical analysis was performed using unpaired two-tailed student's *t*-test with a confidence interval of 99%.

Accession codes. USCD-Nature Signaling Gateway (http://www.signaling-gateway.org): **A002271**, **A001029** and **A002175**.

DOI: 10.1038/ncb1885

22. Lichti, U., Anders, J. & Yuspa, S. H. Isolation and short-term culture of primary keratinocytes, hair follicle populations and dermal cells from newborn mice and keratinocytes from adult mice for *in vitro* analysis and for grafting to immunodeficient mice. *Nature Protoc.* **3,** 799–810 (2008).
23. Takagi, T., Harada, J. & Ishii, S. Murine Schnurri-2 is required for positive selection of thymocytes. *Nature Immunol.* **2,** 1048–1053 (2001).
24. Fields, S. & Song, O. A novel genetic system to detect protein–protein interactions. *Nature* **340,** 245–246 (1989).
25. Fernandez-Salas, E., Sagar, M., Cheng, C., Yuspa, S. H. & Weinberg, W. C. p53 and tumor necrosis factor α regulate the expression of a mitochondrial chloride channel protein. *J. Biol. Chem.* **274,** 36488–36497 (1999).

nature cell biology

DOI: 10.1038/ncb1885

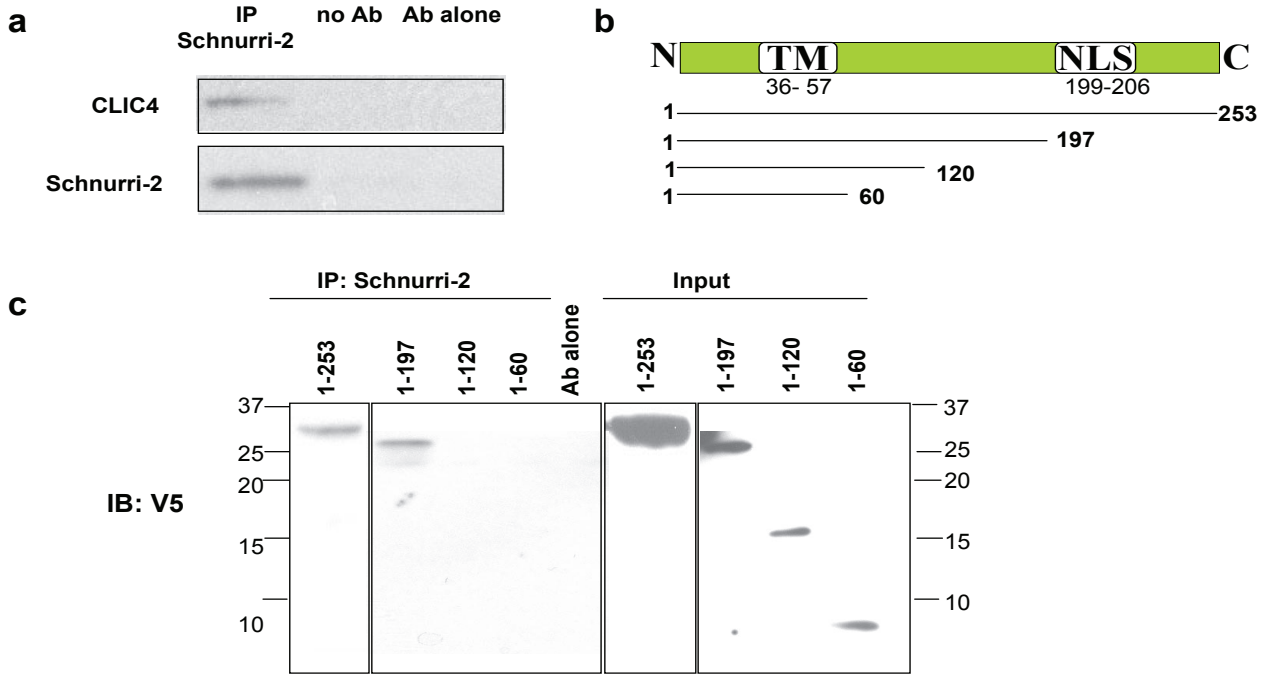

Figure S1 Endogenous and C-terminally deleted CLIC4 coimmunoprecipitates with Schnurri-2. **(a)** Lysates from primary keratinocytes were immunoprecipitated with anti-Schnurri-2 antibody and immunoblotted for CLIC4 and Schnurri-2. **(b)** V5-tagged CLIC4 deletion mutants used for coimmunoprecipitation assay with Schnurri-2. **(c)** Adenoviral deletion constructs of CLIC4 were expressed in primary Balb/c keratinocytes and immunoprecipitated using anti-Schnurri-2 antibody and immunoblotted using anti-V5 antibody. Anti-Schnurri-2 antibody without cell lysates was subjected to the immunoprecipitation and immunoblotting procedure and used as control.

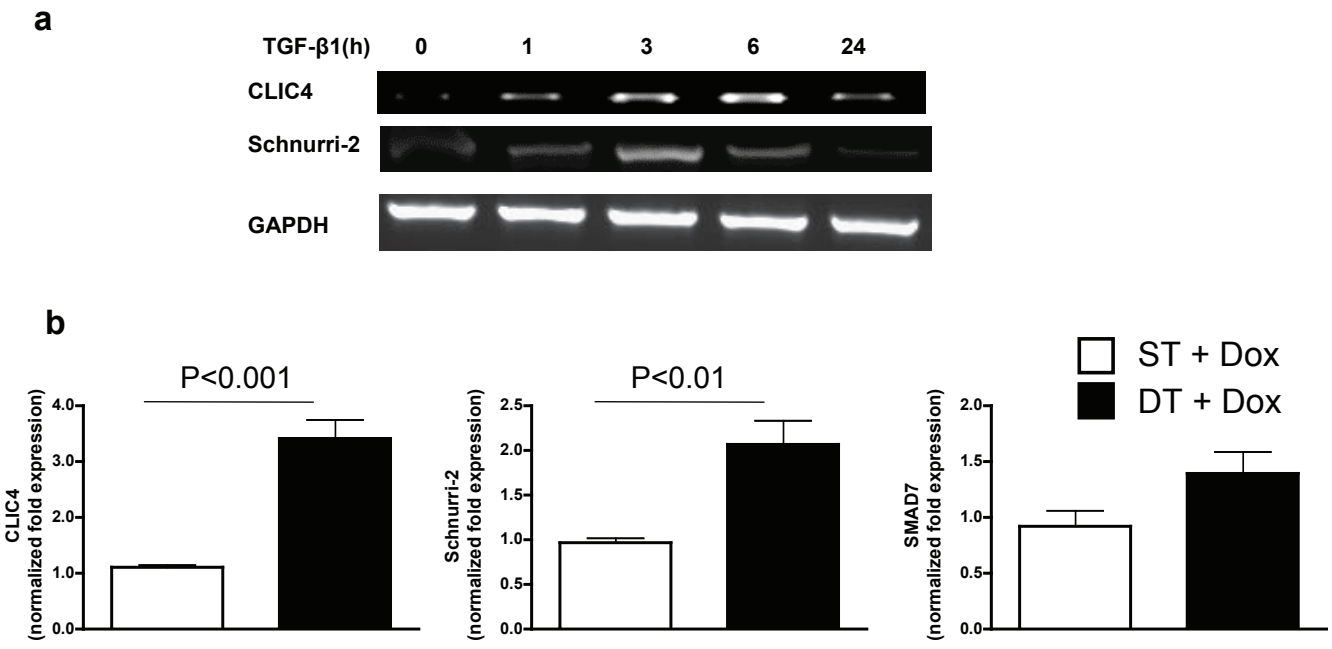

Figure S2 TGF-β enhances transcription of CLIC4 and Schnurri-2 in the skin in vitro and in vivo. **(a)** Primary Balb/c keratinocytes were treated with TGF-β1 (1ng/ml) for indicated times. Total cellular RNA was isolated and subjected to reverse transcription and PCR amplified to detect CLIC4 and Schnurri-2. GAPDH was used as PCR control. **(b)**Real-time PCR analysis of CLIC4, Schnurri-2 and Smad7 mRNA levels in skin of tetOTGFβ1 (ST) and K5/rTA - tetOTGFβ1 (DT) mice fed with doxycycline (Dox) for 4-5 days. RNA was isolated from skin biopsies and cDNA synthesized using High-capacity cDNA kit from Applied Biosystems. Bars represent mean value ± SEM. ST and DT groups contain 5 and 6 animals respectively.

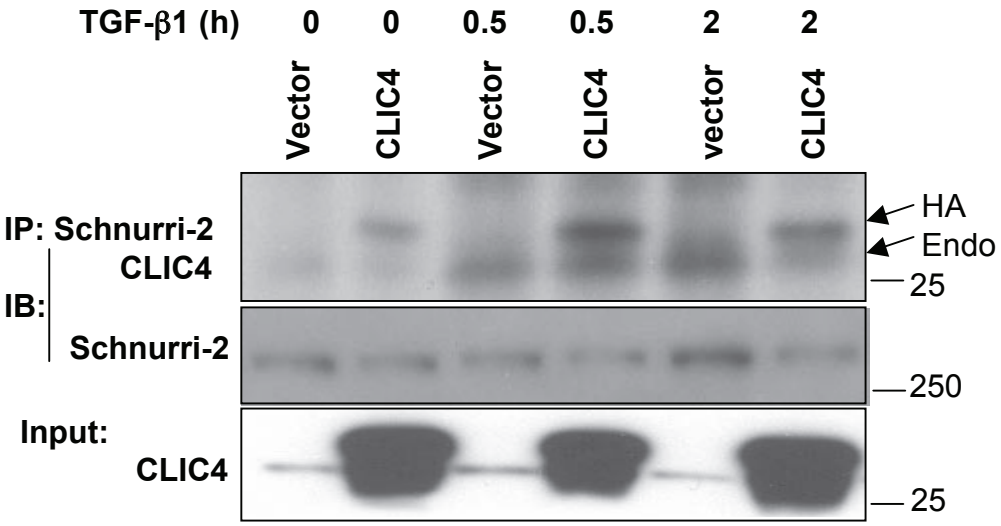

Figure S3 TGF-β enhances interaction of Schnurri-2 with both endogenous and exogenous CLIC4. Cell lysates of keratinocytes transduced with control (vector) or CLIC4 expressing adenoviruses for 16h and treated with TGF-β1 (1 ng/ml) for indicated times were immunoprecipitated with anti-Schnurri-2 antibody and immunoblotted for CLIC4 and Schnurri-2. Arrrows point to HA-tagged exogenous CLIC4 and endogenous CLIC4 protein.

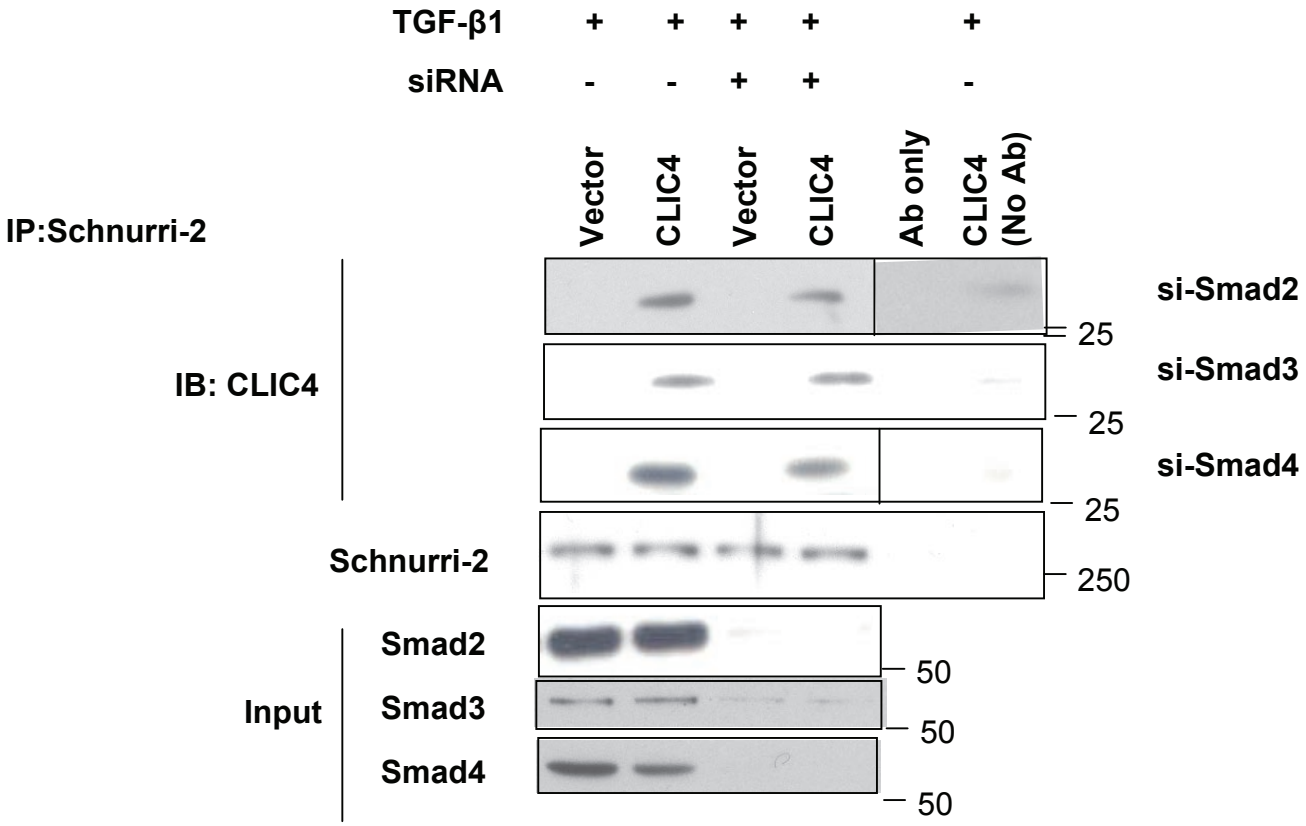

Figure S4 TGF-β dependent interaction of CLIC4 and Schnurri-2 is Smad independent. Primary keratinocytes were transfected with Smad2-3-4 siRNA 48h prior to transduction with empty or CLIC4 adenoviral vectors followed by treatment with TGF-β(1ng/ml) for 1h. Lysates were immunoprecipitated using anti-Schnurri-2 antibody and immunoblotted for CLIC4 and Schnurri-2. Anti-Schnurri-2 antibody without cell lysate and lysate alone without antibody were subjected to immunoprecipitation and used as control. An aliquot of the lysates was used to detect input Smad2, 3 and 4.

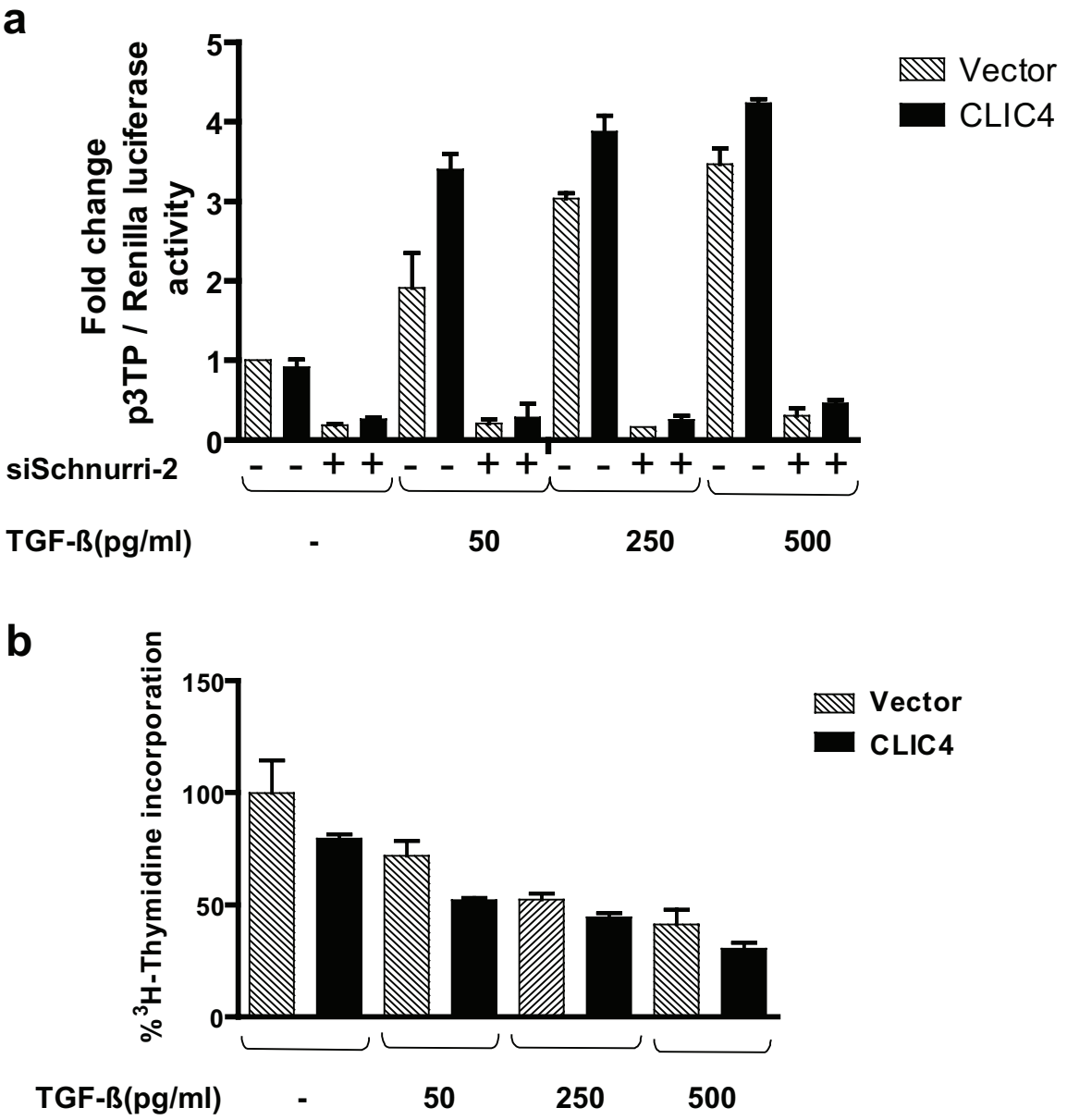

Figure S5 CLIC4 enhances TGF-β reporter activity and TGF-β dependent growth inhibition in a TGF-β dose dependent manner. **(a)** The protocol is same as in Fig 3a in the main text. **(b)** Keratinocytes were transduced with empty or CLIC4 expressing adenoviral constructs +/- TGF-β1 for 16h. 3H-Thymidine incorporation was measured.

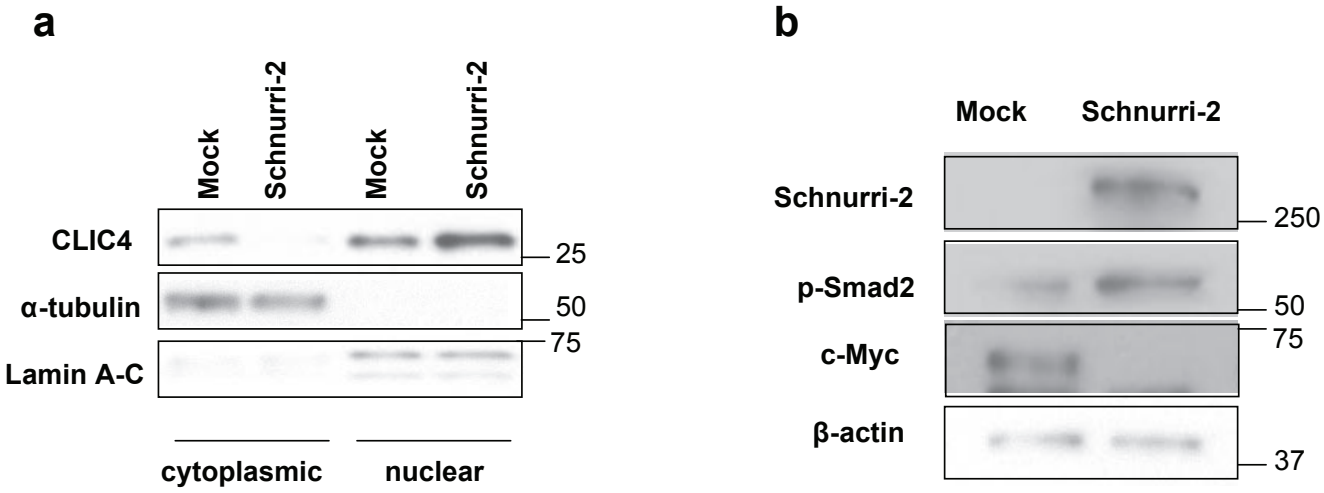

Figure S6 Schnurri-2 enhances CLIC4 nuclear translocation and TGF-β signal transduction. HEK293 cells were mock transfected or transfected with Schnurri-2 expression plasmid pAct-FLAG-hShn2 for 24h. **(a)** Cytoplasmic and nuclear extracts were immunoblotted for CLIC4. α-tubulin and Lamin A/C were used as controls. **(b)** Whole cell lysates were separated by SDS-PAGE and immunoblotted for Schnurri-2, p-Smad2 and c-Myc. β-actin was used as loading control.

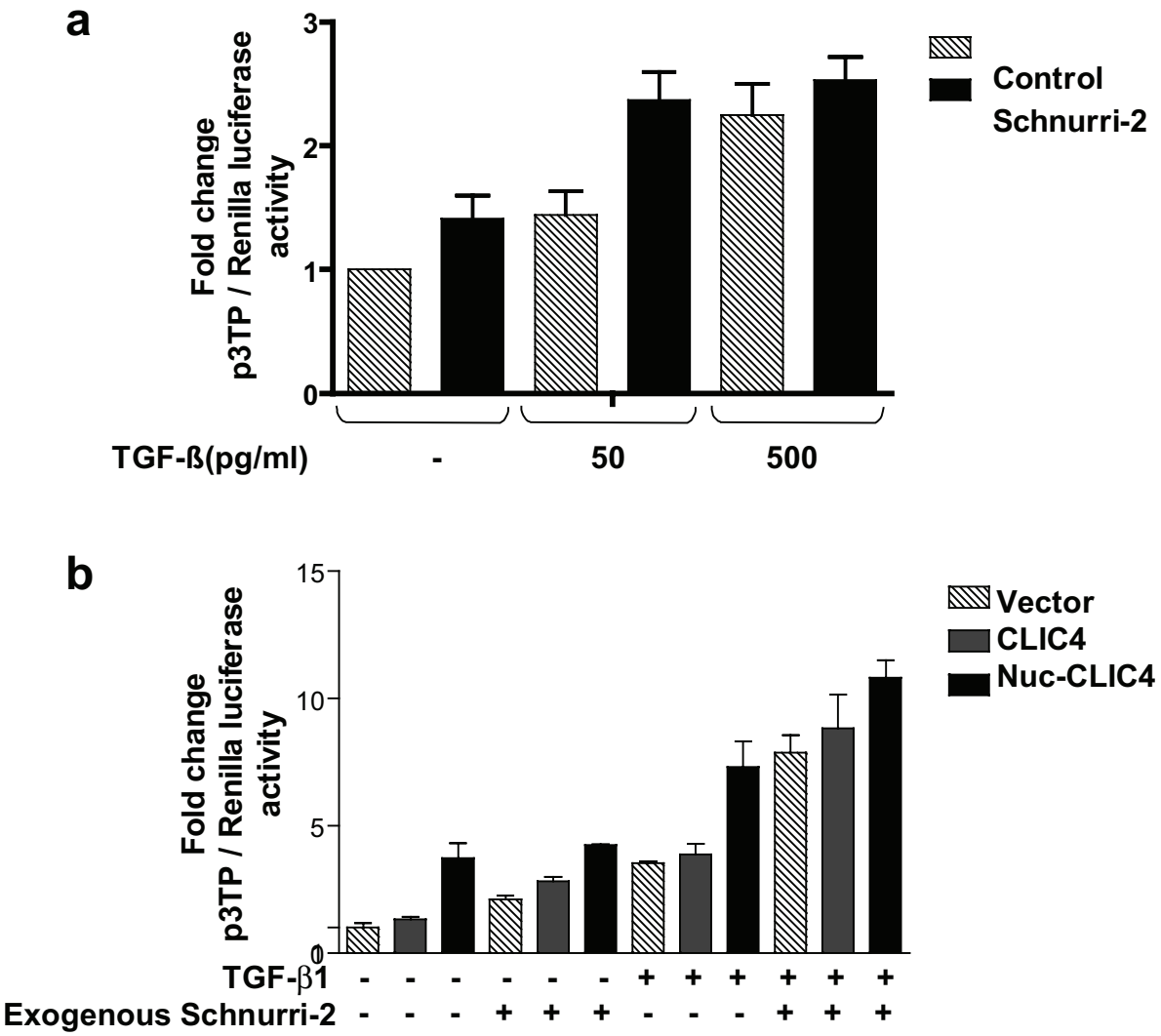

Figure S7 Schnurri-2 dose dependently enhances TGF-β signaling and is essential for modification of TGF-β signaling by wild type but not nuclear targeted CLIC4. **(a)** The protocol is the same as in Figure 2c in the main text. **(b)** Immortalized MEFs from Schnurri-2 knockout mice were transfected with p3TP-lux and pRLTK and pAct-FLAG-hShn2 or lipofectamine alone. Cells were transduced with empty vector, wild type CLIC4 or nuclear targeted CLIC4 adenoviruses +/- TGF-β1 (1 ng/ml) treatment for 14h. Reporter luciferase activity was determined in cell extracts using Dual luciferase reporter assay system (Promega) and normalized to renilla luciferase activity. Data are presented as fold change of untreated Vector sample. Each data point is an average of quadruplicates (n=4) from a representative experiment.

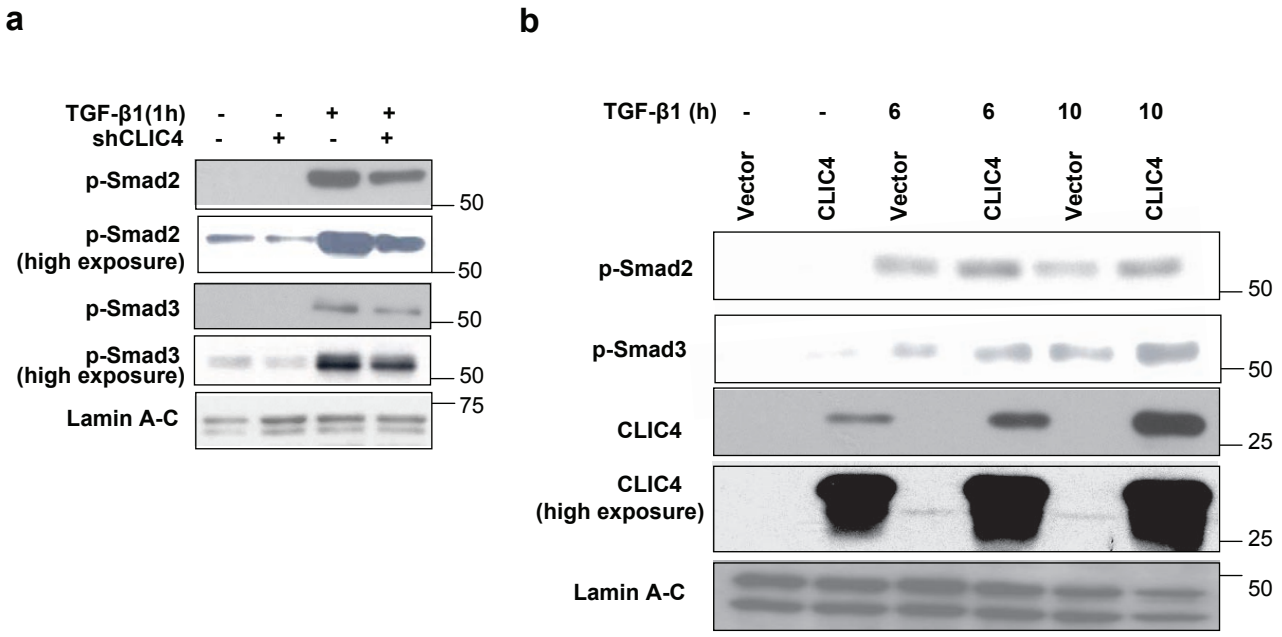

Figure S8 Knockdown of CLIC4 decreases while TGF-β dependent nuclear translocation of CLIC4 sustains p-Smad2/3 levels **(a)** Primary keratinocytes were transduced with adenoviral CLIC4 specific (+) or control non silencing (-) shRNA for 48h +/- TGF-β1 (1 ng/ml) treatment for 1h. Nuclear lysates were immunoblotted for phospho-Smad2 and 3. Lamin A/C was used as loading control. Two exposures are shown to visualize unstimulated p-Smads. **(b)** Primary keratinocytes were transduced with empty or wild-type CLIC4 expressing adenovirus and subsequently treated with TGF-β1 for the times indicated. Nuclear fractions were immunoblotted for phospho-Smad2 and 3 and CLIC4. Lamin A/C was used as loading control. Higher exposures are shown to visualize endogenous CLIC4.

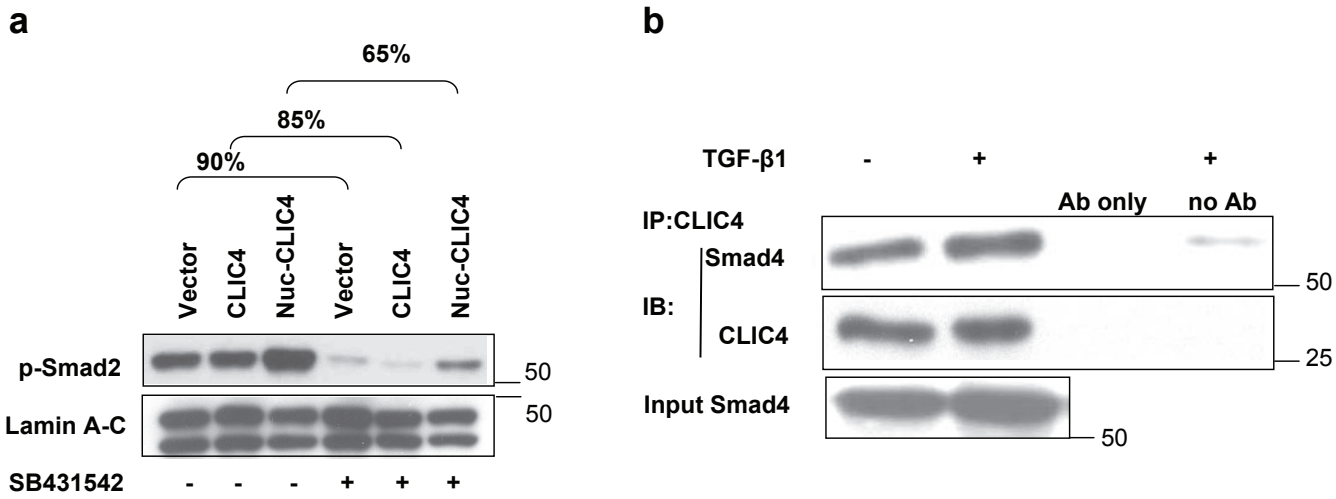

Figure S9 CLIC4 enhances phospho-Smad2 independent of receptor activity and interacts with Smad4 **(a)** Primary keratinocytes were transduced with empty, wild-type or nuclear CLIC4 adenoviruses for 16h and one group was treated with SB431542 for the entire length of transduction. Nuclear lysates were immunoblotted for phospho-Smad2. Lamin A/C was used as loading control. The percent reduction in p-Smad2 levels in the SB431542 treated samples relative to their respective untreated controls is indicated. **(b)** Adenoviral Smad4 was expressed in primary keratinocytes followed by treatment with TGF-β1(1 ng/ml) for 30 min. Lysates were immunoprecipitated using CLIC4 antibody and immunoblotted for Smad4 and CLIC4. An aliquot of the lysates was used directly as input for immunoblotting for Smad4.

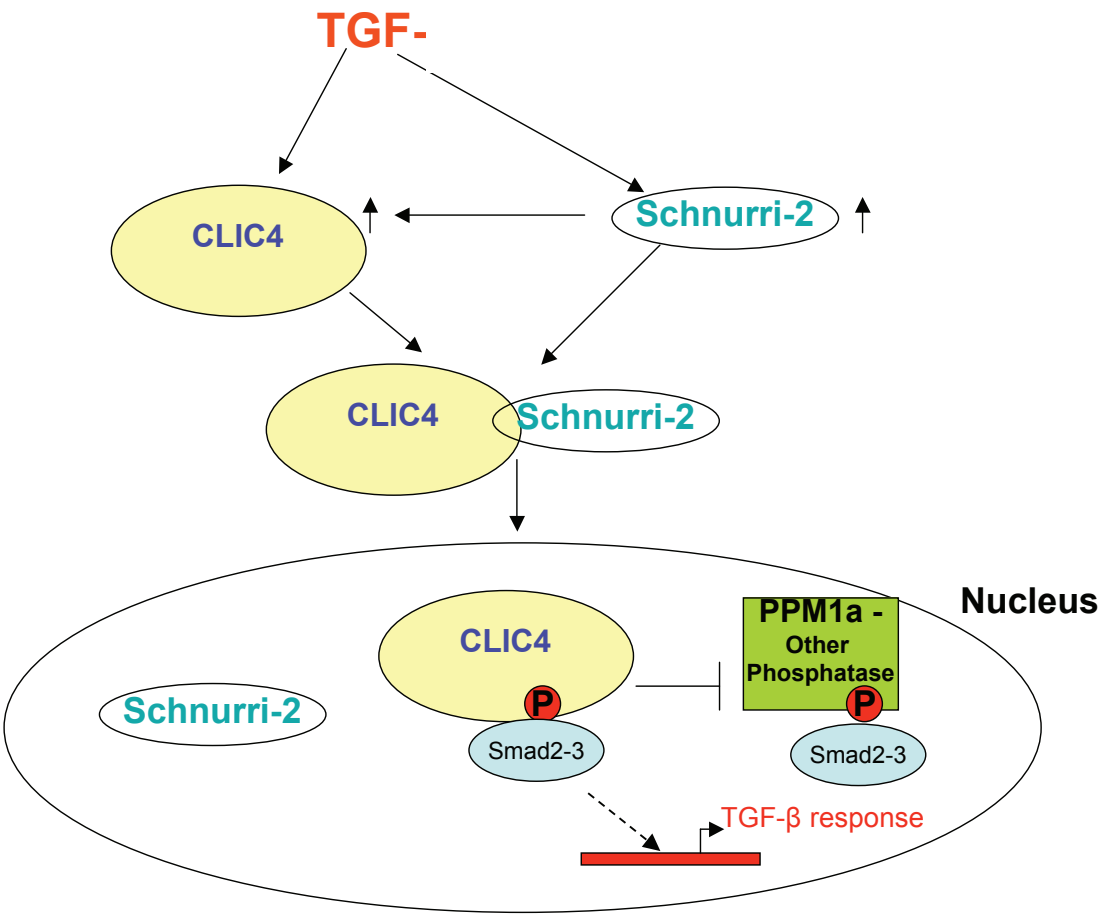

Figure S10 Schematic showing how CLIC4 and Schnurri-2 regulate Smad signaling.

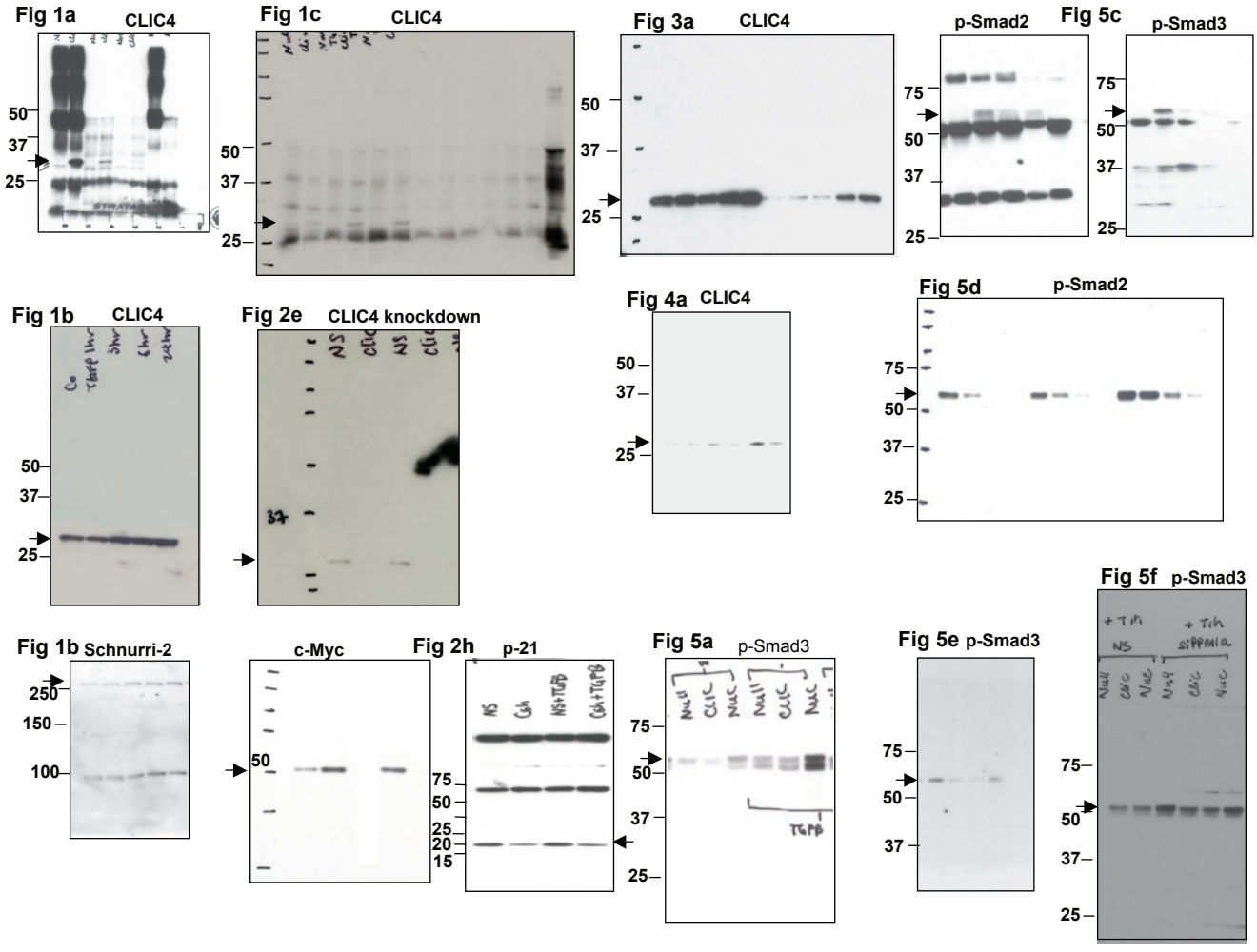

Figure S11 Full scans of western blot data.